

Micromechanics-Based Continuum Constitutive Modeling of Isotropic Non-Cohesive  
Particulate Materials, Informed and Validated by the Discrete Element Method

By

Jonathan A. Fleischmann

A dissertation submitted in partial fulfillment of  
the requirements for the degree of

Doctor of Philosophy  
(Engineering Mechanics)

at the

UNIVERSITY OF WISCONSIN-MADISON

2013

Date of final oral examination: October 25, 2013

The dissertation is approved by the following members of the Final Oral Committee:

Michael E. Plesha, Professor, Engineering Physics

Walter J. Drugan, Professor, Engineering Physics

Daniel C. Kammer, Professor, Engineering Physics

Tuncer B. Edil, Professor, Civil and Environmental Engineering

Fabian Waleffe, Professor, Mathematics



# Dedication

This thesis is written for and dedicated to my wife, Clara Maria Bernadette Fleischmann.



# Acknowledgements

I wish to thank my advisors, Professors Michael Plesha and Walter Drugan, for invaluable assistance at all stages of this research. I also wish to thank the members of my Dissertation Committee: Professors Daniel Kammer and Fabian Waleffe for contributing greatly to both my undergraduate and graduate education; and Professor Tuncer Edil for introducing me to the field of geomechanics. I thank Professor Roderic Lakes for reading and making valuable comments that greatly improved Chapters 3 and 4 of this thesis.



# Contents

<b>1</b>	<b>Introduction</b>	<b>1</b>
<b>2</b>	<b>Literature Review</b>	<b>5</b>
2.1	Constitutive Modeling of Particulate Materials Based on Micromechanics: Elastic Range . . . . .	5
2.2	Constitutive Modeling of Particulate Materials Based on Micromechanics: Plastic Range . . . . .	13
2.3	Constitutive Modeling of Particulate Materials Based on Micromechanics: Discrete Element Method . . . . .	20
<b>3</b>	<b>Direct Micromechanics Derivation and DEM Confirmation of the Elastic Moduli of Isotropic Particulate Materials, Part I: No Particle Rotation</b>	<b>33</b>
3.1	Abstract . . . . .	33
3.2	Introduction . . . . .	34
3.3	Overall Elastic Moduli for Regular Arrays of Uniform Spheres . . . . .	37
3.3.1	Face-Centered Cubic (FCC) Array of Uniform Spheres . . . . .	39
3.3.2	Simple Cubic (SC) Array of Uniform Spheres . . . . .	40
3.3.3	Body-Centered Cubic (BCC) Array of Uniform Spheres . . . . .	41
3.4	Isotropic Effective Elastic Moduli . . . . .	42
3.4.1	Voigt Hypothesis . . . . .	43

3.4.2	Reuss Hypothesis . . . . .	46
3.4.3	Self-Consistent Hypothesis . . . . .	49
3.5	Validation by the Discrete Element Method . . . . .	52
3.6	Discussion . . . . .	59
3.7	Conclusions . . . . .	62
<b>4</b>	<b>Direct Micromechanics Derivation and DEM Confirmation of the Elastic Moduli of Isotropic Particulate Materials, Part II: Particle Rotation</b>	<b>65</b>
4.1	Abstract . . . . .	65
4.2	Introduction . . . . .	66
4.3	Overall Elastic Moduli for Regular Arrays of Uniform Spheres Incorporating the Effect of Particle Rotation . . . . .	68
4.3.1	Face-Centered Cubic (FCC) Array of Uniform Spheres . . . . .	70
4.3.2	Body-Centered Cubic (BCC) Array of Uniform Spheres . . . . .	73
4.3.3	Simple Cubic (SC) Array of Uniform Spheres . . . . .	76
4.4	Isotropic Effective Elastic Moduli Incorporating the Effect of Particle Rotation	80
4.5	Validation by the Discrete Element Method . . . . .	84
4.6	Discussion . . . . .	89
4.7	Conclusions . . . . .	95
<b>5</b>	<b>Determination of Yield Surfaces for Isotropic Non-Cohesive Particulate Materials by the Discrete Element Method, Part I: No Particle Rotation</b>	<b>99</b>
5.1	Abstract . . . . .	99
5.2	Introduction . . . . .	100
5.3	Yield Criteria . . . . .	102
5.4	Methodology . . . . .	105
5.5	Results . . . . .	123

5.6	Discussion . . . . .	131
5.7	Conclusion . . . . .	154
<b>6</b>	<b>Determination of Yield Surfaces for Isotropic Non-Cohesive Particulate Materials by the Discrete Element Method, Part II: Particle Rotation</b>	<b>157</b>
6.1	Abstract . . . . .	157
6.2	Introduction . . . . .	158
6.3	Methodology . . . . .	159
6.4	Results . . . . .	173
6.5	Discussion . . . . .	190
6.6	Conclusion . . . . .	220
<b>7</b>	<b>Micromechanical analysis of Yield in Isotropic Non-Cohesive Particulate Materials, Part I: No Particle Rotation</b>	<b>223</b>
7.1	Abstract . . . . .	223
7.2	Introduction . . . . .	224
7.3	Yield on Slip Planes for Regular Arrays of Uniform Spheres . . . . .	226
7.3.1	Face-Centered Cubic (FCC) Array of Uniform Spheres . . . . .	226
7.3.2	Simple Cubic (SC) Array of Uniform Spheres . . . . .	230
7.3.3	Body-Centered Cubic (BCC) Array of Uniform Spheres . . . . .	232
7.4	Yield in Statistically Isotropic Aggregates of Uniform Spheres . . . . .	233
7.5	Conclusion . . . . .	244
<b>8</b>	<b>Micromechanical analysis of Yield in Isotropic Non-Cohesive Particulate Materials, Part II: Particle Rotation</b>	<b>247</b>
8.1	Abstract . . . . .	247
8.2	Introduction . . . . .	248

8.3	Yield on Slip Planes for Regular Arrays of Uniform Spheres Incorporating the Effect of Particle Rotation . . . . .	250
8.3.1	Face-Centered Cubic (FCC) Array of Uniform Spheres . . . . .	250
8.3.2	Simple Cubic (SC) Array of Uniform Spheres . . . . .	257
8.3.3	Body-Centered Cubic (BCC) Array of Uniform Spheres . . . . .	258
8.4	Yield in Statistically Isotropic Aggregates of Uniform Spheres Incorporating the Effect of Particle Rotation . . . . .	259
8.5	Conclusion . . . . .	266
<b>9</b>	<b>Quantitative Comparison of 2-D and 3-D Discrete Element Simulations of Nominally 2-D Shear Flow</b>	<b>269</b>
9.1	Abstract . . . . .	269
9.2	Introduction . . . . .	270
9.3	Discrete Element Method . . . . .	272
9.4	Methodology . . . . .	275
9.5	Results . . . . .	279
9.6	Analysis . . . . .	282
9.7	Conclusion . . . . .	286
<b>10</b>	<b>Conclusion</b>	<b>289</b>
<b>A</b>	<b>Stiffness Analysis of FCC, SC, and BCC Elementary Cells with Particle Rotation Prohibited</b>	<b>295</b>
A.1	Face-Centered Cubic (FCC) Elementary Cell . . . . .	295
A.2	Simple Cubic (SC) Elementary Cell . . . . .	297
A.3	Body-Centered Cubic (BCC) Elementary Cell . . . . .	299
<b>B</b>	<b>Stiffness Analysis of an FCC Elementary Cell with Unrestrained Particle</b>	

<b>Rotation</b>	<b>303</b>
<b>C Derivation of the Voigt Estimates of the Isotropic Effective Elastic Moduli for a Locally Cubic Material</b>	<b>307</b>
C.1 Averaging Pure Uniaxial Strain . . . . .	309
C.2 Averaging Pure Volumetric Strain . . . . .	311
C.3 Isotropic Effective Elastic Constants . . . . .	312
<b>D Derivation of the Mohr-Coulomb Yield (Failure) Criterion for an Isotropic Particulate Material</b>	<b>315</b>
<b>E Discrete Element Method Critical Time Step Size</b>	<b>321</b>
E.1 Critical Time Step Size for 2-D DEM . . . . .	322
E.1.1 Single Pair of DEM Elements (2-D) . . . . .	324
E.1.2 Triangular Configuration of DEM Elements . . . . .	325
E.1.3 Hexagonal Close-Packing of DEM Elements (2-D) . . . . .	328
E.1.4 Discussion (2-D) . . . . .	331
E.2 Critical Time Step Size for 3-D DEM . . . . .	334
E.2.1 Single Pair of DEM Elements (3-D) . . . . .	338
E.2.2 Tetrahedral Configuration of DEM Elements . . . . .	340
E.2.3 Hexagonal Close-Packing of DEM Elements (3-D) . . . . .	344
E.2.4 Discussion (3-D) . . . . .	350



# Chapter 1

## Introduction

While many phenomenological continuum constitutive models for granular and particulate materials exist, these models do not usually directly relate the microstructural behavior of the particles to the macroscopic particulate material behavior. As a result, these constitutive models are only valid over the range of scenarios for which they were calibrated and tested. This is problematic for predictively modeling the behavior of particulate materials in atypical environments. Such environments include but are not limited to: (1) new geomaterials created from partially or totally recycled materials, such as asphalt (Camargo et al., 2013), (2) manufacturing processes involving non-geological particulate materials, such as in the pharmaceutical industry (Ketterhagen et al., 2009), (3) high strain-rate environments such as high speed ballistic penetration and explosion in sand, of current interest to both the U.S. Navy and U.S. Air Force (Cooper, 2011).

The need for predictive constitutive models for particulate materials in high strain-rate environments, as well as the current state-of-the-art in this area, was discussed at the recent International Workshop on Particulate Materials in Extreme Environments (PMEE 2010) held at the Lawrence Livermore National Laboratory, Livermore, CA, on September 20-24, 2010, hosted by the Air Force Office of Scientific Research (AFOSR). We were invited to

this conference, where we presented the results of Chapter 9 of this thesis [Fleischmann et al. (2013c)] in a talk entitled “Are 2-D DEM Simulations Good Enough?”. This talk proved to be provocative (which was our intention, as the title of the talk suggests), and a lengthy discussion between workshop attendees ensued. Despite some differences of opinion as to the relative value of 2-D versus 3-D DEM simulations, it was universally acknowledged that until unambiguous, *quantitative* links are demonstrated between the micromechanical behavior of particulate materials and their macroscopic behavior, the development of reliable elastoplastic continuum constitutive models for particulate materials applicable in extreme and other atypical environments will not be possible.

This thesis provides a solid beginning at answering this need, by developing unambiguous, quantitative links between *micromechanical* properties of non-cohesive particulate materials, such as local packing geometry, inter-particle contact stiffness, and inter-particle friction coefficient, and their macroscopic material properties in both the elastic and plastic ranges at *low* strain-rates. In particular, in Chapters 3 and 4 [Fleischmann et al. (2013a) and Fleischmann et al. (2013b)] we derive unambiguous, quantitative relationships between the local packing geometry and inter-particle contact stiffnesses of statistically isotropic particulate materials composed of uniform spheres on the microscale and the elastic modulus  $E$  and Poisson’s Ratio  $\nu$  for the particulate material on the macroscale. We also show that previous attempts at deriving such relationships in the elastic range (as recent as the within the last decade) have failed to correctly account for the effect of particle rotation on the microscale, which can lead to zero-energy modes that can significantly effect the behavior of a particulate material even in the (nominally) elastic range.

We significantly advance the state-of-the-art by demonstrating a number of links between the micromechanical behavior of particulate materials and their macroscopic mechanical behavior that were hitherto unknown, including the effects of particle rotation, as well as by providing unambiguous derivations of macroscopic mechanical behavior of statistically

isotropic particulate materials in both the elastic range and at yield, based on the analysis and homogenization of specific local packing geometries under clear micromechanical assumptions involving straightforward force and moment equilibrium rather than the (more nebulous) energy methods employed almost exclusively elsewhere in the literature. These advances have led to the publication of three papers in two well-respected journals in the fields of micromechanics and geomechanics: the *Journal of the Mechanics and Physics of Solids* [Fleischmann et al. (2013a) and Fleischmann et al. (2013b)], and the *International Journal of Geomechanics* [Fleischmann et al. (2013c)].

In Chapters 5–8, we turn our attention from the elastic range to the plastic range, with a micromechanics-based analysis of yield in isotropic non-cohesive particulate materials. First, we determine yield surfaces in 3-D principal stress space using a numerical method known as the discrete element method (DEM) in Chapters 5 and 6. Direct micromechanics derivations follow in Chapters 7 and 8, which are based on analyses of specific local packing geometries and their associated slip planes. As in the elastic range, we perform these direct micromechanics derivations for both the cases when particle rotation is either allowed or not allowed, and this provides valuable insights into the specific effects that particle rotation has on particulate material behavior.

We have informed and validated all of our micromechanics derivations using the 3-D discrete element method (DEM), performing a total of over 2 500 individual computer simulations of true triaxial and direct shear tests on virtual material specimens of 3 000 – 50 000 particles (cohesionless spherical elements). The beauty of DEM is that the simulations can be run with particle rotation either prohibited or unrestrained, which provides a valuable tool for comparison. Moreover, the micromechanical properties of the spherical elements, in particular the inter-element normal and tangential contact stiffnesses  $K_n$  and  $K_t$  and the inter-element friction coefficient  $\mu$ , are known exactly, and the behavior of each element can be monitored precisely throughout the simulations. In this way, element trajectories, as

well as per-element quantities such as friction work and angular velocity, can be monitored throughout the simulations, and the distributions of these quantities can be visualized within the particulate material specimens. The discrete element method, along with the relative merits of 2-D versus 3-D DEM simulations, is discussed in detail in Chapter 9 [Fleischmann et al. (2013c)], and more briefly in Section 2.3.

# Chapter 2

## Literature Review

### 2.1 Constitutive Modeling of Particulate Materials Based on Micromechanics: Elastic Range

A number of researchers have contributed to the published literature on determining effective elastic moduli for particulate/granular materials based on micromechanics. Early work was done by Duffy and Mindlin (1957) and Deresiewicz (1958a) on regular face-centered cubic and simple cubic arrays of uniform spheres (see Sections 3.3.1 and 3.3.2 of this thesis). More recent work has been done by Walton (1987), Chang et al. (1995), Cambou et al. (1995), and Emeriault and Cambou (1996). A good reference for results obtained before 1998 is Cambou (1998).

Let  $K_n$  and  $K_t$  be the normal and tangential inter-particle contact stiffnesses for a particulate material composed of uniform spheres, so that the normal and tangential inter-particle contact forces are given by  $F_n = K_n \delta_n$  and  $F_t = K_t \delta_t$ , where  $\delta_n$  and  $\delta_t$  are the normal and tangential displacements at the point of contact between two spheres. If the macro-scale effective Poisson's ratio and bulk modulus of the particulate material are denoted by  $\nu$  and  $\kappa$ , then Chang et al. (1995) derive the following relationships for an isotropic particulate

material composed of uniform spheres of diameter  $D$ .

$$\alpha = \frac{1 - 4\nu}{1 + \nu}, \quad K_n = \frac{9}{\beta D^2} \kappa, \quad (2.1)$$

where  $\alpha = K_t/K_n$  is the ratio of the tangential to the normal inter-particle contact stiffnesses, and  $\beta$  is the number of contacts per unit volume in the particulate material. Equation (2.1) was previously derived by Walton (1987), and it was also rederived by Cambou et al. (1995). Equation (2.1) depends on the so-called Voigt or kinematic homogenization hypothesis, which maintains that the local strain in an aggregate (in this case particulate) material subjected to uniform strain is the same as the far field strain in that material. Chang et al. (1995) also derive another set of relationships under the so-called Reuss or static homogenization hypothesis, which maintains that the local *stress* in an aggregate material subjected to uniform stress is the same as the far field stress in that material. Under the Reuss hypothesis, Chang et al. (1995) derive

$$\alpha = \frac{1 - 2\nu}{1 + 3\nu}, \quad K_n = \frac{9}{\beta D^2} \kappa, \quad (2.2)$$

for an isotropic particulate material composed of uniform spheres of diameter  $D$ , where  $\alpha = K_t/K_n$  is the ratio of the tangential to the normal inter-particle contact stiffnesses, and  $\beta$  is the number of contacts per unit volume in the particulate material. Chang et al. (1995) also derive more complicated expressions for the case of arbitrary anisotropy in the particulate material. In an earlier study, Chang and Misra (1989) derived the anisotropic stress-strain relations for regular packings of disks (rhombic and hexagonal) in 2-D and spheres (simple cubic only) in 3-D. Equation (2.2) was also rederived by Liao et al. (1997) under what they called the best fit hypothesis. For alternative derivations of equations (2.1) and (2.2), see Section 3.4 of this thesis. Figure 2.1 shows the relationship between  $\alpha = K_t/K_n$  at the inter-particle level and Poisson's ratio  $\nu$  for the macroscopic particulate material predicted by equations (2.1) and (2.2). The Voigt and Reuss curves in Figure 2.1

cross at  $\alpha = 1$  and  $\nu = 0$ .

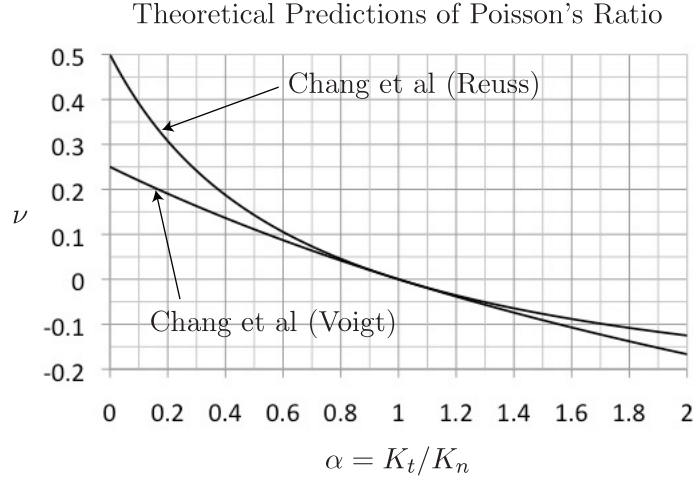


Figure 2.1: Theoretical prediction of Poisson's ratio  $\nu$  as a function of  $\alpha = K_t/K_n$  for a statistically isotropic particulate material derived by Chang et al. (1995) under the Voigt and Reuss hypotheses, given by equations (2.1) and (2.2).

Cambou et al. (1995) rederive equation (2.1) for an isotropic particulate material, but they obtain an expression that is different from (2.2) under their version of the static hypothesis, in which they assume that the average distribution  $f_i$  of the inter-particle contact forces at the local level within a particulate material can be expressed as a function of the orientation direction  $n_i$  and the far field (non-local) stress  $\sigma_{ij}$  as

$$f_i = \zeta \sigma_{ij} n_j + \frac{1 - \zeta}{2} [5n_j \sigma_{jk} n_k - \sigma_{jj}] n_i \quad (2.3)$$

where  $\zeta$  is an internal parameter of the particulate material, which is related to its packing structure. Equation (2.3) was first proposed by Delyon et al. (1990), and it is based on the representation theorems (e.g. Spencer (1987)) under the assumptions that  $f_i$  is linear with respect to  $\sigma_{ij}$  and isotropic with respect to  $n_i$ . Cambou et al. (1995) use the symbol  $\mu$  for  $\zeta$ , but we have renamed it to avoid confusion with either the shear modulus of the material constituting the spheres, the overall shear modulus of the particulate material, or

the inter-particle friction coefficient, all of which are often called  $\mu$ . According to Sidoroff et al. (1993), static equilibrium then requires that

$$\sigma_{ij} = \beta D \int_{\Omega} f_i n_j d\Omega, \quad (2.4)$$

where  $d\Omega = \sin\theta d\varphi d\theta$  is the differential solid angle of the unit sphere  $\Omega$ ,  $\sigma_{ij}$  is the far field stress in the particulate material,  $\beta$  is the average number of contacts per unit volume (as before), and  $D$  is the diameter of the spheres. Under the hypotheses expressed in equations (2.3) and (2.4), Cambou et al. (1995) derive

$$\nu = \frac{2\zeta^2 + \alpha(5 - 10\zeta + 3\zeta^2)}{4\zeta^2 + \alpha(20 - 20\zeta + 6\zeta^2)}, \quad K_n = \frac{9}{\beta D^2} \kappa, \quad (2.5)$$

for an isotropic particulate material composed of uniform spheres of diameter  $D$ , where  $\alpha = K_t/K_n$  is the ratio of the tangential to the normal inter-particle contact stiffnesses and  $\beta$  is the number of contacts per unit volume in the particulate material. Emeriault and Cambou (1996) derive more complicated expressions for an arbitrary anisotropic particulate material. Figure 2.2 shows the relationship between  $\alpha = K_t/K_n$  at the inter-particle level and Poisson's ratio  $\nu$  for the macroscopic particulate material predicted by equation (2.5).

Note that the values of  $K_n$  and  $\alpha = K_t/K_n$  in equations (2.1), (2.2), and (2.5) need not be constant, as they are in the case of a linear elastic inter-particle contact law. According to Hertz-Mindlin contact theory, if two spheres of radius  $R$  are compressed by a normal force  $F_n$  directed along their line of centers, then  $K_n$  and  $\alpha = K_t/K_n$  are given by

$$K_n = \frac{E' a}{1 - \nu'^2}, \quad \alpha = \frac{2(1 - \nu')}{2 - \nu'}, \quad (2.6)$$

where  $E'$  and  $\nu'$  are the elastic modulus and Poisson's ratio for the material constituting the spheres (not the particulate material), and  $a$  is the radius of the circular contact area

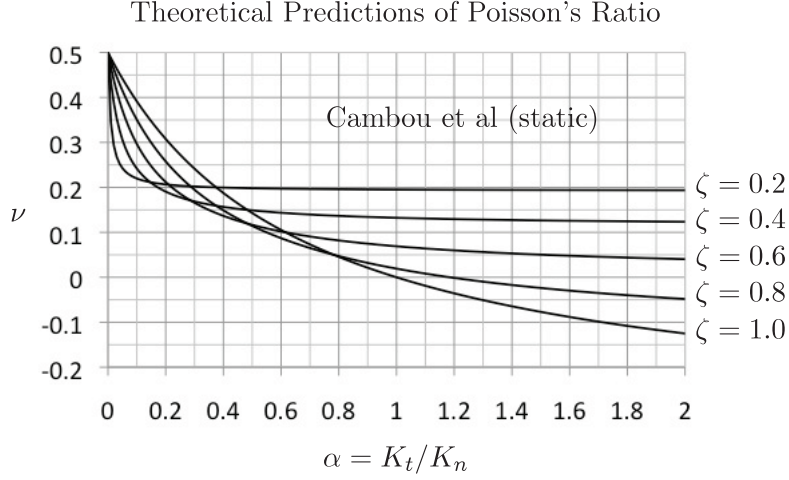


Figure 2.2: Theoretical prediction of Poisson's ratio  $\nu$  as a function of  $\alpha = K_t/K_n$  for a statistically isotropic particulate material derived by Cambou et al. (1995) under their static hypothesis, given by equation (2.5), for different values of the internal material parameter  $\zeta$ .

between the spheres given by

$$a = \left( \frac{3(1 - \nu'^2)}{4E'} F_n R \right)^{1/3}. \quad (2.7)$$

In general, the inter-particle normal force  $F_n$  in equation (2.7) will depend in some way on the confining pressure  $\sigma_0$  on the particulate material, either in an average sense or depending on the local packing structure, and the inter-particle contact law can be linearized about that value of  $F_n$ . For example, for a regular face-centered-cubic array of uniform spheres of radius  $R$ , we can obtain constant values of  $K_n$  and  $\alpha = K_t/K_n$  by letting  $F_n = F_0 = \sqrt{2}R^2\sigma_0$  in equation (2.7), and for a regular simple-cubic array of uniform spheres of radius  $R$ , we can obtain constant values of  $K_n$  and  $\alpha = K_t/K_n$  by letting  $F_n = F_0 = 4R^2\sigma_0$  in equation (2.7).

A useful relationship between the number of contacts per unit volume  $\beta$  and the void

ratio  $e$  within a randomly packed assembly of uniform spheres of radius  $R$  is

$$\beta = \frac{3\bar{n}_c}{8\pi(1+e)R^3}, \quad (2.8)$$

where  $\bar{n}_c$  is the average coordination number in the particulate material, i.e., the average number of contact points per particle. For the derivation, see Nemat-Nasser (2004). Experimental work by Oda (1977) suggests that the average coordination number  $\bar{n}_c$  in random mixtures of (non-uniform) spheres is roughly a function of the void ratio  $e$ . Some empirical formulas relating the coordination number  $\hat{n}$  to the void ratio  $e$  of a particulate material are given in equations (2.9) - (2.12) below, taken from Field (1963), Yanagisawa (1983), Chang et al. (1990), and Ouchiyama and Tanaka (1980), respectively.

$$\bar{n}_c = \frac{12}{1+e}, \quad (2.9)$$

$$\bar{n}_c = 3.183^{(2.469-e)}, \quad (2.10)$$

$$\bar{n}_c = 13.28 - 8e, \quad (2.11)$$

$$\bar{n}_c = \frac{32}{13} \left( \frac{7-e}{1+e} \right). \quad (2.12)$$

Recent work on determining the effective isotropic elastic moduli for particulate/granular materials based on micromechanics has also been done by Trentadue (2004), Suiker and de Borst (2005), Duffaut et al. (2010), and Kruyt et al. (2010). Trentadue (2004) improves the inter-particle contact law given by equations (2.6) and (2.7) by employing Hertz-Cattaneo-Mindlin contact theory, which includes “micro-slip” at inter-particle contact points. To a first approximation, however, the effective elastic constants obtained by Trentadue match those obtained by Chang et al. (1995) under the Reuss hypothesis and Liao et al. (1997) under the best fit hypothesis, which are given by equation (2.2). Trentadue treats only the case of a statistically isotropic particulate material.

Suiker and de Borst (2005) rederive the relations expressed by equation (2.1), along with additional relations for higher order elastic constants corresponding to several strain-gradient micro-polar continuum models. Then they compare the predictions of these models with the wave propagation characteristics of a two-dimensional discrete hexagonal lattice. Their analysis follows that of Chang and Liao (1990) and Chang and Gao (1995) in assuming that discrete particle rotations can be approximated by a continuous particle rotation field, similar to the strain field of classical continuum theory. This particle rotation field is then represented by a Taylor expansion, which can be truncated at whatever order is desired for the strain-gradient continuum model. This approach is problematic in that it cannot capture zero-energy strains or mechanisms due to particle rotation at the microscale. In Chapter 4 of this thesis [Fleischmann et al. (2013b)], we demonstrate both theoretically and via DEM simulations that mechanisms due to particle rotation can and do exist in a randomly packed particulate material, even in the elastic range. Moreover, particle rotation at the local level can be involved in a global elastic strain of the particulate material (i.e., reversible strain at the global level), while, as Goddard (2008) shows, these particle rotations do not contribute to the quasi-static stress power. An attempt at resolving this difficulty in the context of a Cosserat-type continuum framework has been made by Kruyt (2003), but only qualitative results are obtained. Kruyt (2010) extends the work of Suiker and de Borst (2005) to determine the dispersion relations for wave propagation in regular three-dimensional lattices of spherical particles (simple cubic, body centered cubic, and face centered cubic), assuming both normal and tangential inter-particle contact forces (linear spring contact model) and explicitly accounting for the rotational degrees of freedom of the particles.

Duffaut et al. (2010) modify the results of Walton (1987), which are the same as the relations given by equation (2.1), by introducing a parameter to measure micro-slip at inter-particle contacts. This was also done by Bachrach et al. (2000). The motivation for this modification came from an observed discrepancy between the experimentally measured value

of  $\nu$  for a random packing of glass beads and the theoretical prediction of Walton (1987) in the vicinity of  $\alpha \approx 0.9$ . In particular, equation (2.1) underpredicts Poisson’s ratio very significantly when compared to experimental measurements on a random assembly of glass beads, for which Hertz-Mindlin contact theory predicts  $\alpha \approx 0.9$ . Bachrach et al. (2000) suggested that the cause for this discrepancy may be due to slipping at the inter-particle contacts. In Sections 4.5 and 4.6 of this thesis, however, we demonstrate that inter-particle slip cannot account entirely for the discrepancy between the experimental and predicted values of Poisson’s ratio noted by Bachrach et al. (2000) and Duffaut et al. (2010), and we argue that the effect of particle rotation, in particular the mechanisms or zero-energy strains produced by particle rotation in a random assembly of uniform spheres, provide a better explanation for this discrepancy.

In a recent study, Lee et al. (2011) use the Hashin-Shtrikman-Willis variational principle (Hashin and Shtrikman, 1962, Willis, 1977) to obtain overall elastic moduli for heterogeneous polydisperse particulate materials in three-dimensions, where the statistical information for the particulate assemblies (idealized as non-uniform spheres) is based on three-dimensional microtomographic (micro-CT) data. Since the second-order Hashin-Shtrikman-Willis variational principle used by Lee et al. (2011) requires the integration of complex integrands involving the interaction of the Green’s function with first and second order probability functions in three-dimensions, the authors focus on efficient numerical integration techniques necessary for computing the Hashin-Shtrikman-Willis bounds for these tomographically generated systems. The approach of Lee et al. (2011) is powerful, but it is also computationally expensive, and it relies on detailed statistical information for the particulate material fabric. However, while we have criticized the use of variational principles to obtain overall elastic moduli for particulate materials because of their *general* inability to account for the zero-energy strains produced by particle rotation, this may be resolved by the use of the Hashin-Shtrikman-Willis variational principle as extended by Šejnoha and Zeman (2002)

and Procházka and Šejnoha (2004) to include “eigenstrains”, or stress-free strains, which are precisely the zero-energy strains that we have found are critical for understanding the effect of particle rotation on the elastic behavior of particulate materials. Thus, this approach may provide a means for an effective extension of our work in Chapters 3 and 4 of this thesis [Fleischmann et al. (2013a) and Fleischmann et al. (2013b)].

## 2.2 Constitutive Modeling of Particulate Materials Based on Micromechanics: Plastic Range

Several of the same researchers who have used homogenization techniques to obtain effective elastic moduli for particulate materials based on micromechanics have tried to apply similar methods to obtain micromechanics-based elastoplastic models for particulate materials. For example, Emeriault et al. (1996) base their analysis on the static homogenization assumption of Cambou et al. (1995) and Emeriault and Cambou (1996), expressed in equations (2.3) and (2.4), and they derive the yield surface for a particulate material based on the inter-particle slip condition  $F_t = \mu F_n$ , where  $F_t$  and  $F_n$  are the magnitudes of the inter-particle tangential and normal contact forces, respectively, and  $\mu$  is the inter-particle friction coefficient. For an isotropic particulate material, they find that the relationship between the inter-particle friction coefficient  $\mu = \tan \phi_\mu$  (where  $\phi_\mu$  is the microscopic “friction angle” at the inter-particle contacts) and the macroscopic friction angle  $\phi$  for the particulate material at yield is

$$\sin \phi = \tan \phi_\mu \frac{\tan \phi_\mu (3 - \zeta) + \sqrt{4\zeta^2 + \tan^2 \phi_\mu (5 - 3\zeta)^2}}{2\zeta^2 + \tan^2 \phi_\mu (4\zeta^2 - 13\zeta + 11) + \tan \phi_\mu \sqrt{4\zeta^2 + \tan^2 \phi_\mu (5 - 3\zeta)^2}}, \quad (2.13)$$

where the yield of the particulate material on the macroscale follows the well-known Mohr-Coulomb criterion:

$$\frac{|\sigma_1 - \sigma_2|}{2\sqrt{\sigma_1\sigma_2}} \leq \tan \phi, \quad \frac{|\sigma_1 - \sigma_3|}{2\sqrt{\sigma_1\sigma_3}} \leq \tan \phi, \quad \frac{|\sigma_2 - \sigma_3|}{2\sqrt{\sigma_2\sigma_3}} \leq \tan \phi, \quad (2.14)$$

where  $\sigma_1$ ,  $\sigma_2$ , and  $\sigma_3$  are the principal stresses within the particulate material. For a derivation of the Mohr-Coulomb yield criterion as given by equation (2.14), see Appendix D. Emeriault et al. (1996) also derive more complicated yield surfaces for anisotropic particulate materials. The internal parameter  $\zeta$  appearing in equation (2.13) is the same as that appearing in equation (2.3) of Section 2.1. Figure 2.3 shows the relationship between  $\phi_\mu$  and  $\phi$  expressed in equation (2.13) for a range of  $\zeta$ .

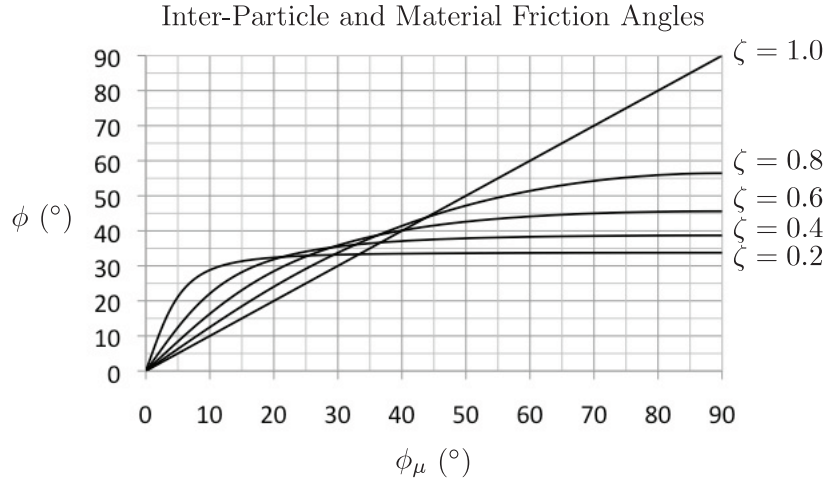


Figure 2.3: The relationship between the inter-particle friction angle  $\phi_\mu = \tan^{-1} \mu$ , where  $\mu$  is the inter-particle friction coefficient, and the macroscopic friction angle  $\phi$  for an isotropic particulate material at yield, derived by Emeriault et al. (1996) under the static hypothesis of Cambou et al. (1995), given by equation (2.13), for different values of the internal material parameter  $\zeta$  described in Section 2.1.

Chang and Hicher (2005) propose a homogenization process for obtaining a macroscopic elastoplastic rate-independent incremental stress-strain relation for a particulate material based on the Reuss hypothesis or best fit hypothesis of Liao et al. (1997), assuming a semi-

phenomenological microscopic elastoplastic material behavior. In particular, they assume that dilation can be represented at the particle scale by

$$\frac{d\delta_n^p}{d\delta_t^p} = \frac{F_t}{F_n} - \tan \phi_0, \quad (2.15)$$

where  $d\delta_n^p$  and  $d\delta_t^p$  are the plastic parts of the relative normal and tangential displacements between two (pseudo)particles,  $F_n$  and  $F_t$  are the corresponding normal and tangential contact forces, and  $\phi_0$  is a material parameter that according to Chang and Hicher can in most cases be considered equal to the inter-particle friction angle  $\phi_\mu$ . They also assume that the yield function at the particle scale can be represented by

$$f(F_n, F_t, \kappa(\delta_t^p)) = F_t - F_n \kappa(\delta_t^p), \quad (2.16)$$

where  $\kappa(\delta_t^p)$  is an isotropic hardening parameter of the form

$$\kappa = \frac{k_{p0} \tan \phi_p \delta_t^p}{|F_n| \tan \phi_p + k_{p0} \delta_t^p}, \quad (2.17)$$

where  $\phi_p$  and  $k_{p0}$  are two more material parameters. The parameter  $k_{p0}$  is the initial slope of the  $\kappa$  versus  $\delta_t^p$  curve, and  $\kappa$  approaches  $\tan \phi_p$  for  $\delta_t^p \gg F_n$ . It must be noted that, although these relations are assumed to exist between individual particles at the particle scale, they do not really represent the micromechanics of the particle interactions themselves, but rather use macroscopic properties of the granular material to describe inter-particle interactions at the particle scale in an ‘‘average’’ sense. For example, neither equation (2.15) nor (2.17) are derived from inter-particle contact mechanics. Under these assumptions, Chang and Hicher (2005) derive an ‘‘inter-particle’’ elastoplastic stiffness tensor  $K_{ij}^c$  so that, for a given contact  $c$ , the increment in the contact force  $dF_i^c$  can be written as a function of the increment in

the contact displacement  $d\delta_j^c$  as

$$dF_i^c = K_{ij}^c d\delta_j^c. \quad (2.18)$$

Using equation (2.18), Chang and Hicher (2005) follow the static (best fit) homogenization process of Liao et al. (1997) to obtain an elastoplastic incremental stress-strain relation

$$d\epsilon_{ij} = \mathcal{M}_{ijkl} d\sigma_{kl}, \quad (2.19)$$

where the fourth-order tensor of second-order elastoplastic compliances  $\mathcal{M}_{ijkl}$  is given by

$$\mathcal{M}_{ijkl} = \Lambda_{im}^{-1} \Lambda_{kn}^{-1} V \sum_c (K_{jl}^c)^{-1} l_m^c l_n^c, \quad (2.20)$$

where the sum is performed over all contacts  $c$  in a representative volume  $V$ ,  $l_i^c$  is the branch vector that connects the centroids of the two particles in contact at  $c$ , and  $\Lambda_{ij} = \sum_c l_i^c l_j^c$  is the fabric tensor for the representative volume. Chang and Hicher (2005) evaluated the sum in equation (2.20) numerically. In order to make the volume representative, they assumed that the orientations of the contacts were at Gauss integration points in spherical coordinates. They claimed that sufficient accuracy was obtained by considering orientations corresponding to 74 fully symmetric integration points. They tested their model against experimental data in the quasi-static range, and they found reasonable agreement. However, because of its dependence on phenomenological relationships such as those expressed in equations (2.15) and (2.17) that do not really exist at the inter-particle level, in that they are not derived from particle interactions, the model of Chang and Hicher (2005) is not really based on micromechanics. Hicher and Chang (2007) have also proposed a micromechanics-based elastoplastic model for unsaturated particulate/granular materials that is rate-*dependent*, but like their rate-independent model, it depends heavily on assumed microscopic behavior that is largely phenomenological.

Another approach to obtaining a micromechanics-based elastoplastic model for particulate materials is taken by Mehrabadi et al. (1993). They derive an incremental elastoplastic continuum constitutive model for a two-dimensional assembly of disks based on the assumption that the microstructure of the particulate assembly can be represented by a probability density function of the inter-particle contact normal vectors. No other information about the particulate material fabric is included in their analysis. In this way, they attempt to simplify the evolution law for the deformation history of the material fabric, which is an essential part of any micromechanics-based elastoplastic constitutive model for a particulate material. Their local yield criterion is taken to be  $F_t = \mu F_n$ , where  $F_t$  and  $F_n$  are the magnitudes of the inter-particle tangential and normal contact forces, respectively, and  $\mu$  is the inter-particle friction coefficient. The local stress tensor is linked to the inter-particle contact forces in a representative volume through equation (2.24) below, and a phenomenological evolution law for the distribution of contact normal vectors is proposed. Mehrabadi et al. (1993) apply a homogenization method based on Taylor (1938), which is an extension of the Voigt homogenization method discussed in Section 3.4.1 of this thesis (and derived in Appendix C) to plasticity, to obtain a macroscopic incremental (rate-independent) continuum constitutive relation for their particulate system. They also briefly discuss the possibility of applying the self-consistent homogenization method proposed by Hill (1965) to their system. Mehrabadi et al. (1993) obtain predictions of shearing deformation from their model that are in *qualitative* agreement with experimental observations of particulate materials. However, they make no *quantitative* comparisons of the predictions they obtain from their model with experimental or numerical (DEM) results. Balendran and Nemat-Nasser (1993) use physical insights gained from the model of Mehrabadi et al to develop a semi-phenomenological elastoplastic model for two-dimensional particulate materials, and show that this model is in better agreement with experimental results than the model of Mehrabadi et al. (1993). The model of Balendran and Nemat-Nasser (1993) is extended to three dimensions by Nemat-Nasser

and Zhang (2002).

A different approach to obtaining a micromechanics-based elastoplastic model for a two-dimensional particulate material is taken by Borja and Wren (1995), who give more attention to capturing the specific effects of the variations and evolution of the microstructure of the material fabric during plastic deformation. They begin by viewing a representative region of a two-dimensional particulate material as a macro-element, and then they derive a local elastoplastic constitutive law for this macro-element. This local elastoplastic constitutive law is based on individual inter-particle contact behavior within the macro-element, consisting of straightforward linear elastic normal and tangential inter-particle contact force-displacement laws  $F_n = K_n \delta_n$  and  $F_t = K_t \delta_t$  and inter-particle slip when the frictional slip condition  $F_t = \mu F_n$  is met, where  $\mu$  is the inter-particle friction coefficient. Then they derive a macroscopic elastoplastic constitutive law by assuming that the particulate material is composed of repeating cells of this macro-element. Borja and Wren (1995) performed numerical simulations using their model with various ordered and disordered macro-elements consisting of 58, 60, 64, and 196 disks, and they found that their model was able to reproduce important qualitative particulate material behavior such as anisotropy, hardening, and dilation. Their results were not quantitatively compared to any other results, obtained by experiment or by DEM. The method of Borja and Wren (1995) is an early example of what today would probably be called a *multiscale* method. More recently, Andrade and Tu (2009) have employed a similar multiscale method to model the elastoplastic behavior of a three-dimensional particulate material using a cubical macro-element consisting of disordered spheres in conjunction with DEM.

Henderson et al. (2001) derive two anisotropic elastoplastic models for particulate material compaction that are based on micromechanics. They obtain their models by employing both the Voigt and Reuss homogenization processes, following the theoretical development of those processes for particulate materials made by Emeriault and Cambou (1996). They in-

clude plastic behavior in the inter-particle contact law, but they do not include inter-particle sliding, because they intend their model to be applicable only to compaction, for which case they assume inter-particle sliding to be negligible. Henderson et al. (2001) compared the predictions of their resulting models with experimental data, and they found that the predictions based on the Reuss approach were more physically realistic than those based on the Voigt approach. They also found that by adjusting parameters in the inter-particle contact law the predictions based on the Reuss approach could be made to match experimental die-pressing data almost perfectly. The model of Henderson et al is limited in that it only applies to the special case of compaction where there is no inter-particle sliding, but it illustrates the failure of the Voigt approach to give quantitatively adequate predictions, even in this (relatively simple) special case.

Anandarajah (2004) and Anandarajah (2008) has developed a model for the elastoplastic deformation of a particulate material that is based on the collapse of force chains in the material. In this model, force chains are assumed to run parallel to the principal stress directions in the particulate material, and the behavior of the force chains is extrapolated from the behavior of simple cubic (SC) and face centered cubic (FCC) representative “micro-elements” of spheres, in which the spheres are allowed to roll and slide relative to one another. Anandarajah (2008) compares the results obtained by this model to results obtained from DEM simulations of triaxial tests on 2914 uniform spheres, and found qualitative agreement. In particular, the critical state line (CSL), which is the relation between the consolidation pressure and void ratio in a particulate material for which no volume change (dilation) occurs during shear deformation, was compared between the model and the DEM simulations, and qualitative agreement was observed.

Recently, Kuhn (2010) has proposed a model for the evolution of a particulate material fabric during plastic deformation. In particular, Kuhn’s model predicts the evolution of the induced anisotropy due to changes in the average inter-particle contact orientations and

average inter-particle contact forces within a particulate material fabric during plastic deformation. Kuhn (2010) also performed three-dimensional DEM simulations on 20 assemblies of 4096 spherical particles subjected to triaxial compression and compared the results of his model to local measurements taken from the DEM simulations. By adjusting material parameters in his model, Kuhn was able to attain quantitative agreement between the DEM measurements and the predictions from the model in regions of uniform plastic deformation within the particulate material fabric.

## 2.3 Constitutive Modeling of Particulate Materials Based on Micromechanics: Discrete Element Method

The discrete (or distinct) element method has been used effectively to numerically model the quasi-static and dynamic behavior of particulate materials since its introduction by Cundall and Strack (1979). Two good references for the current state of the art of the discrete element method, with particular application to geomaterials, including particulate materials, are Jing and Stephansson (2007) and O’Sullivan (2011). In its most basic form, the discrete element method models a particulate medium using a massive collection of distinct rigid elements having simple shapes, such as spheres. Contact between the DEM elements may be modeled by nonlinear Hertz-Mindlin theory, or by the simple linear spring arrangement shown in Figure 2.4. To model friction, the contact history between pairs of elements in contact must be stored. Contact between DEM elements is “soft” (or “penalized”) in the sense that elements are allowed to overlap slightly with a repulsive contact force applied in proportion to the overlap. Let  $u_n$  be the radial overlap distance between two contacting spherical elements, let  $\mathbf{v}_n$  and  $\mathbf{v}_t$  be the relative normal and tangential velocities at the point of contact, and let  $\mathbf{u}_t$  be the elastic part of the total accumulated tangential displacement between the surfaces of the two spheres since the contact was initiated, projected onto the plane of contact and

scaled as necessary to satisfy the frictional sliding criterion  $|\mathbf{F}_t| \leq \mu|\mathbf{F}_n|$  shown in Figure 2.4. Then, according to the linear spring model, the normal and tangential force vectors  $\mathbf{F}_n$  and  $\mathbf{F}_t$  at the point of contact are given by equations (2.21) and (2.22), respectively, where  $K_n$  and  $K_t$  are the normal and tangential elastic contact spring stiffnesses, respectively,  $\mathbf{n}$  is the unit normal vector along the line connecting the centers of the contacting spheres (in the appropriate direction),  $\gamma_n$  and  $\gamma_t$  are normal and tangential viscoelastic damping constants, and  $m_{\text{eff}} = m_i m_j / (m_i + m_j)$  is the effective mass of the two spheres  $i$  and  $j$  (Silbert et al., 2001).

$$\mathbf{F}_n = K_n u_n \mathbf{n} - \gamma_n m_{\text{eff}} \mathbf{v}_n \quad (2.21)$$

$$\mathbf{F}_t = -K_t \mathbf{u}_t - \gamma_t m_{\text{eff}} \mathbf{v}_t. \quad (2.22)$$

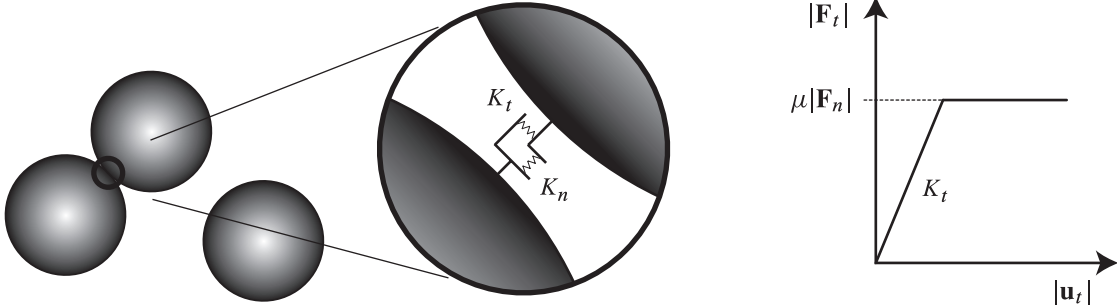


Figure 2.4: Left: Linear spring contact model for spherical DEM elements. Right: Tangential linear contact force-displacement law for spherical DEM elements.

The use of a linear spring contact model allows us to apply the results of Tavaréz and Plesha (2007) and O’Sullivan and Bray (2004) to obtain estimates of the critical time-step size for the explicit time integration scheme. Critical time-step sizes suggested by O’Sullivan and Bray (2004) for 2-D and 3-D DEM simulations are given by equation (2.23). These estimates are based on the standard stability criterion for the central difference explicit integration scheme applied to linear systems,  $\Delta t < (2/\omega_{\text{max}}) \left( \sqrt{1 + \xi^2} - \xi \right)$ , where  $\omega_{\text{max}}$

is the maximum natural frequency of the stiffness and mass matrices associated with the system, and  $\xi$  is the fraction of critical damping in the system at  $\omega_{\max}$  (Cook et al., 2002). For DEM,  $\omega_{\max}$  must be estimated, because internal forces are evaluated in an element-by-element fashion, and hence the stiffness matrix for the system is not formed. The estimate in equation (2.23) ignores the mass proportional damping included in equations (2.21) and (2.22), which has the effect of only slightly decreasing the stability of the system for most problems, since the fraction of critical damping due to mass proportional damping at high frequencies is typically low.

$$\Delta t_{\text{crit}}^{(2\text{-D})} \approx 0.3 \sqrt{\frac{m_{\min}}{K_{\max}}} \quad \Delta t_{\text{crit}}^{(3\text{-D})} \approx 0.2 \sqrt{\frac{m_{\min}}{K_{\max}}} \quad (2.23)$$

The critical time-step sizes given by equation (2.23) include a “safety factor”. For original derivations of alternative estimates of the critical time-step size for 2-D and 3-D DEM based on the Gerschgorin bound, see Appendix E.

For our DEM simulations, we use a modified version of LAMMPS, the Large-scale Atomic/Molecular Massively Parallel Simulator developed at Sandia National Laboratories, which is more commonly used for molecular dynamics simulations than for DEM simulations. For a description of the core features of LAMMPS, see Plimpton (1995). We have added features such as the capability to model non-rigid element clusters and particle damage, as in Jensen et al. (1999), Jensen et al. (2001a), Jensen et al. (2001b), and Tavares and Plesha (2007). A few of the advantages of LAMMPS are that it is open-source, it is easy to expand and modify, and it is optimized for massive parallel computing (see LAMMPS). For 2-D and 3-D visualization of our DEM specimens, we use the open source codes VMD (Humphrey et al., 1996) and ParaView (see ParaView). Since none of the DEM simulations performed for this thesis use element clusters to model individual particles, particles consist of individual (cohesionless) spherical elements only. Hence, in reference to DEM in this thesis, we use

the terms “particle” and “element” interchangeably.

A large number of researchers have used DEM to validate continuum constitutive models for particulate/granular materials since the 1980’s, and a few of these have used DEM to inform the development of their continuum constitutive models based on micromechanics. An early example of this is the work of Bathurst and Rothenburg (1988), who performed DEM simulations on two-dimensional specimens of 1 000 disks to validate their micromechanics-based constitutive relations. The relations obtained by Bathurst and Rothenburg between the elastic constants  $\nu$  and  $\kappa$  and the inter-particle contact stiffnesses  $K_n$  and  $K_t$  correspond to the relations obtained under the Voigt hypothesis, given by equation (2.1), with some differences caused by the fact that their relations were derived for a two-dimensional assembly of disks rather than for a three-dimensional assembly of spheres. For the results of the Voigt and Reuss (or best fit) homogenization hypotheses applied to two-dimensional assemblies of disks as well as three-dimensional assemblies of spheres, see Liao et al. (1997). Bathurst and Rothenburg performed DEM simulations of constrained biaxial compression tests on their specimens and measured Poisson’s ratio  $\nu$  for different inter-particle contact stiffness ratios  $\alpha = K_t/K_n$ . They found good agreement between the measured values and the theoretically predicted values. In particular, for  $\alpha \approx 1$ , Bathurst and Rothenburg found that  $\nu \approx 0$ . They also found that particle rotation in their specimens during the DEM simulations was negligible. It is noteworthy that the DEM specimens used by Bathurst and Rothenburg were nearly close-packed. In Sections 3.5 and 4.5 of this thesis, we report results that we have obtained from our own DEM simulations of constrained triaxial compression tests on three-dimensional specimens consisting of 3 430 and 29 660 uniform spheres, and we note that particle rotation can in fact significantly alter the value of Poisson’s ratio  $\nu$ , particularly for  $\alpha \approx 1$  and greater. This phenomenon appears to be linked to the degree to which inter-particle contacts at the local level are “asymmetric”, and it can be related to a single internal parameter  $\xi$  of the particulate material. See Chapters 3 and 4 of this thesis [Fleischmann

et al. (2013a) and Fleischmann et al. (2013b)] for details.

Chang and Misra (1990) also explored the micromechanical properties of random assemblies of disks and spheres using DEM. They considered only densely packed specimens, with void ratios of  $e \approx 0.1$  for the two-dimensional specimens and  $e \approx 0.5$  for the three-dimensional specimen. The DEM specimens consisted of very few elements, with 276 uniform and 405 non-uniform disks in the two-dimensional specimens and 95 non-uniform spheres in the three-dimensional specimen. Like Bathurst and Rothenburg, Chang and Misra claim that particle rotation is “negligibly small” in the elastic range. They do not make clear what “negligibly small” means, except by appealing to a chart that shows that the maximum particle rotation in the specimens is less than approximately  $10^{-3}$  radians, but whether or not this amount of particle rotation is truly negligible in the elastic range is not addressed. They do make the point that the *mean* particle rotation is very nearly zero, but again whether or not one can conclude from this that the “contribution of rotation is relatively small,” as Chang and Misra conclude, is again not addressed.

Liao et al. (1997) performed DEM simulations on assemblies of 800 to 900 uniform circular disks to test two-dimensional versions of the relations in equations (2.1) and (2.2) and another set of relations derived under what they called the piece-wise fit hypothesis. They performed simulations using disks with  $\alpha = K_t/K_n$  ranging between  $0 \leq \alpha \leq 1$  and measured Poisson’s ratio and Young’s modulus, and they found that the DEM results lay between the theoretical results obtained by the Voigt and piece-wise fit hypotheses.

Calvetti and Emeriault (1999) used DEM to measure the distribution of contact forces in a random assembly of 1159 circular disks of a linear size distribution subjected to biaxial loading. They used these simulations to evaluate the accuracy of theoretical predictions of the elastic constants for the assemblies, such as those given by equation (2.5), based on the homogenization methods of Cambou et al. (1995) and Emeriault and Cambou (1996). They found that these results accurately predicted the elastic behavior of the assemblies if the

disks were constrained to have no rotation, but that the results failed to accurately predict the elastic behavior of the assemblies if the disks were allowed to rotate. Their observations mirror our own observations for three-dimensional assemblies of spheres subjected to triaxial loading, which are given in Sections 3.5 and 4.5 of this thesis.

Kruyt and Rothenburg (2002) used DEM to validate the upper and lower bounds they obtained for the effective elastic moduli for two-dimensional isotropic assemblies of non-rotating particles. One bound was the two-dimensional version of equation (2.1), and the other bound was obtained numerically based on the local packing structure of the individual specimens, according to a method similar to the piece-wise fit hypothesis of Liao et al. (1997). The DEM specimens consisted of 50 000 randomly packed circular disks with log-normal size distributions. They measured the bulk and shear moduli of the specimens for values of  $\alpha = K_t/K_n$  ranging between  $0 \leq \alpha \leq 1$ , and they found that the DEM results lay between the theoretical bounds, as expected.

Jenkins et al. (2005), following earlier work by Jenkins et al. (1989), have used DEM simulations to show that local variations in strain from the the average strain in a particulate material can lead to large discrepancies in the theoretically predicted values of the shear modulus (or Poisson’s ratio) for the particulate material when compared to the measured values. They argue that this local variation is due to a strain “relaxation” between particle pairs deviating from the average strain in the particulate material, which is similar to the argument we make for local strain “mechanisms” due to particle rotation in Chapter 4 of this thesis. They show that this local strain relaxation can decrease the theoretical prediction of the effective shear modulus from equation (2.1) (in terms of the bulk modulus  $\kappa$  and Poisson’s ratio  $\nu$ ) by up to 70%. In contrast, they find that the bulk modulus  $\kappa$  is relatively insensitive to local strain variation, which corresponds to our own observations – see Chapters 3 and 4 of this thesis [Fleischmann et al. (2013a) and Fleischmann et al. (2013b)]. Each DEM specimen for Jenkins et al. (2005) consisted of 10 000 randomly packed spheres of two different radii

in equal numbers.

O’Sullivan et al. (2004) performed a combined experimental and DEM analysis of three dimensional regular arrays of 1 500–2 000 uniform and non-uniform spheres. In their study, they recorded both pre- and post-yield responses of face-centered cubic and rhombic packings of spheres under both triaxial and plane strain loading conditions. They found that DEM was capable of accurately reproducing the experimental results obtained from steel spheres, for which the inter-particle friction angle was measured to be  $\phi_\mu \approx 5.5^\circ$ . They also noted that the post-yield responses of the DEM specimens was sensitive to the coefficient of friction assumed at the particle-boundary interface along the specimen boundaries. During their triaxial DEM simulations, the variation in the average coordination number within the specimens as well as the angle of mobilized friction  $\phi_m = \sin^{-1} [(\sigma_1 - \sigma_3)/(\sigma_1 + \sigma_3)]$  were recorded as functions of axial strain, where  $\sigma_1$  and  $\sigma_3$  denote axial and lateral stresses, respectively. Following up on this work, O’Sullivan and Cui (2009) performed experimental and DEM triaxial tests on irregular packings of approximately 15 000 spheres, using circumferential periodic boundary conditions for the DEM simulations. They found remarkable agreement between plots of the stress ratio versus axial strain obtained from their DEM simulations and experimental triaxial tests, for monotonic and cyclic loading. Moreover, they recorded the variation in the average contact force and coordination number, the average motion of particles, and the evolution of the fabric tensor for the DEM specimens during initial loading and the unload-reload cycles. From their DEM results, O’Sullivan and Cui (2009) were able to identify the gradual formation of force-chains (identified as larger forces supported by vertically oriented inter-element contacts) as axial strain in the triaxial simulations progressed. During subsequent unload-reload cycles, they found that the reduction in the deviator stress during unloading was accompanied by a redistribution of the relative magnitudes of the inter-particle contact forces, but not in a substantial redistribution of the inter-particle contact network geometry. That is, there was no significant collapse of the “strong force networks” or force-chains that

had developed during initial loading.

Durán et al. (2010) have used three-dimensional DEM simulations to systematically compare the different micromechanical formulations of strain that have been used by various researchers for particulate/granular materials, and to assess their accuracy. While the micromechanical formulation of local stress in a particulate/granular material is well-established, there is no corresponding well-established formulation of local strain. Consider a particle  $A$  in a particulate material and one of its contacting neighbors  $B$ , shown in Figure 2.5. For the contact  $c$  between the particle  $A$  and the particle  $B$ , let the branch vector  $l_i^c$  be the vector from the center of the particle  $A$  to the center of the contacting neighbor, and let the vector  $f_i^c$  be the contact force on the particle  $A$  from the particle  $B$ , as shown in Figure 2.5. Then the average local stress tensor over a representative volume including at

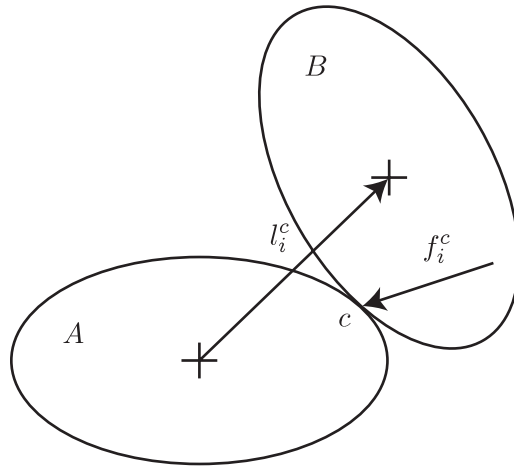


Figure 2.5: Illustration of an inter-particle contact  $c$  between two particles within a particulate material, with the branch vector  $l_i^c$  and the contact force vector  $f_i^c$  shown.

least two particles can be expressed as

$$\sigma_{ij} = \frac{1}{V_\sigma} \sum_c f_i^c l_j^c, \quad (2.24)$$

where the sum is over the contacts between the particles within the representative volume,

and  $V_\sigma$  is the volume of the region containing those particles. Note that the tensor product  $f_i^c l_j^c$  is unique for a given contact  $c$  regardless of which particle plays the role of particle  $A$  in Figure 2.5. For the derivation of equation (2.24), see Nemat-Nasser (2004). Equation (2.24) seems to have been first derived by Love (1927), and it has been rederived many times since. It can be derived either from equilibrium and the Gauss theorem, or by the principle of virtual work. While the use of equation (2.24) is well established in the literature, different formulations for the local strain in a particulate material have been proposed. For example, Bagi (1996) uses the following formulation for the average local strain tensor over a representative volume.

$$\epsilon_{ij} = \frac{1}{V_\epsilon} \sum_e \Delta u_i^e d_j^e, \quad (2.25)$$

where the sum is over the edges of the tetrahedra defining the Delaunay tessellation of the centers of the particles within the representative volume, and  $V_\epsilon$  is the volume of those tetrahedra. For convex particles, the edges  $e$  will include all of the actual contacts, but they will also include so-called “virtual” contacts necessary to complete the Delaunay tessellation. The vector  $d_i^e$  is the so-called complementary area vector of the edge  $e$ , and the vector  $\Delta u_i^e$  is the relative displacement between particles connected by the edge  $e$ . The drawback of Bagi’s strain is that it depends on Delaunay tessellation, which is an  $O(N \log N)$  procedure. Liao et al. (1997) use the following formulation for the average local strain tensor over a representative volume.

$$\epsilon_{ij} = \sum_c \Delta u_i^c l_k^c \Lambda_{jk}^{-1}, \quad (2.26)$$

where the sum is over the contacts between the particles within the representative volume,  $\Lambda_{ij}^{-1}$  is the inverse of the fabric tensor  $\Lambda_{ij} = \sum_c l_i^c l_j^c$  for the representative volume,  $\Delta u_i^c$  is the relative displacement between particles in contact at  $c$ , and  $l_i^c$  is the branch vector. Cambou et al. (2000) use the following formulation for the average local strain tensor over

a representative volume.

$$\epsilon_{ij} = \sum_e \Delta u_i^e l_k^e (\Lambda_{jk}^*)^{-1}, \quad (2.27)$$

where the sum is over the edges of the tetrahedra defining the Delaunay tessellation of the centers of the particles within the representative volume, as in equation (2.25),  $(\Lambda_{ij}^*)^{-1}$  is the inverse of the extended fabric tensor  $\Lambda_{ij}^* = \sum_e l_i^e l_j^e$  for the representative volume,  $\Delta u_i^e$  is the relative displacement between particles connected by the edge  $e$ , and  $l_i^e$  is the branch vector between particles connected by the edge  $e$ . Durán et al. (2010) have shown that, under certain assumptions such as the co-linearity of the complementary area vector  $d_i^e$  and the branch vector  $l_i^e$ , equation (2.27) can be derived from equation (2.25). Durán et al. (2010) compared the predictions of local strain given by equations (2.25) – (2.27) to the macroscopic strain produced during 3-D DEM simulations of isotropic and triaxial loadings. They found that the formulation of strain due to Liao et al. (1997) given by equation (2.26) was unable to reproduce the macroscopic strain. The formulation of strain due to Cambou et al. (2000) given by equation (2.27) performed better, with errors of less than 5%. The formulation of strain due to Bagi (1996) given by equation (2.25) performed best, and was able to reproduce the macroscopic strain within 1% to 2% accuracy. The DEM simulations of Durán et al were performed on a specimen consisting of 250 000 spheres with a log-normal size distribution and volumetric packing density of 0.65.

Kruyt et al. (2010) extend the work of Kruyt and Rothenburg (2002) and Jenkins et al. (2005) to obtain upper and lower bounds for the effective elastic moduli for two-dimensional isotropic assemblies of *rotating* particles. They use the discrete minimum potential energy principle reported by Kruyt and Rothenburg (2004), and in that regard their approach is similar to other variational approaches found in the literature, which we have already critiqued for their general inability to account for the mechanisms or zero-energy strains produced by particle rotation. What is novel, and in our opinion *very important*, in the approach of Kruyt

et al. (2010), however, is the fact that they use *force and moment equilibrium* equations at the microscale to determine the rotation fields for small *sub-assemblies* of elements, which are in turn used in the variational approach at the macroscale. Sub-assemblies of various “orders” are considered, which include progressively more levels of particle neighbors (two-dimensional disks), and these sub-assemblies include what the authors call “near-singular” configurations of disks. Thus, despite the fact that Kruyt et al. (2010) still rely on an energy-based approach to obtain the effective elastic moduli, their approach is capable of capturing zero-energy strains due to particle rotation at the microscale. Kruyt et al. (2010) validate their analytical results with two-dimensional DEM simulations on specimens of 50 000 disks. Chapters 3 and 4 deal with the same issues, but in three-dimensions and using homogenization methods that do not depend on the principle of minimum potential energy. It should be noted that we were unaware of the work of Kruyt et al. (2010) when we wrote (and published) Chapters 3 and 4 [Fleischmann et al. (2013a) and Fleischmann et al. (2013b)] of this thesis. However, we believe that the approach of Kruyt et al. (2010), though at this point still only performed for two-dimensional disks, may eventually provide a reasonable alternative to our approach. At this point, however, essential differences in two and three dimensional particulate material behavior, discussed in Chapter 9 [Fleischmann et al. (2013c)], preclude the possibility of direct *quantitative* comparison of our results with theirs.

It is worth noting that alternatives to the explicit discrete element method have been proposed, for example by Holtzman et al. (2009) and Holtzman et al. (2010), who introduce a variational approach based on the conjugate gradient algorithm that uses the principle of least work or minimum potential energy to find sequential (quasi-static) equilibrium states of a particulate material specimen subjected to incremental displacements of its boundaries. Their method avoids the issue of the critical time step, which can make DEM simulations time consuming (as in any explicit time integration method). Of course, since their method is implicit, it is subject to the well-known disadvantages of implicit methods (such as ill-

conditioning). Holtzman et al. (2009) use their method to determine the shear and bulk moduli of 3-D specimens of approximately 5 000 spheres. Their model's prediction of the bulk modulus compares favorably with experimental data for glass beads, but their prediction of the shear modulus does not. This is unfortunately the common shortcoming of most theoretical treatments of particulate materials in the elastic range. We conjecture that the failure of the variational model to accurately predict the shear modulus is due to the fact that, since this model is based on the minimization of virtual work, it may not properly account for zero-energy rotations in the elastic range. The significance of zero-energy rotations in the elastic range is discussed in detail in Chapter 4 of this thesis.

DEM can be used in some novel and unexpected ways, such as in Silbert (2010), where the author uses DEM to measure the Green's function response to local force perturbations of regular packings of frictionless spheres (in the elastic range). However, DEM is most often employed to simulate the loading conditions encountered in the field of geomechanics, and its use is increasing among researchers in that field (O'Sullivan, 2011). A thorough (and useful) study of the macro and micro behavior of particulate materials under a variety of loading conditions (conventional triaxial, plane strain, and direct shear) typically encountered in the field of geomechanics, employing 3-D DEM simulations on specimens of over 15 000 particles, is performed in the 511-page doctoral dissertation of Zhao (2009).



## Chapter 3

# Direct Micromechanics Derivation and DEM Confirmation of the Elastic Moduli of Isotropic Particulate Materials, Part I: No Particle Rotation <sup>1</sup>

### 3.1 Abstract

We derive the macroscopic elastic moduli of a statistically isotropic particulate aggregate material via the homogenization methods of Voigt (1928) (kinematic hypothesis), Reuss (1929) (static hypothesis), and Hershey (1954) and Kröner (1958) (self-consistent hypothesis), originally developed to treat crystalline materials, from the directionally-averaged elastic moduli of three regular cubic packings of uniform spheres. We determine analytical expressions for these macroscopic elastic moduli in terms of the (linearized) elastic inter-particle contact stiffnesses on the microscale under the three homogenization assumptions for the three cu-

---

<sup>1</sup>This chapter closely follows Fleischmann et al. (2013a).

bic packings (simple, body-centered, and face-centered), assuming no particle rotation. To test these results and those in the literature, we perform numerical simulations using the discrete element method (DEM) to measure the overall elastic moduli of large samples of randomly packed uniform spheres with constant normal and tangential contact stiffnesses (linear spring model). The beauty of DEM is that simulations can be run with particle rotation either prohibited or unrestrained. In this first part of our two-part series of papers, we perform DEM simulations with particle rotation prohibited, and we compare these results with our theoretical results that assumed no particle rotation. We show that the self-consistent homogenization assumption applied to the locally body-centered cubic (BCC) packing most accurately predicts the measured values of the overall elastic moduli obtained from the DEM simulations, in particular Poisson's ratio. Our new analytical self-consistent results lead to significantly better predictions of Poisson's ratio than all prior published theoretical results. Moreover, our results are based on a direct micromechanics analysis of specific geometrical packings of uniform spheres, in contrast to all prior theoretical analyses, which were based on difficult-to-verify hypotheses involving overall inter-particle contact distributions. We continue the analysis begun in this first part for the case of unrestrained particle rotation in Part II, Chapter 4 [Fleischmann et al. (2013b)].

## 3.2 Introduction

We derive the overall elastic moduli for a statistically isotropic particulate aggregate material consisting of randomly oriented arrangements of uniform spheres. At the points of contact between these spheres, we assume that there are both normal and tangential contact stiffnesses, the values for which can be obtained from Hertz-Mindlin contact theory. Moreover, we assume these contact stiffnesses are constant within the range of deformation to which the linear elastic moduli apply. Our approach employs the classical homogenization

methods originally developed to determine theoretically the elastic moduli for a statistically isotropic aggregate material composed of randomly oriented locally cubic crystalline material grains, such as a metal. These homogenization methods were derived by Voigt (1928), Reuss (1929), and Hershey (1954) and Kröner (1958), introducing what are sometimes referred to as the kinematic, static, and self-consistent homogenization hypotheses, respectively. One novel aspect of our approach is that we apply these methods to determine the overall tensor of elastic moduli  $\bar{\mathbf{C}}$  for a statistically isotropic *particulate* material, such as sand or powder, based on the local tensors of elastic moduli  $\mathbf{C}$  for three cubic packings (simple, body-centered, and face-centered) of uniform spheres. In this way, we obtain relationships between the elastic moduli of a statistically isotropic particulate material on the macroscale, and the (linearized) elastic inter-particle contact stiffnesses on the microscale, under each of these three homogenization assumptions and for each of the three cubic packings.

Our results based on the Voigt hypothesis for all three local packings reproduce the results obtained by Walton (1987) and Chang et al. (1995) for an isotropic particulate material under their kinematic hypothesis (analogous to our Voigt hypothesis, but with an assumed uniform distribution of inter-particle contacts, and not based on any specific local packing geometries). Our results based on the Reuss hypothesis also reproduce those obtained by Chang et al. (1995) under their static hypothesis (analogous to our Reuss hypothesis, but again with an assumed uniform distribution of inter-particle contact forces) *for one local packing geometry only*, specifically simple cubic (SC). Our approach also allows us to obtain new results based on the Reuss hypothesis for the face-centered cubic (FCC) and body centered cubic (BCC) local packing geometries, as well as for all three cubic packings via the self-consistent hypothesis of Hershey and Kröner. Moreover, our results are based on direct micromechanical analyses of specific local packing geometries, specifically in that we compute the local tensors of elastic moduli  $C_{ijkl}$  (for the Voigt approach) and compliances  $D_{ijkl}$  (for the Reuss approach) for each local packing geometry, and our assumptions regarding these

microstructural geometries are very clear and specific. This is in contrast to prior researchers who based their theoretical analyses on hypotheses involving overall inter-particle contact distributions assumed to be isotropic in an absolute, rather than a statistical, sense.

After obtaining closed-form analytical expressions for the overall elastic moduli (bulk modulus and Poisson's ratio) of the particulate material in terms of the normal and tangential stiffnesses of the contacts between the particles in the material, we perform numerical simulations using the discrete element method (DEM) to measure the overall elastic moduli for specimens of randomly packed uniform spheres with constant normal and tangential contact stiffnesses (linear spring model), and we compare these results with the theoretical results obtained under the three homogenization assumptions for each of the three cubic packing geometries. In this first part of our two-part series of papers, we perform DEM simulations with particle rotation prohibited, and we compare these results with our theoretical results assuming no particle rotation. We show that our new theoretical results from the self-consistent hypothesis applied to the BCC packing assuming no particle rotation agree most closely with DEM simulations in which particle rotation is prohibited.

We find that, when compared to the measured values of the overall elastic moduli obtained from DEM simulations on specimens of randomly packed uniform spheres, our self-consistent results from the body-centered cubic packing predict values of the elastic moduli, and in particular Poisson's ratio, that are significantly more accurate for the case of no particle rotation than those currently in the literature. We continue the analysis begun in this first part for the case of unrestrained particle rotation in the second part of this two-part study, Chapter 4 [Fleischmann et al. (2013b)], to which we refer simply as Part II in the sequel.

### 3.3 Overall Elastic Moduli for Regular Arrays of Uniform Spheres

For a material with cubic symmetry, the fourth-order tensor of second-order elastic moduli  $C_{ijkl}$  can be written with respect to an arbitrary rectangular Cartesian basis as

$$C_{ijkl} = C_2\delta_{ij}\delta_{kl} + 2C_3I_{ijkl} + (C_1 - C_2 - 2C_3)A_{ijkl}, \quad (3.1)$$

where

$$C_1 = C_{1111} = C_{2222} = C_{3333}, \quad (3.2)$$

$$C_2 = C_{1122} = C_{1133} = C_{2233}, \quad (3.3)$$

$$C_3 = C_{1212} = C_{1313} = C_{2323}, \quad (3.4)$$

are the three independent cubic elastic moduli,  $I_{ijkl}$  is the symmetric fourth-order unit tensor

$$I_{ijkl} = \frac{1}{2}(\delta_{ik}\delta_{jl} + \delta_{il}\delta_{jk}), \quad (3.5)$$

and

$$A_{ijkl} = a_i a_j a_k a_l + b_i b_j b_k b_l + c_i c_j c_k c_l, \quad (3.6)$$

where the vectors  $a_i$ ,  $b_i$ , and  $c_i$  are the orthogonal unit vectors along the principal cubic axes of the material.

Deresiewicz (1958a) reported some of the earliest results concerning the micromechanics of a particulate material. These results were obtained by Duffy and Mindlin (1957) and Deresiewicz (1958b), in which Hertz-Mindlin contact theory was used to analyze both face-centered cubic and simple cubic regular arrays of uniform spheres, shown in Figure 3.1.

According to Deresiewicz, if two like spheres of radius  $R$  are compressed statically by a force

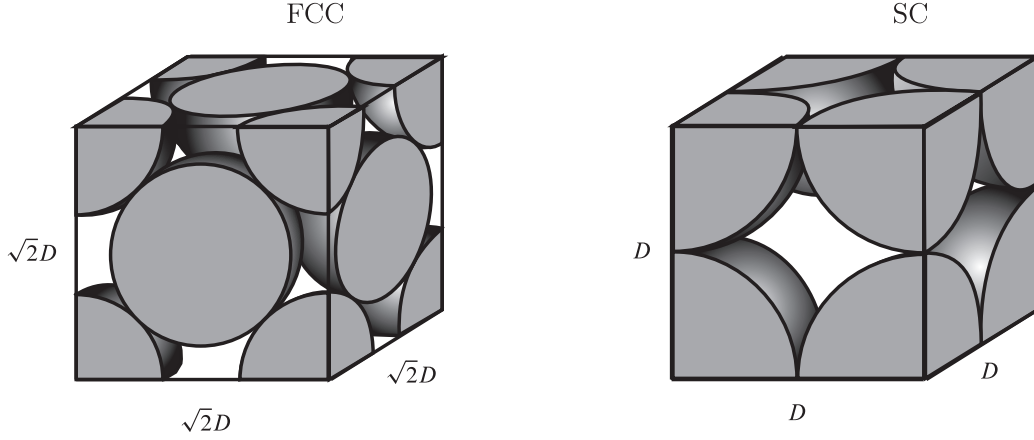


Figure 3.1: Elementary cells of face-centered cubic (left) and simple cubic (right) regular arrays of uniform spheres, where  $D$  is the diameter of the spheres.

$F_n$  directed along their line of centers, then the spheres contact one another on a planar circular area of radius  $q$ , where

$$q = \left( \frac{3(1-\nu^2)}{4E} F_n R \right)^{1/3}, \quad (3.7)$$

where  $E$  and  $\nu$  are the elastic Young's modulus and Poisson's ratio for the material constituting the spheres. According to Deresiewicz, the initial normal and tangential contact stiffnesses between the spheres are then given by

$$K_n = \frac{2\mu q}{1-\nu}, \quad K_t = \frac{4\mu q}{2-\nu}, \quad (3.8)$$

where  $\mu$  is the elastic shear modulus of the sphere material, and the normal and tangential contact forces are given by  $F_n = K_n \delta_n$  and  $F_t = K_t \delta_t$ , where  $\delta_n$  and  $\delta_t$  are normal and tangential contact displacements, respectively.

Note that Hertz-Mindlin contact theory is nonlinear, because the normal and tangential inter-particle contact stiffnesses  $K_n$  and  $K_t$  given in equation (3.8) depend on the normal

contact force  $F_n$  via equation (3.7). However, for the purpose of analyzing the linear elastic behavior of a statistically isotropic aggregate of uniform spheres, we assume these contact stiffnesses are constant within the range of deformation to which the linear elastic moduli apply, about an initial nonzero isotropic compressive stress. In the following subsections, we linearize the Hertz-Mindlin contact law to obtain cubic elastic moduli for three specific arrays of uniform spheres: face-centered cubic (FCC), simple cubic (SC), and body-centered cubic (BCC).

### 3.3.1 Face-Centered Cubic (FCC) Array of Uniform Spheres

Given a regular face-centered cubic array of uniform spheres subjected to an initial isotropic compressive stress  $\sigma_0$  and having the incremental constitutive relation

$$d\sigma_{ij} = C_{ijkl}d\epsilon_{kl}, \quad (3.9)$$

Duffy and Mindlin (1957) obtained the following results:

$$C_1 = \frac{4 - 3\nu}{2 - \nu} \left[ \frac{3\mu^2\sigma_0}{2(1 - \nu)^2} \right]^{1/3}, \quad C_2 = \frac{\nu}{2(4 - 3\nu)}C_1, \quad C_3 = \frac{1}{2}C_1, \quad (3.10)$$

where the cubic elastic moduli  $C_1$ ,  $C_2$ , and  $C_3$  are defined by equations (3.2), (3.3), and (3.4), and  $\mu$  and  $\nu$  are the shear modulus and Poisson's ratio of the sphere material. The initial isotropic compressive stress  $\sigma_0$  gives rise to an initial normal contact force  $F_n = F_0 = \sqrt{2}R^2\sigma_0$  between the spheres. From equation (3.7), this produces an initial contact radius  $q_0$ . This contact radius can be used to linearize the force-displacement laws at the contacts between the spheres by providing constant values for  $K_n$  and  $K_t$ . Solving equations (3.8) with  $q = q_0$

and (3.10) simultaneously for  $C_1$ ,  $C_2$ , and  $C_3$  in terms of  $K_n$ ,  $K_t$ , and  $R$ , we obtain

$$C_1 = \frac{1}{\sqrt{2}R}(K_n + K_t), \quad C_2 = \frac{1}{2\sqrt{2}R}(K_n - K_t), \quad C_3 = \frac{1}{2}C_1, \quad (3.11)$$

for the three independent cubic elastic moduli for a regular face-centered cubic (FCC) array of uniform spheres of radius  $R$  with normal and tangential contact stiffnesses  $K_n$  and  $K_t$ , respectively.

### 3.3.2 Simple Cubic (SC) Array of Uniform Spheres

Given a regular simple cubic array of uniform spheres subjected to an initial isotropic compressive stress  $\sigma_0$ , Deresiewicz (1958b) obtained the following results:

$$d\epsilon_{ii} = 2RN_i d\sigma_{ii}, \quad i = 1, 2, 3 \text{ (no sum)}, \quad (3.12)$$

$$d\epsilon_{ij} = R \left[ \left( T_i \frac{\sigma_{ij}}{\tau_{jk}} \right) d\tau_{jk} + \left( T_j \frac{\sigma_{ji}}{\tau_{ik}} \right) d\tau_{ik} \right], \quad i, j, k = 1, 2, 3 \text{ (no sum)},$$

$$i \neq j \neq k, \quad (3.13)$$

where  $N_i$  and  $T_i$  are the normal and tangential compliances relative to the plane whose normal is parallel to the  $i$  direction, and  $\tau_{jk} = (\sigma_{ij}^2 + \sigma_{ik}^2)^{1/2}$  with  $i \neq j \neq k$  denotes the resultant shear stress on the plane whose normal is parallel to the  $i$  direction. To linearize equation (3.13), we consider only small variations in shear stress from the initial state of zero shear stress, so that  $\sigma_{ij} = d\sigma_{ij}$  and  $\tau_{jk} = d\tau_{jk}$ . Furthermore, we assume that the contact compliances  $N_i = 1/K_n$  and  $T_i = 1/K_t$  are constant, with  $K_n$  and  $K_t$  given by equations (3.8) with  $q = q_0$ , where  $q_0$  is obtained from equation (3.7) with the initial normal contact

force given by  $F_n = F_0 = 4R^2\sigma_0$ . Equations (3.12) and (3.13) then become

$$d\epsilon_{ii} = 2R\frac{1}{K_n}d\sigma_{ii}, \quad d\epsilon_{ij} = 2R\frac{1}{K_t}d\sigma_{ij}, \quad i, j = 1, 2, 3 \text{ (no sum)},$$

$$i \neq j. \tag{3.14}$$

Given the incremental constitutive relation (3.9) with the cubic elastic moduli  $C_1$ ,  $C_2$ , and  $C_3$  defined by equations (3.2), (3.3), and (3.4) as before, we obtain

$$C_1 = \frac{1}{2R}K_n, \quad C_2 = 0, \quad C_3 = \frac{1}{4R}K_t, \tag{3.15}$$

for the three independent cubic elastic moduli for a regular simple cubic (SC) array of uniform spheres of radius  $R$  with normal and tangential contact stiffnesses  $K_n$  and  $K_t$ , respectively.

### 3.3.3 Body-Centered Cubic (BCC) Array of Uniform Spheres

The cubic elastic moduli given in equations (3.11) for face-centered cubic arrays of uniform spheres and in equations (3.15) for simple cubic arrays of uniform spheres can also be obtained more simply by assuming constant normal and tangential contact stiffnesses between the spheres from the start, and calculating the deformation of elementary cells of the FCC and SC lattices subjected to a general state of stress. In this way, we obtain

$$C_1 = \frac{1}{2\sqrt{3}R}(K_n + 2K_t), \quad C_2 = \frac{1}{2\sqrt{3}R}(K_n - K_t), \quad C_3 = \frac{1}{2}(C_1 + C_2), \tag{3.16}$$

for the three independent cubic elastic moduli for a regular body-centered cubic (BCC) array of uniform spheres of radius  $R$  with normal and tangential contact stiffnesses  $K_n$  and  $K_t$ , respectively, as shown in Figure 3.2.

See A for derivations of equations (3.11), (3.15), and (3.16) using the normal and tan-

gential linear spring contact model illustrated in Figure 3.2 (right).

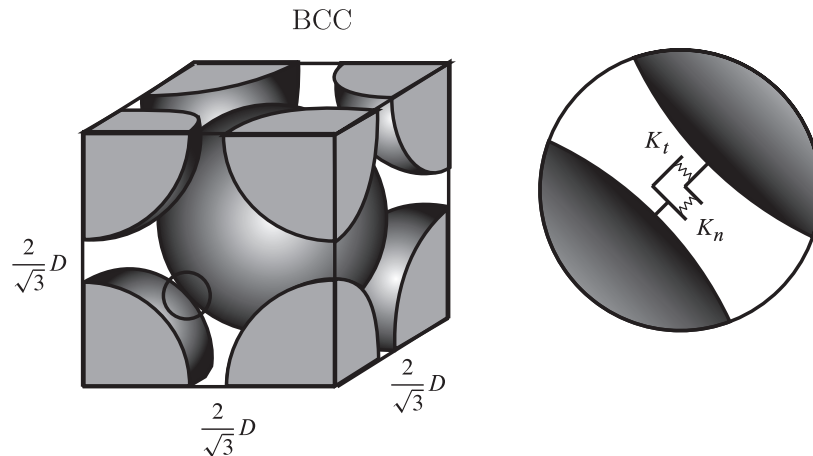


Figure 3.2: Elementary cell of a body-centered cubic regular array of uniform spheres with constant normal and tangential contact stiffnesses  $K_n$  and  $K_t$ , where  $D$  is the diameter of the spheres.

### 3.4 Isotropic Effective Elastic Moduli

In this section, we apply the kinematic, static, and self-consistent homogenization hypotheses of Voigt (1928), Reuss (1929), and Hershey (1954) and Kröner (1958) to determine the overall tensor of elastic moduli  $\bar{\mathbf{C}}$  for a statistically isotropic particulate material based on the local tensors of elastic moduli  $\mathbf{C}$  for the three cubic packings considered in Section 3.3 (obtained either by linearizing the results of Duffy and Mindlin (1957) and Deresiewicz (1958b), or by applying the method of A). Thus the overall tensor of elastic moduli we obtain in e.g. the case of FCC packings would be exact if the particulate material consisted of many randomly-oriented subportions, each of which contained particles only in FCC packings; similar statements apply to the other two cubic packings treated. This is illustrated in Figure 3.3. The results would therefore be expected to be accurate and useful practically if in an actual granular material, one of these three cubic packing types predominates. Also,

as we will see, multiple macroscopic results turn out to be identical for all three packing geometries.

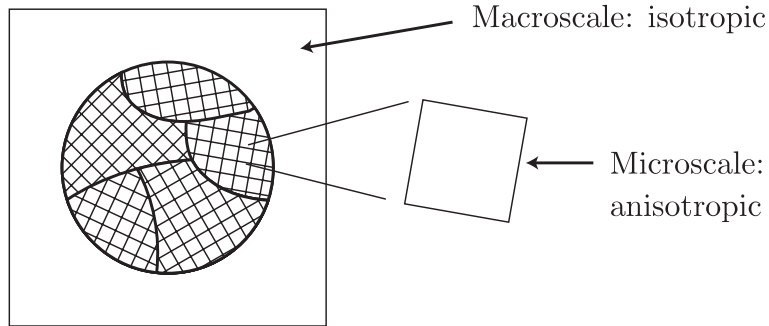


Figure 3.3: Assumption of the homogenization process: the statistically isotropic particulate material consists of many randomly-oriented subportions, each of which contains particles in one of the three cubic packings.

### 3.4.1 Voigt Hypothesis

Voigt (1928) assumed that when an aggregate material is subjected to a state of uniform strain, the individual components of the aggregate will be in the same strain state. It follows that the isotropic fourth-order tensor of effective elastic moduli  $\bar{C}_{ijkl}$  of an isotropic aggregate is simply the orientational average of the elastic modulus tensor of the components:

$$\bar{C}_{ijkl} = \frac{1}{8\pi^2} \int_{\Omega} C_{ijkl} d\Omega, \quad (3.17)$$

where  $d\Omega = \sin\theta d\varphi d\theta d\psi$  is the differential solid angle of the unit sphere  $\Omega$ , and  $\varphi$ ,  $\theta$ , and  $\psi$  are the Euler angles (e.g., Lubarda, 2002). Equation (3.17) gives, upon integration,

$$\bar{C}_{ijkl} = \frac{1}{5}(C_1 + 4C_2 - 2C_3)\delta_{ij}\delta_{kl} + \frac{2}{5}(C_1 - C_2 + 3C_3)I_{ijkl}, \quad (3.18)$$

where  $C_1$ ,  $C_2$ , and  $C_3$  are the cubic elastic moduli for an individual component, and  $I_{ijkl}$  is the symmetric fourth-order unit tensor defined in equation (3.5). If we define the effective

isotropic elastic moduli  $\bar{C}_2 = \bar{C}_{1122}$  and  $\bar{C}_3 = \bar{C}_{1212}$ , then equation (3.18) implies that

$$\bar{C}_2 = \frac{1}{5}C_1 + \frac{4}{5}C_2 - \frac{2}{5}C_3, \quad (3.19)$$

$$\bar{C}_3 = \frac{1}{5}C_1 - \frac{1}{5}C_2 + \frac{3}{5}C_3, \quad (3.20)$$

which are the well-known Voigt estimates of the effective elastic moduli for an isotropic aggregate of cubic crystals (e.g., Hearmon, 1961, Lubarda, 1997).

Although equations (3.19) and (3.20) were originally derived for isotropic polycrystalline materials, the same principle applies to an isotropic particulate material, provided that the packing of the particles can be considered locally cubic and that the applied loading is of a type that keeps all spheres in contact. We will explore the justification of this assumption in a later section. If we employ the cubic elastic moduli  $C_1$ ,  $C_2$ , and  $C_3$  obtained in Section 3.3, given by equations (3.11), (3.15), and (3.16) for the FCC, SC, and BCC packings, respectively, in equations (3.19) and (3.20), we obtain identical results for each of the three local cubic packings:

$$\text{FCC, BCC, SC: } \bar{C}_2 = \frac{\beta D^2}{15} K_n (1 - \alpha), \quad \bar{C}_3 = \frac{\beta D^2}{30} K_n (2 + 3\alpha), \quad (3.21)$$

where  $\alpha = K_t/K_n$  is the ratio of the tangential to the normal inter-particle contact stiffness,  $D$  is the diameter of the spheres, and  $\beta$  is the number of contacts per unit volume in the particulate aggregate, which for the FCC, BCC, and SC regular arrays of uniform spheres is

$$\beta_{\text{FCC}} = \frac{6\sqrt{2}}{D^3}, \quad \beta_{\text{BCC}} = \frac{3\sqrt{3}}{D^3}, \quad \text{and} \quad \beta_{\text{SC}} = \frac{3}{D^3}. \quad (3.22)$$

The isotropic effective elastic moduli  $\bar{C}_2$  and  $\bar{C}_3$  are related to the more familiar bulk

modulus  $\bar{\kappa}$  and Poisson's ratio  $\bar{\nu}$  of the particulate material on the macroscale as

$$\bar{\kappa} = \frac{1}{3} (3\bar{C}_2 + 2\bar{C}_3), \quad \bar{\nu} = \frac{\bar{C}_2}{2(\bar{C}_2 + \bar{C}_3)}. \quad (3.23)$$

From equations (3.21) and (3.23), we obtain the following relations between the normal and tangential inter-particle contact stiffnesses  $K_n$  and  $K_t$  (and  $\alpha = K_t/K_n$ ) and the parameter  $\beta$  on the microscale, and the overall elastic moduli  $\bar{\kappa}$  and  $\bar{\nu}$  of the particulate material on the macroscale, under the Voigt hypothesis for all three local cubic packings:

$$\text{FCC, BCC, SC: } \bar{\kappa} = \frac{\beta D^2}{9} K_n, \quad \bar{\nu} = \frac{1 - \alpha}{4 + \alpha}. \quad (3.24)$$

It is noteworthy that the relations expressed in equations (3.21), and equivalently in equations (3.24), do not depend on the particular packing (FCC, BCC, or SC) used to obtain the cubic elastic moduli  $C_1$ ,  $C_2$ , and  $C_3$  beyond the single parameter  $\beta$ . Moreover,  $\beta$  only influences the bulk modulus  $\bar{\kappa}$ , and not Poisson's ratio  $\bar{\nu}$ , which is (quite surprisingly) completely independent of the geometry of the local packing.

It is also noteworthy that the relations expressed in equations (3.21) and (3.24) are identical to those obtained by Walton (1987) and Chang et al. (1995), under what they called the kinematic hypothesis. In the results of Walton (1987) and Chang et al. (1995), equations (3.21) and (3.24) were derived for any value of the parameter  $\beta$  (and so presumably for any local packing geometry) based on certain assumptions regarding the form of the (globally isotropic) inter-particle contact distribution. Our approach differs substantially from theirs, in that we have performed direct micromechanics analyses of three specific local geometrical arrangements of spheres, while in their approach the form of the overall isotropic distribution of inter-particle contacts is assumed *a priori*, and it has no direct link to any particular local packing geometry. The difference in these approaches will become more clear when we consider homogenization under the Reuss hypothesis in the next section.

Our choice of using the bulk modulus  $\bar{\kappa}$  and Poisson's ratio  $\bar{\nu}$  to characterize the isotropic tensor of effective elastic moduli  $\bar{C}_{ijkl}$  (rather than, for example, the bulk modulus  $\bar{\kappa}$  and shear modulus  $\bar{\mu}$ ), here and in our subsequent analyses, was motivated both “a priori” by a desire to compare our results with other results in the literature such as Chang et al. (1995), and “a posteriori” because of the convenient (and somewhat surprising) way in which  $\bar{\kappa}$  and  $\bar{\nu}$  “split” the microscale variables:  $\bar{\kappa}$  depends only on  $\beta$ ,  $D$ , and  $K_n$  (and not on  $K_t$ ), and  $\bar{\nu}$  depends only on  $\alpha = K_t/K_n$  (and not on  $\beta$  or  $D$ ).

### 3.4.2 Reuss Hypothesis

If we assume that when an aggregate material is subjected to a state of uniform *stress* the individual components of the aggregate will be in the same *stress* state, we obtain different estimates of the effective isotropic elastic moduli for the aggregate material. This approach was taken by Reuss (1929). It follows that the effective elastic compliances of an isotropic aggregate are the orientational averages of the elastic compliances of the components:

$$\bar{D}_{ijkl} = \frac{1}{8\pi^2} \int_{\Omega} D_{ijkl} d\Omega, \quad (3.25)$$

where  $D_{ijkl}$  is the fourth-order tensor of elastic compliances for an individual component. For a material with cubic symmetry having  $D_1 = D_{1111}$ ,  $D_2 = D_{1122}$ , and  $D_3 = D_{1212}$ ,  $D_{ijkl}$  can be written with respect to an arbitrary rectangular Cartesian basis in the same form as  $C_{ijkl}$  in equation (3.1), except with  $D$ 's replacing the  $C$ 's. Thus, equation (3.25) gives, upon integration, results of the same form as those given in equations (3.18), (3.19), and (3.20), except again with  $D$ 's replacing the  $C$ 's. From these results and the relationships between the cubic elastic moduli  $C_1$ ,  $C_2$ , and  $C_3$  and the cubic elastic compliances  $D_1$ ,  $D_2$ , and  $D_3$ ,

it follows that

$$\bar{C}_2 = \frac{(C_1 - C_2)(C_1 + 2C_2) + 2C_3(3C_2 - C_1)}{3C_1 - 3C_2 + 4C_3}, \quad (3.26)$$

$$\bar{C}_3 = \frac{5C_3(C_1 - C_2)}{3C_1 - 3C_2 + 4C_3}, \quad (3.27)$$

which are the well-known Reuss estimates of the effective elastic moduli for an isotropic aggregate of cubic crystals (e.g., Hearmon, 1961, Lubarda, 1997).

Again, we employ the cubic elastic moduli  $C_1$ ,  $C_2$ , and  $C_3$  obtained in Section 3.3, equations (3.11), (3.15), and (3.16) for the FCC, SC, and BCC packings, respectively, in equations (3.26) and (3.27). Unlike the case of the Voigt hypothesis just treated, however, we do not obtain the same estimates for all three local cubic packings. For the locally FCC, BCC, and SC packings, we obtain:

$$\text{FCC: } \bar{C}_2 = \frac{\beta D^2}{6} K_n \frac{(1 - \alpha)(3 + 5\alpha)}{(7 + 13\alpha)}, \quad \bar{C}_3 = \frac{5\beta D^2}{12} K_n \frac{(1 + \alpha)(1 + 3\alpha)}{(7 + 13\alpha)}, \quad (3.28)$$

$$\text{BCC: } \bar{C}_2 = \frac{\beta D^2}{9} K_n \frac{(1 - \alpha)(4 + 5\alpha)}{(4 + 11\alpha)}, \quad \bar{C}_3 = \frac{5\beta D^2}{6} K_n \frac{\alpha(2 + \alpha)}{(4 + 11\alpha)}, \quad (3.29)$$

$$\text{SC: } \bar{C}_2 = \frac{\beta D^2}{3} K_n \left( \frac{1 - \alpha}{3 + 2\alpha} \right), \quad \bar{C}_3 = \frac{\beta D^2}{6} K_n \left( \frac{5\alpha}{3 + 2\alpha} \right). \quad (3.30)$$

From equations (3.23), (3.28), (3.29), and (3.30), we obtain the following relations between the normal and tangential inter-particle contact stiffnesses  $K_n$  and  $K_t$  (and  $\alpha = K_t/K_n$ ) and the parameter  $\beta$  on the microscale, and the overall elastic moduli  $\bar{\kappa}$  and  $\bar{\nu}$  of the particulate material on the macroscale, under the Reuss hypothesis for the locally FCC, BCC, and SC

packings:

$$\text{FCC: } \bar{\kappa} = \frac{\beta D^2}{9} K_n, \quad \bar{\nu} = \frac{3 + 2\alpha - 5\alpha^2}{11 + 24\alpha + 5\alpha^2}, \quad (3.31)$$

$$\text{BCC: } \bar{\kappa} = \frac{\beta D^2}{9} K_n, \quad \bar{\nu} = \frac{4 + \alpha - 5\alpha^2}{8 + 32\alpha + 5\alpha^2}, \quad (3.32)$$

$$\text{SC: } \bar{\kappa} = \frac{\beta D^2}{9} K_n, \quad \bar{\nu} = \frac{1 - \alpha}{2 + 3\alpha}. \quad (3.33)$$

It is noteworthy that the relationship between  $K_n$  and the bulk modulus  $\bar{\kappa}$  expressed in all three equations (3.31), (3.32), and (3.33), derived under the Reuss hypothesis, is the same as that expressed in equation (3.24), where it was derived under the Voigt hypothesis. This is because  $\bar{\kappa} = (1/9)\bar{C}_{ijjj} = (1/9)C_{ijjj}$  is actually a scalar invariant of equation (3.1), and hence it is independent of the orientation of the principal axes in equation (3.6).

It is also noteworthy that the relations expressed in equations (3.30) and (3.33) are identical to those obtained by Chang et al. (1995) for an isotropic particulate material having what they claimed to be an arbitrary local packing (e.g., for any value of  $\beta$ ), under what they called the static hypothesis. Unlike Chang et al. (1995), however, under the Reuss hypothesis we obtain a different relation between  $\alpha$  and  $\bar{\nu}$  for each of the three local cubic packings. All three relations between  $\alpha$  and  $\bar{\nu}$  obtained under the Reuss hypothesis are shown graphically in Figure 3.4, along with the relation given by equation (3.24) for all three local cubic packings under the Voigt hypothesis. We note that, although the results of Chang et al. (1995) under the static hypothesis considered as an *upper bound* on Poisson's ratio are not contradicted by our analysis in this section, our results in this section clearly show that the results of Chang et al. (1995) are not valid for a globally isotropic particulate material with an arbitrary local packing geometry. This demonstrates the value of a direct micromechanics analysis of specific local packing geometries, such as we have performed. In fact, if particle rotation is correctly accounted for, the results of Chang et al. (1995) and the results of this section for the SC local packing fail to provide an upper bound on Poisson's

ratio, as we will show in Part II by a direct micromechanics analysis of particle rotations and by discrete element simulations with unrestrained particle rotation.

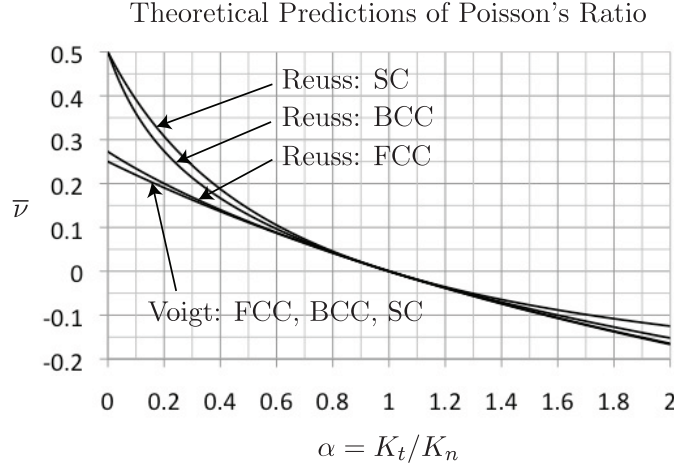


Figure 3.4: Macroscopic Poisson's ratio  $\bar{\nu}$  as a function of  $\alpha = K_t/K_n$  for a statistically isotropic particulate aggregate material derived under the Voigt and Reuss hypotheses using locally cubic elastic moduli obtained from FCC, BCC, and SC regular arrays of uniform spheres.

### 3.4.3 Self-Consistent Hypothesis

Yet another approach to finding the effective elastic moduli for a statistically isotropic aggregate of non-isotropic components with local cubic symmetry was taken by Hershey (1954) and Kröner (1958). This approach is generally called the self-consistent method; it assumes the strain in a single component of an aggregate can be written as

$$\epsilon_{ij}^0 = \mathcal{H}_{ijkl}\epsilon_{kl}, \quad (3.34)$$

where  $\epsilon_{ij}^0$  is the (local) strain in the component and  $\epsilon_{ij}$  is the far field uniform strain in the aggregate. Note that the Voigt method assumes  $\epsilon_{ij}^0 = \epsilon_{ij}$ . For the self-consistent method,

the fourth-order tensor  $\mathcal{H}_{ijkl}$  is given by (e.g., Lubarda, 1997)

$$\mathcal{H}_{ijkl} = I_{ijkl} + h(\delta_{ij}\delta_{kl} + 2I_{ijkl} - 5A_{ijkl}), \quad (3.35)$$

where

$$h = \frac{(C_1 + 2C_2 + 6\bar{C}_3)(C_1 - C_2 - 2\bar{C}_3)}{3 \left[ 8\bar{C}_3^2 + 9C_1\bar{C}_3 + (C_1 - C_2)(C_1 + 2C_2) \right]}, \quad (3.36)$$

and  $I_{ijkl}$  and  $A_{ijkl}$  are given by equations (3.5) and (3.6), respectively. Thus, we now have

$$\bar{C}_{ijkl} = \frac{1}{8\pi^2} \int_{\Omega} \hat{C}_{ijkl} d\Omega, \quad (3.37)$$

where  $\hat{C}_{ijkl} = C_{ijmn}\mathcal{H}_{mnkl}$ . By equating the linear invariants  $\bar{C}_{iijj} = \hat{C}_{iijj}$  and  $\bar{C}_{ijij} = \hat{C}_{ijij}$ , one obtains the following equations for  $\bar{C}_2$  and  $\bar{C}_3$ :

$$3\bar{C}_2 + 2\bar{C}_3 = C_1 + 2C_2, \quad (3.38)$$

$$8\bar{C}_3^3 + (5C_1 + 4C_2)\bar{C}_3^2 - C_3(7C_1 - 4C_2)\bar{C}_3 - C_3(C_1 - C_2)(C_1 + 2C_2) = 0. \quad (3.39)$$

The cubic expression for  $\bar{C}_3$  given by equation (3.39) was originally derived by Kröner (1958).

The advantage of the self-consistent method is that if we instead assume that the *stress* in a single component of the aggregate can be written as

$$\sigma_{ij}^0 = \mathcal{G}_{ijkl}\sigma_{kl}, \quad (3.40)$$

for an appropriately defined fourth-order tensor  $\mathcal{G}_{ijkl}$ , where  $\sigma_{ij}^0$  is the local stress in the component and  $\sigma_{ij}$  is the far field uniform stress in the aggregate, and we follow a similar analysis by defining  $\hat{D}_{ijkl} = D_{ijmn}\mathcal{G}_{mnkl}$  and equating the linear invariants  $\bar{D}_{iijj} = \hat{D}_{iijj}$  and  $\bar{D}_{ijij} = \hat{D}_{ijij}$ , we obtain equations for  $\bar{D}_2$  and  $\bar{D}_3$  that are consistent with the equations

for  $\bar{C}_2$  and  $\bar{C}_3$  given by equations (3.38) and (3.39); see, e.g., Lubarda (1997). This is in contrast to the method employed by Reuss, which assumes  $\sigma_{ij}^0 = \sigma_{ij}$ .

As in Sections 3.4.1 and 3.4.2, we can use equations (3.38) and (3.39) with the cubic elastic moduli  $C_1$ ,  $C_2$ , and  $C_3$  obtained in Section 3.3 to obtain  $\bar{C}_2$  and  $\bar{C}_3$  under the self-consistent hypothesis. As in Section 3.4.2, these depend on the geometry of the local packing. Employing equations (3.11), (3.16), and (3.15) for the locally FCC, BCC, and SC packings, respectively, in equations (3.23), (3.38) and (3.39), we obtain the following relations between the normal and tangential inter-particle contact stiffnesses  $K_n$  and  $K_t$  (and  $\alpha = K_t/K_n$ ) and the parameter  $\beta$  on the microscale and the overall elastic moduli  $\bar{\kappa}$  and  $\bar{\nu}$  of the particulate material on the macroscale under the self-consistent hypothesis:

$$\text{FCC: } \bar{\kappa} = \frac{\beta D^2}{9} K_n, \quad \alpha = \frac{2 + 5\bar{\nu} - 5\bar{\nu}^2 - 8\bar{\nu}^3 - \sqrt{36 - 144\bar{\nu} + 88\bar{\nu}^2 + 280\bar{\nu}^3 - 291\bar{\nu}^4 - 134\bar{\nu}^5 + 169\bar{\nu}^6}}{-4 - 3\bar{\nu} + 6\bar{\nu}^2 + 5\bar{\nu}^3}, \quad (3.41)$$

$$\text{BCC: } \bar{\kappa} = \frac{\beta D^2}{9} K_n, \quad \alpha = \frac{11 + 30\bar{\nu} - 27\bar{\nu}^2 - 46\bar{\nu}^3 - 3\sqrt{81 - 228\bar{\nu} + 202\bar{\nu}^2 + 352\bar{\nu}^3 - 735\bar{\nu}^4 - 92\bar{\nu}^5 + 484\bar{\nu}^6}}{4(-4 - 3\bar{\nu} + 6\bar{\nu}^2 + 5\bar{\nu}^3)}, \quad (3.42)$$

$$\text{SC: } \bar{\kappa} = \frac{\beta D^2}{9} K_n, \quad \alpha = \frac{(1 - 2\bar{\nu})^2(3 - \bar{\nu})}{(1 + \bar{\nu})^2(3 - 4\bar{\nu})}, \quad (3.43)$$

where  $\alpha$  is written in terms of  $\bar{\nu}$  in this case only because the expressions are far more concise than the corresponding expressions for  $\bar{\nu}$  in terms of  $\alpha$ . The self-consistent results for  $\bar{\nu}$  in terms of  $\alpha$  for all three local cubic packings are shown graphically in Figure 3.5, along with the single Voigt relation given by equation (3.24) for all three local cubic packings. A comparison between the  $\bar{\nu}(\alpha)$  curves for an isotropic particulate material with a locally BCC packing structure under all three homogenization hypotheses (Voigt, Reuss, and self-consistent) is given in Figure 3.6. In Section 3.5 we show that the self-consistent results for  $\bar{\nu}(\alpha)$  given in equation (3.42) and shown in Figure 3.6 for a locally BCC packing agree best

with the results obtained by the discrete element method for a random packing of uniform spheres in which particle rotation is prohibited.

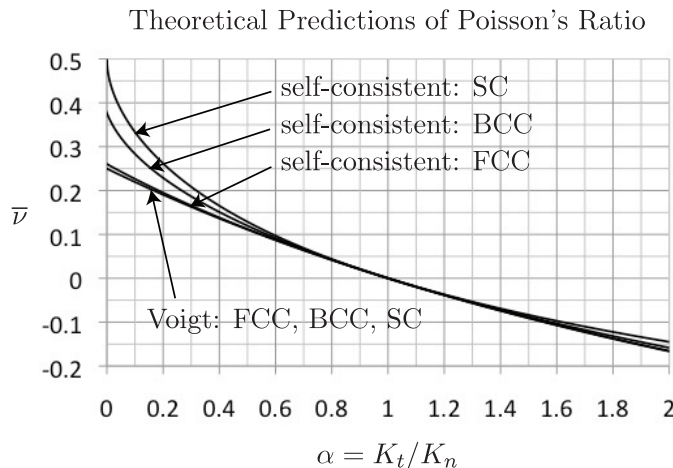


Figure 3.5: Macroscopic Poisson's ratio  $\bar{\nu}$  as a function of  $\alpha = K_t/K_n$  for a statistically isotropic particulate aggregate material derived under the Voigt and self-consistent hypotheses using locally cubic elastic moduli obtained from FCC, BCC, and SC regular arrays of uniform spheres.

### 3.5 Validation by the Discrete Element Method

To test the analytical results of Section 3.4, we performed numerical simulations using the discrete element method (DEM) to measure the macroscopic elastic moduli for randomly packed aggregates of uniform spheres having constant normal and tangential contact stiffnesses  $K_n$  and  $K_t$ , respectively (linear spring contact model). We report the results that we have obtained from six DEM specimens. Specimens 1, 2, and 3 each contained 3 430 randomly packed uniform spheres, and Specimens 4, 5, and 6 each contained 29 660 randomly packed uniform spheres. The specimens are shown in Figure 3.7.

We performed our DEM simulations using the open source code LAMMPS (Large-scale Atomic/Molecular Massively Parallel Simulator) developed at Sandia National Laboratories.

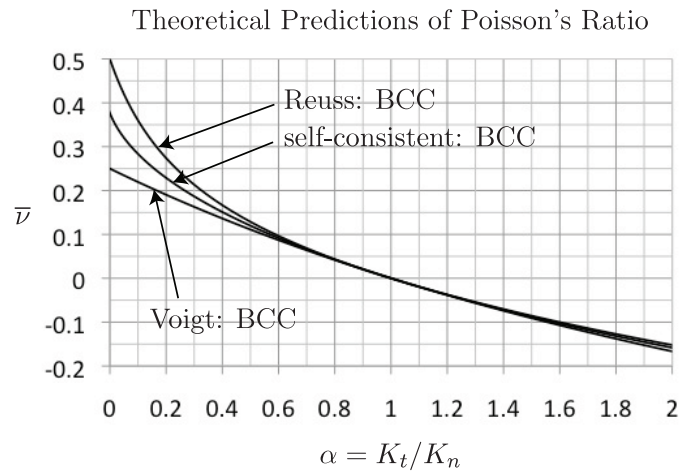


Figure 3.6: Macroscopic Poisson's ratio  $\bar{\nu}$  as a function of  $\alpha = K_t/K_n$  for a statistically isotropic particulate aggregate material derived under the Voigt, Reuss, and self-consistent hypotheses using locally cubic elastic moduli obtained from a BCC regular array of uniform spheres.

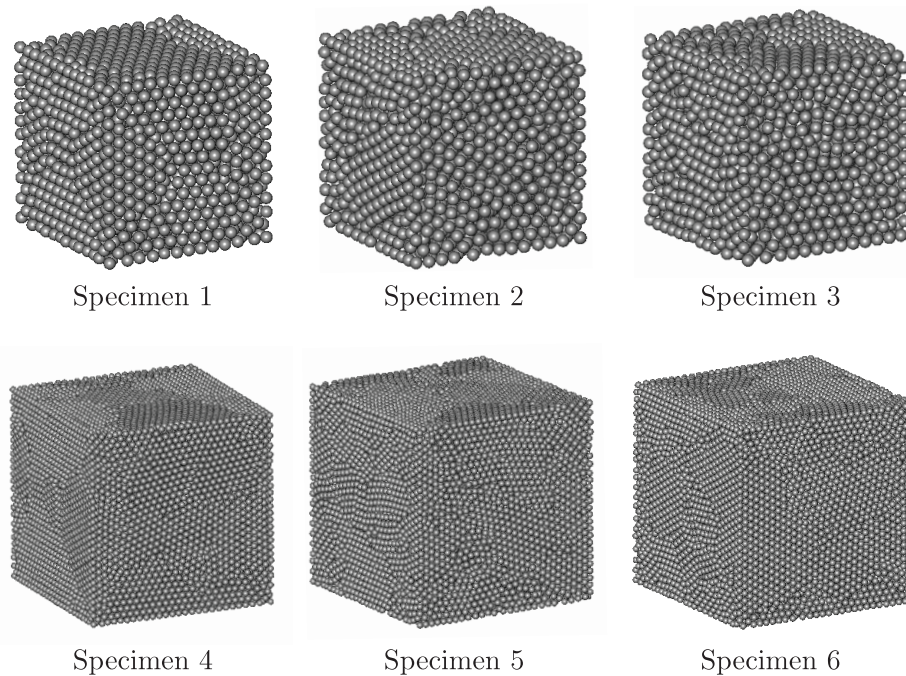


Figure 3.7: Specimens of randomly packed uniform spheres used in the DEM simulations. Specimens 1, 2, and 3 contain 3 430 spherical elements, and Specimens 4, 5, and 6 contain 29 660 spherical elements.

It is a fast, robust, and user-expandable code that can be employed for both molecular dynamics and DEM simulations (see <http://lammmps.sandia.gov>). For a description of the core features of LAMMPS, see Plimpton (1995). To create the specimens, a large volume with cubic shape was populated by a specified number of uniform spherical discrete elements. The elements were given random initial velocities and were then gradually confined by a shrinking cube until a roughly uniform initial compressive stress was achieved in all three directions. For Specimens 1 and 4, inter-particle friction was set to zero throughout the consolidation process. For Specimens 2, 3, 5, and 6, inter-particle friction was present for the initial portion of the consolidation process, and it was set to zero only after the boundary of the confining volume was in its final position, to obtain a dense packing. This resulted in a less ordered packing structure for Specimens 2, 3, 5, and 6 compared to Specimens 1 and 4 (see Figure 3.9).

For all six specimens, after the consolidation process was completed, the inter-particle coefficient of friction was set to infinity to ensure that no inter-particle slip occurred during the DEM simulations. No friction was present on the boundary of the confining volume during the simulations. The resulting initial volumetric packing densities of the six specimens were 0.64, 0.62, 0.62, 0.69, 0.68, and 0.68, respectively. All six of these volume densities correspond to a dense sand (with void ratio  $e \approx 0.5$ ) of roughly uniform particle size (with coefficient of uniformity  $C_u \approx 1$ ), such as Ottawa standard sand (e.g., Bardet, 1997). Note from Figure 3.9 that the packing of the spheres in each of these six specimens was essentially random. In particular, the appearance of regular (hexagonal) packings on the surfaces of the specimens in Figure 3.7 is a surface phenomenon only, caused by the fact that there is no friction between the spheres and the surfaces of the confining volume.

To measure Poisson's ratio  $\bar{\nu}$  for each specimen, the upper surface of the confining volume was lowered with a prescribed quasi-static velocity until an axial strain of  $d\epsilon_z = -0.001$  was obtained. During this time the other five surfaces of the confining volume remained fixed.

Despite these surfaces remaining fixed, however, the *centers* of the spheres in contact with them experienced small but significant displacements normal to the surfaces, due to the compliance of the contacts. Therefore, we monitored  $d\epsilon_x$ ,  $d\epsilon_y$ , and  $d\epsilon_z$ , which were measured to the centers of the spheres in contact with the confining surfaces, and we measured the increments in stress  $d\sigma_x$ ,  $d\sigma_y$ , and  $d\sigma_z$  on all of the surfaces of the confining volume. Using this information, we were able to compute Poisson's ratio for each specimen in two different ways:

$$\bar{\nu}_1 = \frac{d\sigma_x - d\sigma_z \left( \frac{d\epsilon_x}{d\epsilon_z} \right)}{d\sigma_y + d\sigma_z - (d\sigma_x + d\sigma_y) \left( \frac{d\epsilon_x}{d\epsilon_z} \right)}, \quad (3.44)$$

and  $\bar{\nu}_2$  by replacing  $x$  with  $y$  and  $y$  with  $x$  (and 1 with 2) in equation (3.44). Note that, although two values of Poisson's ratio are obtained:  $\bar{\nu}_1$  and  $\bar{\nu}_2$ , the derivation of equation (3.44) assumes material isotropy, which naturally is not perfectly realized in any DEM specimen. For an isotropic specimen, the values of  $\bar{\nu}_1$  and  $\bar{\nu}_2$  would be equal. Thus, comparing  $\bar{\nu}_1$  and  $\bar{\nu}_2$  provides one simple, qualitative test of the isotropy of our specimens. The same DEM simulations were repeated for each specimen with spheres having a ratio of contact stiffnesses  $\alpha = K_t/K_n$  ranging between  $\alpha = 0.0$  (no friction) and  $\alpha = 2.0$ , with  $\alpha$  varied in increments of 0.2.

If we assume Hertz-Mindlin contact, then equation (3.8) implies that  $\alpha = 2(1-\nu)/(2-\nu)$ , where  $\nu$  is Poisson's ratio for the material constituting the spheres (not for the particulate material as a whole). Thus, for a stable elastic material, Hertz-Mindlin contact predicts  $2/3 \leq \alpha \leq 4/3$ . However, since particles are rarely perfectly spherical in a general particulate material, it is useful to consider values of  $\alpha$  that vary beyond the boundaries predicted by Hertz-Mindlin contact theory. Since in the discrete element method the linear spring stiffnesses  $K_n$  and  $K_t$  are user-defined, DEM allows us to test a much larger range of values of  $\alpha$  than physical experiments on a handful of particulate materials would permit.

In the DEM simulations of this first part of our two-part series of papers, the spheres were

allowed full three-dimensional translational freedom of motion, but rotation was prohibited. This was done to facilitate a direct comparison with the theoretical results of Sections 3.3 and 3.4, as well as those of Walton (1987) and Chang et al. (1995), all of which were derived assuming (effectively) no particle rotation. (Note that, although Chang et al. (1995) attempted to include the effect of particle rotation in their analyses, they did so in the context of a “quasi-micro-polar” continuum theory in which the rotation field was assumed to be continuous, and this effectively eliminated the possibility of particle rotations that could lead to zero-energy strains or rotation mechanisms in the particulate material at the local level, as discussed in Part II.) The results are shown in Figure 3.8. Data points for both of the measured values of Poisson’s ratio  $\bar{\nu}_1$  and  $\bar{\nu}_2$  given by equation (3.44) are included in all of the figures as solid squares and solid diamonds. The difference between these data points provides a rough measure of the anisotropy of the specimens, at least in the directions normal to the specimen boundaries. Note that in most of the figures, these data points lie roughly on top of one another.

Figure 3.8 also shows the Voigt, Reuss, and self-consistent curves given by equations (3.24) [Voigt: FCC, BCC, SC], (3.33) [Reuss: SC], (3.42) and (3.43) [self-consistent: BCC and SC, respectively]. Note that the relationship between Poisson’s ratio  $\bar{\nu}$  and  $\alpha = K_t/K_n$  that is given by equation (3.42), the self-consistent result for the local BCC packing, agrees with the values obtained from the DEM simulations better than any of the other theoretical predictions we have considered, including those of Chang et al. (1995), for the case of no particle rotation. As we will see in Part II, when particle rotation is allowed the discrepancy between the DEM measurements of Poisson’s ratio and the theoretical predictions of Chang et al. (1995) only increase.

Note that the theoretical relationship between the bulk modulus  $\bar{\kappa}$ , the normal inter-particle contact stiffness  $K_n$ , and the average number of contacts per unit volume  $\beta$  is the same under all three homogenization hypotheses of Section 3.4. To test this, we measured

## DEM Predictions of Poisson's Ratio

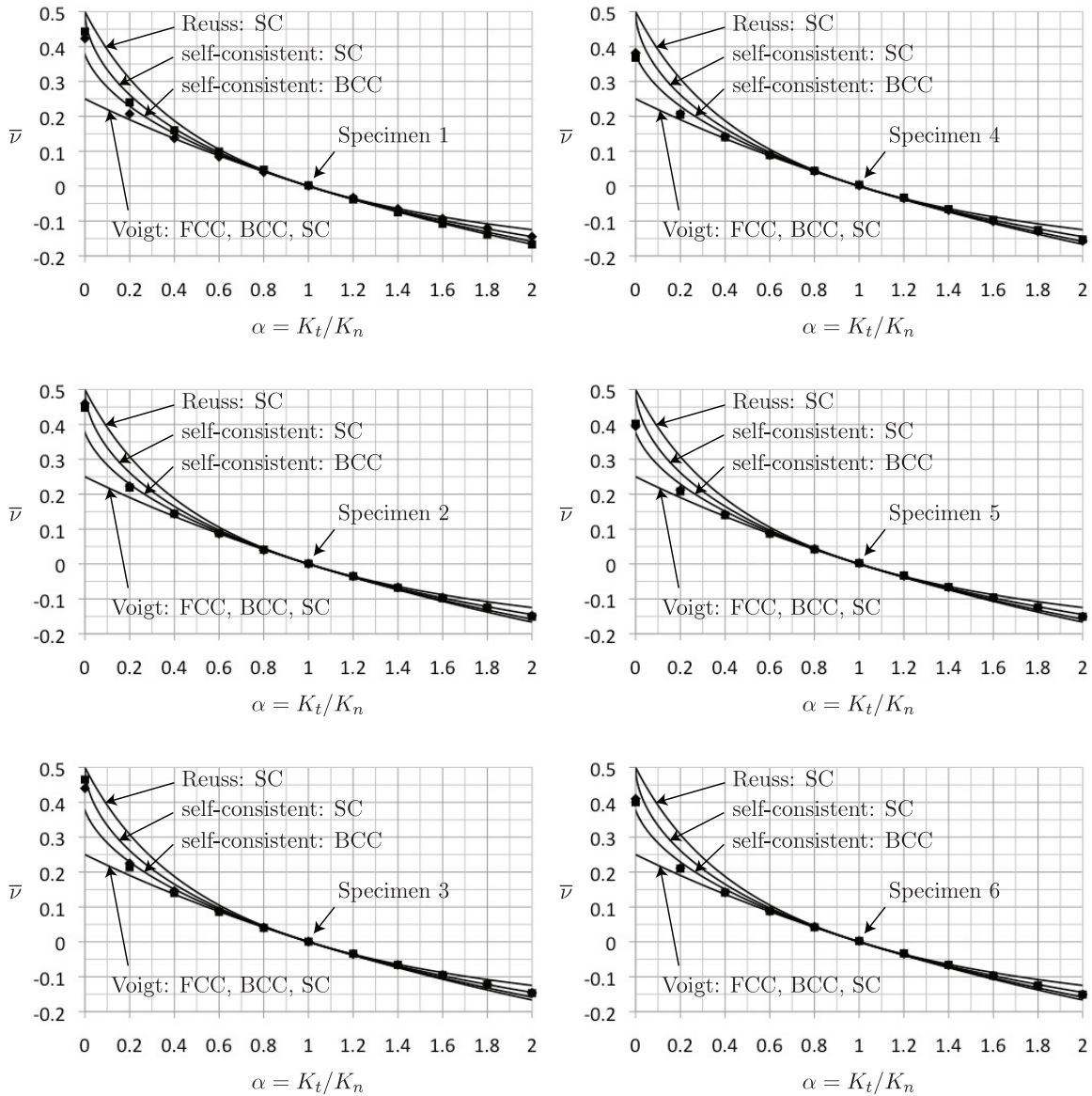


Figure 3.8: Macroscopic Poisson's ratio  $\bar{\nu}$  versus  $\alpha = K_t/K_n$  obtained from DEM simulations on six specimens of randomly packed uniform spheres with constant normal and tangential contact stiffnesses  $K_n$  and  $K_t$ , in which the spheres were not allowed to rotate. Also shown are the theoretical curves given by the Voigt, Reuss, and self-consistent equations (3.24) [Voigt: FCC, BCC, SC], (3.33) [Reuss: SC], (3.42) and (3.43) [self-consistent: BCC and SC, respectively].

the bulk modulus of the six DEM specimens described in this section independently of Poisson's ratio by subjecting the specimens to a uniform volumetric strain, and measuring the stress increments on the surfaces of the confining volume. The measured values of the bulk modulus in terms of the normal contact stiffness  $K_n$  and the diameter of the spheres  $D$  for the six DEM specimens were found to be  $\bar{\kappa}_1 = 0.58K_n/D$ ,  $\bar{\kappa}_2 = 0.47K_n/D$ ,  $\bar{\kappa}_3 = 0.49K_n/D$ ,  $\bar{\kappa}_4 = 0.66K_n/D$ ,  $\bar{\kappa}_5 = 0.57K_n/D$ , and  $\bar{\kappa}_6 = 0.58K_n/D$ , respectively. The average number of contacts per unit volume in the six DEM specimens were measured to be  $\beta_1 = 5.4/D^3$ ,  $\beta_2 = 4.4/D^3$ ,  $\beta_3 = 4.5/D^3$ ,  $\beta_4 = 6.2/D^3$ ,  $\beta_5 = 5.4/D^3$ , and  $\beta_6 = 5.5/D^3$ , respectively. Thus, the theoretical value of  $\bar{\kappa} = K_n\beta D^2/9$  predicted by equations (3.24), (3.31) – (3.33), and (3.41) – (3.43) for the six DEM specimens is  $\bar{\kappa} = 0.60K_n/D$  for Specimen 1,  $\bar{\kappa} = 0.49K_n/D$  for Specimen 2,  $\bar{\kappa} = 0.50K_n/D$  for Specimen 3,  $\bar{\kappa} = 0.69K_n/D$  for Specimen 4,  $\bar{\kappa} = 0.60K_n/D$  for Specimen 5, and  $\bar{\kappa} = 0.61K_n/D$  for Specimen 6, which differ from the measured values by about 3%, 4%, 2%, 5%, 5%, and 5%, respectively.

We also monitored friction work between the spheres throughout the DEM simulations, and we verified that *there was no inter-particle slip* during the DEM simulations (i.e., friction work was zero). This is in agreement with the assumptions made in the theoretical derivations of Sections 3.3 and 3.4, and in the prior theoretical studies of Walton (1987) and Chang et al. (1995). No inter-particle slip is also in agreement with the notion of elastic behavior. It is noteworthy, however, that in physical experiments on sand or other particulate materials, it is almost impossible to verify that no inter-particle slip takes place, which makes the notion of an elastic range for a particulate material somewhat ambiguous. This is one reason why the DEM simulations are necessary to confirm our theoretical analyses, since we can be sure that we are strictly within the elastic range.

## 3.6 Discussion

A number of issues related to the effects of particle rotation will arise in Part II, and so we leave the bulk of our discussion until then. We can, however, already consider the validity of our assumption of locally cubic packing structure in particulate materials, which was implicit in the analyses of Section 3.4. We first note that our results under the Voigt hypothesis did not, in the end, depend on what type of local cubic packing was assumed, but only on the number of contacts per unit volume  $\beta$  and the inter-particle contact stiffnesses  $K_n$  and  $K_t$ . We also note that equations (3.21) and (3.24) reproduce exactly the results of Chang et al. (1995), which were obtained without assuming a locally cubic packing structure in the particulate material. This suggests that these results did not depend on any specific assumption regarding the local packing structure. Under the Reuss and self-consistent hypotheses, however, there was substantial dependence on the local packing structure (see Figures 3.4 and 3.5).

In Section 3.5, we found that  $\beta D^3 = \{5.4, 4.4, 4.5, 6.2, 5.4, 5.5\}$  for Specimens 1 – 6, respectively, where  $D$  denotes the diameter of the particles in the specimens. From equation (3.22), we have  $\beta_{\text{FCC}} D^3 \approx 8.5$ ,  $\beta_{\text{BCC}} D^3 \approx 5.2$ , and  $\beta_{\text{SC}} D^3 = 3$ . Thus, the average number of contacts per unit volume in each of the six DEM specimens corresponds most closely to that of the BCC packing. This is in general agreement with what was observed in Section 3.5: the theoretical relationship between Poisson’s ratio  $\bar{\nu}$  and  $\alpha = K_t/K_n$  given by equation (3.42), which is the self-consistent result for the local BCC packing, agrees best with the values obtained from the DEM simulations. The value of  $\beta D^3$  does not give much information about the local packing structure of the specimens, however.

One way to identify the local packing structure in the specimens is to use a radial distribution function. The radial distribution function  $g(r)$  counts the average number of particles at a distance  $r$  from the center of each particle, normalized by the volume of the differential

shell of thickness  $dr$  in which the particle is located. While commonly used in molecular dynamics, the radial distribution function is not ideally suited for discrete systems in general, since for a regular lattice the curve  $g(r)$  will consist of spikes, and the height of these spikes will depend on the size of the differential shell element, with the height going to infinity as  $dr \rightarrow 0$ . For our purposes, however, the radial distribution function will be useful, since we can compare the positions and relative heights of the spikes for the six DEM specimens versus the three regular cubic packings, with  $dr = 10^{-2}D$  fixed for consistency. Note that the radial distribution function is independent of angle, so it will not be altered if the principal axes of the local cubic packings are not oriented along the same directions. Thus, we expect the radial distribution function to give some indication of the extent to which the local packing geometry of a DEM specimen is cubic, even if that specimen is an isotropic aggregate of locally cubic packings.

Figure 3.9 shows the radial distribution functions for each of the six DEM specimens, as well as the radial distribution functions for the SC, BCC, and FCC regular arrays of uniform spheres. Note that the packing structure of all six specimens is significantly less ordered than that of the regular cubic arrays. This is a confirmation that the overall packing structure of the specimens is indeed random. Note also, however, that the radial distribution functions for Specimen 1 and Specimen 4 exhibit marked spikes at the same radial distances as the radial distribution function of the FCC packing (with an extra spike at  $r/D \approx 1.9$  corresponding to the BCC packing), which supports our hypothesis that the local packing structure of these specimens is at least approximately cubic in nature. Despite the fact that the radial distribution functions for Specimens 2, 3, 5, and 6 do not suggest a locally cubic packing structure, we have seen that the self-consistent equation (3.42) agrees with the  $\bar{v}(\alpha)$  curves for these specimens very well.

Finally, we consider whether or not the DEM specimens used in Section 3.5 can truly be said to be statistically isotropic. Hill (1956) suggests that for a homogenization process

## Radial Distribution Functions

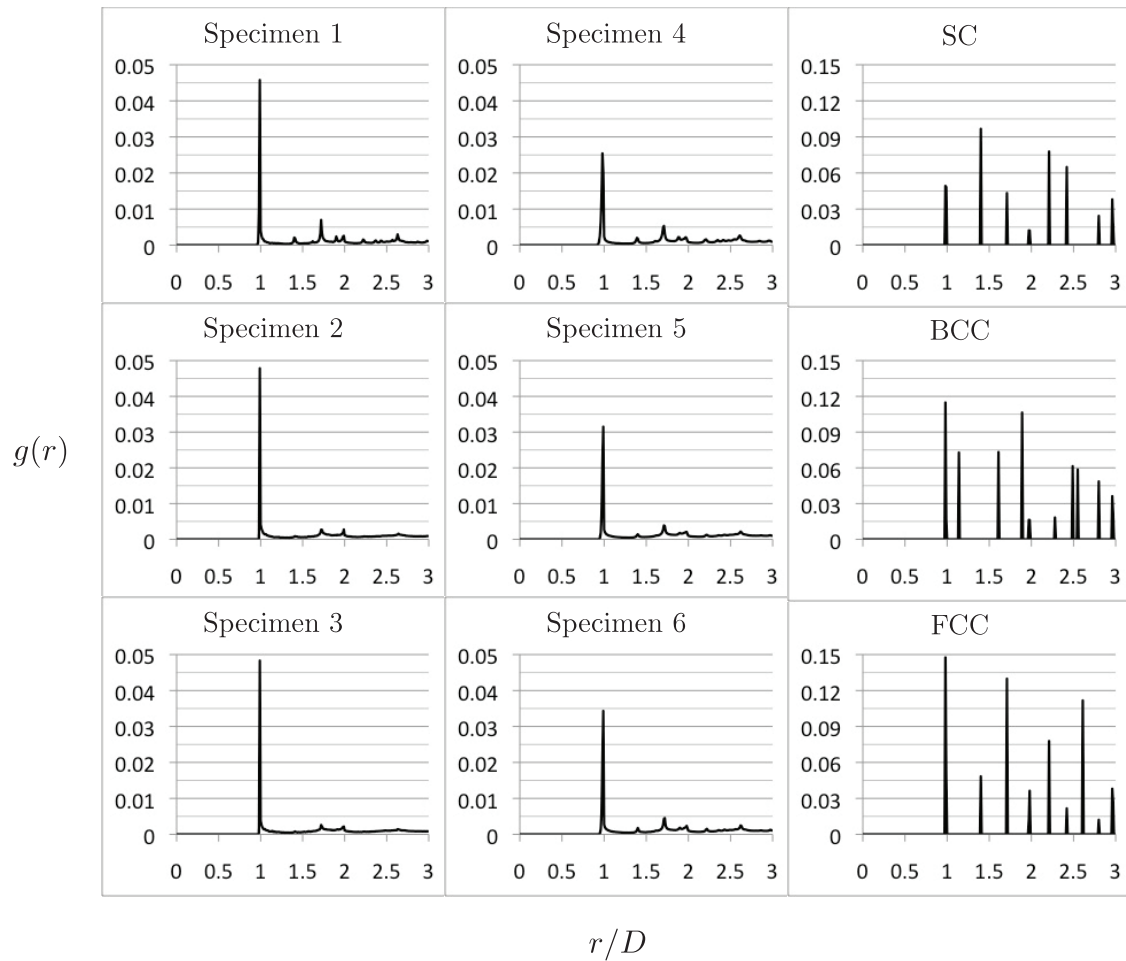


Figure 3.9: Radial distribution functions  $g(r)$  for DEM Specimens 1 – 6, and the SC, BCC, and FCC regular arrays. In our calculations of  $g(r)$  we have used  $dr = 10^{-2}D$ , where  $D$  is the diameter of the spheres.

like those of Section 3.4 to be valid, the smallest dimension of the material specimen in question should be approximately 1 000 times larger than the largest dimension of its essential micro-constituent, which for the analyses of Section 3.4 is an elementary cell. For the DEM simulation specimens with 3 430 and 29 660 spheres of diameter  $D$ , the length of the specimens were approximately  $15D$  and  $30D$ , respectively. Since the edge-length of an elementary cell of an SC, BCC, or FCC packing of uniform spheres is between  $D$  and  $\sqrt{2}D$ , the DEM specimens in question are far from satisfying Hill's condition. Unfortunately, to accurately simulate a statistically isotropic specimen with an essential micro-constituent dimension between  $D$  and  $\sqrt{2}D$  according to Hill's condition would require more than  $10^7$  spheres, which is beyond our computational resources.

### 3.7 Conclusions

We have applied the homogenization methods of Voigt (1928) (the kinematic hypothesis), Reuss (1929) (the static hypothesis), and Hershey (1954) and Kröner (1958) (the self-consistent hypothesis) to obtain the effective isotropic elastic moduli for a statistically isotropic assembly of spheres having constant normal and tangential inter-particle contact stiffnesses, using the elastic moduli derived from regular cubic lattices. In contrast to previous work in the literature, our results are based on direct micromechanical analyses of specific local packing geometries. Our results reproduce those of Walton (1987) and Chang et al. (1995) under the kinematic hypothesis for all of the local packing geometries that we considered (FCC, BCC, and SC), and the results of Chang et al. (1995) under the static hypothesis for the simple cubic (SC) local packing geometry. Our approach also allowed us to obtain new results from the static hypothesis for FCC and BCC local packing geometries, as well as new results for all three local packing geometries from the self-consistent homogenization hypothesis. Our results also show that the results of Chang et al. (1995) under

the static hypothesis at best give only an upper bound on Poisson's ratio *for the case of no particle rotation*, and do not hold for arbitrary local packing geometries.

To test our theoretical results, we performed DEM simulations on six randomly packed specimens of uniform spheres, having constant normal and tangential contact stiffnesses  $K_n$  and  $K_t$ , respectively (linear spring contact model). In this Part I of our two-part series of papers, our theoretical analyses and our DEM simulations were all performed with particle rotation prohibited. There were several major advantages to using DEM to test our theoretical results, as opposed to, for example, using experiments on physical particles such as glass beads. First and foremost for this Part I, we could prohibit particle rotation in the DEM simulations, providing a direct test of the validity of our theoretical analyses and those published previously with no particle rotation assumed. Moreover, we were able to reproduce our theoretical assumption of constant contact stiffness exactly, without having to make any assumptions regarding the actual contact behavior of the physical particles, thus eliminating one source of uncertainty. We were also able to assign precise values to the normal and tangential contact stiffnesses, and thus measure Poisson's ratio for a large range of specific values of  $\alpha = K_t/K_n$ , and we could verify that no inter-particle slip took place during our DEM simulations.

While the effects of particle rotation will be explored in Part II, we already note that our theoretical results obtained under the self-consistent homogenization assumption, particularly that based on the body-centered cubic local packing geometry, are capable of providing remarkably good agreement with the results we obtained from our DEM simulations with no particle rotation, even when compared to the best theoretical estimates currently in the published literature. We continue our analysis with the case of particle rotation in Part II.



## Chapter 4

# Direct Micromechanics Derivation and DEM Confirmation of the Elastic Moduli of Isotropic Particulate Materials, Part II: Particle Rotation <sup>1</sup>

### 4.1 Abstract

In Part I, Chapter 3 [Fleischmann et al. (2013a)], we performed theoretical analyses of three cubic packings of uniform spheres (simple, body-centered, and face-centered) assuming no particle rotation, employed these results to derive the effective elastic moduli for a statistically isotropic particulate material, and assessed these results by performing numerical discrete element method (DEM) simulations with particle rotations prohibited. In this second part, we explore the effect that particle rotation has on the overall elastic moduli of a statistically isotropic particulate material. We do this both theoretically, by re-analyzing

---

<sup>1</sup>This chapter closely follows Fleischmann et al. (2013b).

the elementary cells of the three cubic packings with particle rotation allowed, which leads to the introduction of an internal parameter to measure zero-energy rotations at the local level, and numerically via DEM simulations in which particle rotation is unrestrained. We find that the effects of particle rotation cannot be neglected. For unrestrained particle rotation, we find that the self-consistent homogenization assumption applied to the locally body-centered cubic packing incorporating particle rotation effects most accurately predicts the measured values of the overall elastic moduli obtained from the DEM simulations, in particular Poisson’s ratio. Our new self-consistent results and theoretical modeling of particle rotation effects together lead to significantly better theoretical predictions of Poisson’s ratio than all prior published results. Moreover, our results are based on a direct micromechanics analysis of specific geometrical packings of uniform spheres, in contrast to prior theoretical analyses based on hypotheses involving overall inter-particle contact distributions. Thus, our results permit a direct assessment of the reasons for the theory-experiment discrepancies noted in the literature with regard to previous theoretical derivations of the macroscopic elastic moduli for particulate materials, and our new theoretical results greatly narrow such discrepancies.

## 4.2 Introduction

In the first of this two-part series, Chapter 3 [Fleischmann et al. (2013a)], to which we refer simply as Part I in the sequel, we performed theoretical analyses of three cubic packings of uniform spheres (simple, body-centered, and face-centered) assuming no particle rotation. We used the resulting tensors of cubic elastic moduli  $\mathbf{C}$  to obtain tensors of effective elastic moduli  $\overline{\mathbf{C}}$  for a statistically isotropic particulate material with locally cubic packing structure, using the homogenization methods of Voigt (1928) (kinematic hypothesis), Reuss (1929) (static hypothesis), and Hershey (1954) and Kröner (1958) (self-consistent hypothe-

sis). While the assumption of no particle rotation can be justified for certain regular cubic packings as the number of elementary cells becomes large (as we confirm herein), it cannot be justified in general for statistically isotropic assemblies that have only a *locally* cubic packing structure. In this second part of our two-part series, we re-analyse the three cubic packings with the effect of particle rotation included. We prove by several simple theoretical examples that particle rotation can produce zero-energy strains or mechanisms in a particulate material, and that they significantly alter the predicted value of Poisson's ratio for a particulate material in the elastic range. To account for the effect of particle rotation, we introduce a micromechanics-motivated internal parameter that leads to new theoretical predictions for the elastic moduli under all three homogenization assumptions.

After obtaining closed-form analytical expressions for the overall elastic moduli (bulk modulus and Poisson's ratio) of the particulate material in terms of the normal and tangential stiffnesses of the contacts between the particles in the material, we perform numerical simulations using the discrete element method (DEM) to measure the overall elastic moduli for specimens of randomly packed uniform spheres with constant normal and tangential contact stiffnesses (linear spring model), and we compare these results with the theoretical results obtained under the three homogenization assumptions for each of the three cubic packing geometries. In Part I, our DEM simulations were performed with particle rotation prohibited. In this second part, our DEM simulations are performed under identical conditions as in Part I, but with particle rotation unrestrained. The overall elastic moduli are again measured from the DEM simulations, and the results are compared both to those of the DEM simulations performed in Part I and to the theoretical results obtained in this second part, which include the effects of particle rotation. We show that our new theoretical results from the self-consistent hypothesis applied to the BCC packing including particle rotation agree most closely with DEM simulations in which particle rotation is unrestrained, and that these are significantly different from the results obtained in Part I when particle

rotation was prohibited.

Our method of including the effects of mechanisms produced by particle rotation is in contrast to the work of other researchers, such as Chang et al. (1995) and Chang and Gao (1995), who include particle rotation only within the context of micro-polar or quasi-micro-polar continuum theory. The micro-polar or quasi-micro-polar continuum approach cannot capture the zero-energy strains or mechanisms produced by particle rotations, and therefore cannot accurately predict Poisson's ratio for an isotropic particulate material. We find that, when compared to the measured values of the overall elastic moduli obtained from DEM simulations on specimens of randomly packed uniform spheres, our analytical self-consistent results from the body-centered cubic packing that include the effect of particle rotation predict values of the elastic moduli, and in particular Poisson's ratio, that are significantly more accurate than those currently in the literature.

### 4.3 Overall Elastic Moduli for Regular Arrays of Uniform Spheres Incorporating the Effect of Particle Rotation

In Section 2 of Part I, we derived the three independent cubic elastic moduli  $C_1$ ,  $C_2$ , and  $C_3$  for three regular cubic packings of uniform spheres: face-centered cubic (FCC), simple cubic (SC), and body-centered cubic (BCC), under the assumption that no particle rotation occurred during deformation. These cubic elastic moduli were given in terms of the radius of the spheres  $R$  and the normal and tangential inter-particle contact stiffnesses  $K_n$  and  $K_t$ .

They are repeated here for reference:

FCC, no particle rotation:

$$C_1 = \frac{1}{\sqrt{2}R}(K_n + K_t), \quad C_2 = \frac{1}{2\sqrt{2}R}(K_n - K_t), \quad C_3 = \frac{1}{2}C_1, \quad (4.1)$$

BCC, no particle rotation:

$$C_1 = \frac{1}{2\sqrt{3}R}(K_n + 2K_t), \quad C_2 = \frac{1}{2\sqrt{3}R}(K_n - K_t), \quad C_3 = \frac{1}{2}(C_1 + C_2), \quad (4.2)$$

SC, no particle rotation:

$$C_1 = \frac{1}{2R}K_n, \quad C_2 = 0, \quad C_3 = \frac{1}{4R}K_t, \quad (4.3)$$

The assumption that the particles (spheres) do not rotate turns out to be quite significant. Despite this fact, the assumption of no particle rotation can be justified for certain regular cubic arrays in the limit as the number of elementary cells becomes large, due to the symmetry of the inter-particle contacts; we provide explicit DEM verification of this later in this section. However, if a statistically isotropic particulate material has only *locally* cubic packing structure, then the assumption of no particle rotation can no longer be justified. What is even more problematic from the point of view of continuum modeling is that some of these particle rotations may be mechanisms. In other words, some quasi-static particle rotations may result in zero energy change in the system, but still cause plastic (irreversible) strain. This violates Drucker's postulate. Moreover, particle rotation at the local level may be involved in a global elastic strain of the particulate material, while, as Goddard (2008) shows, these particle rotations do not contribute to the quasi-static stress power. Mechanisms due to particle rotation can occur anywhere that there are local asymmetries in the distribution of inter-particle contacts. In the following subsections, we consider the effect of particle rotation in each of the three elementary cells shown in Figure 4.1.

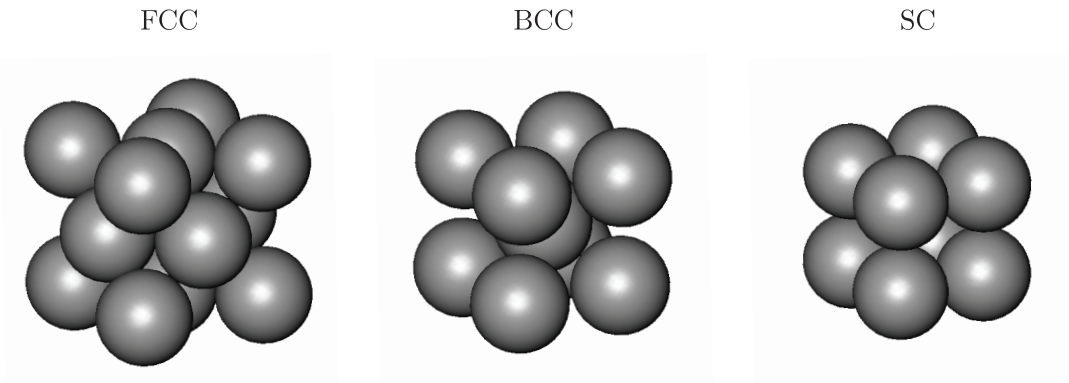


Figure 4.1: Elementary cells of face-centered cubic (left), body-centered cubic (center), and simple cubic (right) regular arrays of uniform spheres.

### 4.3.1 Face-Centered Cubic (FCC) Array of Uniform Spheres

If we consider a single elementary cell of an FCC array of uniform spheres (Figure 4.1, left), then for loading parallel to the principal axes, if the spheres are not allowed to rotate, Poisson's ratio is

$$\nu_{\text{FCC}} = \frac{C_2}{C_1 + C_2} = \frac{1 - \alpha}{3 + \alpha} \quad (4.4)$$

with  $C_1$  and  $C_2$  given by equation (4.1) and  $\alpha = K_t/K_n$ . Figure 4.2 plots equation (4.4), as well as measurements of Poisson's ratio  $\nu$  as a function of  $\alpha$  for the single elementary cell obtained from numerical simulations using the discrete element method. For one set of DEM simulations, the spheres were not allowed to rotate, while for the other set, rotation was unrestrained. In all of the DEM simulations, the lateral surfaces of the cell were constrained while an axial strain was applied quasi-statically along one of the principal axes (the  $z$  axis), and Poisson's ratio was computed from the principal stress increments  $d\sigma_x$ ,  $d\sigma_y$ , and  $d\sigma_z$  according to equation (3.44) of Part I. No friction was present on the boundary of the elementary cell during the deformation. As Figure 4.2 shows, when the spheres are not allowed to rotate, the DEM results for Poisson's ratio are in perfect agreement with the theoretical predictions of equation (4.4). When the spheres are allowed to rotate, however, the DEM

results for Poisson’s ratio no longer agree with the theoretical predictions of equation (4.4), but are consistently (and significantly) higher. Note that we were able to verify that there was *no inter-particle slip* in all of the DEM simulations referred to in Figure 4.2.

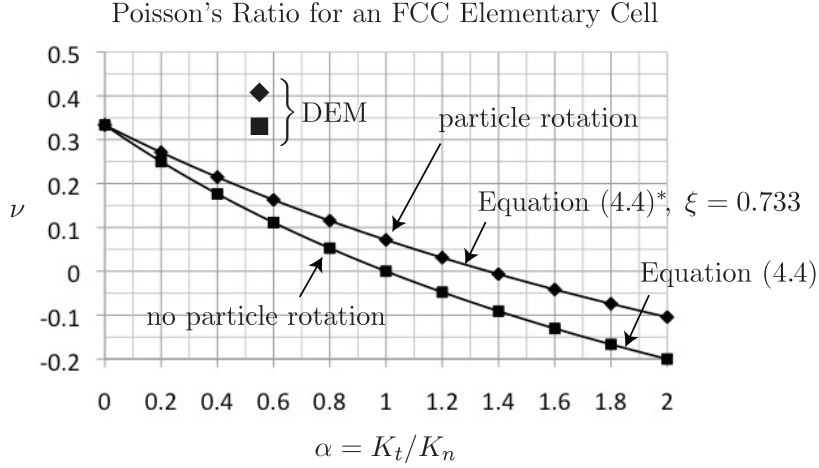


Figure 4.2: Poisson’s ratio  $\nu$  as a function of  $\alpha = K_t/K_n$  for a single elementary cell of an FCC array of uniform spheres. The data points represent values obtained by numerical simulations performed using the discrete element method (DEM) in which the particles were either allowed or not allowed to rotate. The theoretical curves are from equations (4.4) and (4.4)\* [which is equation (4.4) with  $\alpha$  replaced by  $\alpha^* = \xi\alpha$ ] with  $\xi = 11/15 \approx 0.733$ .

It is not difficult to theoretically determine the effect of particle rotation on the cubic elastic moduli of a single FCC elementary cell with no friction between the spheres and the boundary of the cell. First, we note that equation (4.1) can be re-derived for the case of no particle rotation by considering a single FCC elementary cell subjected to a state of pure uniaxial strain  $\epsilon_{11} = -\delta_{11}/(\sqrt{2}D)$  (with  $\epsilon_{22} = \epsilon_{33} = 0$ ). It can be shown by an analysis of the inter-particle normal and tangential contact forces within the FCC cell that the forces normal to the cell faces are  $F_{11} = -2(K_n + K_t)\delta_{11}$  and  $F_{22} = F_{33} = -(K_n - K_t)\delta_{11}$ , where contributions from inter-particle contacts on the faces and interior of the cell have been included, and where, since the “material” cube is measured only to the centers of the outer spheres, the normal and tangential stiffnesses of the contacts on the faces contribute half of

their full values. From these the expressions for  $C_1$  and  $C_2$  in terms of  $K_n$  and  $K_t$  given in equation (4.1) can be derived in a straightforward way, since  $\sigma_{11} = F_{11}/(2D^2) = C_1\epsilon_{11}$ , and  $\sigma_{22} = \sigma_{33} = F_{22}/(2D^2) = F_{33}/(2D^2) = C_2\epsilon_{11}$ . Similarly, the expression for  $C_3$  in terms of  $K_n$  and  $K_t$  given in equation (4.1) can be derived by considering a single FCC elementary cell subjected to a state of pure shear.

If a single FCC elementary cell in which particle rotation is unrestrained is subjected to a state of pure uniaxial strain along one of its principal axes, then due to the symmetry of the loading, only the spheres at the eight corners of the cell will experience rotation. Note that in the FCC packing, each corner sphere is in contact with three face-centered spheres: two on faces parallel to the axis of deformation and one on a face normal to the axis of deformation. If each corner sphere remains in contact with all three face-centered spheres throughout the deformation, then an analysis of the stiffness matrix for the FCC elementary cell with rotational degrees of freedom leads to  $F_{11} = -2(K_n + \xi K_t)\delta_{11}$  and  $F_{22} = F_{33} = -(K_n - \xi K_t)\delta_{11}$  with  $\xi = 11/15$ . This analysis is given in detail in B. It follows that the cubic elastic moduli for the FCC elementary cell with unrestrained particle rotation are

$$C_1 = \frac{1}{\sqrt{2}R}(K_n + \xi K_t), \quad C_2 = \frac{1}{2\sqrt{2}R}(K_n - \xi K_t), \quad C_3 = \frac{1}{2}C_1, \quad (4.5)$$

with  $\xi = 11/15 \approx 0.733$ .

If the deformation in the single FCC elementary cell we have just described is sufficiently large, then infinitesimal gaps will form between the corner spheres and the face-centered spheres on faces normal to the axis of deformation. In this case, if particle rotation is unrestrained and no tangential force is applied to the boundaries of the cell, it can be shown by a similar analysis that the cubic elastic moduli for the FCC elementary cell are again given by equation (4.5), but now with  $\xi = 0.5$ . If particle rotation is prohibited, then gaps on the faces normal to the deformation may still form, but they do not affect the cubic elastic

moduli (i.e.,  $\xi = 1$ ).

Our theoretical analysis is confirmed by the DEM simulations described at the beginning of this section. If we substitute the expressions for  $C_1$  and  $C_2$  given by equation (4.5) into equation (4.4), and call the resulting expression equation (4.4)\* where  $\alpha^* = \xi\alpha$  replaces  $\alpha$ , then the  $\nu(\alpha)$  curve predicted by equation (4.4)\* with  $\xi = 0.733$  agrees perfectly with the curve that was obtained numerically by DEM simulations in which particle rotation was unrestrained, as shown in Figure 4.2.

We commented earlier that the assumption of no particle rotation *is* valid for certain regular cubic arrays in the limit as the number of elementary cells becomes large. This is in fact true for the regular FCC array even when the number of elementary cells is only moderately large. We have confirmed this by DEM simulations on  $2 \times 2 \times 2$ ,  $3 \times 3 \times 3$ , and  $7 \times 7 \times 7$  arrays of FCC elementary cells, containing totals of 63, 172, and 1688 uniform spheres, respectively. The results are shown in Figure 4.3. For a  $7 \times 7 \times 7$  FCC array, the data points obtained from DEM simulations in which particle rotation was *unrestrained* match those obtained from a single FCC elementary cell in which particle rotation was prohibited, which is predicted by equation (4.4) or by equation (4.4)\* with  $\xi = 1$ , as shown in Figure 4.3; this is the minimum array size for which this match occurs.

### 4.3.2 Body-Centered Cubic (BCC) Array of Uniform Spheres

If we consider a single elementary cell of a BCC array of uniform spheres (Figure 4.1, center), then for loading parallel to the principal axes, if the spheres are not allowed to rotate, Poisson's ratio is

$$\nu_{\text{BCC}} = \frac{C_2}{C_1 + C_2} = \frac{1 - \alpha}{2 + \alpha} \quad (4.6)$$

with  $C_1$  and  $C_2$  given by equation (4.2). It is quite easy to show theoretically that if particle rotation is allowed for a single BCC elementary cell loaded parallel to the principal axes with

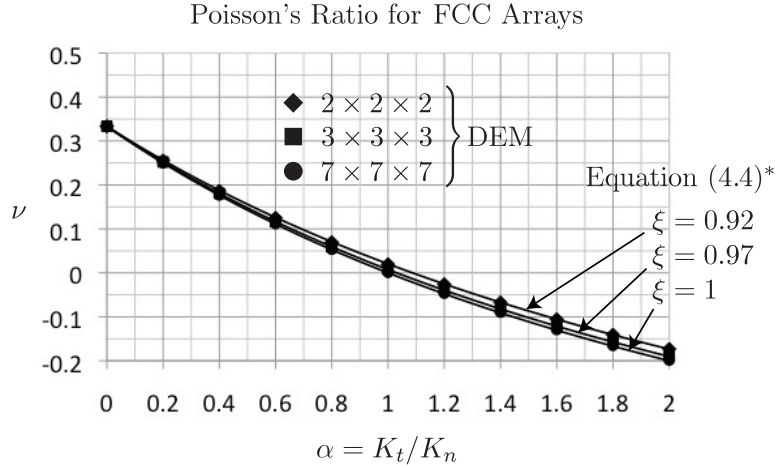


Figure 4.3: Poisson's ratio  $\nu$  as a function of  $\alpha = K_t/K_n$  for  $2 \times 2 \times 2$ ,  $3 \times 3 \times 3$ , and  $7 \times 7 \times 7$  arrays of FCC elementary cells, containing totals of 63, 172, and 1688 uniform spheres, respectively. The data points represent values obtained by numerical simulations performed using the discrete element method (DEM) in which particle rotation was unrestrained. The theoretical curves are from equation (4.4)\* [which is equation (4.4) with  $\alpha$  replaced by  $\alpha^* = \xi\alpha$ ] with  $\xi = 0.92$ ,  $\xi = 0.97$ , and  $\xi = 1$ . The  $7 \times 7 \times 7$  array is the minimum size for which  $\xi = 1$ .

no friction on the boundary of the cell, then  $\nu_{\text{BCC}} = 0.5$  regardless of  $\alpha$ . This is confirmed by DEM simulations analogous to those performed on the single FCC elementary cell considered in Section 4.3.1. Figure 4.4 plots equation (4.6), as well as measurements of Poisson's ratio  $\nu$  as a function of  $\alpha$  for the single elementary cell obtained from numerical simulations using the discrete element method. For one set of DEM simulations, the spheres were not allowed to rotate, while for the other set, rotation was unrestrained. No friction was present on the boundary of the elementary cell during the deformation. As Figure 4.4 shows, when the spheres are not allowed to rotate, the DEM results for Poisson's ratio are in perfect agreement with the theoretical predictions of equation (4.6). When the spheres are allowed to rotate, however, the DEM results for Poisson's ratio no longer agree with the theoretical predictions of equation (4.6), but are consistently (and significantly) higher. Note that we were able to verify that there was *no inter-particle slip* in either of the DEM simulations

referred to in Figure 4.4.

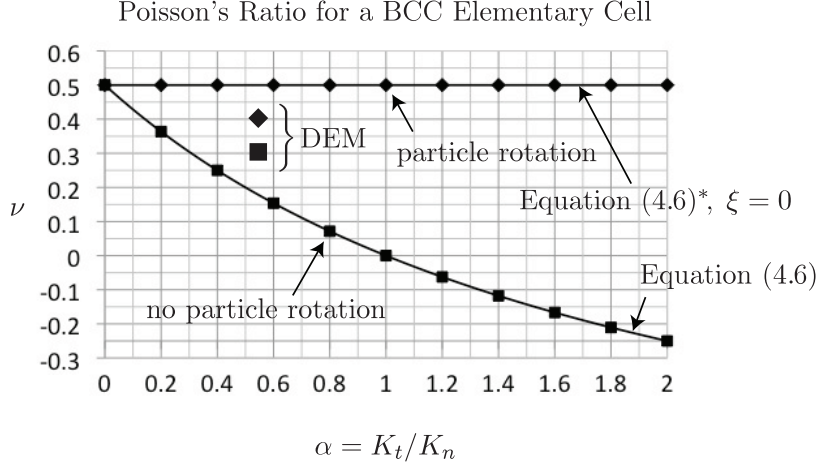


Figure 4.4: Poisson's ratio  $\nu$  as a function of  $\alpha = K_t/K_n$  for a single elementary cell of a BCC array of uniform spheres. The data points represent values obtained by numerical simulations performed using the discrete element method (DEM) in which the particles were either allowed or not allowed to rotate. The theoretical curves are from equations (4.6) and (4.6)\* [which is equation (4.6) with  $\alpha$  replaced by  $\alpha^* = \xi\alpha$ ] with  $\xi = 0$ .

Indeed, for any sort of deformation, if the spheres in a BCC elementary cell are free to rotate and there is no tangential force applied to the boundaries, there will be no inter-particle tangential displacement regardless of  $K_t$ . This follows immediately from moment equilibrium applied to the eight spheres on the boundaries of the cell. Thus, the effect of particle rotation for a single BCC elementary cell with particle rotation unrestrained is equivalent to the inter-particle tangential stiffness being zero. In analogy to the cases of the FCC and SC elementary cells, we can write the modified cubic elastic moduli for a single BCC elementary cell incorporating particle rotation as

$$C_1 = \frac{1}{2\sqrt{3}R}(K_n + 2\xi K_t), \quad C_2 = \frac{1}{2\sqrt{3}R}(K_n - \xi K_t), \quad C_3 = \frac{1}{2}(C_1 + C_2), \quad (4.7)$$

with  $\xi = 0$ .

Our theoretical analysis is confirmed by the DEM simulations described at the beginning

of this section. If we substitute the expressions for  $C_1$  and  $C_2$  given by equation (4.7) into equation (4.6), and call the resulting expression equation (4.6)\* where  $\alpha^* = \xi\alpha$  replaces  $\alpha$ , then the  $\nu(\alpha)$  curve predicted by equation (4.6)\* with  $\xi = 0$  agrees exactly with the curve that was obtained numerically by DEM simulations in which particle rotation was unrestrained, as shown in Figure 4.4. It is noteworthy that, due to geometric nonlinearities, if the pre-compression on the single BCC elementary cell in the DEM simulations results in an initial overlap of the spheres of  $0.01D$ , where  $D$  is the sphere diameter, then the DEM results for Poisson's ratio are actually  $\nu = 0.508$ . However, if the pre-compression on the single BCC elementary cell is reduced so that the initial overlap of the spheres is  $0.001D$ , then the DEM result for Poisson's ratio becomes  $\nu = 0.5008$ , and this result can be brought arbitrarily close to the theoretical result of  $\nu = 0.5$  by further reducing the initial overlap of the spheres.

Unlike the case of the FCC elementary cells, however, it takes a significant number of BCC elementary cells to restrain particle rotation. Figure 4.5 shows the results of DEM simulations on  $9 \times 9 \times 9$ ,  $18 \times 18 \times 18$ , and  $27 \times 27 \times 27$  arrays of BCC elementary cells, containing totals of 1 729, 12 691, and 41 635 uniform spheres, respectively. For a  $27 \times 27 \times 27$  BCC array, the data points obtained from DEM simulations in which particle rotation was unrestrained match approximately those obtained from a single BCC elementary cell in which particle rotation was prohibited (the match is good for  $\alpha \leq 1.0$ , but it diverges slightly for  $\alpha > 1.0$ ), which is predicted by equation (4.6) or by equation (4.6)\* with  $\xi = 1$ , as shown in Figure 4.5; this is the minimum array size for which this approximate match occurs.

### 4.3.3 Simple Cubic (SC) Array of Uniform Spheres

A single elementary cell of a SC array of uniform spheres (Figure 4.1, right) shows no Poisson effect when loaded parallel to the principal axes (because  $C_2 = 0$ ). However, particle rotation can affect the shear behavior of a single SC elementary cell when asymmetries exist in the

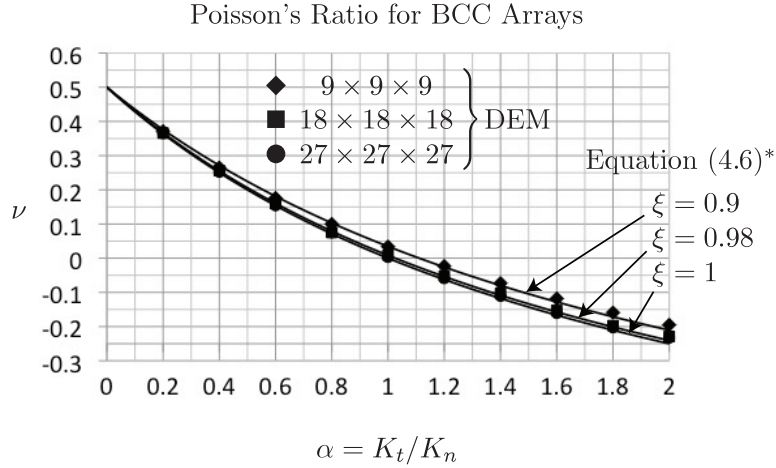


Figure 4.5: Poisson's ratio  $\nu$  as a function of  $\alpha = K_t/K_n$  for  $9 \times 9 \times 9$ ,  $18 \times 18 \times 18$ , and  $27 \times 27 \times 27$  arrays of BCC elementary cells, containing totals of 1 729, 12 691, and 41 635 uniform spheres, respectively. The data points represent values obtained by numerical simulations performed using the discrete element method (DEM) in which particle rotation was unrestrained. The theoretical curves are from equation (4.6)\* [which is equation (4.6) with  $\alpha$  replaced by  $\alpha^* = \xi\alpha$ ] with  $\xi = 0.9$ ,  $\xi = 0.98$ , and  $\xi = 1$ . The  $27 \times 27 \times 27$  array is the minimum size for which  $\xi \approx 1$ .

distribution of inter-particle contacts, which result in shearing mechanisms. To illustrate this point with a simple example, consider an elementary cell of a simple cubic array of uniform spheres subjected to pure shear for which particle rotation *is allowed* to occur, as shown in Figure 4.6. If all of the inter-particle contacts in the SC elementary cell shown in Figure 4.6 are active, then a simple calculation shows that the shear strain is  $2\epsilon_{xy} = \Delta/2R$ , and the shear stress is  $\sigma_{xy} = 4K_t\delta_t/(4R)^2$ , where  $\delta_t = \Delta - 2R\theta$  and  $R$  is the radius of the spheres. Moment balance at the particle level requires that  $K_t\delta_t = K_t2R\theta$ , from which it follows that  $\Delta = 2\delta_t$ . Thus, it follows in this case that  $C_3 = \sigma_{xy}/(2\epsilon_{xy}) = K_t/(4R)$ , which is the same as the value reported for the SC elementary cell in equation (4.3) obtained assuming *no* particle rotation. Note that in this case the distribution of inter-particle contacts in Figure 4.6 is symmetric.

Next consider the same SC elementary cell subjected to pure shear shown in Figure 4.6,

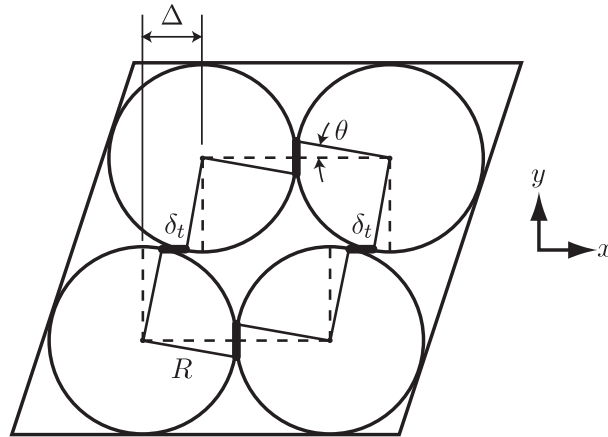


Figure 4.6: An elementary cell of an SC array of uniform spheres subjected to pure shear. If all inter-particle contacts are active, then  $C_3 = K_t/(4R)$ , which is the same as when no particle rotation is allowed, and corresponds to  $\xi = 1.0$  in equation (4.8). However, if a single infinitesimal gap is introduced between the two visible spheres at the bottom of the cell so that one inter-particle contact in the  $y$ - $z$  plane is lost, then  $C_3 = 0.5K_t/(4R)$ , which corresponds to  $\xi = 0.5$  in equation (4.8).

but this time with a single infinitesimal gap introduced between the two visible spheres at the bottom of the cell, so that there is no resistance to relative rotation at what would otherwise have been the contact point between those two spheres in the  $y$ - $z$  plane. It follows that, while the shear strain is the same as it was in the preceding paragraph when all of the inter-particle contacts were active, and moment equilibrium at the particle level still requires that  $K_t\delta_t = K_t2R\theta$  (in the absence of moments at the inter-particle contacts), the shear stress now becomes  $\sigma_{xy} = 2K_t\delta_t/(4R)^2$ , from which it follows that  $C_3 = 0.5K_t/(4R)$ , which is *half* of the value reported for the SC elementary cell in equation (4.3) assuming no particle rotation. Note that in this case the distribution of inter-particle contacts in Figure 4.6 is no longer symmetric.

Finally, consider the same SC elementary cell subjected to pure shear shown in Figure 4.7, in which an infinitesimal gap exists between all pairs of particles having their contact plane with unit normal in the  $x$ -direction. This arrangement provides no resistance to shear stress, and so  $C_3 = 0$ .

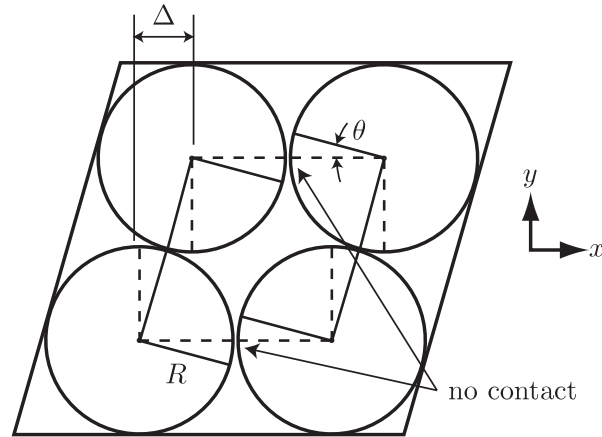


Figure 4.7: An elementary cell of an SC array of uniform spheres subjected to pure shear, with no inter-particle contacts in the  $y$ - $z$  plane. For this arrangement  $C_3 = 0$ , which corresponds to  $\xi = 0$  in equation (4.8).

These simple examples suggest that if we consider the possibility of zero-energy shearing mechanisms due to particle rotation and asymmetry in the distribution of inter-particle contacts, the cubic elastic moduli for a single SC elementary cell become

$$C_1 = \frac{1}{2R}K_n, \quad C_2 = 0, \quad C_3 = \frac{1}{4R}\xi K_t, \quad (4.8)$$

where  $0 \leq \xi \leq 1$  is an internal parameter measuring the presence of shearing mechanisms due to particle rotation and asymmetries in the distribution of inter-particle contacts. In the preceding three examples, we found by direct analysis that  $\xi = 1.0$ ,  $\xi = 0.5$ , or  $\xi = 0$ , respectively, depending on the number of inter-particle contacts providing resistance to shear deformation. Note that in all three of these examples the resistance of the elementary cell to normal stress (and hence the value of  $C_1$ ) is the same.

## 4.4 Isotropic Effective Elastic Moduli Incorporating the Effect of Particle Rotation

In Section 3 of Part I, we derived relations between the overall elastic moduli  $\bar{\kappa}$  and  $\bar{\nu}$  of a statistically isotropic particulate material on the macroscale, and the normal and tangential inter-particle contact stiffnesses  $K_n$  and  $K_t$  (and  $\alpha = K_t/K_n$ ) and the average number of inter-particle contacts per unit volume  $\beta$  on the microscale, for all three local cubic packings under the Voigt, Reuss, and self-consistent hypotheses. If equations (4.5), (4.7), and (4.8) are used for the cubic elastic moduli instead of equations (4.1), (4.2), and (4.3), then the only change in the relations obtained in Section 3 of Part I is that  $K_t$  is replaced by an “effective”  $K_t^* = \xi K_t$ , and  $\alpha$  is replaced by an “effective”  $\alpha^* = \xi\alpha = K_t^*/K_n$ , where  $0 \leq \xi \leq 1$  is an internal parameter measuring the presence of shearing mechanisms due to particle rotation and asymmetries in the distribution of inter-particle contacts. Note that  $K_n$  remains unchanged. If  $\xi = 0$  then all inter-particle contacts contain shearing mechanisms, and  $K_t$  becomes zero. If  $\xi = 1$  then there are no shearing mechanisms, and  $K_t$  is unaltered.

Thus, we obtain the following relations between the normal and tangential inter-particle contact stiffnesses  $K_n$  and  $K_t$  (and  $\alpha = K_t/K_n$ ) and the parameter  $\beta$  on the microscale, and the overall elastic moduli  $\bar{\kappa}$  and  $\bar{\nu}$  of the particulate material on the macroscale, under the Voigt, Reuss, and self-consistent hypotheses for the locally FCC, BCC, and SC packings:

$$\text{Voigt, Reuss, self-consistent: FCC, BCC, SC:} \quad \bar{\kappa} = \frac{\beta D^2}{9} K_n, \quad (4.9)$$

$$\text{Voigt: FCC, BCC, SC:} \quad \bar{\nu} = \frac{1 - \alpha^*}{4 + \alpha^*}, \quad (4.10)$$

$$\text{Reuss: FCC:} \quad \bar{\nu} = \frac{3 + 2\alpha^* - 5\alpha^{*2}}{11 + 24\alpha^* + 5\alpha^{*2}}, \quad (4.11)$$

$$\text{Reuss: BCC:} \quad \bar{\nu} = \frac{4 + \alpha^* - 5\alpha^{*2}}{8 + 32\alpha^* + 5\alpha^{*2}}, \quad (4.12)$$

$$\text{Reuss: SC:} \quad \bar{\nu} = \frac{1 - \alpha^*}{2 + 3\alpha^*}, \quad (4.13)$$

$$\begin{aligned} \text{self-consistent: FCC:} \quad \alpha^* = \\ \frac{2 + 5\bar{\nu} - 5\bar{\nu}^2 - 8\bar{\nu}^3 - \sqrt{36 - 144\bar{\nu} + 88\bar{\nu}^2 + 280\bar{\nu}^3 - 291\bar{\nu}^4 - 134\bar{\nu}^5 + 169\bar{\nu}^6}}{-4 - 3\bar{\nu} + 6\bar{\nu}^2 + 5\bar{\nu}^3}, \end{aligned} \quad (4.14)$$

$$\begin{aligned} \text{self-consistent: BCC:} \quad \alpha^* = \\ \frac{11 + 30\bar{\nu} - 27\bar{\nu}^2 - 46\bar{\nu}^3 - 3\sqrt{81 - 228\bar{\nu} + 202\bar{\nu}^2 + 352\bar{\nu}^3 - 735\bar{\nu}^4 - 92\bar{\nu}^5 + 484\bar{\nu}^6}}{4(-4 - 3\bar{\nu} + 6\bar{\nu}^2 + 5\bar{\nu}^3)}, \end{aligned} \quad (4.15)$$

$$\text{self-consistent: SC:} \quad \alpha^* = \frac{(1 - 2\bar{\nu})^2(3 - \bar{\nu})}{(1 + \bar{\nu})^2(3 - 4\bar{\nu})}, \quad (4.16)$$

where  $\alpha^* = \xi\alpha = \xi K_t/K_n$ , and where  $\alpha^*$  is written in terms of  $\bar{\nu}$  in the self-consistent case only because the expressions are far more concise than the corresponding expressions for  $\bar{\nu}$  in terms of  $\alpha^*$ .

In Section 4.3.1, for a single FCC cell with unrestrained particle rotation and no tangential force applied to the boundaries, we found by direct analysis that  $\xi = 0.733$  or  $\xi = 0.5$ , depending on whether or not certain infinitesimal inter-particle gaps exist. We also found by DEM simulations on  $2 \times 2 \times 2$ ,  $3 \times 3 \times 3$ , and  $7 \times 7 \times 7$  arrays of FCC cells with unrestrained particle rotation that  $\xi = 0.92$ ,  $\xi = 0.97$ , and  $\xi = 1$ , respectively, as shown in Figure 4.3. In Section 4.3.2, for a single BCC cell with unrestrained particle rotation and no tangential force applied to the boundaries, we found by direct analysis that  $\xi = 0$ . We also found by DEM simulations on  $9 \times 9 \times 9$ ,  $18 \times 18 \times 18$ , and  $27 \times 27 \times 27$  arrays of BCC cells with unrestrained particle rotation that  $\xi = 0.9$ ,  $\xi = 0.98$ , and  $\xi = 1$ , respectively, as shown in Figure 4.5. For both the FCC and BCC arrays, the *minimum* number of cells was found that

effectively restrained particle rotation (i.e., resulted in  $\xi = 1$ ), and this is the number that was reported. Note that significantly more cells were required to restrain particle rotation in the BCC array than were required in the FCC array. In Section 4.3.3, for a single SC cell subjected to pure shear with unrestrained particle rotation, we found by direct analysis that  $\xi = 1.0$ ,  $\xi = 0.5$ , or  $\xi = 0$ , depending on the number of infinitesimal inter-particle gaps introduced. Note that if  $\xi = 0$  then equations (4.12), (4.13), and (4.16) predict that  $\bar{\nu} = 0.5$  for all values of  $\alpha$ . This suggests that in the presence of sufficiently many shearing mechanisms, the particulate material acts effectively as a fluid, with no resistance to shear stress. The case of  $\xi = 0$  is illustrated by the SC elementary cell considered in Figure 4.7, and by the single BCC elementary cell with unrestrained particle rotation. It should be noted, however, that these two illustrative cases are not isotropic. For further discussion of the arrangement shown in Figure 4.7, see Bardet and Vardoulakis (2001) and Kruyt (2003).

While it is clear that (infinitely) many rotational mechanisms exist in a single BCC elementary cell when no tangential force is applied to the spheres in contact with the cell boundary, for such mechanisms to exist in a *statistically isotropic aggregate* of BCC elementary cells, it would be necessary for some kind of local asymmetry to exist in the inter-particle contact distribution. Such local asymmetry could be caused by a series of aligned BCC elementary cells. Note that a diagonal alignment of BCC cells would result in what is called a “force-chain” in the geomechanics literature. The existence of force-chains in particulate materials is well known, as noted by Mitchell and Soga (2005). Force-chains, sometimes called strong force networks, refer to isolated paths of high inter-particle contact forces within a particulate material under load. The areas outside of these force-chains, sometimes called weak clusters, experience much smaller inter-particle contact forces. Many researchers, such as Cundall and Strack (1979) and Oda (1997), have observed that during plastic shear, particles within force-chains do not slide, but rather the columns of particles within the force-chains buckle. In an elastic context, the buckling of local force-chains in a particulate

material (which implies the existence of local mechanisms due to particle rotation) would result in an increase in Poisson’s ratio when compared to a particulate material without such mechanisms, as predicted by equations (4.10) – (4.16) when  $\xi < 1$ .

It is intriguing to consider the relationship between the parameter  $\xi$  and other internal geometrical parameters of a (statistically isotropic) particulate material, such as the average number of contacts per unit volume  $\beta$ , or the average coordination number  $\bar{n}_c$ , which is related to  $\beta$  (see, e.g., Nemat-Nasser, 2004). Note, however, that in equation (4.9), the value of  $\beta$  is unaffected by  $\xi$ . This is because the particle rotations and infinitesimal gaps considered in the preceding subsections did not affect the *normal* component of the inter-particle contact forces, and so did not change the bulk modulus  $\bar{\kappa}$ . Hence, the average number of contacts per unit volume  $\beta$  should still include the “missing” contacts that in some of these examples gave rise to  $\xi < 1$ . Thus, the internal parameter  $\xi$  cannot depend exclusively on either  $\beta$  or  $\bar{n}_c$ . Rather, we hypothesize that the internal parameter  $\xi$  for an overall isotropic particulate material is related to *local asymmetry* in the inter-particle contact force distribution. Finding a relationship between the internal parameter  $\xi$  and a quantifiable measure of asymmetry in the inter-particle contact force distribution of a particulate material at the local level, which must involve the fabric tensor of the particulate material (e.g., Durán et al., 2010), is a subject of continuing research.

Recent work in determining the effective isotropic elastic moduli for a particulate (or granular) material based on micromechanics, with an attempt to include the effect of particle rotation, has been performed by Suiker and de Borst (2005). They rederive the relations expressed by the Voigt equation (4.10) with  $\xi = 1$  (but without the internal parameter), along with additional relations for higher order elastic constants corresponding to several strain-gradient micro-polar continuum models. Then they compare the predictions of these models with the wave propagation characteristics of a two-dimensional discrete hexagonal lattice. Their analysis follows that of Chang and Liao (1990) and Chang and Gao (1995) in assuming

that discrete particle rotations can be approximated by a continuous particle rotation field, similar to the strain field of classical continuum theory. This particle rotation field is then represented by a Taylor expansion, which can be truncated at whatever order is desired for the strain-gradient continuum model. This approach is problematic in that it cannot capture the zero-energy strains or mechanisms due to particle rotation at the microscale. Both the simple example of this section and the DEM results of Section 4.5 demonstrate that mechanisms due to particle rotation can and do exist in a random assembly of spherical particles, and these mechanisms affect the elastic properties of the material (specifically Poisson’s ratio), despite the fact that they do not contribute to the quasi-static stress power (Goddard, 2008). As will be shown in the following section, none of these prior theoretical models incorporating particle rotation can come close to matching our DEM simulations for precisely these reasons, whereas the theoretical models derived here can.

## 4.5 Validation by the Discrete Element Method

To test the analytical results of Section 4.4, we performed numerical simulations using the discrete element method (DEM) to measure the macroscopic elastic moduli for randomly packed aggregates of uniform spheres having constant normal and tangential contact stiffnesses  $K_n$  and  $K_t$ , respectively. We report the results that we have obtained from six DEM specimens. Specimens 1, 2, and 3 each contained 3 430 randomly packed uniform spheres, and Specimens 4, 5, and 6 each contained 29 660 randomly packed uniform spheres. The specimens are shown in Figure 7 of Part I.

We performed the DEM simulations using the open source code LAMMPS, described in Part I. The setup procedure and initial geometries of the six DEM specimens used in this part of our two-part series are identical to those of the six DEM specimens used in Part I. For a discussion of the initial packing geometries, including the average number of contacts

per unit volume and the radial distribution functions for the specimens, see Section 3.5 and Figure 3.9 of Part I.

To measure Poisson's ratio  $\bar{\nu}$  for each specimen, we followed the procedure described by the paragraph including equation (3.44) in Part I. To explore the effect of particle rotation in the DEM simulations of this second part of our two-part series, the spheres were allowed full three-dimensional translational and rotational freedom of motion. The results are shown in Figure 4.8. Data points for both of the measured values of Poisson's ratio  $\bar{\nu}_1$  and  $\bar{\nu}_2$  given by equation (3.44) of Part I are included in all of the figures as solid squares and solid diamonds. The difference between these data points provides a rough measure of the anisotropy of the specimens, at least in the directions normal to the specimen boundaries. Note that in most of the figures, these data points lie roughly on top of one another.

Figure 4.8 also shows the Voigt (4.10), Reuss (4.13), and self-consistent (4.15), (4.16) curves, with  $\xi = \{0.75, 0.6, 0.55, 0.85, 0.8, 0.75\}$  for Specimens 1 – 6, respectively, where the values of the internal parameter  $\xi$  were chosen to fit the DEM data points. Also shown in Figure 4.8 by dotted lines are all of the same curves with  $\xi = 1$ , which correspond to the curves shown in Figure 8 of Part I. Note that when the rotation of the spheres is not restrained, the value of Poisson's ratio in all six specimens is strictly and significantly greater than zero when  $\alpha = 1.0$  ( $K_t = K_n$ ). This is in disagreement with the results of Section 3.3 in Part I, which do not account for the effect of particle rotation, as well as the results of Chang et al. (1995) for both an isotropic and a general anisotropic particulate material (not necessarily having a locally cubic packing structure) under both the kinematic and static hypotheses, all of which predict  $\bar{\nu} = 0$  when  $\alpha = 1.0$ . This phenomenon *is* captured, however, by equations (4.10), (4.13), (4.15), and (4.16), with  $\xi < 1.0$ . In particular, the relationship between Poisson's ratio  $\bar{\nu}$  and  $\alpha = K_t/K_n$  that is given by equation (4.15), the self-consistent result for the local BCC packing, with  $\xi = \{0.75, 0.6, 0.55, 0.85, 0.8, 0.75\}$  for Specimens 1 – 6, respectively, agrees with the values obtained from the DEM simulations better than any

of the other theoretical predictions we have considered thus far.

We also monitored friction work between the spheres throughout the DEM simulations, and we verified that *there was no inter-particle slip* during the DEM simulations, regardless of whether or not particle rotation was allowed (i.e., friction work was zero). Thus, inter-particle slip, and consequently plastic deformation, was not involved in the discrepancy between the values of Poisson's ratio predicted by the Voigt (4.10), Reuss (4.13), and self-consistent (4.15), (4.16) equations, with  $\xi = 1$ , which also correspond to the equations of Section 3 in Part I, and the values that were measured from the DEM simulations when particle rotation was allowed. As noted above, this discrepancy increased as  $\alpha$  increased, but was remedied when the Voigt, Reuss, and self-consistent equations were used with  $\xi = \{0.75, 0.6, 0.55, 0.85, 0.8, 0.75\}$  for Specimens 1 – 6, respectively. Note that, because Chang et al. (1995) predict  $\bar{\nu} = 0$  when  $\alpha = 1.0$  not only for a statistically isotropic particulate material, but also for a general anisotropic particulate material, their theoretical predictions cannot be reconciled with our DEM results when particle rotation is involved. We postulate that the internal parameter  $\xi$  measures zero-energy rotations or mechanisms in the particulate material at the local level (as it was directly shown to do in the explicit cases analyzed in Sections 4.3.1 - 4.3.2), which exist even when the particulate material is statistically isotropic and when no inter-particle slip occurs, and which, as we discussed at the end of Section 4.4, are not accounted for in the quasi-micro-polar and micro-polar theories of Chang et al. (1995), Chang and Gao (1995), Suiker and de Borst (2005), and others.

Our postulation of the existence of zero-energy rotations or mechanisms in a statistically isotropic particulate material [which we have directly confirmed: see the last two paragraphs of this section] is similar to the postulation made by Jenkins et al. (2005), who, following earlier work by Jenkins et al. (1989), have used DEM simulations to show that *local deviations* in strain from the the average (macroscopic) strain in a particulate material can lead to *large* discrepancies between the theoretically predicted values of the macroscopic shear modulus

## DEM Predictions of Poisson's Ratio

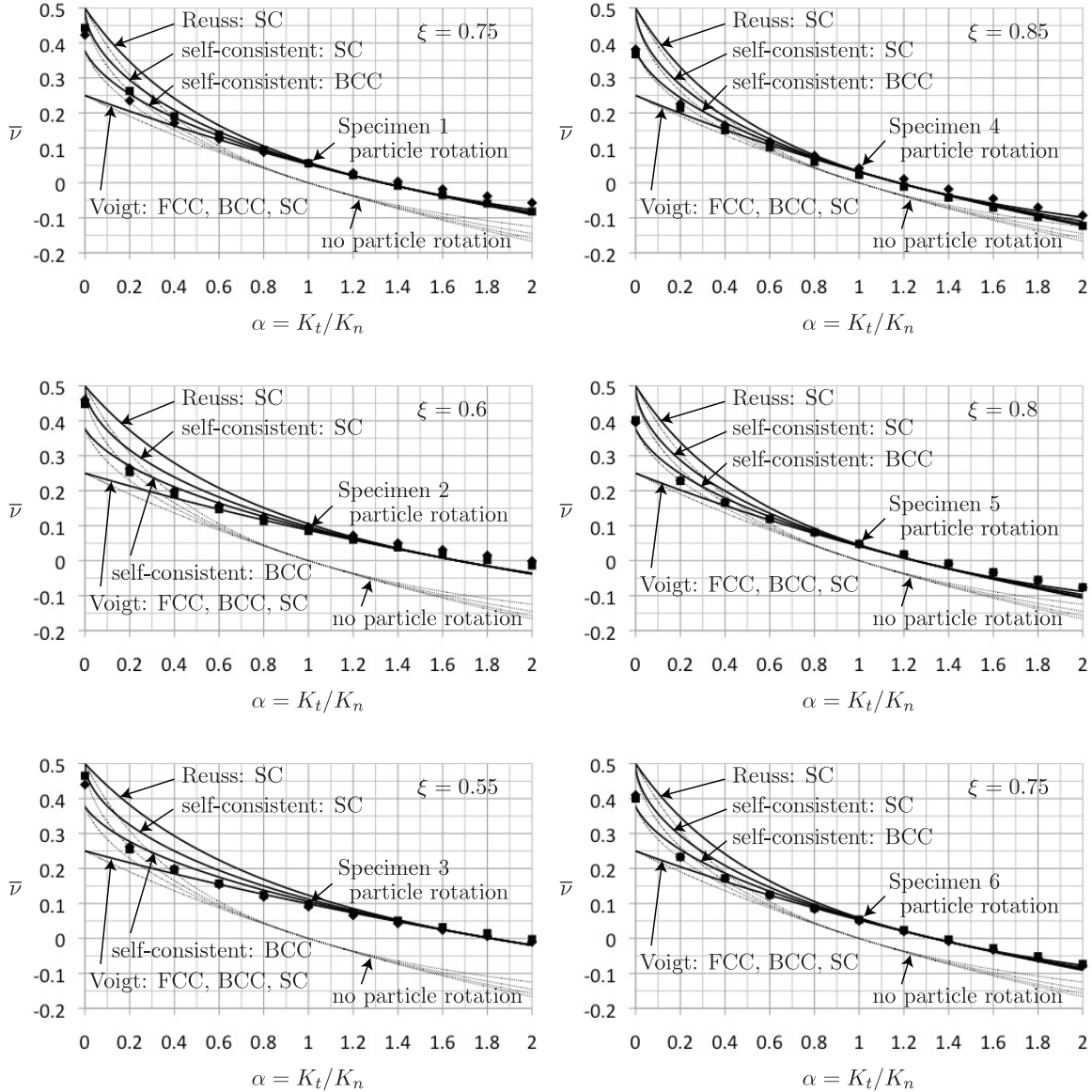


Figure 4.8: Macroscopic Poisson's ratio  $\bar{\nu}$  versus  $\alpha = K_t/K_n$  obtained from DEM simulations on six specimens of randomly packed uniform spheres with constant normal and tangential contact stiffnesses  $K_n$  and  $K_t$ , in which the spheres were allowed to rotate. Also shown are the theoretical curves given by equations (4.10) [Voigt: FCC, BCC, SC], (4.13) [Reuss: SC], (4.15) and (4.16) [self-consistent: BCC and SC, respectively], with  $\xi = \{0.75, 0.6, 0.55, 0.85, 0.8, 0.75\}$  for Specimens 1 – 6, respectively. Observe that the analytical self-consistent homogenization result for the local BCC packing, equation (4.15), agrees most closely with the DEM simulations.

(or Poisson’s ratio) for the particulate material and the numerically measured values. They argue that this local deviation is due to strain “relaxation” between particle pairs, which is similar to our argument for local strain “mechanisms” due to particle rotation. Jenkins et al. (2005) show that this local strain relaxation can decrease the theoretical prediction of the effective shear modulus obtained from equation (3.24) of Part I, or equations (4.9) and (4.10) with  $\xi = 1$  (where the shear modulus is obtained in terms of the bulk modulus  $\bar{\kappa}$  and Poisson’s ratio  $\bar{\nu}$ ), by up to 70%. In contrast, they found that the bulk modulus  $\bar{\kappa}$  is relatively insensitive to local strain variation. This is in perfect agreement with our observations in Section 4.4 and in this section regarding Poisson’s ratio. The DEM specimens used by Jenkins et al. (2005) consisted of 10 000 randomly packed spheres of two different radii in equal numbers.

We have confirmed the existence of rotational mechanisms within our DEM specimens by monitoring the angular velocities of individual particles throughout the DEM simulations described in this section. We found that particles in some of the specimens experienced angular velocities in excess of *ten times* the average angular velocity of the particles in those specimens during a simulation. This can be quantified by the ratio  $\langle \Omega \rangle_{\max} / \langle \Omega \rangle_{\text{avg}}$ , where  $\Omega$  is the magnitude of the angular velocity of an individual particle in a specimen, the angled brackets  $\langle \rangle$  denote root-mean-square time average over the course of a simulation, and the subscripts “max” and “avg” denote maximum and rms-average values over all particles in the specimen. We computed this ratio for each specimen during the simulation with  $\alpha = 1.0$ , and the resulting values were  $\langle \Omega \rangle_{\max} / \langle \Omega \rangle_{\text{avg}} = \{10.3, 8.37, 9.31, 32.9, 70.0, 36.4\}$  for Specimens 1 – 6, respectively.

Figure 4.9 shows clusters of particles in Specimens 2 and 6 that experienced angular velocities in excess of two times the rms-average particle angular velocity at a particular time during the DEM simulations with  $\alpha = 1.0$ . The particles with  $\Omega > 2\Omega_{\text{avg}}$  are shown as spheres in Figure 4.9, while the other particles (i.e., with  $\Omega \leq 2\Omega_{\text{avg}}$ ) are shown as dots.

The spheres are shaded according to the magnitude of their angular velocities. Particles with  $\Omega > 5\Omega_{\text{avg}}$  and  $\Omega > 10\Omega_{\text{avg}}$  are magnified and shown next to Specimens 2 and 6, respectively. Figure 4.9, together with the measured values of  $\langle\Omega\rangle_{\text{max}}/\langle\Omega\rangle_{\text{avg}}$  for all of the specimens, shows that rotational mechanisms were present during the simulations. There appears, however, to be no correlation between  $\langle\Omega\rangle_{\text{max}}/\langle\Omega\rangle_{\text{avg}}$  and the internal parameter  $\xi$  for our DEM specimens.

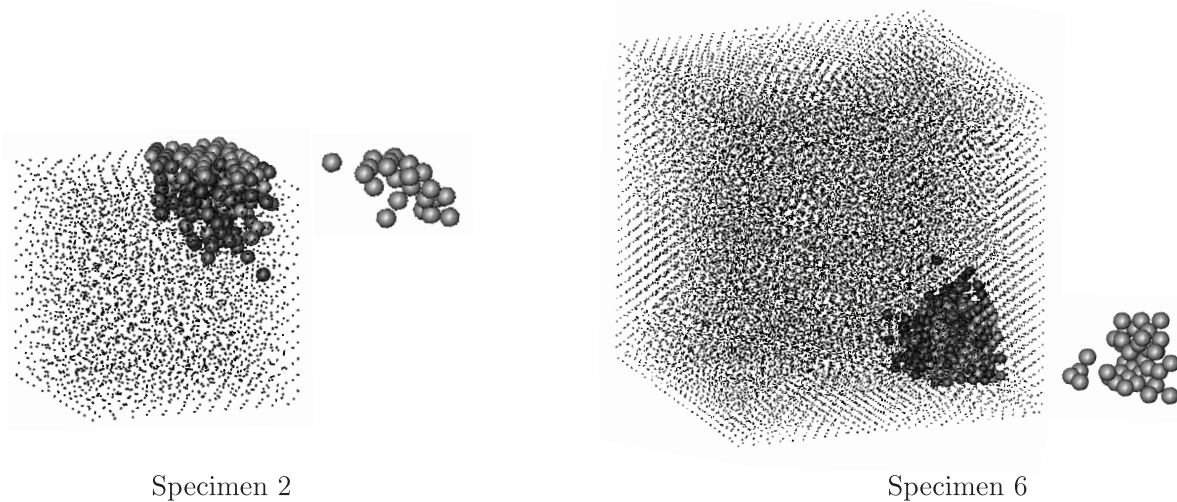


Figure 4.9: Rotational mechanisms in DEM Specimens 2 and 6. The particles represented as spheres in each specimen experienced rotations in excess of 2 times the rms-average particle rotation in the specimen. The magnified spheres next to Specimens 2 and 6 represent particles that experienced rotations in excess of 5 and 10 times the rms-average particle rotation, respectively.

## 4.6 Discussion

If we assume Hertz-Mindlin contact, then equation (3.8) of Part I [Chapter 3] implies that  $\alpha = 2(1 - \nu)/(2 - \nu)$ , where  $\alpha = K_t/K_n$  and  $\nu$  is Poisson's ratio for the material constituting the spheres (not for the particulate material as a whole). Thus, for a particulate material composed of uniform spheres, if the spheres are composed of a stable elastic material then

$\alpha$  is bounded by  $2/3 \leq \alpha \leq 4/3$ , and if the spheres are composed of a stable elastic material with  $0 \leq \nu \leq 1/2$  then  $\alpha$  is bounded by  $2/3 \leq \alpha \leq 1$ . For materials with  $\nu \approx 0.3$  (such as quartz), Hertz-Mindlin contact implies that  $\alpha \approx 0.8$ . Thus, the accuracy of theoretical models for values of  $\alpha$  in the vicinity of 0.8, and more generally for values of  $\alpha$  between  $2/3$  and 1, is of great practical importance. Figure 4.10 shows the  $\bar{\nu}(\alpha)$  curve for Specimen 3 in the region  $2/3 \leq \alpha \leq 4/3$  with unrestrained particle rotation, along with the theoretical curves given by the Voigt (4.10), Reuss (4.13), and self-consistent (4.15), (4.16) equations, with  $\xi = 0.55$  and  $\xi = 1$ .

Also shown in Figure 4.10 for comparison is an experimental data point for spherical glass beads. For glass beads,  $\nu \approx 0.2$ , and Hertz-Mindlin contact theory predicts  $\alpha \approx 0.9$ . Thus, the Voigt (4.10), Reuss (4.13), and self-consistent (4.15), (4.16) equations with  $\xi = 1$ , which also correspond to the equations of Section 3 in Part I derived assuming no particle rotation, all predict that Poisson's ratio for an isotropic packing of spherical glass beads should be  $\bar{\nu} \approx 0.02$ . However, according to Bachrach et al. (2000), the experimentally measured value of Poisson's ratio for a random packing of spherical glass beads is  $\bar{\nu} \approx 0.15$ , over seven times larger than the theoretical predictions of Section 3 in Part I. Note from Figure 4.10, however, that the values of  $\bar{\nu}$  predicted by the Voigt (4.10), Reuss (4.13), and self-consistent (4.15), (4.16) equations of Section 4.4 with  $\xi = 0.55$  are much closer to the experimentally measured value of  $\bar{\nu}$ , ranging between  $\bar{\nu} \approx 0.11$  and  $\bar{\nu} \approx 0.14$  for  $\alpha \approx 0.9$ . It should be noted that the value of the internal parameter  $\xi = 0.55$  was chosen to match the DEM data points obtained from Specimen 3, and by adjusting the internal parameter  $\xi$  any of the modified curves could be made to pass through the single experimental data point for glass beads. Specimen 3 was chosen in Figure 4.10 for illustrative purposes, because it shows the largest effect of particle rotation of the six DEM specimens tested, and because the values of Poisson's ratio in the vicinity of  $\alpha \approx 0.9$  are the closest to that measured experimentally for spherical glass beads.

Unfortunately, although it is illustrative, the experimental data point for glass beads

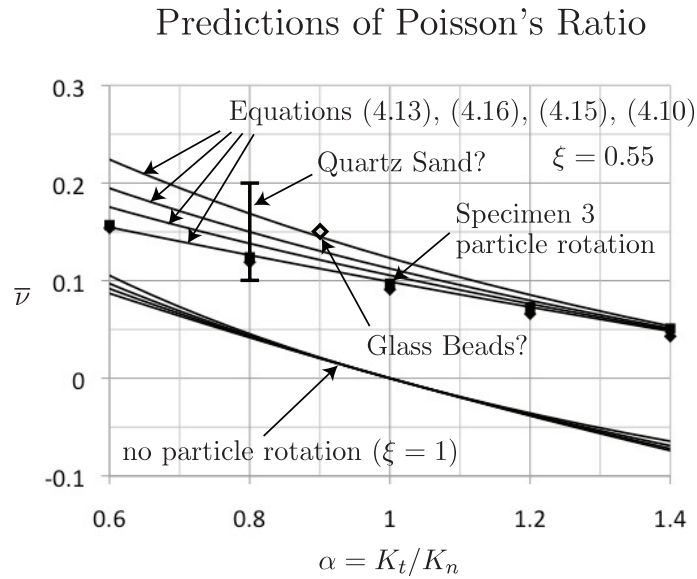


Figure 4.10: Macroscopic Poisson's ratio  $\bar{\nu}$  for  $\alpha = K_t/K_n$  bounded by  $2/3 \leq \alpha \leq 4/3$ , which is the range of possible values for  $\alpha$  assuming Hertz-Mindlin contact between spheres composed of a stable elastic material. DEM data points are from Specimen 3 with unrestrained particle rotation. Also shown are the theoretical curves given by equations (4.10) [Voigt], (4.13) [Reuss: SC], (4.15) and (4.16) [self-consistent: BCC and SC, respectively], with  $\xi = 0.55$  and  $\xi = 1$ . Also shown is an experimental data point for glass beads, for which the value of  $\alpha \approx 0.9$  is uncertain because it assumes no inter-particle slip. A range of experimentally measured values of Poisson's ratio for quartz sand is also shown, for which the value of  $\alpha \approx 0.8$  is uncertain for the same reason.

provides limited information for the purpose of testing our theory. This is because, as noted by Bachrach et al. (2000), we do not know whether or not there was inter-particle slip between the glass beads during the experiment, and hence we do not know whether the value of  $\alpha \approx 0.9$  predicted by Hertz-Mindlin contact theory (assuming no inter-particle slip) is correct for the glass beads. The same is true of the experimentally measured values of Poisson's ratio for quartz sand, which typically fall in the range  $0.1 < \bar{\nu} < 0.2$  (e.g., Mitchell and Soga, 2005). This is one reason the discrete element method was essential to test the validity of our theoretical results, since the value of  $\alpha$  for any given physical particulate material (such as glass beads) is not known exactly, and at best provides only one data point, while using DEM we could adjust  $\alpha$  over a large range of exactly known values by adjusting the inter-particle tangential contact stiffness  $K_t$ . Nevertheless, we note from Figure 4.10 that the range of experimentally measured values of Poisson's ratio for quartz sand with  $\alpha \approx 0.8$  compares well with our DEM simulation results obtained from Specimen 3.

Bachrach et al. (2000) noted the discrepancy between the experimentally measured value of  $\bar{\nu}$  for a random packing of glass beads and the theoretical prediction of Walton (1987), which is identical to equation (4.10) with  $\xi = 1$ . Bachrach et al. (2000) suggested that the cause for this discrepancy may be due to slipping at the inter-particle contacts. A similar approach was taken by Trentadue (2004), who replaced the Hertz-Mindlin contact law in equation (3.8) of Part I with a Hertz-Cattaneo-Mindlin contact law, which includes a parameter  $\zeta$  to account for micro-slip at inter-particle contacts, and by Duffaut et al. (2010), who also modified the results of Walton (1987) by introducing a parameter to account for micro-slip at inter-particle contacts. While slipping at inter-particle contacts may be partially responsible for the very large discrepancy between the experimentally measured value of  $\bar{\nu} \approx 0.15$  for a random packing of glass beads and the values predicted by the methods of Section 3 in Part I (with no particle rotation), slipping at inter-particle contacts

cannot explain the discrepancy between the values of  $\bar{\nu}$  that were measured from our DEM simulations and the values predicted by the methods of Section 3 in Part I, since we can verify that no slipping occurred between any of the particles in our DEM simulations. Indeed, by using DEM simulations to explore the effect of eliminating particle rotation, we believe we have identified an important contributing factor to the discrepancy between theoretical and experimentally measured values of Poisson's ratio in particulate materials, particularly in the vicinity of  $\alpha \approx 1$ .

Another approach to the homogenization of particulate materials was taken by Cambou et al. (1995). Like Walton (1987) and Chang et al. (1995), Cambou et al. (1995) did not analyze specific local particle arrangements, but instead assumed a form for the distribution of inter-particle contact forces a priori. However, in addition to rederiving equation (3.24) of Part I or equation (4.10) with  $\xi = 1$  under the Voigt hypothesis, Cambou et al. (1995) introduced an internal parameter  $\mu$  in their "static localization method" (analogous to homogenization under the Reuss hypothesis) that measures the fraction of the deviatoric stress in the particulate material supported by the normal components of the inter-particle contact forces, from  $2/5$  for  $\mu = 1$  to  $1$  for  $\mu = 0$ . Specifically, they assumed the average distribution  $f_i$  of the inter-particle contact forces at the local level within a particulate material can be expressed as a function of the orientation direction  $n_i$  and the far field (non-local) stress  $\sigma_{ij}$  as

$$f_i = \mu \sigma_{ij} n_j + \frac{1 - \mu}{2} [5 n_j \sigma_{jk} n_k - \sigma_{jj}] n_i. \quad (4.17)$$

Equation (4.17) was first proposed by Delyon et al. (1990), and it is based on the representation theorems (e.g., Spencer, 1987) under the assumptions that  $f_i$  is linear with respect to  $\sigma_{ij}$  and isotropic with respect to  $n_i$ . Static equilibrium then requires that

$$\sigma_{ij} = \beta D \int_{\Omega} f_i n_j d\Omega, \quad (4.18)$$

where  $d\Omega = \sin\theta d\varphi d\theta d\psi$  is the differential solid angle of the unit sphere  $\Omega$ ,  $\sigma_{ij}$  is the far field stress in the particulate material,  $\beta$  is the average number of contacts per unit volume, and  $D$  is the diameter of the spheres. Under the hypotheses expressed in equations (4.17) and (4.18), the relationship obtained by Cambou et al. (1995) between Poisson's ratio  $\bar{\nu}$  and  $\alpha = K_t/K_n$  by their static localization method is

$$\bar{\nu} = \frac{2\mu^2 + \alpha(5 - 10\mu + 3\mu^2)}{4\mu^2 + \alpha(20 - 20\mu + 6\mu^2)}. \quad (4.19)$$

Emeriault and Cambou (1996) derive more complicated expressions for an arbitrary anisotropic particulate material. If  $\mu = 1$ , then equation (4.19) is identical to equation (4.13) with  $\xi = 1$ , which is the same as the relation obtained by Chang et al. (1995) under their static hypothesis. Note that if  $\mu = 0$ , then none of the deviatoric stress in the particulate material is carried by the tangential components of the inter-particle contact forces. Thus, the role of  $\mu$  in the analysis of Cambou et al is similar to the role of  $\xi$  in our analysis. For  $\mu < 1$ , equation (4.19) does in fact predict a value of Poisson's ratio that is strictly greater than zero when  $\alpha = 1.0$ , which is in general agreement with what we have observed in our DEM simulations. However, as Figure 4.11 shows, for no value of  $\mu$  can the  $\bar{\nu}(\alpha)$  curve given by equation (4.19) be made to match the curve obtained from our DEM simulations as closely as the curve given by equation (4.15).

While the internal parameter  $\xi$  cannot depend exclusively on the average number of contacts per unit volume  $\beta$  for reasons discussed in Section 4.4, we note that for the six DEM specimens described in the preceding section, there is, in fact, a strong correlation between  $\xi$  and  $\beta$ . Figure 4.12 illustrates this correlation. It is noteworthy that the correlation between  $\xi$  and  $\beta$  observed in the DEM specimens appears to be independent of the number of spheres in the specimens (i.e., 3 430 or 29 660). This suggests that the particle rotation effects observed in the DEM simulations described in Section 4.5 are not simply due to boundary effects, nor

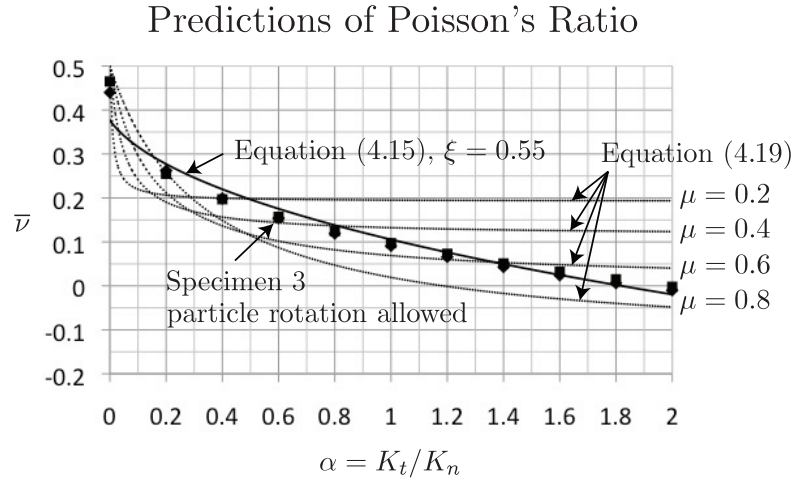


Figure 4.11: The relationship between Poisson's ratio  $\bar{\nu}$  and  $\alpha = K_t/K_n$  as obtained by Cambou et al. (1995) by their static localization method, given by equation (4.19), for a range of values of their internal parameter  $\mu$ . Also shown are the DEM data points from Specimen 3 with unrestrained particle rotation, and the curve given by the self-consistent equation (4.15) with  $\xi = 0.55$ .

to the fact that the specimens are too small to represent a statistically isotropic particulate material. The best-fit line to the data points in Figure 4.12 is given by

$$\xi = 0.164\beta D^3 - 0.143 \quad (4.20)$$

with an  $R^2$  value of 0.905.

## 4.7 Conclusions

Building on the work of Part I, we have explored the effects of particle rotation on the elastic moduli of a statistically isotropic particulate material with locally cubic packing structure. We found that particle rotation effects *must* be properly accounted for to accurately predict the values of Poisson's ratio that were measured by our DEM simulations on six randomly packed specimens of uniform spheres, having constant normal and tangential contact stiff-

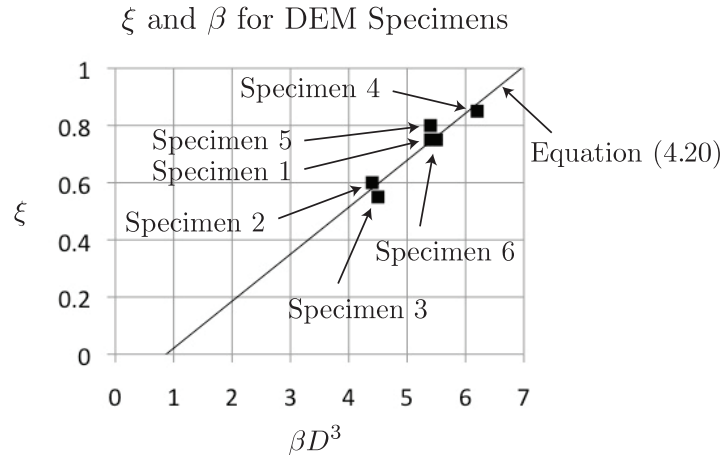


Figure 4.12: Correlation between the internal parameter  $\xi$  and the average number of contacts per unit volume  $\beta$  for the six DEM specimens tested in Section 4.5, where  $D$  is the diameter of the spheres.

nesses  $K_n$  and  $K_t$ , respectively.

There were several advantages to using DEM to test our theoretical results, as opposed to, for example, using experiments on physical particles such as glass beads. First, we were able to reproduce our theoretical assumption of constant contact stiffness exactly, without having to make any assumptions regarding the actual contact behavior of the physical particles, thus eliminating one source of uncertainty. We were also able to assign precise values to the normal and tangential contact stiffnesses, and thus measure Poisson's ratio for a large range of specific values of  $\alpha = K_t/K_n$ . Finally, we were able to adjust the DEM simulations to either allow or prohibit particle rotation, and in this way study the effect of particle rotation on the values of Poisson's ratio. Specifically, we were able to prove that particle rotation was responsible for the values of Poisson's ratio predicted by the DEM simulations in the vicinity of  $\alpha = 1$  being significantly higher than the theoretical predictions of Walton (1987) and Chang et al. (1995), which do not account for the mechanisms (i.e., zero-energy deformations) produced by particle rotation. In particular, the results of Chang et al. (1995) under the static hypothesis *do not* provide an upper bound on Poisson's ratio if particle rotation is

allowed. This is despite the fact that Chang et al. (1995) attempted to include the effects of particle rotation via a “quasi-micro-polar” continuum theory. The inability of their approach to match the DEM simulation results appears to be due to the fact that the micro-polar or quasi-micro-polar continuum approach cannot capture the zero-energy strains or mechanisms produced by particle rotations, which we have shown can and do exist in random assemblies of uniform spheres where there are local asymmetries in the distribution of inter-particle contacts.

We also showed that this discrepancy between the theoretical and DEM predictions of Poisson’s ratio could not be caused by inter-particle slip, since no inter-particle slip took place in our DEM simulations. This is a significant observation, since Bachrach et al. (2000) have hypothesized that inter-particle slip could be the cause for the (same) discrepancy between the theoretical prediction of Poisson’s ratio by Walton and the experimentally measured value of Poisson’s ratio for a random packing of uniform glass beads with  $\alpha \approx 0.9$ . While inter-particle slip may have taken place and contributed to the discrepancy, it cannot serve as the sole explanation, since the discrepancy still exists when no inter-particle slip takes place. It might also be noted that the results of such a comparison with experiment are difficult to interpret, since the theoretical value of Poisson’s ratio depends on  $\alpha$ , and  $\alpha$  depends on the contact model assumed, which may itself be imperfect for the glass beads.

Based on a micromechanics analysis of the effect of particle rotation and the effect of the mechanisms caused by particle rotation in each of the three cubic elementary cells (FCC, BCC, and SC), we showed how our theoretical results could be modified by the introduction of an internal parameter  $\xi$ , which gave rise to an effective tangential stiffness  $K_t^* = \xi K_t$ , and hence an effective  $\alpha^* = \xi\alpha$ , where  $0 \leq \xi \leq 1$  is a measure of the presence of shearing mechanisms due to particle rotation induced by local asymmetries in the distribution of inter-particle contacts. If  $\xi = 0$  then all inter-particle contacts contain shearing mechanisms, and  $\alpha^* = 0$ . If  $\xi = 1$  then there are no shearing mechanisms, and  $\alpha^* = \alpha$ . With this modifi-

cation, our theoretical results obtained under the self-consistent homogenization assumption, particularly that based on the body-centered cubic local packing geometry, are capable of providing remarkably good agreement with the results we obtained from our DEM simulations, especially when compared to the best theoretical estimates currently in the published literature.

## Chapter 5

# Determination of Yield Surfaces for Isotropic Non-Cohesive Particulate Materials by the Discrete Element Method, Part I: No Particle Rotation

### 5.1 Abstract

We perform numerical simulations using the discrete element method (DEM) to determine yield surfaces for large samples of randomly packed uniform spheres with constant normal and tangential contact stiffnesses (linear spring model) and uniform inter-particle friction coefficient  $\mu$ . The beauty of DEM is that the simulations can be run with particle rotation either prohibited or unrestrained, which provides a valuable tool for comparison, and the micromechanical properties of the spheres, especially the inter-particle friction coefficient  $\mu$ , are known exactly. Since each discrete spherical element represents an individual particle, we use the terms “element” and “particle” interchangeably. For the results presented in this

chapter, all DEM simulations were performed with particle rotation prohibited. In Chapter 6, DEM simulations are performed with particle rotations allowed.

## 5.2 Introduction

In the field of geomechanics, particularly in the study of soils, the most important mechanical property is the yield criterion. This is because, for most applications, the mechanical behavior of a geomaterial within the elastic range is of less importance than the point at which the geomaterial yields. For particulate geomaterials, this yielding usually takes the form of inter-particle sliding rather than destruction of the individual particles. Notable exceptions apply. For example, the elastic behavior of a geomaterial is crucial in the determination of the seismic wave speed (Bachrach et al., 2000), as we note in Chapter 4 of this thesis and Fleischmann et al. (2013b). Also, individual particle damage has been observed in physical experiments, including both direct shear and triaxial tests, particularly for large-scale geomaterials such as railway ballast (Indraratna et al., 1998), and this “micro-scale” particle damage can affect the geomaterial’s plastic (particularly post-yield) behavior (Jensen et al., 2001b). However, yielding due to inter-particle sliding remains the predominant mode of failure for particulate geomaterials in common applications.

The need for a mechanical characterization of isotropic particulate materials extends beyond the field of geomechanics. In this context, the yield criterion remains crucial in the standard formulation of an elastoplastic continuum constitutive model, as it does for any material. In the classical elastoplastic formulation, the yield (or failure) criterion defines a material’s transition from elastic to plastic mechanical behavior. Typically, yield criteria take the form of three-dimensional surfaces in either principal stress space or principal strain space (e.g., Lubarda, 2002, Simo and Hughes, 1998). We use the more common principal stress space characterization of yield criteria.

In this chapter, we report results from numerical simulations using the discrete element method (DEM), which were performed on six randomly packed specimens of 3 430–29 660 uniform spherical elements with uniform inter-element (Coulomb) friction. For the purpose of comparison, the DEM simulations of this chapter and the next were performed on the same (geometric) DEM specimens as those used in Chapter 3 [Fleischmann et al. (2013a)] and Chapter 4 [Fleischmann et al. (2013b)]. Since each spherical element represents an individual particle, we use the terms “element” and “particle” interchangeably. Numerous simulations were performed on each specimen for a wide range of values of the inter-element friction coefficient  $\mu$ . The numerical simulations corresponded to quasi-static constant-volume (three-dimensional) true triaxial tests. By varying the (quasi-static) strain rates and monitoring the stresses in the three triaxial directions throughout these simulations, we obtain complete yield surfaces for each of the six specimens for a wide range of values of  $\mu$ .

From these yield surfaces, we obtain relationships for all six DEM specimens between the inter-particle friction coefficient  $\mu$  on the microscale and the material friction angle  $\phi$  on the macroscale. We find that for a given value of the inter-particle friction coefficient  $\mu$ , the values of the material friction angle  $\phi$  exhibit very little scatter. (We examine the relationship between  $\mu$  and  $\phi$  in greater detail in Chapters 7 and 8.) We compare the yield surfaces obtained by DEM to those predicted by several well known yield-criteria, and find that the Lade-Duncan yield criterion provides the best characterization of the data points, particularly those corresponding to DEM simulations of extension. We also monitor inter-particle friction work within each specimen during the DEM simulations, both globally and on an element-by-element basis, and we examine the relationship between the friction work and the inter-particle friction coefficient.

In this chapter, as we did in Chapter 3 [Fleischmann et al. (2013a)] for the elastic range, we report results obtained from DEM simulations in which particle rotation was prohibited. In Chapter 6, we report results analogous to the results of this chapter, obtained from DEM

simulations with unrestrained particle rotation, as we did in Chapter 4 [Fleischmann et al. (2013b)] for the elastic range.

### 5.3 Yield Criteria

The Mohr-Coulomb yield (or failure) criterion is the oldest and still one of the most used yield criteria for particulate materials in general, and geomaterials in particular. For non-cohesive particulate materials, the classical Mohr-Coulomb yield criterion is characterized by the following three-dimensional surface in principal stress space:

$$\frac{|\sigma_i - \sigma_j|}{2\sqrt{\sigma_i\sigma_j}} = \tan \phi, \quad i \neq j, \quad i, j = 1, 2, 3, \quad (5.1)$$

where  $\phi$  is the (macroscopic) friction angle for the particulate material. For particulate materials, the friction angle  $\phi$  is a “strength” characteristic, somewhat analogous to yield stress. For non-cohesive particulate materials,  $\phi$  is also called the “angle of repose”. In equation (5.1) it is assumed that the principal stresses  $\sigma_1$ ,  $\sigma_2$ , and  $\sigma_3$  all have the same sign, which must be the case if the particulate material is non-cohesive. In the geomechanics literature,  $\sigma_1$ ,  $\sigma_2$ , and  $\sigma_3$  are generally assumed to be positive in compression, but equation (5.1) is true independent of this convention. If equality “=” is replaced by inequality “<”, then equation (5.1) defines the elastic range (in principal stress space) for a non-cohesive isotropic particulate material with friction angle  $\phi$ . For a derivation of equation (5.1), see Appendix D.

The Mohr-Coulomb yield criterion is not typically characterized as we have done in equation (5.1). Rather, it is more typically characterized in terms of the hydrostatic pressure  $p = (\sigma_1 + \sigma_2 + \sigma_3)/3$  and the Lode angle  $\theta$  (e.g., Bardet, 1997). The Lode angle is an angle on the plane of constant hydrostatic pressure  $p$  in principal stress space, which is called the

$\pi$ -plane. There are different versions of the Lode angle in the literature, and we will use the definition in which  $\theta$  is measured from one of the principal stress directions projected onto the  $\pi$ -plane, as shown in Figure 5.1. Due to material frame invariance, the Mohr-Coulomb

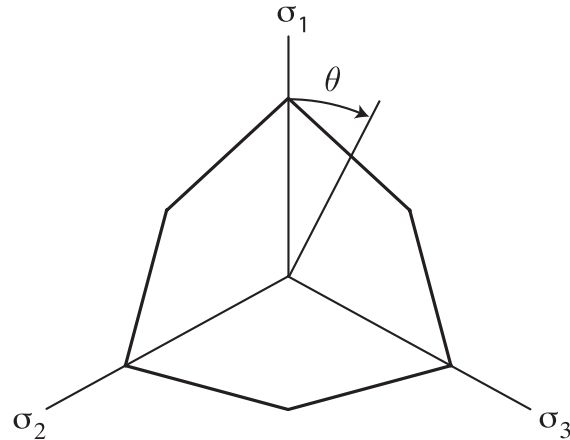


Figure 5.1: The intersection of the Mohr-Coulomb yield surface with the plane of constant hydrostatic pressure  $p$  (called the  $\pi$ -plane) in principal stress space, with the principal stresses  $\sigma_1$ ,  $\sigma_2$ , and  $\sigma_3$  positive in compression. The Lode angle  $\theta$  is measured from any of the principal stress directions projected onto the  $\pi$ -plane.

yield criterion (and all yield criteria) must be independent of the labeling of the principal stresses  $\sigma_1$ ,  $\sigma_2$ , and  $\sigma_3$ . Thus, as shown in Figure 5.1, the Mohr-Coulomb yield criterion must exhibit  $120^\circ$  rotational symmetry, as well as reflective symmetry about each of the three projected principal stress directions on the  $\pi$ -plane. Therefore, the specific principal stress direction from which the Lode angle  $\theta$  is measured is arbitrary, and the Lode angle varies between  $0 \leq \theta \leq 60^\circ$ .

Other yield criteria for non-cohesive particulate materials exist, such as the Drucker-Prager criterion, which is simply a cone in principal stress space with vertex at the origin and axis along the line  $\sigma_1 = \sigma_2 = \sigma_3$ . The Drucker-Prager criterion can be characterized in principal stress space by the surface  $I_1 - a\sqrt{J_2} = 0$ , where  $I_1 = 3p = \sigma_1 + \sigma_2 + \sigma_3$  is the first stress invariant,  $J_2 = [(\sigma_1 - \sigma_2)^2 + (\sigma_2 - \sigma_3)^2 + (\sigma_3 - \sigma_1)^2]/6$  is the second deviatoric

stress invariant, and  $a$  is a material parameter. The intersection of the Drucker-Prager yield surface with the  $\pi$ -plane is a circle. Both the Mohr-Coulomb and the Drucker-Prager yield surfaces scale linearly with the hydrostatic pressure  $p$ , as shown in Figure 5.2.

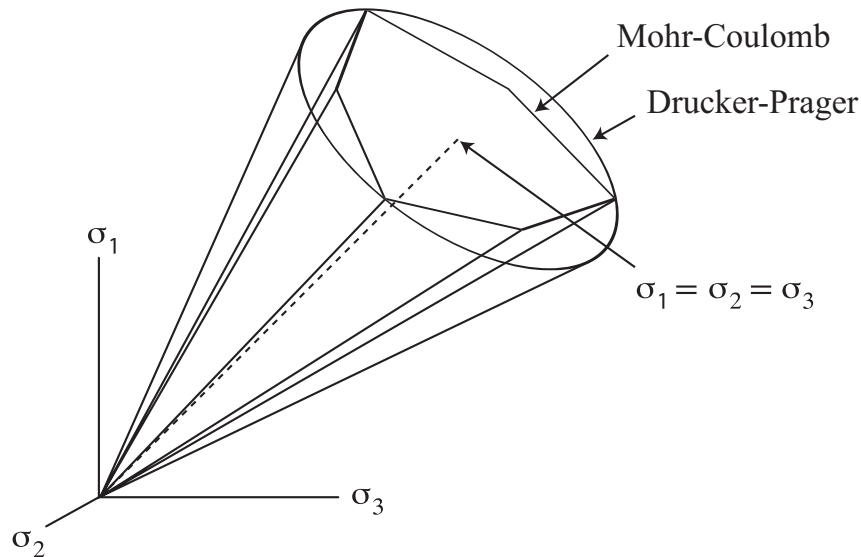


Figure 5.2: The Mohr-Coulomb and Drucker-Prager yield surfaces in principal stress space for a non-cohesive particulate material, with the principal stresses  $\sigma_1$ ,  $\sigma_2$ , and  $\sigma_3$  positive in compression.

Other (phenomenological) yield criteria include the Lade-Duncan and Matsuoka-Nakai criteria (Bardet, 1990). The Lade-Duncan criterion is characterized in principal stress space by the surface  $I_1^3 - bI_3 = 0$ , where  $I_3 = \sigma_1\sigma_2\sigma_3$  is the third stress invariant, and  $b$  is a material parameter. The Matsuoka-Nakai – also called the Spatially Mobilized Plane or SMP (Matsuoka and Sun, 2006) – criterion is characterized in principal stress space by the surface  $I_1I_2 - cI_3 = 0$ , where  $I_2 = \sigma_1\sigma_2 + \sigma_2\sigma_3 + \sigma_3\sigma_1$  is the second stress invariant, and  $c$  is a material parameter.

A host of phenomenological variations on these yield criteria can be defined, all of which lie between the Mohr-Coulomb and Drucker-Prager criteria, and all of which have slightly

different Lode angle dependences (Bardet, 1990). Typically, the material parameters for these yield criteria (e.g.,  $\phi$ ,  $a$ ,  $b$ , and  $c$ ) are chosen so that the yield surfaces coincide at a Lode angle of  $\theta = 0$ , since this is the location in principal stress space corresponding to the standard triaxial test, for which  $\sigma_1 \neq \sigma_2 = \sigma_3 = \text{constant}$ .

## 5.4 Methodology

For this chapter, we performed a total of 1 296 numerical simulations using the discrete element method (DEM) to determine yield surfaces in principal stress space for randomly packed aggregates of uniform spheres having constant normal and tangential contact stiffnesses  $K_n$  and  $K_t$ , respectively (linear spring contact model), and uniform inter-particle friction coefficient  $\mu$ , with particle rotation prohibited. We report the results that we have obtained from the same six DEM specimens that were tested in Sections 3.5 and 4.5 of this thesis, and in Fleischmann et al. (2013a) and Fleischmann et al. (2013b). Specimens 1, 2, and 3 each contained 3 430 randomly packed uniform spheres, and Specimens 4, 5, and 6 each contained 29 660 randomly packed uniform spheres. The specimens are shown in Figure 3.7 of Section 3.5, which is repeated here as Figure 5.3 for convenience.

As in Chapters 3 and 4, we performed our DEM simulations using LAMMPS, the open-source “Large-scale Atomic/Molecular Massively Parallel Simulator” software developed at Sandia National Laboratories (Plimpton, 1995), which is described briefly in Section 3.5 and in more detail in Section 9.3. We have modified our own version of LAMMPS in several ways: some major, such as adding the capability of monitoring inter-element friction work following Jensen et al. (2001b); some minor, such as removing an artificially imposed limit on the maximum value of the inter-element friction coefficient (of  $\mu = 1.0$ ) that was in place in the standard code.

The setup procedures and initial geometries of the six specimens used in this section are

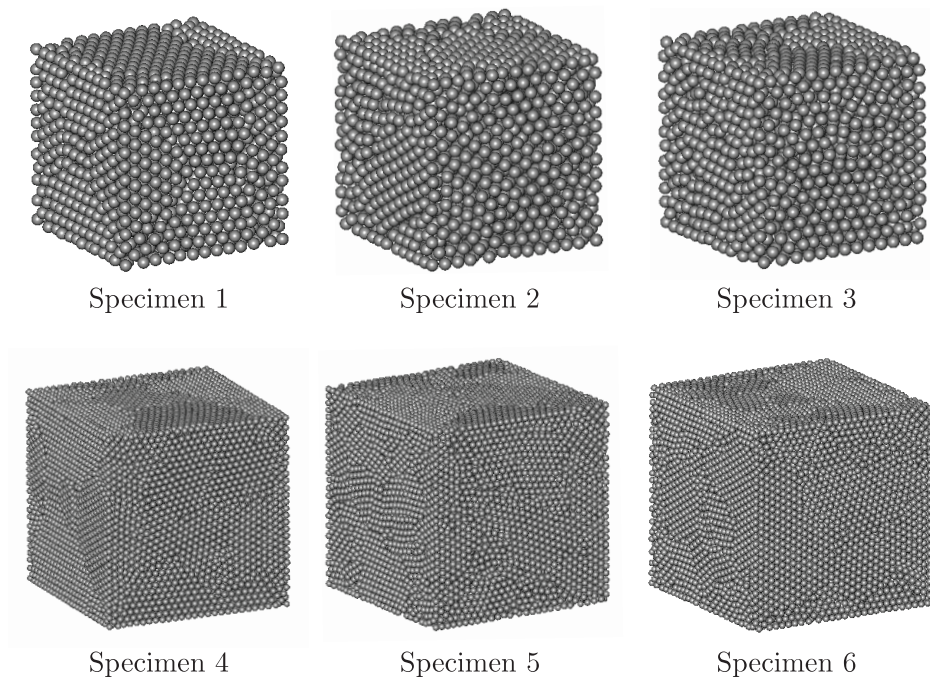


Figure 5.3: Specimens of randomly packed uniform spheres used in the DEM simulations. Specimens 1, 2, and 3 contain 3 430 spherical elements, and Specimens 4, 5, and 6 contain 29 660 spherical elements.

identical to those of the six specimens used in Section 3.5 and Fleischmann et al. (2013a) and Section 4.5 and Fleischmann et al. (2013b). For a discussion of the initial packing geometries, including the average number of contacts per unit volume and the radial distribution functions for the specimens, see Section 3.5 and Section 3.6, or Fleischmann et al. (2013a). For convenience, we repeat here the initial volumetric packing densities of the six specimens, which were 0.64, 0.62, 0.62, 0.69, 0.68, and 0.68, respectively. All six of these volume densities correspond to a dense sand (with void ratio  $e \approx 0.5$ ) of roughly uniform particle size (with coefficient of uniformity  $C_u \approx 1$ ), such as Ottawa standard sand (e.g., Bardet, 1997). Figure 3.9 of Section 3.6 shows that the packing of the spheres in each of these six specimens is essentially random.

To compute yield surfaces for the specimens, true triaxial simulations were performed under constant volume conditions, in which the upper wall of the confining cube was lowered or raised at a constant strain rate  $\dot{\epsilon}_z = \pm 0.01$ , and the lateral walls of the confining cube were expanded or contracted at various predetermined lateral strain rates. To obtain a single yield surface, sixteen DEM simulations were performed with lateral strain rates of  $\dot{\epsilon}_x = \{\mp 0.005, \mp 0.0057, \mp 0.0064, \mp 0.0071, \mp 0.0079, \mp 0.0086, \mp 0.0093, \mp 0.01\}$  and  $\dot{\epsilon}_y = \{\mp 0.005, \mp 0.0043, \mp 0.0036, \mp 0.0029, \mp 0.0021, \mp 0.0014, \mp 0.0007, 0\}$  in such a way that the (small strain) volumetric strain rate was zero:  $\dot{\epsilon} = \dot{\epsilon}_x + \dot{\epsilon}_y + \dot{\epsilon}_z = 0$ . In this way, an approximately constant volume condition was maintained. The variation in the lateral strain rates was necessary to obtain different values of the intermediate principal stress during the simulations, so that each simulation could produce a data point for the yield surface at a different Lode angle on the  $\pi$ -plane. Note that all of these strain rates are low enough that the particulate material response can be considered quasi-static. The walls of the confining cube were frictionless, and the total force on each wall was measured continually throughout the simulations, so that the stresses  $\sigma_x$ ,  $\sigma_y$ , and  $\sigma_z$  on the walls of the confining cube were known at all times. The simulations were run to a total axial strain of  $\epsilon_z = \pm 0.1$  (or

10% axial strain in either compression or extension, depending on the simulation). In all of the DEM simulations performed for the present chapter, the spheres were allowed full three-dimensional translational freedom of motion, but particle rotation was prohibited. For Chapter 6, DEM simulations analogous to those of this chapter were performed with particle rotations allowed.

The sixteen DEM simulations described in the preceding paragraph were performed on each of the six specimens with nine different values of the inter-element friction coefficient  $\mu = \{0.01, 0.1, 0.2, 0.3, 0.4, 0.5, 0.6, 0.7, 0.8\}$ , requiring a total of 144 DEM simulations per specimen. During these sixteen simulations, which were performed on a particular specimen with a particular inter-element friction coefficient, the measured principal stress triple  $(\sigma_1, \sigma_2, \sigma_3)$ , with  $\sigma_i = \sigma_x$ ,  $\sigma_j = \sigma_y$ , and  $\sigma_k = \sigma_z$ , where  $i, j, k \in \{1, 2, 3\}$  with  $i \neq j \neq k$ , could be converted into six unit vectors in principal stress space (for the six different assignments of  $i, j$ , and  $k$ ) and projected onto any  $\pi$ -plane, which is a plane in principal stress space for which  $\sigma_1 + \sigma_2 + \sigma_3$  is constant. Thus, six data points could be plotted on the  $\pi$ -plane for every measured stress triple  $(\sigma_x, \sigma_y, \sigma_z)$ . For consistency, the data points for all of the DEM simulations were projected onto the same  $\pi$ -plane, although the actual hydrostatic pressure  $p = (\sigma_1 + \sigma_2 + \sigma_3)/3$  for the individual simulations varied. Note that for the yield surfaces we obtain in this way to be comparable, we must implicitly assume that the yield surface depends linearly on the hydrostatic pressure  $p$ , and that the particulate material has no strength when  $p = 0$ . We will return to this assumption in the discussion section that follows.

To determine the yield surface, the  $16(\times 6)$  data points were plotted on the  $\pi$ -plane for axial strains ( $|\epsilon_z|$ ) of  $\{1\%, 2\%, 3\%, 4\%, 5\%, 6\%, 7\%, 8\%\}$  (in either compression or extension). The yield surface was then found by determining the set of data points on the  $\pi$ -plane for which the principal stresses were maximum, after which the principal stresses either remained fixed or began to decrease. It was found that the maximal yield surface occurred

at 4%–6% axial strain for Specimens 1–3 (with 3 430 particles), and at 6%–8% axial strain for Specimens 4–6 (with 29 660 particles), after which time the yield surface either remained approximately fixed or began to collapse.

By way of example, Figure 5.4 shows the data points on the  $\pi$ -plane obtained from DEM simulations performed on Specimen 1 with inter-element friction coefficients of  $\mu = 0.2$  (top) and  $\mu = 0.5$  (bottom) for axial strains of 1%–8% in either compression or extension, depending on the data point. The symmetry due to material frame invariance (i.e., the cyclic renaming of the principal stress directions) is included in the figure, resulting in  $16 \times 6 = 96$  data points on the  $\pi$ -plane for each value of the axial strain. For convenience, the principal stress directions are shown positive in compression, which is commonly done in the field of geomechanics. Also shown on Figure 5.4 are the yield surfaces according to the Mohr-Coulomb yield criterion with (macroscopic) friction angles  $\phi = 34^\circ$  (top) and  $\phi = 53^\circ$  (bottom), chosen to match the data points at a Lode angle of zero.

Figures 5.5–5.9 show the corresponding results for Specimens 2–6, respectively, with inter-element friction coefficients of  $\mu = 0.2$  (top) and  $\mu = 0.5$  (bottom). Analogous DEM simulations and analyses were performed for all six specimens for all nine values of the inter-element friction coefficient  $\mu$ , and the matching “material” or macroscopic friction angle  $\phi$  (at a Lode angle of zero) corresponding to the classical Mohr-Coulomb yield criterion was determined for each (with an accuracy of approximately  $\pm 0.25^\circ$ ).

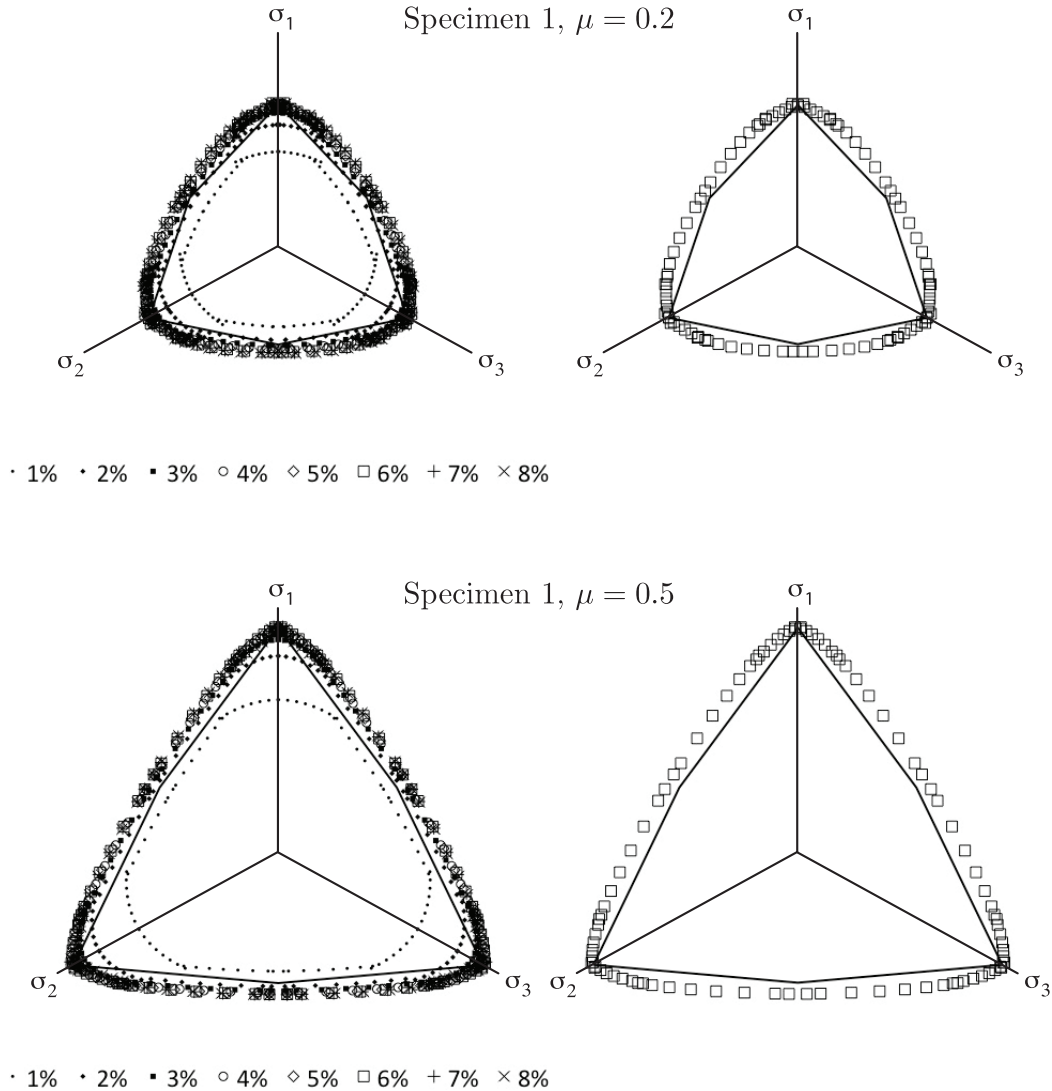


Figure 5.4: Left: Data points on the  $\pi$ -plane obtained from one set of DEM simulations performed on Specimen 1 with an inter-element friction coefficient of  $\mu = 0.2$  (top) and  $\mu = 0.5$  (bottom), with particle rotation prohibited. Right: Maximal yield surfaces. The solid line in both diagrams is the Mohr-Coulomb yield surface with a macroscopic friction angle of  $\phi = 34.0^\circ$  (top) and  $\phi = 53.0^\circ$  (bottom), chosen to match the data points at a Lode angle of zero. The data points for 1%, 2%, ..., 8% designate the axial strain in either compression or extension (depending on the Lode angle).

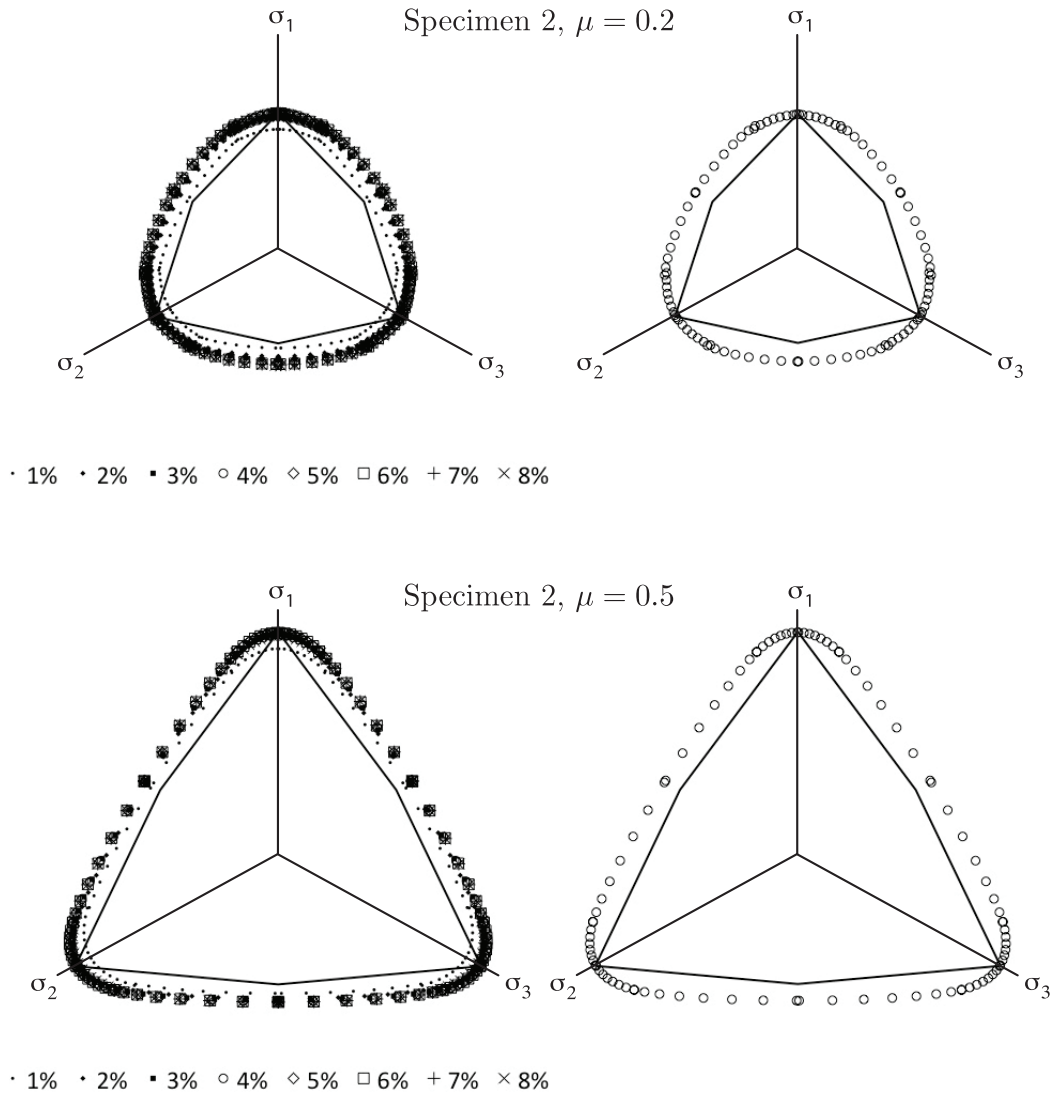


Figure 5.5: Left: Data points on the  $\pi$ -plane obtained from one set of DEM simulations performed on Specimen 2 with an inter-element friction coefficient of  $\mu = 0.2$  (top) and  $\mu = 0.5$  (bottom), with particle rotation prohibited. Right: Maximal yield surfaces. The solid line in both diagrams is the Mohr-Coulomb yield surface with a macroscopic friction angle of  $\phi = 32.5^\circ$  (top) and  $\phi = 52.5^\circ$  (bottom), chosen to match the data points at a Lode angle of zero. The data points for 1%, 2%, ..., 8% designate the axial strain in either compression or extension (depending on the Lode angle).

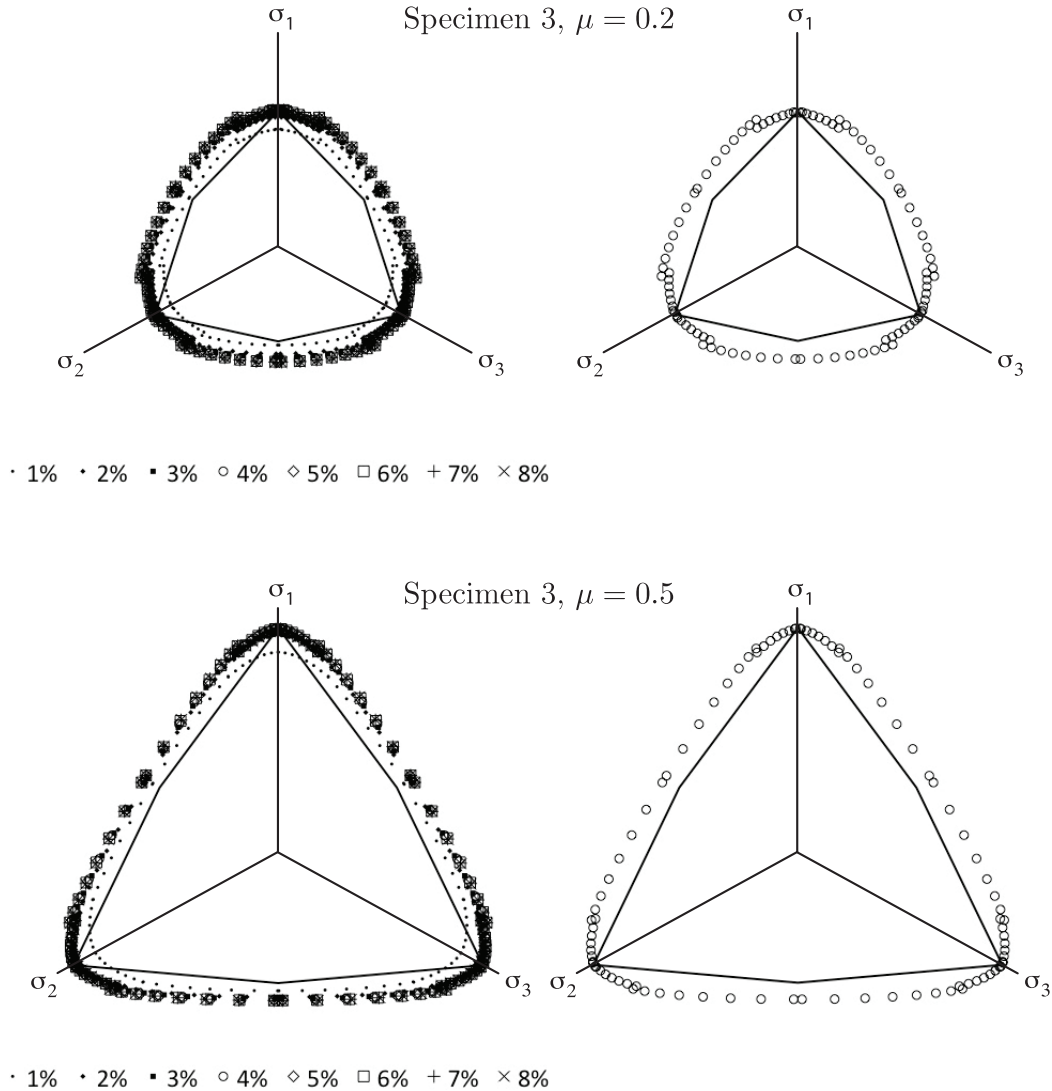


Figure 5.6: Left: Data points on the  $\pi$ -plane obtained from one set of DEM simulations performed on Specimen 3 with an inter-element friction coefficient of  $\mu = 0.2$  (top) and  $\mu = 0.5$  (bottom), with particle rotation prohibited. Right: Maximal yield surfaces. The solid line in both diagrams is the Mohr-Coulomb yield surface with a macroscopic friction angle of  $\phi = 32.5^\circ$  (top) and  $\phi = 53.0^\circ$  (bottom), chosen to match the data points at a Lode angle of zero. The data points for 1%, 2%, ..., 8% designate the axial strain in either compression or extension (depending on the Lode angle).

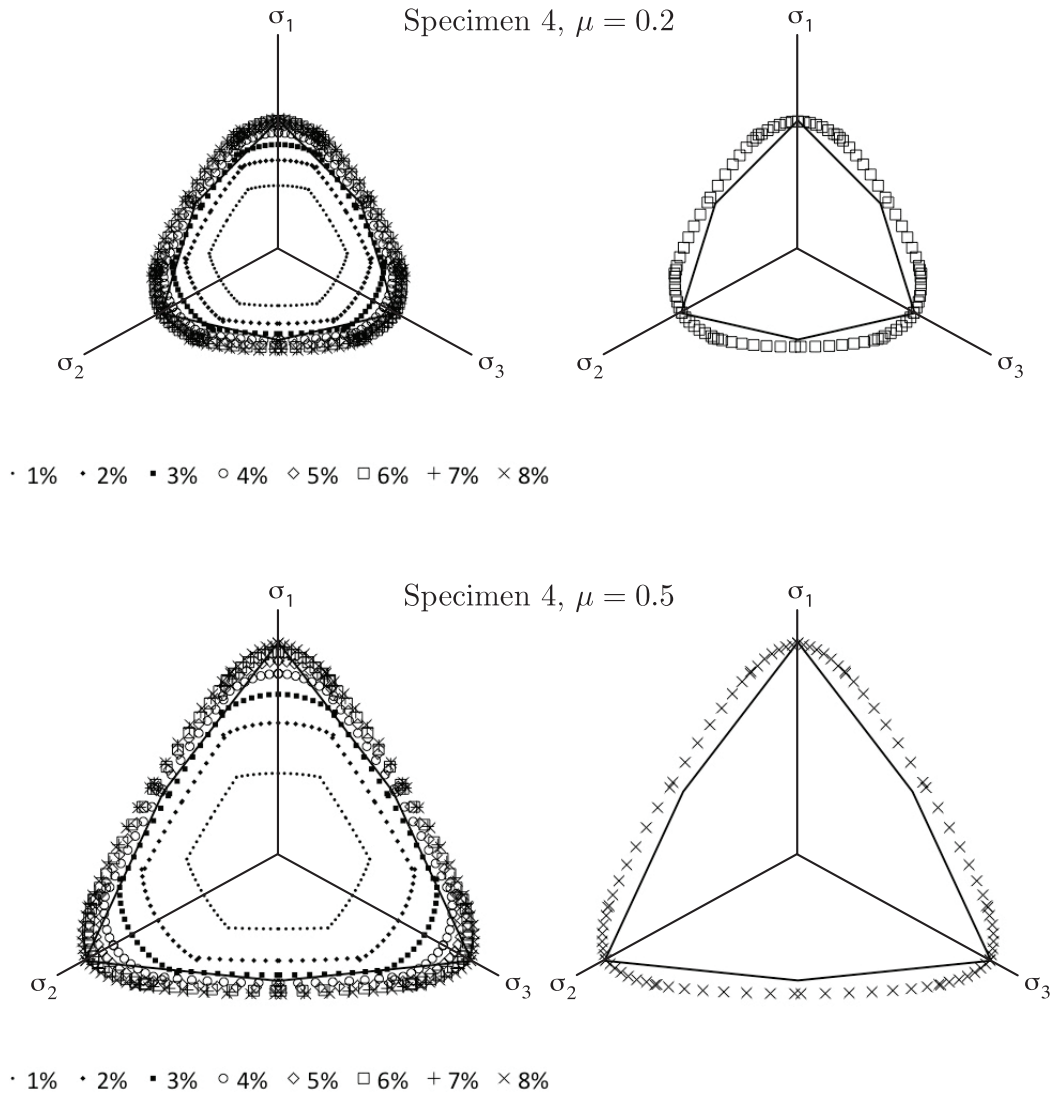


Figure 5.7: Left: Data points on the  $\pi$ -plane obtained from one set of DEM simulations performed on Specimen 4 with an inter-element friction coefficient of  $\mu = 0.2$  (top) and  $\mu = 0.5$  (bottom), with particle rotation prohibited. Right: Maximal yield surfaces. The solid line in both diagrams is the Mohr-Coulomb yield surface with a macroscopic friction angle of  $\phi = 31.0^\circ$  (top) and  $\phi = 50.0^\circ$  (bottom), chosen to match the data points at a Lode angle of zero. The data points for 1%, 2%, ..., 8% designate the axial strain in either compression or extension (depending on the Lode angle).

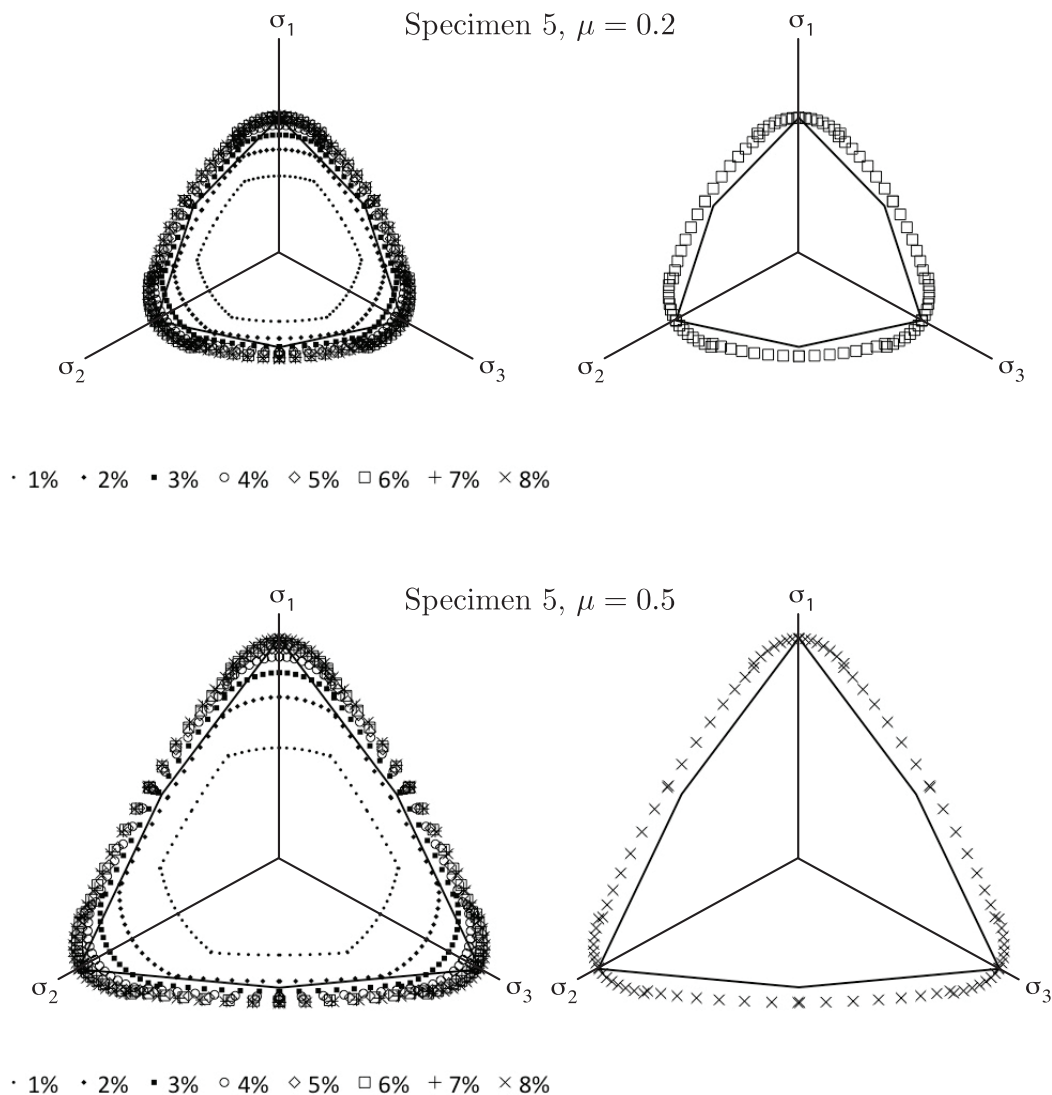


Figure 5.8: Left: Data points on the  $\pi$ -plane obtained from one set of DEM simulations performed on Specimen 5 with an inter-element friction coefficient of  $\mu = 0.2$  (top) and  $\mu = 0.5$  (bottom), with particle rotation prohibited. Right: Maximal yield surfaces. The solid line in both diagrams is the Mohr-Coulomb yield surface with a macroscopic friction angle of  $\phi = 32.5^\circ$  (top) and  $\phi = 52.0^\circ$  (bottom), chosen to match the data points at a Lode angle of zero. The data points for 1%, 2%, ..., 8% designate the axial strain in either compression or extension (depending on the Lode angle).

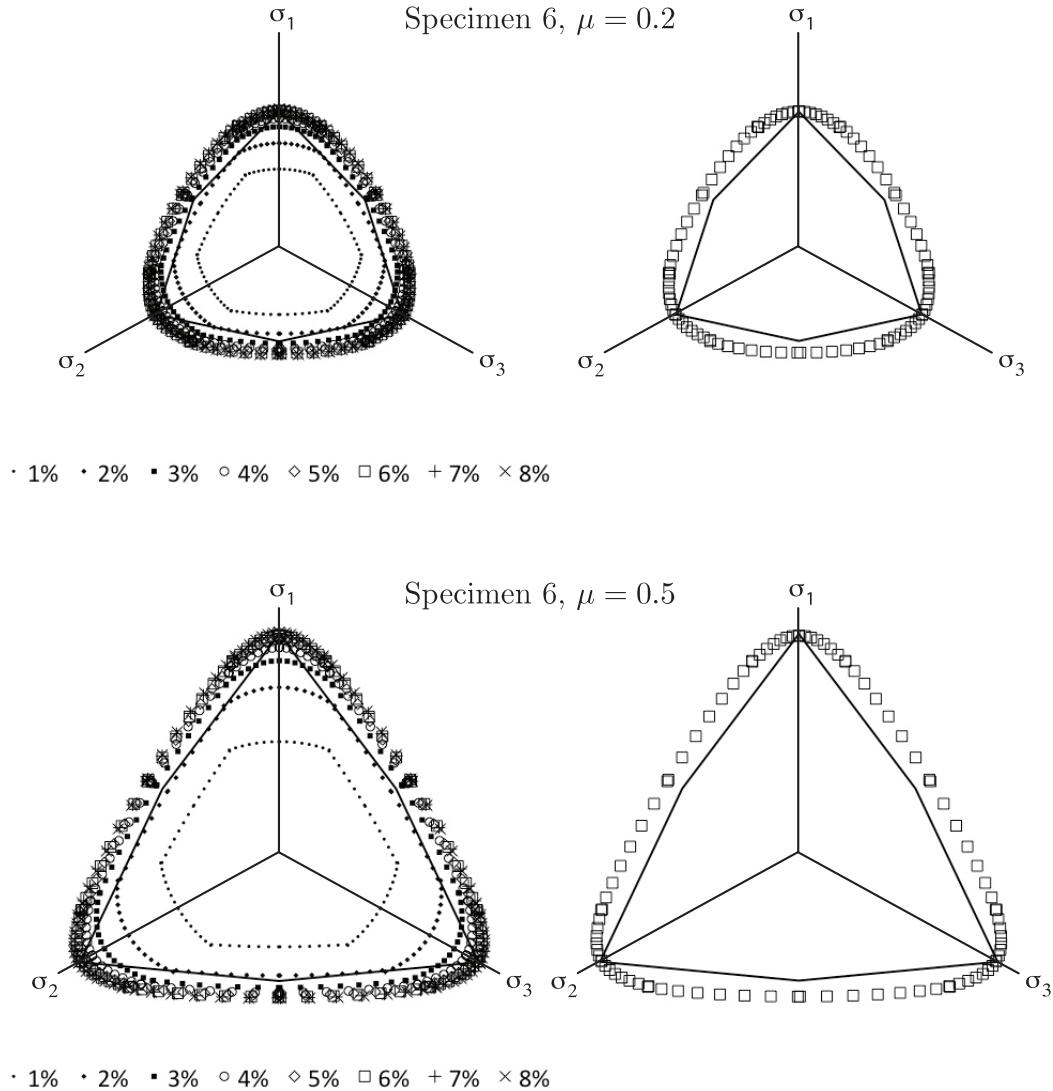


Figure 5.9: Left: Data points on the  $\pi$ -plane obtained from one set of DEM simulations performed on Specimen 6 with an inter-element friction coefficient of  $\mu = 0.2$  (top) and  $\mu = 0.5$  (bottom), with particle rotation prohibited. Right: Maximal yield surfaces. The solid line in both diagrams is the Mohr-Coulomb yield surface with a macroscopic friction angle of  $\phi = 32.5^\circ$  (top) and  $\phi = 51.5^\circ$  (bottom), chosen to match the data points at a Lode angle of zero. The data points for 1%, 2%, ..., 8% designate the axial strain in either compression or extension (depending on the Lode angle).

One of the enhancements we have added to our version of LAMMPS is the monitoring of inter-particle friction work, as defined by Jensen et al. (2001b). In particular, if contacting discrete elements  $i$  and  $j$  experience relative sliding, then the magnitude of the tangential component of the inter-element contact force is  $F_t^{ij} = \mu N^{ij}$ , where  $N^{ij}$  is the normal component of the inter-element contact force and  $\mu$  is the inter-element friction coefficient. The friction work for the element pair  $ij$  over a given time interval  $\Delta t = [t_k, t_{k+1}]$  is then  $U_f^{ij} = F_t^{ij} \Delta s^{ij}$ , where  $\Delta s^{ij}$  is the magnitude of the incremental relative tangential *sliding* displacement at the contact point between elements  $i$  and  $j$  corresponding to the time interval  $\Delta t$ . This expression assumes  $\Delta t$  is small, as in the size of the critical time step for DEM (Appendix E). Note that when the discrete elements are allowed to rotate (as they are by default, although particle rotation is not allowed in the current chapter),  $\Delta s^{ij}$  will include a contribution due to the rotation of the elements  $i$  and  $j$ . Given the definitions in this paragraph, the total friction work in a DEM specimen can be computed at any time during a simulation as

$$U_f = \sum_{\Delta t} \sum_{i=0}^{N-1} \sum_{j=i+1}^N U_f^{ij}, \quad (5.2)$$

where the first sum is taken over all time steps prior to the time at which  $U_f$  is being computed, and  $N$  is the total number of discrete elements in the specimen.

Using this capability, the total accumulated friction work  $U_f$  for each specimen for each value of the inter-particle friction coefficient  $\mu$  was recorded throughout the DEM simulations. By way of example, Figure 5.10 shows the total friction work  $U_f$  (Joules) as a function of strain at Lode angles of  $\theta = 0$  and  $\theta = 60^\circ$  for Specimen 1 with inter-element friction coefficients of  $\mu = 0.2$  (top) and  $\mu = 0.5$  (bottom), for axial strains of 1%–8% in either compression ( $\theta = 0$ ) or extension ( $\theta = 60^\circ$ ). Figures 5.11–5.15 show the corresponding results for Specimens 2–6, respectively, with inter-element friction coefficients of  $\mu = 0.2$  (top) and  $\mu = 0.5$  (bottom).

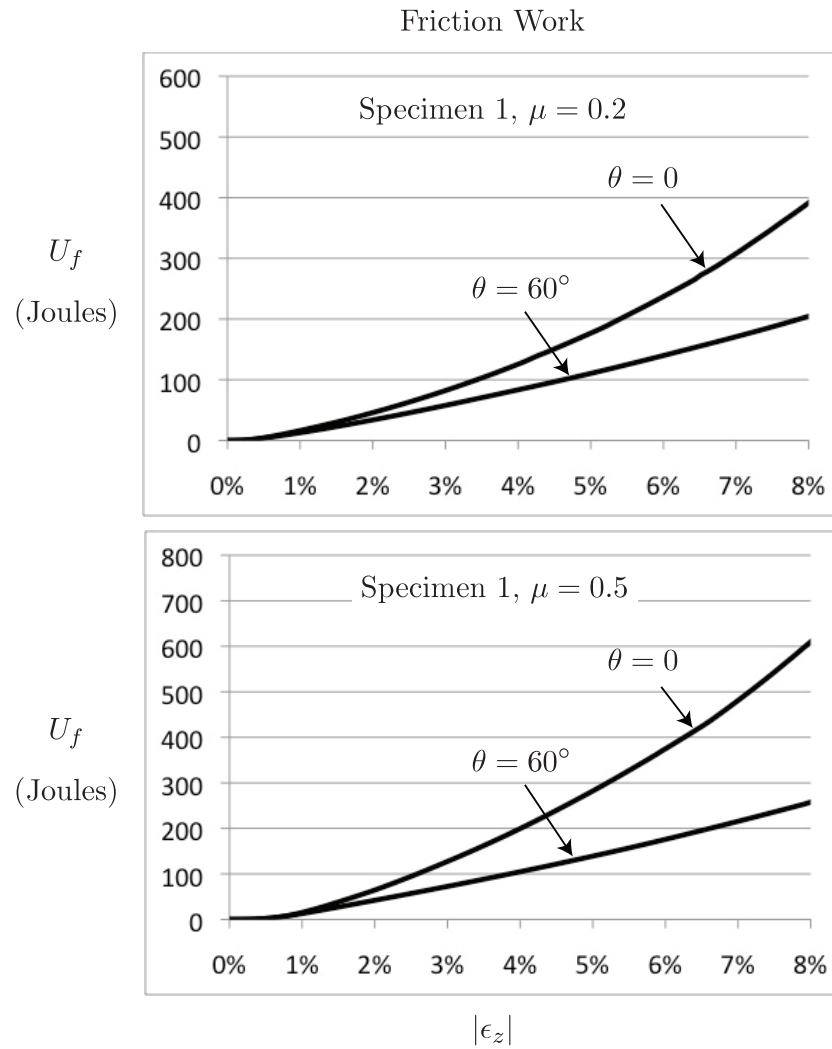


Figure 5.10: Total accumulated friction work  $U_f$  as a function of strain for Specimen 1 with an inter-element friction coefficient of  $\mu = 0.2$  (top) and  $\mu = 0.5$  (bottom), with particle rotation prohibited. The two curves correspond to the data points on the yield surfaces shown in Figure 5.4 at Lode angles of  $\theta = 0$  and  $\theta = 60^\circ$ .

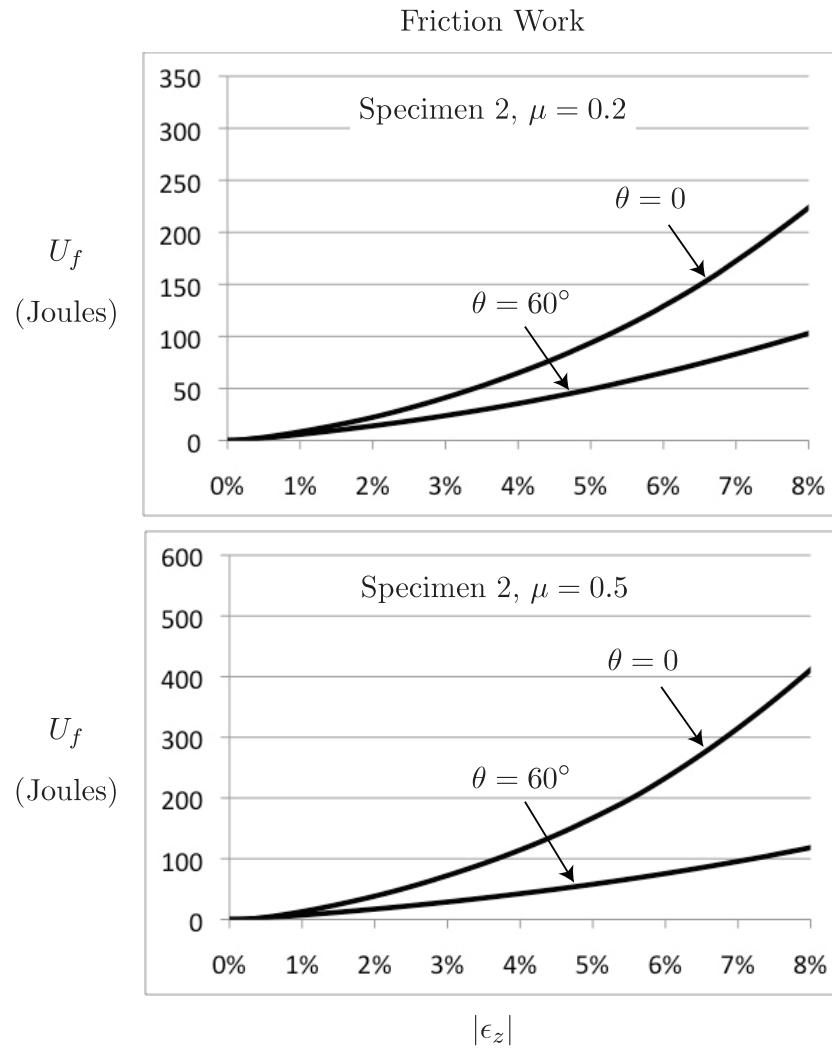


Figure 5.11: Total accumulated friction work  $U_f$  as a function of strain for Specimen 2 with an inter-element friction coefficient of  $\mu = 0.2$  (top) and  $\mu = 0.5$  (bottom), with particle rotation prohibited. The two curves correspond to the data points on the yield surfaces shown in Figure 5.5 at Lode angles of  $\theta = 0$  and  $\theta = 60^\circ$ .

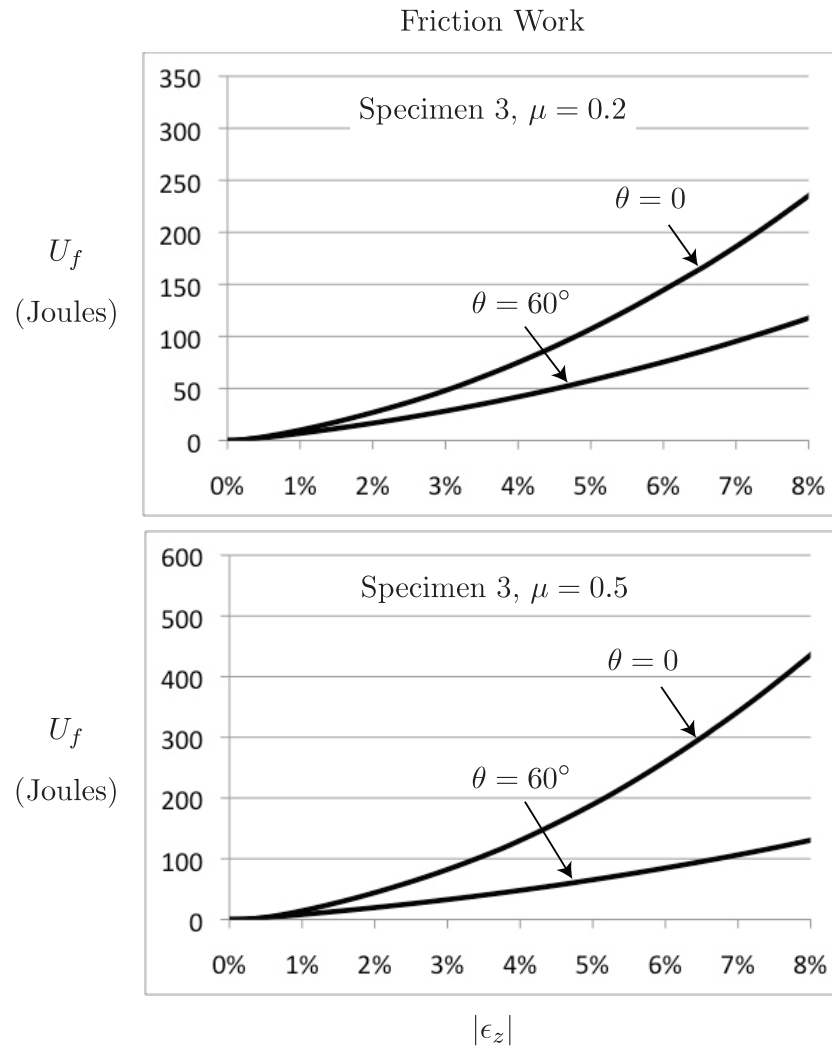


Figure 5.12: Total accumulated friction work  $U_f$  as a function of strain for Specimen 3 with an inter-element friction coefficient of  $\mu = 0.2$  (top) and  $\mu = 0.5$  (bottom), with particle rotation prohibited. The two curves correspond to the data points on the yield surfaces shown in Figure 5.6 at Lode angles of  $\theta = 0$  and  $\theta = 60^\circ$ .

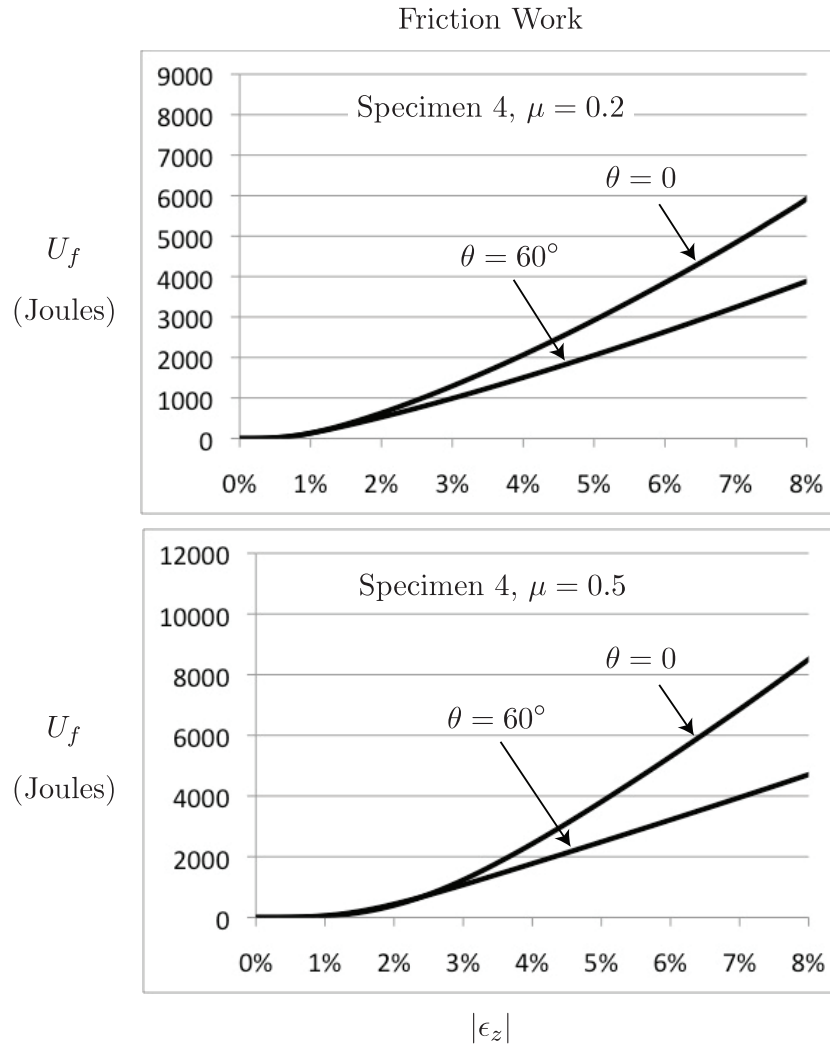


Figure 5.13: Total accumulated friction work  $U_f$  as a function of strain for Specimen 4 with an inter-element friction coefficient of  $\mu = 0.2$  (top) and  $\mu = 0.5$  (bottom), with particle rotation prohibited. The two curves correspond to the data points on the yield surfaces shown in Figure 5.7 at Lode angles of  $\theta = 0$  and  $\theta = 60^\circ$ .

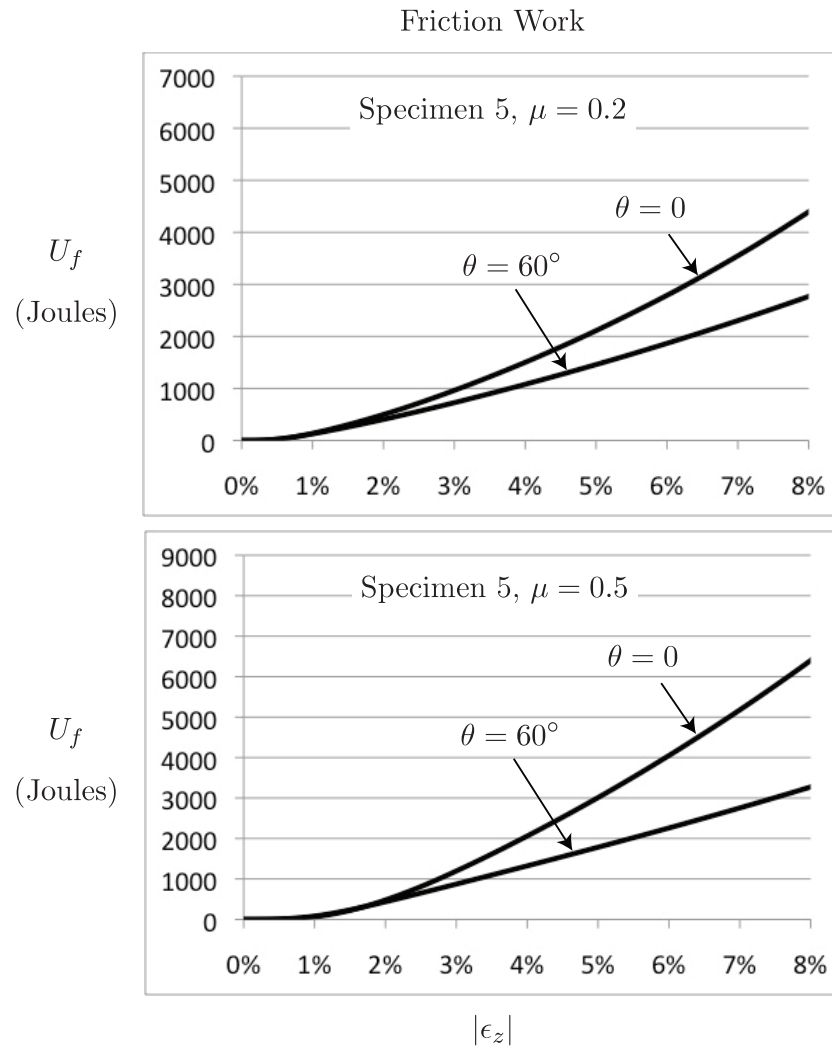


Figure 5.14: Total accumulated friction work  $U_f$  as a function of strain for Specimen 5 with an inter-element friction coefficient of  $\mu = 0.2$  (top) and  $\mu = 0.5$  (bottom), with particle rotation prohibited. The two curves correspond to the data points on the yield surfaces shown in Figure 5.8 at Lode angles of  $\theta = 0$  and  $\theta = 60^\circ$ .

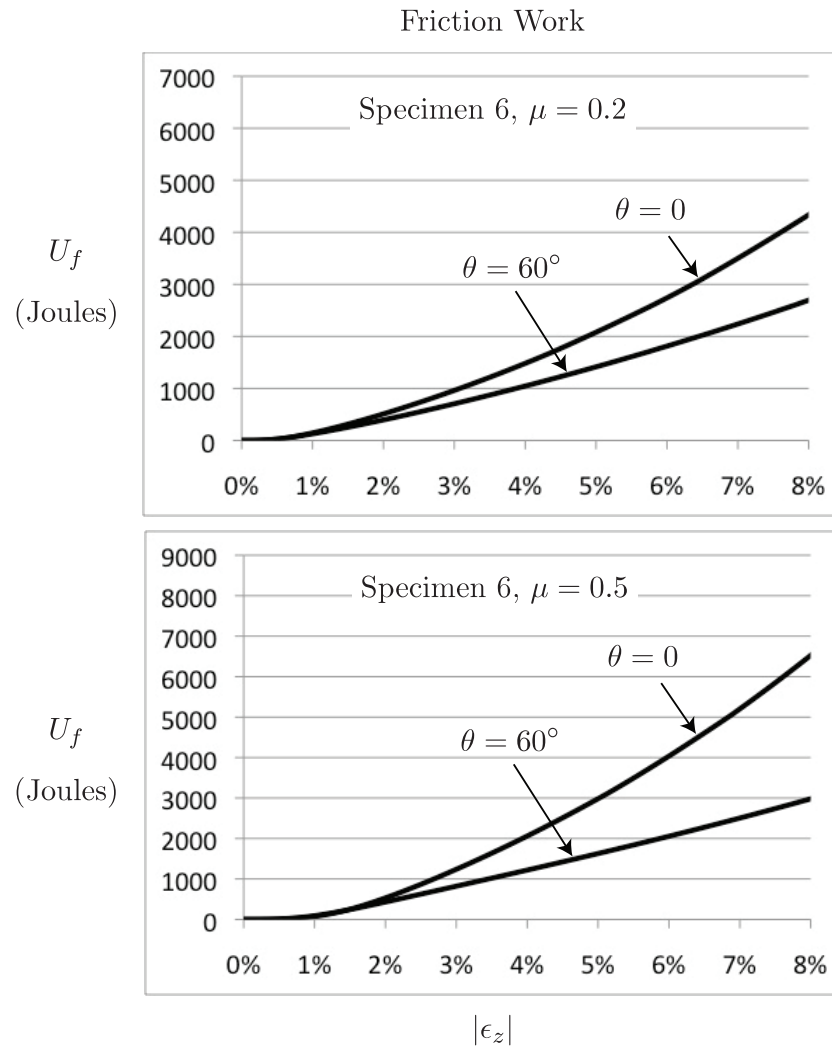


Figure 5.15: Total accumulated friction work  $U_f$  as a function of strain for Specimen 6 with an inter-element friction coefficient of  $\mu = 0.2$  (top) and  $\mu = 0.5$  (bottom), with particle rotation prohibited. The two curves correspond to the data points on the yield surfaces shown in Figure 5.9 at Lode angles of  $\theta = 0$  and  $\theta = 60^\circ$ .

## 5.5 Results

Figures 5.16–5.21 show the 54 yield surfaces that were obtained from the DEM simulations described in Section 5.4, performed on Specimens 1–6 with nine different values of the inter-element friction coefficient  $0.01 \leq \mu \leq 0.8$ , with particle rotation prohibited. Also shown are the corresponding Mohr-Coulomb yield surfaces, with the macroscopic friction angle  $\phi$  chosen in each case to match the data points at a Lode angle of zero.

Figure 5.22 shows the resulting relationship between the macroscopic (material) friction angle  $\phi$  corresponding to the classical Mohr-Coulomb yield criterion and the microscopic (inter-particle) friction angle  $\phi_\mu = \tan^{-1} \mu$  for each specimen, where  $\mu$  is the inter-element friction coefficient ( $0.6^\circ \leq \phi_\mu \leq 39^\circ$ ). Recall that the material friction angle  $\phi$  was chosen to make the Mohr-Coulomb yield surface match the yield surface determined by DEM at a Lode angle of zero, with an accuracy of approximately  $\pm 0.25^\circ$ . Note that for each of the six specimens represented in Figure 5.22 there are nine data points, corresponding to the nine different values of the inter-element friction coefficient, and each of these data points came from one of the yield surfaces shown in Figures 5.16–5.21, each of which required sixteen DEM simulations. Thus, Figure 5.22 represents a total of 864 DEM simulations.

To extend the relationship between  $\phi_\mu$  and  $\phi$  shown in Figure 5.22 for values up to  $\phi_\mu \approx 90^\circ$ , an additional 432 DEM simulations were run on the smaller Specimens 1–3 with inter-element friction coefficients  $\mu = \{0.9, 1.0, 1.2, 1.5, 2.0, 3.0, 5.0, 10.0, 100.0\}$ . The resulting extended relationship between  $\phi_\mu$  and  $\phi$  for Specimens 1–3 is shown in Figure 5.23. In the interest of space, we have not included figures showing the individual yield surfaces for  $\mu > 0.8$  for Specimens 1–3 analogous to Figures 5.16–5.18. There is little to learn from seeing these yield surfaces, beyond the values of  $\phi$  chosen to match the data points at a Lode angle of zero, which are shown in Figure 5.23, since for  $\phi_\mu \geq 56^\circ$  ( $\mu \geq 1.5$ ) the yield surfaces are near-perfect triangles.

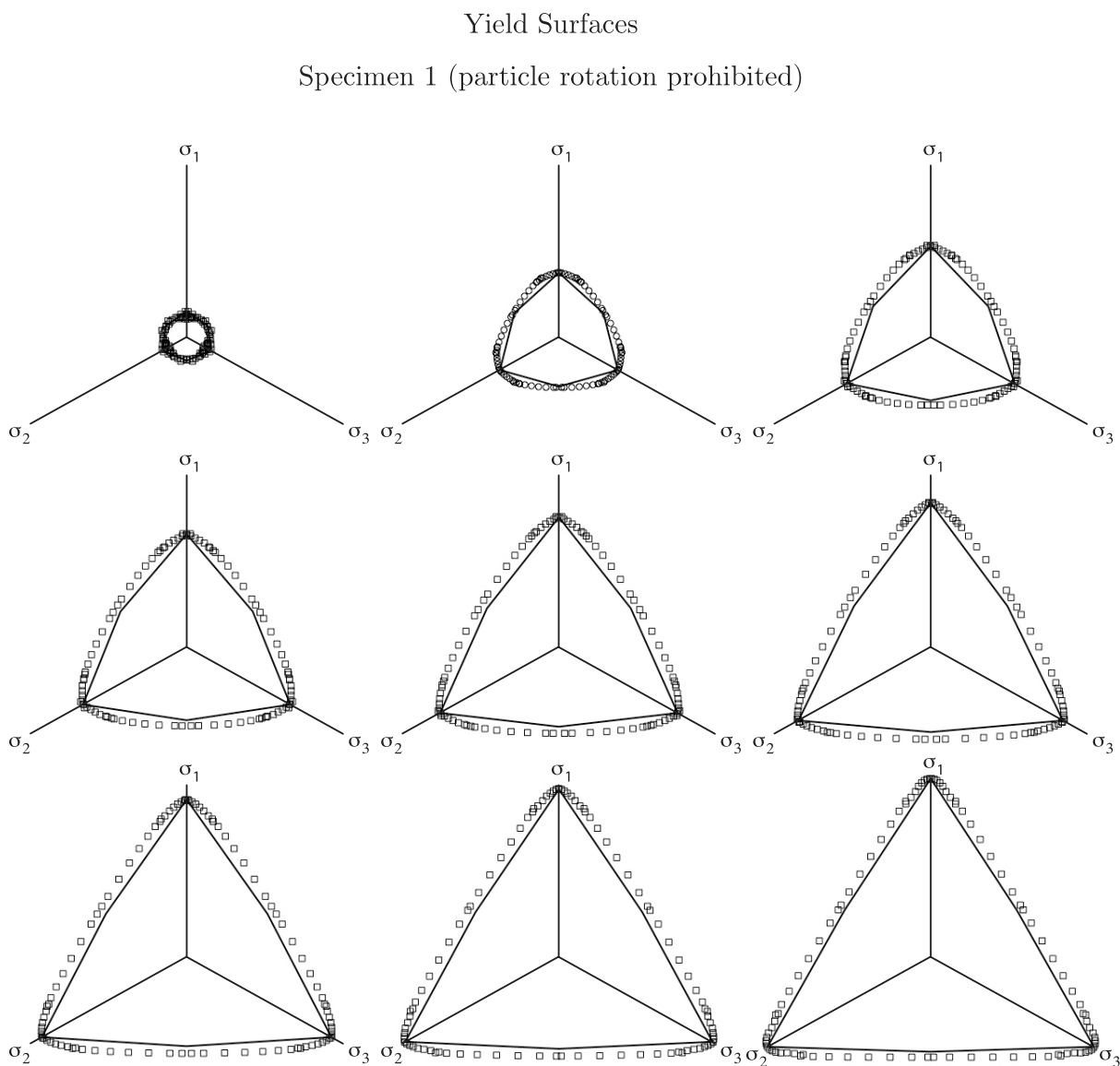


Figure 5.16: Yield surfaces obtained by DEM simulations performed on Specimen 1 with 3430 randomly packed uniform spheres with inter-element friction coefficients (from upper left to lower right) of  $\mu = \{0.01, 0.1, 0.2, 0.3, 0.4, 0.5, 0.6, 0.7, 0.8\}$ , with particle rotation prohibited. Also shown for comparison are the Mohr-Coulomb yield surfaces with values of the macroscopic friction angle  $\phi = \{10.5, 24.5, 34.0, 41.5, 47.5, 53.0, 58.5, 63.0, 68.0\}^\circ$  chosen to match the data points at a Lode angle of zero.

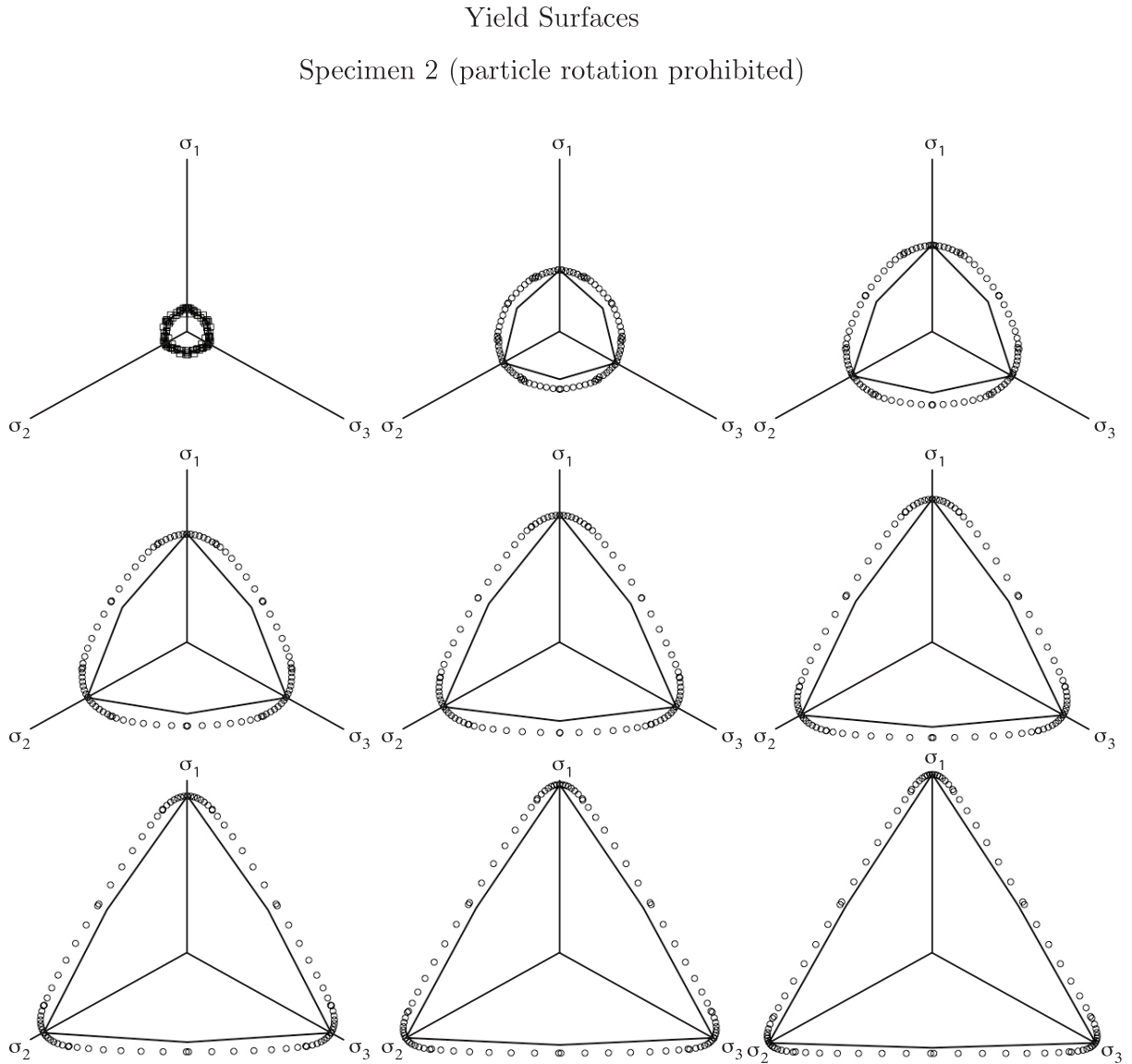


Figure 5.17: Yield surfaces obtained by DEM simulations performed on Specimen 2 with 3430 randomly packed uniform spheres with inter-element friction coefficients (from upper left to lower right) of  $\mu = \{0.01, 0.1, 0.2, 0.3, 0.4, 0.5, 0.6, 0.7, 0.8\}$ , with particle rotation prohibited. Also shown for comparison are the Mohr-Coulomb yield surfaces with values of the macroscopic friction angle  $\phi = \{10.0, 23.5, 32.5, 40.0, 46.5, 52.5, 58.0, 63.0, 68.0\}^\circ$  chosen to match the data points at a Lode angle of zero.

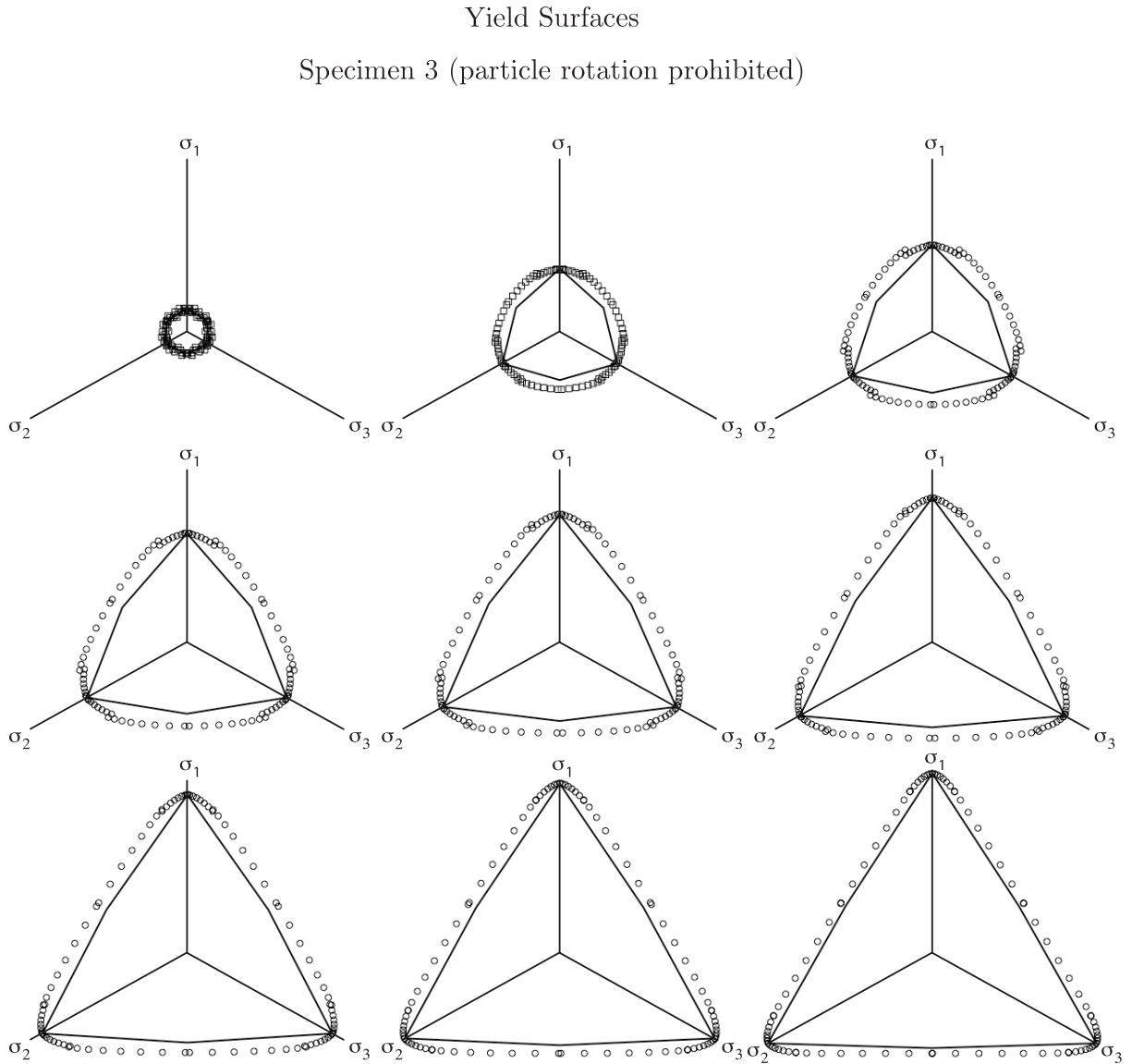


Figure 5.18: Yield surfaces obtained by DEM simulations performed on Specimen 3 with 3430 randomly packed uniform spheres with inter-element friction coefficients (from upper left to lower right) of  $\mu = \{0.01, 0.1, 0.2, 0.3, 0.4, 0.5, 0.6, 0.7, 0.8\}$ , with particle rotation prohibited. Also shown for comparison are the Mohr-Coulomb yield surfaces with values of the macroscopic friction angle  $\phi = \{9.5, 24.0, 32.5, 40.0, 46.5, 53.0, 58.5, 63.5, 68.5\}^\circ$  chosen to match the data points at a Lode angle of zero.

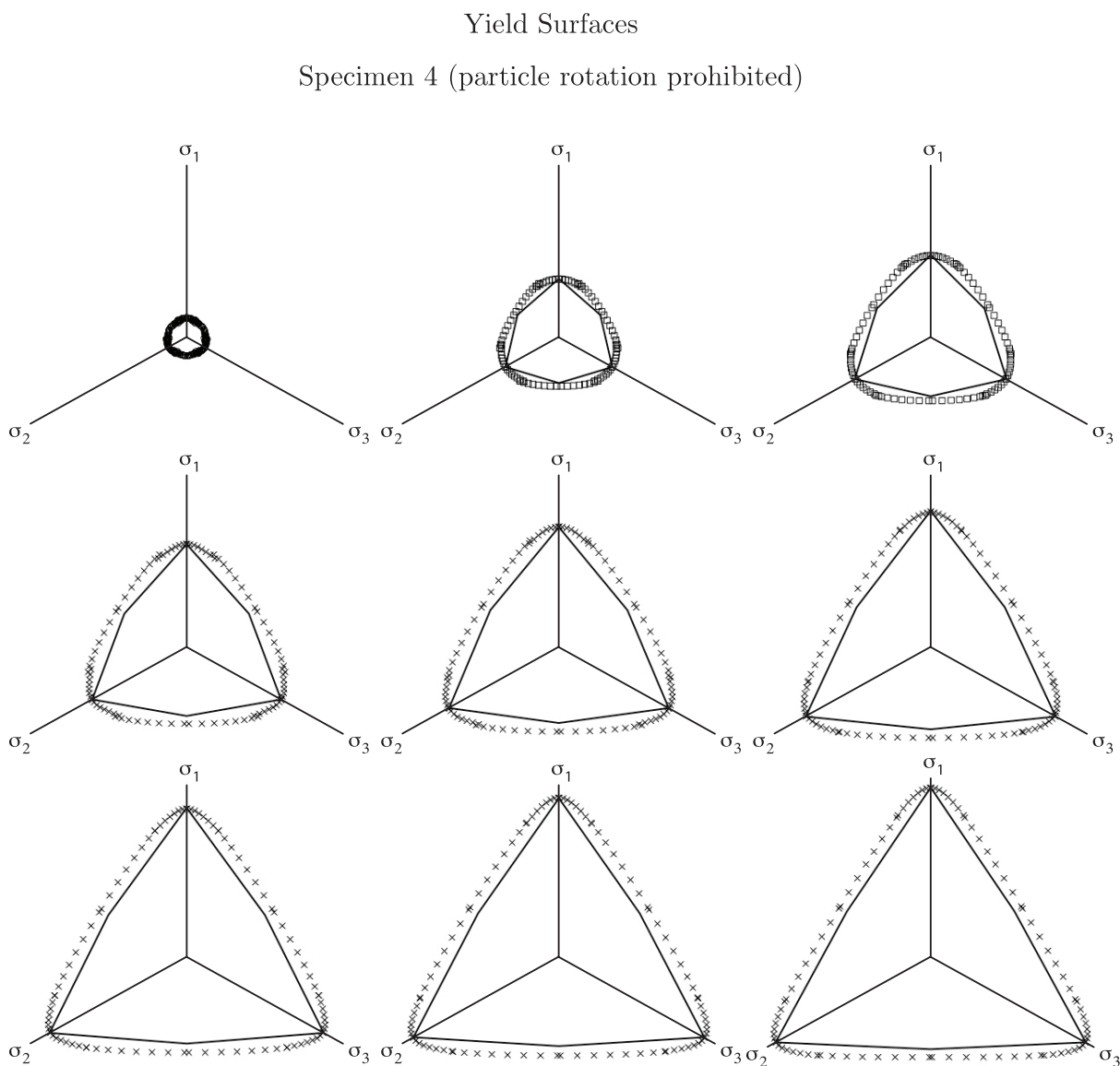


Figure 5.19: Yield surfaces obtained by DEM simulations performed on Specimen 4 with 29 660 randomly packed uniform spheres with inter-element friction coefficients (from upper left to lower right) of  $\mu = \{0.01, 0.1, 0.2, 0.3, 0.4, 0.5, 0.6, 0.7, 0.8\}$ , with particle rotation prohibited. Also shown for comparison are the Mohr-Coulomb yield surfaces with values of the macroscopic friction angle  $\phi = \{8.0, 22.5, 31.0, 38.0, 44.0, 50.0, 55.0, 59.0, 63.5\}^\circ$  chosen to match the data points at a Lode angle of zero.

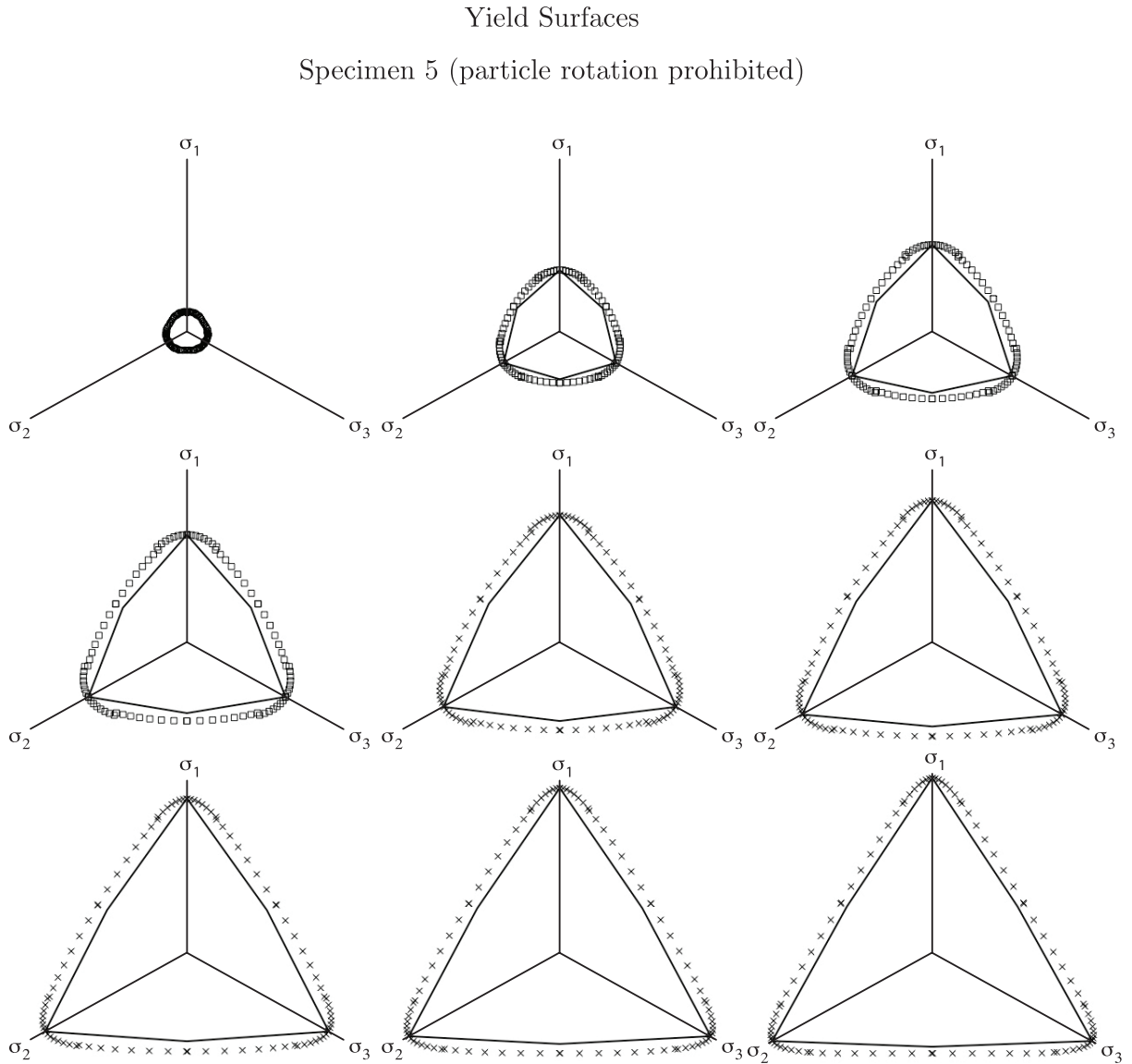


Figure 5.20: Yield surfaces obtained by DEM simulations performed on Specimen 5 with 29 660 randomly packed uniform spheres with inter-element friction coefficients (from upper left to lower right) of  $\mu = \{0.01, 0.1, 0.2, 0.3, 0.4, 0.5, 0.6, 0.7, 0.8\}$ , with particle rotation prohibited. Also shown for comparison are the Mohr-Coulomb yield surfaces with values of the macroscopic friction angle  $\phi = \{8.0, 23.5, 32.5, 39.5, 46.5, 52.0, 57.0, 61.5, 66.0\}^\circ$  chosen to match the data points at a Lode angle of zero.

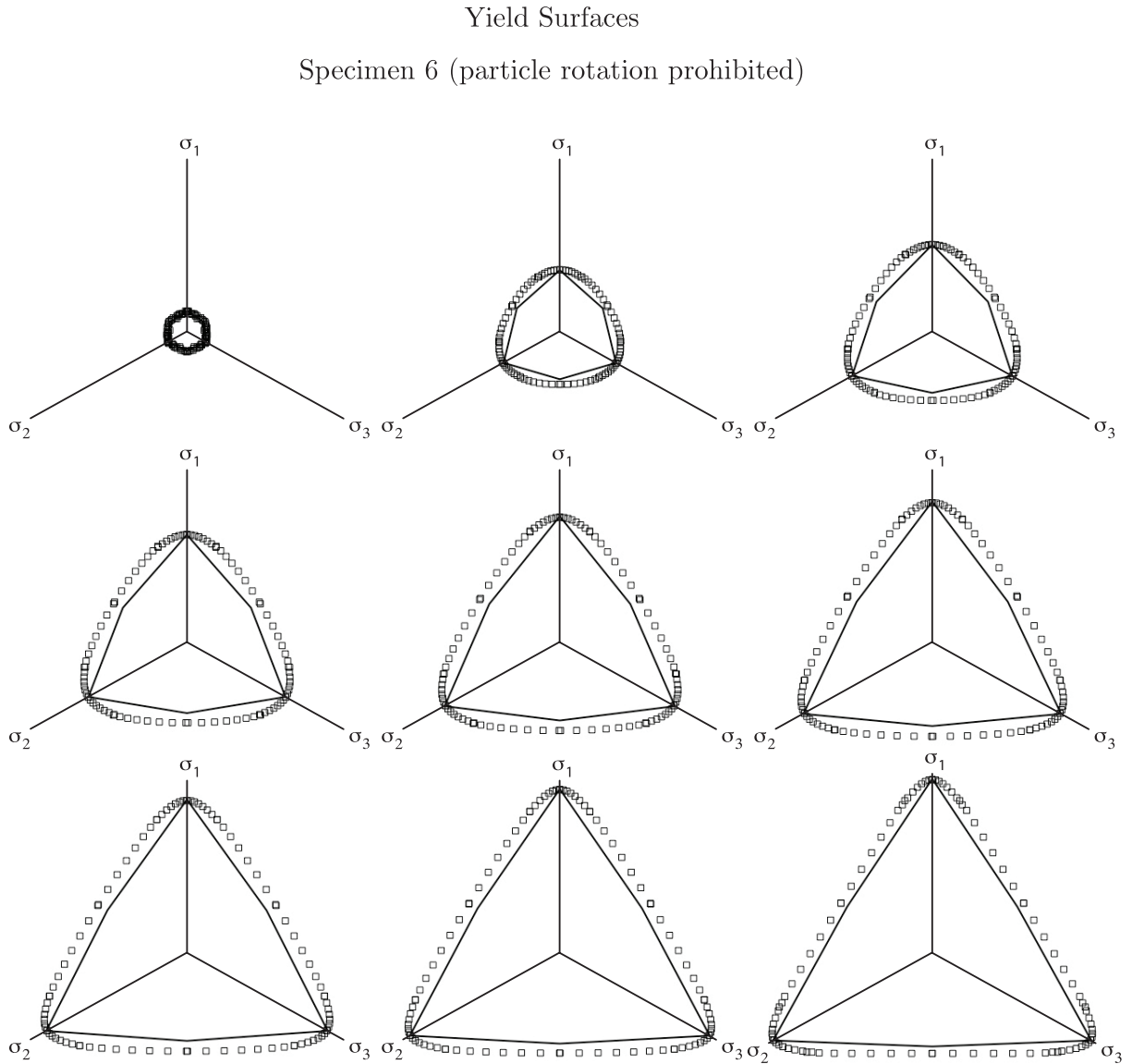


Figure 5.21: Yield surfaces obtained by DEM simulations performed on Specimen 6 with 29 660 randomly packed uniform spheres with inter-element friction coefficients (from upper left to lower right) of  $\mu = \{0.01, 0.1, 0.2, 0.3, 0.4, 0.5, 0.6, 0.7, 0.8\}$ , with particle rotation prohibited. Also shown for comparison are the Mohr-Coulomb yield surfaces with values of the macroscopic friction angle  $\phi = \{8.5, 23.5, 32.5, 39.5, 46.0, 51.5, 56.5, 61.0, 65.5\}^\circ$  chosen to match the data points at a Lode angle of zero.

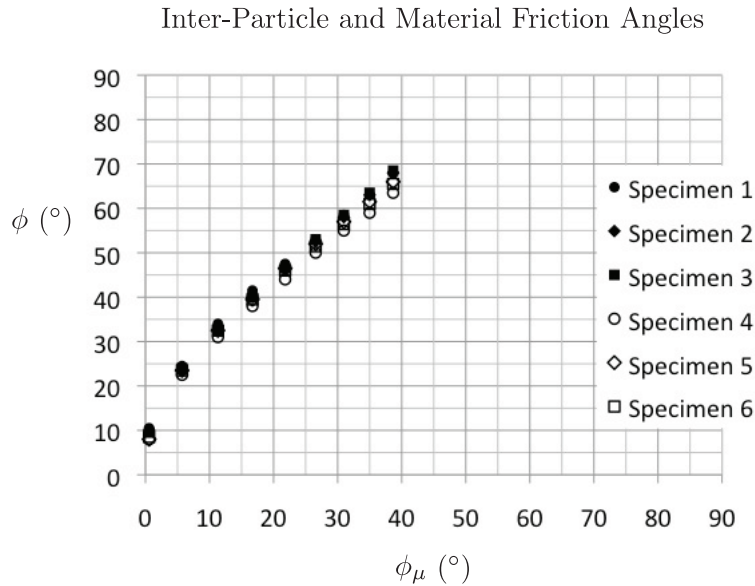


Figure 5.22: The relationship between the inter-particle friction coefficient  $\mu$  or the inter-particle friction angle  $\phi_\mu = \tan^{-1} \mu$  and the macroscopic or material friction angle  $\phi$  based on the yield surfaces shown in Figures 5.16–5.21, obtained from the 864 DEM simulations described in this section for six specimens of 3 430–29 660 randomly packed uniform spheres, with particle rotation prohibited.

The total accumulated friction work  $U_f$  in each specimen was recorded throughout the DEM simulations, as described in Section 5.4. Figures 5.10–5.15 of Section 5.4 show that for a given DEM specimen with a given inter-element friction coefficient  $\mu$ , the relationship between  $U_f$  and strain depends on the Lode angle  $\theta$ . Moreover, the relationship between  $U_f$  and strain is not linear. However, for the purpose of comparison, at a given Lode angle, the average rate of friction work can be determined (by linear regression for  $0\% \leq |\epsilon_z| \leq 8\%$ ) for each DEM specimen for each value of the inter-element friction coefficient  $\mu$ . Figure 5.24 shows the resulting relationship between the average rate of friction work (Joules/in/in) and the microscopic friction angle  $\phi_\mu = \tan^{-1} \mu$ , where  $\mu$  is the inter-element friction coefficient, for Specimens 1–3 with  $0.01 \leq \mu \leq 100.0$ , (with particle rotation prohibited), at Lode angles of  $\theta = 0$  (top) and  $\theta = 60^\circ$  (bottom). Figure 5.25 shows the corresponding relationships for Specimens 4–6 with  $0.01 \leq \mu \leq 0.8$ .

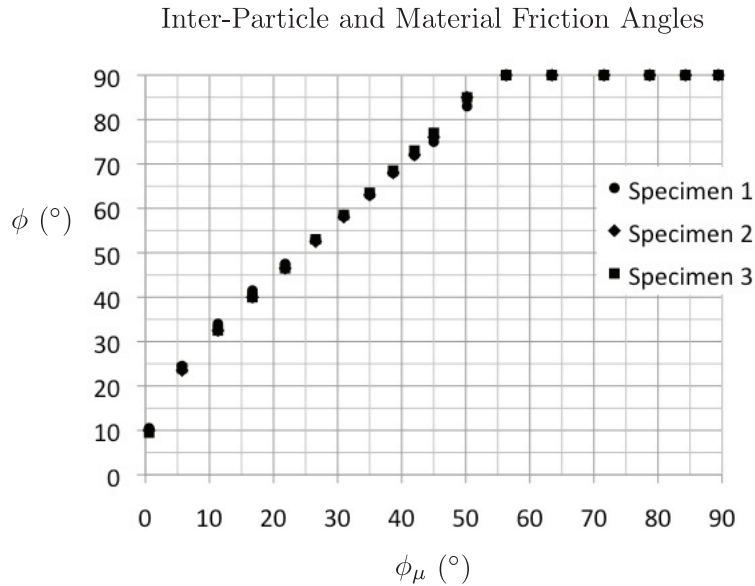


Figure 5.23: The relationship between the inter-particle friction coefficient  $\mu$  or the inter-particle friction angle  $\phi_\mu = \tan^{-1} \mu$  and the macroscopic or material friction angle  $\phi$ , obtained from 864 DEM simulations described in this section for three specimens of 3 430 randomly packed uniform spheres, with particle rotation prohibited.

## 5.6 Discussion

The validity of Figures 5.22 and 5.23 depend on several assumptions implicit in our method of projecting stress triples  $(\sigma_1, \sigma_2, \sigma_3)$  onto the  $\pi$ -plane from the origin in principal stress space. First, we assume a priori that the particulate materials represented by Specimens 1–6 have essentially zero strength when the hydrostatic pressure  $p = 0$ . Since the hydrostatic pressure is nonzero in all of our DEM simulations, this assumption is not tested by our simulations. However, the assumption of zero strength when  $p = 0$  is equivalent to the assumption that the particulate material being modeled is *non-cohesive*. Since our DEM simulations include no inter-element cohesive forces, this assumption is reasonable. Note from Figures 5.22 and 5.23 that the strength of the particulate material (as represented by the material friction angle  $\phi$ ) does *not* go to zero as the inter-particle friction coefficient  $\mu$  (and  $\phi_\mu$ ) goes to zero. Chapter 7 provides a micromechanics-based explanation of this phenomenon.

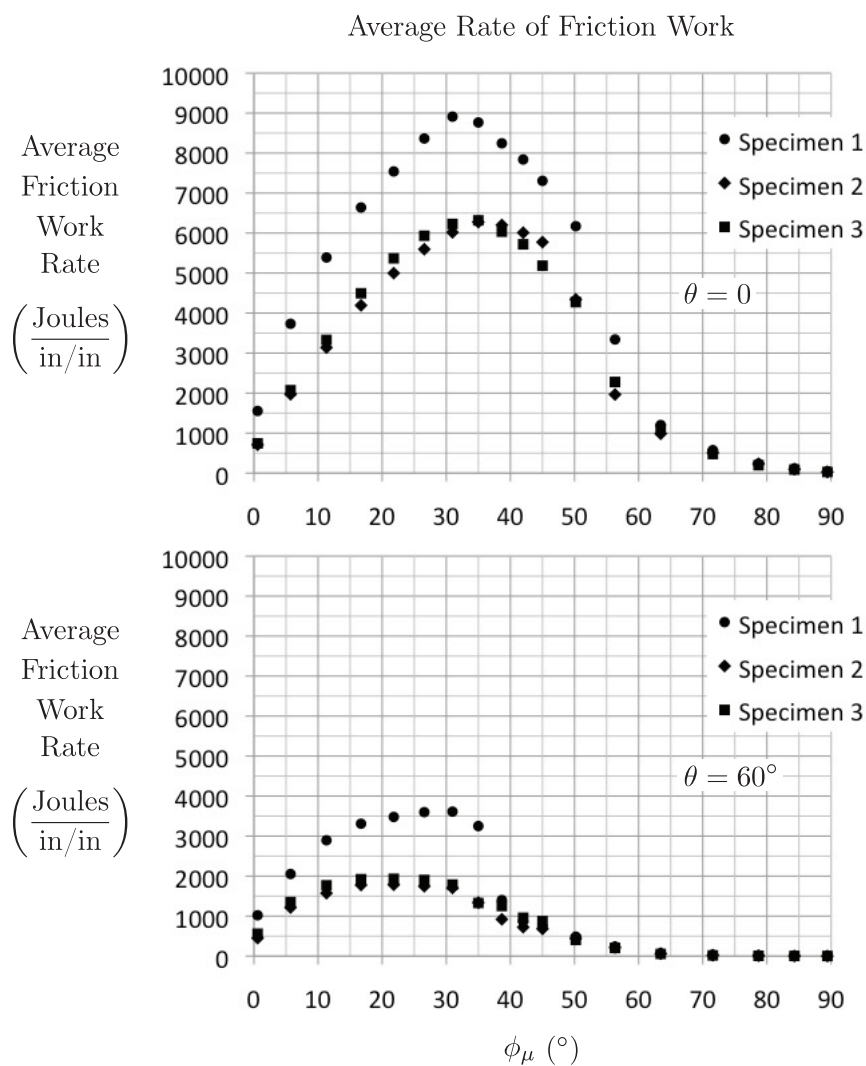


Figure 5.24: The relationship between the inter-particle friction angle  $\phi_\mu = \tan^{-1} \mu$  (where  $\mu$  is the inter-element friction coefficient,  $0.01 \leq \mu \leq 100.0$ ) and the average rate of friction work in Specimens 1–3 at Lode angles of  $\theta = 0$  (top) and  $\theta = 60^\circ$  (bottom), with particle rotation prohibited.

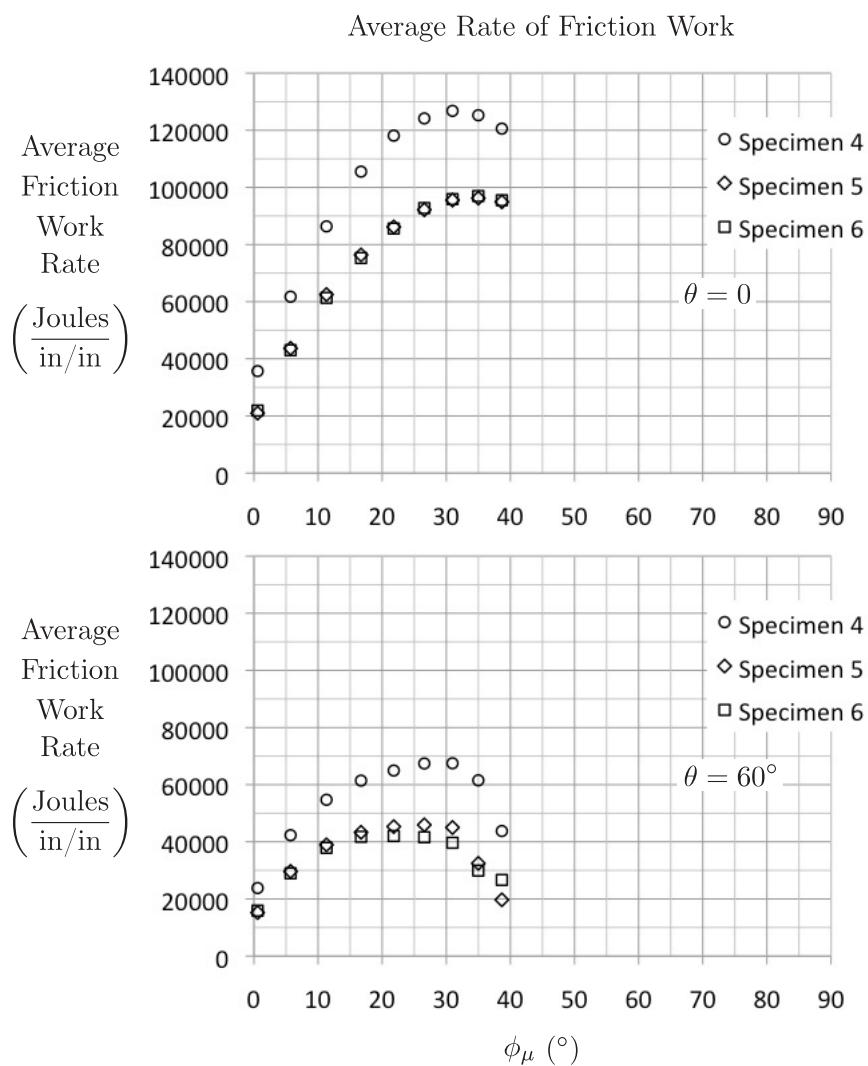


Figure 5.25: The relationship between the inter-particle friction angle  $\phi_\mu = \tan^{-1} \mu$  (where  $\mu$  is the inter-element friction coefficient,  $0.01 \leq \mu \leq 0.8$ ) and the average rate of friction work in Specimens 4–6 at Lode angles of  $\theta = 0$  (top) and  $\theta = 60^\circ$  (bottom), with particle rotation prohibited.

Second, since the hydrostatic pressure on the specimens was not constant during the simulations, our method assumes implicitly that the yield surface is linearly related to the hydrostatic pressure  $p$ , as noted in Section 5.4. In fact, for a given specimen with a given inter-element friction coefficient  $\mu$ , the variation in  $p = (\sigma_1 + \sigma_2 + \sigma_3)/3$  was observed and recorded during the sixteen DEM simulations with varying  $\dot{\epsilon}_1$ ,  $\dot{\epsilon}_2$ , and  $\dot{\epsilon}_3$  (needed to obtain the data points for the yield surface, as described in Section 5.4). For Specimens 1–6, with  $0.1 < \mu < 1.0$  and  $1\% \leq \epsilon_i \leq 8\%$ , the variation in  $p$  during the sixteen DEM simulations was approximately (1)  $1 \text{ MPa} < p < 4 \text{ MPa}$ , (2)  $0.4 \text{ MPa} < p < 3 \text{ MPa}$ , (3)  $0.5 \text{ MPa} < p < 3 \text{ MPa}$ , (4)  $3 \text{ MPa} < p < 5 \text{ MPa}$ , (5)  $2 \text{ MPa} < p < 4 \text{ MPa}$ , and (6)  $2 \text{ MPa} < p < 4 \text{ MPa}$ . For all six specimens, the largest pressure discontinuity between simulations occurs at the transition from compression to extension, which occurs between adjacent data points on the yield surfaces (projected onto the  $\pi$ -plane) at a Lode angle of  $\theta \approx 20^\circ$ .

Note that, despite this observed variation in  $p$  from specimen to specimen during the simulations, the data points in Figures 5.22 and 5.23 from all six specimens are quite closely clustered for each value of  $\mu$  (or  $\phi_\mu$ ). This provides some evidence in support of our assumption of linearity, at least within the range of  $p$  experienced by our specimens during our DEM simulations. Moreover, the observable “continuity” of each yield surface (projected onto the  $\pi$ -plane), which is obtained from the sixteen DEM simulations performed on a given specimen with a given value of  $\mu$ , provides further evidence in support of our assumption of linearity. That is, since the value of the hydrostatic pressure  $p$  was observed to “jump” by a factor of approximately 100%–500% in all six specimens (e.g., from 4 MPa to 1 MPa in Specimen 1, from 3 MPa to 0.5 MPa in Specimen 3, and from 4 MPa to 2 MPa in Specimen 5) between “adjacent” DEM simulations at  $\theta \approx 20^\circ$  (at the transition from compression to extension), the fact that most of the yield surfaces shown in Figures 5.16–5.21 exhibit *little or no* discontinuity at a Lode angle  $\theta \approx 20^\circ$  is a strong confirmation of our assumption of the linearity of the yield surfaces for the range of pressures noted for each specimen in the

preceding paragraph. It cannot be expected that the relationship between the yield surface and  $p$  would be precisely linear, however, and so exceptions are to be expected. One of the most notable exceptions appears in Specimen 3 with  $\mu = 0.2$  at a Lode angle of  $\theta = 18^\circ$ , as shown in Figure 5.26.

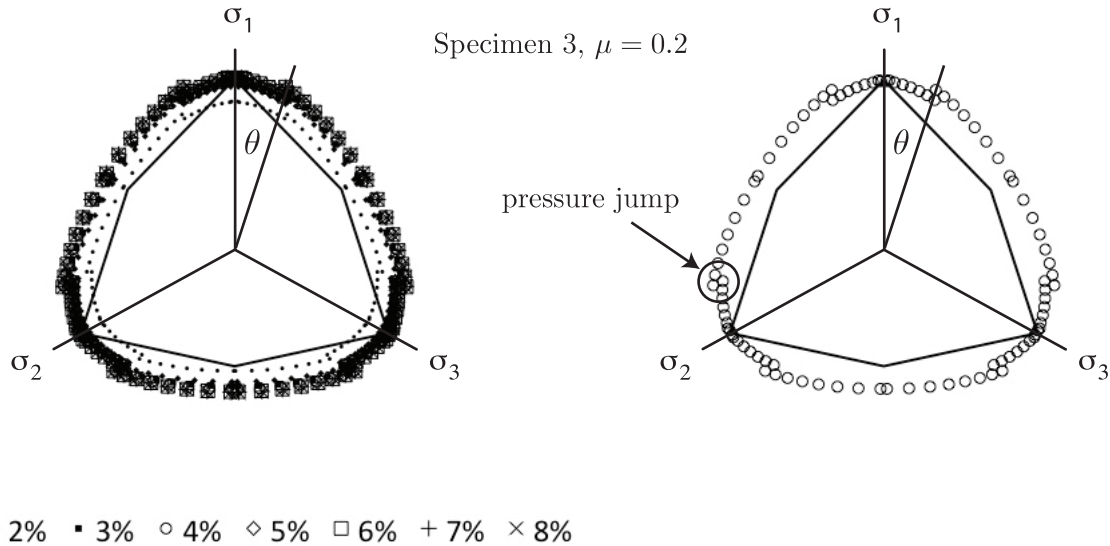


Figure 5.26: Observable discontinuity in the data points on the  $\pi$ -plane obtained from one set of DEM simulations performed on Specimen 3 with an inter-element friction coefficient of  $\mu = 0.2$ . The discontinuity occurs at a Lode angle of  $\theta = 18^\circ$ , where there is a jump in the hydrostatic pressure from  $p \approx 0.8$  MPa to  $p \approx 1$  MPa at adjacent data points.

Figures 5.16–5.21 show the Mohr-Coulomb yield surfaces with material friction angles  $\phi$  chosen to match the yield surfaces determined by DEM for each specimen for each value of  $\mu$  at a Lode angle of  $\theta = 0$ . Other yield surfaces for non-cohesive particulate materials include the Drucker-Prager, Lade-Duncan, and Matsuoka-Nakai surfaces (Bardet, 1990), as described in Section 5.3. Figures 5.27–5.32 show the yield surfaces determined by DEM for Specimens 1–6 with  $\mu = 0.2$  (top) and  $\mu = 0.5$  (bottom), with particle rotation prohibited. Also shown in Figures 5.27–5.32 are Mohr-Coulomb, Drucker-Prager, Lade-Duncan (left) and Matsuoka-Nakai (right) yield surfaces, with material parameters chosen to match the DEM data points at a Lode angle of zero.

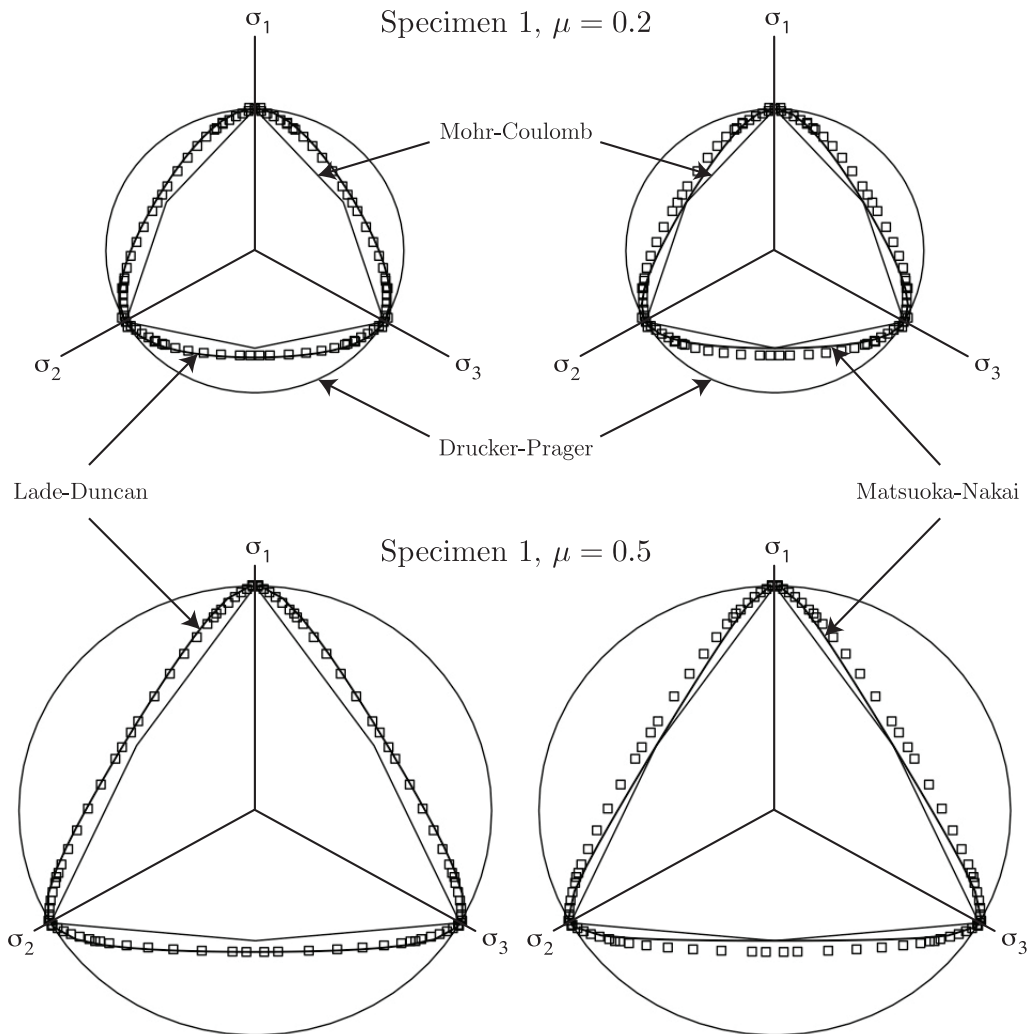


Figure 5.27: Yield surfaces obtained by DEM simulations performed on Specimen 1 with inter-element friction coefficients of  $\mu = 0.2$  (top) and  $\mu = 0.5$  (bottom), with particle rotation prohibited. Also shown are Mohr-Coulomb, Drucker-Prager, Lade-Duncan (left) and Matsuoka-Nakai (right) yield surfaces, with material parameters chosen to match the data points at a Lode angle of  $\theta = 0$ .

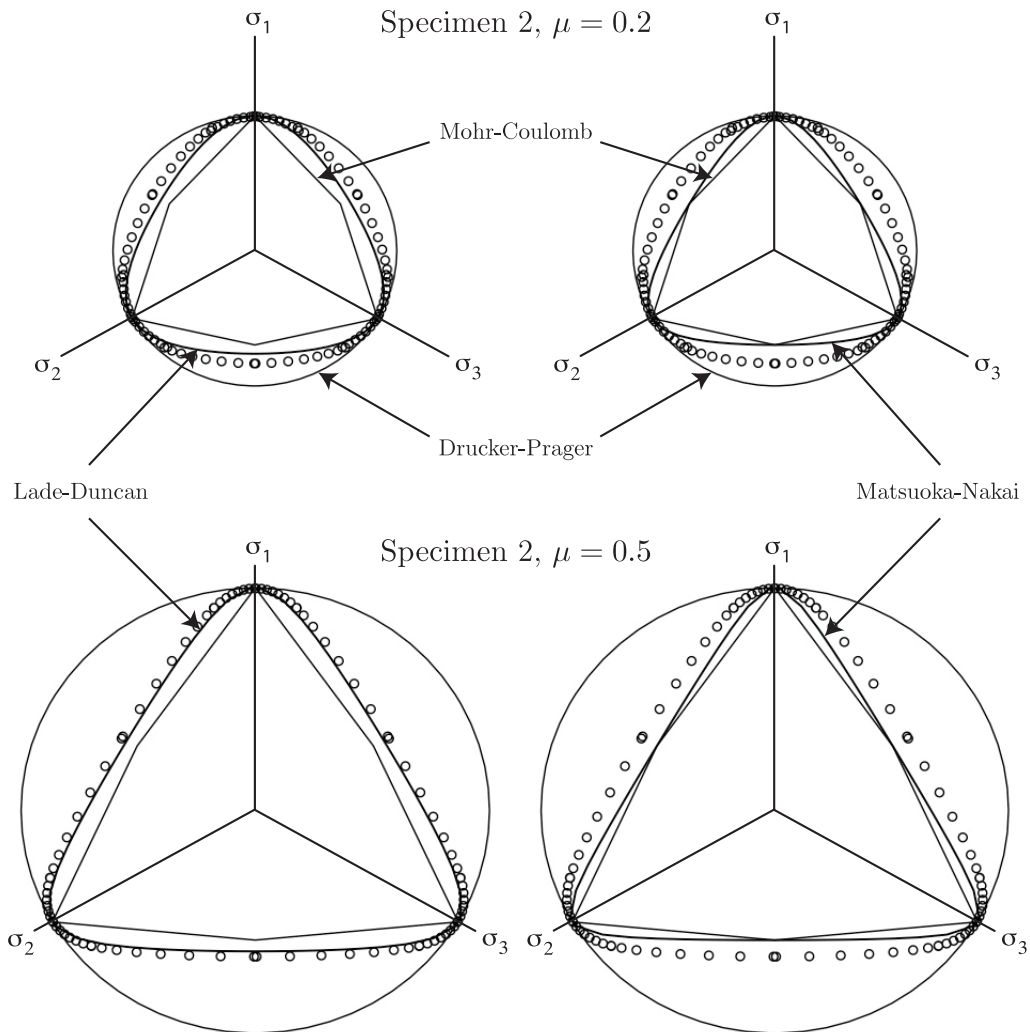


Figure 5.28: Yield surfaces obtained by DEM simulations performed on Specimen 2 with inter-element friction coefficients of  $\mu = 0.2$  (top) and  $\mu = 0.5$  (bottom), with particle rotation prohibited. Also shown are Mohr-Coulomb, Drucker-Prager, Lade-Duncan (left) and Matsuoka-Nakai (right) yield surfaces, with material parameters chosen to match the data points at a Lode angle of  $\theta = 0$ .

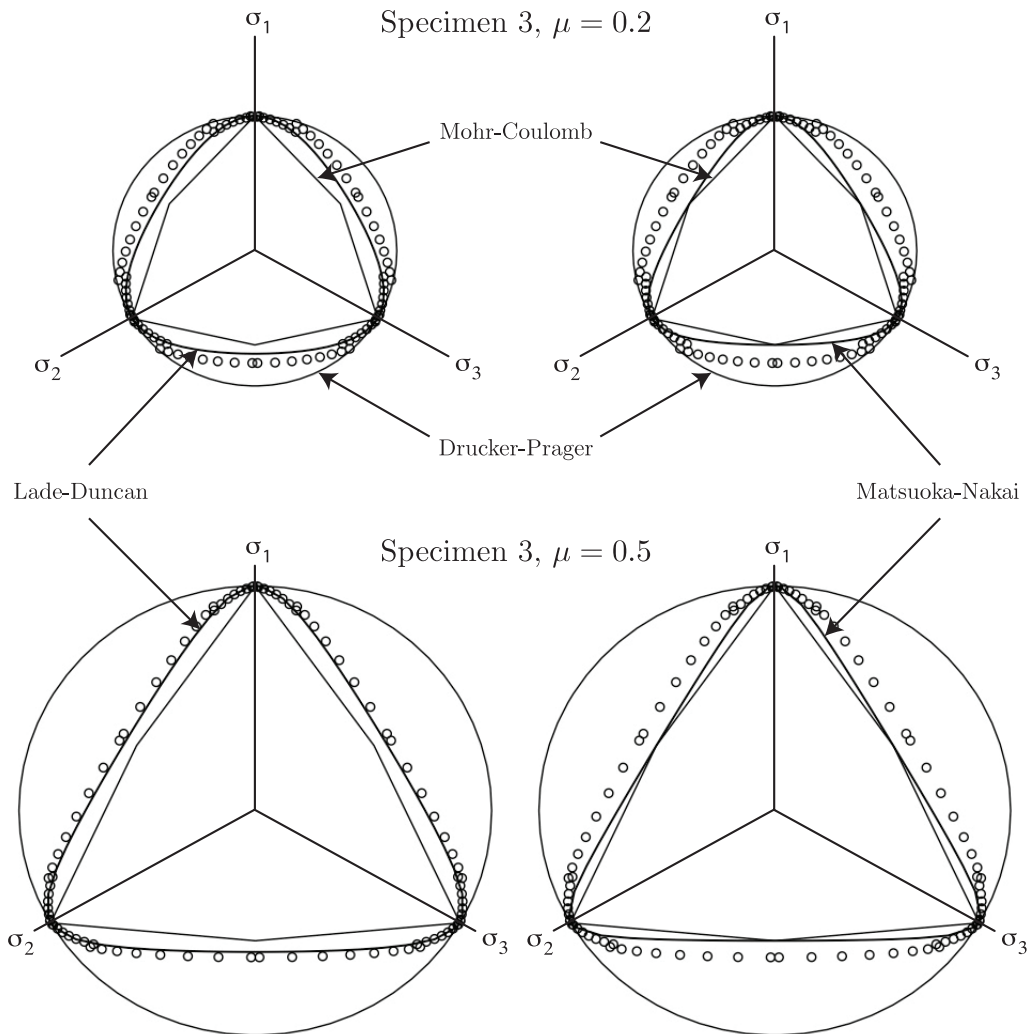


Figure 5.29: Yield surfaces obtained by DEM simulations performed on Specimen 3 with inter-element friction coefficients of  $\mu = 0.2$  (top) and  $\mu = 0.5$  (bottom), with particle rotation prohibited. Also shown are Mohr-Coulomb, Drucker-Prager, Lade-Duncan (left) and Matsuoka-Nakai (right) yield surfaces, with material parameters chosen to match the data points at a Lode angle of  $\theta = 0$ .

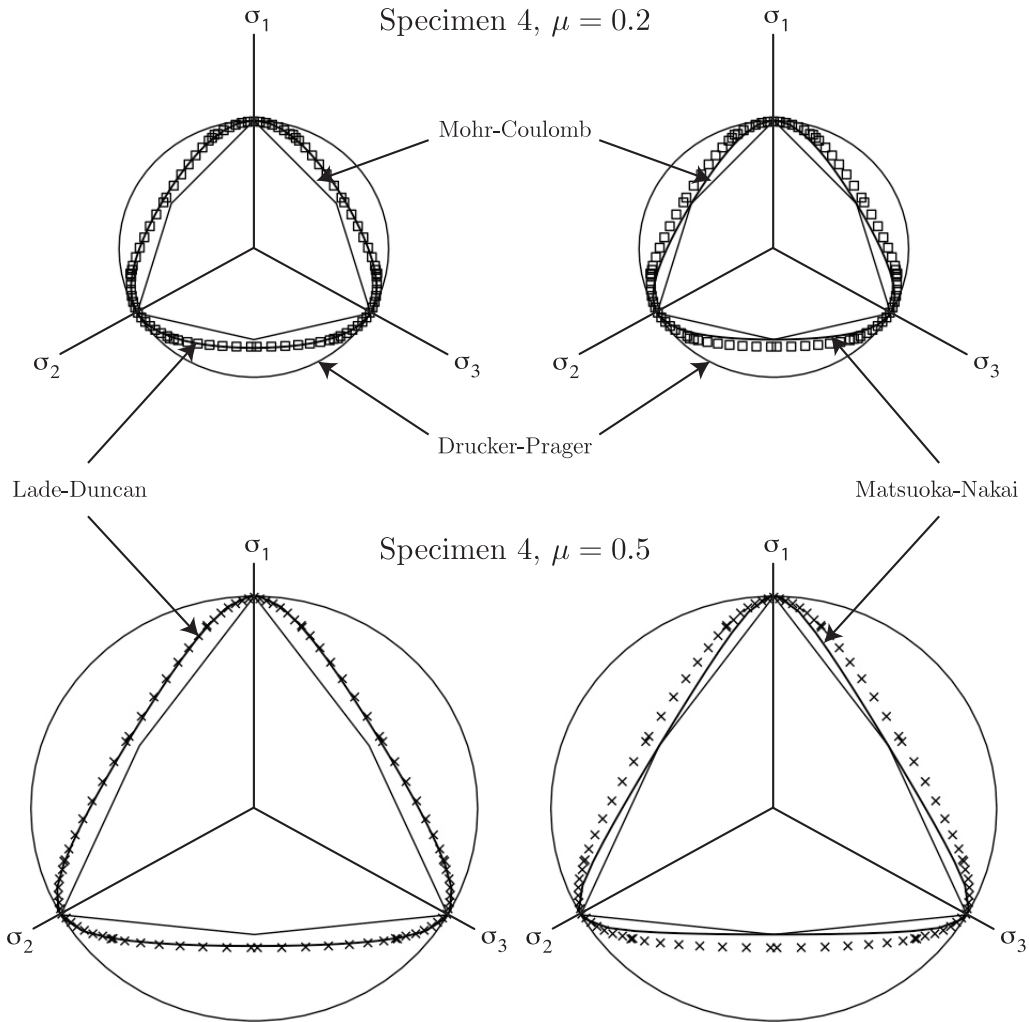


Figure 5.30: Yield surfaces obtained by DEM simulations performed on Specimen 4 with inter-element friction coefficients of  $\mu = 0.2$  (top) and  $\mu = 0.5$  (bottom), with particle rotation prohibited. Also shown are Mohr-Coulomb, Drucker-Prager, Lade-Duncan (left) and Matsuoka-Nakai (right) yield surfaces, with material parameters chosen to match the data points at a Lode angle of  $\theta = 0$ .

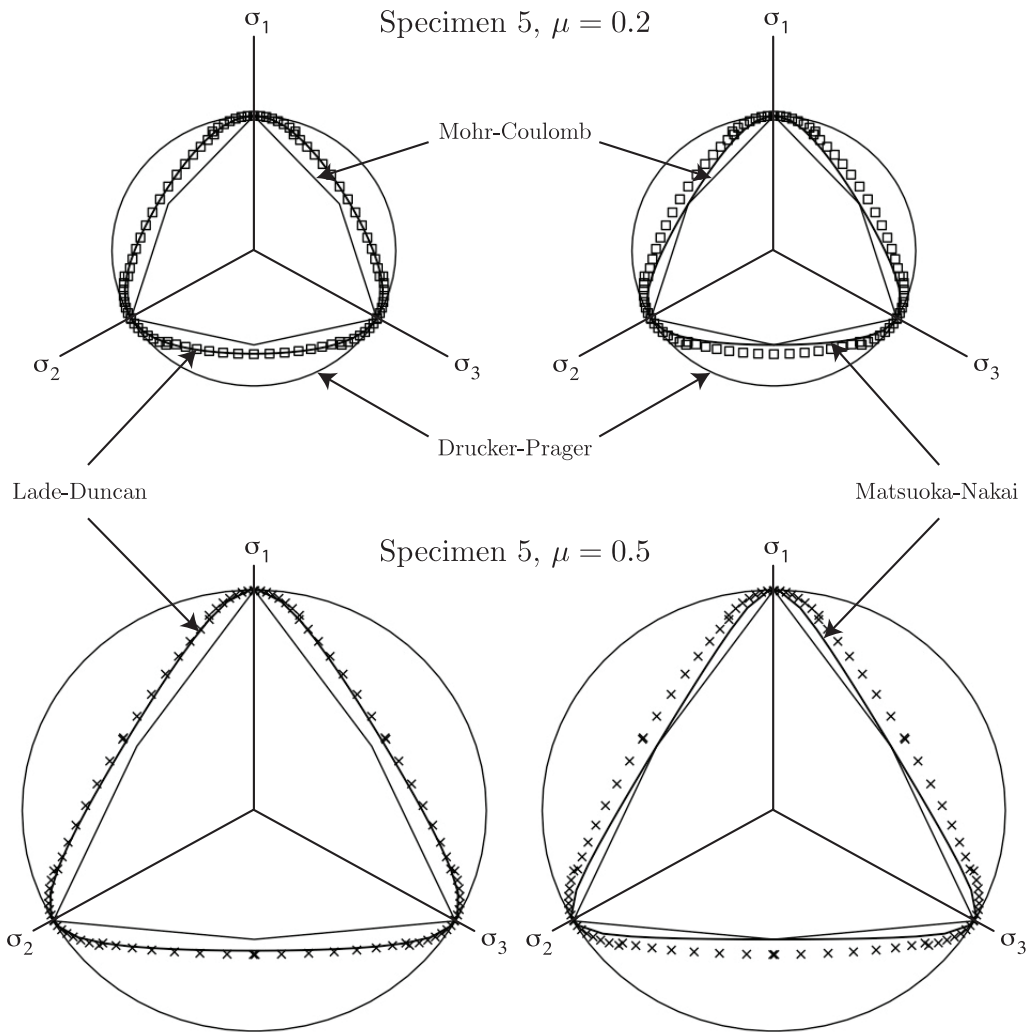


Figure 5.31: Yield surfaces obtained by DEM simulations performed on Specimen 5 with inter-element friction coefficients of  $\mu = 0.2$  (top) and  $\mu = 0.5$  (bottom), with particle rotation prohibited. Also shown are Mohr-Coulomb, Drucker-Prager, Lade-Duncan (left) and Matsuoka-Nakai (right) yield surfaces, with material parameters chosen to match the data points at a Lode angle of  $\theta = 0$ .

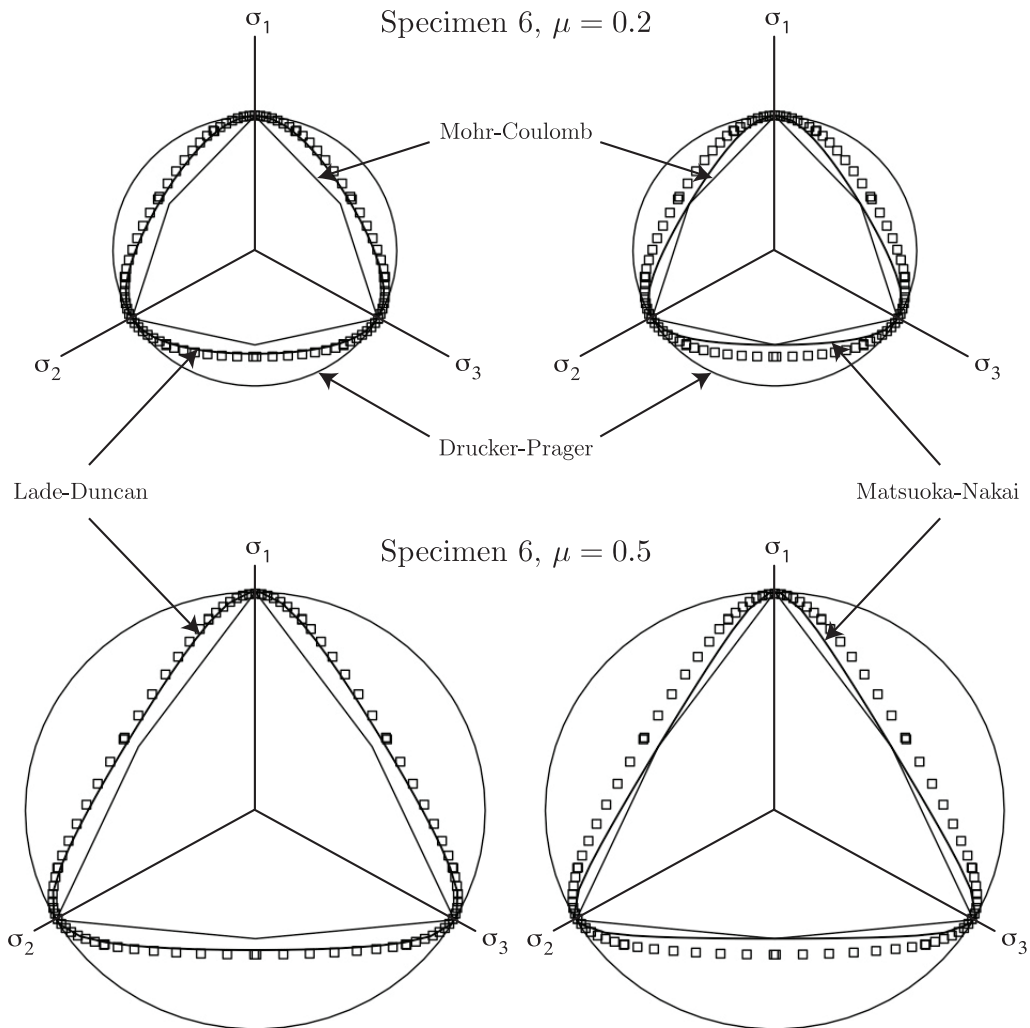


Figure 5.32: Yield surfaces obtained by DEM simulations performed on Specimen 6 with inter-element friction coefficients of  $\mu = 0.2$  (top) and  $\mu = 0.5$  (bottom), with particle rotation prohibited. Also shown are Mohr-Coulomb, Drucker-Prager, Lade-Duncan (left) and Matsuoka-Nakai (right) yield surfaces, with material parameters chosen to match the data points at a Lode angle of  $\theta = 0$ .

Note that the Matsuoka-Nakai and Mohr-Coulomb yield surfaces coincide at Lode angles of  $\theta = 0$  and  $\theta = 60^\circ$ , while the Lade-Duncan and Mohr-Coulomb yield surfaces only coincide at a Lode angle of  $\theta = 0$ , where all four yield surfaces in Figures 5.27–5.32 were forced to coincide by our choice of material parameters. Recall from Section 5.3 that both the Matsuoka-Nakai and Lade-Duncan yield surfaces lie between the Mohr-Coulomb and Drucker-Prager yield surfaces, the last being a circle on the  $\pi$ -plane in principal stress space. Figures 5.27–5.32 show that the relative performance of the yield surfaces depend on both the specimen geometry (packing) and the inter-particle friction coefficient  $\mu$ . For Specimens 1 and 4, the data points tend to lie between the Lade-Duncan and Matsuoka-Nakai surfaces. For Specimens 2, 3, 5, and 6, on the other hand, the data points tend to lie between the Lade-Duncan and Drucker-Prager surfaces. For all six specimens, the data points correspond most closely with the Lade-Duncan yield surface, and this correspondence improves as  $\mu$  increases. The correspondence with the Lade-Duncan yield surface is most pronounced for Specimens 1, 4, and 5, for all values of  $\mu$ .

It must be emphasized that the material friction angles  $\phi$  of Figures 5.22 and 5.23, chosen to match the yield surfaces of Figures 5.16–5.21 at a Lode angle of  $\theta = 0$ , are the *peak* friction angles for the particulate material being modeled by DEM, sometimes denoted  $\phi_p$  in the geomechanics literature (e.g., Bardet, 1997). Another important strength property of particulate materials is the *residual* friction angle  $\phi_r$ , which is generally different from the peak friction angle  $\phi_p$ . See Section 9.6 of Chapter 9 of this thesis (Fleischmann et al., 2013c) for a discussion of typical values of the peak and residual friction angles for well-graded sand as an example.

In particulate materials, irreversible strain generally occurs *before* the peak friction angle. Indeed, if “elastic” is strictly defined as the range for which strain energy is fully reversible, then the strain at which a particulate material leaves the elastic range can be very small indeed. It is well known to researchers in the field of geomechanics that there is very little

“elastic range” for dry sand, since instabilities in the material fabric can produce a small amount of irreversible strain almost immediately upon loading. According to Mitchell and Soga (2005), irrecoverable strains can develop in uncemented normally consolidated sands at strains as low as  $\epsilon = 0.007\%$ . Figures 5.10–5.15 show that friction work (and hence irrecoverable strain) occurs at or before  $|\epsilon_z| = 1\%$  for all six specimens, with  $\mu = 0.2$  or  $\mu = 0.5$  and  $\theta = 0$  or  $\theta = 60^\circ$ . On the other hand, Figures 5.4–5.9 show that yield associated with the peak friction angle  $\phi$  occurs at approximately  $4\% \leq |\epsilon_z| \leq 6\%$  for Specimens 1–3 and at approximately  $6\% \leq |\epsilon_z| \leq 8\%$  for Specimens 4–6, after which time the yield surface either remains approximately fixed or begins to collapse.

Another (perhaps more familiar) way of presenting the information that is contained in Figures 5.4–5.9 is to graph the ratio of axial stress to lateral stress versus axial strain for DEM simulations corresponding to various Lode angles. In the DEM simulations corresponding to Lode angles of  $\theta = 0$  and  $\theta = 60^\circ$ ,  $\sigma_{\text{axial}} = \sigma_z$ ,  $\epsilon_{\text{axial}} = \epsilon_z$ , and  $\sigma_{\text{lateral}} = \sigma_x = \sigma_y$ . Recall from Section 5.4 that the macroscopic (peak) friction angles  $\phi$  for each specimen for each inter-element friction coefficient  $\mu$  were chosen to match the data points obtained from the DEM simulations corresponding to a Lode angle of  $\theta = 0$ . Figures 5.33–5.38 show the stress-strain curves for Specimens 1–6, respectively, with an inter-element friction coefficient of  $\mu = 0.2$  (top) and  $\mu = 0.5$  (bottom), at Lode angles of  $\theta = 0$  and  $\theta = 60^\circ$ . Recall from Section 5.4 that the DEM simulations are of true triaxial tests performed under constant volume conditions.

The magnitude of the axial strain  $|\epsilon_z|$  corresponding to the peak friction angle  $\phi$  also corresponds to the peak value of the stress ratio  $\sigma_{\text{axial}}/\sigma_{\text{lateral}}$  in Figures 5.33–5.38. Thus, these figures confirm that the axial strain corresponding to the (peak) material friction angle ranges from approximately  $4\% \leq |\epsilon_{\text{axial}}| \leq 6\%$  for Specimens 1–3 and approximately  $6\% \leq |\epsilon_{\text{axial}}| \leq 8\%$  for Specimens 4–6. This agrees with the maximal yield surfaces identified from the data points in Figures 5.4–5.9. Note that the stress-strain curves in the range

$1\% < |\epsilon_{\text{axial}}| < 4\%$  do not represent the elastic behavior of the particulate material, since plastic strain is already occurring in this range, as confirmed by the existence of non-zero friction work in the specimens for  $|\epsilon_{\text{axial}}| > 1\%$ .

Regarding the average rate of friction work in Specimens 1–3, shown in Figure 5.24, it is significant that while the rate of friction work in Specimen 1 is significantly larger – roughly 40% larger at a Lode angle of  $\theta = 0$  – than the rate of friction work in either Specimens 2 or 3 for  $0 < \phi_{\mu} \leq 56^{\circ}$  ( $0 < \mu \leq 1.5$ ), Figure 5.23 shows that the material friction angles  $\phi$  for Specimens 1–3 (at a Lode angle of  $\theta = 0$ ) are very close to the same over the same range of  $\phi_{\mu}$  ( $\mu$ ), with a variation of at most 5%. Taken together, Figures 5.23 and 5.24 seem to imply that the material friction angle and the rate of friction work in a specimen are uncorrelated. The same is true of Specimens 4–6, since, while Figure 5.25 shows that the friction work rate in Specimen 4 is roughly 30% larger (at a Lode angle of  $\theta = 0$ ) than that of either Specimens 5 or 6, Figure 5.22 shows that the material friction angles  $\phi$  for Specimens 4–6 (at a Lode angle of  $\theta = 0$ ) exhibit a variation of less than 6%.

As we have noted in other chapters, such as Chapters 3 and 4, one of the great advantages of using the Discrete Element Method is the amount of data that one can obtain and analyze *at the element level*. For example, in addition to the cumulative friction work, we can also visually inspect the friction work experienced by every individual element in a DEM specimen at any time during a simulation. In this way, it is possible to determine whether failure (sliding) occurs primarily along identifiable slip planes within a specimen, or whether failure (sliding) is randomly dispersed throughout the specimen during yielding. Figure 5.39 shows the friction work experienced by each element in Specimen 5 at 4% axial strain in compression during the DEM simulation corresponding to a Lode angle of  $\theta = 0$  on the yield surface shown in Figure 5.8 (bottom) with an inter-element friction coefficient of  $\mu = 0.5$ . On the left side of Figure 5.39, the gray scale of each element denotes the friction work experienced by that element, varying from white for elements experiencing no friction work

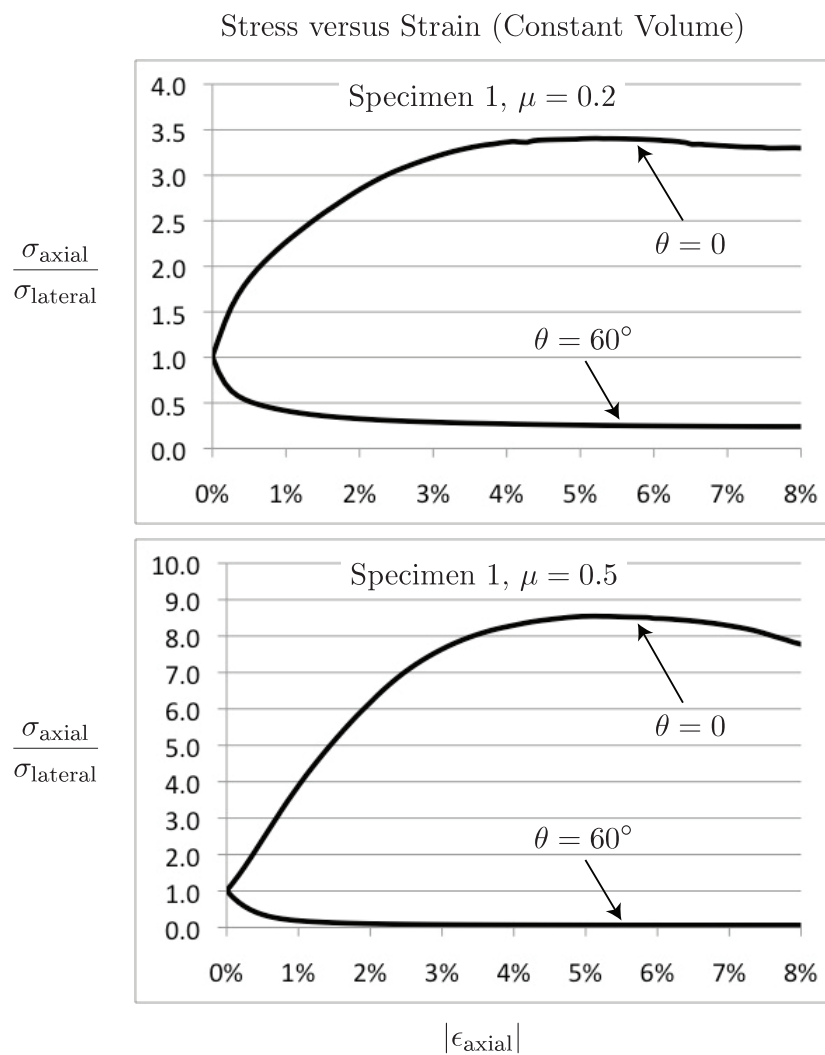


Figure 5.33: Stress ratio as a function of axial strain for Specimen 1 with an inter-element friction coefficient of  $\mu = 0.2$  (top) and  $\mu = 0.5$  (bottom), with particle rotation prohibited. The two curves correspond to the data points on the yield surfaces shown in Figure 5.4 at Lode angles of  $\theta = 0$  and  $\theta = 60^\circ$ .

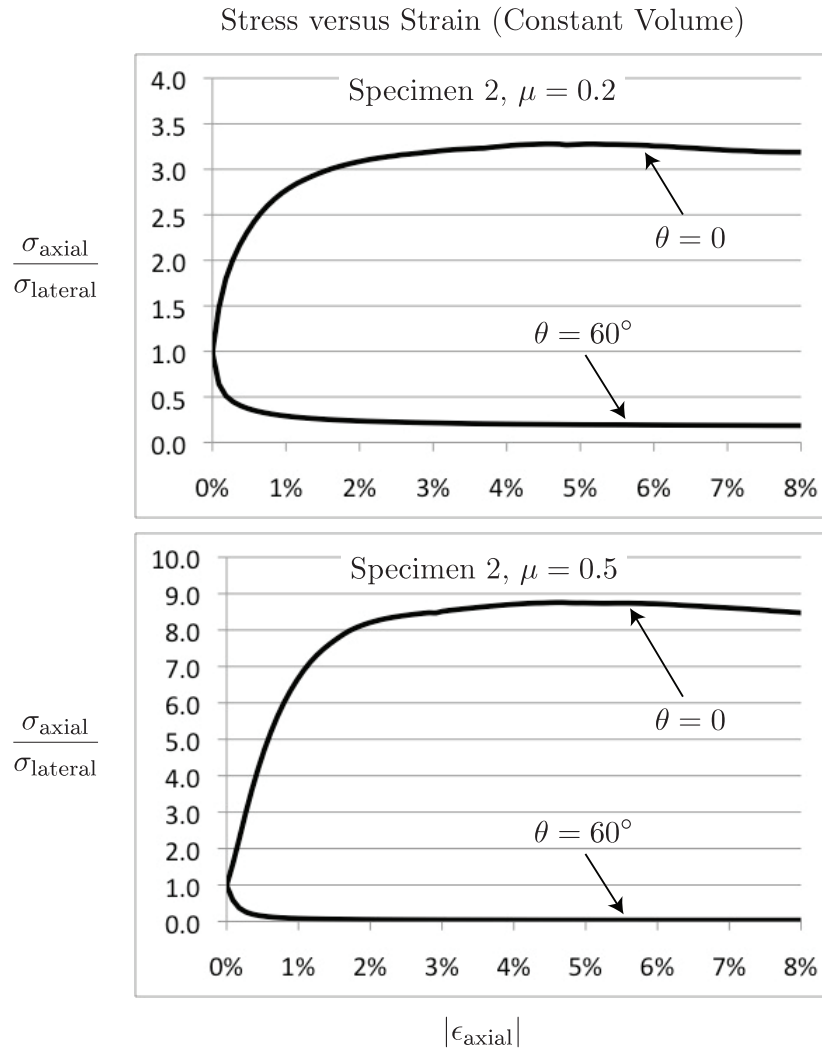


Figure 5.34: Stress ratio as a function of axial strain for Specimen 2 with an inter-element friction coefficient of  $\mu = 0.2$  (top) and  $\mu = 0.5$  (bottom), with particle rotation prohibited. The two curves correspond to the data points on the yield surfaces shown in Figure 5.5 at Lode angles of  $\theta = 0$  and  $\theta = 60^\circ$ .

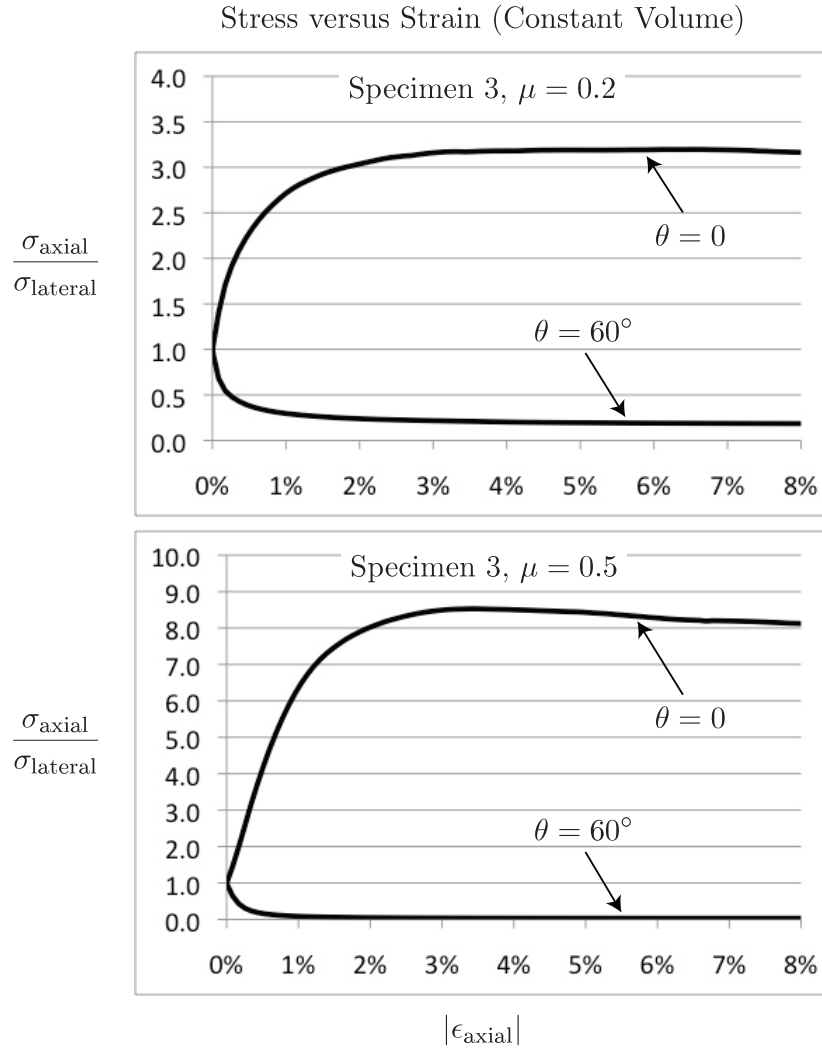


Figure 5.35: Stress ratio as a function of axial strain for Specimen 3 with an inter-element friction coefficient of  $\mu = 0.2$  (top) and  $\mu = 0.5$  (bottom), with particle rotation prohibited. The two curves correspond to the data points on the yield surfaces shown in Figure 5.6 at Lode angles of  $\theta = 0$  and  $\theta = 60^\circ$ .

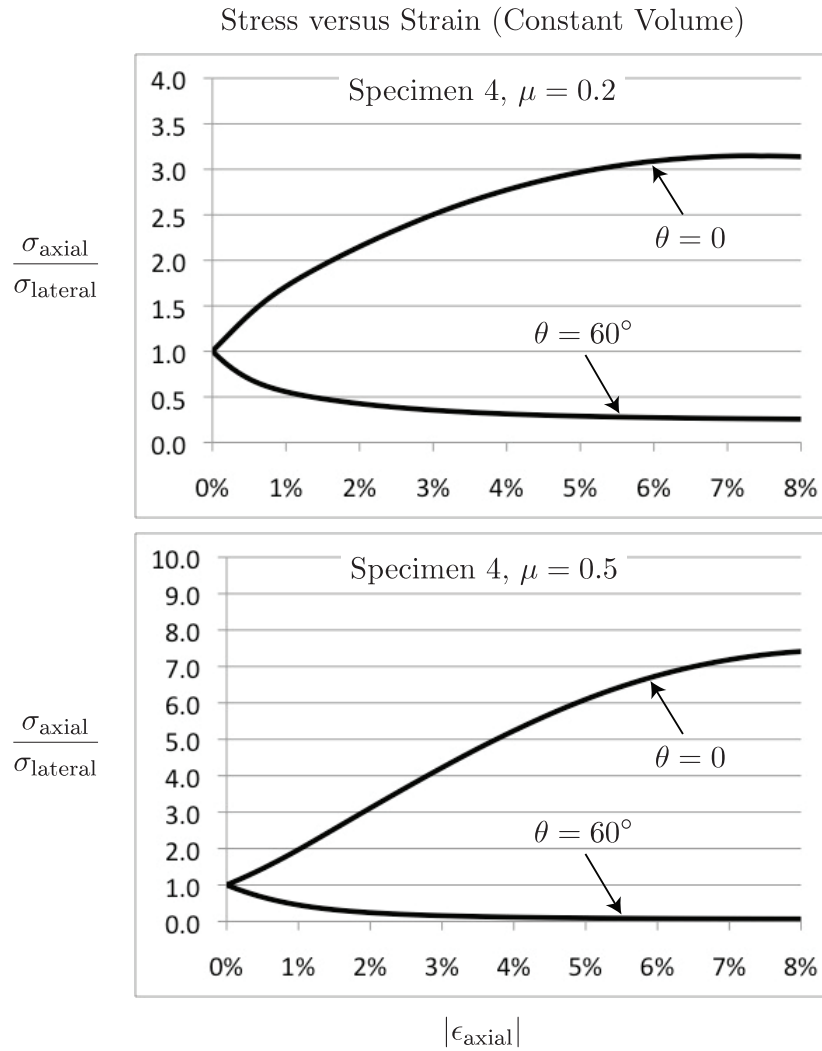


Figure 5.36: Stress ratio as a function of axial strain for Specimen 4 with an inter-element friction coefficient of  $\mu = 0.2$  (top) and  $\mu = 0.5$  (bottom), with particle rotation prohibited. The two curves correspond to the data points on the yield surfaces shown in Figure 5.7 at Lode angles of  $\theta = 0$  and  $\theta = 60^\circ$ .

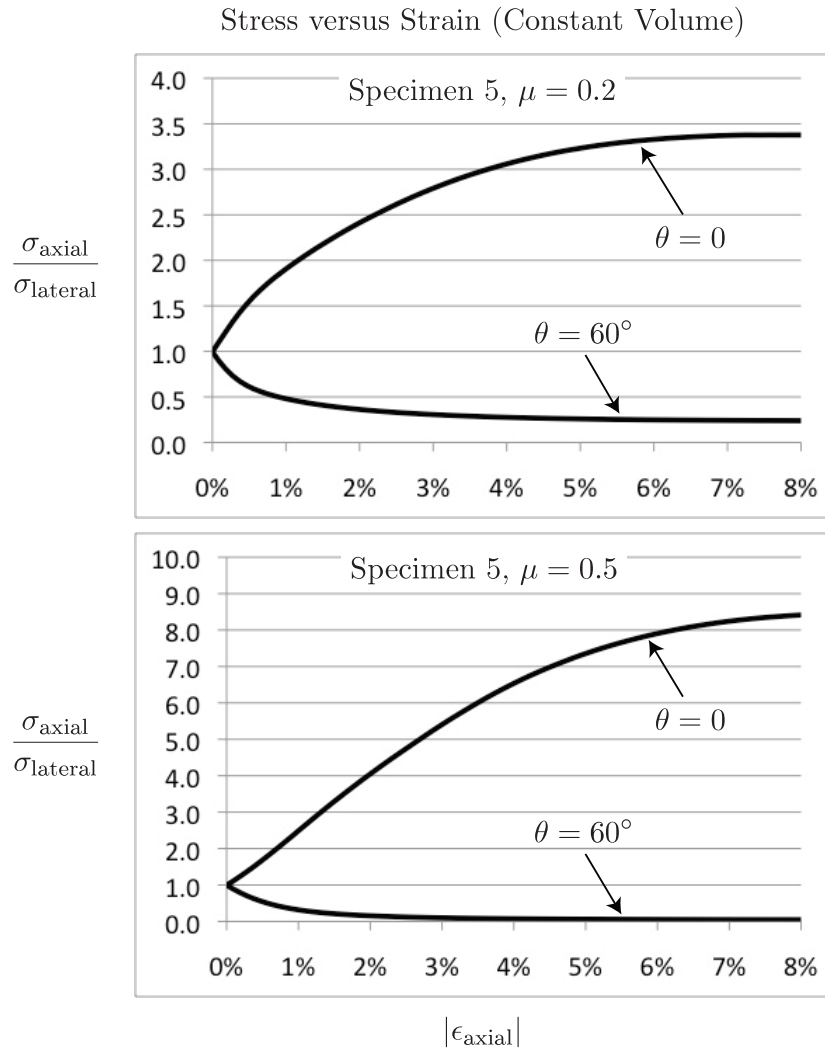


Figure 5.37: Stress ratio as a function of axial strain for Specimen 5 with an inter-element friction coefficient of  $\mu = 0.2$  (top) and  $\mu = 0.5$  (bottom), with particle rotation prohibited. The two curves correspond to the data points on the yield surfaces shown in Figure 5.8 at Lode angles of  $\theta = 0$  and  $\theta = 60^\circ$ .

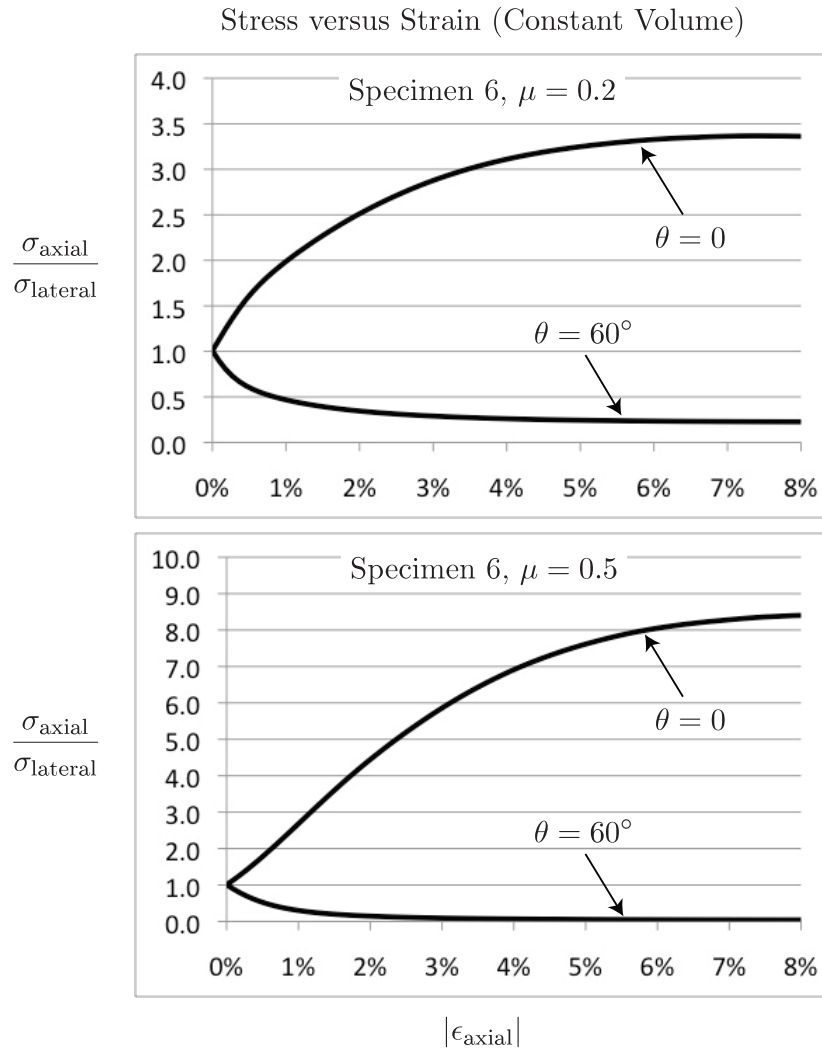


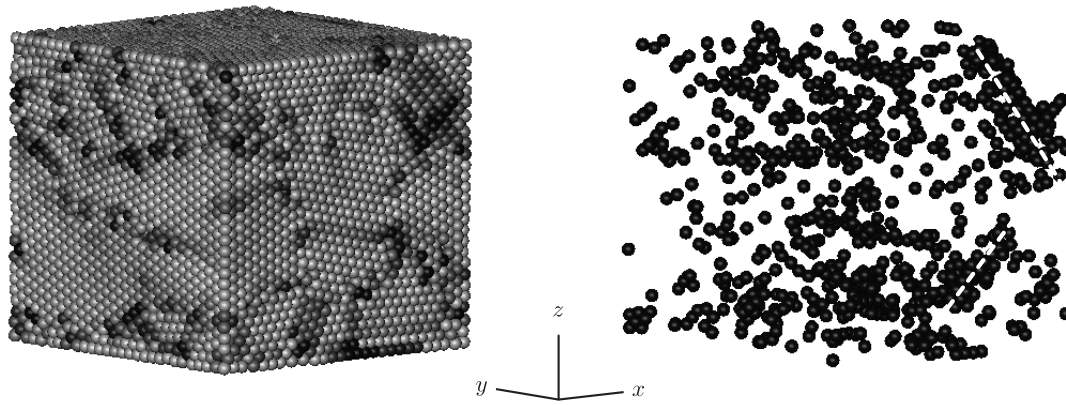
Figure 5.38: Stress ratio as a function of axial strain for Specimen 6 with an inter-element friction coefficient of  $\mu = 0.2$  (top) and  $\mu = 0.5$  (bottom), with particle rotation prohibited. The two curves correspond to the data points on the yield surfaces shown in Figure 5.9 at Lode angles of  $\theta = 0$  and  $\theta = 60^\circ$ .

to black for elements experiencing friction work greater than or equal to 40 Joules. On the right side of Figure 5.39, only the elements experiencing friction work greater than or equal to 40 Joules are shown.

Several distinct slip planes can be identified in the specimen shown in Figure 5.39, and these slip planes are highlighted by white dotted lines on the right side of the figure. The orientations of the specimen shown in Figure 5.39 were chosen to facilitate the visual identification of these slip planes. While Figure 5.39 shows that at least three distinct slip planes exist in Specimen 5 at 4% axial strain in compression (at a Lode angle of  $\theta = 0$ ), the figure also shows that significantly many smaller local slip-systems also exist, and these appear to be randomly distributed throughout the specimen. The same general trends can be seen in Figure 5.40, which again shows the friction work experienced by each element in Specimen 5 with  $\mu = 0.5$ , but this time at 4% axial strain in *extension* during the DEM simulation corresponding to a Lode angle of  $\theta = 60^\circ$ . On the left side of Figure 5.40, the gray scale of each element varies from white for elements experiencing no friction work to black for elements experiencing friction work greater than or equal to 30 Joules. On the right side of Figure 5.40, only the elements experiencing friction work greater than or equal to 30 Joules are shown.

Since the information conveyed by Figures 5.39 and 5.40 is primarily visual, it is difficult to quantify. However, by inspecting various specimens, we have found that the picture conveyed by Figures 5.39 and 5.40 is typical of the larger 29 660-element specimens (4–6), with several identifiable slip planes, but also with significantly many smaller local slip-systems that appear to be randomly distributed throughout the specimen. The smaller 3 430-element specimens (1–3), on the other hand, do not show any clear slip planes. In all six specimens, the friction work tends to begin to accumulate in clusters of elements near the centers of the specimens, after which the region of the specimen experiencing friction work grows outward toward the surfaces of the specimens.

## Friction Work



## Specimen 5

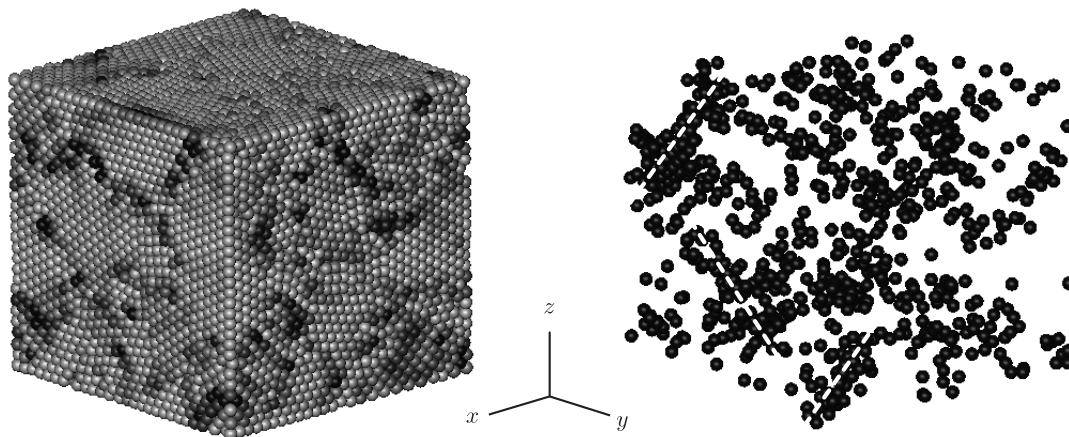
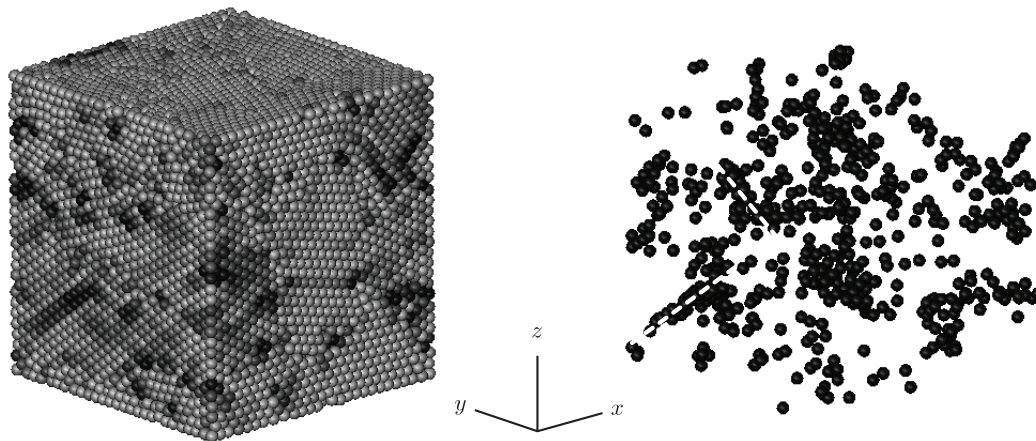


Figure 5.39: Friction work (designated by gray scale) experienced by each element in Specimen 5 at  $|\epsilon_z| = 4\%$  axial strain (compression) during the DEM simulation corresponding to a Lode angle of  $\theta = 0$  on the yield surface shown in Figure 5.8 with an inter-element friction coefficient of  $\mu = 0.5$ , with particle rotation prohibited. Black elements experience friction work greater than or equal to 40 Joules. Visually identifiable local slip planes are highlighted by white dotted lines on the right.

## Friction Work



Specimen 5

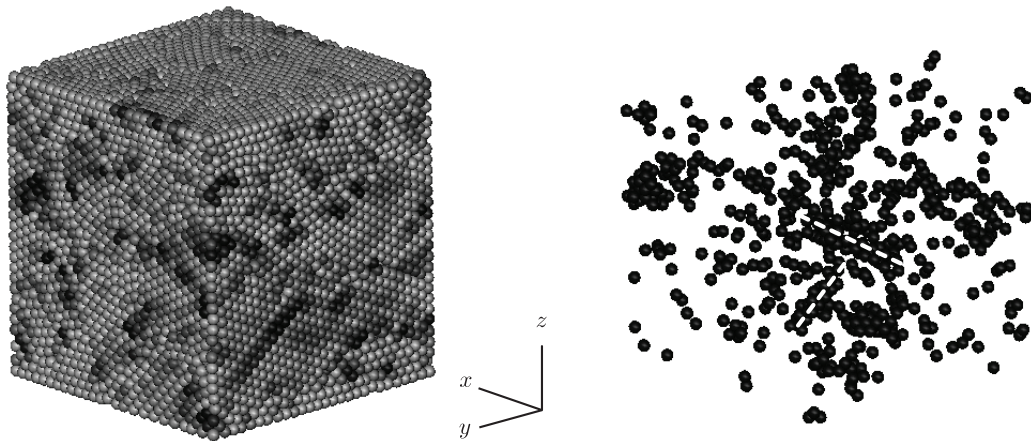


Figure 5.40: Friction work (designated by gray scale) experienced by each element in Specimen 5 at  $|\epsilon_z| = 4\%$  axial strain (extension) during the DEM simulation corresponding to a Lode angle of  $\theta = 60^\circ$  on the yield surface shown in Figure 5.8 with an inter-element friction coefficient of  $\mu = 0.5$ , with particle rotation prohibited. Black elements experience friction work greater than or equal to 30 Joules. Visually identifiable local slip planes are highlighted by white dotted lines on the right.

The fact that failure appears to be primarily a local phenomenon in the specimens we have tested in this chapter is encouraging for the development of a micromechanics-based continuum constitutive model for particulate materials, since all continuum constitutive models depend on the assumption that at some scale there exists a representative volume element and associated definitions of local stress and strain tensors that can be related to global stress and strain tensors via methods of homogenization.

## 5.7 Conclusion

We have performed DEM simulations on six specimens of randomly packed uniform spheres having a uniform inter-particle friction coefficient  $\mu$ . Multiple simulations were performed for each specimen, with  $\mu$  ranging from  $0.01 \leq \mu \leq 100.0$  for Specimens 1–3 (with 3 430 elements) and  $0.01 \leq \mu \leq 0.8$  for Specimens 4–6 (with 29 660 elements). For each specimen and for each inter-element friction coefficient  $\mu$  we performed sixteen DEM simulations under various true triaxial (constant-volume) strain conditions in order to obtain data points for the yield surface in principal stress space for a full range of values of the Lode angle  $0 \leq \theta \leq 60^\circ$  on the  $\pi$ -plane. This amounted to a total of 1 296 simulations, which were performed using a modified version of the open-source code LAMMPS (Plimpton, 1995, LAMMPS) running on a 12-processor Mac Pro workstation.

The main results of this chapter are the yield surfaces shown in Figures 5.16–5.21 for Specimens 1–6, respectively, and the resulting relationships between the inter-particle friction coefficient  $\mu$  or the inter-particle friction angle  $\phi_\mu = \tan^{-1} \mu$  on the microscale and the material friction angle  $\phi$  on the macroscale for each specimen, which are shown in Figures 5.22 and 5.23. We will return to this relationship in Chapter 6 for the case of particle rotation, and in Chapters 7 and 8 where we derive relationships between  $\phi_\mu$  and  $\phi$  by analytical means based on micromechanics. We note here that the data points obtained from all

six randomly packed specimens of 3 430–29 660 elements exhibit very little scatter, with a maximum variation of about 8%.

Comparing the shapes of the yield surfaces obtained from our DEM simulations to those predicted by the Mohr-Coulomb, Drucker-Prager, Lade-Duncan, and Matsuoka-Nakai (SMP) criteria for given values of the material friction angle  $\phi$ , we found that the DEM data points are best represented for all values of the Lode angle  $\theta$  by the Lade-Duncan yield criterion, in particular for  $\theta = 60^\circ$ , which corresponds to extension.

Also noteworthy is the fact that the average rate of friction work in the specimens does not appear to be correlated to the material friction angle  $\phi$  (or to the inter-particle friction coefficient  $\mu$ ). In particular, in Specimen 1 we see an average rate of friction work that is over 50% greater than in Specimens 2 and 3, while the material friction angles for all three specimens is virtually the same for every value of the inter-particle friction coefficient  $\mu$ . The same observation can be made regarding Specimens 4–6. Friction work on an element-by-element basis was also useful for visually identifying slip systems within the specimens, both at the onset of yield and during plastic deformation, as we illustrate for Specimen 5 in Figures 5.39 and 5.40.

As in Chapter 3 [Fleischmann et al. (2013a)], all of the results in this chapter were obtained from DEM simulations in which particle rotation was prohibited. We continue our analysis with the case of unrestrained particle rotation in Chapter 6, which follows. A micromechanical analysis of the DEM results presented in this chapter is given in Chapter 7, assuming no particle rotation, and the corresponding micromechanical analysis for the case of particle rotation is given in Chapter 8.



## Chapter 6

# Determination of Yield Surfaces for Isotropic Non-Cohesive Particulate Materials by the Discrete Element Method, Part II: Particle Rotation

### 6.1 Abstract

In Chapter 5, we used the discrete element method (DEM) to determine yield surfaces for large samples of randomly packed uniform spheres with constant normal and tangential contact stiffnesses (linear spring model) and uniform inter-particle friction coefficient  $\mu$  with particle rotation prohibited. In this chapter, we continue the analysis begun in Chapter 5 for the case of unrestrained particle rotation. We compare the resulting yield surfaces to the Mohr-Coulomb, Drucker-Prager, Lade-Duncan, and Matsuoka-Nakai yield surfaces, and determine the relationship between the resulting material friction angle  $\phi$  on the macroscale and the inter-particle friction coefficient  $\mu$  on the microscale. In all of the DEM simulations

performed for this chapter, the spheres were allowed full three-dimensional translational and rotational freedom of motion.

## 6.2 Introduction

As we note in the Introduction to Part I, Section 5.2, the yield surface for an isotropic particulate material, which is usually characterized by the material friction angle  $\phi$ , is of great practical importance. Not only is the yield surface a critical component of the classical formulation of an elastoplastic continuum constitutive model for a particulate material, the shear strength, determined by the material friction angle  $\phi$ , is possibly the most important mechanical characteristic of a geomaterial in practice.

In Chapter 5, we used the discrete element method (DEM) to determine yield surfaces for particulate material specimens of 3 430–29 660 randomly packed uniform spheres with constant normal and tangential contact stiffnesses (linear spring model) and uniform inter-particle friction coefficient  $\mu$  with particle rotation prohibited. We performed 1 296 individual DEM simulations to obtain full yield surfaces for each specimen for a wide range of inter-particle friction coefficients  $\mu$ :  $0.01 \leq \mu \leq 100.0$  for Specimens 1–3 (with 3 430 elements) and  $0.01 \leq \mu \leq 0.8$  for Specimens 4–6 (with 29 660 elements). We used these yield surfaces to determine the relationship between the resulting material friction angle  $\phi$  on the macroscale and the inter-particle friction coefficient  $\mu$  (or the inter-particle friction angle  $\phi_\mu = \tan^{-1} \mu$ ) on the microscale for each DEM specimen. We also monitored inter-particle friction work within each specimen, and noted the presence of slip planes.

For the results reported in Chapter 5, all of the DEM simulations were performed with particle rotation prohibited, as was the case in Chapter 3 for the elastic range. The restriction of no particle rotation is unique to DEM (it cannot be enforced in physical experiments), and the results provide us with valuable micromechanical insight, particularly when we compare

the results for which particle rotation was prohibited to the results for which particle rotation was unrestrained, as was done in Chapters 3 [Fleischmann et al. (2013a)] and 4 [Fleischmann et al. (2013b)] for the elastic range. In this chapter, we report results obtained from DEM simulations in which particle rotation is unrestrained.

### 6.3 Methodology

The methodology for this chapter is completely analogous to that of Chapter 5, with the sole exception that in the DEM simulations performed for the current chapter, the rotation of the spheres was not (artificially) restrained. That is, the spheres were allowed full three-dimensional translational *and rotational* freedom of motion, analogous to the simulations of Chapter 4 in the elastic range.

Thus, for the current chapter we performed an additional 1 296 numerical simulations using the discrete element method (DEM) with unrestrained particle rotation to determine yield surfaces in principal stress space for randomly packed aggregates of uniform spheres having constant normal and tangential contact stiffnesses  $K_n$  and  $K_t$ , respectively (linear spring contact model), and uniform inter-particle friction coefficient  $\mu$ . The simulations were performed on the same six DEM specimens used in Chapters 3, 4, and 5 of this thesis. Specimens 1, 2, and 3 each contained 3 430 randomly packed uniform spheres, and Specimens 4, 5, and 6 each contained 29 660 randomly packed uniform spheres. The specimens are shown in Figures 3.7 and 5.3. The DEM simulations were performed using LAMMPS (Plimpton, 1995), which is described briefly in Sections 3.5 and 5.4, and in more detail in Sections 2.3 and 9.3, of this thesis.

Analogous to Figure 5.4, Figure 6.1 shows the data points on the  $\pi$ -plane obtained from DEM simulations performed on Specimen 1, with unrestrained particle rotation, with inter-element friction coefficients of  $\mu = 0.2$  (top) and  $\mu = 0.5$  (bottom) for axial strains of

1%–8% in either compression or extension, depending on the data point. For convenience, the principal stress directions are shown positive in compression, which is commonly done in the field of geomechanics. Also shown on Figure 6.1 are the yield surfaces according to the Mohr-Coulomb yield criterion with (macroscopic) friction angles  $\phi = 24.0^\circ$  (top) and  $\phi = 33.0^\circ$  (bottom), chosen to match the data points at a Lode angle of zero.

Figures 6.2–6.6 show the corresponding results for Specimens 2–6, respectively, with inter-element friction coefficients of  $\mu = 0.2$  (top) and  $\mu = 0.5$  (bottom). Once again, analogous DEM simulations and analyses were performed for all six specimens, with unrestrained particle rotation, for all nine values of the inter-element friction coefficient  $\mu$ , and the matching “material” or macroscopic friction angle  $\phi$  (at a Lode angle of zero) corresponding to the classical Mohr-Coulomb yield criterion was determined for each (with an accuracy of approximately  $\pm 0.25^\circ$ ). It was found that the maximal yield surfaces occurred at 4%–6% axial strain for all six specimens, after which time the yield surfaces either remained approximately fixed or in some instances began to collapse. See Section 5.4 for a detailed description of the DEM simulations used to generate the data points in Figures 6.1–6.6.

Also analogous to Section 5.4, the total accumulated friction work  $U_f$  for each specimen for each value of the inter-particle friction coefficient  $\mu$  was recorded throughout the DEM simulations. By way of example, Figure 6.7 shows the total friction work  $U_f$  (Joules) as a function of strain at Lode angles of  $\theta = 0$  and  $\theta = 60^\circ$  for Specimen 1 with inter-element friction coefficients of  $\mu = 0.2$  (top) and  $\mu = 0.5$  (bottom), for axial strains of 1%–8% in either compression ( $\theta = 0$ ) or extension ( $\theta = 60^\circ$ ). Figures 6.8–6.12 show the corresponding results for Specimens 2–6, respectively, with inter-element friction coefficients of  $\mu = 0.2$  (top) and  $\mu = 0.5$  (bottom). See Section 5.4 for a detailed description of the DEM simulations used to generate Figures 6.7–6.12.

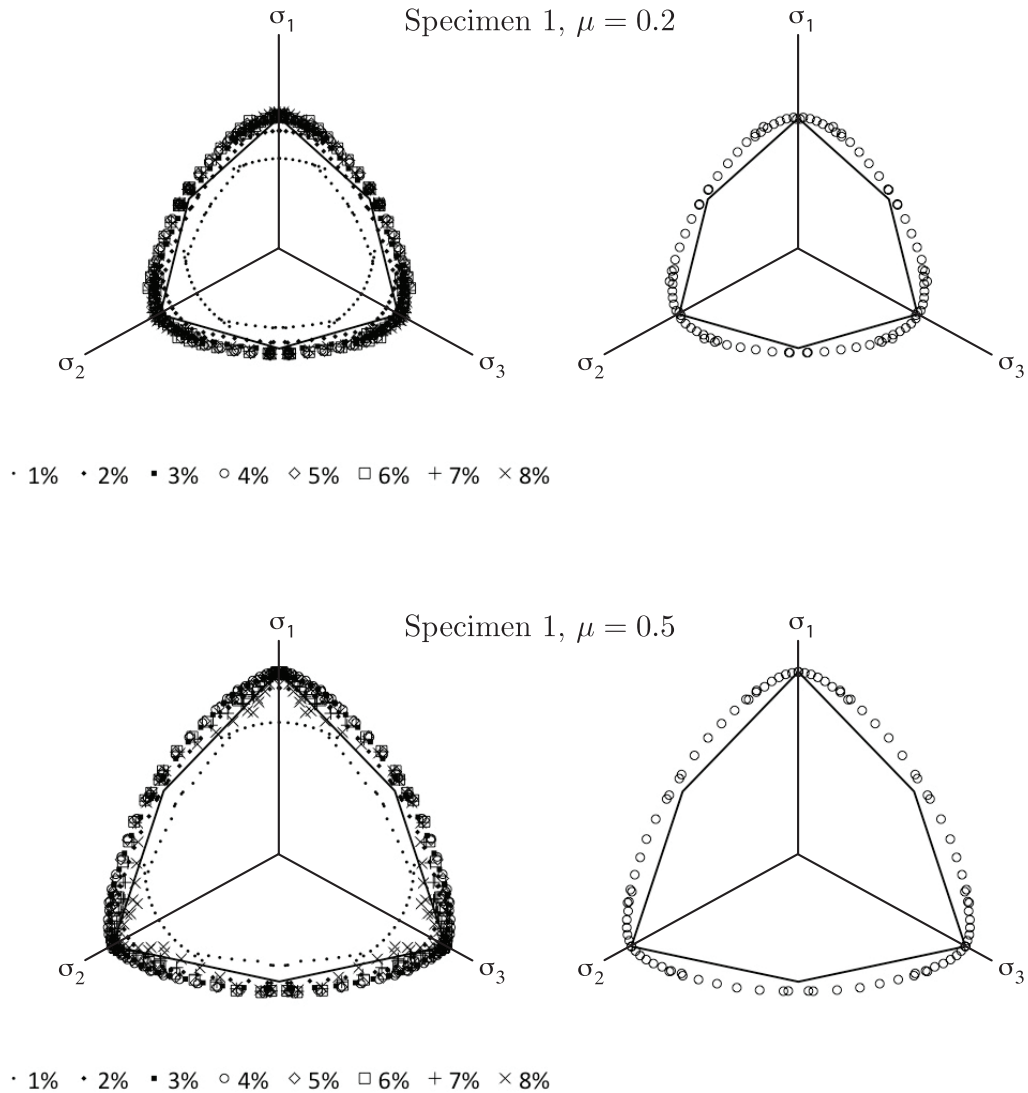


Figure 6.1: Left: Data points on the  $\pi$ -plane obtained from one set of DEM simulations performed on Specimen 1 with an inter-element friction coefficient of  $\mu = 0.2$  (top) and  $\mu = 0.5$  (bottom), with particle rotation allowed. Right: Maximal yield surfaces. The solid line in both diagrams is the Mohr-Coulomb yield surface with a macroscopic friction angle of  $\phi = 24.0^\circ$  (top) and  $\phi = 33.0^\circ$  (bottom), chosen to match the data points at a Lode angle of zero. The data points for 1%, 2%, ..., 8% designate the axial strain in either compression or extension (depending on the Lode angle).

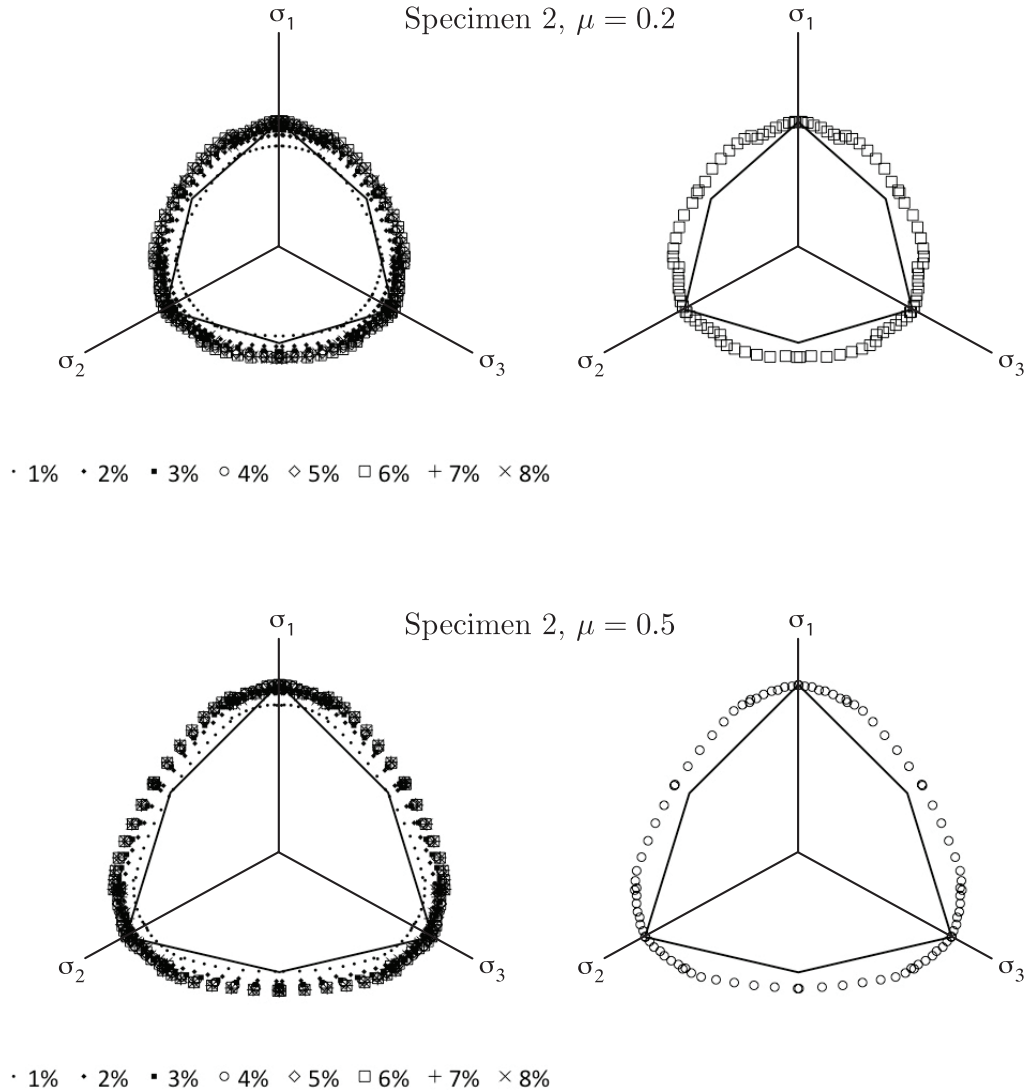


Figure 6.2: Left: Data points on the  $\pi$ -plane obtained from one set of DEM simulations performed on Specimen 2 with an inter-element friction coefficient of  $\mu = 0.2$  (top) and  $\mu = 0.5$  (bottom), with particle rotation allowed. Right: Maximal yield surfaces. The solid line in both diagrams is the Mohr-Coulomb yield surface with a macroscopic friction angle of  $\phi = 23.0^\circ$  (top) and  $\phi = 30.5^\circ$  (bottom), chosen to match the data points at a Lode angle of zero. The data points for 1%, 2%, ..., 8% designate the axial strain in either compression or extension (depending on the Lode angle).

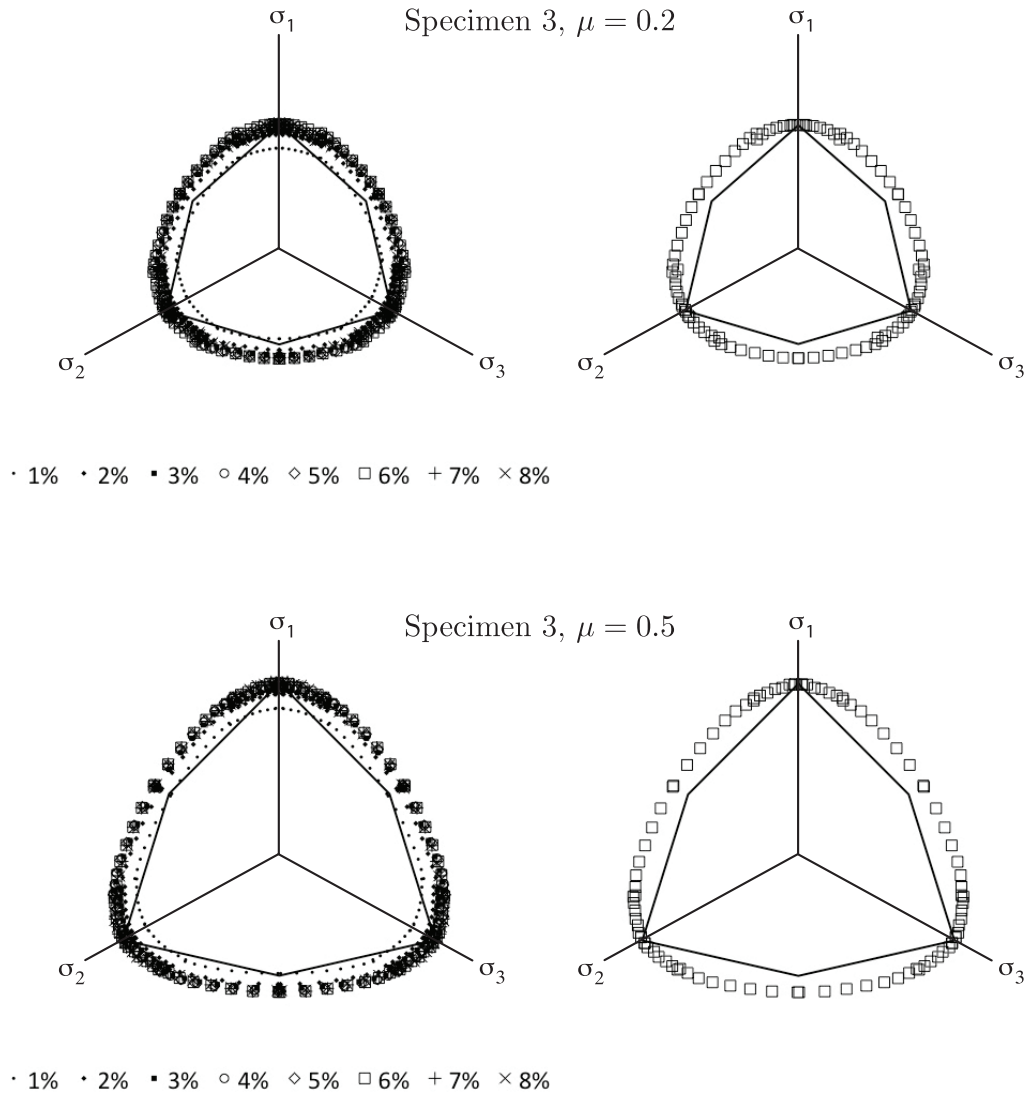


Figure 6.3: Left: Data points on the  $\pi$ -plane obtained from one set of DEM simulations performed on Specimen 3 with an inter-element friction coefficient of  $\mu = 0.2$  (top) and  $\mu = 0.5$  (bottom), with particle rotation allowed. Right: Maximal yield surfaces. The solid line in both diagrams is the Mohr-Coulomb yield surface with a macroscopic friction angle of  $\phi = 23.0^\circ$  (top) and  $\phi = 31.0^\circ$  (bottom), chosen to match the data points at a Lode angle of zero. The data points for 1%, 2%, ..., 8% designate the axial strain in either compression or extension (depending on the Lode angle).

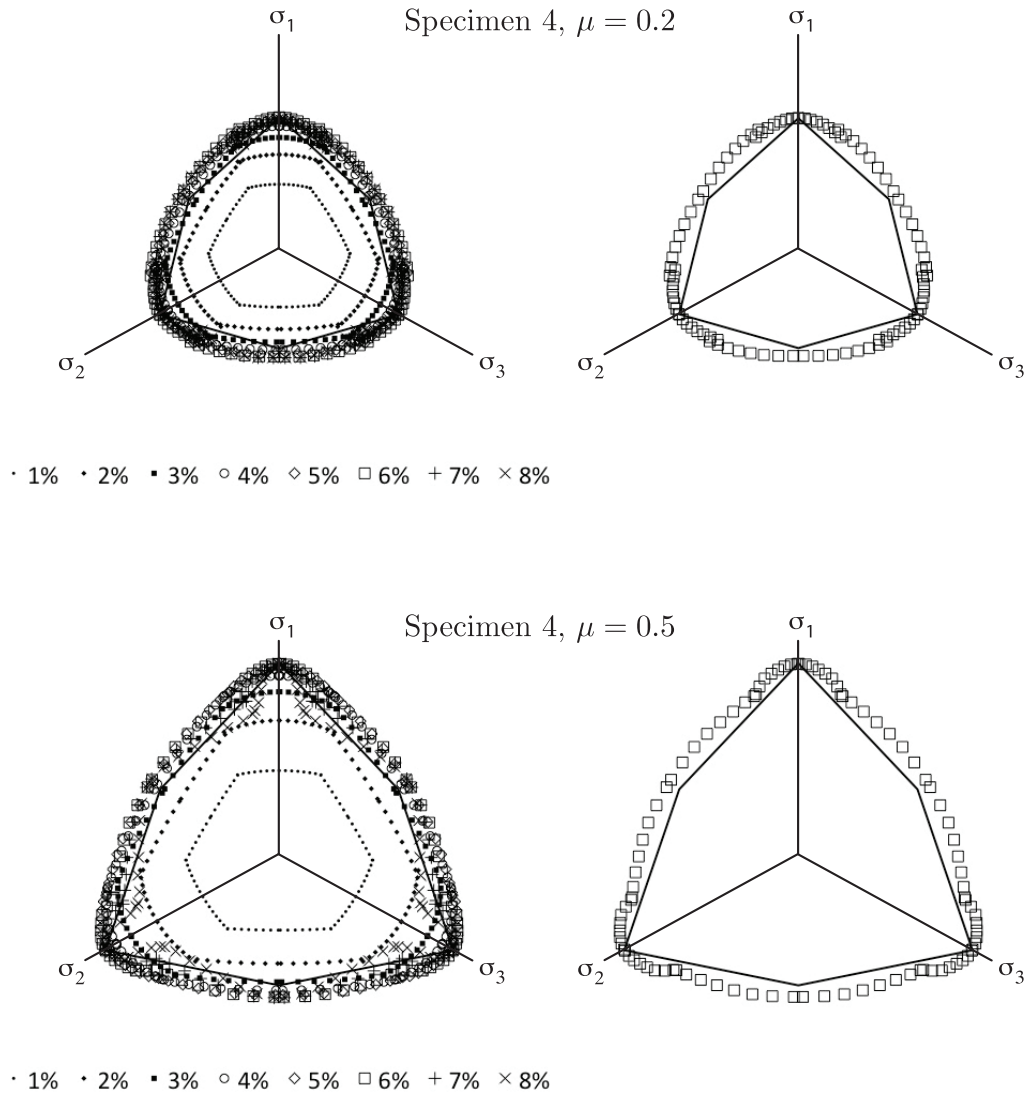


Figure 6.4: Left: Data points on the  $\pi$ -plane obtained from one set of DEM simulations performed on Specimen 4 with an inter-element friction coefficient of  $\mu = 0.2$  (top) and  $\mu = 0.5$  (bottom), with particle rotation allowed. Right: Maximal yield surfaces. The solid line in both diagrams is the Mohr-Coulomb yield surface with a macroscopic friction angle of  $\phi = 24.0^\circ$  (top) and  $\phi = 34.5^\circ$  (bottom), chosen to match the data points at a Lode angle of zero. The data points for 1%, 2%, ..., 8% designate the axial strain in either compression or extension (depending on the Lode angle).

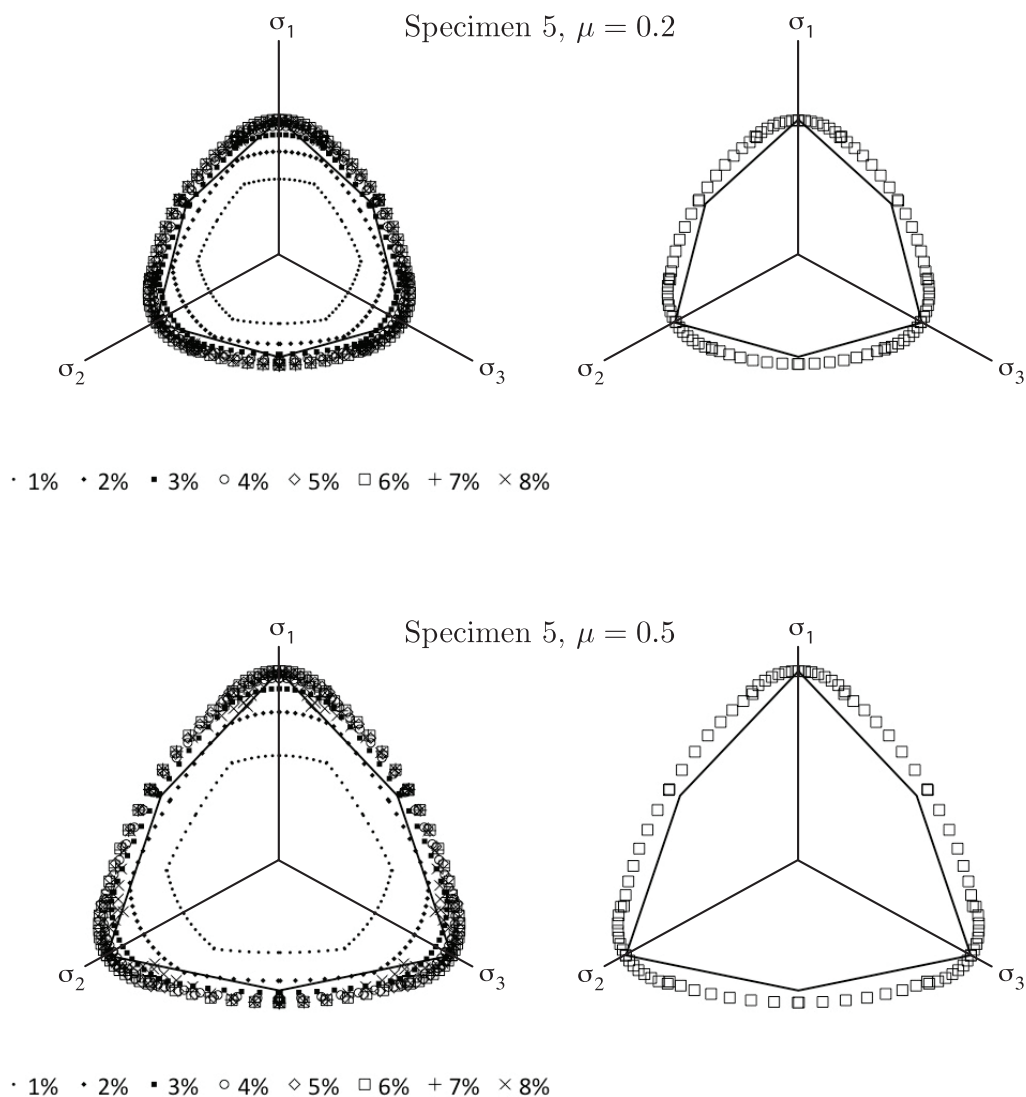


Figure 6.5: Left: Data points on the  $\pi$ -plane obtained from one set of DEM simulations performed on Specimen 5 with an inter-element friction coefficient of  $\mu = 0.2$  (top) and  $\mu = 0.5$  (bottom), with particle rotation allowed. Right: Maximal yield surfaces. The solid line in both diagrams is the Mohr-Coulomb yield surface with a macroscopic friction angle of  $\phi = 25.0^\circ$  (top) and  $\phi = 34.0^\circ$  (bottom), chosen to match the data points at a Lode angle of zero. The data points for 1%, 2%, ..., 8% designate the axial strain in either compression or extension (depending on the Lode angle).

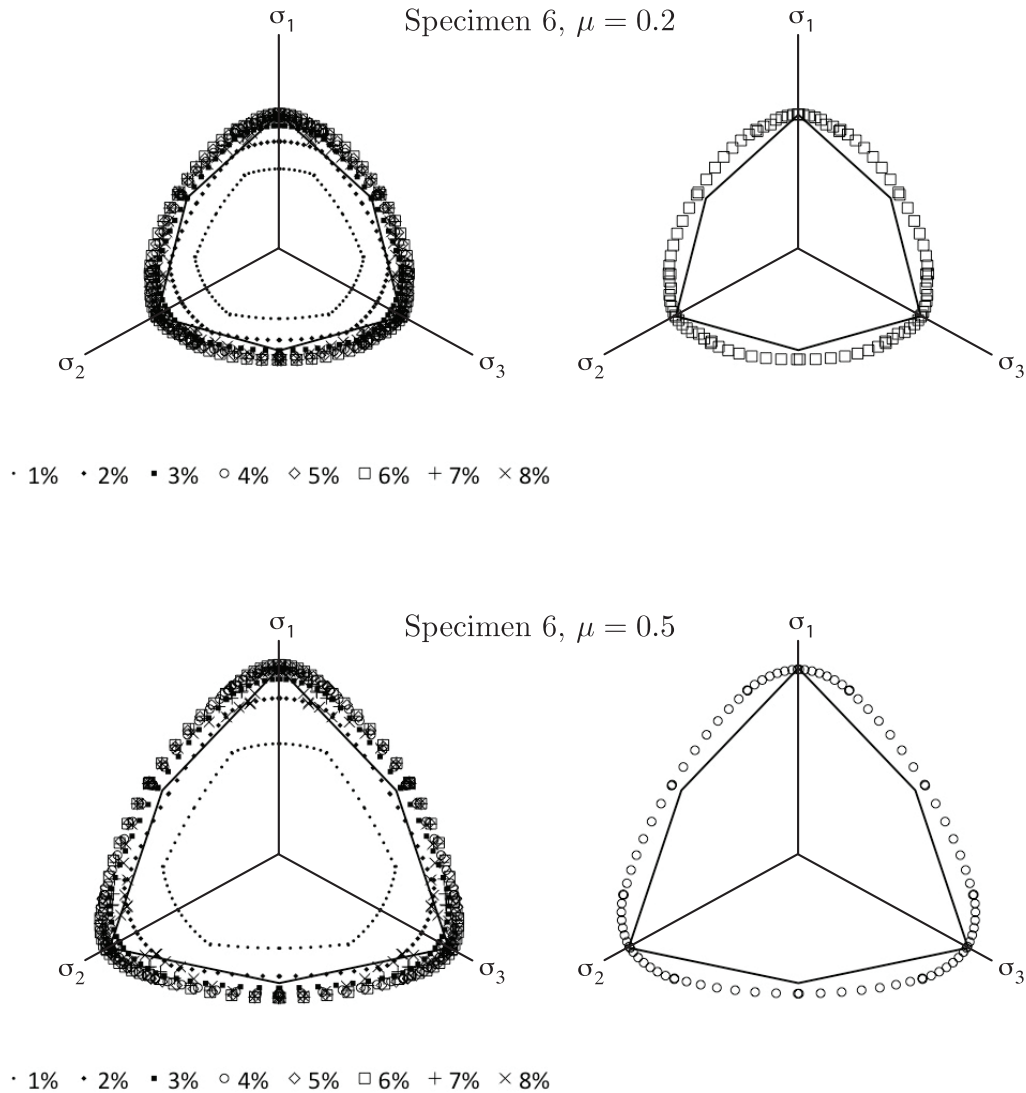


Figure 6.6: Left: Data points on the  $\pi$ -plane obtained from one set of DEM simulations performed on Specimen 6 with an inter-element friction coefficient of  $\mu = 0.2$  (top) and  $\mu = 0.5$  (bottom), with particle rotation allowed. Right: Maximal yield surfaces. The solid line in both diagrams is the Mohr-Coulomb yield surface with a macroscopic friction angle of  $\phi = 24.5^\circ$  (top) and  $\phi = 33.5^\circ$  (bottom), chosen to match the data points at a Lode angle of zero. The data points for 1%, 2%, ..., 8% designate the axial strain in either compression or extension (depending on the Lode angle).

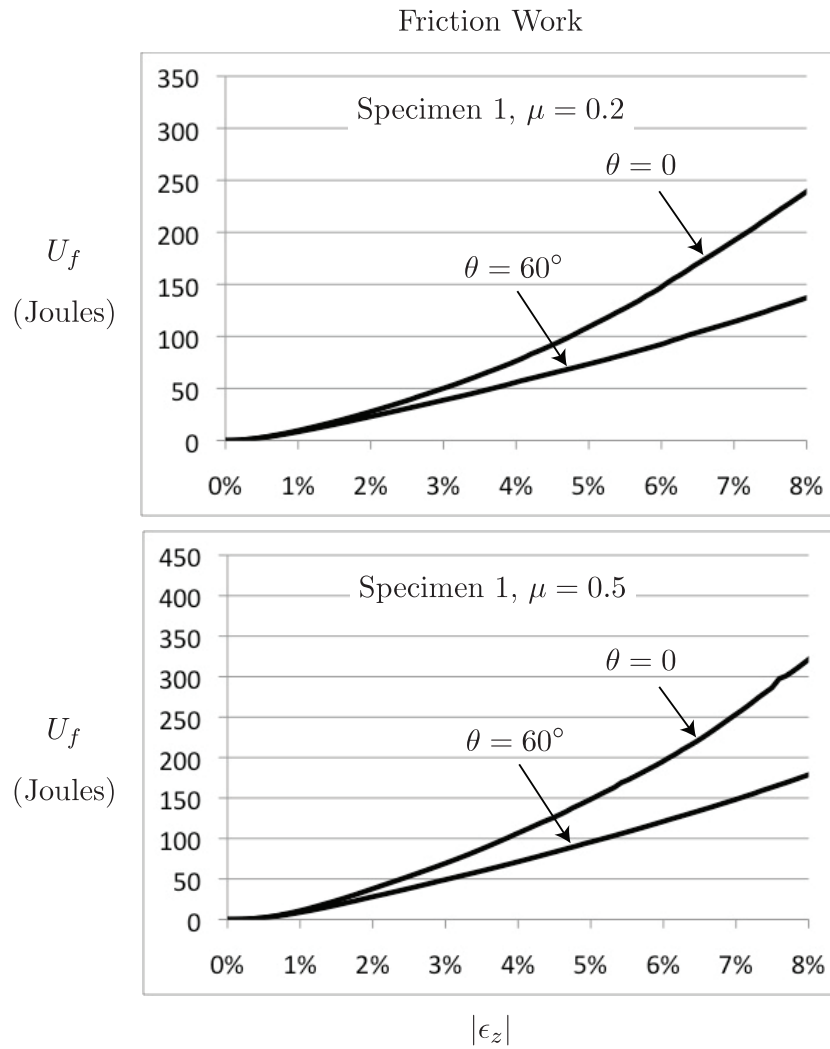


Figure 6.7: Total accumulated friction work  $U_f$  as a function of strain for Specimen 1 with an inter-element friction coefficient of  $\mu = 0.2$  (top) and  $\mu = 0.5$  (bottom), with particle rotation allowed. The two curves correspond to the data points on the yield surfaces shown in Figure 6.1 at Lode angles of  $\theta = 0$  and  $\theta = 60^\circ$ .

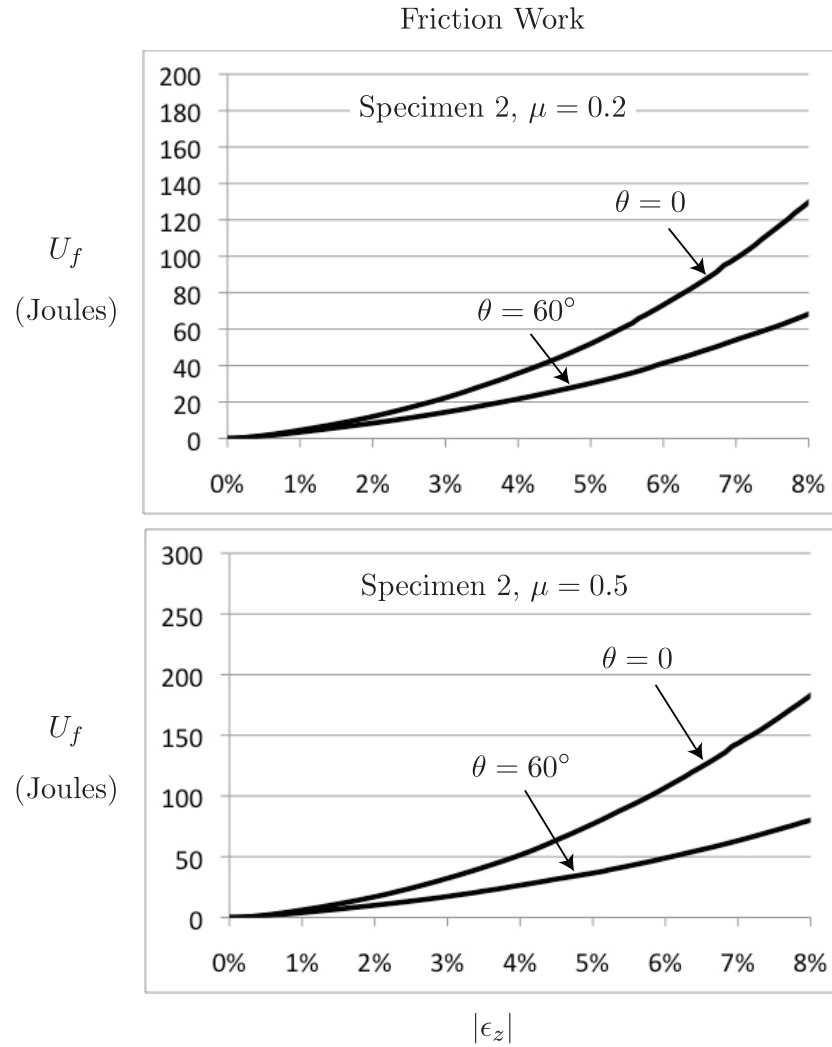


Figure 6.8: Total accumulated friction work  $U_f$  as a function of strain for Specimen 2 with an inter-element friction coefficient of  $\mu = 0.2$  (top) and  $\mu = 0.5$  (bottom), with particle rotation allowed. The two curves correspond to the data points on the yield surfaces shown in Figure 6.2 at Lode angles of  $\theta = 0$  and  $\theta = 60^\circ$ .

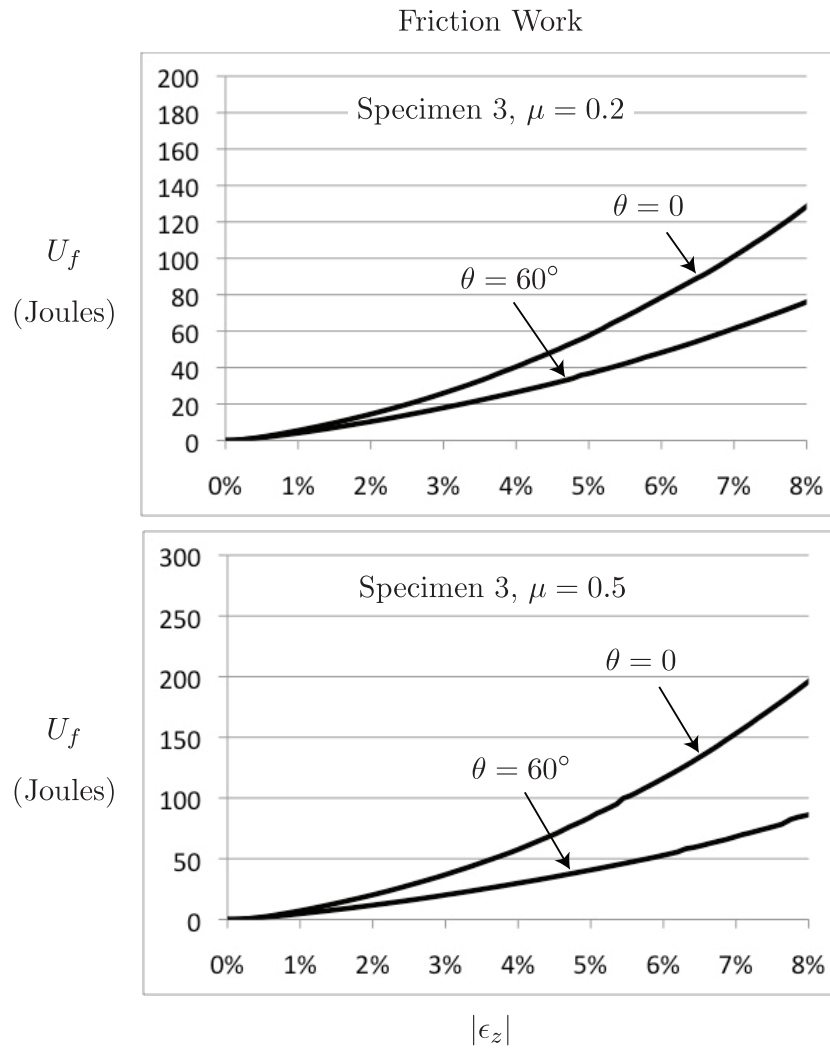


Figure 6.9: Total accumulated friction work  $U_f$  as a function of strain for Specimen 3 with an inter-element friction coefficient of  $\mu = 0.2$  (top) and  $\mu = 0.5$  (bottom), with particle rotation allowed. The two curves correspond to the data points on the yield surfaces shown in Figure 6.3 at Lode angles of  $\theta = 0$  and  $\theta = 60^\circ$ .

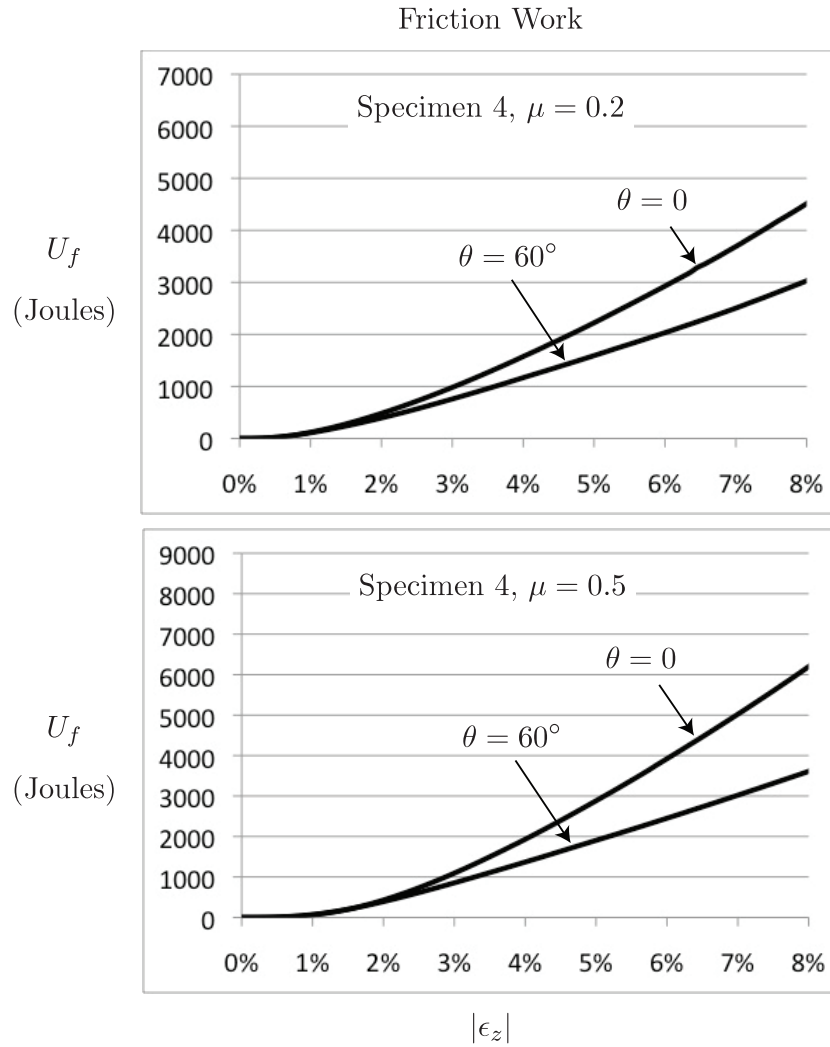


Figure 6.10: Total accumulated friction work  $U_f$  as a function of strain for Specimen 4 with an inter-element friction coefficient of  $\mu = 0.2$  (top) and  $\mu = 0.5$  (bottom), with particle rotation allowed. The two curves correspond to the data points on the yield surfaces shown in Figure 6.4 at Lode angles of  $\theta = 0$  and  $\theta = 60^\circ$ .

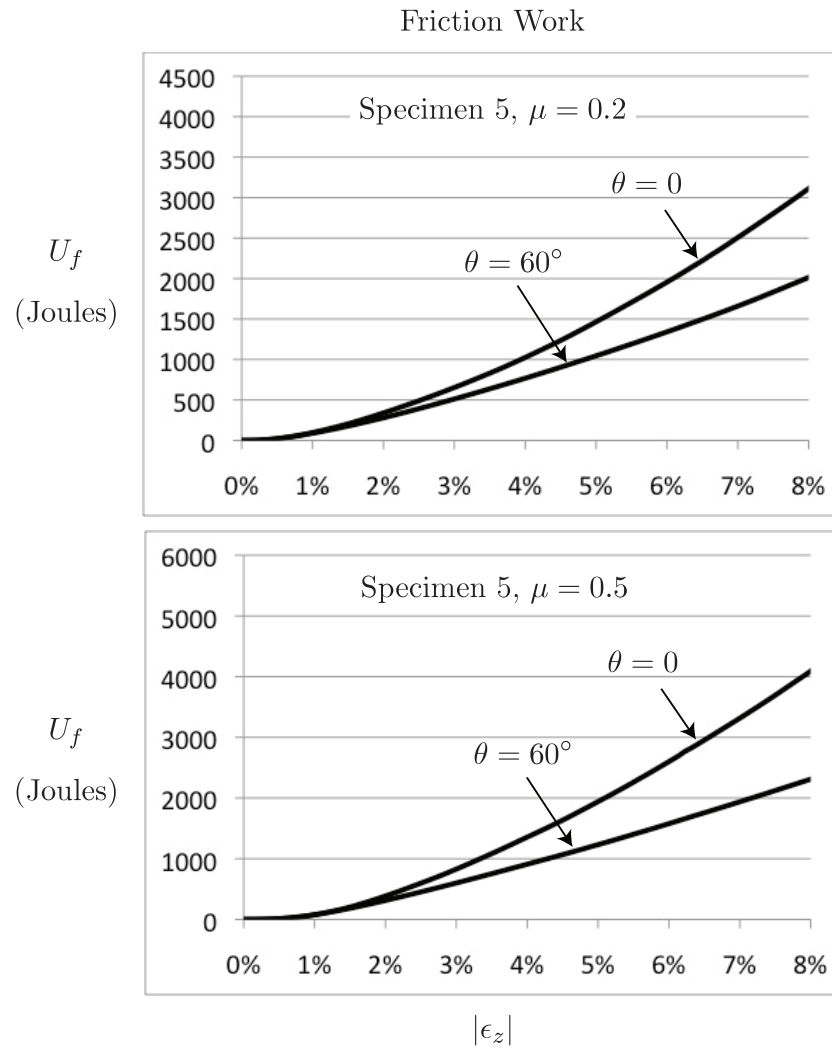


Figure 6.11: Total accumulated friction work  $U_f$  as a function of strain for Specimen 5 with an inter-element friction coefficient of  $\mu = 0.2$  (top) and  $\mu = 0.5$  (bottom), with particle rotation allowed. The two curves correspond to the data points on the yield surfaces shown in Figure 6.5 at Lode angles of  $\theta = 0$  and  $\theta = 60^\circ$ .

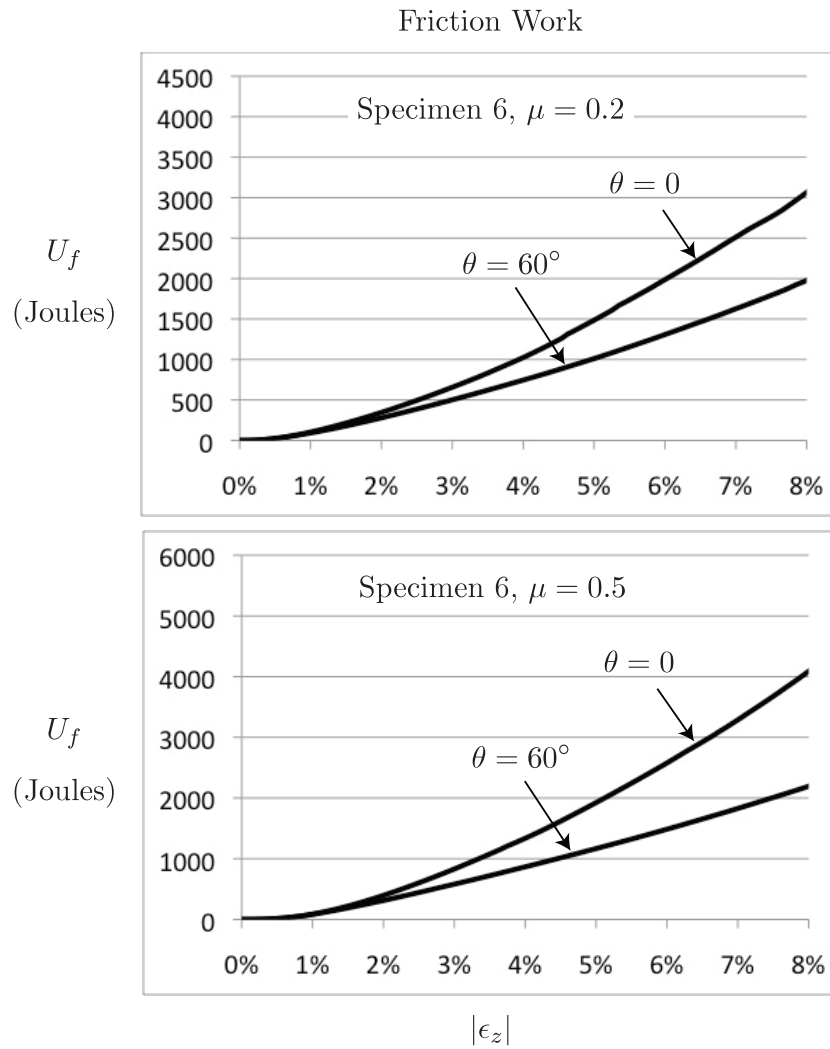


Figure 6.12: Total accumulated friction work  $U_f$  as a function of strain for Specimen 6 with an inter-element friction coefficient of  $\mu = 0.2$  (top) and  $\mu = 0.5$  (bottom), with particle rotation allowed. The two curves correspond to the data points on the yield surfaces shown in Figure 6.6 at Lode angles of  $\theta = 0$  and  $\theta = 60^\circ$ .

## 6.4 Results

The figures in this section are direct analogues of the figures in Section 5.5, except with unrestrained particle rotation (i.e., particle rotation allowed). Figures 6.13–6.18 show the 54 yield surfaces that were obtained from the DEM simulations described in Section 6.3, performed on Specimens 1–6 with nine different values of the inter-element friction coefficient  $0.01 \leq \mu \leq 0.8$ , with particle rotation allowed. Also shown are the corresponding Mohr-Coulomb yield surfaces, with the macroscopic friction angle  $\phi$  chosen in each case to match the data points at a Lode angle of zero. For comparison, Figures 6.19–6.24 show the yield surfaces given in Figures 5.16–5.21 with particle rotation prohibited and in Figures 6.13–6.18 with particle rotation allowed, for Specimens 1–6, respectively. In all cases, the smaller yield surfaces in Figures 6.19–6.24 correspond to unrestrained particle rotation (from Figures 6.13–6.18), and the larger yield surfaces correspond to particle rotation prohibited (from Figures 5.16–5.21).

Figure 6.25 shows the resulting relationship between the macroscopic (material) friction angle  $\phi$  corresponding to the classical Mohr-Coulomb yield criterion and the microscopic (inter-particle) friction angle  $\phi_\mu = \tan^{-1} \mu$  for each specimen, where  $\mu$  is the inter-element friction coefficient ( $0.6^\circ \leq \phi_\mu \leq 39^\circ$ ). Recall that the material friction angle  $\phi$  was chosen to make the Mohr-Coulomb yield surface match the yield surface determined by DEM at a Lode angle of zero, with an accuracy of approximately  $\pm 0.25^\circ$ . For comparison, Figure 6.26 shows the relationships given in Figure 5.22 with particle rotation prohibited and in Figure 6.25 with particle rotation allowed. As in Section 5.5, additional simulations were run on the smaller Specimens 1–3 with inter-element friction coefficients in the range  $0.9 \leq \mu \leq 100.0$  to extend the relationship between  $\phi_\mu$  and  $\phi$  shown in Figure 6.25 for values up to  $\phi_\mu \approx 90^\circ$ . The resulting extended relationship between  $\phi_\mu$  and  $\phi$  for Specimens 1–3 is shown in Figure 6.27.

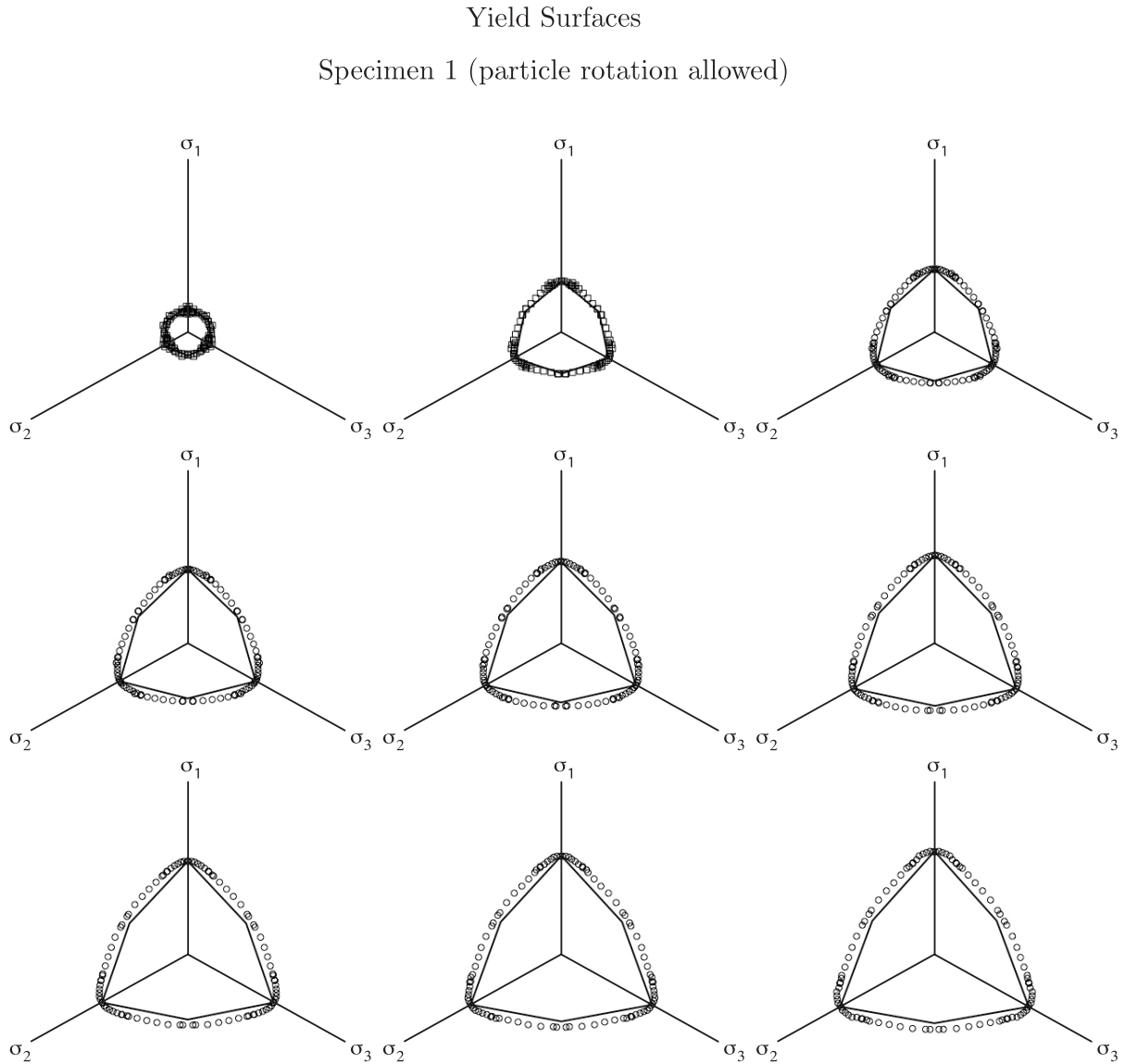


Figure 6.13: Yield surfaces obtained by DEM simulations performed on Specimen 1 with 3430 randomly packed uniform spheres with inter-element friction coefficients (from upper left to lower right) of  $\mu = \{0.01, 0.1, 0.2, 0.3, 0.4, 0.5, 0.6, 0.7, 0.8\}$ , with particle rotation allowed. Also shown for comparison are the Mohr-Coulomb yield surfaces with values of the macroscopic friction angle  $\phi = \{10.5, 20.0, 24.0, 28.0, 30.5, 33.0, 35.0, 36.5, 38.0\}^\circ$  chosen to match the data points at a Lode angle of zero.

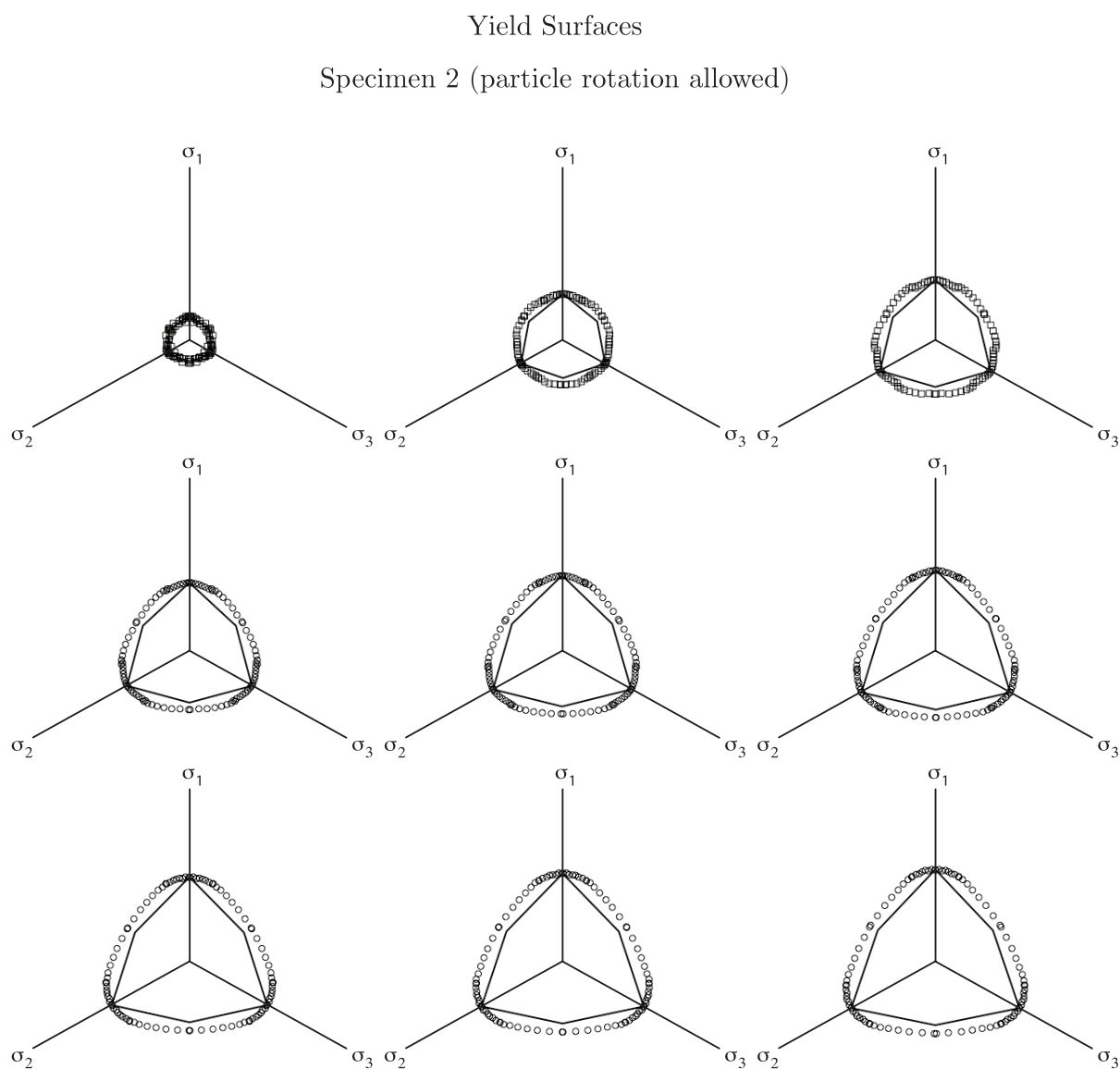


Figure 6.14: Yield surfaces obtained by DEM simulations performed on Specimen 2 with 3430 randomly packed uniform spheres with inter-element friction coefficients (from upper left to lower right) of  $\mu = \{0.01, 0.1, 0.2, 0.3, 0.4, 0.5, 0.6, 0.7, 0.8\}$ , with particle rotation allowed. Also shown for comparison are the Mohr-Coulomb yield surfaces with values of the macroscopic friction angle  $\phi = \{10.0, 18.0, 23.0, 26.0, 28.5, 30.5, 32.0, 33.0, 34.0\}^\circ$  chosen to match the data points at a Lode angle of zero.

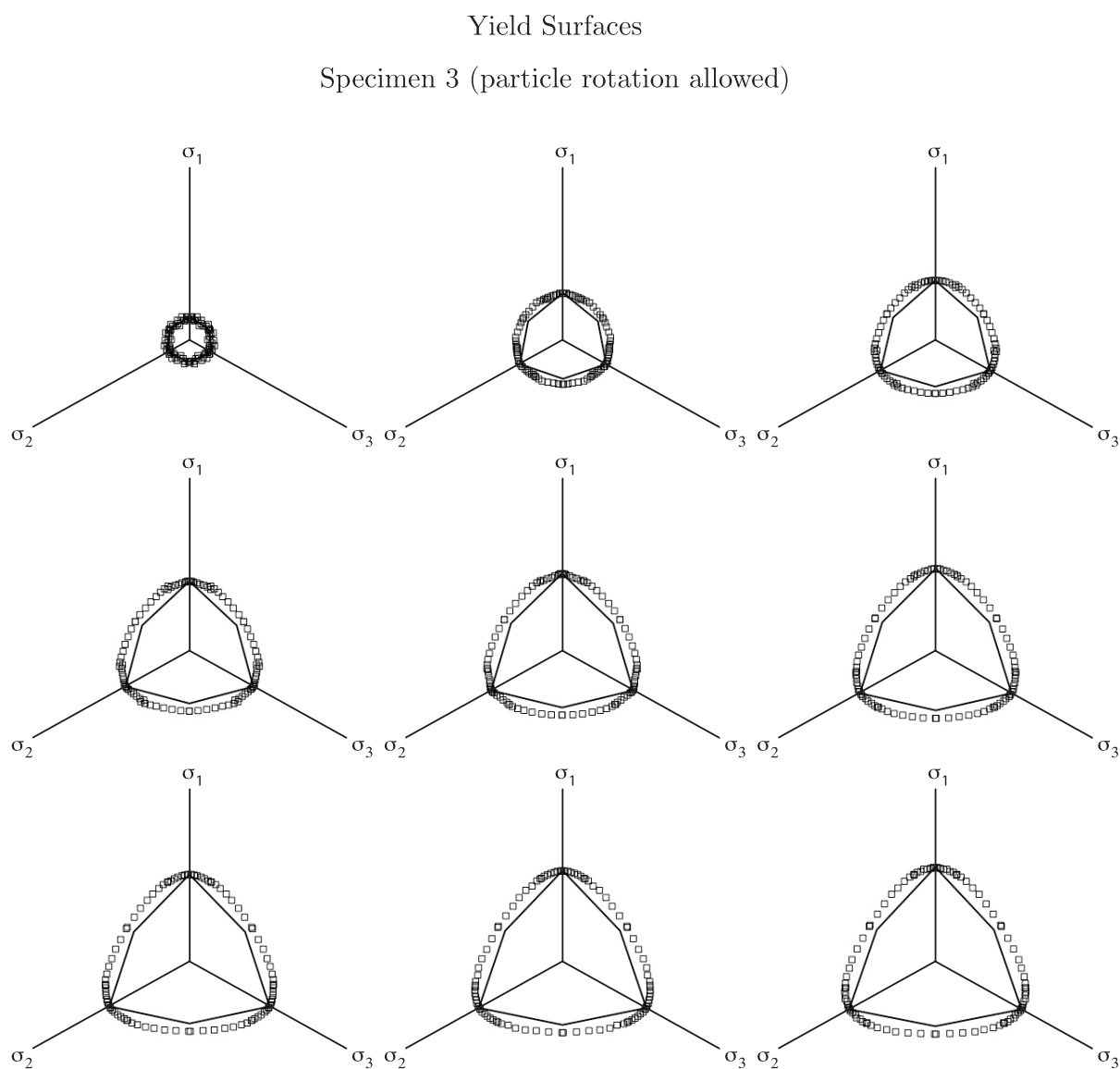


Figure 6.15: Yield surfaces obtained by DEM simulations performed on Specimen 3 with 3430 randomly packed uniform spheres with inter-element friction coefficients (from upper left to lower right) of  $\mu = \{0.01, 0.1, 0.2, 0.3, 0.4, 0.5, 0.6, 0.7, 0.8\}$ , with particle rotation allowed. Also shown for comparison are the Mohr-Coulomb yield surfaces with values of the macroscopic friction angle  $\phi = \{9.5, 18.5, 23.0, 26.5, 29.0, 31.0, 32.5, 34.0, 35.0\}^\circ$  chosen to match the data points at a Lode angle of zero.

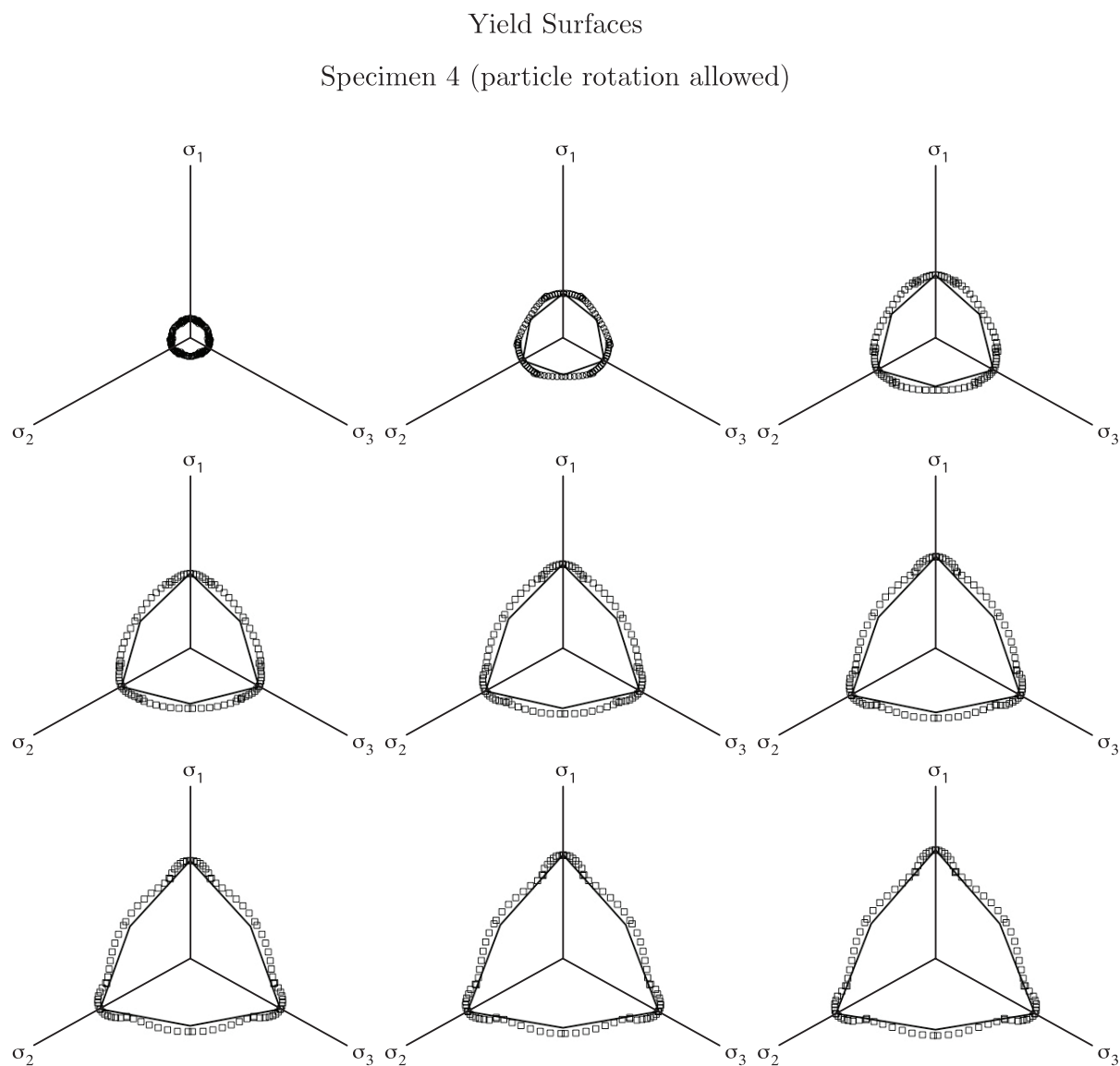


Figure 6.16: Yield surfaces obtained by DEM simulations performed on Specimen 4 with 29 660 randomly packed uniform spheres with inter-element friction coefficients (from upper left to lower right) of  $\mu = \{0.01, 0.1, 0.2, 0.3, 0.4, 0.5, 0.6, 0.7, 0.8\}$ , with particle rotation allowed. Also shown for comparison are the Mohr-Coulomb yield surfaces with values of the macroscopic friction angle  $\phi = \{8.0, 17.5, 24.0, 28.5, 31.5, 34.5, 36.5, 38.5, 40.0\}^\circ$  chosen to match the data points at a Lode angle of zero.

## Yield Surfaces

Specimen 5 (particle rotation allowed)

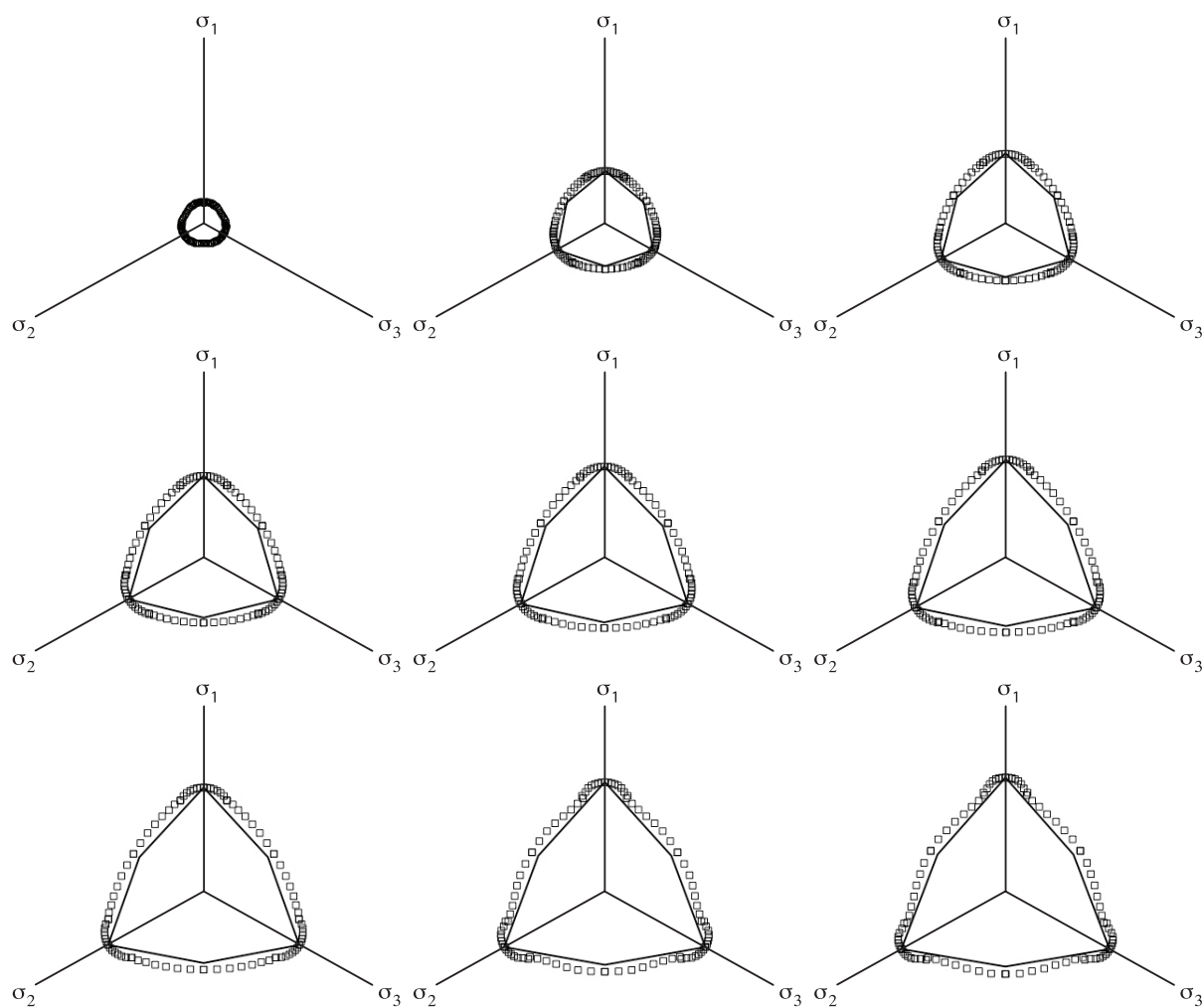


Figure 6.17: Yield surfaces obtained by DEM simulations performed on Specimen 5 with 29 660 randomly packed uniform spheres with inter-element friction coefficients (from upper left to lower right) of  $\mu = \{0.01, 0.1, 0.2, 0.3, 0.4, 0.5, 0.6, 0.7, 0.8\}$ , with particle rotation allowed. Also shown for comparison are the Mohr-Coulomb yield surfaces with values of the macroscopic friction angle  $\phi = \{8.0, 19.0, 25.0, 28.5, 31.5, 34.0, 36.0, 37.5, 39.0\}^\circ$  chosen to match the data points at a Lode angle of zero.

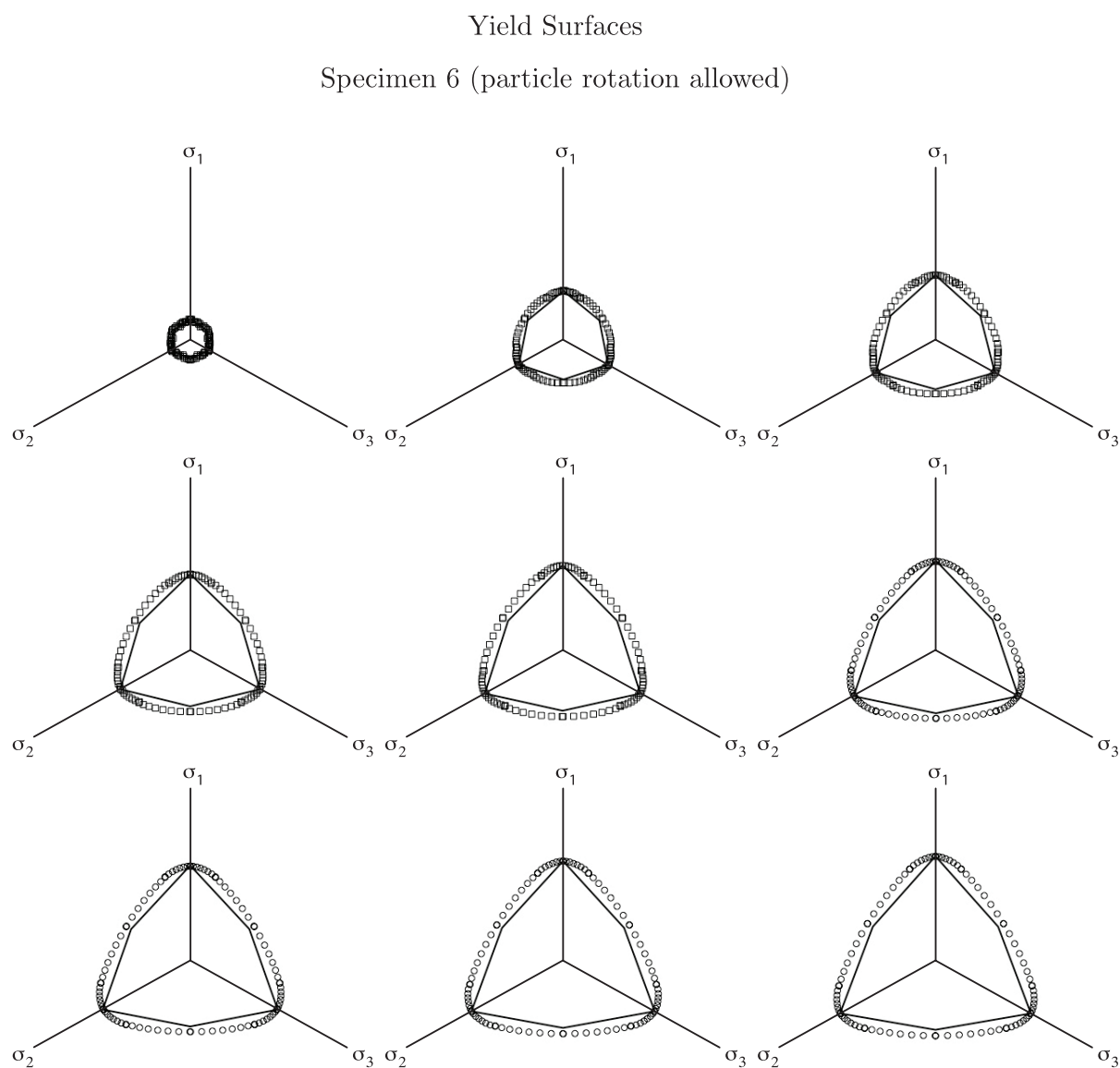


Figure 6.18: Yield surfaces obtained by DEM simulations performed on Specimen 6 with 29 660 randomly packed uniform spheres with inter-element friction coefficients (from upper left to lower right) of  $\mu = \{0.01, 0.1, 0.2, 0.3, 0.4, 0.5, 0.6, 0.7, 0.8\}$ , with particle rotation allowed. Also shown for comparison are the Mohr-Coulomb yield surfaces with values of the macroscopic friction angle  $\phi = \{8.5, 19.0, 24.5, 28.5, 31.5, 33.5, 35.5, 37.0, 38.5\}^\circ$  chosen to match the data points at a Lode angle of zero.

## Yield Surfaces

Specimen 1 (particle rotation: allowed vs. prohibited)

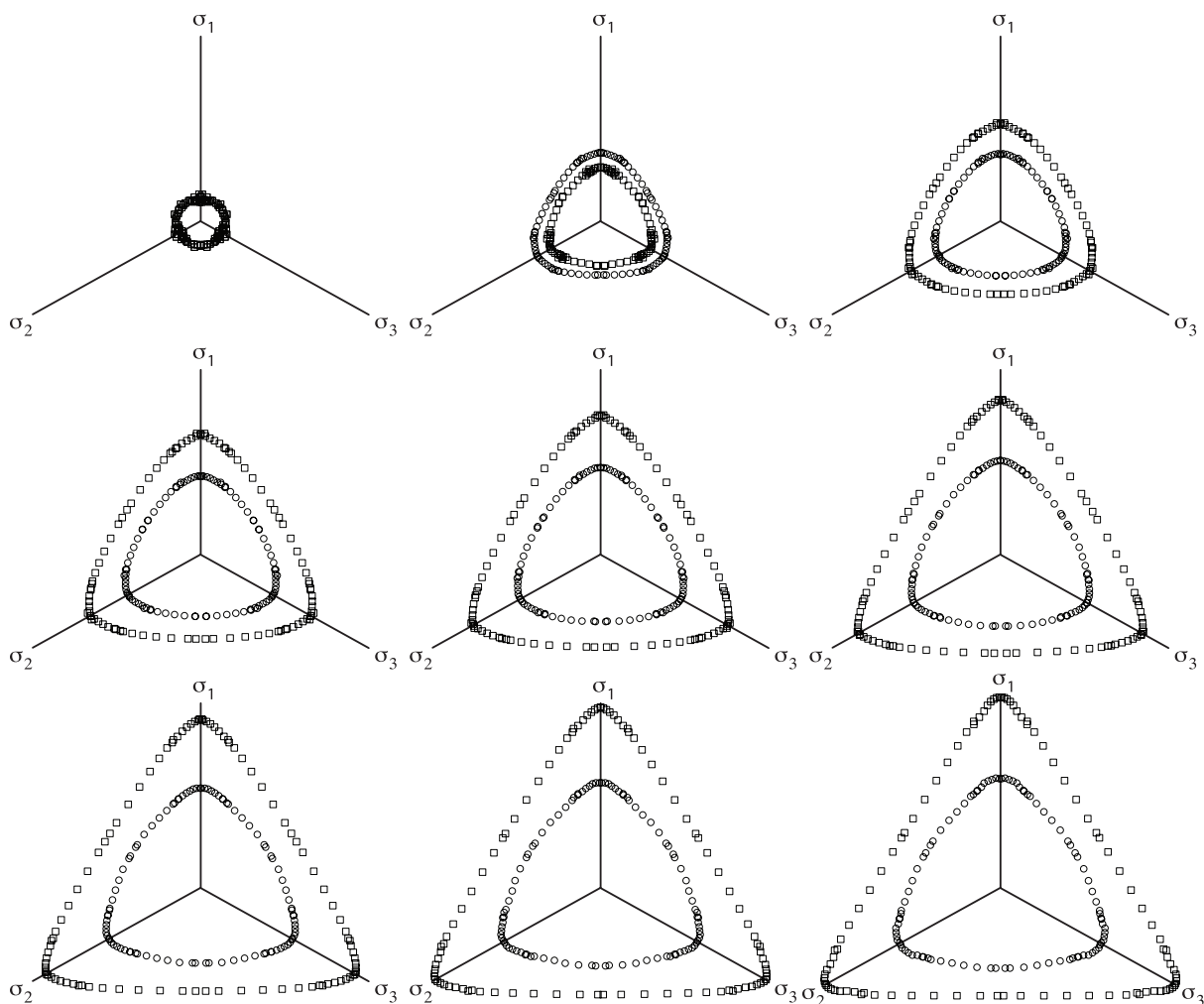


Figure 6.19: Yield surfaces obtained by DEM simulations performed on Specimen 1 with 3430 randomly packed uniform spheres with inter-element friction coefficients (from upper left to lower right) of  $\mu = \{0.01, 0.1, 0.2, 0.3, 0.4, 0.5, 0.6, 0.7, 0.8\}$ , with particle rotation allowed (smaller yield surfaces, from Figure 6.13) or prohibited (larger yield surfaces, from Figure 5.16), shown together for comparison.

## Yield Surfaces

Specimen 2 (particle rotation: allowed vs. prohibited)

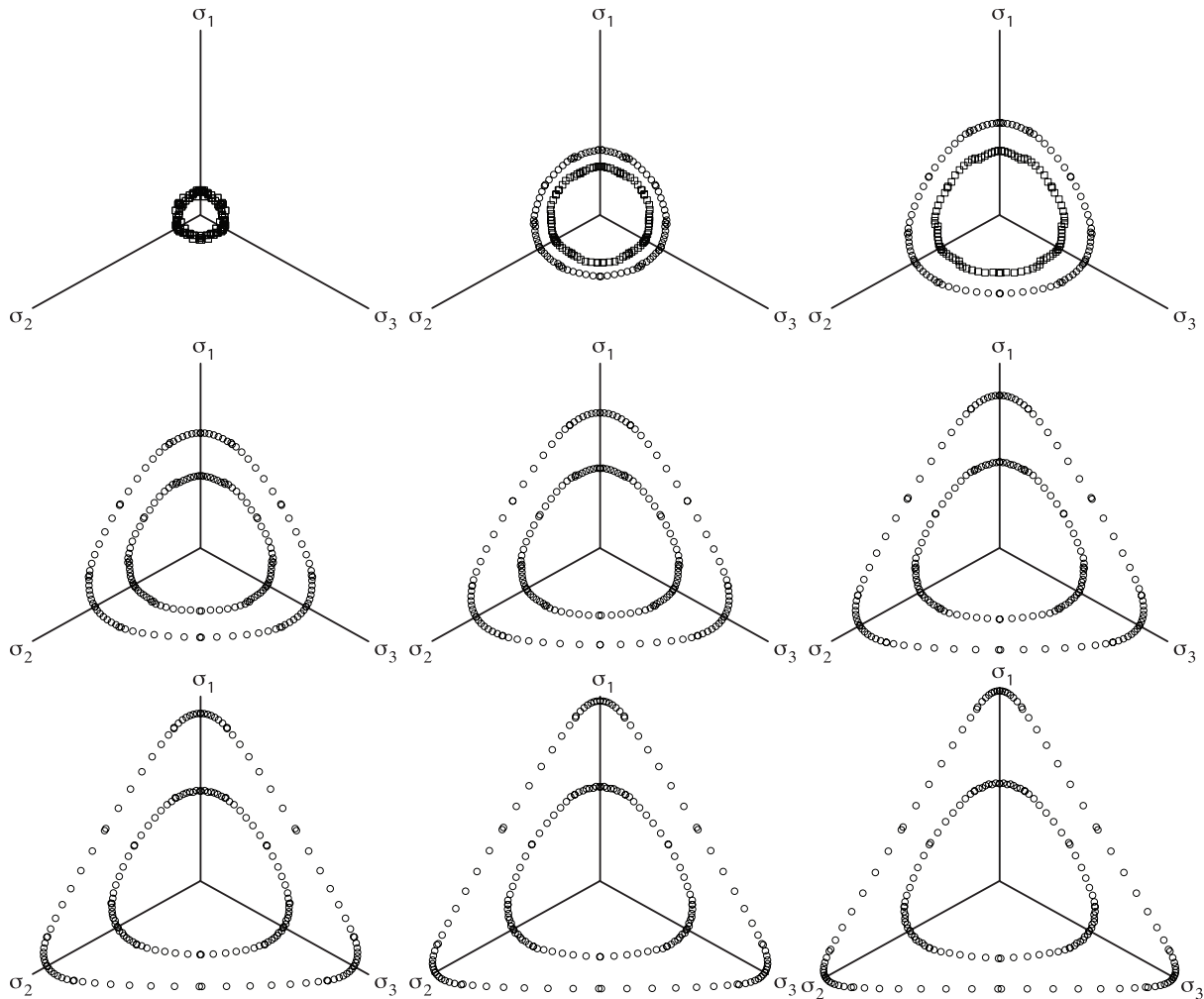


Figure 6.20: Yield surfaces obtained by DEM simulations performed on Specimen 2 with 3430 randomly packed uniform spheres with inter-element friction coefficients (from upper left to lower right) of  $\mu = \{0.01, 0.1, 0.2, 0.3, 0.4, 0.5, 0.6, 0.7, 0.8\}$ , with particle rotation allowed (smaller yield surfaces, from Figure 6.14) or prohibited (larger yield surfaces, from Figure 5.17), shown together for comparison.

## Yield Surfaces

Specimen 3 (particle rotation: allowed vs. prohibited)

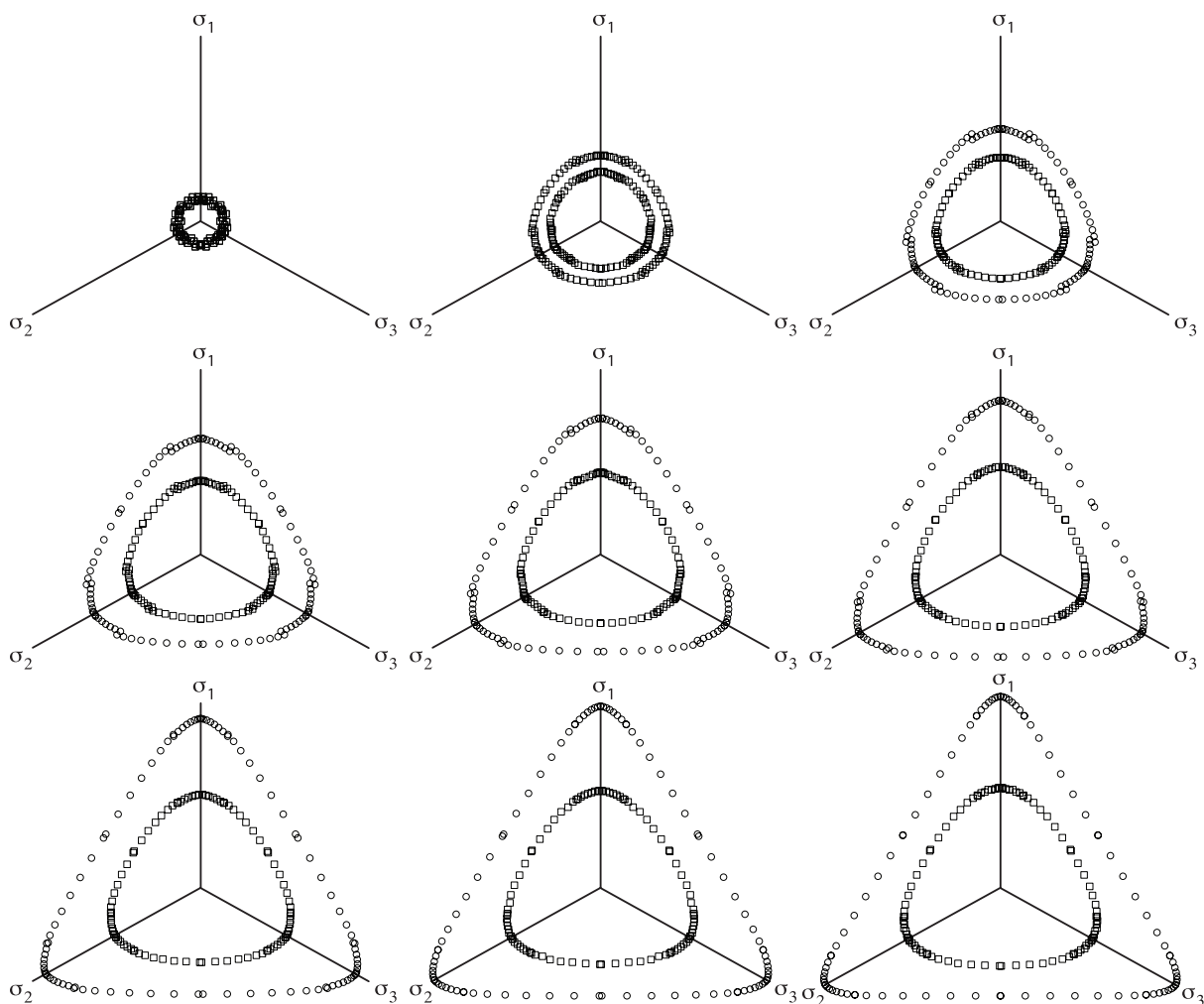


Figure 6.21: Yield surfaces obtained by DEM simulations performed on Specimen 3 with 3430 randomly packed uniform spheres with inter-element friction coefficients (from upper left to lower right) of  $\mu = \{0.01, 0.1, 0.2, 0.3, 0.4, 0.5, 0.6, 0.7, 0.8\}$ , with particle rotation allowed (smaller yield surfaces, from Figure 6.15) or prohibited (larger yield surfaces, from Figure 5.18), shown together for comparison.

## Yield Surfaces

Specimen 4 (particle rotation: allowed vs. prohibited)

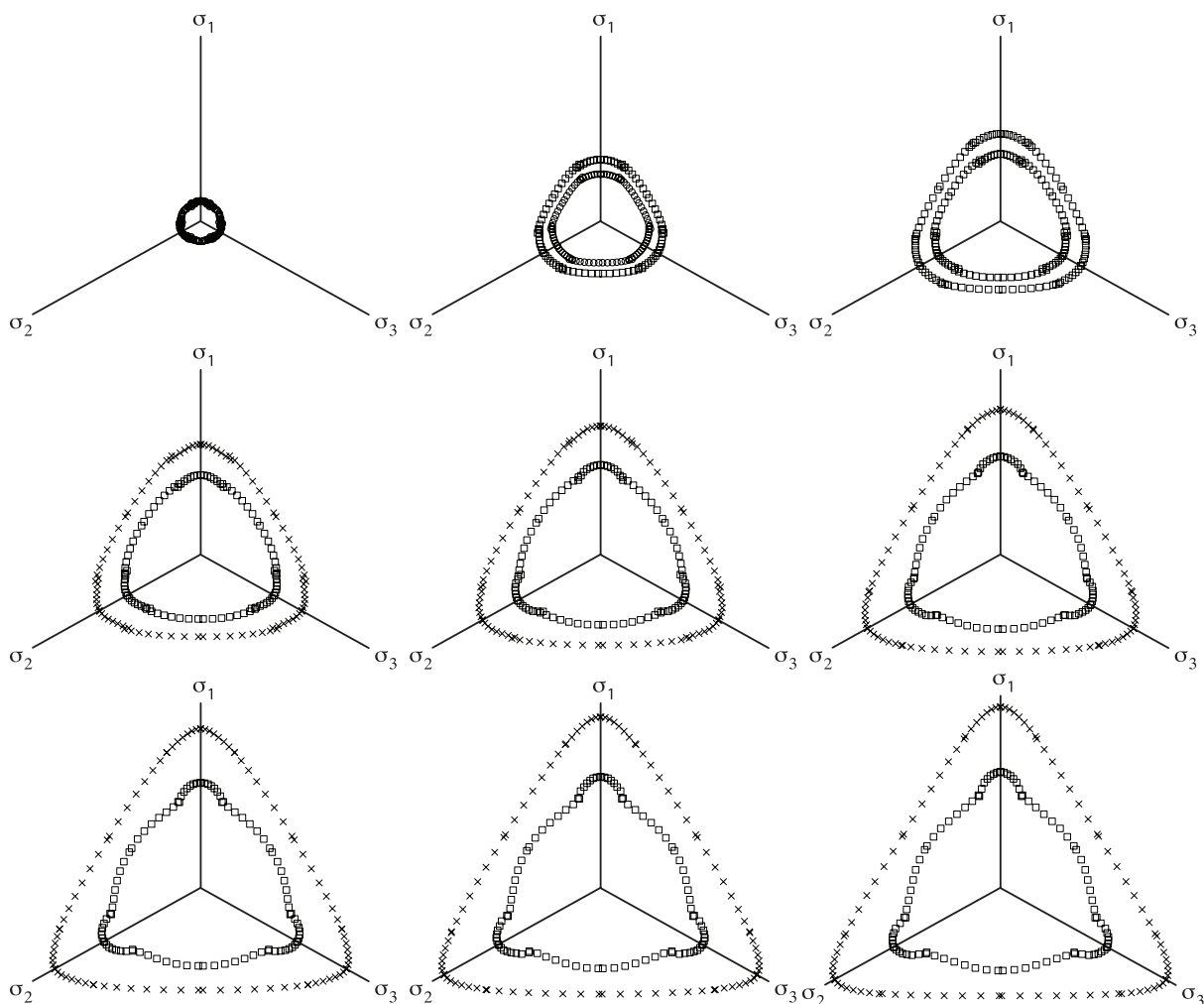


Figure 6.22: Yield surfaces obtained by DEM simulations performed on Specimen 4 with 29 660 randomly packed uniform spheres with inter-element friction coefficients (from upper left to lower right) of  $\mu = \{0.01, 0.1, 0.2, 0.3, 0.4, 0.5, 0.6, 0.7, 0.8\}$ , with particle rotation allowed (smaller yield surfaces, from Figure 6.16) or prohibited (larger yield surfaces, from Figure 5.19), shown together for comparison.

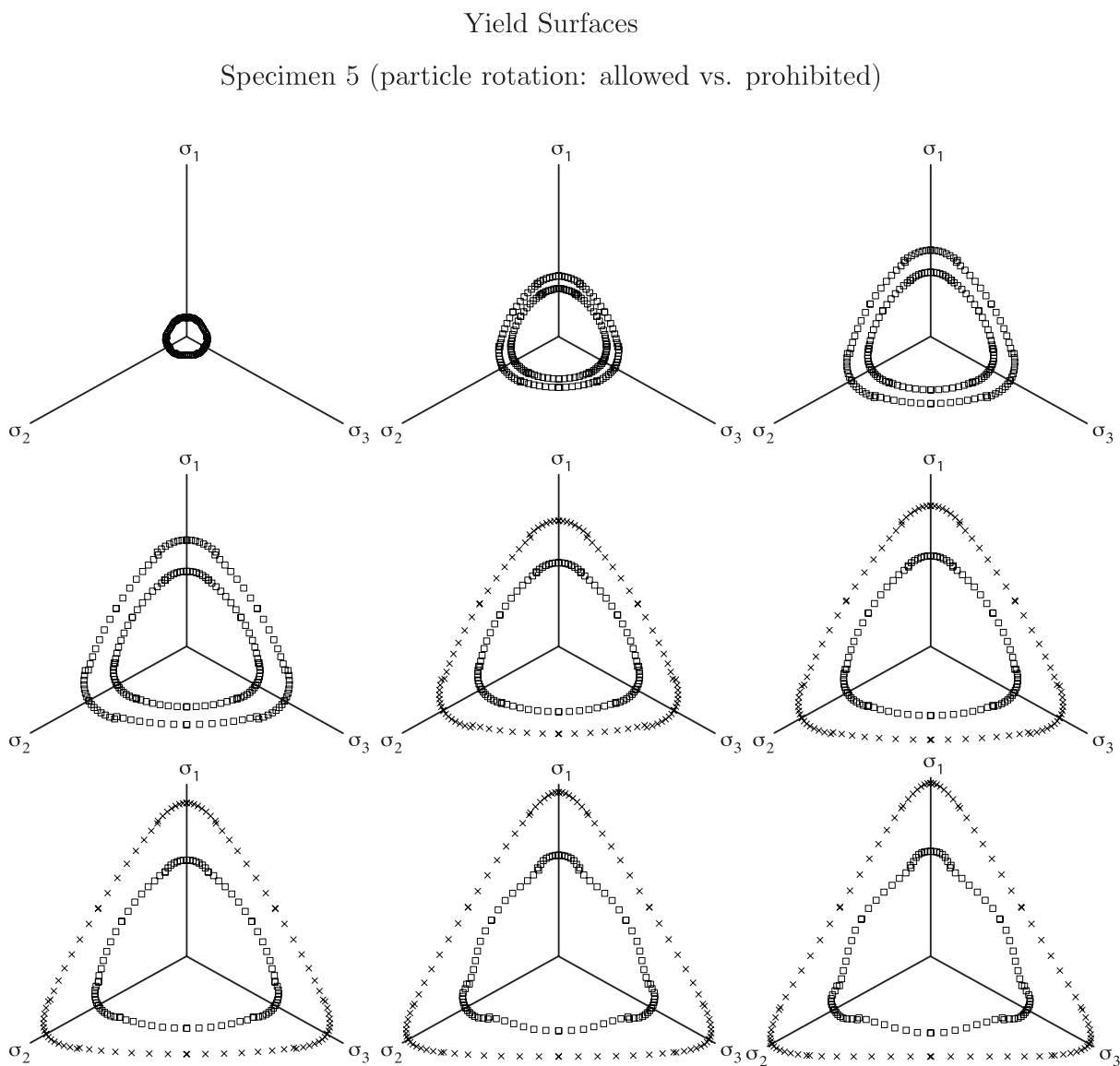


Figure 6.23: Yield surfaces obtained by DEM simulations performed on Specimen 5 with 29 660 randomly packed uniform spheres with inter-element friction coefficients (from upper left to lower right) of  $\mu = \{0.01, 0.1, 0.2, 0.3, 0.4, 0.5, 0.6, 0.7, 0.8\}$ , with particle rotation allowed (smaller yield surfaces, from Figure 6.17) or prohibited (larger yield surfaces, from Figure 5.20), shown together for comparison.

## Yield Surfaces

Specimen 6 (particle rotation: allowed vs. prohibited)

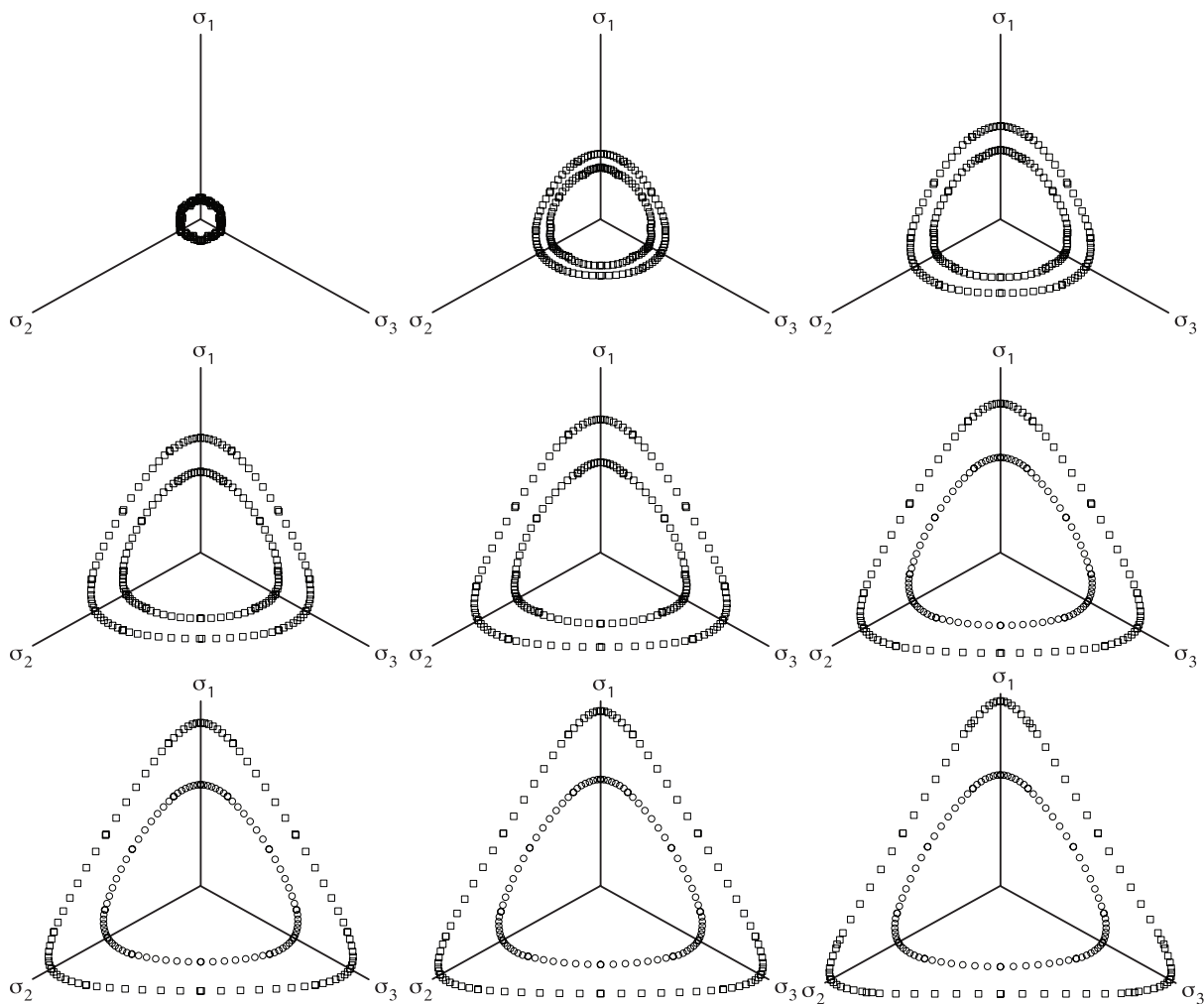


Figure 6.24: Yield surfaces obtained by DEM simulations performed on Specimen 6 with 29 660 randomly packed uniform spheres with inter-element friction coefficients (from upper left to lower right) of  $\mu = \{0.01, 0.1, 0.2, 0.3, 0.4, 0.5, 0.6, 0.7, 0.8\}$ , with particle rotation allowed (smaller yield surfaces, from Figure 6.18) or prohibited (larger yield surfaces, from Figure 5.21), shown together for comparison.

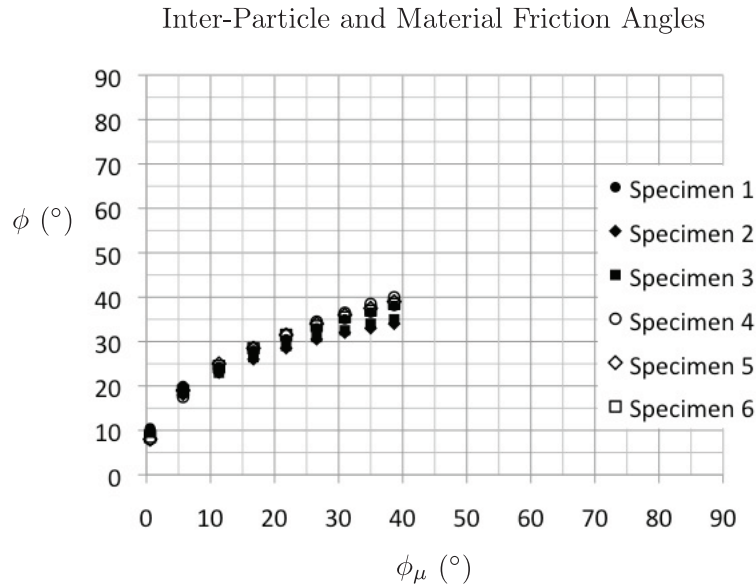


Figure 6.25: The relationship between the inter-particle friction coefficient  $\mu$  or the inter-particle friction angle  $\phi_\mu = \tan^{-1} \mu$  and the macroscopic or material friction angle  $\phi$  based on the yield surfaces shown in Figures 5.16–5.21, obtained from the 864 DEM simulations described in this section for six specimens of 3 430–29 660 randomly packed uniform spheres, with particle rotation allowed.

Since the total accumulated friction work  $U_f$  in each specimen was recorded throughout the DEM simulations, as described in Section 6.3, the average rate of friction work could be determined (by linear regression for  $0\% \leq |\epsilon_z| \leq 8\%$ ) for each DEM specimen for each value of the inter-element friction coefficient  $\mu$ , as in Chapter 5. Figure 6.28 shows the resulting relationship between the average rate of friction work (Joules/in/in) and the microscopic friction angle  $\phi_\mu = \tan^{-1} \mu$ , where  $\mu$  is the inter-element friction coefficient, for Specimens 1–3 with  $0.01 \leq \mu \leq 100.0$ , (with particle rotation allowed), at Lode angles of  $\theta = 0$  (top) and  $\theta = 60^\circ$  (bottom). Figure 6.29 shows the corresponding relationships for Specimens 4–6 with  $0.01 \leq \mu \leq 0.8$ .

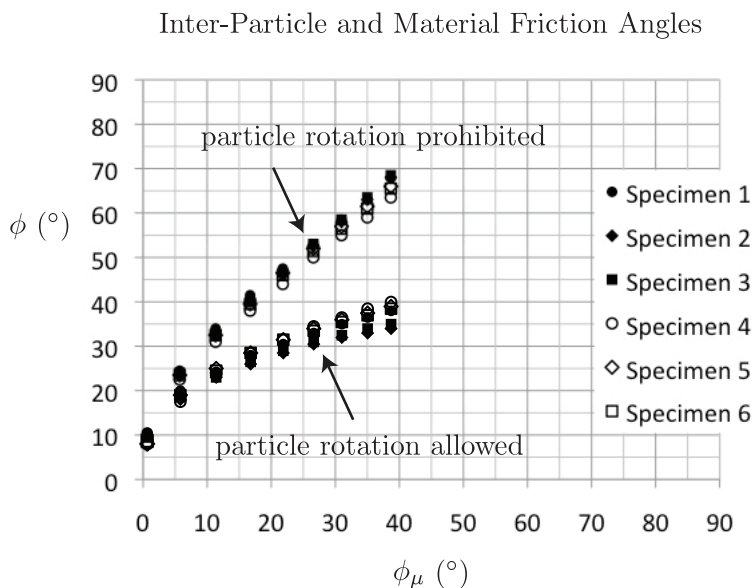


Figure 6.26: The relationship between the inter-particle friction angle  $\phi_{\mu} = \tan^{-1} \mu$  and the macroscopic or material friction angle  $\phi$  from Figure 6.25 with particle rotation allowed and from Figure 5.22 with particle rotation prohibited, shown together for comparison.

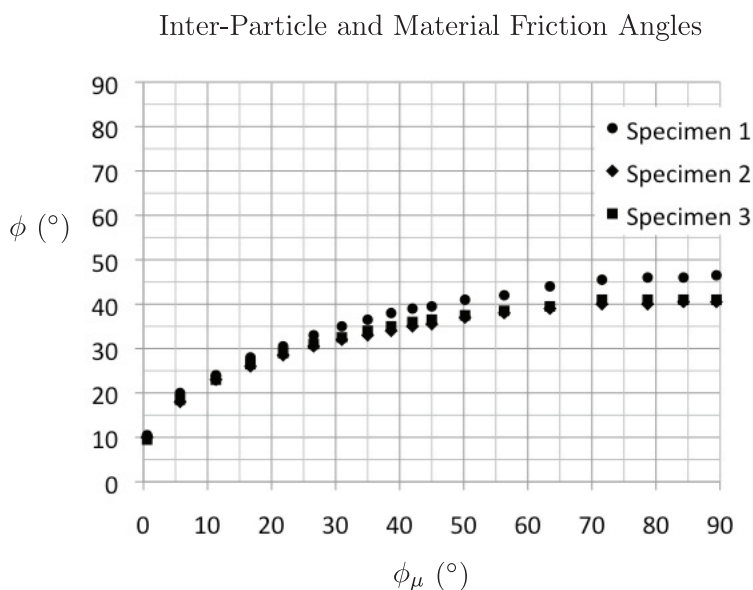


Figure 6.27: The relationship between the inter-particle friction coefficient  $\mu$  or the inter-particle friction angle  $\phi_{\mu} = \tan^{-1} \mu$  and the macroscopic or material friction angle  $\phi$ , obtained from 864 DEM simulations described in this section for three specimens of 3 430 randomly packed uniform spheres, with particle rotation allowed.

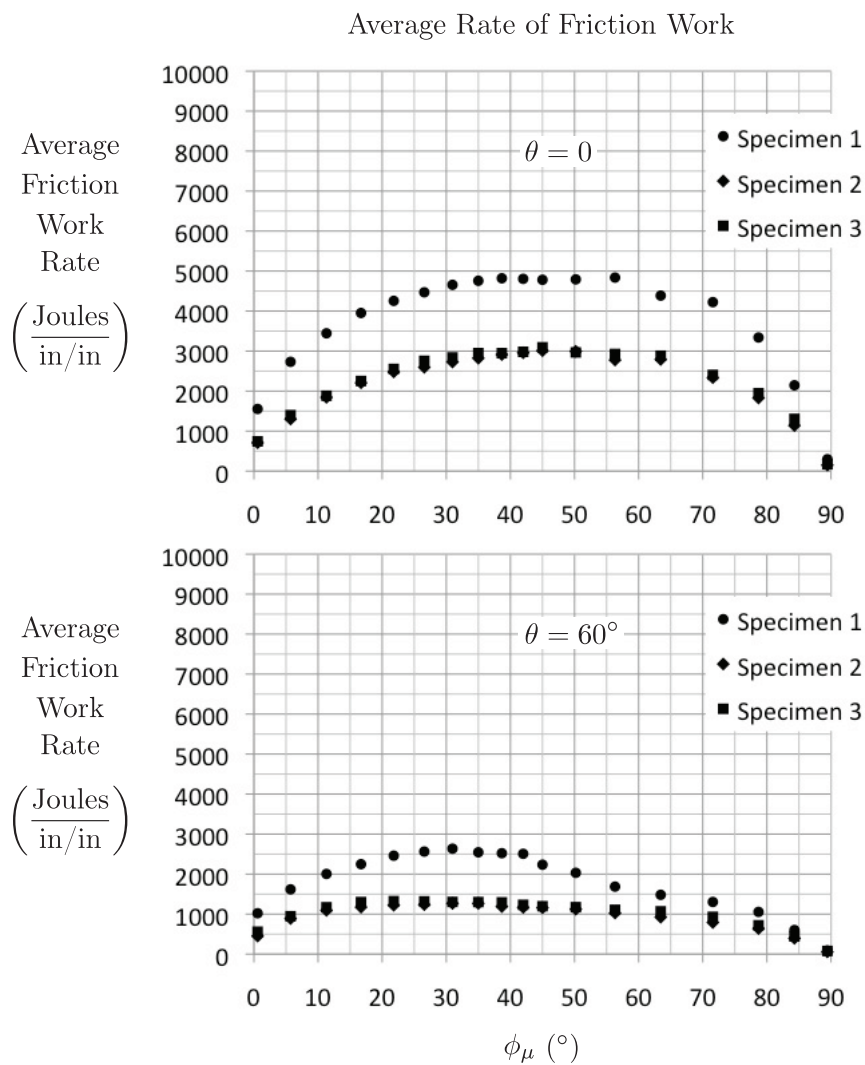


Figure 6.28: The relationship between the inter-particle friction angle  $\phi_\mu = \tan^{-1} \mu$  (where  $\mu$  is the inter-element friction coefficient,  $0.01 \leq \mu \leq 100.0$ ) and the average rate of friction work in Specimens 1–3 at Lode angles of  $\theta = 0$  (top) and  $\theta = 60^\circ$  (bottom), with particle rotation allowed.

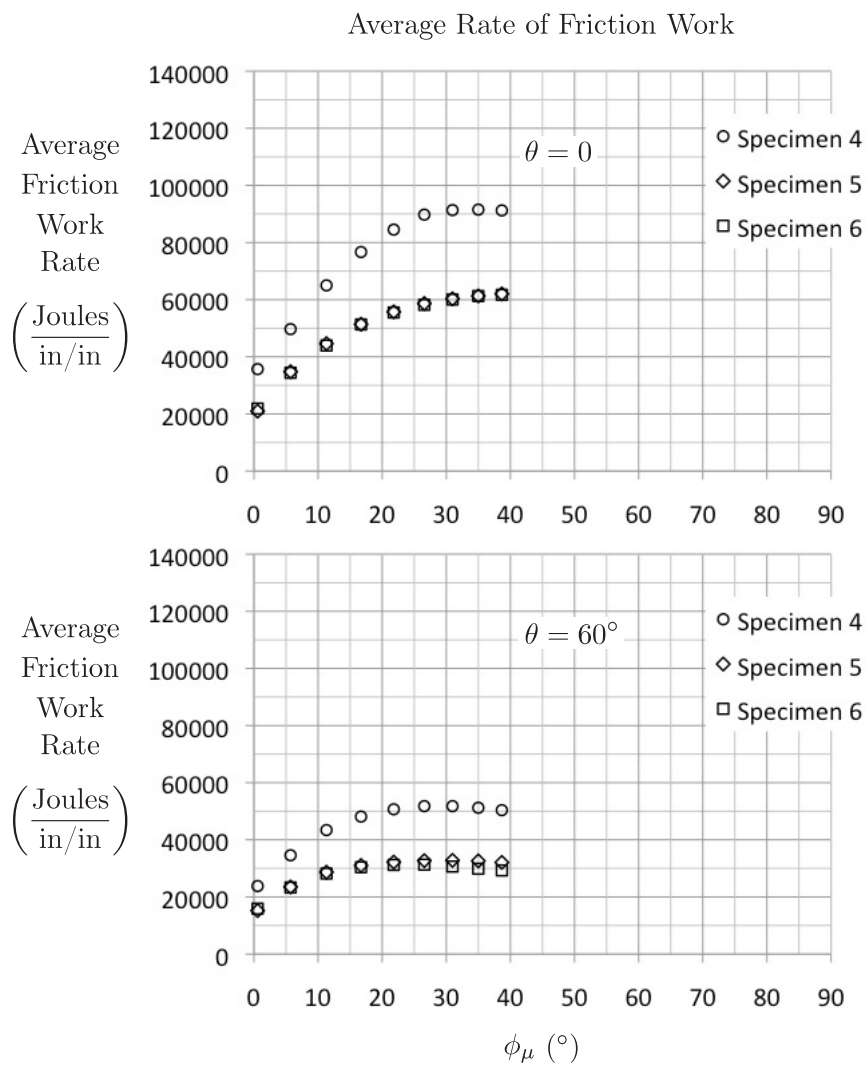


Figure 6.29: The relationship between the inter-particle friction angle  $\phi_\mu = \tan^{-1} \mu$  (where  $\mu$  is the inter-element friction coefficient,  $0.01 \leq \mu \leq 0.8$ ) and the average rate of friction work in Specimens 4–6 at Lode angles of  $\theta = 0$  (top) and  $\theta = 60^\circ$  (bottom), with particle rotation allowed.

## 6.5 Discussion

We begin with the important observation that, since the spheres in the DEM simulations performed for this chapter were allowed full rotational as well as translational freedom of motion, the results of this chapter are more representative of the true physical behavior of a particulate material composed of uniform spheres than are those of Part I, Chapter 5. As may be expected, the material friction angle  $\phi$  for each specimen for each value of the inter-particle friction coefficient  $\mu$  is significantly lower when particle rotation is allowed as compared to when particle rotation is prohibited. This can be observed in a direct comparison of the yield surfaces shown in Figures 5.16–5.21 in Section 5.5 and Figures 6.13–6.18 in Section 6.4, and even more clearly in a comparison of the relationship between the inter-particle friction angle  $\phi_\mu = \tan^{-1} \mu$  and the material friction angle  $\phi$  shown in Figures 5.22 and 5.23 in Section 5.5 and Figures 6.25 and 6.27 in Section 6.4.

The relationship between the “micro” and “macro” friction angles  $\phi_\mu$  and  $\phi$  shown in Figures 6.25 and 6.27 can be directly compared to the relationship derived by Emeriault et al. (1996), which is given by equation (2.13) in Section 2.2. Figure 6.30 shows the relationship between  $\phi_\mu$  and  $\phi$  determined by the DEM simulations of this chapter (with particle rotation allowed) and the relationship derived by Emeriault et al. (1996) for three different values of their internal material parameter  $\zeta$ . (For curves corresponding to other values of  $\zeta$ , see Figure 2.3 in Section 2.2.) Note that the material parameter  $\zeta$  is called  $\mu$  in Emeriault et al. (1996), but we have renamed it both in equation (2.13) and in this chapter (for obvious reasons). The meaning of the material parameter  $\zeta$  is explained in Section 2.1 of this thesis. First, we note that the correspondence between our DEM data points and the curves derived by Emeriault et al. (1996) for the three values of  $\zeta$  shown in Figure 6.30 is reasonably good overall. However, we also note that *no* single value of  $\zeta$  produces a curve that provides a *very* good match with the DEM data points for any specimen for *all* values of  $\phi_\mu$  at the same

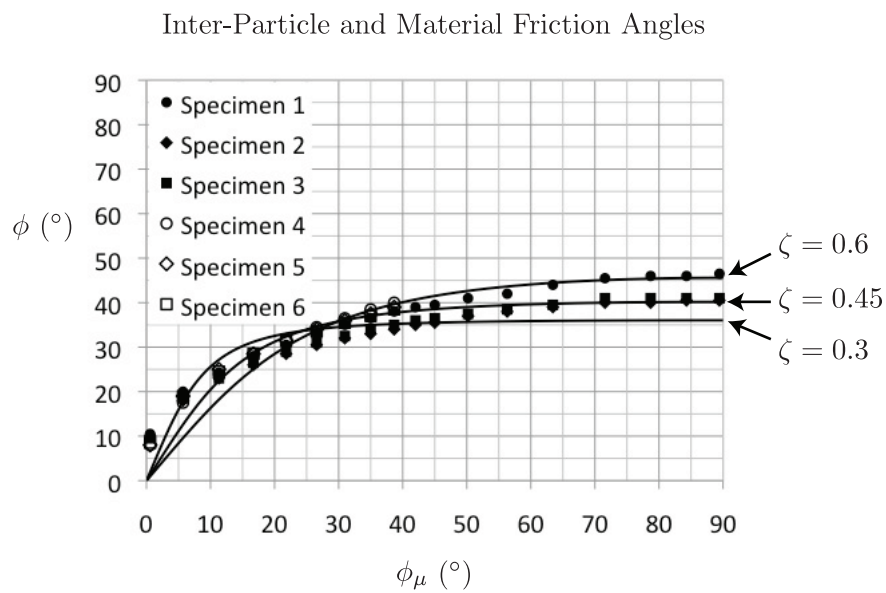


Figure 6.30: The relationship between the inter-particle friction coefficient  $\mu$  or the inter-particle friction angle  $\phi_{\mu} = \tan^{-1} \mu$  and the macroscopic or material friction angle  $\phi$  obtained from the DEM simulations described in this section (with particle rotation allowed), along with the curves derived by Emeriault et al. (1996), given by equation (2.13) in Section 2.2, for three values of the internal material parameter  $\zeta$ .

time. We will return to this point in Chapter 8 of this thesis.

Figures 6.13–6.18 show the Mohr-Coulomb yield surfaces with material friction angles  $\phi$  chosen to match the yield surfaces determined by DEM for each specimen for each value of  $\mu$  at a Lode angle of  $\theta = 0$ . Other yield surfaces for non-cohesive particulate materials include the Drucker-Prager, Lade-Duncan, and Matsuoka-Nakai surfaces (Bardet, 1990), as described in Section 5.3. Figures 6.31–6.36 show the yield surfaces determined by DEM for Specimens 1–6 with  $\mu = 0.2$  (top) and  $\mu = 0.5$  (bottom), with particle rotation allowed. Also shown in Figures 6.31–6.36 are Mohr-Coulomb, Drucker-Prager, Lade-Duncan (left) and Matsuoka-Nakai (right) yield surfaces, with material parameters chosen to match the DEM data points at a Lode angle of zero. Figures 6.37–6.39 show the same information for Specimens 1–3 with  $\mu = 0.8$  (top) and  $\mu = 1.2$  (bottom).

Since the DEM simulations performed for this chapter are more physically realistic than those performed for Chapter 5 in the sense that particle rotation is unrestrained, it is interesting to see which of these yield surfaces provides the best overall fit to the DEM data points in Figures 6.31–6.36, and to compare these figures to Figures 5.27–5.32 in Chapter 5 with particle rotation prohibited. First, the same trends are observable for Specimens 1–3 regardless of whether particle rotation is allowed or prohibited: for Specimen 1, the data points tend to lie between the Lade-Duncan and Matsuoka-Nakai surfaces; for Specimens 2 and 3, the data points tend to lie between the Lade-Duncan and Drucker-Prager surfaces. For Specimens 4–6 with particle rotation allowed, the data points match the Lade-Duncan yield surface almost exactly for all values of  $\mu$ . For Specimens 1–3, the correspondence with the Lade-Duncan yield surface improves as the inter-particle friction coefficient  $\mu$  increases, particularly for  $\mu > 0.5$ , as shown in Figures 6.37–6.39.

A comparison of Figures 6.31–6.36 with Figures 5.27–5.32 shows that particle rotation does not seem to play a significant role in the relative performance of the yield surfaces for our DEM specimens, and that the Lade-Duncan yield surface provides a very good

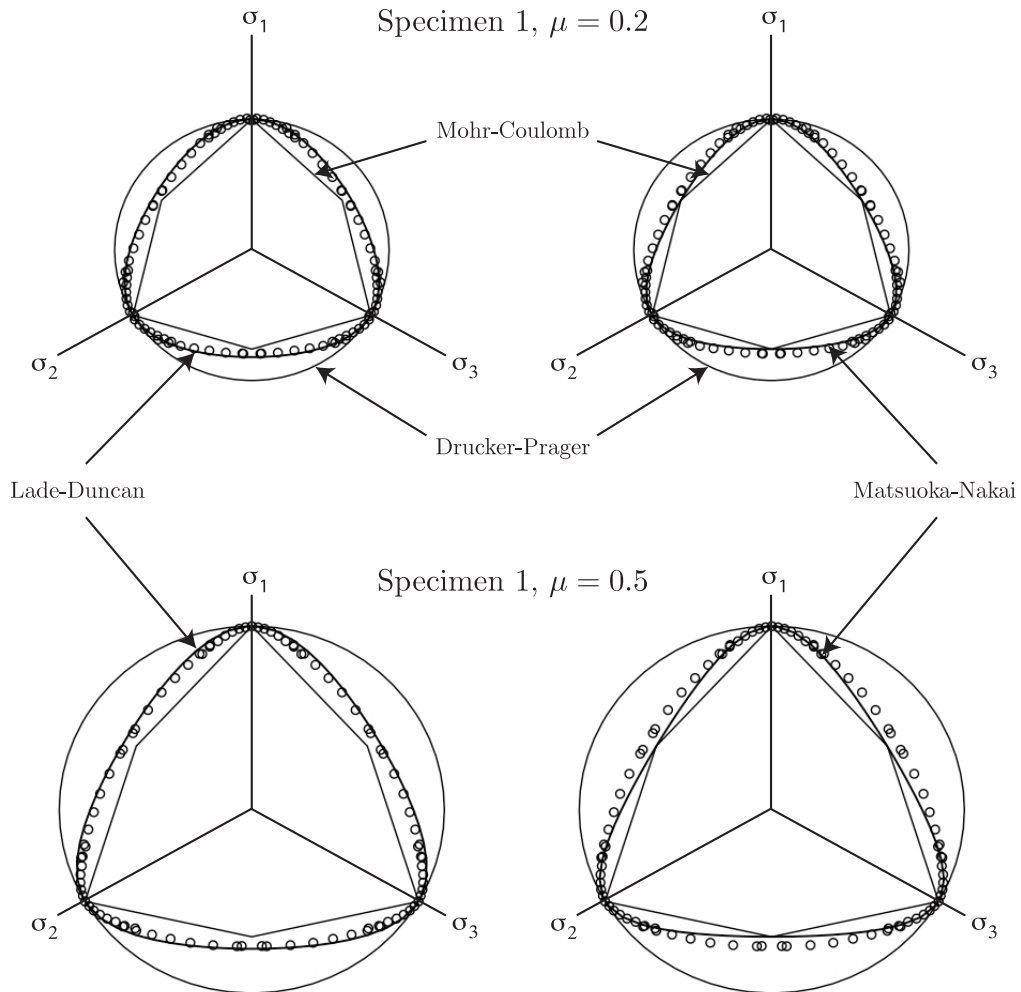


Figure 6.31: Yield surfaces obtained by DEM simulations performed on Specimen 1 with inter-element friction coefficients of  $\mu = 0.2$  (top) and  $\mu = 0.5$  (bottom), with particle rotation allowed. Also shown are Mohr-Coulomb, Drucker-Prager, Lade-Duncan (left) and Matsuoka-Nakai (right) yield surfaces, with material parameters chosen to match the data points at a Lode angle of  $\theta = 0$ .

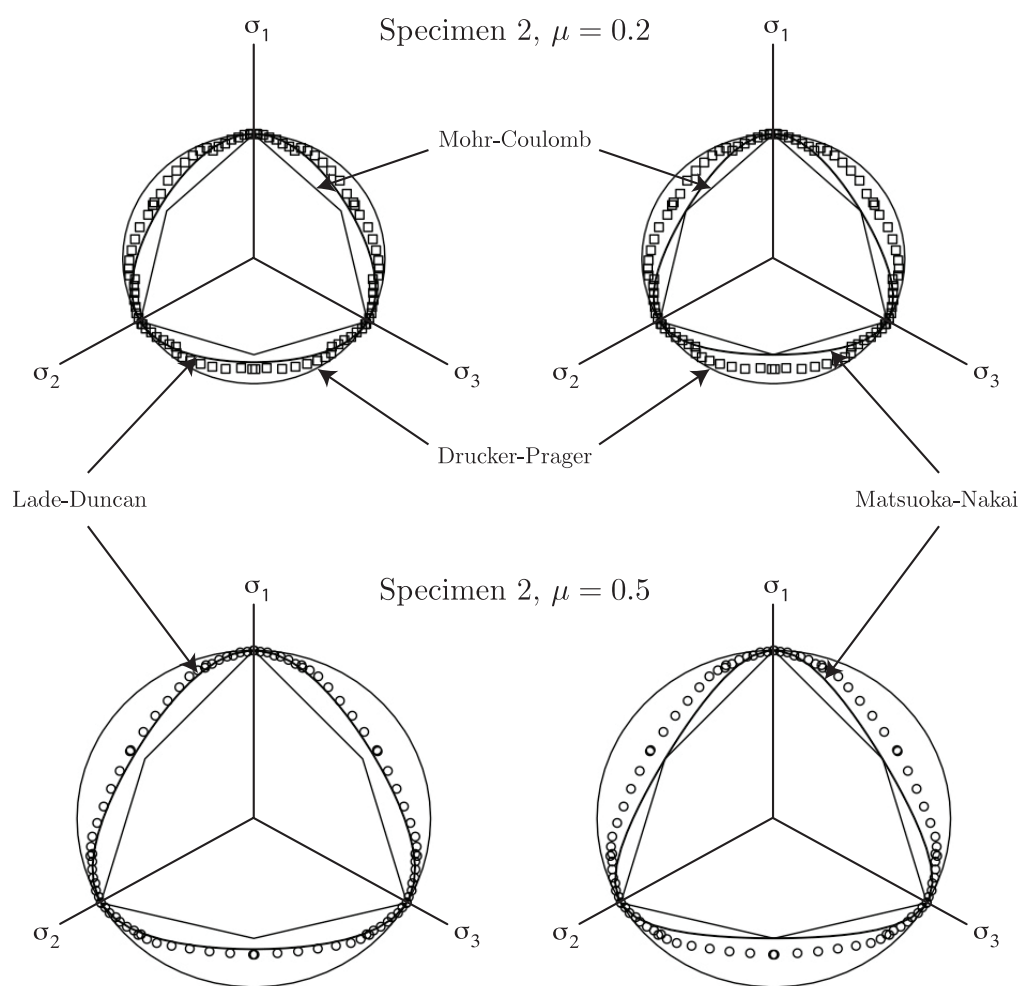


Figure 6.32: Yield surfaces obtained by DEM simulations performed on Specimen 2 with inter-element friction coefficients of  $\mu = 0.2$  (top) and  $\mu = 0.5$  (bottom), with particle rotation allowed. Also shown are Mohr-Coulomb, Drucker-Prager, Lade-Duncan (left) and Matsuoka-Nakai (right) yield surfaces, with material parameters chosen to match the data points at a Lode angle of  $\theta = 0$ .

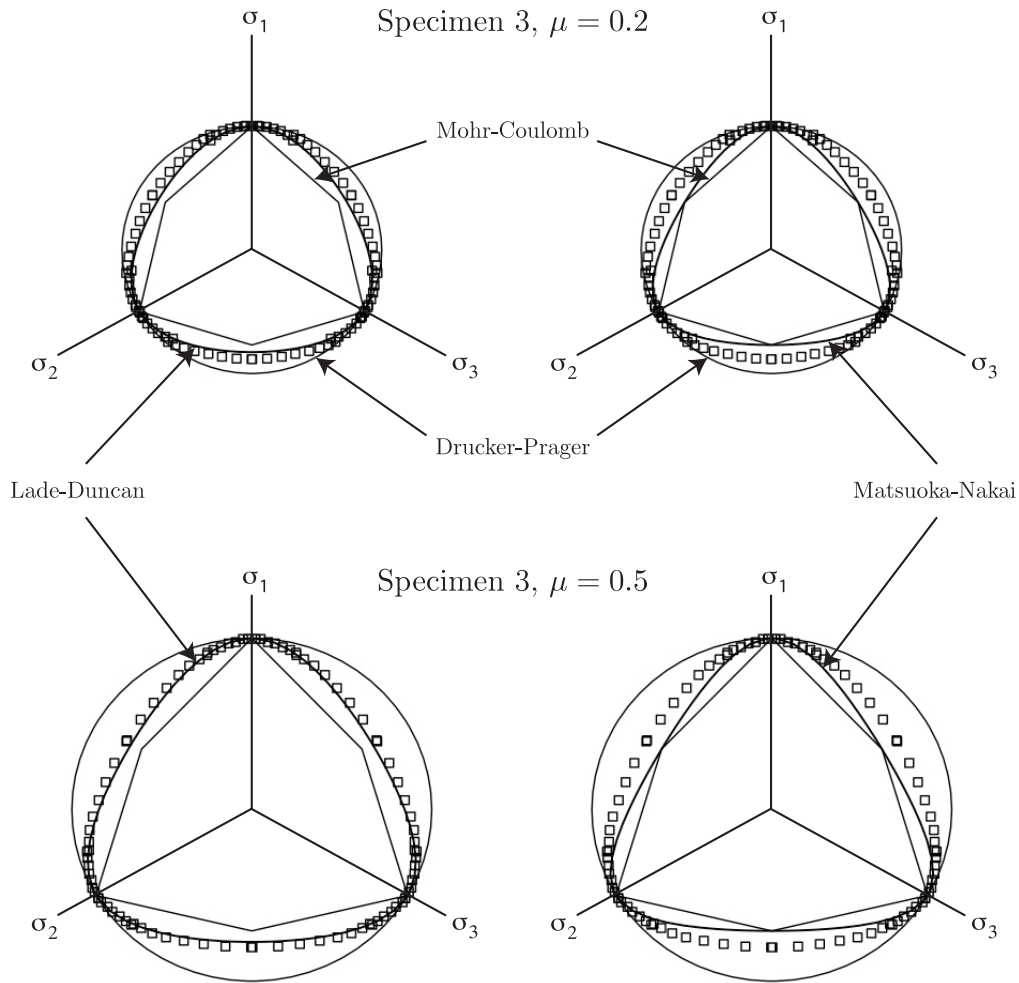


Figure 6.33: Yield surfaces obtained by DEM simulations performed on Specimen 3 with inter-element friction coefficients of  $\mu = 0.2$  (top) and  $\mu = 0.5$  (bottom), with particle rotation allowed. Also shown are Mohr-Coulomb, Drucker-Prager, Lade-Duncan (left) and Matsuoka-Nakai (right) yield surfaces, with material parameters chosen to match the data points at a Lode angle of  $\theta = 0$ .

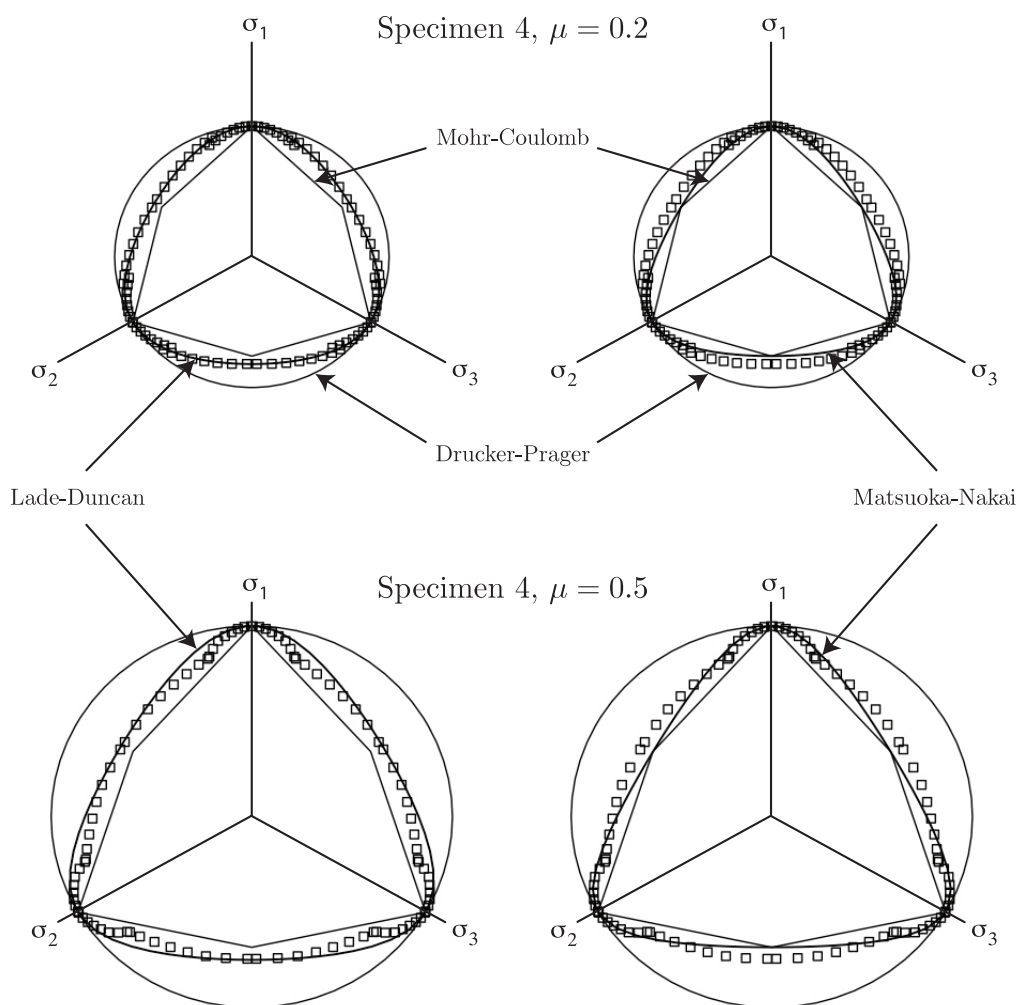


Figure 6.34: Yield surfaces obtained by DEM simulations performed on Specimen 4 with inter-element friction coefficients of  $\mu = 0.2$  (top) and  $\mu = 0.5$  (bottom), with particle rotation allowed. Also shown are Mohr-Coulomb, Drucker-Prager, Lade-Duncan (left) and Matsuoka-Nakai (right) yield surfaces, with material parameters chosen to match the data points at a Lode angle of  $\theta = 0$ .

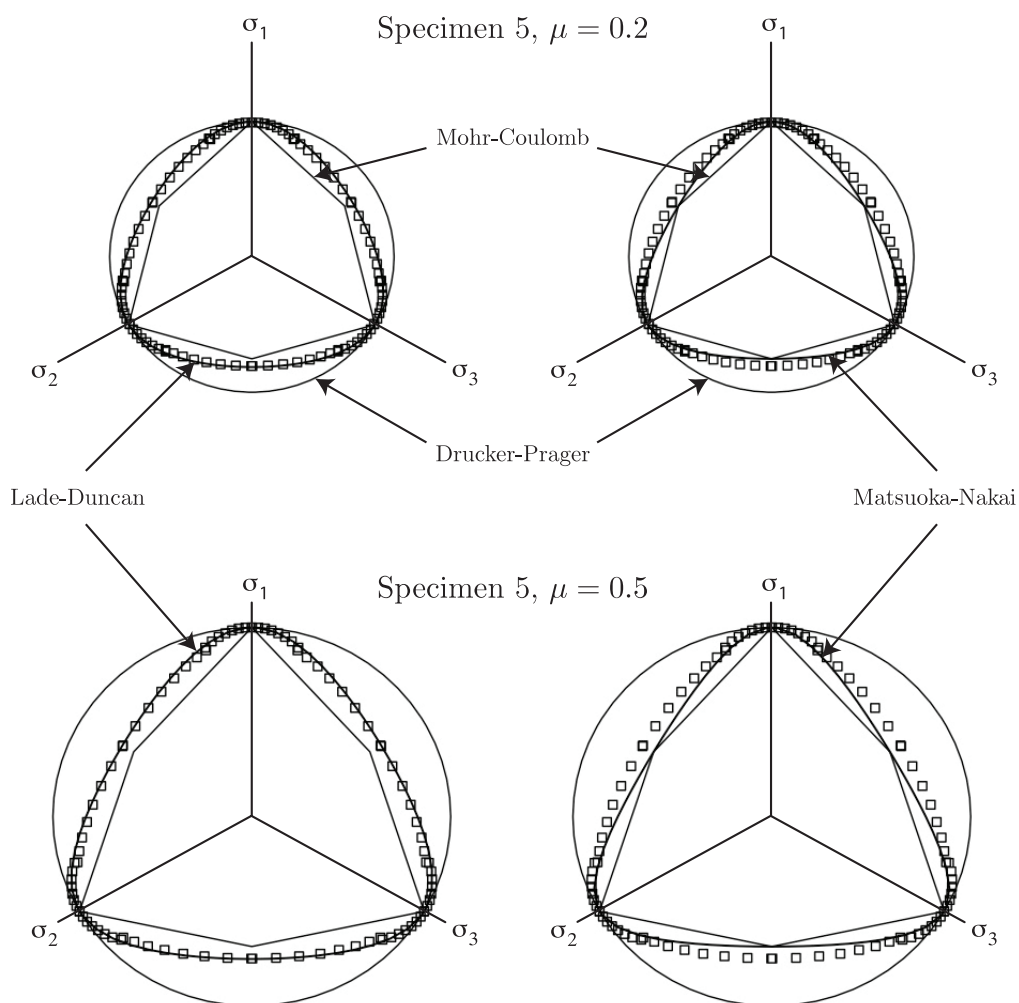


Figure 6.35: Yield surfaces obtained by DEM simulations performed on Specimen 5 with inter-element friction coefficients of  $\mu = 0.2$  (top) and  $\mu = 0.5$  (bottom), with particle rotation allowed. Also shown are Mohr-Coulomb, Drucker-Prager, Lade-Duncan (left) and Matsuoka-Nakai (right) yield surfaces, with material parameters chosen to match the data points at a Lode angle of  $\theta = 0$ .

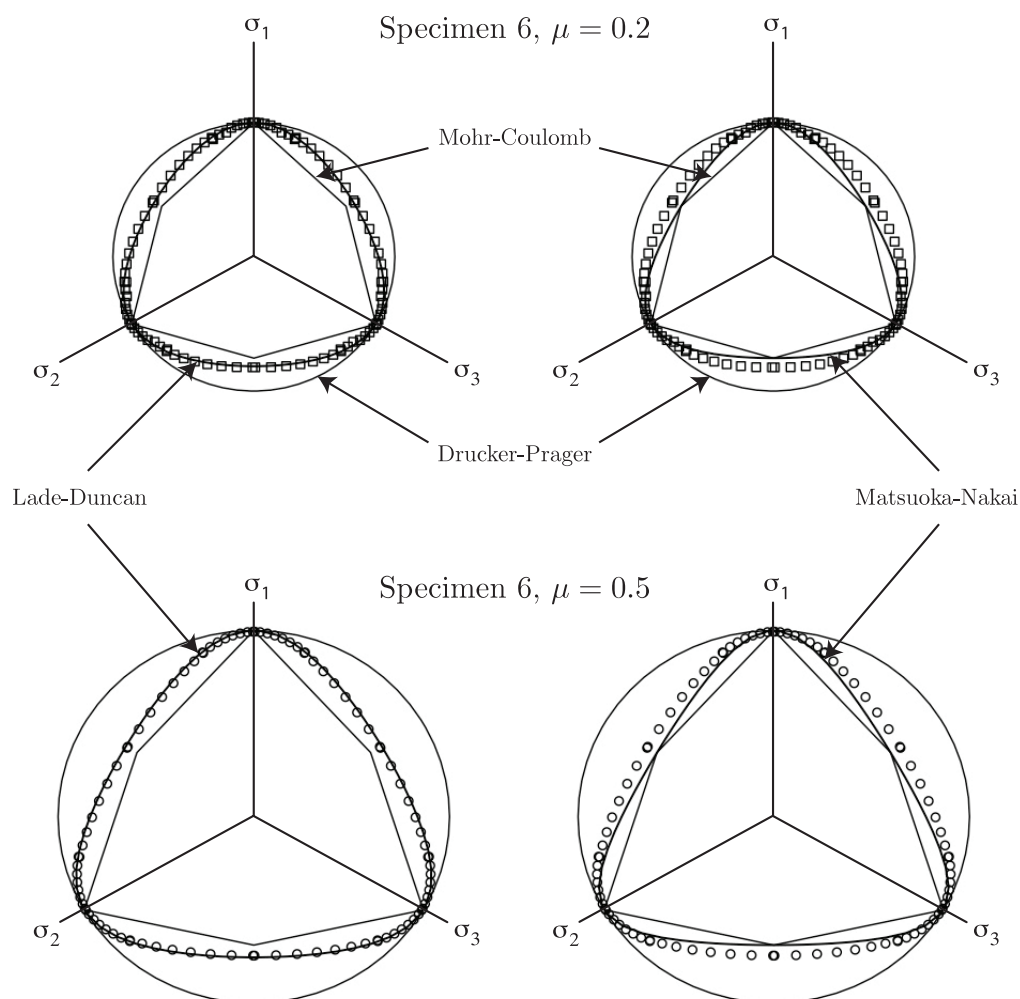


Figure 6.36: Yield surfaces obtained by DEM simulations performed on Specimen 6 with inter-element friction coefficients of  $\mu = 0.2$  (top) and  $\mu = 0.5$  (bottom), with particle rotation allowed. Also shown are Mohr-Coulomb, Drucker-Prager, Lade-Duncan (left) and Matsuoka-Nakai (right) yield surfaces, with material parameters chosen to match the data points at a Lode angle of  $\theta = 0$ .

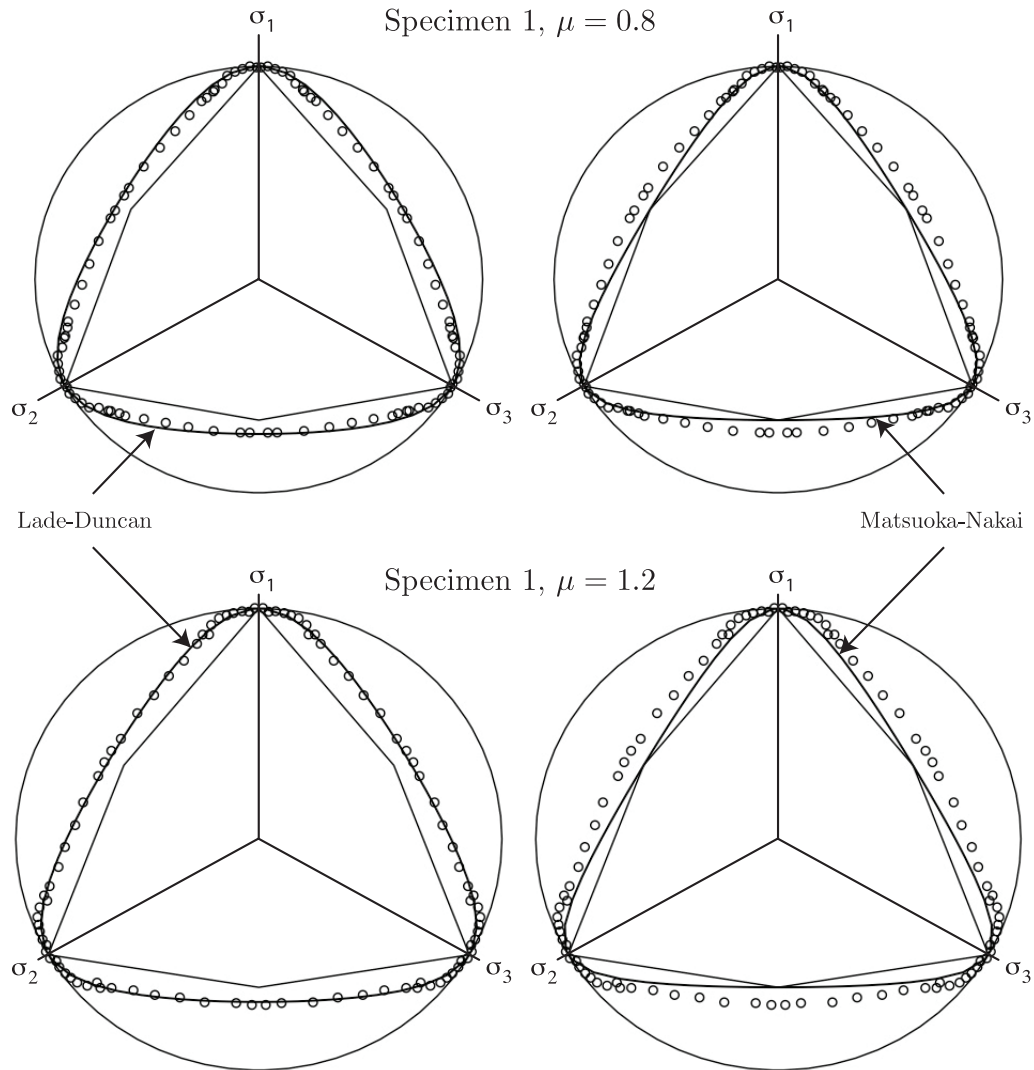


Figure 6.37: Yield surfaces obtained by DEM simulations performed on Specimen 1 with inter-element friction coefficients of  $\mu = 0.8$  (top) and  $\mu = 1.2$  (bottom), with particle rotation allowed. Also shown are Mohr-Coulomb, Drucker-Prager, Lade-Duncan (left) and Matsuoka-Nakai (right) yield surfaces, with material parameters chosen to match the data points at a Lode angle of  $\theta = 0$ .

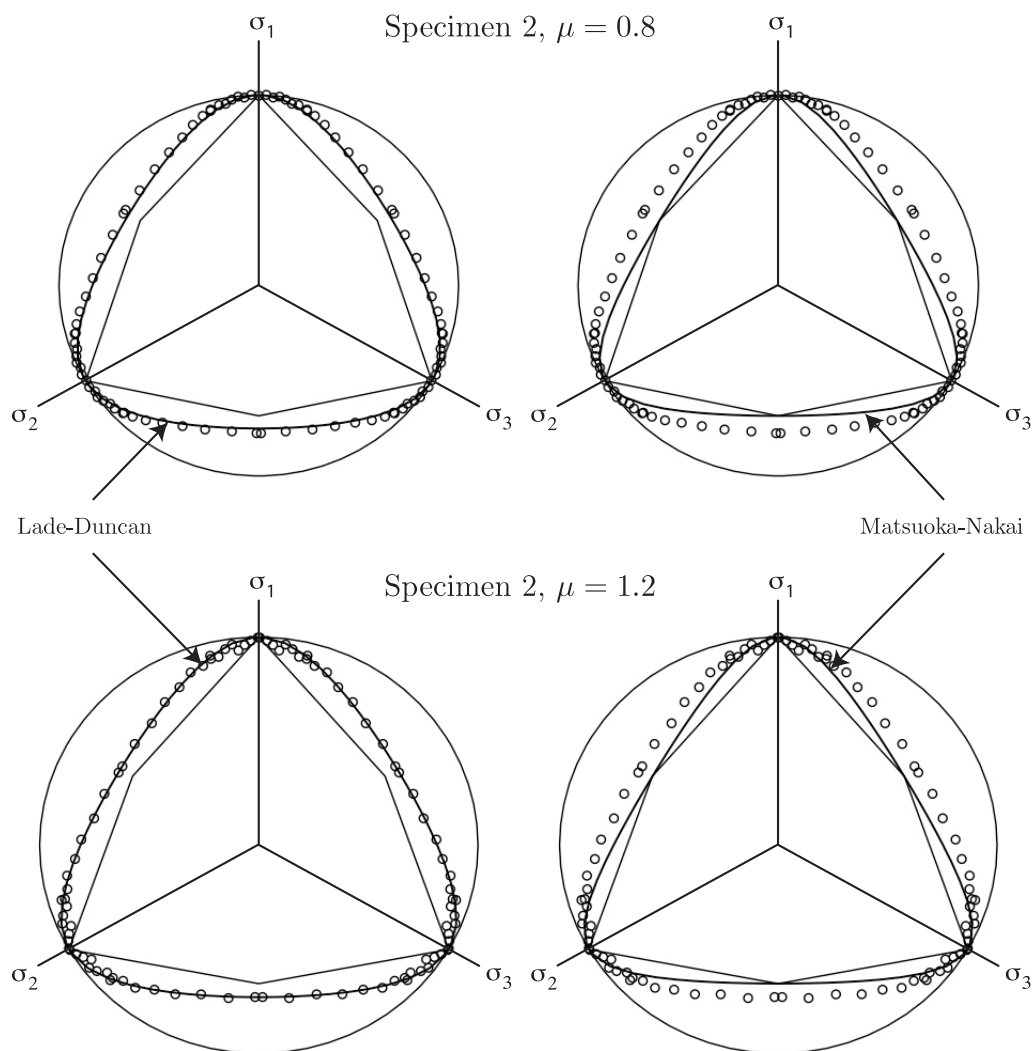


Figure 6.38: Yield surfaces obtained by DEM simulations performed on Specimen 2 with inter-element friction coefficients of  $\mu = 0.8$  (top) and  $\mu = 1.2$  (bottom), with particle rotation allowed. Also shown are Mohr-Coulomb, Drucker-Prager, Lade-Duncan (left) and Matsuoka-Nakai (right) yield surfaces, with material parameters chosen to match the data points at a Lode angle of  $\theta = 0$ .

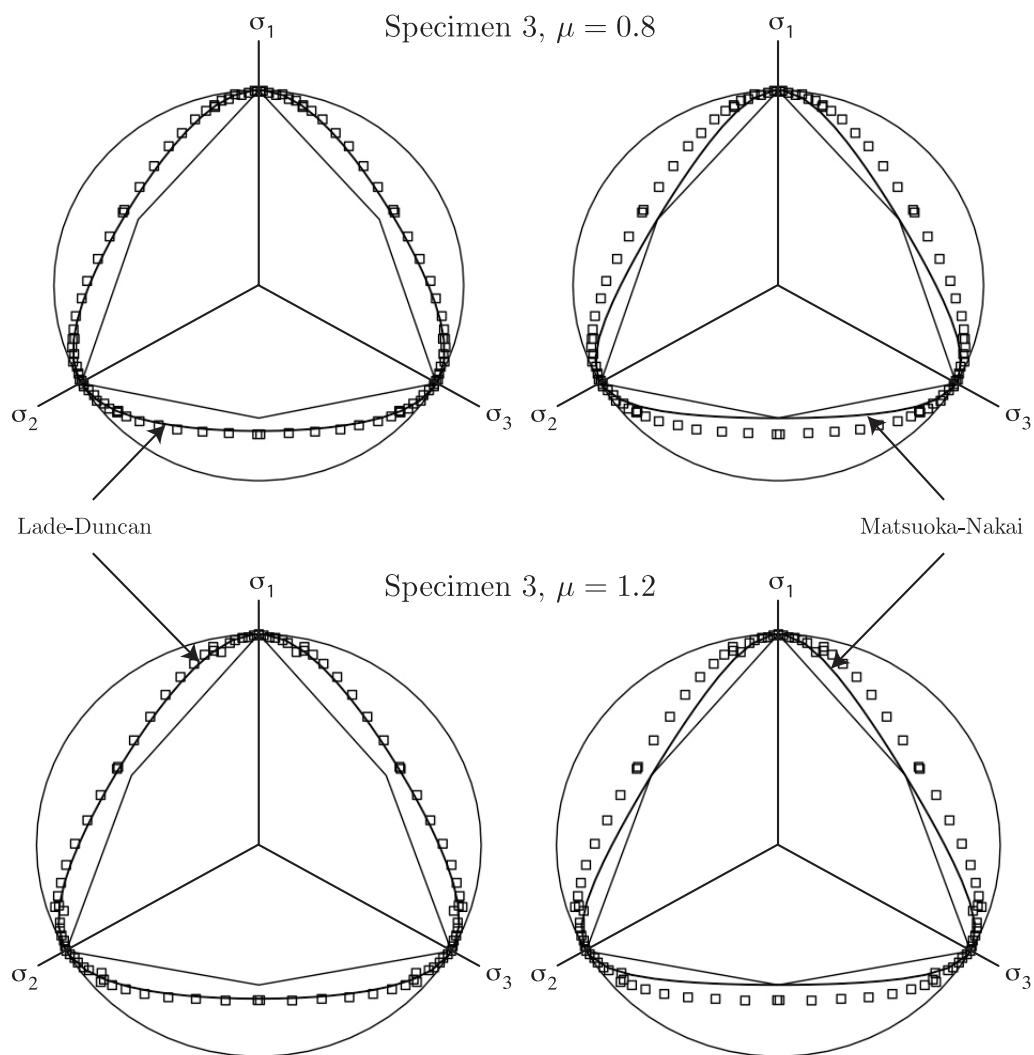


Figure 6.39: Yield surfaces obtained by DEM simulations performed on Specimen 3 with inter-element friction coefficients of  $\mu = 0.8$  (top) and  $\mu = 1.2$  (bottom), with particle rotation allowed. Also shown are Mohr-Coulomb, Drucker-Prager, Lade-Duncan (left) and Matsuoka-Nakai (right) yield surfaces, with material parameters chosen to match the data points at a Lode angle of  $\theta = 0$ .

characterization of the DEM data points regardless of whether particle rotation is allowed or prohibited.

As one might expect, the total accumulated friction work  $U_f$  in each specimen is smaller when particle rotation is allowed than when particle rotation is prohibited. This can be seen by a direct comparison of Figures 6.7–6.12 with Figures 5.10–5.15. The form of the  $U_f$  versus  $|\epsilon_z|$  curve is essentially the same regardless of whether or not particle rotation is allowed. As noted in Section 5.6, the material friction angle  $\phi$  is the *peak* friction angles for the particulate material specimens (Bardet, 1997). As in the case of no particle rotation, these peak friction angles do not correspond to the initiation of irreversible strain, which occurs with the initiation of friction work at or before  $|\epsilon_z| = 1\%$  for all six specimens, with  $\mu = 0.2$  or  $\mu = 0.5$  and  $\theta = 0$  or  $\theta = 60^\circ$ , as shown in Figures 6.7–6.12, while yield associated with the peak friction angle  $\phi$  occurs at approximately  $4\% \leq |\epsilon_z| \leq 6\%$  for all six specimens, as shown in Figures 6.1–6.6. This is expected for non-cohesive particulate materials, since, as noted in Section 5.6, irrecoverable strains can develop in uncemented normally consolidated sands at strains as low as  $\epsilon = 0.007\%$  (Mitchell and Soga, 2005).

Analogous to Figures 5.33–5.38 for the case of no particle rotation, Figures 6.40–6.45 show the stress-strain curves for Specimens 1–6, respectively, with particle rotation allowed, with inter-element friction coefficients of  $\mu = 0.2$  (top) and  $\mu = 0.5$  (bottom), at Lode angles of  $\theta = 0$  and  $\theta = 60^\circ$ , for which  $\sigma_{\text{axial}} = \sigma_z$ ,  $\epsilon_{\text{axial}} = \epsilon_z$ , and  $\sigma_{\text{lateral}} = \sigma_x = \sigma_y$ . Note that the peak friction angle  $\phi$  corresponds to the peak value of the stress ratio  $\sigma_{\text{axial}}/\sigma_{\text{lateral}}$  in the stress-strain curves of Figures 6.40–6.45. Thus, the stress-strain curves confirm that the axial strain corresponding to the (peak) material friction angle ranges from approximately  $4\% \leq |\epsilon_{\text{axial}}| \leq 6\%$  for all six specimens, which agrees with the maximal yield surfaces identified from the data points in Figures 6.1–6.6.

Regarding the average rate of friction work in the DEM specimens during the simulations, which is shown in Figure 6.28 for Specimens 1–3 and in Figure 6.29 for Specimens 4–6, several

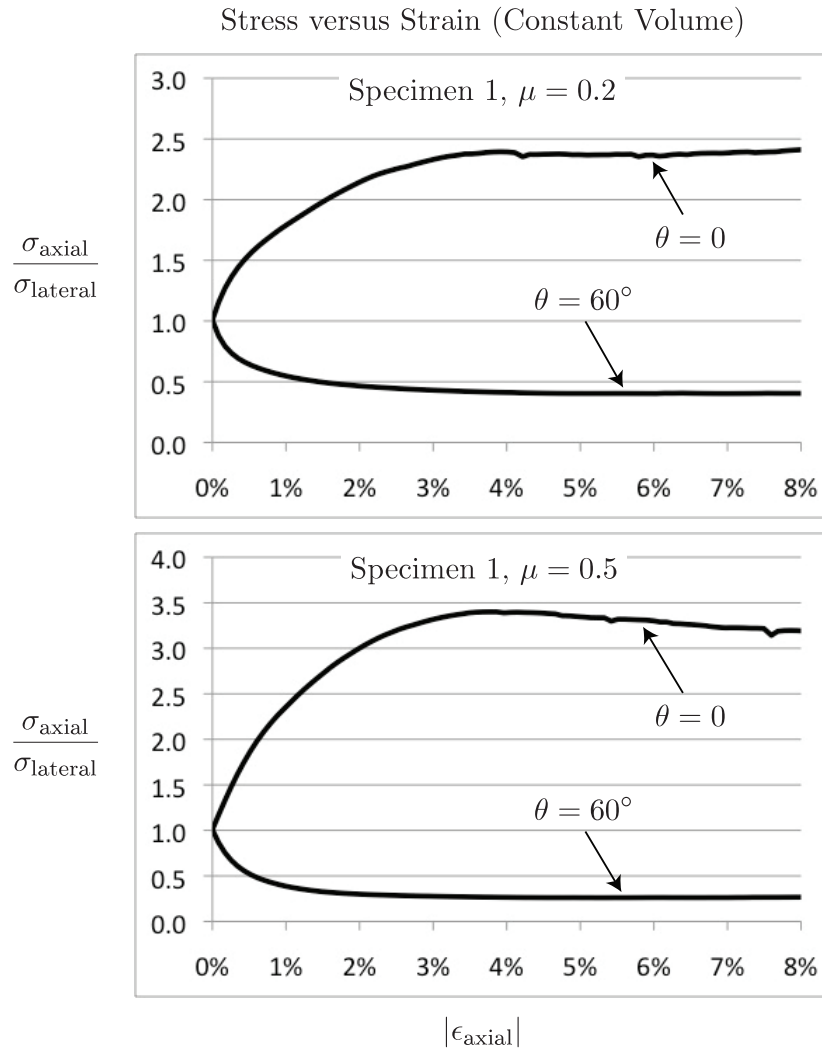


Figure 6.40: Stress ratio as a function of axial strain for Specimen 1 with an inter-element friction coefficient of  $\mu = 0.2$  (top) and  $\mu = 0.5$  (bottom), with particle rotation allowed. The two curves correspond to the data points on the yield surfaces shown in Figure 6.1 at Lode angles of  $\theta = 0$  and  $\theta = 60^\circ$ .

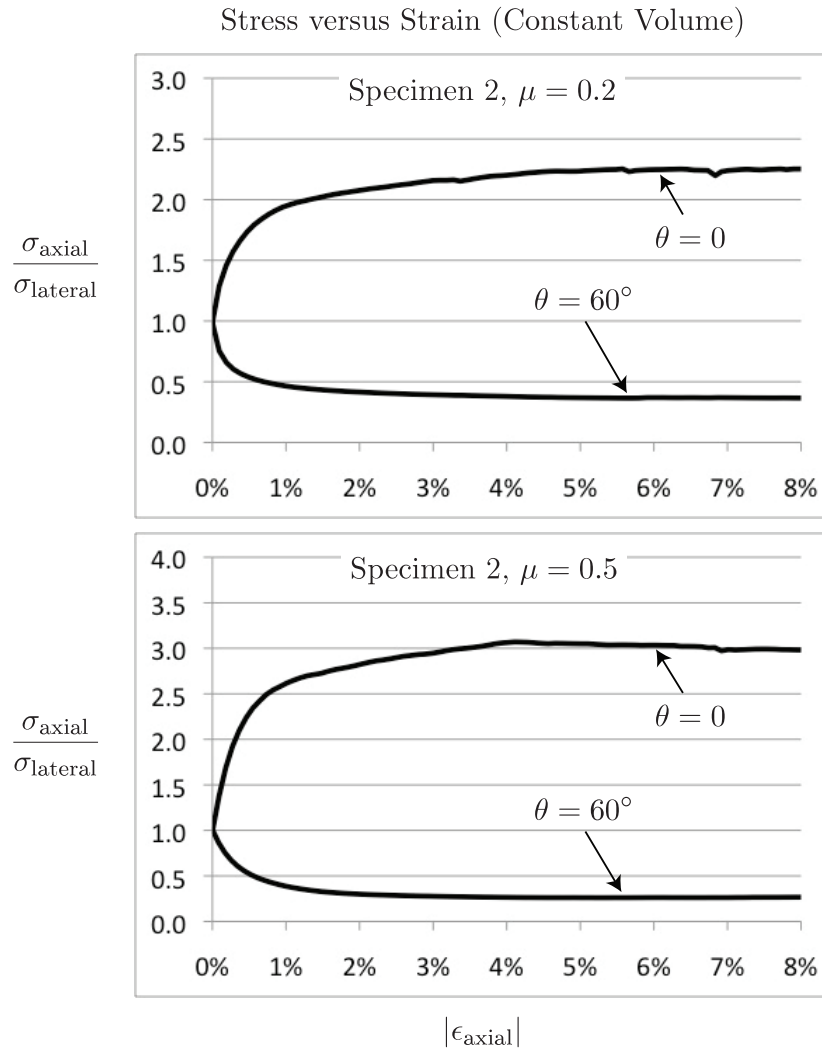


Figure 6.41: Stress ratio as a function of axial strain for Specimen 2 with an inter-element friction coefficient of  $\mu = 0.2$  (top) and  $\mu = 0.5$  (bottom), with particle rotation allowed. The two curves correspond to the data points on the yield surfaces shown in Figure 6.2 at Lode angles of  $\theta = 0$  and  $\theta = 60^\circ$ .

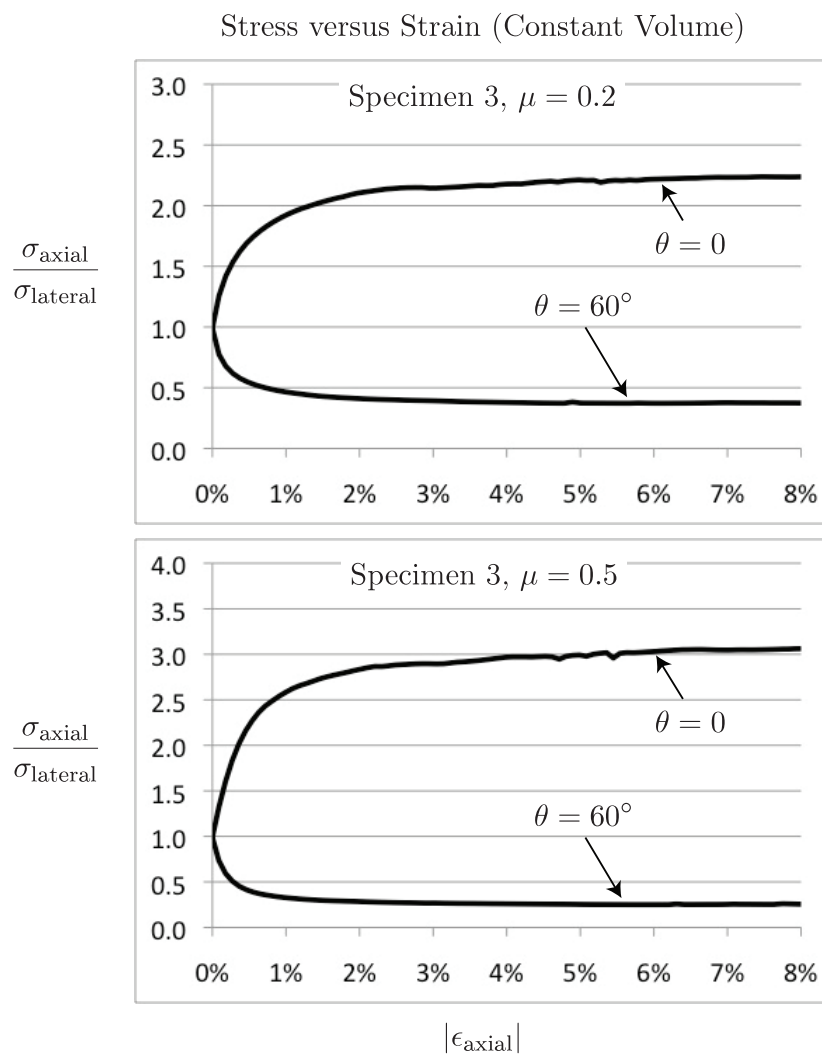


Figure 6.42: Stress ratio as a function of axial strain for Specimen 3 with an inter-element friction coefficient of  $\mu = 0.2$  (top) and  $\mu = 0.5$  (bottom), with particle rotation allowed. The two curves correspond to the data points on the yield surfaces shown in Figure 6.3 at Lode angles of  $\theta = 0$  and  $\theta = 60^\circ$ .

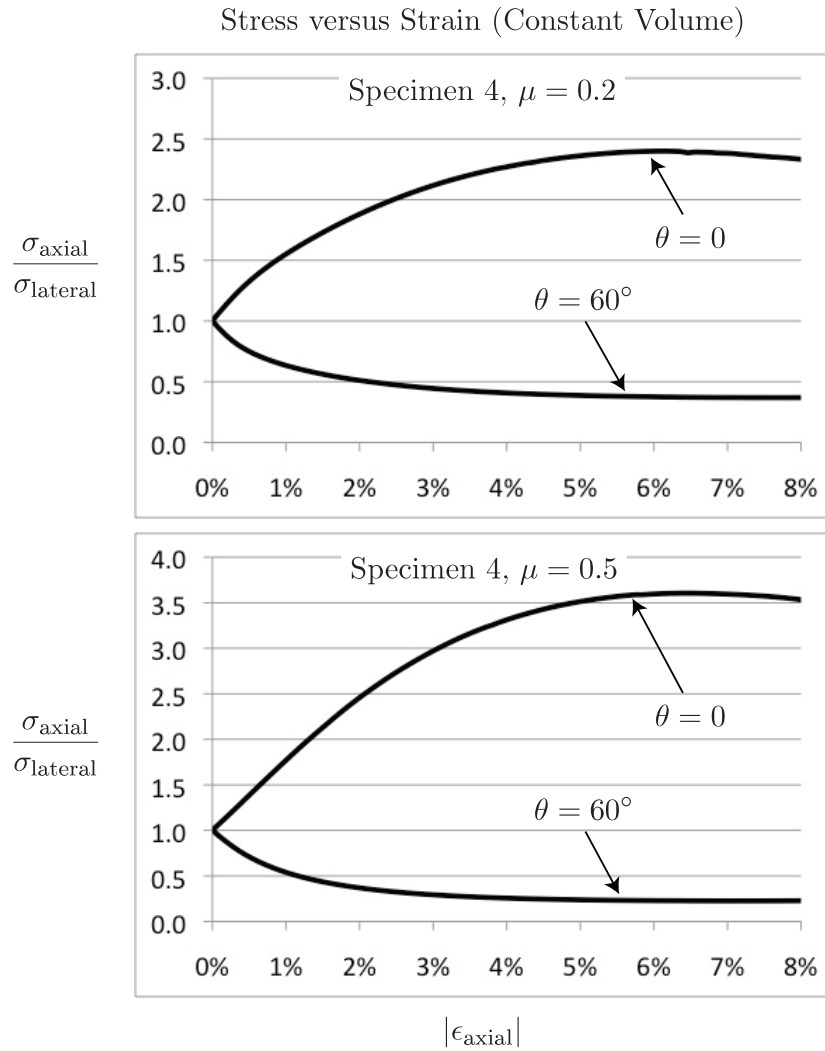


Figure 6.43: Stress ratio as a function of axial strain for Specimen 4 with an inter-element friction coefficient of  $\mu = 0.2$  (top) and  $\mu = 0.5$  (bottom), with particle rotation allowed. The two curves correspond to the data points on the yield surfaces shown in Figure 6.4 at Lode angles of  $\theta = 0$  and  $\theta = 60^\circ$ .

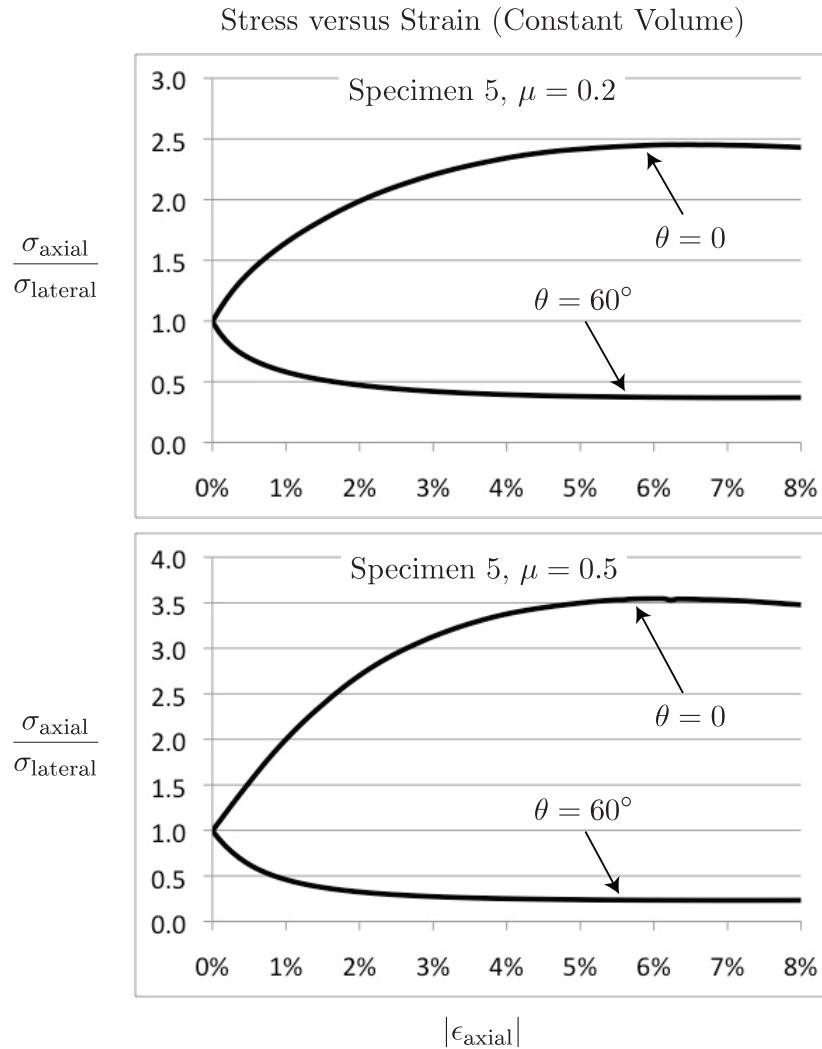


Figure 6.44: Stress ratio as a function of axial strain for Specimen 5 with an inter-element friction coefficient of  $\mu = 0.2$  (top) and  $\mu = 0.5$  (bottom), with particle rotation allowed. The two curves correspond to the data points on the yield surfaces shown in Figure 6.5 at Lode angles of  $\theta = 0$  and  $\theta = 60^\circ$ .

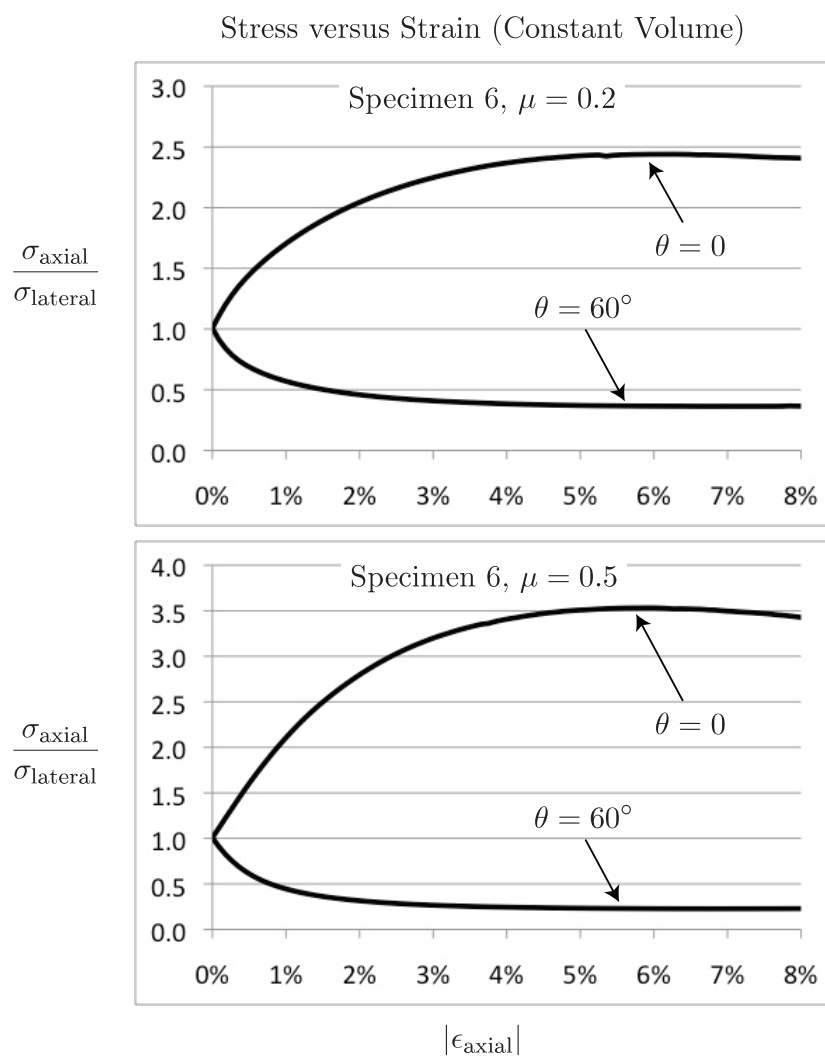


Figure 6.45: Stress ratio as a function of axial strain for Specimen 6 with an inter-element friction coefficient of  $\mu = 0.2$  (top) and  $\mu = 0.5$  (bottom), with particle rotation allowed. The two curves correspond to the data points on the yield surfaces shown in Figure 6.6 at Lode angles of  $\theta = 0$  and  $\theta = 60^\circ$ .

observations can be made. First, as noted in Section 5.6 for the case of no particle rotation, the rate of friction work and the material friction angle in the specimens appear to be uncorrelated, since there is a significantly larger variation in the rate of friction work between Specimen 1 and either Specimens 2 or 3, and between Specimen 4 and either Specimens 5 or 6, than there is in the material friction angle  $\phi$  for the same sets of specimens. In particular, at  $\phi_\mu = 26.6^\circ$  ( $\mu = 0.5$ ), between Specimens 1 and 2 the variation in the average rate of friction work is 72% while the variation in the material friction angle  $\phi$  is 8%. Second, regarding the rate of friction work for Specimens 1–3 shown in Figure 6.28, for  $\theta = 0$ , the friction work rate as a function of  $\phi_\mu$  is nearly symmetric about  $\phi_\mu = 45^\circ$ . This symmetry was not observed for the case of no particle rotation in Figure 5.24, and it is less pronounced for  $\theta = 60^\circ$  in Figure 6.28. However, regardless of Lode angle and whether or not particle rotation is allowed, the average rate of friction work goes to zero as  $\mu \rightarrow \infty$  ( $\phi_\mu \rightarrow 90^\circ$ ), while the material friction angle remains finite: either  $\phi = 90^\circ$  with particle rotation prohibited, or  $40^\circ < \phi < 47^\circ$  with particle rotation allowed.

Figures 6.46 and 6.47 show the friction work experienced by each element in Specimen 5 at 4% axial strain in compression and extension, respectively, during the DEM simulation corresponding to Lode angles of  $\theta = 0$  and  $\theta = 60^\circ$ , respectively, on the yield surface shown in Figure 6.5 (bottom), with an inter-element friction coefficient of  $\mu = 0.5$ . On the left side of Figures 6.46 and 6.47, the gray scale of each element denotes the friction work experienced by that element, varying from white for elements experiencing no friction work to black for elements experiencing friction work greater than or equal to 40 Joules in Figure 6.46 and 30 Joules in Figure 6.47. On the right side of Figures 6.46 and 6.47, only the elements experiencing friction work greater than or equal to 40 Joules or 30 Joules, respectively, are shown. Comparing Figures 6.46 and 6.47 with Figures 5.39 and 5.40, we observe that the general appearance of the per-element friction work distribution within Specimen 5 is similar whether or not particle rotation is allowed. However, there are some distinctions. Note that

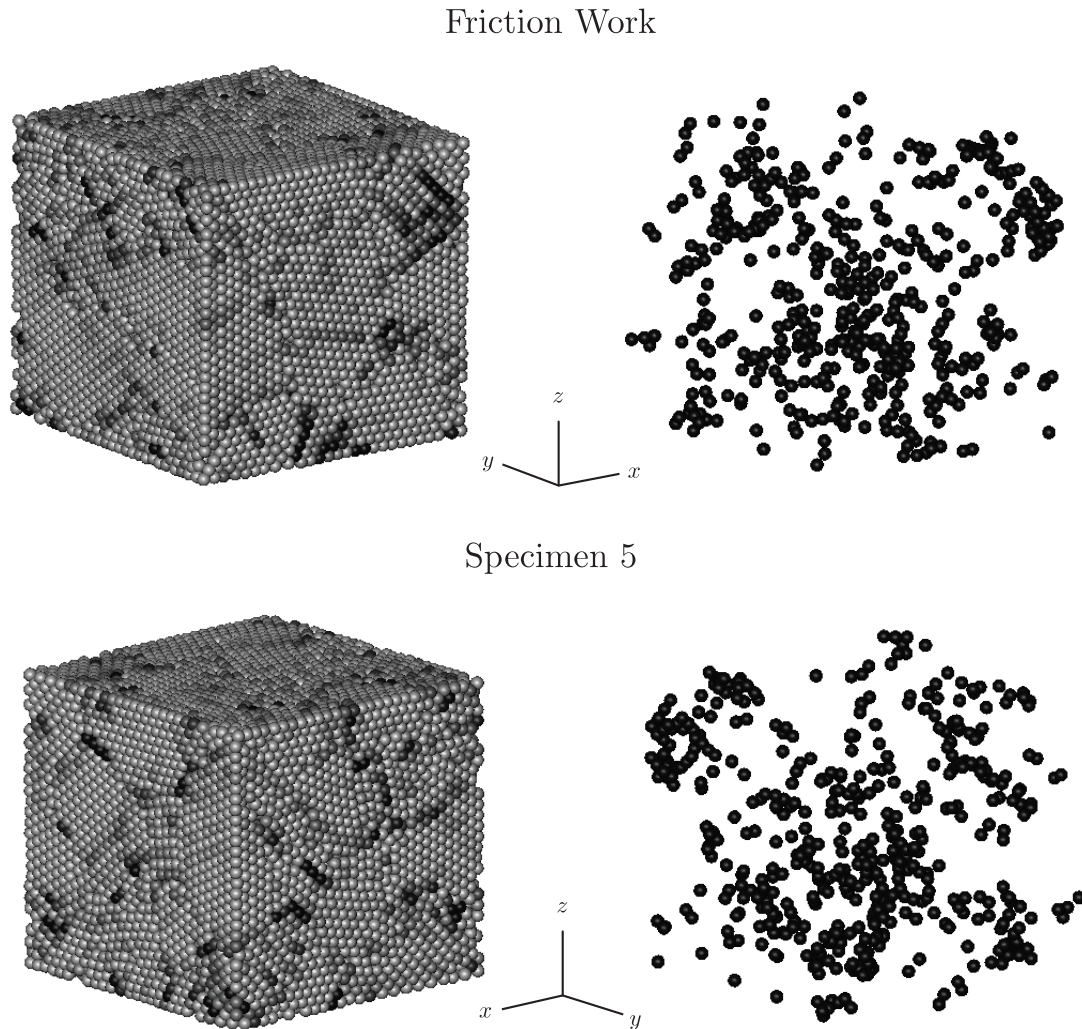
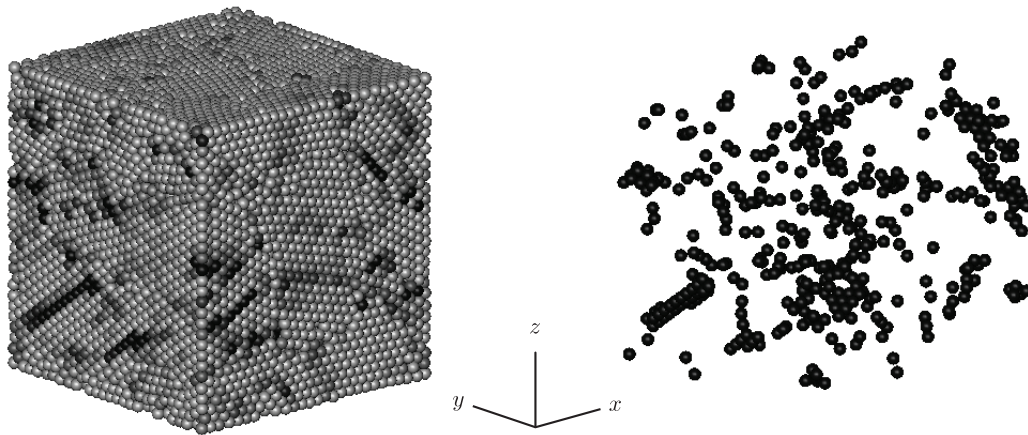


Figure 6.46: Friction work (designated by gray scale) experienced by each element in Specimen 5 at  $|\epsilon_z| = 4\%$  axial strain (compression) during the DEM simulation corresponding to a Lode angle of  $\theta = 0$  on the yield surface shown in Figure 6.5 with an inter-element friction coefficient of  $\mu = 0.5$ , with particle rotation allowed. Black elements experience friction work greater than or equal to 40 Joules. At this strain (4%), no local slip planes can be visually identified by per-element friction work.

## Friction Work



Specimen 5

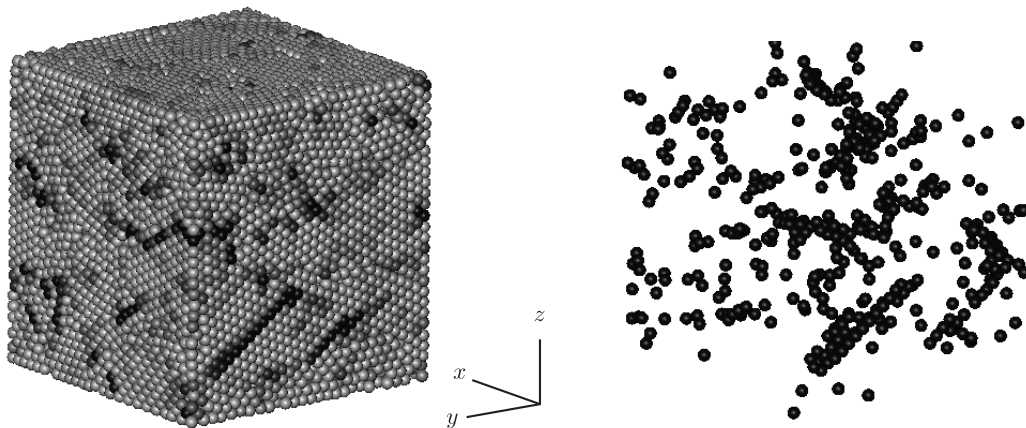


Figure 6.47: Friction work (designated by gray scale) experienced by each element in Specimen 5 at  $|\epsilon_z| = 4\%$  axial strain (extension) during the DEM simulation corresponding to a Lode angle of  $\theta = 60^\circ$  on the yield surface shown in Figure 6.5 with an inter-element friction coefficient of  $\mu = 0.5$ , with particle rotation allowed. Black elements experience friction work greater than or equal to 30 Joules. At this strain (4%), no local slip planes can be visually identified by per-element friction work.

the orientations of Specimen 5 in Figures 6.46 and 5.39 and in Figures 6.47 and 5.40 are intentionally the same, to facilitate comparison. A close comparison shows that elements in some regions of Specimen 5 that experience significant friction work when particle rotation is prohibited experience little or no friction work when particle rotation is allowed. Also, fewer (if any) slip planes can be visually identified by per-element friction work when particle rotation is allowed, and friction work appears to occur instead along “chains” of elements. This is in general agreement with the observations of Oda (1997), who observed that failure in real sand seems to occur when force-chains or “strong force networks” of contacting particles become unstable and “buckle”, which would result in friction work being highest along these buckling force-chains due to elements in the force-chains sliding relative to adjacent elements outside of the force-chains, in so-called “weak clusters”.

Since particle rotation was allowed in the DEM simulations performed for this chapter, we can also examine the angular velocities of individual particles within the specimens. As we did for the elastic range in Section 4.5, we can compute the ratio  $\langle \Omega \rangle_{\max}^{\leq |\epsilon_{\text{axial}}|} / \langle \Omega \rangle_{\text{avg}}^{\leq |\epsilon_{\text{axial}}|}$  for each specimen for a range of values of the axial strain  $|\epsilon_{\text{axial}}|$ , where  $\Omega$  is the magnitude of the angular velocity of an individual particle in a specimen, the angled brackets  $\langle \rangle^{\leq |\epsilon_{\text{axial}}|}$  denote root-mean-square time average over the course of a simulation up to the axial strain  $|\epsilon_{\text{axial}}|$ , and the subscripts “max” and “avg” denote maximum and rms-average values over all particles in the specimen. Figures 6.48 and 6.49 show this ratio as a function of axial strain  $|\epsilon_{\text{axial}}|$  for Specimens 1–3 and Specimens 4–6, respectively, during the DEM simulations corresponding to Lode angles of  $\theta = 0$  (top) and  $\theta = 60^\circ$  (bottom) on the yield surface shown in Figure 6.5 with an inter-element friction coefficient of  $\mu = 0.5$ . Figures 6.48 and 6.49 show that the maximum angular velocity of particles within Specimens 1–3 can be anywhere from 10 to 60 times the average particle angular velocity, and the maximum angular velocity of particles within Specimens 4–6 is frequently in excess of 100 times the average particle angular velocity, for both  $\theta = 0$  and  $\theta = 60^\circ$ .

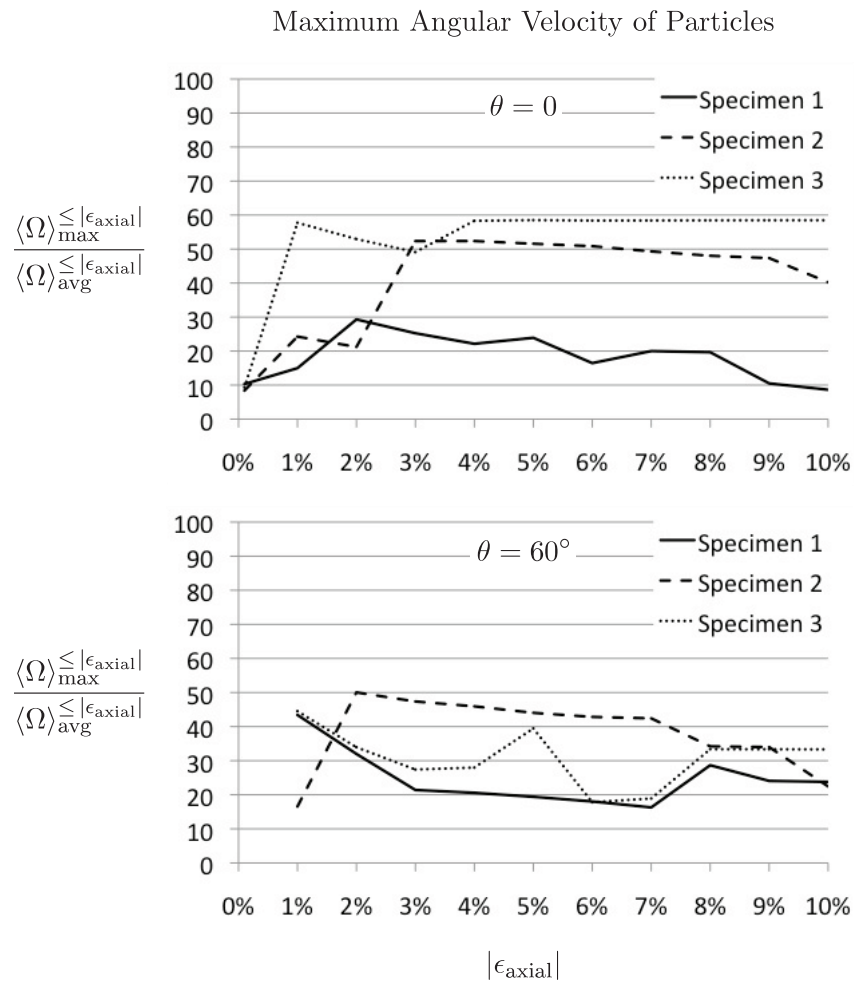


Figure 6.48: The ratio of maximum to rms-average angular velocity of particles, where the angled brackets  $\langle \rangle^{\leq |\epsilon_{\text{axial}}|}$  denote root-mean-square time average over the course of a simulation up to the axial strain  $|\epsilon_{\text{axial}}|$ , as a function of  $|\epsilon_{\text{axial}}|$  for Specimens 1–3 with inter-element friction coefficient  $\mu = 0.5$  at Lode angles of  $\theta = 0$  (top) and  $\theta = 60^\circ$  (bottom).

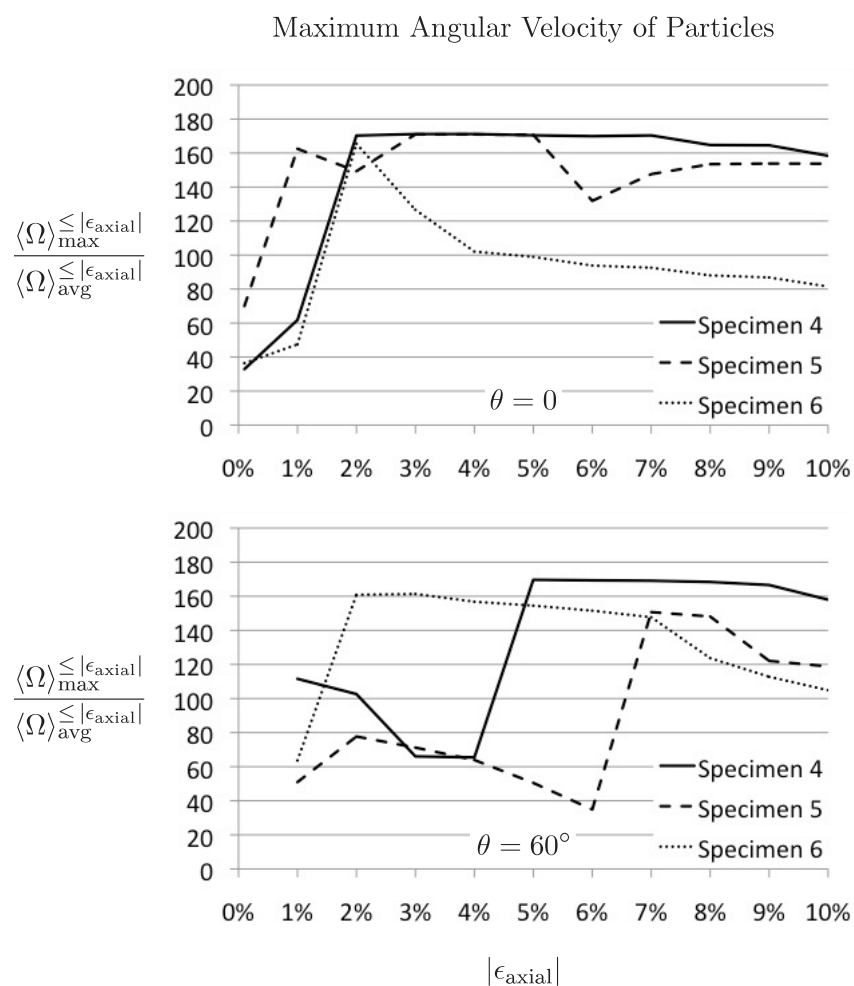


Figure 6.49: The ratio of maximum to rms-average angular velocity of particles, where the angled brackets  $\langle \rangle^{\leq |\epsilon_{\text{axial}}|}$  denote root-mean-square time average over the course of a simulation up to the axial strain  $|\epsilon_{\text{axial}}|$ , as a function of  $|\epsilon_{\text{axial}}|$  for Specimens 4–6 with inter-element friction coefficient  $\mu = 0.5$  at Lode angles of  $\theta = 0$  (top) and  $\theta = 60^\circ$  (bottom).

For the simulations performed for this chapter, the Discrete Element Method also allows us to examine the rotation of individual particles, as we did in Figure 4.9 of Section 4.5. Figures 6.50 and 6.51 show the rotational kinetic energy of elements in Specimen 5 at an axial strain of  $|\epsilon_z| = 4\%$  during the DEM simulation corresponding to Lode angles of  $\theta = 0$  and  $\theta = 60^\circ$ , respectively, on the yield surface shown in Figure 6.5 (bottom), with an inter-element friction coefficient of  $\mu = 0.5$ . Black elements have rotational kinetic energy greater than or equal to 100 nano-Joules in both figures. For reference, the mass of each element (sphere) in all six specimens is 5.24 g. Note that the per-element rotational kinetic energy is small because the DEM simulations are quasi-static.

Figures 6.50 and 6.51 confirm the existence of force-chains in Specimen 5 at  $|\epsilon_z| = 4\%$  axial strain. Note that contacting elements in strong force networks will experience larger rotational kinetic energy than elements in the surrounding weak-clusters as the force-chains become unstable and buckle. Numerous such chains of elements can be seen in Figures 6.50 and 6.51 on the right. Note that no clear slip planes can be seen in Figures 6.50 and 6.51. This suggests that the buckling of force-chains is the dominant mode of failure during the initiation of yield. A comparison of Figure 6.50 with 6.51 also shows that more particle rotation occurs in Specimen 5 during compression than during extension.

As axial strain increases, slip planes begin to appear. Figures 6.52 and 6.53 show the rotational kinetic energy of elements in Specimen 5 at an axial strain of  $|\epsilon_z| = 7\%$  during the DEM simulation corresponding to Lode angles of  $\theta = 0$  and  $\theta = 60^\circ$ , respectively, on the yield surface shown in Figure 6.5 (bottom), with an inter-element friction coefficient of  $\mu = 0.5$ . Black elements have rotational kinetic energy greater than or equal to 200 nano-Joules in Figure 6.52, and 100 nano-Joules in Figure 6.53. Figures 6.52 and 6.53 reveal that at an axial strain of  $|\epsilon_z| = 7\%$ , particle rotation in Specimen 5 occurs primarily on well-defined global slip planes, during both compression ( $\theta = 0$ ) and extension ( $\theta = 60^\circ$ ). These slip systems remain active in Specimen 5 over a range of axial strain of approximately  $7\% \leq |\epsilon_z| \leq 9\%$ .

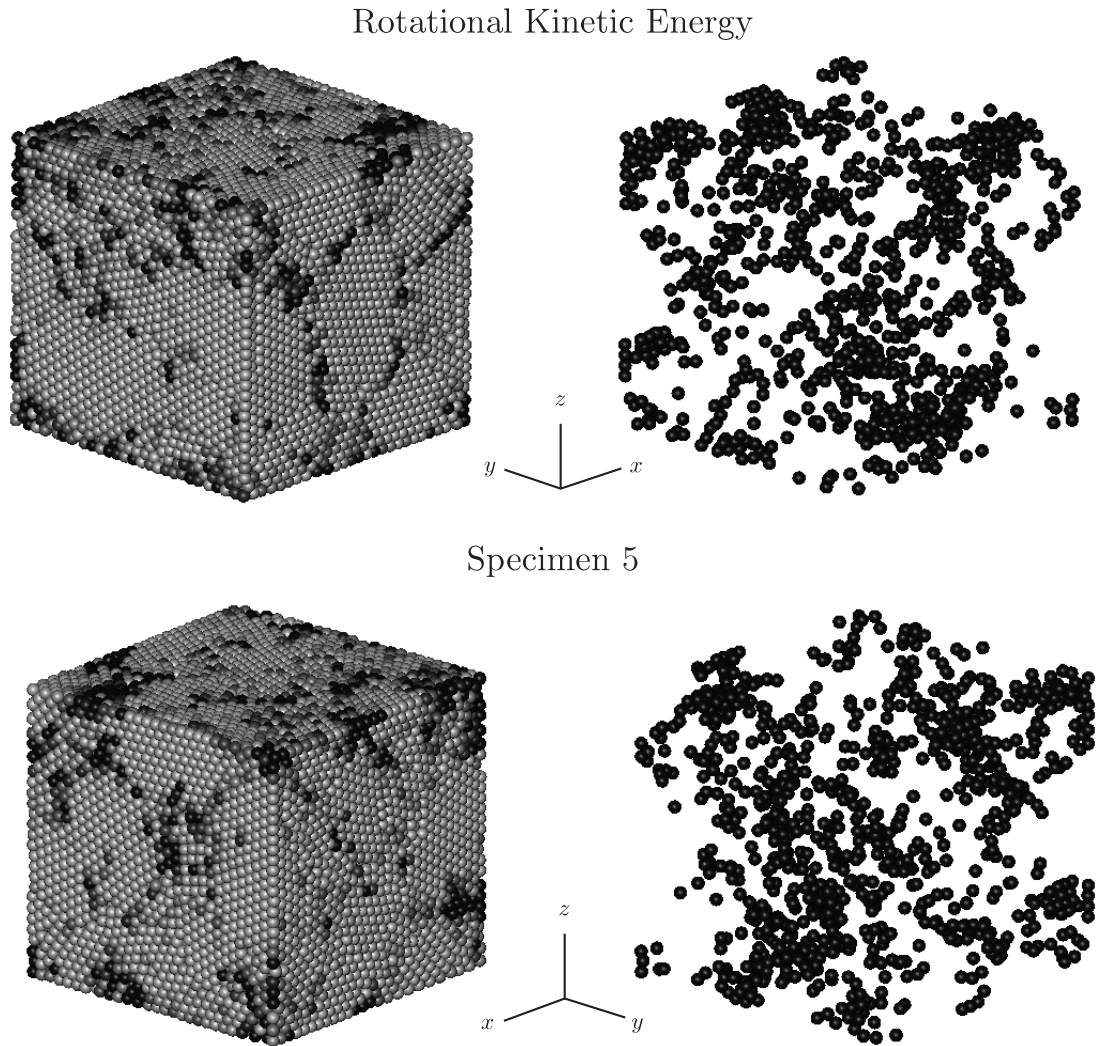


Figure 6.50: Rotational kinetic energy (designated by gray scale) of each element in Specimen 5 at  $|\epsilon_z| = 4\%$  axial strain (compression) during the DEM simulation corresponding to a Lode angle of  $\theta = 0$  on the yield surface shown in Figure 6.5 with an inter-element friction coefficient of  $\mu = 0.5$ . Black elements have rotational kinetic energy greater than or equal to 100 nano-Joules. At this strain (4%), no local slip planes can be visually identified by per-element rotational kinetic energy.

## Rotational Kinetic Energy

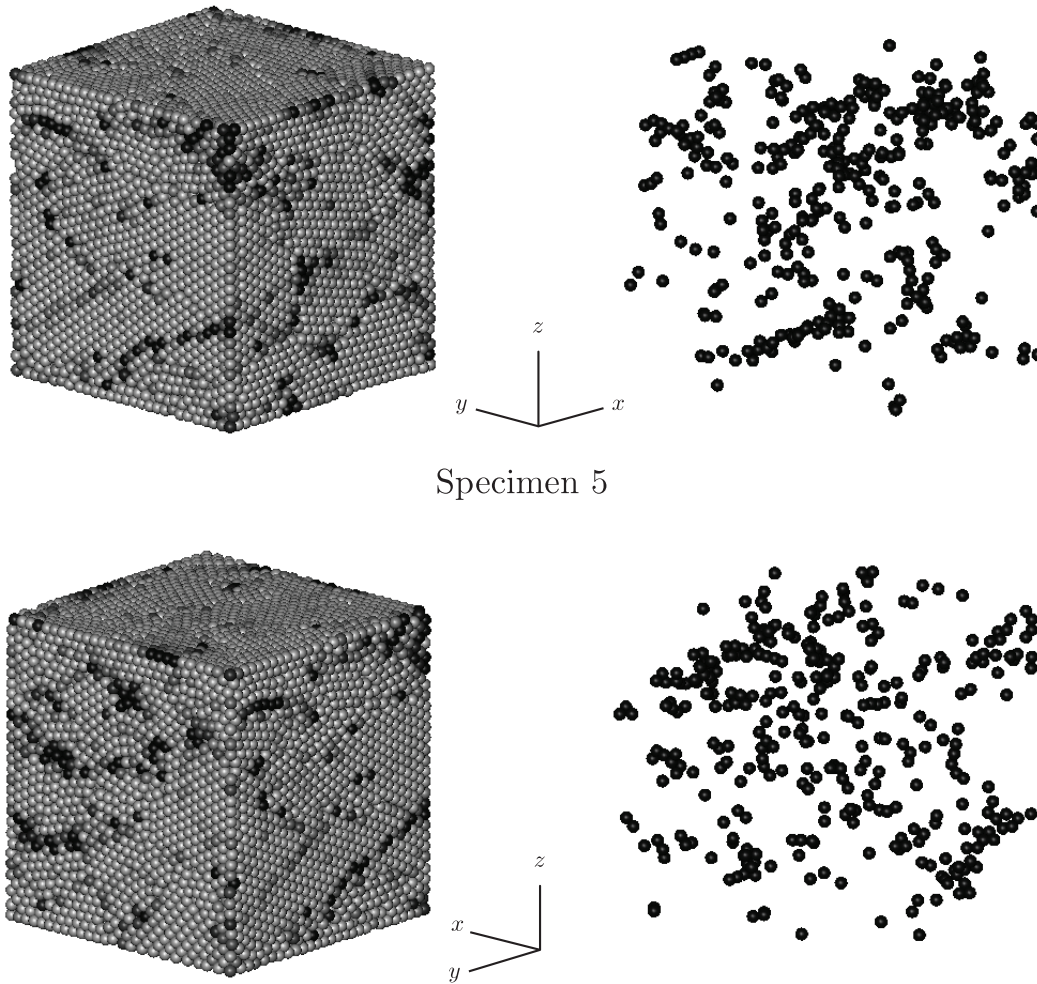


Figure 6.51: Rotational kinetic energy (designated by gray scale) of each element in Specimen 5 at  $|\epsilon_z| = 4\%$  axial strain (extension) during the DEM simulation corresponding to a Lode angle of  $\theta = 60^\circ$  on the yield surface shown in Figure 6.5 with an inter-element friction coefficient of  $\mu = 0.5$ . Black elements have rotational kinetic energy greater than or equal to 100 nano-Joules. At this strain (4%), no local slip planes can be visually identified by per-element rotational kinetic energy.

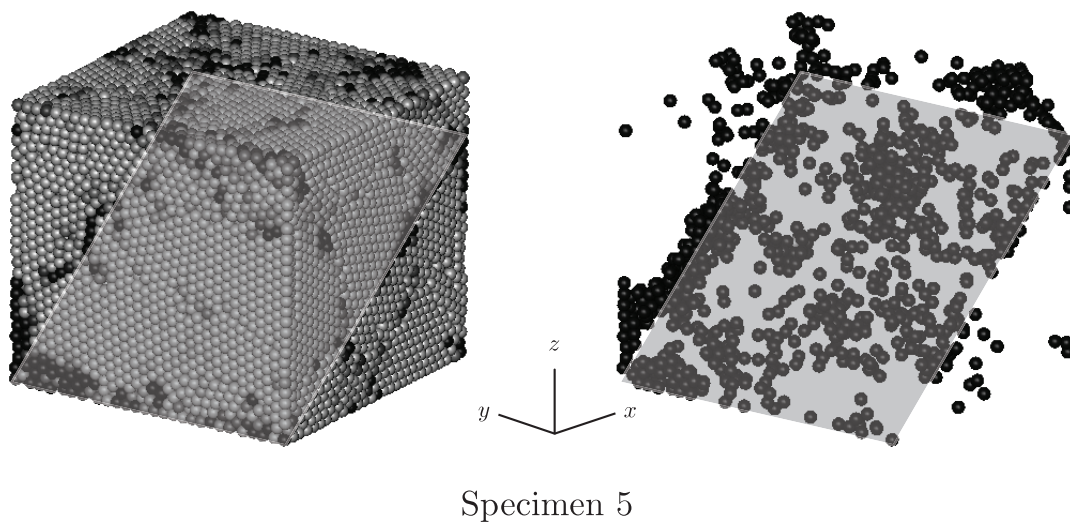


Figure 6.52: Rotational kinetic energy (designated by gray scale) of each element in Specimen 5 at  $|\epsilon_z| = 7\%$  axial strain (compression) during the DEM simulation corresponding to a Lode angle of  $\theta = 0$  on the yield surface shown in Figure 6.5 with an inter-element friction coefficient of  $\mu = 0.5$ . Black elements have rotational kinetic energy greater than or equal to 200 nano-Joules. At this strain (7%), a well-defined global slip plane (shaded) can be visually identified by per-element rotational kinetic energy.

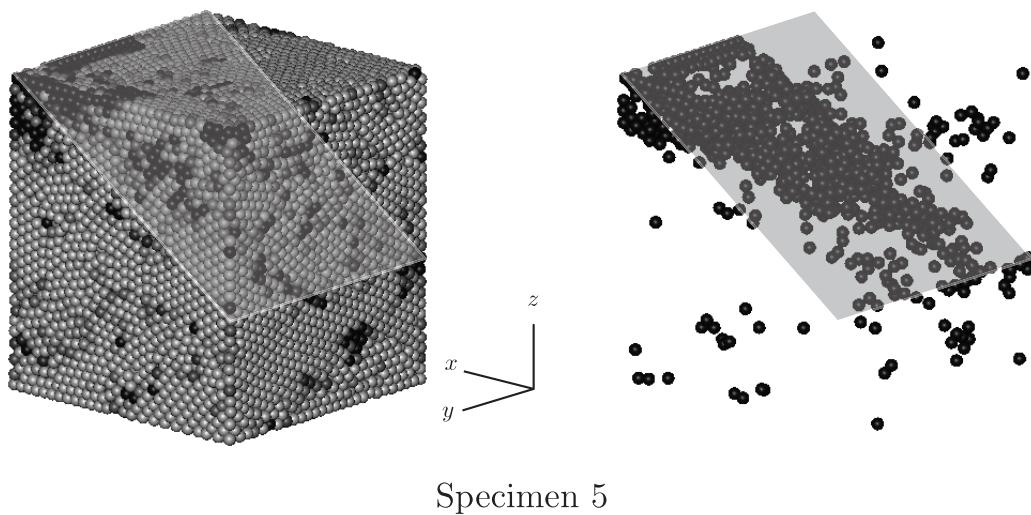


Figure 6.53: Rotational kinetic energy (designated by gray scale) of each element in Specimen 5 at  $|\epsilon_z| = 7\%$  axial strain (extension) during the DEM simulation corresponding to a Lode angle of  $\theta = 60^\circ$  on the yield surface shown in Figure 6.5 with an inter-element friction coefficient of  $\mu = 0.5$ . Black elements have rotational kinetic energy greater than or equal to 100 nano-Joules. At this strain (7%), a well-defined global slip plane (shaded) can be visually identified by per-element rotational kinetic energy.

Referring to Figure 6.44, the (peak) material friction angle  $\phi$  is reached in Specimen 5 for both  $\theta = 0$  and  $\theta = 60^\circ$  at  $|\epsilon_z| \approx 6\%$  axial strain with the maximum value of the stress ratio  $\sigma_{\text{axial}}/\sigma_{\text{lateral}}$ . Thus, we note from Figures 6.50–6.53 that the mode of failure in Specimen 5 for both  $\theta = 0$  and  $\theta = 60^\circ$  seems to change dramatically from the buckling of force-chains during the initiation of yielding, at an axial strain of  $|\epsilon_z| = 4\%$ , shortly *before* the (peak) material friction angle  $\phi$  is reached, to sliding along well-defined global slip planes during sustained yielding, at an axial strain of  $|\epsilon_z| = 7\%$ , immediately *after* the (peak) material friction angle  $\phi$  is reached.

## 6.6 Conclusion

In this chapter, we have extended the results of Chapter 5 to include the effects of particle rotation. We have determined yield surfaces on the  $\pi$ -plane for a full range of Lode angles  $0 \leq \theta \leq 60^\circ$  for six DEM specimens consisting of 3 430–29 660 randomly packed uniform spheres with uniform inter-element friction coefficient  $\mu$ , with  $0.01 \leq \mu \leq 100.0$  for the 3 430-element specimens and  $0.01 \leq \mu \leq 0.8$  for the 29 660-element specimens. The data points on the  $\pi$ -plane were obtained for each specimen for each inter-element friction coefficient from sixteen DEM simulations of true triaxial tests under constant-volume conditions, which amounted to 1 296 simulations (in addition to the 1 296 simulations performed for Chapter 5, performed using a modified version of the open-source code LAMMPS (Plimpton, 1995, LAMMPS) running on a 12-processor Mac Pro workstation.

As in Chapter 5, the main results of this chapter are the yield surfaces themselves, shown in Figures 6.13–6.18 for Specimens 1–6, respectively, and the resulting relationships between the inter-particle friction coefficient  $\mu$  (or the inter-particle friction angle  $\phi_\mu = \tan^{-1} \mu$ ) on the microscale and the (peak) material friction angle  $\phi$  on the macroscale for each specimen, which are shown in Figures 6.25 and 6.27. We will return to this relationship

in Chapter 8 where we derive relationships between  $\phi_\mu$  and  $\phi$  by analytical means based on micromechanics.

A comparison of the shapes of the yield surfaces obtained from our DEM simulations with those predicted by the Mohr-Coulomb, Drucker-Prager, Lade-Duncan, and Matsuoka-Nakai criteria for given values of the material friction angle  $\phi$  shows that the DEM data points are best represented for all values of the Lode angle  $\theta$  by the Lade-Duncan yield criterion, in particular for  $\theta = 60^\circ$  (extension). A comparison of the yield surfaces obtained in this chapter with those obtained in Chapter 5 shows that the relative performance of the yield criteria for each specimen is essentially the same regardless of whether particle rotation is allowed or prohibited in the DEM simulations.

We took advantage of the discrete element method to explore friction work on an element-by-element basis within each specimen, and to compute the average rate of friction work in each specimen as a function of the inter-element friction coefficient  $\mu$ , which is shown in Figures 6.28 and 6.29. We found that the average rate of friction work within the specimens can vary by more than 50% without significantly altering the material friction angle  $\phi$ . We also monitored particle rotation, and plotted the ratio of maximum particle angular velocity to average particle angular velocity in each specimen for an inter-element friction coefficient of  $\mu = 0.5$ , which according to Mitchell and Soga (2005) is a typical value of the inter-particle friction coefficient for quartz sand, both wet and dry. We found that the maximum angular velocity of particles within the specimens was frequently over 100 times the average angular velocity.

An exploration of friction work and rotational kinetic energy of individual particles within one of the specimens allowed us to observe modes of failure, both at the initiation of yield and during sustained yielding. We found that before the peak material friction angle is reached, the primary mode of failure appears to be the buckling of force-chains, with no well-defined slip planes present in the specimen, while after the peak material friction angle

is reached, the failure mode shifts to sliding along well-defined slip planes. This can be seen in Figures 6.50–6.53 showing the rotational kinetic energy of the particles in Specimen 5 (consisting of 29 660 spheres) at axial strains of 4% and 7%, before and immediately after the (peak) material friction angle is reached (at an axial strain of approximately 6%). The transition from local force-chain buckling before the peak material friction angle is reached to sliding along well-defined slip planes after the peak material friction angle is reached is clearly illustrated by comparing these figures.

## Chapter 7

# Micromechanical analysis of Yield in Isotropic Non-Cohesive Particulate Materials, Part I: No Particle Rotation

### 7.1 Abstract

We now turn our attention to a direct micromechanics derivation of the yield surface for a statistically isotropic non-cohesive particulate material to correspond with the yield surfaces obtained by DEM simulations in Chapter 5. We base our derivation on a direct micromechanical analysis of three local packing geometries: face-centered cubic (FCC), simple cubic (SC), and body-centered cubic (BCC), as we did for the elastic range in Chapter 3. In this chapter, as in Chapter 3 and the DEM simulations performed for Chapter 5, we assume that no particle rotation occurs. In Chapter 8, as in Chapter 4 and the DEM simulations performed for Chapter 6, we will remove this restriction. By itself, the assumption of no particle rotation is generally unrealistic, but it is useful to lay a theoretical foundation for the case of particle rotation that follows in Chapter 8.

## 7.2 Introduction

In Chapter 5, we used the Discrete Element Method (DEM) to determine complete yield surfaces in three-dimensional principal stress space (on the  $\pi$ -plane) for a series of specimens of 3 430–29 660 randomly packed uniform spheres. In these DEM simulations, the inter-particle contact forces are modeled as linear springs in both the normal and tangential directions before the initiation of sliding, with  $F_n = K_n \delta_n$  and  $F_t = K_t \delta_t$  for  $F_t < \mu F_n$  and  $\delta_n > 0$  (i.e., no inter-particle cohesion), and with the initiation of inter-particle tangential sliding occurring when the Coulomb friction criterion  $F_t = \mu F_n$  is reached, where  $\mu$  is the inter-particle friction coefficient. For each specimen, sets of DEM simulations of true triaxial tests were performed to obtain complete yield surfaces on a  $\pi$ -plane for a full range of Lode angles  $0 \leq \theta \leq 60^\circ$ . The same DEM simulations were repeated for each specimen for a wide range of inter-particle friction coefficients: with  $0.01 \leq \mu \leq 100.0$  for the 3 430-element specimens (Specimens 1–3) and  $0.01 \leq \mu \leq 0.8$  for the 29 660-element specimens (Specimens 4–6). See Section 5.4 for a description of these simulations.

From the yield surfaces in Chapter 5, we obtained a relationship between the inter-particle friction coefficient  $\mu$  and the peak material friction angle  $\phi$  for each specimen (corresponding to a Lode angle of zero, or compression). This relationship can be expressed in terms of an inter-particle friction angle  $\phi_\mu = \tan^{-1} \mu$  and the peak material friction angle  $\phi$ . Alternatively, the same relationship could be expressed in terms of the inter-particle friction coefficient  $\mu$  and a material or macroscopic friction coefficient  $\mu_{\text{macro}} = \tan \phi$  associated with the peak material friction angle  $\phi$ . The resulting relationship between  $\phi_\mu$  and  $\phi$  for the case of no particle rotation is shown in Figure 5.22 for all six specimens for  $0.01 \leq \mu \leq 0.8$  and in Figure 6.27 for Specimens 1–3 for  $0.01 \leq \mu \leq 100.0$ .

In this chapter, we perform a micromechanical analysis of the initiation of yield along slip planes in three specific local packing geometries of uniform spheres: face-centered cubic

(FCC), simple cubic (SC), and body-centered cubic (BCC). We use these results to analytically relate the inter-particle friction coefficient  $\mu$  to the material friction angle  $\phi$  in a statistically isotropic assembly of (non-cohesive) uniform spheres under the static homogenization hypothesis. The implicit assumption in such an analysis is that in a statistically isotropic assembly slip occurs locally in one or more randomly oriented locally-cubic packings of spheres along one or more of the slip planes associated with these locally-cubic packings. This approach is analogous to the approach successfully employed for the elastic range in Chapters 3 and 4 [Fleischmann et al. (2013a,b)].

The usefulness of our analytical approach rests on its ability to model true isotropic particulate materials. To judge whether or not our approach succeeds in doing this, we compare the  $\phi$  versus  $\phi_\mu$  curves determined theoretically in this chapter to those obtained for the DEM specimens of Chapter 5. We find that the relationship between  $\phi_\mu$  and  $\phi$  derived theoretically for a locally FCC (but globally isotropic) particulate material provides a reasonably good match for all six DEM specimens, particularly Specimen 4 consisting of 29 660 spheres. We also introduce a generalized model based on a micromechanical characterization of the geometry of any local slip system, which generalizes the slip systems of the local FCC, BCC, and SC packings. We find that this generalized model can be adjusted to match the DEM data points even more closely (with particle rotation prohibited).

In analogy with Chapter 3 for the elastic range, the DEM simulations of Chapter 5 were performed with particle rotation prohibited, and the corresponding micromechanical analysis of this chapter likewise assumes that no particle rotation takes place during yielding. By itself, the assumption of no particle rotation is generally unrealistic, but it is useful for comparison with and to lay a theoretical foundation for the case of particle rotation that follows in Chapter 8.

## 7.3 Yield on Slip Planes for Regular Arrays of Uniform Spheres

In this section, we determine the slip planes and yield conditions for three regular cubic arrays of uniform spheres: face-centered cubic (FCC), simple cubic (SC), and body-centered cubic (BCC). For analyses of the elastic behavior of the same three cubic arrays, including the definitions of the fourth-order tensor of second-order elastic moduli  $C_{ijkl}$  and the linearization of the inter-particle contact force laws, see Section 3.3.

### 7.3.1 Face-Centered Cubic (FCC) Array of Uniform Spheres

In a regular face-centered cubic array of uniform spheres subjected to an initial isotropic compressive stress  $\sigma_0$ , the initial normal contact force between the spheres is  $F_n = F_0 = \sqrt{2}r^2\sigma_0$  (Deresiewicz, 1958a). This initial normal contact force  $F_n$  can be used to linearize the inter-particle Hertz-Mindlin contact force-displacement law by providing constant values for the inter-particle normal and tangential contact stiffnesses  $K_n$  and  $K_t$  from equations (3.7) and (3.8) of Section 3.3.

Figure 7.1 shows an elementary cell of the face-centered cubic (FCC) array of uniform spheres with the visible spheres numbered, and three of the 12 crystallographically similar slip planes. Figure 7.2 shows all 14 spheres in an FCC elementary cell in four separate layers viewed in a direction normal to the three slip planes shown in Figure 7.1. The numbering of the spheres in Figure 7.2 corresponds to the numbering of the visible spheres in Figure 7.1. The unit vector normal to the slip planes shown in Figure 7.1 is  $\hat{u}_n = (\hat{i} + \hat{j} + \hat{k})/\sqrt{3}$ . The preferential slip directions on the slip planes for each layer shown in Figure 7.2 relative to

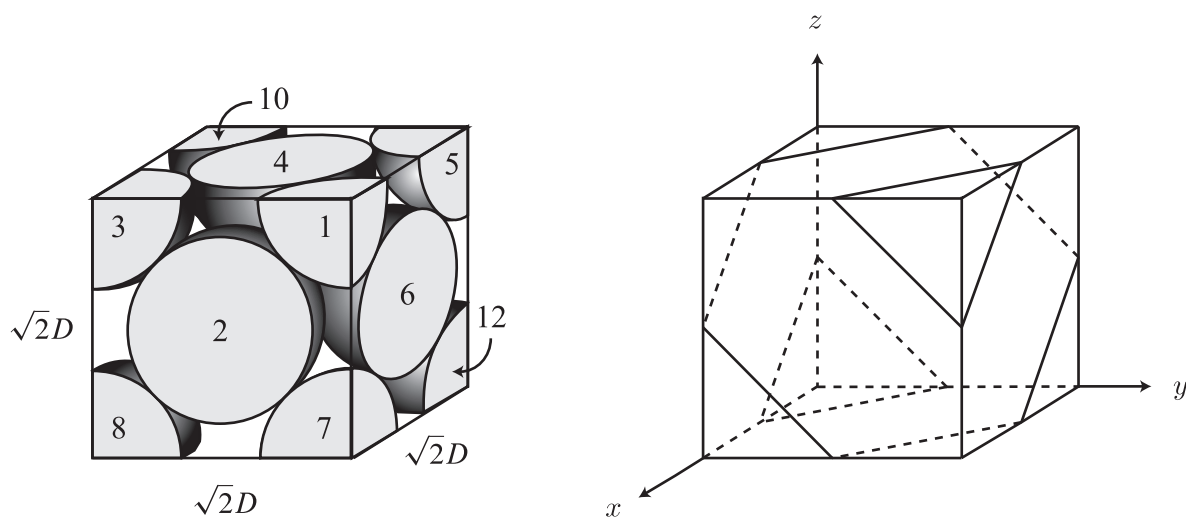


Figure 7.1: Left: Elementary cell of the face-centered cubic (FCC) array of uniform spheres analyzed in this section. Right: Three of the 12 crystallographically similar slip planes for the FCC regular cubic array.

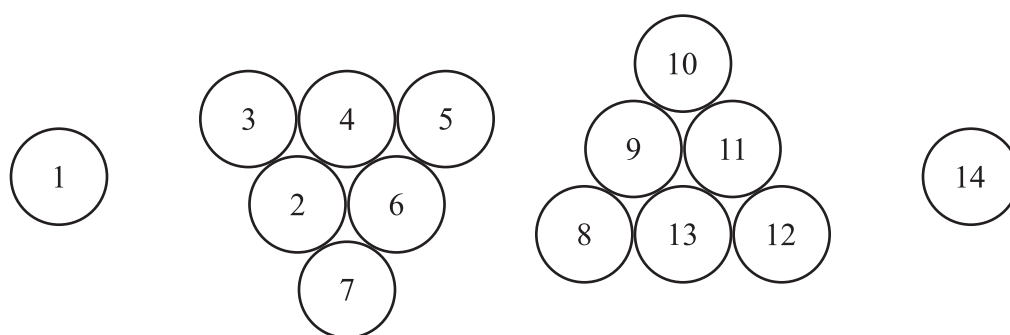


Figure 7.2: Four separate layers of spheres in an FCC elementary cell viewed in a direction normal to the three slip planes shown in Figure 7.1. The numbering of the spheres corresponds to the numbering of the visible spheres in Figure 7.1.

the layer underneath it, viewed in the  $-\hat{u}_n$  direction, are given by

$$\hat{u}_1 = -\frac{2}{\sqrt{6}}\hat{i} + \frac{1}{\sqrt{6}}\hat{j} + \frac{1}{\sqrt{6}}\hat{k}, \quad (7.1)$$

$$\hat{u}_2 = \frac{1}{\sqrt{6}}\hat{i} - \frac{2}{\sqrt{6}}\hat{j} + \frac{1}{\sqrt{6}}\hat{k}, \quad (7.2)$$

$$\hat{u}_3 = \frac{1}{\sqrt{6}}\hat{i} + \frac{1}{\sqrt{6}}\hat{j} - \frac{2}{\sqrt{6}}\hat{k}. \quad (7.3)$$

The unit vectors  $\hat{u}_1$ ,  $\hat{u}_2$ , and  $\hat{u}_3$  are the preferential slip directions on the three slip planes shown in Figure 7.1 (right) with unit normal vector  $\hat{u}_n = (\hat{i} + \hat{j} + \hat{k})/\sqrt{3}$ , and are shown in Figure 7.3 next to an FCC elementary cell viewed in the  $-\hat{u}_n$  direction. The preferential slip directions and unit normal vectors for the other nine crystallographically similar slip planes are obtained by renaming the coordinate axes.

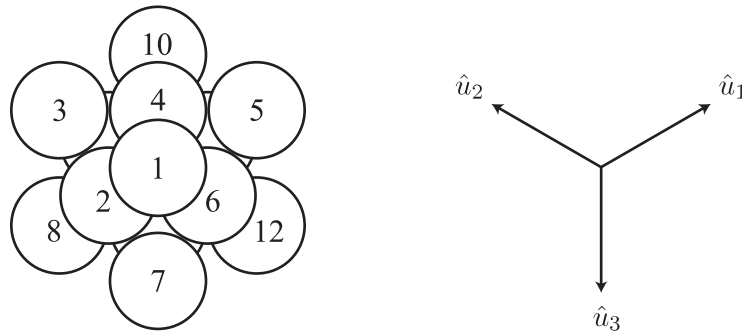


Figure 7.3: The preferential slip directions for each layer of an FCC elementary cell relative to the layer underneath it, viewed in a direction normal to the three slip planes shown in Figure 7.1. The numbering of the spheres corresponds to the numbering of the spheres in Figure 7.1 and Figure 7.2.

Note that when layers of spheres above and below a slip plane in an FCC elementary cell slide relative to one another in one of the preferential slip directions  $\hat{u}_1$ ,  $\hat{u}_2$ , or  $\hat{u}_3$ , they will experience motion normal to the slip plane in the  $\hat{u}_n$  direction as well as in the slip direction  $\hat{u}_i$ . This motion normal to the slip plane results in dilation. Also note that both the normal and tangential inter-particle contact forces between the contacting spheres contribute to the

resultant forces in both the  $\hat{u}_i$  and  $\hat{u}_n$  directions, tangent and normal to the slip plane. Figure 7.4 shows the path of a single sphere  $A$  in one of the layers of spheres on one of the slip planes in an FCC elementary cell shown in Figures 7.2 and 7.3 as the sphere begins to slide over two spheres  $B$  and  $C$  in the layer of spheres underneath it, in the preferential slip direction  $\hat{u}_i$ , on a slip plane with unit normal  $\hat{u}_n$ . The contact radius between sphere  $A$

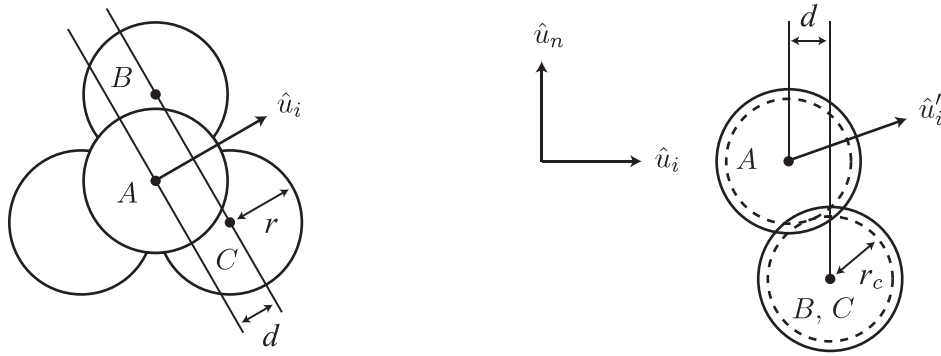


Figure 7.4: The path of a single sphere  $A$  in one of the layers of spheres in an FCC elementary cell shown in Figures 7.2 and 7.3 as it slides over two spheres  $B$  and  $C$  in the layer underneath in the preferential slip direction  $\hat{u}_i$  on a slip plane with unit normal  $\hat{u}_n$ . The initial motion of sphere  $A$  is in the  $\hat{u}'_i$  direction.

and each of the spheres  $B$  and  $C$  projected onto the  $\hat{u}_i$ - $\hat{u}_n$  plane shown in Figure 7.4 on the right is  $r_c = \sqrt{3}r/2$ , and the distance that sphere  $A$  must travel in the  $\hat{u}_i$  direction before a maximum dilation is reached is  $d = r/\sqrt{3}$ . The unit vector  $\hat{u}'_i$  in the direction of the *initial* motion of sphere  $A$  can be written in terms of the unit vectors  $\hat{u}_i$  and  $\hat{u}_n$  as

$$\hat{u}'_i = \sin(\cos^{-1}(1/3)) \hat{u}_i + (1/3)\hat{u}_n, \quad (7.4)$$

which gives  $\hat{u}'_1 = (-\hat{i} + \hat{j} + \hat{k})/\sqrt{3}$ ,  $\hat{u}'_2 = (\hat{i} - \hat{j} + \hat{k})/\sqrt{3}$ , and  $\hat{u}'_3 = (\hat{i} + \hat{j} - \hat{k})/\sqrt{3}$ . The *initial* dilation angle  $\psi$  between the unit vector  $\hat{u}'_i$  and the slip plane with unit normal  $\hat{u}_n$  is therefore

$$\psi = \cos^{-1} \hat{u}'_i \cdot \hat{u}_n = \sin^{-1}(1/3) \approx 19.47^\circ. \quad (7.5)$$

According to Vermeer and de Borst (1984), this is only slightly larger than the typical initial dilation angle for dense sand of  $15^\circ$ .

Consider two layers of spheres in an FCC array of uniform spheres on a slip plane subjected to normal and tangential stresses  $\sigma_n$  and  $\sigma_t$  in the  $\hat{u}_n$  and  $\hat{u}_i$  directions, respectively. Note that we need only consider the free-body diagram of sphere  $A$  in contact with spheres  $B$  and  $C$  in Figure 7.4 as sphere  $A$  begins to slide over spheres  $B$  and  $C$  in the direction  $\hat{u}'_i$  to determine the ratio of forces in the  $\hat{u}_i$  and  $\hat{u}_n$  directions, and hence the ratio of stresses  $\sigma_t$  and  $\sigma_n$ , necessary for force equilibrium on the slip plane at the initiation of yield. Let  $F_n$  and  $F_t$  denote the normal and tangential inter-particle contact forces, respectively, between sphere  $A$  and each of the spheres  $B$  and  $C$ , which by symmetry must be the same. If we assume that at the initiation of yield  $F_t = \mu F_n$ , where  $\mu$  is the inter-particle friction coefficient, then the free-body diagram of sphere  $A$  shows that the ratio of stresses tangent and normal to the slip plane at the initiation of yield is

$$\mu_{\text{slip}}^{\text{FCC}} = \frac{\sigma_t}{\sigma_n} = \frac{\cos(30^\circ) \sin \psi + \mu \cos \psi}{\cos(30^\circ) \cos \psi - \mu \sin \psi} = \frac{\sqrt{3} + 4\sqrt{2}\mu}{2\sqrt{6} - 2\mu} \quad (7.6)$$

which characterizes the local material friction coefficient  $\mu_{\text{slip}}^{\text{FCC}}$  for each slip plane in a regular FCC array of uniform spheres at the initiation of yield in terms of the inter-particle friction coefficient  $\mu$ , with particle rotation prohibited.

### 7.3.2 Simple Cubic (SC) Array of Uniform Spheres

Figure 7.5 shows an elementary cell of the simple cubic (SC) array of uniform spheres with the visible spheres numbered, and one of the three crystallographically similar slip planes. The unit vector normal to the slip plane shown in Figure 7.5 is  $\hat{u}_n = \hat{k}$ , and the preferential slip direction is any direction in the  $x$ - $y$  plane. The unit normal vectors and preferential slip directions for the other two crystallographically similar slip planes are obtained by renaming

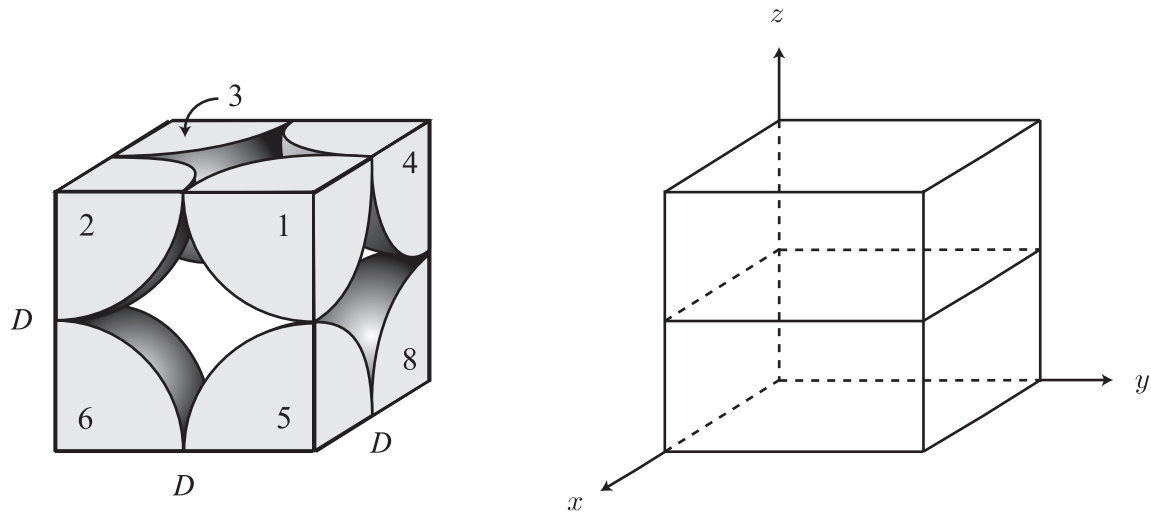


Figure 7.5: Left: Elementary cell of the simple cubic (SC) array of uniform spheres analyzed in this section. Right: One of the three crystallographically similar slip planes for the SC regular cubic array.

the coordinate axes. The slip systems for the SC packing involve no *initial* dilation. Hence,  $\psi = 0$ .

Clearly, if  $F_n$  and  $F_t$  denote the normal and tangential inter-particle contact forces, then force equilibrium on the slip plane requires simply that  $\sigma_t/\sigma_n = F_t/F_n$ . If we assume that at the initiation of yield  $F_t = \mu F_n$ , where  $\mu$  is the inter-particle friction coefficient, then the ratio of stresses tangent and normal to the slip plane at the initiation of yield is

$$\mu_{\text{slip}}^{\text{SC}} = \frac{\sigma_t}{\sigma_n} = \mu \quad (7.7)$$

which characterizes the local material friction coefficient  $\mu_{\text{slip}}^{\text{SC}}$  for each slip plane in a regular SC array of uniform spheres at the initiation of yield in terms of the inter-particle friction coefficient  $\mu$ , with particle rotation prohibited.

### 7.3.3 Body-Centered Cubic (BCC) Array of Uniform Spheres

Figure 7.6 shows an elementary cell of the body-centered cubic (BCC) array of uniform spheres with the visible spheres numbered, and one of the six crystallographically similar slip planes. The unit vector normal to the slip plane shown in Figure 7.6 is  $\hat{u}_n = (\hat{i} + \hat{j})/\sqrt{2}$ ,

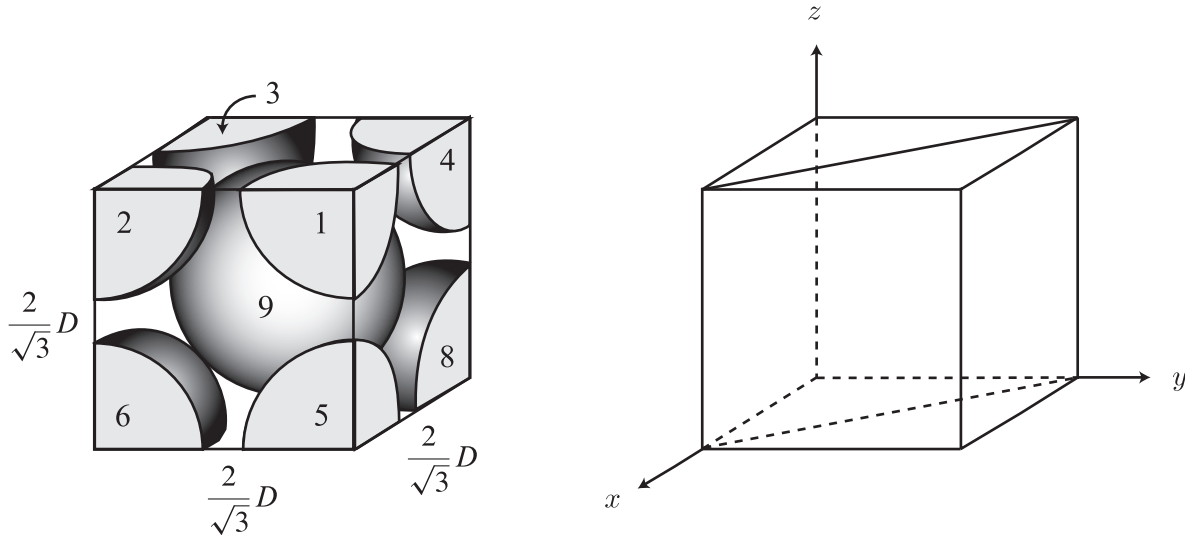


Figure 7.6: Left: Elementary cell of the body-centered cubic (BCC) array of uniform spheres analyzed in this section. Right: One of the six crystallographically similar slip planes for the BCC regular cubic array.

and the preferential slip directions on that slip plane are  $\hat{u}_{\pm} = \pm(-\hat{i} + \hat{j})/\sqrt{2}$ . The unit normal vectors and preferential slip directions for the other five crystallographically similar slip planes are obtained by renaming the coordinate axes. Note that for sliding on the “standard” slip planes in the BCC array there is no *initial* dilation. Hence,  $\psi = 0$ .

If we consider the free-body diagram of sphere 9 in contact with spheres 1 and 5 in Figure 7.6 as spheres 1 and 5 begin to slide over sphere 9 in the direction  $\hat{u}_{\pm}$ , we can determine the ratio of forces in the  $\hat{u}_{\pm}$  and  $\hat{u}_n$  directions, and hence the ratio of stresses  $\sigma_t$  and  $\sigma_n$ , necessary for force equilibrium on the slip plane at yield. Let  $F_n$  and  $F_t$  denote the normal and tangential inter-particle contact forces, respectively, between each of spheres 1 and 5 and sphere 9, which by symmetry must be the same. If we assume that at the

initiation of yield  $F_t = \mu F_n$ , where  $\mu$  is the inter-particle friction coefficient, then the free-body diagram of sphere 9 shows that the ratio of stresses tangent and normal to the slip plane at the initiation of yield is

$$\mu_{\text{slip}}^{\text{BCC}} = \frac{\sigma_t}{\sigma_n} = \frac{\mu}{\cos(\sin^{-1}(1/\sqrt{3}))} \quad (7.8)$$

which characterizes the local material friction coefficient  $\mu_{\text{slip}}^{\text{BCC}}$  for each slip plane in a regular BCC array of uniform spheres at the initiation of yield in terms of the inter-particle friction coefficient  $\mu$ , with particle rotation prohibited.

## 7.4 Yield in Statistically Isotropic Aggregates of Uniform Spheres

For a statistically isotropic polycrystalline material, once the yield stress  $\tau_Y$  associated with each slip system of the local crystals has been determined, homogenization processes analogous to those employed in Section 3.4 can be used to determine the initial yield surface for the material, provided the local crystals are randomly oriented and every orientation is equally represented. Such homogenization processes for locally cubic materials were originally developed by Taylor (1938), Bishop and Hill (1951a), and Bishop and Hill (1951b) to determine the plastic behavior of metals having locally cubic crystalline grains. Hill (1965) used the self-consistent method to analytically determine implicit equations for the polycrystalline elastoplastic moduli based on the corresponding moduli of the constituent crystals. Similar analyses had been performed earlier by Kröner (1961) and Budiansky and Wu (1962). Hutchinson (1970) used the analytical results of Hill (1965) to compute the yield surface for a statistically isotropic aggregate of FCC crystalline grains.

In the analysis of this chapter, we will employ the static homogenization method. Under

the static hypothesis, it is assumed that when an aggregate material is subjected to a uniform state of stress the individual material subportions will experience the same state of stress. In the elastic range, this assumption leads to the homogenization method of Reuss (1929), which was successfully employed for statistically isotropic particulate materials in Section 3.4.2 of Chapter 3 [Fleischmann et al. (2013a)]. Taylor (1938) applied the static hypothesis to determine the yield criterion for a polycrystalline aggregate material in terms of the yield conditions on the slip systems in the local crystals. If the strength of the individual (randomly oriented) crystalline grains in a polycrystalline aggregate are *pressure-independent*, then the Tresca yield criterion holds for the aggregate material, which states that yield occurs when

$$\frac{1}{2}|\bar{\sigma}_i - \bar{\sigma}_j| = \bar{\tau}_Y, \quad i \neq j, \quad i, j \in \{1, 2, 3\}, \quad (7.9)$$

for any combination of the principal stresses  $\bar{\sigma}_1$ ,  $\bar{\sigma}_2$ , and  $\bar{\sigma}_3$ . Assuming that the orientations of the local crystals are randomly oriented and every orientation is equally represented, then under the static hypothesis the macroscopic yield stress for the aggregate material is simply equal to the (minimum) yield stress associated with the slip systems in the constituent crystalline grains, or

$$\bar{\tau}_Y = \tau_Y. \quad (7.10)$$

According to Hutchinson (1970), equation (7.9) is still valid under the assumptions of the self-consistent method, except the relationship between the macroscopic yield stress  $\bar{\tau}_Y$  in the aggregate material and the (minimum) yield stress  $\tau_Y$  along the local slip systems is more complicated, and it generally involves the elastic properties of both the local and aggregate materials (Hill, 1965).

For a non-cohesive particulate material whose strength is *pressure-dependent*, the Tresca yield criterion generalizes to the Mohr-Coulomb yield criterion, derived in Appendix D. According to the Mohr-Coulomb yield criterion, yield in a statistically isotropic particulate

aggregate material is governed by the maximum ratio of tangential to normal stress  $\bar{\sigma}_t/\bar{\sigma}_n$  on any spatially-oriented plane in the aggregate material, which occurs when

$$\frac{|\bar{\sigma}_i - \bar{\sigma}_j|}{2\sqrt{\bar{\sigma}_i\bar{\sigma}_j}} = \mu_{\text{macro}}, \quad i \neq j, \quad i, j \in \{1, 2, 3\}, \quad (7.11)$$

for any combination of the principal stresses  $\bar{\sigma}_1$ ,  $\bar{\sigma}_2$ , and  $\bar{\sigma}_3$ , where  $\mu_{\text{macro}}$  is the macroscopic or material friction coefficient for the particulate aggregate material (called  $\mu$  in the derivation of Appendix D). In the study of particulate materials, the macroscopic friction coefficient  $\mu_{\text{macro}}$  is usually represented by a macroscopic or material friction angle  $\phi = \tan^{-1} \mu_{\text{macro}}$ , which is also the angle of repose of the particulate aggregate material.

If all local packing geometries and associated slip planes are randomly oriented and equally represented in a particulate aggregate material, then, under the static hypothesis, yield in the particulate aggregate material will occur when the maximum ratio of tangential to normal stress  $\bar{\sigma}_t/\bar{\sigma}_n$  on any spatially-oriented plane in the aggregate material is equal to the smallest ratio  $\sigma_t/\sigma_n = \mu_{\text{slip}}$  that causes sliding on any slip system in the local packings of uniform spheres, or

$$\mu_{\text{macro}} = \mu_{\text{slip}}, \quad (7.12)$$

as illustrated in Figure 7.7, where  $\mu_{\text{slip}}$  is given in terms of the inter-particle friction coefficient  $\mu$  for each of the local cubic packings in Section 7.3.

Figure 7.8 shows the resulting relationship between the inter-particle friction coefficient  $\mu$  expressed as an inter-particle friction angle  $\phi_\mu = \tan^{-1} \mu$  and the material friction angle  $\phi = \tan^{-1} \mu_{\text{macro}}$  for locally FCC, BCC, and SC statistically isotropic particulate aggregate materials with  $\mu_{\text{macro}} = \mu_{\text{slip}}^{\text{FCC}}$ ,  $\mu_{\text{macro}} = \mu_{\text{slip}}^{\text{BCC}}$ , and  $\mu_{\text{macro}} = \mu_{\text{slip}}^{\text{SC}}$ , given by equations (7.6), (7.8), and (7.7), respectively. Note that the predicted curve for a locally FCC particulate aggregate material and the DEM data points obtained in Chapter 5 for Specimen 4 consisting of 29 660 spheres (with particle rotation prohibited) match quite well for  $0.2 \leq \mu \leq 0.8$

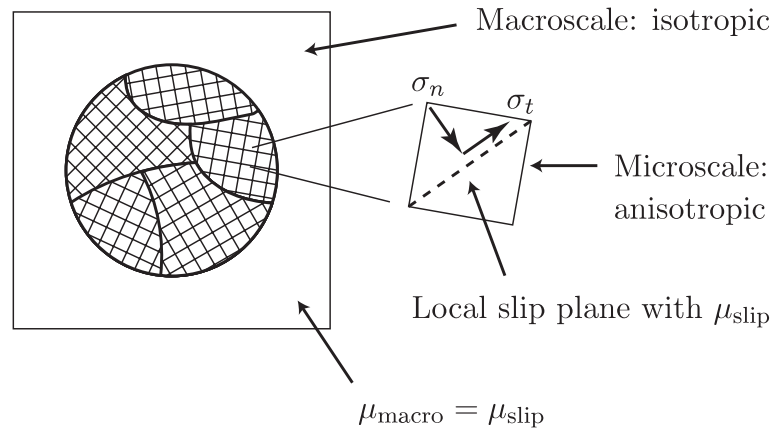


Figure 7.7: Static homogenization hypothesis for yield: the statistically isotropic particulate material consists of many randomly-oriented subportions with specific local packings and associated local slip planes.

( $10^\circ \leq \phi_\mu \leq 40^\circ$ ). The curves predicted for locally BCC and SC particulate aggregate materials, on the other hand, are far from the DEM data points.

It should be noted that the average number of inter-particle contacts per unit volume for all six DEM specimens tested in Chapters 3–6 were initially closest to that of the BCC packing ( $\beta_{\text{BCC}} \approx 5.2/D^3$ , where  $D$  is the diameter of the particles), as noted in Section 3.6. We also saw in Figure 3.8 of Section 3.5 that the *elastic* behavior of all six DEM specimens, in particular the relationship between Poisson’s ratio for the particulate material and the ratio of tangential to normal inter-particle contact stiffnesses  $\alpha = K_t/K_n$ , are modeled most closely by the self-consistent homogenization hypothesis applied to a statistically isotropic aggregate of local BCC packings of uniform spheres. However, Figure 7.8 shows clearly that the *yielding* behavior of the same six DEM specimens, in particular the relationship between the inter-particle friction angle  $\phi_\mu$  (or coefficient  $\mu = \tan \phi_\mu$ ) and the particulate material friction angle  $\phi$ , are not well modeled by the (static) yielding behavior of a statistically isotropic aggregate of local BCC packings of uniform spheres. The FCC curve in Figure 7.8 is clearly superior, although it also fails to capture the material friction angle  $\phi$  when  $\mu = 0$  (and  $\phi_\mu = 0^\circ$ ), which is also the initial dilation angle  $\psi$  of the DEM specimens.

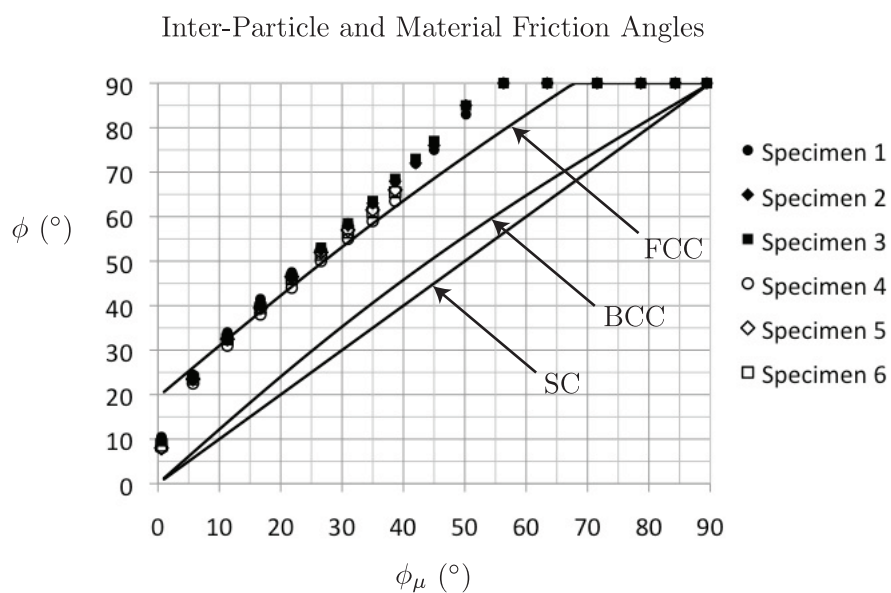


Figure 7.8: The relationship between the inter-particle friction coefficient  $\mu$  expressed as an inter-particle friction angle  $\phi_{\mu} = \tan^{-1} \mu$  and the material friction angle  $\phi = \tan^{-1} \mu_{\text{macro}}$  predicted for a statistically isotropic particulate aggregate material composed of locally FCC, BCC, and SC regular arrays of uniform spheres, assuming no particle rotation. Also shown are the data points obtained in Chapter 5 for Specimens 1–6 (shown previously in Figures 5.22 and 5.23) from DEM simulations with particle rotation prohibited.

Note also that for the *initiation* of sliding on the standard slip planes in the three local cubic packings considered in Section 7.3, only the FCC packing produces dilation, with an initial dilation angle of  $\psi \approx 19.47^\circ$ . For the initiation of yield on the standard slip planes in both the SC and BCC packings,  $\psi = 0$ . The initial volumetric packing densities of all six of the DEM specimens tested in Chapters 3–6 were approximately 0.66, with a void ratio  $e \approx 0.5$ , which is typical of dense sand having uniform, well-rounded particles (e.g., Bardet, 1997). (For comparison, the volumetric packing density of an FCC packing is roughly 0.74, that of a BCC packing is roughly 0.68, and that of an SC packing is roughly 0.52.) Since dense sands experience dilation, with a typical initial dilation angle of  $\psi \approx 15^\circ$  (Vermeer and de Borst, 1984), we therefore may expect our randomly-packing DEM specimens to experience dilation as well. Indeed, the initial dilation angle  $\psi$  in our DEM specimens is easily measured, since it is equal to the friction angle  $\phi$  in the absence of inter-particle friction. Thus, Figure 7.8 shows that the initial dilation angle  $\psi$  for all six DEM specimens is approximately  $\psi \approx 10^\circ$ .

Thus, considering the initial dilation angle of our DEM specimens, it is clear why the FCC curve in Figure 7.8 models the DEM data more closely than the BCC or SC curves, since of the three local cubic packings only the FCC packing produces initial dilation. Another possible explanation for the superiority of the FCC curve in Figure 7.8 is that the friction angles  $\phi$  obtained for the DEM specimens in Chapter 5 are *peak* friction angles, rather than friction angles associated with the true *initiation* of yield, as noted in Chapter 5. Thus, since the local FCC packing is the most “stable” of the three local cubic packings, as slip begins to occur in a particulate material during the initiation of yield, the spheres may tend to realign themselves into a packing similar to the FCC packing along slip planes, or more likely into an “intermediate” packing geometry between the SC, BCC, and FCC packings, regardless of the initial packing geometry of the spheres. Note that the characterization of the peak friction angle rather than the initiation of yield is typical for particulate materials,

since, as noted in Section 5.6, the true initiation of “yield” in particulate materials typically occurs at very small strains, with irrecoverable strains developing in uncemented normally consolidated sands at strains as low as  $\epsilon = 0.007\%$  (Mitchell and Soga, 2005).

The considerations of the preceding two paragraphs serve to motivate the introduction of a generalized local packing model, capable of reproducing all three of the local cubic packings analyzed in Section 7.3, but also capable of representing local packing geometries having a full range of initial dilation angles  $\psi$ . To this end, we generalize the contact geometry between spheres  $A$ ,  $B$ , and  $C$  shown in Figure 7.4 for the FCC packing to allow any orientation of spheres on an arbitrary slip plane, as shown in Figure 7.9. In this model, we use two angles

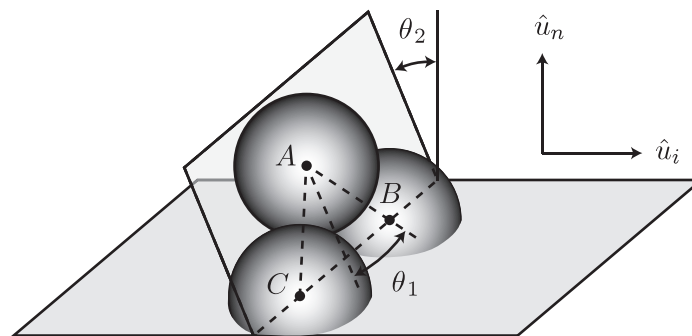


Figure 7.9: The path of a single sphere  $A$  in one of the layers of spheres as it slides over two spheres  $B$  and  $C$  in the layer underneath in the preferential slip direction  $\hat{u}_i$  on an arbitrary slip plane with unit normal  $\hat{u}_n$ . The initial motion of sphere  $A$  is in the direction normal to the plane containing the centers of spheres  $A$ ,  $B$ , and  $C$ .

$\theta_1$  and  $\theta_2$  to characterize the geometry of spheres  $A$ ,  $B$ , and  $C$ , in contact on an arbitrary slip plane, as sphere  $A$  begins to slide over spheres  $B$  and  $C$ . The angle  $\theta_2 = \psi$  is the initial dilation angle, and the angle  $\theta_1$  characterizes what we call the “v-belt effect” in Chapter 9 [Fleischmann et al. (2013c)], which is an intuitive way of understanding (nominally 2-D) yielding in a physically three-dimensional particulate material.

As in Section 7.3.1, we need only consider the free-body diagram of sphere  $A$  in contact with spheres  $B$  and  $C$  in Figure 7.9, as sphere  $A$  begins to slide over spheres  $B$  and  $C$  in the

direction normal to the plane containing the centers of spheres  $A$ ,  $B$ , and  $C$ , to determine the ratio of forces in the  $\hat{u}_i$  and  $\hat{u}_n$  directions, and hence the ratio of stresses  $\sigma_t$  and  $\sigma_n$ , necessary for force equilibrium on the slip plane at the initiation of yield. Let  $F_n$  and  $F_t$  denote the normal and tangential inter-particle contact forces, respectively, between sphere  $A$  and each of the spheres  $B$  and  $C$ , which by symmetry must be the same. If we assume that at the initiation of yield  $F_t = \mu F_n$ , where  $\mu$  is the inter-particle friction coefficient, then the free-body diagram of sphere  $A$  shows that the ratio of stresses tangent and normal to the slip plane at the initiation of yield is

$$\mu_{\text{slip}} = \frac{\sigma_t}{\sigma_n} = \frac{\cos \theta_1 \sin \theta_2 + \mu \cos \theta_2}{\cos \theta_1 \cos \theta_2 - \mu \sin \theta_2} \quad (7.13)$$

which characterizes the local material friction coefficient  $\mu_{\text{slip}}$  for an arbitrary slip plane in an array of uniform spheres at the initiation of yield in terms of the inter-particle friction coefficient  $\mu$  and the angles  $\theta_1$  and  $\theta_2 = \psi$ , with particle rotation prohibited. Note that equation (7.13) generalizes equations (7.6), (7.7), and (7.8), with  $\theta_1 = 30^\circ$  and  $\theta_2 = \sin^{-1}(1/3) \approx 19.47^\circ$  for the FCC packing,  $\theta_1 = \sin^{-1}(1/\sqrt{3}) \approx 35.26^\circ$  and  $\theta_2 = 0$  for the BCC packing, and  $\theta_1 = \theta_2 = 0$  for the SC packing.

Zhou and Dinsmore (2009) have performed a statistical study of the distribution of inter-particle contact forces in random assemblies of spheres in three dimensions and disks in two dimensions (under a variety of stress conditions). This study reveals an approximately uniform distribution of inter-force angles  $\theta$  measured between adjacent normal inter-particle contact forces in a three dimensional random assembly of uniform spheres between the geometric bounds of  $\theta_{\min} = 60^\circ$  and  $\theta_{\max} = 180^\circ$ , with a slight peak at each of the two geometric bounds. Zhou and Dinsmore (2009) hypothesize that the peak at  $\theta_{\max} = 180^\circ$  is due to the presence of force chains, which for the sake of stability favor straight propagation through the particulate assembly. This translates to  $30^\circ \leq \theta_1 \leq 90^\circ$  in Figure 7.9. Hence, if we

assume that a statistically isotropic assembly of uniform spheres is composed of equally represented subportions having local packing geometries given by the generalized model of equation (7.13) with  $30^\circ \leq \theta_1 \leq 90^\circ$  uniformly distributed, we may use  $\theta_1 = \bar{\theta}_1 = 60^\circ$  in equation (7.13), which gives the following generalized model for a statistically isotropic assembly of uniform spheres:

$$\mu_{\text{macro}} = \mu_{\text{slip}} = \frac{\sigma_t}{\sigma_n} = \frac{\sin \psi + 2\mu \cos \psi}{\cos \psi - 2\mu \sin \psi} \quad (7.14)$$

where  $\mu$  is the inter-particle friction coefficient,  $\psi$  is the initial dilation angle, and the material friction angle is given by  $\phi = \tan^{-1} \mu_{\text{macro}}$ .

Figure 7.10 shows the relationship between  $\phi_\mu = \tan^{-1} \mu$ , and  $\phi = \tan^{-1} \mu_{\text{macro}}$  given by equation (7.14) with  $\psi = 10^\circ$ , along with the DEM data points obtained in Chapter 5 for Specimens 1–6 (with particle rotation prohibited). Note that the relationship between  $\phi$  and  $\phi_\mu$  obtained in Chapter 5 for all six DEM specimens of randomly packed uniform spheres (with particle rotation prohibited) is predicted quite well by equation (7.14) with an initial dilation angle of  $\psi = 10^\circ$  in the range  $0 \leq \mu \leq 1$  ( $0 \leq \phi_\mu \leq 45^\circ$ ), particularly for Specimens 1–3. This is quite remarkable considering the fact that the only parameter chosen by us to match the data points was the initial dilation angle  $\psi$ , which was chosen to match the (approximate) material friction angle  $\phi$  at  $\mu = 0$  ( $\phi_\mu = 0$ ) for all six DEM specimens.

Finally, it is worth noting that in the case where the distribution of  $\theta_1$  in Figure 7.9 is not uniform or is not bounded by  $30^\circ \leq \theta_1 \leq 90^\circ$  (as in an assembly of spheres with non-uniform size), then equation (7.13) should be used with values of  $\theta_1 = \bar{\theta}_1 \neq 60^\circ$  based on the specific distribution of  $\theta_1$  in the assembly. Figure 7.11 shows various curves predicted by equation (7.13) with  $\theta_2 = \psi = 10^\circ$  and  $\theta_1 = \{30, 40, 50, 60, 70, 80\}^\circ$ , along with the DEM data points obtained in Chapter 5 for Specimens 1–6 (with particle rotation prohibited), for comparison.

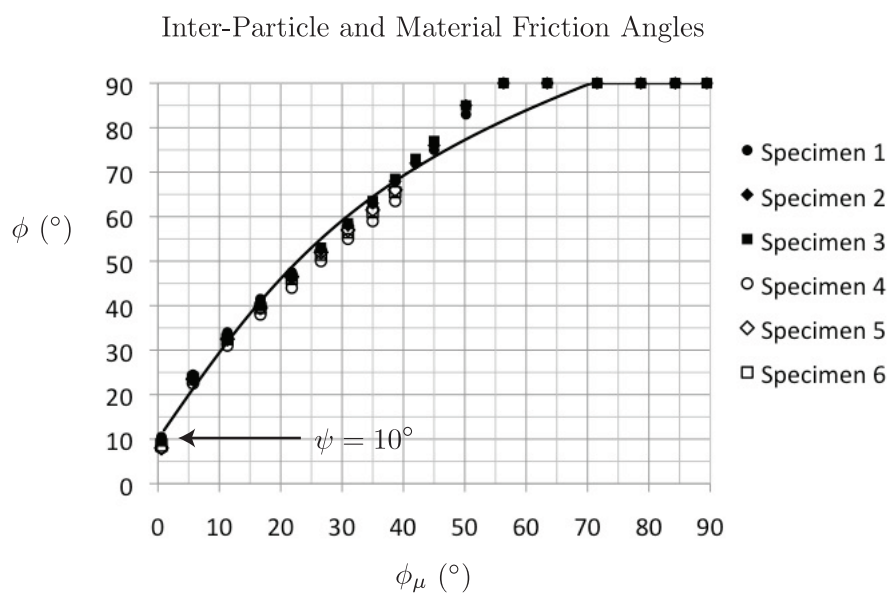


Figure 7.10: The relationship between the inter-particle friction coefficient  $\mu$  expressed as an inter-particle friction angle  $\phi_\mu = \tan^{-1} \mu$  and the material friction angle  $\phi = \tan^{-1} \mu_{\text{macro}}$  predicted for a statistically isotropic particulate aggregate material by the generalized model given by equation (7.14) with  $\psi = 10^\circ$ , assuming no particle rotation. Also shown are the data points obtained in Chapter 5 for Specimens 1–6 (shown previously in Figures 5.22 and 5.23) from DEM simulations with particle rotation prohibited.

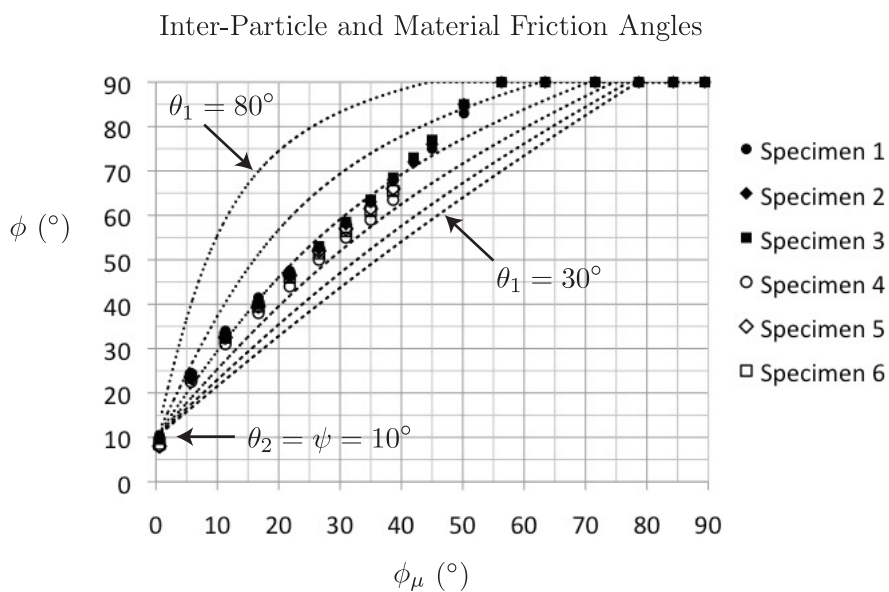


Figure 7.11: The relationship between the inter-particle friction coefficient  $\mu$  expressed as an inter-particle friction angle  $\phi_{\mu} = \tan^{-1} \mu$  and the material friction angle  $\phi = \tan^{-1} \mu_{\text{macro}}$  predicted for a statistically isotropic particulate aggregate material by the generalized model given by equation (7.13) with  $\theta_2 = \psi = 10^{\circ}$  and  $\theta_1 = \{30, 40, 50, 60, 70, 80\}^{\circ}$ , assuming no particle rotation. Also shown are the data points obtained in Chapter 5 for Specimens 1–6 (shown previously in Figures 5.22 and 5.23) from DEM simulations with particle rotation prohibited.

## 7.5 Conclusion

We analyzed the conditions for yield on the standard slip planes in local face-centered cubic (FCC), body-centered cubic (BCC), and simple cubic (SC) regular packings of uniform spheres to determine local material friction coefficients  $\mu_{\text{slip}}$  governing yield on the standard slip planes in each of the local packings in terms of the inter-particle friction coefficient  $\mu$ , given by equations (7.6), (7.8), and (7.7) for the local FCC, BCC, and SC packings, respectively. We used these results to analyze the yield conditions for a statistically isotropic particulate aggregate material composed of randomly packed uniform spheres.

Assuming that a randomly packed particulate material can be idealized as an aggregate material consisting of randomly-oriented subportions with specific local packings (either cubic or generalized) and applying the static homogenization hypothesis, we have assumed that the *macroscopic* material friction coefficient for the aggregate material  $\mu_{\text{macro}}$  is equal to the local material friction coefficient  $\mu_{\text{slip}}$  for the slip planes in the (predominant) local packing, where the material friction angle for the statistically isotropic particulate material is  $\phi = \tan^{-1} \mu_{\text{macro}}$ . Thus,  $\mu_{\text{macro}}$  (and hence  $\phi$ ) is related to the inter-particle friction coefficient  $\mu$  via  $\mu_{\text{slip}}$  for each of the local packings.

If a statistically isotropic particulate material consists of randomly-oriented subportions or “grains” of particles arranged (at least predominantly) in one of the three cubic packings or the generalized local packing discussed below, then the slip planes for the local packings will also be randomly-oriented. Thus, despite the fact that we consider yield of the local packings along specific, predetermined slip planes, we do *not* thereby constrain the statistically isotropic particulate aggregate material to yield along slip planes with any specific spatial orientation. The same observation was made for statistically isotropic polycrystalline aggregate materials on the molecular scale by Taylor (1938).

We found that the relationship between the inter-particle friction coefficient  $\mu$  expressed

as an inter-particle friction angle  $\phi_\mu = \tan^{-1} \mu$  and the macroscopic or material friction angle  $\phi = \tan^{-1} \mu_{\text{macro}}$  predicted for a statistically isotropic particulate aggregate material composed of locally FCC regular arrays of uniform spheres (with  $\mu_{\text{macro}} = \mu_{\text{slip}}^{\text{FCC}}$ ) provided a good approximation to the same relationship obtained from DEM simulations performed on six specimens of 3 430–29 660 randomly packed uniform spheres in Chapter 5, with particle rotation prohibited, as shown in Figure 7.8.

We also introduced a generalized model given by equations (7.13) and (7.14) relating  $\mu_{\text{slip}}$  to the inter-particle friction coefficient  $\mu$  for inter-particle contacts on an arbitrary slip plane with two geometric parameters  $\theta_1$  and  $\theta_2$ , where  $\theta_2 = \psi$  is the initial dilation angle, and  $\theta_1$  characterizes what we call the “v-belt effect” in Chapter 9 [Fleischmann et al. (2013c)], which is an intuitive way of understanding (nominally 2-D) yielding in a physically three-dimensional particulate material. This model generalizes the results for all three local cubic packings, and it allows us to match the DEM data points from Chapter 5 even more closely by choosing appropriate values for  $\theta_1$  and  $\theta_2$  in equation (7.13) – or just the initial dilation angle  $\psi$  if equation (7.14) is used for a statistically isotropic assembly of uniform spheres – as shown in Figure 7.10.

Like the DEM simulations performed for Chapter 5, the theoretical derivations of this chapter were carried out with particle rotation prohibited. To model the results obtained from the DEM simulations performed for Chapter 6, we continue our analysis with the case of particle rotation in Chapter 8.



## Chapter 8

# Micromechanical analysis of Yield in Isotropic Non-Cohesive Particulate Materials, Part II: Particle Rotation

### 8.1 Abstract

We extend the theoretical results of Chapter 7 (Part I) to include the effect of particle rotation, as we did in Chapter 4 for the elastic range. In particular, we analyze the motion of particles on the standard slip planes of the face-centered cubic (FCC), simple cubic (SC), and body-centered cubic (BCC) arrays of uniform spheres, including the effect of particle rotation. This leads to a generalized model relating the inter-particle friction coefficient  $\mu$  and the material friction coefficient  $\mu_{\text{macro}}$  or the material friction angle  $\phi = \tan^{-1} \mu_{\text{macro}}$  for a statistically isotropic (non-cohesive) particulate material consisting of uniform spheres. We compare this relation with the relation obtained from the DEM simulations performed for Chapter 6, in which particle rotation was unrestrained, and we find that the match is excellent. In particular, our relation provides a significantly better match with the DEM

data points of Chapter 6 than the relation derived by Emeriault et al. (1996). Also, our derivation shows that the material friction angle  $\phi$  depends in part on the *elastic* properties of the spheres, in particular on the ratio of the tangential to the normal inter-particle contact stiffness  $\alpha = K_t/K_n$ . This dependence is not included in the relation derived by Emeriault et al. (1996). Moreover, we show that the relation between  $\phi_\mu$  and  $\phi$  depends on the parameter  $\xi$  that was introduced by us in Chapter 4 [Fleischmann et al. (2013b)] to characterize the effect of particle rotation in the elastic range, and this dependence becomes pronounced as  $\mu \rightarrow \infty$  ( $\phi_\mu \rightarrow 90^\circ$ ). In Chapter 4 [Fleischmann et al. (2013b)], we showed that the parameter  $\xi$  can be understood as providing a quantitative measure of the presence of zero-energy modes or mechanisms in a particulate material.

## 8.2 Introduction

In Chapter 6, we used the Discrete Element Method (DEM) to determine yield surfaces for six specimens of 3 430–29 660 randomly packed uniform spheres with constant normal and tangential inter-particle contact stiffnesses  $K_n$  and  $K_t$  (linear spring model), and uniform inter-particle friction coefficients  $\mu$ . The DEM simulations were performed on each specimen for a wide range of inter-particle friction coefficients, with  $0.01 \leq \mu \leq 100.0$  for the 3 430-element Specimens 1–3 and  $0.01 \leq \mu \leq 0.8$  for the 29 660-element Specimens 4–6. The resulting yield surfaces allowed us to determine the (peak) material friction angle  $\phi$  for each DEM specimen for each value of the inter-particle friction coefficient  $\mu$  at a Lode angle of zero on the  $\pi$ -plane, corresponding to the (maximum) stress ratio  $\sigma_{\text{axial}}/\sigma_{\text{lateral}}$  at yield in a true-triaxial compressive test, and this resulted in a relationship between the inter-particle friction coefficient  $\mu$  on the microscale (which can also be expressed as an inter-particle friction angle  $\phi_\mu = \tan^{-1} \mu$ ) and the material friction angle  $\phi$  on the macroscale (which can also be expressed as a macroscopic friction coefficient  $\mu_{\text{macro}} = \tan \phi$ ).

In this chapter, we perform a micromechanical analysis of the initiation of yield along the standard slip planes in three regular cubic arrays of uniform spheres: face-centered cubic (FCC), simple cubic (SC), and body-centered cubic (BCC), including the effect of particle rotation. We perform a *direct micromechanics derivation* of the yield conditions for the standard slip systems in a local FCC packing of uniform spheres, and we generalize this derivation to include slip planes in arbitrary packing geometries. Applying the static homogenization hypothesis, we propose a generalized model relating the material friction angle  $\phi$  in a statistically isotropic (non-cohesive) particulate aggregate material composed of uniform spheres to the inter-particle friction coefficient  $\mu$ , incorporating the effect of particle rotation. The resulting relation between the inter-particle friction coefficient  $\mu$  (or the inter-particle friction angle  $\phi_\mu = \tan^{-1} \mu$ ) and the material friction angle  $\phi$  (or the macroscopic friction coefficient  $\mu_{\text{macro}} = \tan \phi$ ) depends on the material initial dilation angle  $\psi$ , as it did in Chapter 7 with particle rotation prohibited. However, with the effect of particle rotation included, this relation also depends on the number of “active” layers in the slip systems, as well as on the *elastic* properties of both the local and aggregate particulate materials. In particular, the relation between  $\mu$  and  $\phi$  depends on the ratio  $\alpha = K_t/K_n$  and on the internal parameter  $\xi$  introduced in Chapter 4 [Fleischmann et al. (2013b)] to quantify the presence of zero-energy modes or shear mechanisms in the aggregate material. These dependences become increasingly pronounced as  $\mu \rightarrow \infty$  ( $\phi_\mu \rightarrow 90^\circ$ ).

Comparing the theoretical relation between the inter-particle and material friction angles  $\phi_\mu$  and  $\phi$  derived in this chapter with the results obtained by the discrete element method for the six DEM specimens of Chapter 6 (with particle rotation allowed), we find excellent agreement. In particular, our relation provides a significantly better match with the DEM data points of Chapter 6 than the relation derived by Emeriault et al. (1996), also based on a static homogenization hypothesis, which is to our knowledge the only other micromechanics-based derivation of this relation in the literature.

## 8.3 Yield on Slip Planes for Regular Arrays of Uniform Spheres Incorporating the Effect of Particle Rotation

In this section, we consider how particle rotation affects the yield conditions derived in Section 7.3 on the slip planes for three regular cubic arrays of uniform spheres: face-centered cubic (FCC), simple cubic (SC), and body-centered cubic (BCC).

### 8.3.1 Face-Centered Cubic (FCC) Array of Uniform Spheres

Figure 7.1 in Section 7.3.1 shows an elementary cell of the face-centered cubic (FCC) array of uniform spheres with the visible spheres numbered, and three of the 12 crystallographically similar slip planes. Figure 7.2 in Section 7.3.1 shows all 14 spheres in an FCC elementary cell in four separate layers viewed in a direction normal to the three slip planes shown in Figure 7.1. The numbering of the spheres in Figure 7.2 corresponds to the numbering of the visible spheres in Figure 7.1. The preferential slip directions  $\hat{u}_i$  on the slip planes shown in Figure 7.1 (right) with unit normal vector  $\hat{u}_n$  are shown in Figure 7.3 next to an FCC elementary cell viewed in the  $-\hat{u}_n$  direction. The initial dilation angle for these slip systems is  $\psi = \sin^{-1}(1/3) \approx 19.47^\circ$ .

Figure 8.1 shows a group of eleven spheres on three layers within a slip system with preferential slip direction  $\hat{u}_i$  and unit normal  $\hat{u}_n$  viewed in the  $\hat{u}_i$ - $\hat{u}_n$  plane. We will first consider the case in which only the spheres on a single layer are free to rotate (spheres *A*, *E*, *F*, *G*, and *H* in Figure 8.1). The uppermost layer of spheres in Figure 8.1 experiences a displacement in the  $\hat{u}_i$  direction while the bottommost layer of spheres remains fixed. Let  $\sigma_n$  and  $\sigma_t$  be the stresses normal and tangent to the slip plane on the uppermost layer of spheres, in the  $\hat{u}_n$  and  $\hat{u}_i$  directions, respectively. Then, as in Section 7.3.1, the ratio of

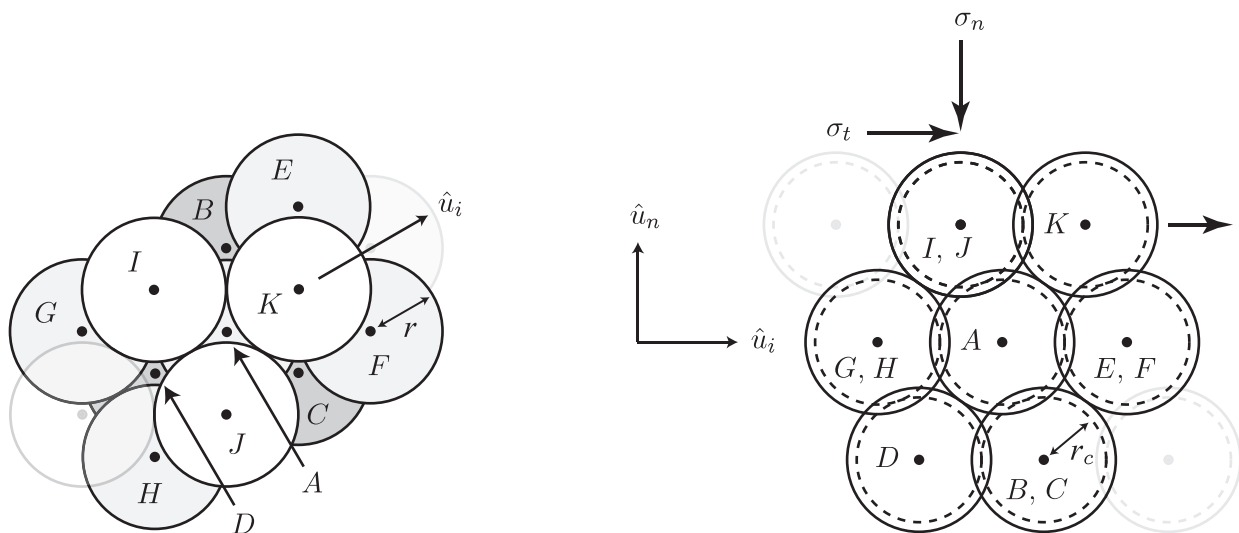


Figure 8.1: Eleven spheres (lettered A–K for reference) on three layers in a standard slip system of a FCC array of uniform spheres, (left:) viewed in the  $-\hat{u}_n$  direction, and (right:) viewed in the  $\hat{u}_i$ – $\hat{u}_n$  plane, where the direction  $\hat{u}_i$  is one of the three preferential slip directions associated with the slip planes shown in Figure 7.1, which are shown in Figure 7.3, and the direction  $\hat{u}_n$  is normal to the slip plane.

stresses tangent and normal to the slip plane will be

$$\mu_{\text{slip}}^{\text{FCC}} = \frac{\sigma_t}{\sigma_n} = \frac{F_n \cos(30^\circ) \sin \psi + F_t \cos \psi}{F_n \cos(30^\circ) \cos \psi - F_t \sin \psi}, \quad (8.1)$$

where  $F_n$  and  $F_t$  denote the normal and tangential inter-particle contact forces between sphere A and spheres B and C in Figure 8.1, which by symmetry must be the same. In Section 7.3.1 with particle rotation prohibited, we assumed that  $F_t = \mu F_n$  at yield. With particle rotation allowed, however, we cannot assume a priori that sphere A will *slide* relative to spheres B, C, I, and J rather than *rolling without slip* relative to spheres B, C, I, and J and *sliding* relative to spheres E, F, G, and H on the same plane.

Let  $F'_n$  and  $F'_t$  denote the normal and tangential inter-particle contact forces between sphere A and each of spheres E, F, G, and H in Figure 8.1 (which are the same). Note that the motion of the upper two layers of spheres in Figure 8.1 in the  $\hat{u}_i$  direction will

cause contact between sphere  $A$  and spheres  $D$  and  $K$  to be lost at the moment motion begins. Thus, we may ignore the contact forces between sphere  $A$  and spheres  $D$  and  $K$  in our analysis of yield with particle rotation allowed, as we did in Section 7.3.1 with particle rotation prohibited. In other words, we assume that strong force networks or force-chains of types  $\langle I, J \rangle \rightarrow \langle A \rangle \rightarrow \langle B, C \rangle$  and  $\langle G, H \rangle \rightarrow \langle A \rangle \rightarrow \langle E, F \rangle$  exist during the motions analyzed in this section, and force-chains of type  $\langle D \rangle \rightarrow \langle A \rangle \rightarrow \langle K \rangle$  *do not* exist during this motion. Unlike Section 7.3.1, however, without further assumptions the free-body diagram of sphere  $A$  is statically indeterminate. Thus, we solve the problem for two separate boundary conditions: (1) constant normal stress, in which  $\sigma_n$  in the  $\hat{u}_n$  direction is constant, and (2) constant volume, in which motion is purely in the  $\hat{u}_i$  direction. While the constant normal stress boundary condition make the free-body diagram of sphere  $A$  statically determinate, the solution of the constant volume boundary condition problem depends on the force-displacement laws for the spheres, and in particular on the ratio of the inter-particle tangential and normal contact stiffnesses  $\alpha = K_t/K_n$ .

### Constant Normal Stress

Figure 8.2 shows the free-body diagram of sphere  $A$  with constant normal stress boundary conditions. If  $\sigma_n$  is to remain constant, then the motion of sphere  $A$  must be in the  $\hat{u}'_i$  direction (at an angle  $\psi$  relative to the slip plane). We will assume initially that  $F_n = F_0$  and  $F'_n = \eta_0 F_0$ . Moment balance for sphere  $A$  implies that  $F_t = F'_t$ . Thus, if  $\eta_0 > 1$ , sliding will occur between sphere  $A$  and spheres  $B$  and  $C$  in Figure 8.1, and equation (8.1) is the same as equation (7.6) for the case of no particle rotation. If  $\eta_0 \leq 1$ , however, then sliding occurs between sphere  $A$  and spheres  $E$ ,  $F$ ,  $G$ , and  $H$  in Figure 8.1. Thus, at yield  $F'_t = \mu F'_n = \mu \eta_0 F_0$ . We will assume  $\eta_0 \leq 1$ .

Before motion occurs,  $F_t = F'_t = 0$ , and we have  $\sigma_n A_0 = 2F_0 \cos(30^\circ) \cos \psi$  for some reference area  $A_0$  on the slip plane. At yield, moment equilibrium for sphere  $A$  implies that

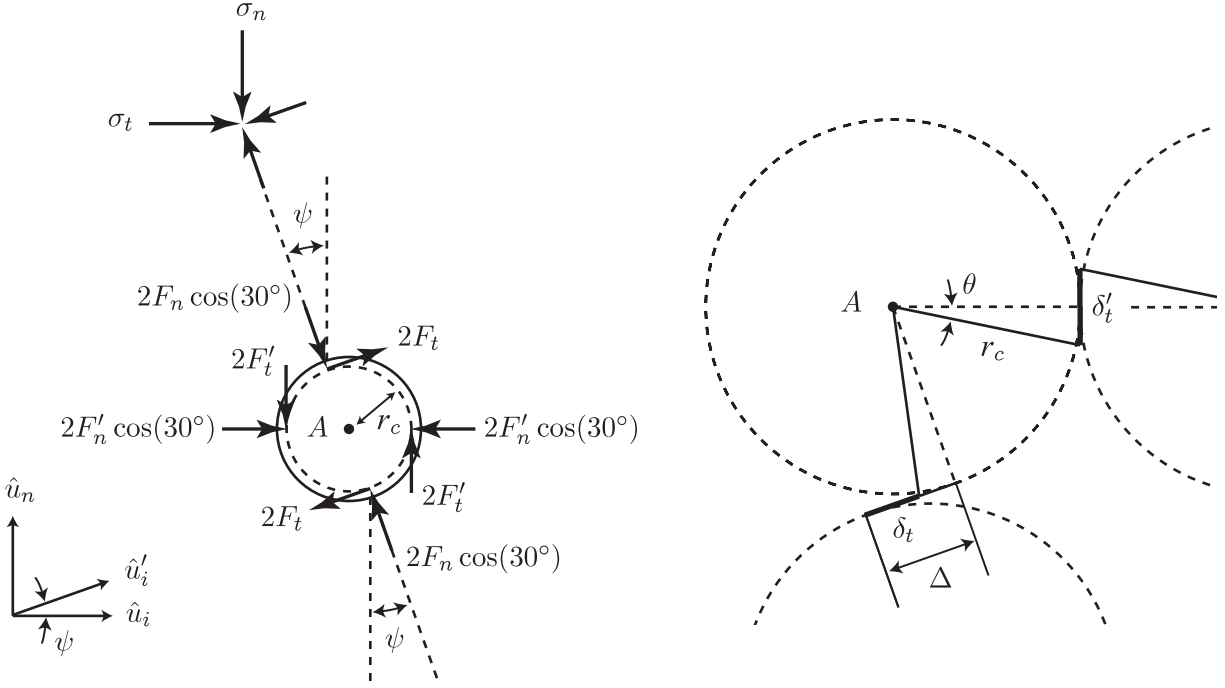


Figure 8.2: Free-body diagram of sphere  $A$  with constant normal stress boundary conditions.

$F_t = F'_t = \mu\eta_0 F_0$ , and we have  $\sigma_n A_0 = 2F_n \cos(30^\circ) \cos \psi - 2\mu\eta_0 F_0$ . Since the normal stress  $\sigma_n$  is constant, we can equate  $\sigma_n$  before and after yield to find  $F_n$  at yield, and equation 8.1 becomes

$$\text{Constant Normal Stress: } \mu_{\text{slip}}^{\text{FCC}} = \frac{\sigma_t}{\sigma_n} = \tan \psi + \mu\eta_0 \sec(30^\circ) \sec^2 \psi, \quad (8.2)$$

which characterizes the local material friction coefficient  $\mu_{\text{slip}}^{\text{FCC}}$  for each slip plane in a regular FCC array of uniform spheres at the initiation of yield under constant normal stress boundary conditions in terms of the inter-particle friction coefficient  $\mu$ , with particle rotation allowed. Note that equation (8.2) is the equation of a line, with  $\mu_{\text{slip}}^{\text{FCC}} = \tan \psi$  at  $\mu = 0$ . Figure 8.3 shows the resulting relationships between  $\phi_\mu = \tan^{-1} \mu$  and  $\phi_{\text{slip}}^{\text{FCC}} = \tan^{-1} \mu_{\text{slip}}^{\text{FCC}}$  given by equation (8.2) with  $\eta_0 = \{1, 0.5, 0.25\}$ .

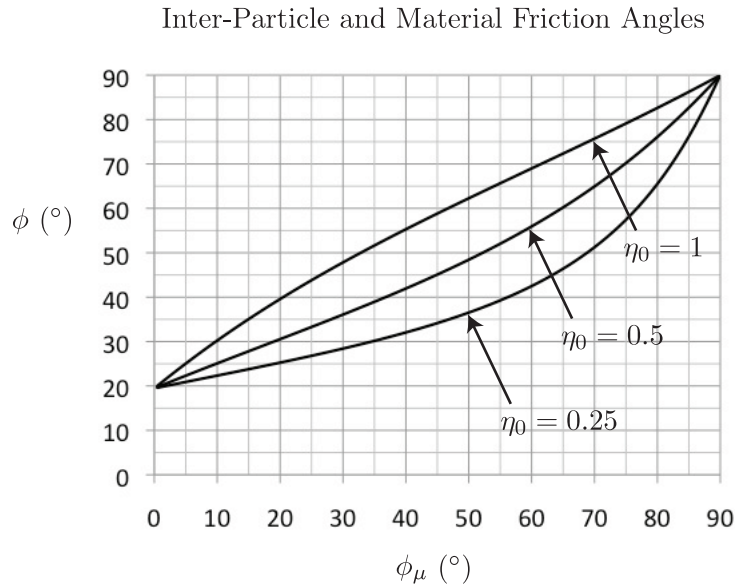


Figure 8.3: The relationship between the inter-particle friction coefficient  $\mu$  expressed as an inter-particle friction angle  $\phi_\mu = \tan^{-1} \mu$  and the local material friction angle  $\phi_{\text{slip}}^{\text{FCC}} = \tan^{-1} \mu_{\text{slip}}^{\text{FCC}}$  given by equation (8.2), with  $\eta_0 = \{1, 0.5, 0.25\}$ .

### Constant Volume

Figure 8.4 shows the free-body diagram of sphere  $A$  with constant volume boundary conditions. Note that, if the displacement of sphere  $A$  is in the  $\hat{u}_i$  direction (on the slip plane), then  $\sigma_n$  cannot remain constant. Consider the displacement  $\Delta \hat{u}_i$  shown in Figure 8.4. The normal and tangential contact forces between sphere  $A$  and spheres  $B$  and  $C$  are  $F_n = K_n \delta_n$  and  $F_t = K_t \delta_t$ , respectively, where  $\delta_n$  and  $\delta_t$  are the relative displacements between spheres  $A$  and spheres  $B$  and  $C$  normal and tangent to the contact planes, and  $K_n$  and  $K_t$  are the inter-particle contact stiffnesses in the normal and tangential directions, respectively, relative to the inter-particle contact planes. (Note:  $\delta_n$  and  $\delta_t$  are not in the directions normal and tangent to the slip plane like the stresses  $\sigma_n$  and  $\sigma_t$ .) As in the case of constant normal stress, we will assume initially that  $F_n = F_0 = K_n \delta_0$  and  $F'_n = \eta_0 F_0$ . Once again, if  $\eta_0 \leq 1$  sliding occurs between sphere  $A$  and spheres  $E$ ,  $F$ ,  $G$ , and  $H$  in Figure 8.1. Thus, at yield

$$F'_t = \mu F'_n = \mu \eta_0 F_0.$$

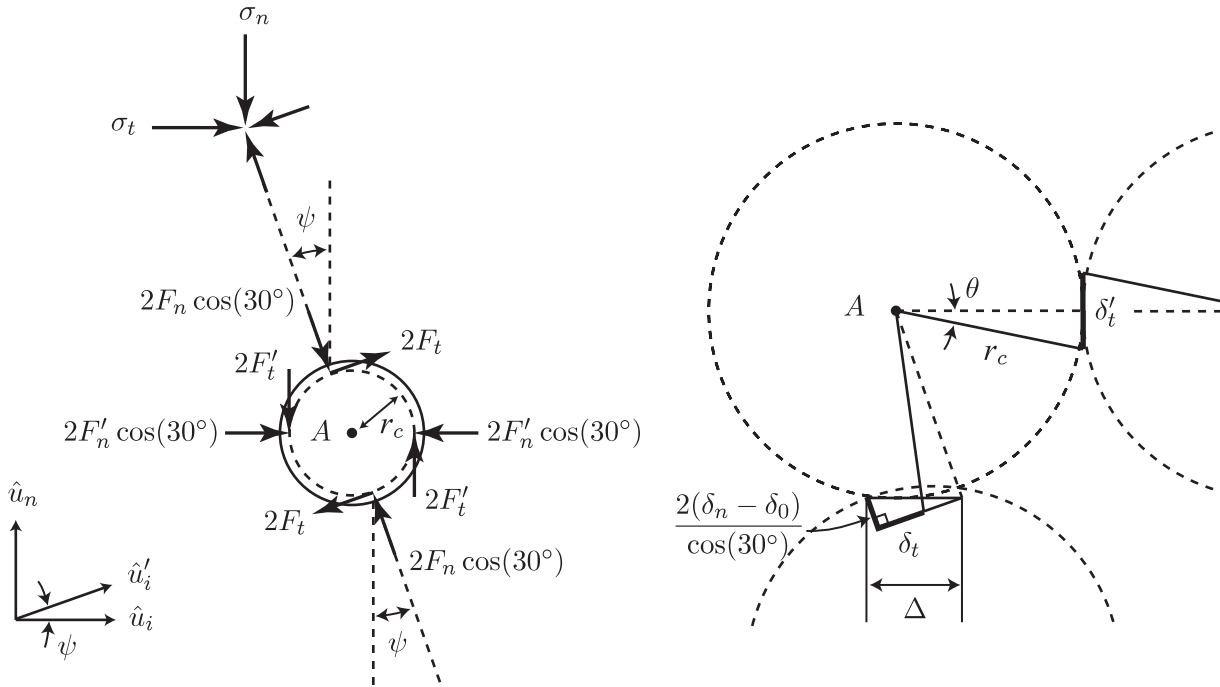


Figure 8.4: Free-body diagram of sphere  $A$  with constant volume boundary conditions.

If sphere  $A$  rotates clockwise through an angle  $\theta$  during the displacement  $\Delta \hat{u}_i$ , then employing small angle approximations we have  $\delta_n = \delta_0 + (\Delta/2) \cos(30^\circ) \sin \psi$  and  $\delta_t = \Delta \cos \psi - r_c \theta$ , where  $r_c = r \cos(30^\circ)$ ,  $r$  is the radius of the spheres, and  $\delta_0 = F_0/K_n$ . By symmetry, if sphere  $A$  rotates clockwise through an angle  $\theta$ , then spheres  $E$ ,  $F$ ,  $G$ , and  $H$  must do so likewise. Thus,  $\delta'_t = 2r_c \theta$ , and moment equilibrium for sphere  $A$  implies that  $F_t = K_t \delta_t = F'_t = K_t \delta'_t = K_t 2r_c \theta$ , which implies that  $\Delta = 3r_c \theta / \cos \psi$  and  $\theta = \mu \eta_0 F_0 / (2K_t r_c)$ , giving

$$\delta_n = \delta_0 \left( 1 + \frac{3\mu\eta_0}{4\alpha} \cos(30^\circ) \tan \psi \right) \quad \text{and} \quad \delta_t = \delta_0 \frac{\mu\eta_0}{\alpha}, \quad (8.3)$$

where  $\alpha = K_t/K_n$ . With  $F_n = K_n \delta_n$  and  $F_t = K_t \delta_t$ , equation 8.1 becomes

$$\text{Constant Volume:} \quad \mu_{\text{slip}}^{\text{FCC}} = \frac{\sigma_t}{\sigma_n} = \frac{\cos(30^\circ) \sin \psi + \mu \eta \cos \psi}{\cos(30^\circ) \cos \psi - \mu \eta \sin \psi}, \quad (8.4)$$

with  $\eta$  given by

$$\eta = \frac{F'_n}{F_n} = \frac{\eta_0}{1 + \frac{3\mu\eta_0}{4\alpha} \cos(30^\circ) \tan \psi}, \quad (8.5)$$

where  $\alpha = K_t/K_n$  is the ratio of the tangential to the normal inter-particle contact stiffnesses for the spheres. Equations (8.4) and (8.5) characterize the local material friction coefficient  $\mu_{\text{slip}}^{\text{FCC}}$  for each slip plane in a regular FCC array of uniform spheres at the initiation of yield under constant volume boundary conditions in terms of the inter-particle friction coefficient  $\mu$ , with particle rotation allowed. Figures 8.5 and 8.6 show the resulting relationships between  $\phi_\mu = \tan^{-1} \mu$  and  $\phi_{\text{slip}}^{\text{FCC}} = \tan^{-1} \mu_{\text{slip}}^{\text{FCC}}$  given by equations (8.4) and (8.5) with  $\alpha = K_t/K_n = 1$  and  $\eta_0 = \{1, 0.5, 0.25\}$ , and with  $\alpha = K_t/K_n = \{1, 0.5, 0.25, 0.125\}$  and  $\eta_0 = 1$ , respectively.

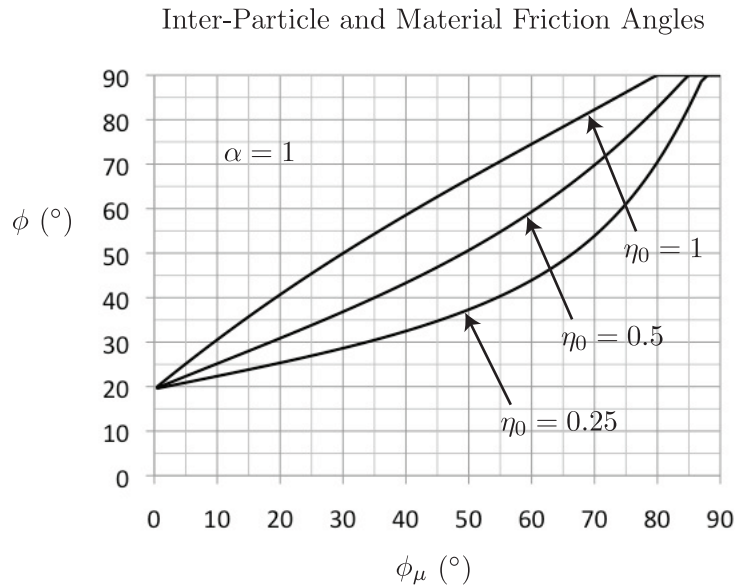


Figure 8.5: The relationship between the inter-particle friction coefficient  $\mu$  expressed as an inter-particle friction angle  $\phi_\mu = \tan^{-1} \mu$  and the local material friction angle  $\phi_{\text{slip}}^{\text{FCC}} = \tan^{-1} \mu_{\text{slip}}^{\text{FCC}}$  given by equations (8.4) and (8.5), with  $\alpha = K_t/K_n = 1$  and  $\eta_0 = \{1, 0.5, 0.25\}$ .

Finally, increasing the number of active (rotating) layers in the slip systems is essentially equivalent to adding tangential springs with stiffness  $K_t$  in series. Thus, *increasing* the number of active or rotating layers of spheres in a standard slip system of an FCC array of

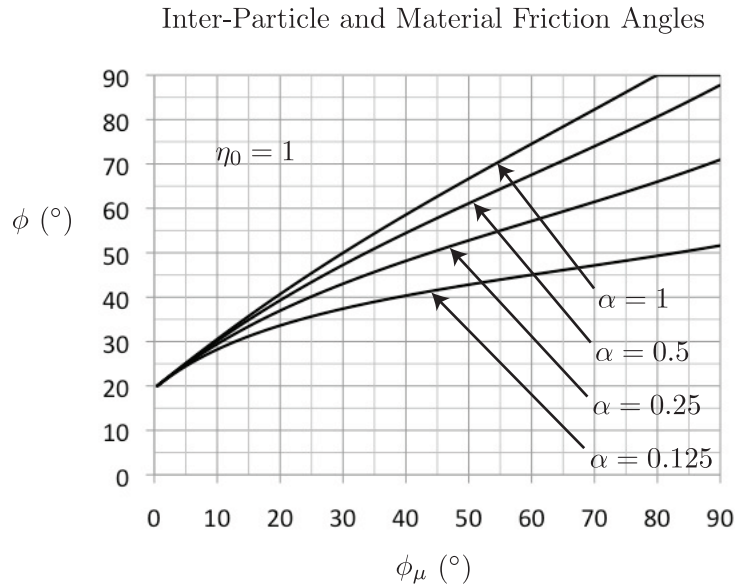


Figure 8.6: The relationship between the inter-particle friction coefficient  $\mu$  expressed as an inter-particle friction angle  $\phi_\mu = \tan^{-1} \mu$  and the local material friction angle  $\phi_{\text{slip}}^{\text{FCC}} = \tan^{-1} \mu_{\text{slip}}^{\text{FCC}}$  given by equations (8.4) and (8.5), with  $\alpha = K_t/K_n = \{1, 0.5, 0.25, 0.125\}$  and  $\eta_0 = 1$ .

uniform spheres under constant volume boundary conditions by a factor of  $n$  is equivalent to *decreasing*  $\alpha$  in equation (8.5) by a factor of  $1/n$ .

### 8.3.2 Simple Cubic (SC) Array of Uniform Spheres

Figure 7.5 in Section 7.3.2 shows an elementary cell of the simple cubic (SC) array of uniform spheres and one of the three crystallographically similar slip planes. The slip systems for the SC packing involve no initial dilation. Hence,  $\psi = 0$ . In Section 4.3.3, we analyzed the shearing deformation of an SC array of uniform spheres along one of the standard slip planes in the elastic range, including the effect of particle rotation. As we noted there, moment equilibrium at the particle level requires that the inter-particle tangential contact force  $F_t$  be the same between all of the contacting spheres. Thus, whether slip occurs first at the contacts parallel or perpendicular to the slip plane depends on the ratio  $\eta = F'_t/F'_n$  of the

inter-particle normal contact forces between spheres on the slip plane to those off of the slip plane. Since the slip systems in the SC packing involve no initial dilation, all inter-particle normal forces will remain the same during the initiation of yielding (assuming only small displacement from the initial regular packing geometry). Thus,  $\eta = \eta_0$  is constant. If the SC array is initially composed of evenly spaced uniform spheres with the same normal contact stiffness  $K_n$ , then  $\eta = \eta_0 = 1$ , and slip will occur at contacts parallel and perpendicular to the slip plane simultaneously. Assuming that  $\eta_0 \leq 1$ , yield will occur when  $F_t = \mu\eta F_n = \mu\eta_0 F_n$ , where  $\mu$  is the inter-particle friction coefficient. Thus, we have

$$\mu_{\text{slip}}^{\text{SC}} = \mu\eta_0, \quad (8.6)$$

which characterizes the local material friction coefficient  $\mu_{\text{slip}}^{\text{SC}}$  for each slip plane in a regular SC array of uniform spheres at the initiation of yield in terms of the inter-particle friction coefficient  $\mu$ , with particle rotation allowed.

### 8.3.3 Body-Centered Cubic (BCC) Array of Uniform Spheres

Figure 7.6 in Section 7.3.3 shows an elementary cell of the body-centered cubic (BCC) array of uniform spheres and one of the six crystallographically similar slip planes. As noted in Section 7.3.3, the slip systems for the BCC packing involve no initial dilation, and hence  $\psi = 0$ . If particle rotation is allowed, then the spheres in a BCC array will provide no resistance to relative motion in the direction tangent to the standard slip planes. Thus,

$$\mu_{\text{slip}}^{\text{BCC}} = 0 \quad (8.7)$$

is the local material friction coefficient for the standard slip planes in a regular BCC array of uniform spheres when particle rotation is allowed.

## 8.4 Yield in Statistically Isotropic Aggregates of Uniform Spheres Incorporating the Effect of Particle Rotation

If we employ the static homogenization hypothesis  $\mu_{\text{macro}} = \mu_{\text{slip}}$  that we used in Chapter 7, then the Mohr-Coulomb yield criterion is again given by

$$\frac{|\bar{\sigma}_i - \bar{\sigma}_j|}{2\sqrt{\bar{\sigma}_i \bar{\sigma}_j}} = \mu_{\text{macro}} = \mu_{\text{slip}}, \quad i \neq j, \quad i, j \in \{1, 2, 3\}, \quad (8.8)$$

for any combination of the principal stresses  $\bar{\sigma}_1$ ,  $\bar{\sigma}_2$ , and  $\bar{\sigma}_3$ , and the material friction angle is given by  $\phi = \tan^{-1} \mu_{\text{macro}} = \tan^{-1} \mu_{\text{slip}}$ . It follows that the relationship between  $\phi_\mu = \tan^{-1} \mu$  and  $\phi$  for a statistically isotropic locally FCC, BCC, or SC particulate aggregate material is given by equations (8.2)–(8.5), (8.7), or (8.6), respectively, and is shown for a locally FCC particulate aggregate material under constant volume boundary conditions in Figure 8.6 for a range of  $\alpha = K_t/K_n$ .

If we repeat the analysis of Section 8.3.1 for the arbitrary arrangement of particles on the slip plane shown in Figure 7.9, with the effect of particle rotation included, we obtain the following straightforward generalizations of equation (8.2) and equations (8.4) and (8.5) for the constant normal stress and constant volume boundary conditions:

$$\text{Constant Normal Stress:} \quad \mu_{\text{macro}} = \mu_{\text{slip}} = \tan \theta_2 + \mu \eta_0 \sec \theta_1 \sec^2 \theta_2, \quad (8.9)$$

$$\text{Constant Volume:} \quad \mu_{\text{macro}} = \mu_{\text{slip}} = \frac{\cos \theta_1 \sin \theta_2 + \mu \eta \cos \theta_2}{\cos \theta_1 \cos \theta_2 - \mu \eta \sin \theta_2}, \quad (8.10)$$

where  $\eta = F'_n/F_n$  is the ratio of the inter-particle normal contact forces between spheres on the slip plane to those off of the slip plane, given by

$$\eta = \frac{\eta_0}{1 + n \frac{3\mu\eta_0}{4\alpha^{**}} \cos \theta_1 \tan \theta_2}, \quad (8.11)$$

where  $\alpha^{**} = \xi^* \alpha = \xi^* K_t / K_n$  is the “effective” ratio of the tangential to the normal inter-particle contact stiffnesses for the spheres in the slip system during yield, and  $n$  is the number of active (rotating) layers in the slip system. Equations (8.9)–(8.11) characterize the local material friction coefficient  $\mu_{\text{slip}}$  for an arbitrary slip plane in an array of uniform spheres at the initiation of yield under constant normal stress and constant volume boundary conditions in terms of the inter-particle friction coefficient  $\mu$  and the angles  $\theta_1$  and  $\theta_2 = \psi$ , with particle rotation allowed.

The internal parameter  $\xi^*$  has the same meaning as the internal parameter  $\xi$  introduced in Chapter 4 [Fleischmann et al. (2013b)] for the elastic range. That is,  $\xi^*$  quantifies the presence of zero-energy modes or shearing mechanisms in a particulate material due to particle rotation and asymmetries in the distribution of inter-particle contacts. We distinguish  $\xi^*$  at yield from  $\xi$  because we expect more shearing mechanisms to be present when the peak material friction angle  $\phi$  is reached than were present in the elastic range. If  $\xi^* = 0$ , then all inter-particle contacts contain shearing mechanisms during yield, and  $\eta = 0$ , which results in  $\mu_{\text{slip}} = \tan \theta_2 = \tan \psi$  in equation (8.10), and the material friction angle is equal to the initial dilation angle  $\phi = \psi$  for all values of the inter-particle friction coefficient  $\mu$ . An example of this is yield on the standard slip planes in the local BCC packing, for which  $\xi^* = 0$  and  $\phi = \psi = 0$ . Another example is the case where only force chains of type  $\langle I, J \rangle \rightarrow \langle A \rangle \rightarrow \langle B, C \rangle$  exist in the slip system shown in Figure 8.1, for which  $\xi^* = 0$  and  $\phi = \psi = \sin^{-1}(1/3) \approx 19.47^\circ$ . If  $\xi^* = 1$ , then no shearing mechanisms are present, and the relationship between  $\mu_{\text{slip}}$  and the inter-particle friction coefficient  $\mu$  depends on  $\theta_1$ ,  $\theta_2 = \psi$ ,  $\alpha$ , and  $n$ , as it did for the local FCC packing in equations (8.4) and (8.5).

Note that equation (8.10) is a direct extension of equation (7.13) incorporating the effect of particle rotation, and as before  $\theta_2 = \psi$  is the initial dilation angle, and  $\theta_1$  characterizes what we call the “v-belt effect” in Chapter 9 [Fleischmann et al. (2013c)], which is an intuitive way of understanding (nominally 2-D) yielding in a physically three-dimensional

particulate material. Equation (8.9) and equations (8.10) and (8.11) reproduce the equations in Section 8.3 for  $\mu_{\text{slip}}^{\text{FCC}}$  with  $\theta_1 = 30^\circ$  and  $\theta_2 = \sin^{-1}(1/3) \approx 19.47^\circ$ ,  $\mu_{\text{slip}}^{\text{SC}}$  with  $\theta_1 = \theta_2 = 0$ , and  $\mu_{\text{slip}}^{\text{BCC}}$  with  $\theta_2 = 0$  and  $\xi^* = 0$  (or  $\eta_0 = 0$ ). To avoid the introduction of a third angle in the derivation of equation (8.9) and equations (8.10) and (8.11), we have assumed that the (normal) contact angle between spheres on the generalized slip plane shown in Figure 7.9 relative to the preferential slip direction  $\hat{u}_i$  is also equal to  $\theta_1$ .

As in Chapter 7, for a random assembly of uniform spheres, since the angle  $\theta_1$  is geometrically bounded and (approximately) uniformly distributed between  $30^\circ \leq \theta_1 \leq 90^\circ$  (Zhou and Dinsmore, 2009), we may use  $\theta_1 = \bar{\theta}_1 = 60^\circ$  in equation (8.9) and equations (8.10) and (8.11). Moreover, it is reasonable to assume that  $\eta_0 = 1$  in a statistically isotropic assembly. This gives the following simplified generalized model for a statistically isotropic assembly of uniform spheres incorporating the effect of particle rotation:

$$\text{Constant Normal Stress:} \quad \mu_{\text{macro}} = \mu_{\text{slip}} = \tan \psi + 2\mu \sec^2 \psi, \quad (8.12)$$

$$\text{Constant Volume:} \quad \mu_{\text{macro}} = \mu_{\text{slip}} = \frac{\sin \psi + 2\mu\eta \cos \psi}{\cos \psi - 2\mu\eta \sin \psi}, \quad (8.13)$$

where  $\mu$  is the inter-particle friction coefficient,  $\psi$  is the initial dilation angle, and  $\eta$  is given by

$$\eta = \frac{1}{1 + n \frac{3\mu}{8\alpha^{**}} \tan \psi}, \quad (8.14)$$

where  $\alpha^{**} = \xi^* \alpha = \xi^* K_t / K_n$  as before, and  $n$  is the number of active (rotating) layers in the slip system. The material friction angle is given by  $\phi = \tan^{-1} \mu_{\text{macro}}$ .

As always, the merit of the generalized models given by equations (8.9)–(8.11) or by equations (8.12)–(8.14) rests on their ability to model true isotropic particulate materials. Figure 8.7 shows the relationship between the inter-particle friction coefficient  $\mu$  expressed as an inter-particle friction angle  $\phi_\mu = \tan^{-1} \mu$  and the material friction angle  $\phi$  obtained

from the DEM simulations of Chapter 6, performed on randomly packed assemblies of 3 430–29 660 uniform spheres under constant volume boundary conditions with particle rotation allowed. Also shown in Figure 8.7 are the curves predicted by equations (8.13) and (8.14) with  $n = 3$ ,  $\psi = 10^\circ$ , and  $\xi^* = \{0.06, 0.08, 0.09\}$ . Figure 8.7 shows an exceptional match

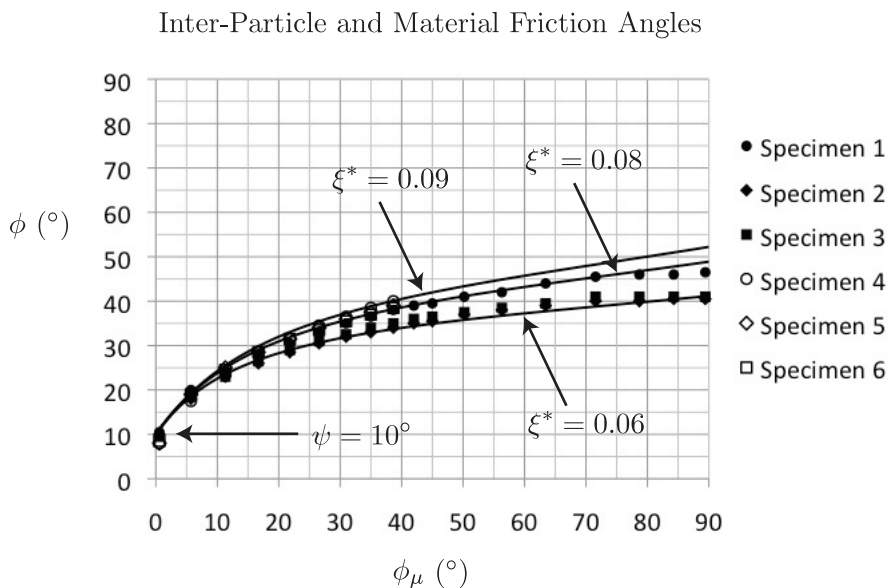


Figure 8.7: The relationship between the inter-particle friction coefficient  $\mu$  expressed as an inter-particle friction angle  $\phi_\mu = \tan^{-1} \mu$  and the material friction angle  $\phi$  obtained from the DEM simulations of Chapter 6 performed under constant volume boundary conditions with particle rotation allowed, along with the curves predicted by equations (8.13) and (8.14) with  $n = 3$ ,  $\psi = 10^\circ$ , and  $\xi^* = \{0.06, 0.08, 0.09\}$ .

between the  $\phi$  versus  $\phi_\mu$  curves predicted by equations (8.13) and (8.14) and the DEM data points obtained in Chapter 6. The quality of this match is remarkable for the following reasons:

First, while an examination of the form of equation (8.14) shows that infinitely many combinations of  $n$  and  $\xi^*$  could have produced the same curves shown in Figure 8.7, the value of  $n = 3$  is based on observations of actual slip planes in the DEM specimens during yielding, shown for Specimen 5 in Figures 6.52 and 6.53, and the same value of  $n = 3$  was used for all six DEM specimens. Recalling that the values of the internal parameter  $\xi$  chosen

in Chapter 4 [Fleischmann et al. (2013b)] to match the *elastic* behavior (specifically Poisson's ratio) of the same DEM specimens were  $\xi = \{0.75, 0.6, 0.55, 0.85, 0.8, 0.75\}$  for Specimens 1–6, respectively, the choice of  $n = 3$  results in values of  $\xi^*$  that are approximately 10% of the respective values of  $\xi$  for the same specimens in the elastic range. In fact, an adequate match to the data points for all six DEM specimens is obtained if we simply let  $\xi^* = 0.1\xi$ . Given this observation, the only remaining parameter in the generalized model given by equations (8.13) and (8.14) needed to match the DEM data points is the initial dilation angle  $\psi = 10^\circ$ , which is the same as the value chosen in Chapter 7 for the case of no particle rotation, and which was chosen to match the material friction angle  $\phi \approx 10^\circ$  at  $\mu = 0$  ( $\phi_\mu = 0$ ) for all six DEM specimens.

The fact that  $\xi^* \approx 0.1\xi$  agrees with our observations in Section 6.5, where we noted the presence of force chain buckling during yielding *before* the peak friction angle  $\phi$  was reached, followed by the mobilization of slip planes (involving particle rotation) *after* the peak friction angle was reached. The buckling of force chains implies a rearrangement of particles in favor of lower energy, and this suggests an *increase* in the presence of shearing mechanisms, which implies a *decrease* in  $\xi^*$  compared to  $\xi$  in the elastic range. Thus, by the time the peak friction angle  $\phi$  is reached, a value of  $\xi^* \approx 0.1\xi$  is not unreasonable.

Finally, the curves predicted by equations (8.13) and (8.14) provide a significantly better match to the DEM data points of Chapter 6 (under constant volume conditions with particle rotation allowed) than those derived by Emeriault et al. (1996), which are given by equation (2.13) in Section 2.2 of this thesis, for any value of their internal parameter  $\zeta$  as illustrated in Figure 8.8. The internal parameter  $\zeta$  (or “ $\mu$ ”) of Emeriault et al. (1996) corresponds roughly to our internal parameter  $\xi$ , as discussed in Section 4.6, where  $\zeta$  is referred to as “ $\mu$ ” as it is in Cambou et al. (1995) and Emeriault et al. (1996). Note that the model of Emeriault et al. (1996) does not allow the material friction angle  $\phi$  to be nonzero when  $\mu = 0$ , whereas we observe a nonzero value of  $\phi = \psi$  when  $\mu = 0$  in all of our DEM specimens,

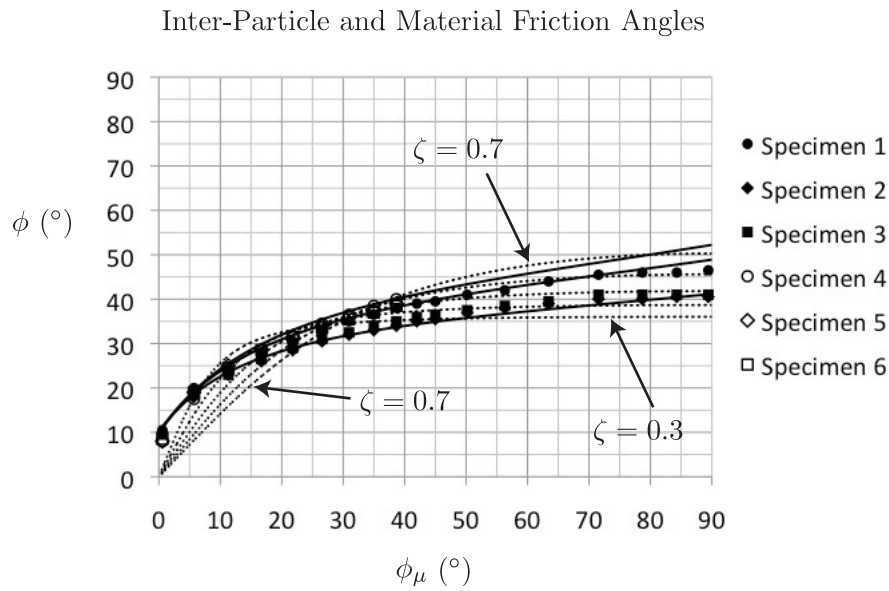


Figure 8.8: The relationship between the inter-particle friction coefficient  $\mu$  expressed as an inter-particle friction angle  $\phi_\mu = \tan^{-1} \mu$  and the material friction angle  $\phi$  obtained from the DEM simulations of Chapter 6 performed on randomly packed assemblies of 3 430–29 660 uniform spheres under constant volume boundary conditions with particle rotation allowed, along with the curves predicted by equations (8.13) and (8.14) with  $n = 3$ ,  $\psi = 10^\circ$ , and  $\xi^* = \{0.06, 0.08, 0.09\}$  (solid lines), and the relation derived by Emeriault et al. (1996), given by equation (2.13) in Section 2.2, with  $\zeta = \{0.3, 0.4, 0.5, 0.6, 0.7\}$  (dotted lines).

regardless of whether particle rotation is allowed or prohibited, as noted first in Section 5.6. Moreover, the shapes of the curves predicted by the model of Emeriault et al. (1996) given by equation (2.13) cannot match the DEM data points of Chapter 6 for both  $\mu \rightarrow 0$  and  $\mu \rightarrow \infty$  ( $\phi_\mu \rightarrow 0$  and  $\phi_\mu \rightarrow 90^\circ$ ) at the same time for any value of the internal parameter  $\zeta$ . On the other hand, the curves predicted by our generalized model given by equations (8.13) and (8.14) have shapes that are able to match the DEM data points exceptionally well for all values of the inter-particle friction coefficient  $\mu$  given appropriate choices of the internal parameter  $\xi^* \approx 0.1\xi$  and the initial dilation angle  $\psi$ .

It is worth noting that numerical (DEM) and experimental triaxial tests on regular packings (face-centered cubic and rhombic) of 1 500–2 000 spheres have been performed by O’Sullivan et al. (2004). In this study, the physical and numerical triaxial tests were performed on regular FCC packings of uniform steel spheres with inter-particle friction angle  $\phi_\mu \approx 5.5^\circ$  with the principal directions of the cubic packing aligned with the axial and lateral directions of the triaxial apparatus. It was found that the mean peak angle of mobilized friction for these FCC specimens was  $\phi_m \approx 24^\circ$ , with  $\phi_m = \sin^{-1}[(\sigma_1 - \sigma_3)/(\sigma_1 + \sigma_3)]$ , where  $\sigma_1$  and  $\sigma_3$  were the measured axial and lateral stresses during the triaxial tests, respectively. It is important to note that in this calculation, O’Sullivan et al. (2004) are not computing the friction angle of the FCC packing on its preferred slip planes, as we do in Section 8.3.1, since the orientation of the preferred slip planes (a geometric property of the packing) are not likely to align with the orientation of the plane of maximum  $\sigma_t/\sigma_n$  (a function of the loading) during the triaxial tests. This is in contrast with our analyses of the conditions for sliding along the preferred slip planes in *local* regular packings, which is applicable only to a statistically isotropic particulate material in which every orientation of the local (regular or generalized) packings are equally represented, so that the plane of maximum  $\sigma_t/\sigma_n$  in the specimen can always be assumed to coincide with *some* local preferred slip plane, as we discuss in Section 7.4 when we introduce our (static) homogenization assumption.

O’Sullivan and Cui (2009) performed numerical (DEM) and physical triaxial tests on *random* assemblies of uniform and non-uniform chrome steel spheres with an inter-particle friction coefficient of  $\mu = 0.096$  ( $\phi_\mu \approx 5.5^\circ$ ). In this study, for a random assembly of approximately 15 000 spheres with a void ratio of approximately 0.62, a peak material friction angle of  $\phi \approx 19^\circ$  was measured both experimentally and by DEM, which we note is in remarkable agreement with our own DEM results of Chapter 6 (with  $\mu = 0.1$ ) and with the corresponding prediction of our generalized (constant volume) model with the parameters chosen for Figure 8.7. O’Sullivan and Cui (2009) also monitor and record the variation in the average contact force and coordination number, the average motion of particles, and the evolution of the fabric tensor for their DEM specimens during monotonic and cyclic loading, both pre- and post-yield. A discussion of post-yield behavior, however, takes us beyond the scope of this chapter, in which we have dealt only with the initiation of yield.

## 8.5 Conclusion

We have obtained a generalized model incorporating the effect of particle rotation that predicts the material friction angle  $\phi = \tan^{-1} \mu_{\text{macro}}$  or the material friction coefficient  $\mu_{\text{macro}}$  for a statistically isotropic non-cohesive particulate material on the macroscale in terms of the inter-particle friction coefficient  $\mu$  or inter-particle friction angle  $\phi_\mu = \tan^{-1} \mu$  between individual particles on the microscale. This was done by analyzing specific local packings, in particular the local face-centered cubic (FCC) packing and its generalizations, to obtain  $\mu_{\text{slip}}$  on the local slip planes, and applying the very simple (static) homogenization hypothesis  $\mu_{\text{macro}} = \mu_{\text{slip}}$ .

Despite the simplicity of this homogenization hypothesis, we found that for constant volume boundary conditions the relationship between  $\mu_{\text{macro}}$  and  $\mu$  depends both on the initial dilation angle  $\psi$  of the particulate material and on the *elastic* properties of the individual

particles, specifically on the ratio of the inter-particle tangential and normal contact stiffnesses  $\alpha = K_t/K_n$ . This ratio is also of great importance to Poisson's ratio for a particulate material in the elastic range (Fleischmann et al., 2013b). In this respect, the constant volume model of this chapter is similar to results obtained for locally FCC metals using the self-consistent homogenization hypothesis (Hutchinson, 1970). Moreover, introducing an internal parameter  $\xi^*$  with the same intuitive meaning as the internal parameter  $\xi$  introduced in Chapter 4 for the elastic range allowed us to obtain excellent agreement between the generalized model given by equations (8.13) and (8.14) and the relationship between  $\phi_\mu$  and  $\phi$  obtained in Chapter 6 from DEM simulations performed on randomly packed assemblies of 3 430–29 660 uniform spheres under constant volume boundary conditions with particle rotation allowed, for all values of the inter-particle friction coefficient  $\mu$ . It is particularly noteworthy that our generalized model, which is based on a relatively simple and direct micromechanical analysis of translational and rotational particle motion and force equilibrium on local slip planes, can provide this excellent match to the DEM data points of Chapter 6 for all values of  $\mu$ , including the limiting behavior as  $\mu \rightarrow 0$  and  $\mu \rightarrow \infty$ , while the model of Emeriault et al. (1996), which is based on a more complicated derivation following that of Cambou et al. (1995), discussed in Sections 2.1, 2.2, and 4.6, is unable to provide as good a match to the DEM data points over the full range of  $\mu$  for any value of their internal parameter.

In addition to providing a clear micromechanical understanding of the *form* of the relationship between  $\mu$  and  $\mu_{\text{macro}}$ , our generalized model may also provide a practically useful *predictive* model. While the only material parameter needed in equation (8.12) for the constant normal stress case is the initial dilation angle  $\psi$ , we can reduce the number of material parameters in equations (8.13) and (8.14) for the constant volume case as well, given the observation that we may heuristically let  $n = 3$  and  $\xi^* = 0.1\xi$ , with  $\xi$  given in terms of the average number of contacts per unit volume  $\beta$  in the particulate material by equation (4.20),

with  $\beta$  given in terms of the average coordination number  $\bar{n}_c$  and the void ratio  $e$  in the particulate material by equations (2.8)–(2.12), and with  $\alpha = K_t/K_n = 2(1 - \nu)/(2 - \nu)$ , where  $\nu$  is Poisson’s ratio for the material constituting the spheres (not for the particulate material as a whole). Then equations (8.13) and (8.14) provide a relationship between the inter-particle friction coefficient  $\mu$  on the microscale and the material friction coefficient  $\mu_{\text{macro}}$  or the material friction angle  $\phi = \tan^{-1} \mu_{\text{macro}}$  on the macroscale, for the case of constant volume, in terms of the initial dilation angle  $\psi$  and the void ratio  $e$  for the particulate material as a whole and Poisson’s ratio  $\nu$  for the material constituting the spheres. More work is clearly necessary, however, to gain a deeper understanding of the internal parameter  $\xi^*$  and to predictively characterize the number of active slip planes  $n$  in the constant volume case, although for all six randomly packed DEM specimens consisting of 3 430–29 660 spheres tested in Chapter 6, the value  $n = 3$  provided a good match to the data points.

## Chapter 9

# Quantitative Comparison of Two-Dimensional and Three-Dimensional Discrete Element Simulations of Nominally Two-Dimensional Shear Flow <sup>1</sup>

### 9.1 Abstract

We report results obtained from numerical simulations of direct (or ring) shear tests on ASTM standard graded (Ottawa) sand using the discrete element method (DEM) with periodic boundary conditions in both two and three dimensions. We quantitatively compare the data obtained from these simulations to experimental data for ASTM standard graded sand. Our results show that the three-dimensional effects of non-planar inter-particle contact forces

---

<sup>1</sup>This chapter closely follows Fleischmann et al. (2013c).

and particle motion are significant in the three-dimensional DEM simulations, even during nominally two-dimensional shear flow. Moreover, the three-dimensional DEM simulations accurately predict the peak and residual friction angles of ASTM standard graded sand. On the other hand, the two-dimensional DEM simulations fail to accurately predict the peak and residual friction angles. We argue that the failure of the two-dimensional DEM simulations and the success of the three-dimensional DEM simulations to provide quantitatively accurate predictions of peak and residual friction angles is due largely to the respective absence or presence of three-dimensional effects, including non-planar inter-particle contact forces and non-planar particle motion, in these DEM simulations.

## 9.2 Introduction

The discrete (or distinct) element method has been used effectively to numerically model the quasi-static and dynamic behavior of particulate materials, especially dry or saturated sand, since its introduction by Cundall and Strack (1979). Because of the large amount of experimental data available in the literature for comparison, the direct (box) shear test or the ring shear test have been frequently modeled by DEM (see, e.g., Jensen et al., 2001a,b, Zhang and Thornton, 2002, Liu et al., 2005, Liu, 2006, Cui and O'Sullivan, 2006, Cheng and Minh, 2009, Zhou et al., 2009, Wang and Gutierrez, 2009, Orlando et al., 2009, Yan and Ji, 2010). Due to constraints in computational resources, many contemporary DEM simulations are still performed in two dimensions, meaning that all motion and all DEM inter-element contact forces have been constrained to exist only in the plane of the nominally two-dimensional loading and shearing motion. For example, of the references cited above, only Cui and O'Sullivan (2006), Orlando et al. (2009), and Yan and Ji (2010) perform three-dimensional DEM simulations, while the rest perform two-dimensional DEM simulations. Compared to DEM simulations performed in three dimensions, DEM simulations performed in two

dimensions have the obvious advantage of decreasing the number of elements needed to model a physical specimen of the same dimensions, thereby reducing the run-time of the simulation correspondingly. Moreover, the complexity of certain optimized contact algorithms, such as the cell-list algorithm, can be lowered significantly when all inter-element contacts lie in a single plane (see, e.g., Frenkel and Smit, 2002), and the minimum stable time-step size for a two-dimensional DEM simulation is significantly larger than for a three-dimensional DEM simulation (O’Sullivan and Bray, 2004).

It seems reasonable to expect that the error introduced by the idealizations of a two-dimensional DEM simulation would be minimal for nominally two-dimensional loading and shearing motion, such as in a direct shear or ring shear test. However, our research has shown that even for a ring shear test in which the particle size is much smaller than the size of the specimen (thereby minimizing boundary effects) the residual friction angle predicted by a two-dimensional and a three-dimensional DEM simulation differ substantially. We argue that this is due largely to the non-negligible inter-particle contact forces and particle motion that both occur in the nominally “out-of-plane” direction during a three-dimensional DEM simulation. Such “out-of-plane” motion was observed experimentally in direct shear tests on Ottawa sand by Guler et al. (1999) using image analysis techniques. We track such motion of particles in our three-dimensional DEM simulation, and we show that the displacement of particles within the shear zone in the “out-of-plane” direction can be more than 10% of their displacement in the direction of shearing motion. Moreover, we show by an analysis of the inter-particle contact forces in our DEM simulations that the geometry of the inter-particle contacts in the three-dimensional simulation causes an increase in the apparent friction during sliding motion when compared to the two-dimensional simulation, which leads to a significant increase in the predicted value of the peak and residual friction angles. By analogy, this increase is similar to the enhancement of friction provided by a “v-belt” and pulley system when compared to a flat belt and pulley system. Comparing the peak and residual friction

angles predicted by the DEM simulations to those of ASTM standard graded (Ottawa) sand, we find that the three-dimensional DEM simulation gives *quantitatively* correct results, while the results obtained from the two-dimensional DEM simulation are only *qualitatively* correct. Taken together, our findings suggest that if quantitatively correct predictions of the behavior of a particulate material are needed, then it is necessary to run fully three-dimensional DEM simulations, even if the behavior in question is generally regarded as two-dimensional in character, such as in the case of the direct box or ring shear tests.

### 9.3 Discrete Element Method

In its most basic form, the discrete element method models a particulate medium using a massive collection of distinct rigid elements having simple shapes, such as circles (or bars) in 2-D or spheres in 3-D. Contact between the DEM elements may be modeled by nonlinear Hertz-Mindlin theory, or by a simple linear spring arrangement as shown in Figure 9.1. Friction is modeled as shown in Figure 9.1 at the right. To model friction, the contact

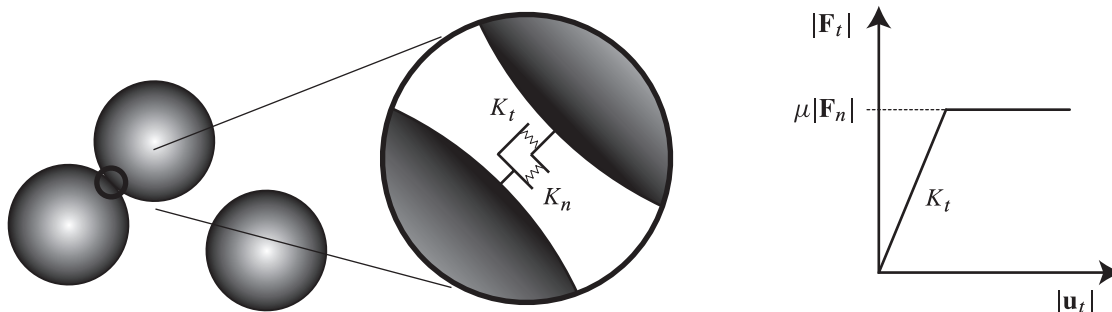


Figure 9.1: Linear spring contact model (left) and tangential contact force-displacement law (right) for spherical DEM elements with Coulomb friction.

history between pairs of elements in contact must be stored. Contact between DEM elements is “soft” in the sense that elements are allowed to overlap before a corrective contact force is applied. To be more specific, let  $u_n$  in equation (9.1) be the radial overlap distance between

two contacting spherical elements, let  $\mathbf{v}_n$  and  $\mathbf{v}_t$  in equations (9.1) and (9.2) be the relative normal and tangential velocities at the point of contact, and let  $\mathbf{u}_t$  in equation (9.2) be the elastic part of the total accumulated tangential displacement between the surfaces of the two spheres since the contact was initiated, projected onto the plane of contact and scaled as necessary to satisfy the frictional sliding criterion  $|\mathbf{F}_t| \leq \mu|\mathbf{F}_n|$  shown in Figure 9.1. Then, using the linear spring model, the normal and tangential force vectors  $\mathbf{F}_n$  and  $\mathbf{F}_t$  at the point of contact are given by equations (9.1) and (9.2), respectively, where  $K_n$  and  $K_t$  are the normal and tangential elastic contact spring stiffnesses,  $\mathbf{n}$  is the unit normal vector along the line connecting the centers of the contacting spheres (in the appropriate direction),  $\gamma_n$  and  $\gamma_t$  are normal and tangential viscoelastic damping constants, and  $m_{\text{eff}} = m_i m_j / (m_i + m_j)$  is the effective mass of the two spheres having masses  $m_i$  and  $m_j$  (Silbert et al., 2001). Once the inter-element contact forces are calculated, the translational and rotational motion of the elements are obtained by applying an explicit time integration scheme, such as the central difference algorithm described in Cook et al. (2002) or the Verlet algorithm described in Frenkel and Smit (2002).

$$\mathbf{F}_n = K_n u_n \mathbf{n} - \gamma_n m_{\text{eff}} \mathbf{v}_n \quad (9.1)$$

$$\mathbf{F}_t = -K_t \mathbf{u}_t - \gamma_t m_{\text{eff}} \mathbf{v}_t \quad (9.2)$$

For the simulations in this paper, we have chosen to use the linear spring model exclusively, for the following two reasons. First, we believe that the simplicity of the linear spring contact algorithm will bring into sharper focus the differences between the 2-D and 3-D simulations. Furthermore, for deformations that feature large sliding displacements, such as shear zone formation and subsequent slip, prior work has shown relative insensitivity of results to the elastic portion of the DEM inter-element contact behavior (Di Renzo and Di Maio, 2004). The use of the linear spring contact model allows us to apply the results of O'Sullivan and Bray (2004) to obtain a reliable critical time-step size, which is given in terms of the

minimum element mass  $m_{\min}$  and the maximum inter-element contact spring stiffness  $K_{\max}$  by equations (9.3) and (9.4) for 2-D and 3-D DEM simulations, respectively.

$$\Delta t_{\text{crit}}^{(2\text{-D})} \approx 0.3 \sqrt{\frac{m_{\min}}{K_{\max}}} \quad (9.3)$$

$$\Delta t_{\text{crit}}^{(3\text{-D})} \approx 0.2 \sqrt{\frac{m_{\min}}{K_{\max}}} \quad (9.4)$$

This estimate is based on the standard stability criterion for the central difference explicit time integration scheme applied to linear systems,  $\Delta t < (2/\omega_{\max}) (\sqrt{1 + \xi^2} - \xi)$ , where  $\omega_{\max}$  is the maximum natural frequency of the stiffness and mass matrices associated with the system, and  $\xi$  is the fraction of critical damping at  $\omega_{\max}$  (Cook et al., 2002). For DEM,  $\omega_{\max}$  must be estimated, because internal forces are evaluated in an element-by-element fashion, and hence the stiffness matrix for the system is not formed. The estimates in equations (9.3) and (9.4) ignore the mass proportional damping included in equations (9.1) and (9.2), which has the effect of only slightly decreasing the stability of the system for most problems, since the fraction of critical damping due to mass proportional damping at high frequencies is small. [For original derivations of alternative estimates of the critical time-step size for 2-D and 3-D DEM based on the Gerschgorin bound, see Appendix E.]

For our DEM simulations, we use a modified version of LAMMPS, the Large-scale Atomic/Molecular Massively Parallel Simulator developed at Sandia National Laboratories, which can be used for molecular dynamics simulations as well as for DEM simulations (Plimpton, 1995). A few of the advantages of LAMMPS are that it is open-source, it is easy to expand and modify, and it is optimized for massive parallel computing. More information about LAMMPS can be found at the LAMMPS [www](http://www.lammps.org) site (LAMMPS).

## 9.4 Methodology

To explore three-dimensional effects in direct shear tests, we have performed both 2-D and 3-D DEM simulations of direct (ring) shear tests on Ottawa standard graded sand. Ottawa sand particles typically have a Krumbein roundness and sphericity between 0.7 and 0.9 (Cho et al., 2006). In general, values of Krumbein roundness and sphericity above 0.6 indicate high roundness, values between 0.4 and 0.6 indicate medium roundness, and values below 0.4 indicate low roundness. A perfect sphere has a Krumbein roundness and sphericity of exactly 1.0. We chose to model Ottawa sand in our DEM simulations because its physical behavior is well known, and because its particles are well rounded, thus enhancing the ability of spherical DEM elements to model its behavior.

The sand specimens in the 2-D and 3-D simulations each consisted of 50 000 spherical DEM elements between upper and lower bounding surfaces, which were modeled as solid rigid bodies composed of overlapping spheres. Figure 9.2 shows portions of the 2-D and 3-D specimens used in the DEM simulations, with the upper and lower bounding surfaces shaded. Since the packing densities (or void ratios) of a 2-D specimen and a 3-D specimen are not geometrically comparable, and since we desired the 2-D and 3-D specimens to be as comparable as possible, a maximum initial packing density was sought for both specimens by the following preparation procedure. First, randomly placed DEM elements were generated between the upper and lower bounding surfaces in both specimens. Then the friction between the DEM elements was turned off, and the upper and lower bounding surfaces were brought together with a prescribed compressive force, after which the bounding surfaces were vibrated until no further increase in packing density (or decrease in void ratio) was observed in either the 2-D specimen or the 3-D specimen. Finally, the friction between the DEM elements was turned back on, the lower bounding surface was fixed, and a constant compressive force was applied to the upper bounding surface. In the 3-D simulation, both the  $x$  and  $z$  boundaries

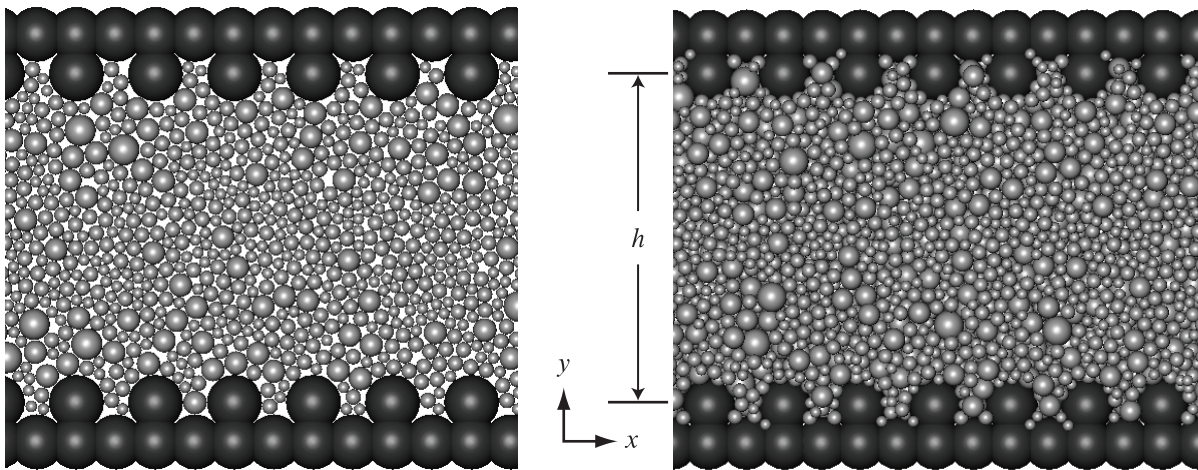


Figure 9.2: Portions of the initial specimens for the 2-D (left) and 3-D (right) DEM direct (ring) shear simulations.

were periodic. In the 2-D simulation, the  $x$  boundary was periodic, and the elements were constrained to move only in the  $x$ - $y$  plane (i.e., no motion was allowed in the  $z$  direction).

Elements of four different sizes were used, with diameters of 0.3 mm, 0.4 mm, 0.6 mm, and 0.8 mm. The distribution of the elements was chosen to match the particle size distribution of standard graded (Ottawa) sand, as specified in ASTM standard C 778-06. The particle size distribution is shown in Figure 9.3. Note that the particle size distribution is percent by weight (or volume), rather than percent by number of particles. Also note that when computing individual element weights for the 2-D simulation, the elements were treated as spheres rather than rods, so that the same number of elements of each size were used in both the 2-D and 3-D simulations. After preparation, the initial void ratio of the 3-D specimen was approximately  $e = 0.43$ , which corresponds to densely packed sand. While the void ratio of a 2-D specimen is generally not geometrically comparable to that of real sand, it is possible to calculate a “pseudo 3-D” void ratio for the 2-D specimen (Di Maio and Di Renzo, 2007), where the elements in the 2-D specimen are treated as spheres and the thickness of

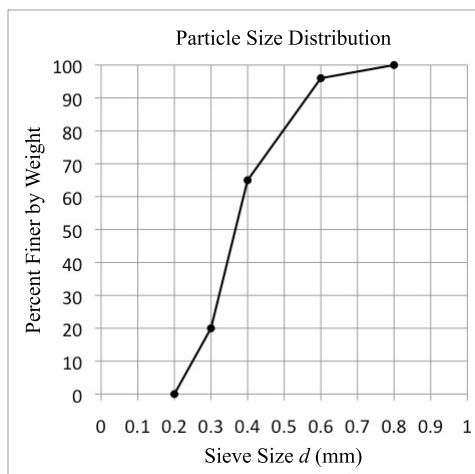


Figure 9.3: Particle size distribution for the 2-D and 3-D DEM direct (ring) shear simulations, corresponding to the particle size distribution of standard graded (Ottawa) sand, as specified in ASTM standard C 778-06.

the 2-D specimen is taken to be the average diameter of the elements. Using this approach, the initial “pseudo 3-D” void ratio of the 2-D specimen after preparation was approximately  $e = 0.45$ .

The direct shear test DEM simulations were carried out under constant normal-stress conditions in both 2-D and 3-D. The lower bounding surface was fixed, and a uniform normal compressive stress of 1 MPa was applied to the upper bounding surface. A constant shear displacement velocity of 100 mm/s in the horizontal ( $x$ ) direction was applied to the upper bounding surface. It may be noted that, while a normal compressive stress of 1 MPa is typical for direct shear tests on sand, a shear displacement velocity of 100 mm/s is somewhat higher than those typically used for quasi-static direct shear tests. However, an exploration of the effect of using different displacement velocities performed by the authors showed that increasing the prescribed velocity by an order of magnitude had no significant effect on the results of the DEM simulations, other than to introduce some high frequency vibrations during fully developed (critical state) shear, primarily in the 3-D simulation. In particular, increasing the prescribed displacement velocity by an order of magnitude had no effect on

the peak or residual friction angles predicted by the DEM simulations. The dimensions of the 3-D specimen were  $h = 8.7$  mm (initially) by 30 mm in the  $x$  direction by 10 mm in the  $z$  direction. The dimensions of the 2-D specimen were  $h = 8.7$  mm (initially) by 850 mm in the  $x$  direction. Note that, because of the periodic boundary conditions in the  $x$  direction, both the 2-D and 3-D DEM simulations model a direct *ring* shear test more closely than a direct *box* shear test, where the  $y$  direction corresponds to the radial direction, and the  $x$  direction corresponds to the  $\theta$  direction. The use of periodic boundary conditions in the  $x$  and  $z$  directions in the simulations allows us to assume that the physical dimensions of the specimens in the  $x$  and  $z$  directions are both much larger than the diameter of the largest DEM element. This is important, since the experimental results of Cerato and Lutenecker (2006) suggest that to obtain a value of the residual friction angle that is independent of specimen size, the horizontal dimension of a direct shear test specimen must be at least 50 times larger than the largest particle diameter.

Inter-element DEM contact forces were modeled by linear springs, as described in an earlier section. The normal spring stiffness was taken to be  $K_n = 10^9$  N/mm, and the tangential spring stiffness was taken to be  $K_t = 8(10^8)$  N/mm. The normal spring stiffness  $K_n$  was chosen to be on the order of magnitude corresponding to the normal stiffness predicted by nonlinear Hertz-Mindlin theory for quartz spheres of diameter  $d \approx 0.5$  mm if a radial strain of  $\epsilon_r = 0.001$  at the point of contact is assumed, where the modulus of elasticity for quartz is taken to be  $E = 8(10^{10})$  Pa; see equation (9.5). The tangential spring stiffness is obtained from the relationship expressed in equation (9.6), which is obtained from Hertz-Mindlin contact theory (Elata and Berryman, 1996). When using equations (9.5) and (9.6), we have taken Poisson's ratio for quartz to be  $\nu = 0.3$ .

$$K_n = Ed \frac{\sqrt{\epsilon_r}}{(1 - \nu^2)} \quad (9.5)$$

$$K_t = \frac{2(1-\nu)}{2-\nu} K_n \quad (9.6)$$

As we mentioned earlier, the shearing behavior of a granular medium does not appear to be very sensitive to the exact values of  $K_n$  and  $K_t$ . The damping coefficients in equations (9.1) and (9.2) were taken to be  $\gamma_n = 40 \text{ s}^{-1}$  and  $\gamma_t = 20 \text{ s}^{-1}$ . This damping was included only to smooth the (otherwise somewhat noisy) numerical output. An exploration of different damping coefficients performed by the authors showed that they had no effect on the peak or residual friction angles predicted by the DEM simulations. The coefficient of sliding friction between the elements was taken to be  $\mu = 0.5$  (or  $\phi_\mu = 26^\circ$ ), which corresponds to the coefficient of sliding friction between quartz surfaces, wet or dry (Mitchell and Soga, 2005). The minimum element mass in both the 2-D and the 3-D simulations was approximately  $m_{\min} = 4(10^{-5}) \text{ g}$ , which is based on a density of  $0.003 \text{ g/mm}^3$  for quartz. From equations (9.3) and (9.4), this led to our choices of time step sizes of  $\Delta t^{(2\text{-D})} = 6(10^{-8}) \text{ s}$  and  $\Delta t^{(3\text{-D})} = 4(10^{-8}) \text{ s}$  for the 2-D and 3-D simulations, respectively.

## 9.5 Results

One of the greatest advantages of the discrete element method over experimental methods for exploring the behavior of particulate media is the amount of information that can be obtained at the micro-scale. In addition to measuring the average shear force on the upper bounding surface and the overall dilation of the 2-D and 3-D specimens as functions of horizontal ( $x$  direction) displacement, we were also able to track the displacements of individual particles in different regions of the shear flow. Thus, in the 3-D simulation, we were able to measure the motion of particles in the “out-of-plane” ( $z$ ) direction throughout the shear test.

The normalized average shear stress as a function of the displacement of the upper surface in the horizontal ( $x$ ) direction for both the 2-D and 3-D DEM simulations is shown in

Figure 9.4, along with dilation as a percent of the initial thickness of the specimen in the  $y$  direction. Note that, despite qualitative similarity, there is a significant quantitative difference

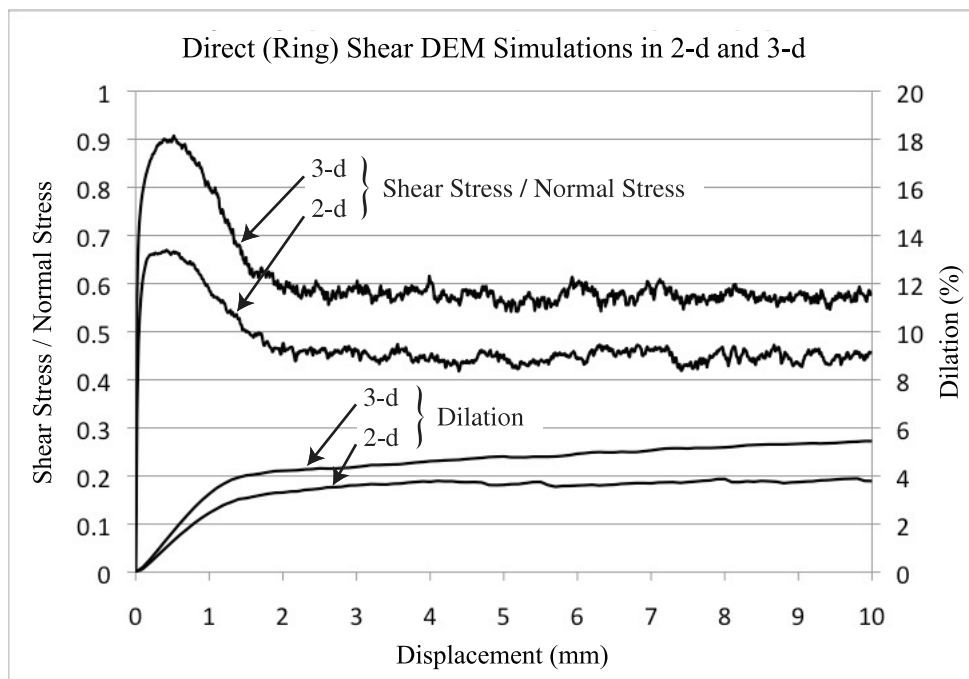


Figure 9.4: The normalized average shear stress and dilation as functions of the horizontal ( $x$  direction) displacement of the upper surface of the specimens for the 2-D and 3-D DEM direct (ring) shear simulations.

between the peak and residual friction angles predicted by the 2-D and 3-D simulations. We will return to this point in the analysis section that follows. Also note that the normalized average shear stress, which is the ratio of the average shear stress to the applied normal stress, is identical to the ratio of the average shear force to the applied normal force in each simulation. Since the average shear force and the applied normal force are known unambiguously for both the 2-D and 3-D simulations, we are able to avoid ambiguities regarding how stress is calculated in 2-D versus 3-D.

For the 3-D DEM simulation, the maximum displacement of elements in the “out-of-plane” ( $z$ ) direction within different vertically stratified regions of the 3-D specimen is shown in Figure 9.5. Each of the vertically stratified regions, which are designated in Figure 9.5

at the right with dashed lines, is approximately 2 mm thick. The maximum “out-of-plane” ( $z$ ) displacement of the elements in each of these regions is graphed in Figure 9.5 at the left as a function of the horizontal displacement of the upper bounding surface of the specimen during the shear test. Note that in the 2-D simulation, no element displacement was allowed

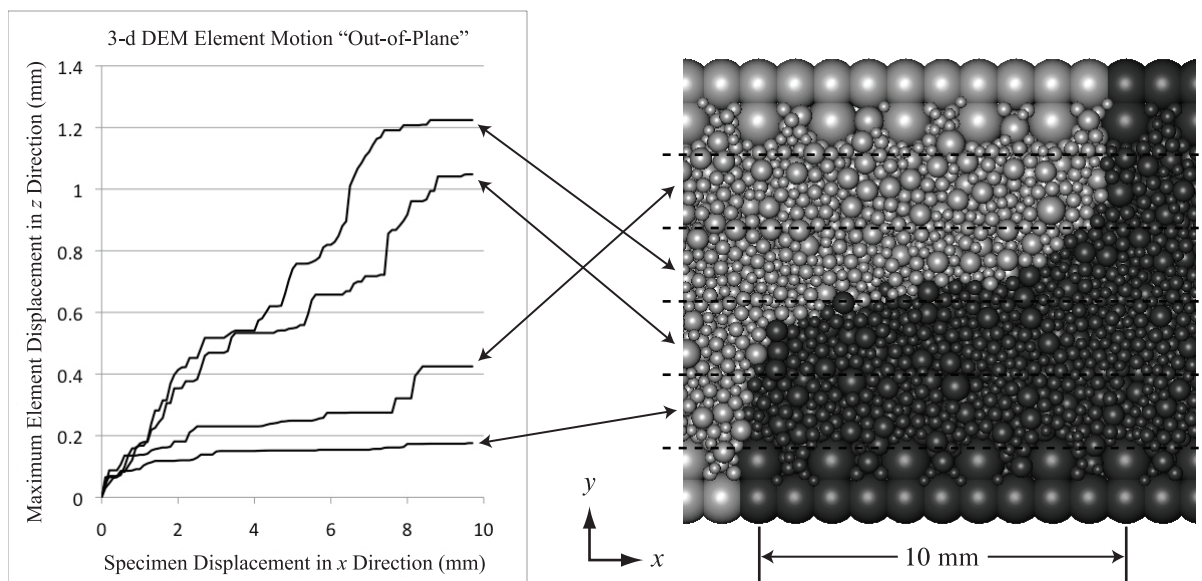


Figure 9.5: Maximum displacement in the “out-of-plane” ( $z$ ) direction for elements in the 3-D DEM simulation (left) within different vertical strata of the specimen (right) as functions of the horizontal ( $x$  direction) displacement of the upper surface of the specimen.

in the “out-of-plane” ( $z$ ) direction. However, Figure 9.5 shows that in the 3-D simulation, elements near the center of the specimen travelled more than 1.2 mm in the “out-of-plane” ( $z$ ) direction during the shear test. Thus, in a 3-D shear test simulation, a single element can move a distance in the “out-of-plane” direction that is more than 10% of the distance it moves in the direction of shear. We will return to this point in the analysis section that follows. The final accumulated shear displacement in the  $x$  direction within the 3-D specimen is also shown by the color of the elements in Figure 9.5 at the right, where the boundary between the black and the white elements was vertical at the start of the simulation. Note from Figure 9.5 that the shear zone comprises a vertical span of approximately 4 mm near

the center of the specimen, and that particle motion in the “out-of-plane” ( $z$ ) direction is greatest within this shear zone. We will track the motion of individual particles within the shear zone in the analysis section that follows.

## 9.6 Analysis

The first point to note is that the overall appearance of both the 2-D and the 3-D DEM results is correct for densely packed sand, as described in Mitchell and Soga (2005). In particular, for densely packed sand, we expect the peak friction angle  $\phi_p$  to be significantly higher than the residual (or critical state) friction angle  $\phi_r$ . According to Bardet (1997), typical values of the peak friction angle and the residual friction angle for densely packed well-graded sands are  $38^\circ < \phi_p < 46^\circ$  and  $30^\circ < \phi_r < 34^\circ$ , respectively. The peak and residual friction angles predicted by our simulations are easily computed from Figure 9.4 as the inverse tangent of the ratio of shear stress to normal stress. Thus, our 2-D DEM simulation predicts  $\phi_p \approx 34^\circ$  and  $\phi_r \approx 24^\circ$ , and the 3-D DEM simulation predicts  $\phi_p \approx 42^\circ$  and  $\phi_r \approx 30^\circ$ . Since the peak friction angle depends on the initial packing of the specimen, we will concentrate on comparing the residual friction angle  $\phi_r$  with experimentally determined values. For ASTM standard graded Ottawa sand with  $D_{50} = 0.35$  mm and  $C_u = 1.7$ , which corresponds to the specimens used in both our 2-D and 3-D DEM simulations, Cho et al. (2006) report a residual friction angle of  $\phi_r = 30^\circ$ . For the particles of the ASTM standard graded Ottawa sand used in their experiments, Cho et al. (2006) report an average roundness of 0.8 and sphericity of 0.9. These are lower than the values for the perfectly spherical particles used in our 2-D and 3-D DEM simulations, which have a roundness and sphericity of 1.0 exactly. Despite this fact, we note that the value of the residual friction angle  $\phi_r \approx 30^\circ$  predicted by the 3-D DEM simulation is identically the same as the experimentally determined value for ASTM standard graded (Ottawa) sand. On the other hand, the value of  $\phi_r \approx 24^\circ$  predicted

by the 2-D DEM simulation is substantially low.

If we form a ratio of the values of  $\tan \phi_r$  predicted by the 3-D and 2-D DEM simulations, as shown in equation (9.7),

$$\alpha = \frac{\tan \phi_r^{(3-D)}}{\tan \phi_r^{(2-D)}}, \quad (9.7)$$

we find that  $\alpha \approx 1.3$ . To explain the reason why  $\alpha \neq 1.0$  (i.e., why the 2-D and 3-D DEM simulations disagree in their prediction of  $\phi_r$ ), we first consider the equilibrium of forces in the  $y$ - $z$  plane for the 2-D simulation versus the 3-D simulation, as illustrated in Figure 9.6. In

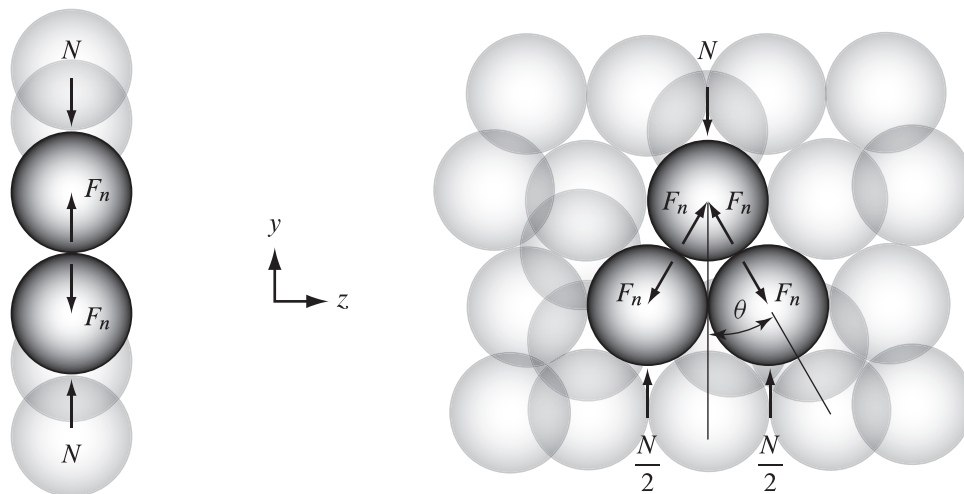


Figure 9.6: Forces in the  $y$ - $z$  plane for a hypothetical packing of uniform spheres in the 2-D DEM simulation (left) and in the 3-D DEM simulation (right).

the following discussion, we will call forces that have a component in the  $z$  direction “out-of-plane forces”. Obviously, there can be no out-of-plane forces in a 2-D simulation. However, it is equally obvious that for an arbitrary packing of elements, there will be out-of-plane forces in a 3-D simulation. This is illustrated in Figure 9.6 for a particular packing of elements.

Consider the simple geometry of forces depicted in Figure 9.6. If the projection of the normal contact force between two elements onto the  $y$ - $z$  plane in the 2-D simulation is  $(F_n)_{y,z} = N$ , where  $N$  is the force that is transferred to the elements from the upper and lower boundaries, then the projection of the analogous normal contact force onto the  $y$ - $z$

plane in the 3-D simulation is  $(F_n)_{y,z} = 0.5N(\cos\theta)^{-1}$ . If we ignore particle rotation, for the purposes of theoretical comparison only, then the shear force in the  $x$  direction during sliding in the 2-D case will be simply  $(F_t)_x = \mu(F_n)_{y,z} = \mu N$ . In the 3-D case, however, the shear force will be  $(F_t)_x = 2\mu(F_n)_{y,z} = \mu N(\cos\theta)^{-1}$  (where the factor of 2 accounts for the fact that in the 3-D packing there are two contacts where there is only one in 2-D). This gives  $\alpha = (\cos\theta)^{-1}$ . The minimum possible value of  $\theta$  for a packing of uniform spheres is  $\theta = 30^\circ$ , which gives  $\alpha \approx 1.2$ . For a cubic close packing of uniform spheres,  $\theta = 45^\circ$ , which gives  $\alpha \approx 1.4$ . While these two values cannot be viewed as strict lower and upper bounds on  $\alpha$ , it is interesting to note that the observed value of  $\alpha \approx 1.3$  falls exactly between the two.

In our DEM simulations, the elements are not uniform in size, and the geometry of the inter-element contacts is not regular. Figure 9.7 shows a  $y$ - $z$  cross section of the 3-D DEM specimen within the shear zone during fully developed shear flow, with normal inter-element contact forces shown. It is clear from Figure 9.7 that the true situation regarding the

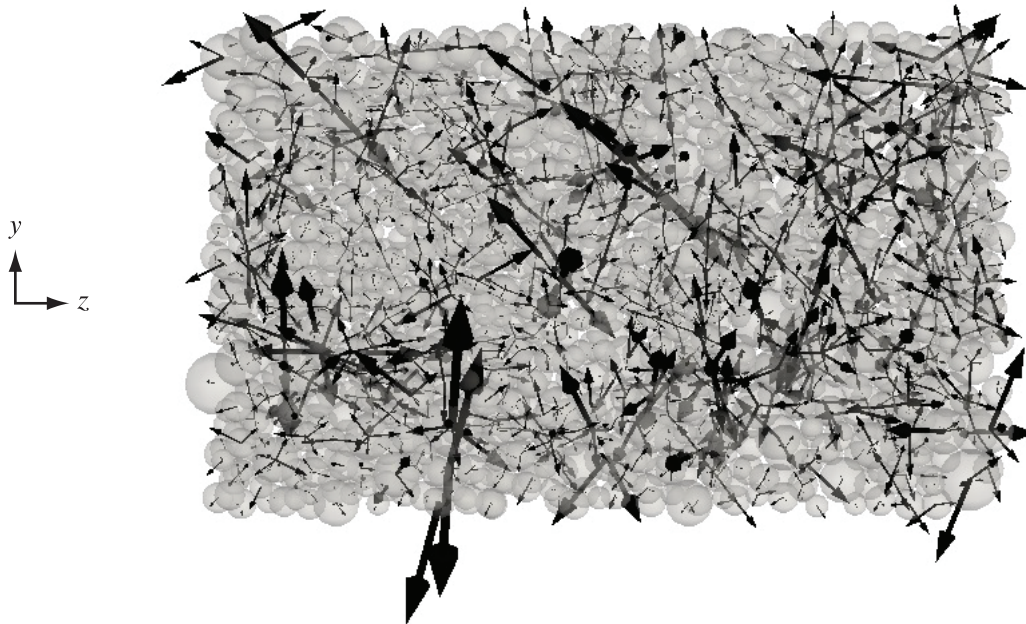


Figure 9.7: Normal contact forces in the  $y$ - $z$  plane for a section of the shear zone during fully developed shear flow in the 3-D DEM simulation.

inter-element contact forces is much more complicated than the simplified picture given in Figure 9.6. In an attempt to quantify the true situation, we have summed the magnitudes of the normal contact forces projected onto the  $y$ - $z$  plane between all pairs of elements during fully developed shear flow for both the 2-D and the 3-D DEM simulations, and we have computed the time-average of these values. We found that

$$\frac{\langle \sum (F_n)_{y,z}^{(2-D)} \rangle}{N^{(2-D)}} \approx 36, \quad \text{and} \quad \frac{\langle \sum (F_n)_{y,z}^{(3-D)} \rangle}{N^{(3-D)}} \approx 58, \quad (9.8)$$

where the sums in equation (9.8) are computed over all inter-element contacts in either specimen, and  $N$  is the total normal force applied to the upper surface of either specimen. Under certain assumptions, the ratio of the values given in equation (9.8) may be expected to provide an estimate of  $\alpha$ . This results in an estimate of  $\alpha \approx 1.6$ . We note that this estimate is somewhat higher than the observed value of  $\alpha \approx 1.3$ .

Another important factor that influences the behavior of the 2-D DEM simulation is that the *motion* of elements as well as the inter-element contact forces is constrained to lie entirely in the  $x$ - $y$  plane. However, tracking individual elements in the 3-D simulation reveals that there is, in fact, significant motion in the  $z$  direction, as was shown in Figure 9.5. The paths of seven such elements within the shear zone of the 3-D DEM simulation are shown in Figure 9.8. Note that elements within the shear zone of the 3-D simulation can move as much as four times their own diameter in the “out-of-plane” direction ( $z$ ) during the course of the direct shear simulation, during which time the same elements move less than approximately thirty times their own diameter in the direction of shear ( $x$ ). This represents a significant difference when compared to the behavior of elements in the 2-D DEM simulation, since in the 3-D DEM simulation the displacement of elements within the shear zone in the “out-of-plane” direction can be more than 10% of their displacement in the direction of the (nominally two-dimensional) shearing motion. This observation agrees with experimental

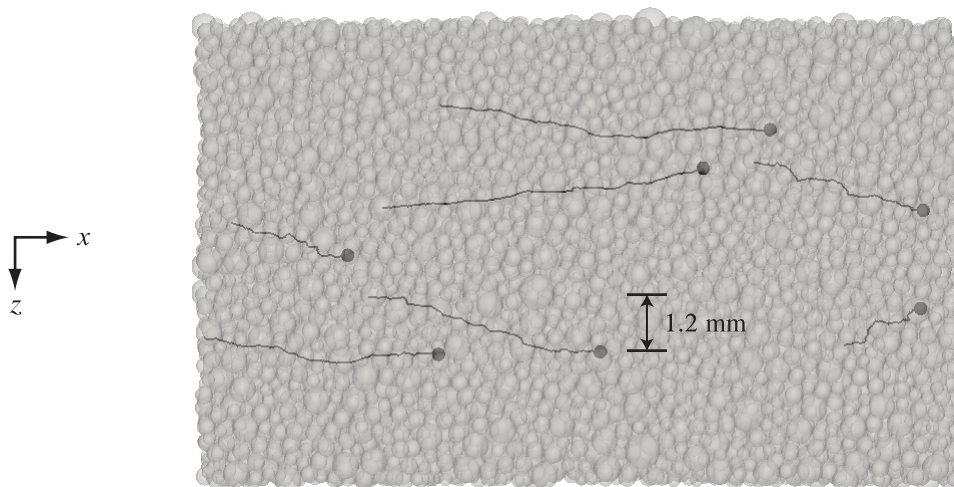


Figure 9.8: Particle trajectories in an  $x$ - $z$  planar cross-section within the shear zone of the 3-D DEM simulation, viewed from above.

observations made by Guler et al. (1999) using image analysis techniques, in which sand particles were seen to periodically “disappear” and “reappear” during direct shear tests when the medium was viewed from the side (i.e., a cross-section in the  $x$ - $y$  plane). The motion of elements in the  $z$  direction in the 3-D DEM simulation may provide one reason why the observed value of  $\alpha \approx 1.3$  is lower than the value of  $\alpha \approx 1.6$  that is predicted by summing the magnitudes of the normal inter-element contact forces in the  $y$ - $z$  plane. Since elements in the 3-D simulation have an additional degree of freedom in which to move, the system is thereby “softened”.

## 9.7 Conclusion

We have shown a 3-D DEM simulation of nominally two-dimensional shear flow can predict the residual friction angle  $\phi_r$  of ASTM standard graded sand with *quantitative* accuracy. On the other hand, a 2-D DEM simulation, while predicting the *qualitative* behavior of a particulate material correctly, fails to predict the residual friction angle with quantitative

accuracy. There appear to be several factors that cause the results obtained from 3-D DEM simulations to differ from those obtained from 2-D DEM simulations, and which cause the 3-D DEM results to predict more accurately the true behavior of a particulate material. We have attempted to explain some of the micro-mechanisms that contribute to the discrepancy between the residual friction angle predicted by the 2-D and the 3-D simulations. These micro-mechanisms include an increase in apparent friction in the 3-D simulation caused by the presence of forces in the “out-of-plane” ( $z$ ) direction, which is similar to the increase in apparent friction between a “v-belt” and pulley compared to a flat belt and pulley. At the same time, there appear to be “softening” effects present in the 3-D simulation that are lacking in the 2-D simulation, such as “out-of-plane” particle motion, which are caused by the added degree of freedom. Although our micro-mechanical considerations provide some quantitative explanation of the difference in the residual friction angles predicted by the 2-D and 3-D DEM simulations, it is difficult to predict the error in the results obtained from a 2-D DEM simulation in a reliable way. If quantitatively correct predictions of the behavior of a particulate material are desired, then a 3-D DEM analysis is probably required. If qualitatively correct results are all that is needed, then a 2-D DEM simulation may be acceptable. For related studies, see Chen et al. (2007), Ng (2009), and Dang and Meguid (2010).



# Chapter 10

## Conclusion

In this thesis, we obtain a number of significant relationships between the micromechanical properties of particulate materials, such as the ratio of the tangential to normal inter-particle contact stiffnesses  $\alpha = K_t/K_n$ , which for spherical particles is related to Poisson's ratio  $\nu$  of the material constituting the spheres by  $\alpha = 2(1 - \nu)/(2 - \nu)$ , and the inter-particle friction coefficient  $\mu$ ; and the macroscopic properties of the particulate materials, such as the macroscopic Poisson's ratio  $\bar{\nu}$  (Chapters 3, 4) and the material friction angle  $\phi$  (Chapters 5, 6, 7, 8). All of our theoretical relationships have been validated by the discrete element method, or DEM (Sections 3.5, 4.5, and Chapters 5, 6, 9). Using a numerical method such as the discrete element method to validate theoretical results of the kind derived in this thesis has several advantages over using experimental data. First, the properties of the particles on the microscale are known exactly in the numerical simulations, thus reducing variables that in experiments might affect the results in unexpected ways that are difficult to control. Second, the discrete element method allowed us to perform numerical simulations in which particles could have their rotational velocities artificially restrained. Performing DEM simulations with particle rotation either allowed or prohibited proved to be *very* advantageous. First, it provided an extra control to test theoretical results against, which has resulted in virtually

all of our analyses being split into two parts: “Part I: No Particle Rotation” and “Part II: Particle Rotation”. Second, by comparing our theoretical results with particle rotation either prohibited or allowed to results published by other researchers, we discovered that many researchers had implicitly ignored the effects of particle rotation without realizing it, particularly in the elastic range, leading to theoretical results that match our DEM simulations and corresponding theoretical results with particle rotation prohibited, but fail to match our DEM simulations and corresponding theoretical results with particle rotation allowed.

This discovery has already lead to the publication of two papers: Fleischmann et al. (2013a) (Part I) and Fleischmann et al. (2013b) (Part II) in the *Journal of the Mechanics and Physics of Solids*, appearing as Chapters 3 and 4 in this thesis, which show that local shearing mechanisms or zero-energy energy modes due to particle rotation can alter the relationship between the local ratio of the inter-particle tangential to normal contact stiffnesses  $\alpha = K_t/K_n$  and the macroscopic Poisson’s ratio  $\bar{\nu}$  in a statistically isotropic particulate material. We found that the degree to which these local shearing mechanisms can affect the macroscopic Poisson’s ratio can be characterized by a single internal parameter  $\xi$ , which appears to be strongly correlated to the average number of contacts per unit volume  $\beta$  in the particulate material via equation (4.20), which can in turn be related to the void ratio  $e$  via equations (2.8)–(2.12). We have followed up on the success of our published analyses of the elastic range with derivations of the relationship between the inter-particle friction coefficient  $\mu$  and the material friction angle  $\phi$  for a statistically isotropic non-cohesive particulate material, which appear in Chapters 5–8. In Chapter 8, we show that again the ratio of the inter-particle tangential to normal contact stiffnesses  $\alpha = K_t/K_n$  comes into play, along with the internal parameter  $\xi^* \approx 0.1\xi$ .

Essentially, all of the results of this thesis have one common theme: A detailed micromechanical analysis of specific *anisotropic* local packing geometries can lead to general models

for statistically *isotropic* particulate materials based on standard homogenization methods that significantly improve the current state of the art. This is because the models in the literature are almost exclusively based on the assumption of *local* isotropy in a particulate material, which for example can eliminate mechanisms caused by *asymmetry* in inter-particle contacts. However, statistical or *global* isotropy in a particulate material *does not* require *local* isotropy, since a locally anisotropic material (or packing geometry) can occur in equally represented randomly oriented subportions in a statistically isotropic particulate material, analogous to “grains” in a statistically isotropic metal. As a result, the micromechanical behavior of locally asymmetric packing geometries can significantly affect the overall properties of a statistically isotropic particulate material, as we saw for Poisson’s ratio in Chapters 3 and 4 [Fleischmann et al. (2013a,b)].

In addition to directly validating the theoretical results of Chapters 3, 4, 7, and 8, we performed a number of exploratory DEM simulations for their own sake, such as those of Chapters 5, 6, and 9 [Fleischmann et al. (2013c)]. In Chapters 5 and 6, in addition to obtaining the relationship between the inter-particle friction coefficient  $\mu$  or  $\phi_\mu = \tan^{-1} \mu$  and the material friction angle  $\phi$  used to validate the results of Chapters 7 and 8, we also obtained complete yield surfaces for six DEM specimens of 3 430–29 660 randomly packed uniform spheres on the  $\pi$ -plane for a full range of Lode angles, and we found that the Lade-Duncan yield criterion performed very well for all specimens at all values of the Lode angle, in particular that of  $60^\circ$  (extension). We also used DEM to visually examine failure modes in the DEM specimens due to particle rotation and inter-particle friction (local force-chain buckling at strains prior to that of the peak friction angle followed by particle rotation on global slip planes after the peak friction angle has been achieved), and we measured the average rate of friction work in the DEM specimens as a function of the inter-particle friction coefficient  $\mu$ . In Chapter 9 [Fleischmann et al. (2013c)], we showed that three-dimensional (3-D) DEM simulations of direct (ring) shear tests are capable of predicting the material

friction angle of dense ASTM standard C 778-06 (Ottawa) sand with *quantitative* accuracy ( $\phi_p \approx 42^\circ$  and  $\phi_r \approx 30^\circ$ ), while two-dimensional (2-D) DEM simulations fail to predict the material friction angle due to a combination of factors including softening effects caused by particle motion in the “out-of-plane” direction offset by a simple increase in apparent friction in the 3-D simulations due to a so-called “v-belt” effect.

As we said in the Introduction (Chapter 1) of this thesis, the final aim of our micromechanical analyses has been to create complete, *quantitative* links between the micromechanical properties of particulate materials and their macroscopic material properties, in order to facilitate *predictive* elastoplastic continuum constitutive models of particulate materials based on their micromechanical properties. We have succeeded in creating such a quantitative link for the elastic range, evidenced by the success of the model of Chapter 4 in capturing the effect of particle rotation to accurately predict the macroscopic Poisson’s ratio  $\bar{\nu}$  in six dense randomly packed DEM specimens of 3 430–29 660 uniform spheres tested in Chapter 4. This model also allows us to obtain a theoretical justification for the experimentally measured macroscopic Poisson’s ratio for quartz sand and glass beads, which cannot be explained by either the model of Chapter 3 with particle rotation prohibited or previous models in the published literature (e.g., Chang et al., 1995, Chang and Gao, 1995, Suiker and de Borst, 2005). In particular, for  $\alpha$  near 1.0, these models exhibit error in excess of several hundred percent when compared either to glass beads (for which  $\alpha \approx 0.9$ ) or to our DEM specimens. We have shown that the error relative to our DEM specimens is due to the effect of particle rotation, but is *not* due to inter-particle *slip* as assumed by Bachrach et al. (2000) and Trentadue (2004). While Cambou et al. (1995) propose a model that includes an internal parameter “ $\mu$ ” (renamed  $\zeta$  by us in Section 2.1), which is somewhat analogous to our internal parameter  $\xi$ , for no value of their internal parameter can the relationship between  $\alpha$  and  $\bar{\nu}$  be made to match our DEM results as closely as our model with an appropriate choice of  $\xi$ , as shown in Figure 4.11.

We have succeeded in creating a quantitative link between macroscopic and micromechanical properties in a statistically isotropic non-cohesive particulate material at the point of yield, evidenced by the success of the constant volume model of Chapter 8 in accurately predicting the material friction angle  $\phi$  in six dense randomly packed DEM specimens of 3 430–29 660 uniform spheres tested in Chapter 6. In particular, with appropriate choices of initial dilation angle  $\psi$  and internal parameter  $\xi^* \approx 0.1\xi$ , our constant volume model of the relationship between  $\phi$  and  $\phi_\mu = \tan^{-1} \mu$ , where  $\mu$  is the inter-particle friction coefficient, matches our DEM results more closely than the model of Emeriault et al. (1996), which is based on the model of Cambou et al. (1995), for any value of their internal parameter  $\zeta$  (or “ $\mu$ ”), as shown in Figure 8.8. To test the accuracy of the constant normal stress model of Chapter 8, we may use the results from the 3-D DEM simulation performed for Chapter 9 under constant normal stress conditions. Since the particle size distribution is not uniform, we will not use equation 8.12, but rather we will use equation 8.9 with  $\theta_1 = \bar{\theta}_1 \approx 53^\circ$ , which corresponds to a simple average of the bounds on  $\theta_1$  for the particle size distribution used in Chapter 9. Figure 9.4 shows that the initial dilation angle in the 3-D DEM simulation is  $\theta_2 = \psi \approx \tan^{-1}(0.03h) \approx 14.63^\circ$ . Thus, with the inter-particle friction coefficient  $\mu = 0.5$  used in Chapter 9, equation 8.9 predicts that  $\phi_p = \tan^{-1} \mu_{\text{macro}} \approx 49^\circ$ , which is within 20% of the measured value of  $\phi_p \approx 42^\circ$ .

Future work includes (1) obtaining a theoretical (micromechanics-based) derivation of the yield surface for all values of the Lode angle that improves the Mohr-Coulomb yield surface and explains the success of the Lade-Duncan surface in describing yield surfaces obtained from DEM simulations for the six specimens in Chapters 5 and 6, (2) extending our theoretical (micromechanics-based) model to include plastic deformation beyond the initiation of yield, for which we already have a large amount of DEM data from the simulations of Chapters 5 and 6, and (3) exploring more local packing geometries, and obtaining quantitative relationships between the material fabric (i.e., packing geometry) and the internal

parameters  $\xi$  and  $\xi^*$  used in the models of Chapters 3, 4, 7, and 8. We intend to address all three of these points in the near future, as we continue to build on the results of this thesis, employing DEM to inform and validate elastoplastic continuum constitutive models for statistically isotropic particulate materials based on micromechanical analyses of specific local packing geometries.

## Appendix A

# Stiffness Analysis of FCC, SC, and BCC Elementary Cells with Particle Rotation Prohibited

In this appendix, we derive the cubic elastic moduli  $C_1$ ,  $C_2$ , and  $C_3$  given in equations (3.11), (3.15), and (3.16) for FCC, SC, and BCC elementary cells, respectively, with particle rotation prohibited. We do so by assuming constant normal and tangential contact stiffnesses ( $K_n$  and  $K_t$ , respectively) between the uniform spheres of diameter  $D = 2R$ , and calculating the deformation of the elementary cells subjected to pure uniaxial compression and pure shear in directions parallel to the principal axes.

### A.1 Face-Centered Cubic (FCC) Elementary Cell

To determine  $C_1$  and  $C_2$ , we apply a state of pure uniaxial normal strain

$$\epsilon_{11} = -\frac{2\delta}{\sqrt{2}D}, \quad \epsilon_{22} = \epsilon_{33} = \epsilon_{12} = \epsilon_{13} = \epsilon_{23} = 0, \quad (\text{A.1})$$

to a single FCC elementary cell as shown in Figure A.1 (left), where the 3-axis is positive out of the page. The dashed lines represent the inter-particle contacts on the face of the cube, and the dotted lines represent the inter-particle contacts on the interior of the cube. Only the contacts for the upper half of the cube are shown. The forces  $F_1$  and  $F_2$  (and  $F_3$ ,

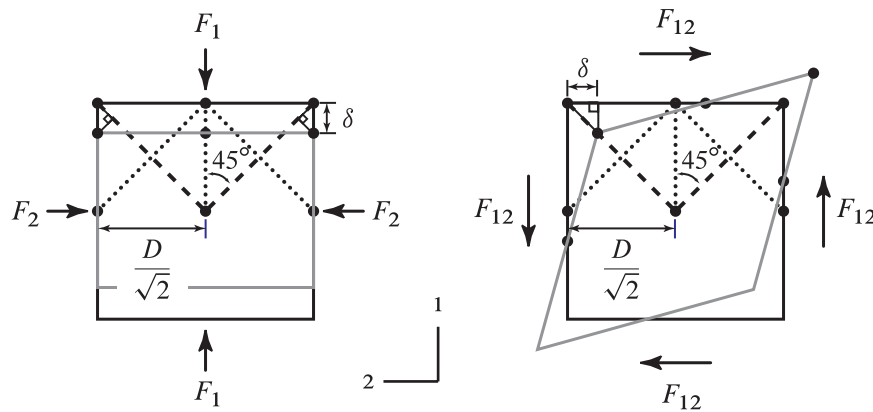


Figure A.1: A single FCC elementary cell in a state of pure uniaxial normal strain (left) and pure shear strain (right), viewed from the  $(0, 0, 1)$ -direction.

which is not shown) are determined from the normal and tangential displacements of the inter-particle contacts, in terms of the normal and tangential spring stiffnesses  $K_n$  and  $K_t$ . Summing the forces from the contacts in the cube, and noting that the spring stiffnesses on the four faces have one half their regular values because each is shared by two cubes, we have

$$F_1 = 4(K_n + K_t)\delta, \quad F_2 = F_3 = 2(K_n - K_t)\delta. \quad (\text{A.2})$$

From these and the cubic Hooke's law for the elementary cell, we have

$$\sigma_{11} = -\frac{F_1}{2D^2} = C_1\epsilon_{11}, \quad \sigma_{22} = \sigma_{33} = -\frac{F_2}{2D^2} = -\frac{F_3}{2D^2} = C_2\epsilon_{11}. \quad (\text{A.3})$$

Combining equations (A.1), (A.2), and (A.3), we find

$$C_1 = \frac{1}{\sqrt{2}R}(K_n + K_t), \quad C_2 = \frac{1}{2\sqrt{2}R}(K_n - K_t). \quad (\text{A.4})$$

To determine  $C_3$ , we apply a state of pure shear strain

$$\epsilon_{12} = -\frac{\delta}{\sqrt{2}D}, \quad \epsilon_{11} = \epsilon_{22} = \epsilon_{33} = \epsilon_{13} = \epsilon_{23} = 0, \quad (\text{A.5})$$

to a single FCC elementary cell as shown in Figure A.1 (right). The shear force  $F_{12}$  is obtained from a similar procedure as that employed above for the normal forces:

$$F_{12} = 2(K_n + K_t)\delta. \quad (\text{A.6})$$

From this and the cubic Hooke's law for the elementary cell, we have

$$\sigma_{12} = -\frac{F_{12}}{2D^2} = 2C_3\epsilon_{12}. \quad (\text{A.7})$$

Combining equations (A.5), (A.6), and (A.7), we find

$$C_3 = \frac{1}{2\sqrt{2}R}(K_n + K_t). \quad (\text{A.8})$$

Equations (A.4) and (A.8) reproduce equation (3.11) of Section 3.3.1.

## A.2 Simple Cubic (SC) Elementary Cell

To determine  $C_1$  and  $C_2$ , we apply a state of pure uniaxial normal strain

$$\epsilon_{11} = -\frac{2\delta}{D}, \quad \epsilon_{22} = \epsilon_{33} = \epsilon_{12} = \epsilon_{13} = \epsilon_{23} = 0, \quad (\text{A.9})$$

to a single SC elementary cell as shown in Figure A.2 (left), where the 3-axis is positive out of the page. The dashed lines represent the contacts on the edges of the cube. Proceeding

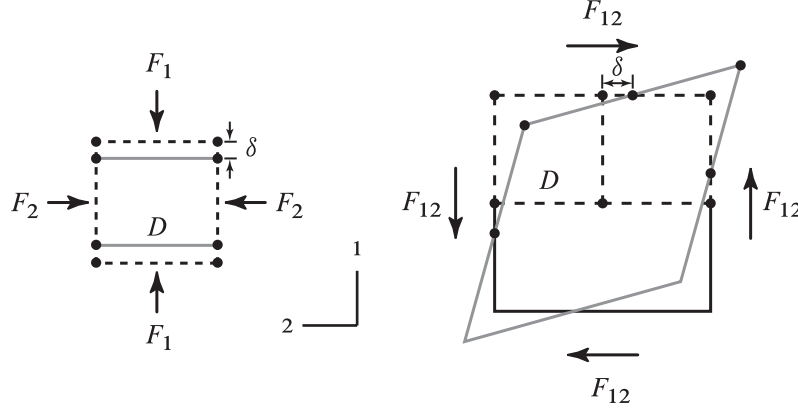


Figure A.2: A single SC elementary cell in a state of pure uniaxial normal strain (left) and a cube built from eight SC elementary cells in a state of pure shear strain (right), viewed from the  $(0, 0, 1)$ -direction.

as before, but noting that the spring stiffnesses on the edges have one fourth their regular values because each is shared by four cubes, we have

$$F_1 = 2K_n\delta, \quad F_2 = F_3 = 0. \quad (\text{A.10})$$

Combining equations (A.9), (A.10), and the cubic Hooke's law for the elementary cell:  $\sigma_{11} = -F_1/D^2 = C_1\epsilon_{11}$  and  $\sigma_{22} = \sigma_{33} = -F_2/D^2 = -F_3/D^2 = C_2\epsilon_{11}$ , we find

$$C_1 = \frac{1}{2R}K_n, \quad C_2 = 0. \quad (\text{A.11})$$

To determine  $C_3$ , we apply a state of pure shear strain

$$\epsilon_{12} = -\frac{\delta}{2D}, \quad \epsilon_{11} = \epsilon_{22} = \epsilon_{33} = \epsilon_{13} = \epsilon_{23} = 0, \quad (\text{A.12})$$

to a cube built from eight SC cells as shown in Figure A.2 (right), where the 3-axis is positive

out of the page. The dashed lines represent the contacts on the edges of the cells. Only the contacts for the upper half of the cube are shown. Proceeding as before, and noting that the spring stiffnesses on the front and back faces have one half their regular values because each is shared by two cubes, we have

$$F_{12} = 2K_t\delta. \quad (\text{A.13})$$

Combining equations (A.12), (A.13), and the cubic Hooke's law for the elementary cell:  $\sigma_{12} = -F_{12}/(4D^2) = 2C_3\epsilon_{12}$ , we find

$$C_3 = \frac{1}{4R}K_t. \quad (\text{A.14})$$

Equations (A.11) and (A.14) reproduce equation (3.15) of Section 3.3.2.

### A.3 Body-Centered Cubic (BCC) Elementary Cell

To determine  $C_1$  and  $C_2$ , we apply a state of pure uniaxial normal strain

$$\epsilon_{11} = -\frac{2\delta\sqrt{3}}{2D}, \quad \epsilon_{22} = \epsilon_{33} = \epsilon_{12} = \epsilon_{13} = \epsilon_{23} = 0, \quad (\text{A.15})$$

to a single BCC elementary cell as shown in Figure A.3, viewed from the  $(0, 0, 1)$ -direction (left), and viewed from the  $(0, 1, 1)$ -direction (right). The dotted lines represent the inter-particle contacts on the interior of the cube. Only the contacts for the upper half of the cube are shown. Proceeding as before, we find

$$F_1 = \frac{4}{3}(K_n + 2K_t)\delta, \quad F_2 = F_3 = \frac{4}{3}(K_n - K_t)\delta. \quad (\text{A.16})$$

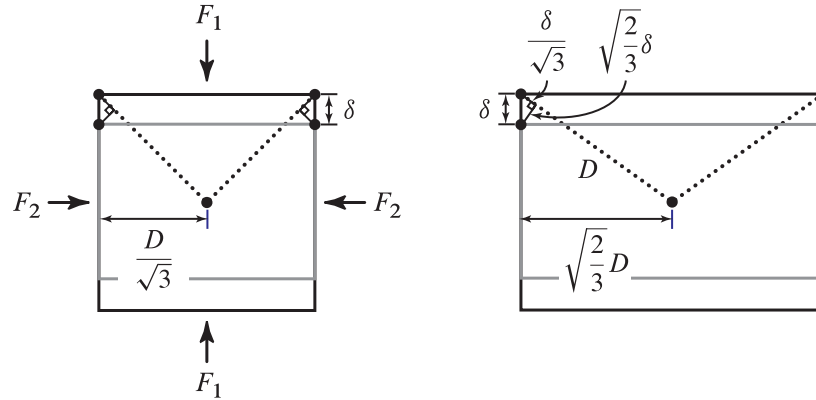


Figure A.3: A single BCC elementary cell in a state of pure uniaxial normal strain, viewed from the  $(0, 0, 1)$ -direction (left), and viewed from the  $(0, 1, 1)$ -direction (right).

Combining equations (A.15), (A.16), and the cubic Hooke's law for the elementary cell:  $\sigma_{11} = -3F_1/(4D^2) = C_1\epsilon_{11}$  and  $\sigma_{22} = \sigma_{33} = -3F_2/(4D^2) = -3F_3/(4D^2) = C_2\epsilon_{11}$ , we find

$$C_1 = \frac{1}{2\sqrt{3}R}(K_n + 2K_t), \quad C_2 = \frac{1}{2\sqrt{3}R}(K_n - K_t). \quad (\text{A.17})$$

To determine  $C_3$ , we apply a state of pure shear strain

$$\epsilon_{12} = -\frac{\delta\sqrt{3}}{2D}, \quad \epsilon_{11} = \epsilon_{22} = \epsilon_{33} = \epsilon_{13} = \epsilon_{23} = 0, \quad (\text{A.18})$$

to a single BCC elementary cell as shown in Figure A.4, viewed from the  $(0, 0, 1)$ -direction (left), and viewed from the  $(1, -1, 0)$ -direction (right). Proceeding as before, we find

$$F_{12} = \frac{2}{3}(2K_n + K_t)\delta. \quad (\text{A.19})$$

Combining equations (A.18), (A.19), and the cubic Hooke's law for the elementary cell:  $\sigma_{12} = -3F_{12}/(4D^2) = 2C_3\epsilon_{12}$ , we find

$$C_3 = \frac{1}{4\sqrt{3}R}(2K_n + K_t). \quad (\text{A.20})$$

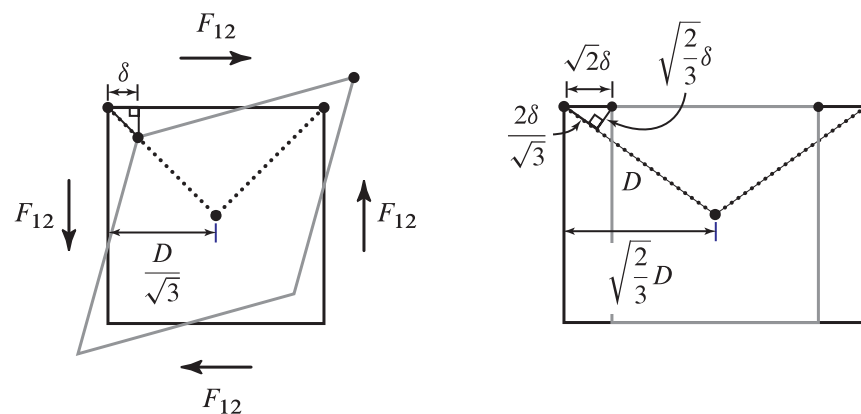


Figure A.4: A single BCC elementary cell in a state of pure shear strain, viewed from the  $(0,0,1)$ -direction (left), and viewed from the  $(1,-1,0)$ -direction (right).

Equations (A.17) and (A.20) reproduce equation (3.16) of Section 3.3.3.



## Appendix B

# Stiffness Analysis of an FCC Elementary Cell with Unrestrained Particle Rotation

In this appendix, we consider the stiffness of a single FCC elementary cell with unrestrained particle rotation subjected to a state of pure uniaxial compression along one of its principal axes:  $-\delta_{11}$ ,  $\delta_{22} = \delta_{33} = 0$ . In Section 4.3.1, we reported that an analysis of the inter-particle normal and tangential contact forces within a single FCC cell with *no particle rotation* for this state of deformation gives  $F_{11} = -2(K_n + K_t)\delta_{11}$  and  $F_{22} = F_{33} = -(K_n - K_t)\delta_{11}$  for the forces normal to the cell faces, and we noted that the normal and tangential stiffnesses of the contacts on the cell faces must contribute only half of their full values if the FCC cell is considered to be a constitutive material element of a larger material array. We also note, however, that if a single FCC cell is considered alone, then all of the contact forces must be included with their full values, and the measured forces normal to the cell faces will actually be  $F_{11} = -3(K_n + K_t)\delta_{11}$  and  $F_{22} = F_{33} = -(3/2)(K_n - K_t)\delta_{11}$ . This is verified by DEM simulations.

If a single FCC elementary cell in which particle rotation is *unrestrained* is subjected to the state of pure uniaxial compression described in the last paragraph, then due to the symmetry

of the loading only the spheres at the eight corners of the cell will experience rotation, and we can simplify our analysis by considering only the four spheres in contact at one corner of the FCC cell where only the corner sphere has rotational degrees of freedom. Figure B.1 shows the four spheres that we will analyze. These four spheres are in the configuration of a tetrahedron. For the state of pure uniaxial compression in the  $\hat{e}_1$  direction:  $-\delta_{11}$ ,

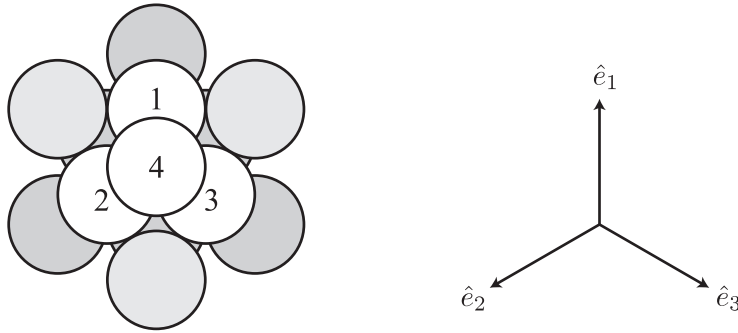


Figure B.1: The four numbered spheres that we analyze, which are in the configuration of a tetrahedron, and the principal directions for a single FCC elementary cell.

$\delta_{22} = \delta_{33} = 0$ , Spheres 1 and 4 in Figure B.1 experience a displacement of  $-\delta_{11}/2$  in the  $\hat{e}_1$  direction, and Spheres 2 and 3 remain fixed. If we denote the force contribution in the  $\hat{e}_i$  direction from the contact between Spheres  $a$  and  $b$  as  $(f_{ab})_{ii}$  (no sum), then we have

$$(f_{12})_{11} = (f_{13})_{11} = -(1/4)(K_n + K_t)\delta_{11}, \quad (\text{B.1})$$

$$(f_{12})_{22} = (f_{13})_{33} = -(1/4)(K_n - K_t)\delta_{11}, \quad (\text{B.2})$$

$$(f_{12})_{33} = (f_{13})_{22} = 0. \quad (\text{B.3})$$

Because Spheres 2 and 3 remain fixed, we have

$$(f_{23})_{11} = (f_{23})_{22} = (f_{23})_{33} = 0. \quad (\text{B.4})$$

If Sphere 4 has rotational degrees of freedom  $\delta\theta_1$ ,  $\delta\theta_2$ , and  $\delta\theta_3$  about the principal axes  $\hat{e}_1$ ,

$\hat{e}_2$ , and  $\hat{e}_3$ , respectively, then for small rotations we have

$$(f_{24})_{11} = -(1/4)(K_n + K_t)\delta_{11} - R\delta\theta_2 K_t/\sqrt{2}, \quad (\text{B.5})$$

$$(f_{24})_{22} = 0, \quad (\text{B.6})$$

$$(f_{24})_{33} = -(1/4)(K_n - K_t)\delta_{11} + R\delta\theta_2 K_t/\sqrt{2}, \quad (\text{B.7})$$

$$(f_{34})_{11} = -(1/4)(K_n + K_t)\delta_{11} + R\delta\theta_3 K_t/\sqrt{2}, \quad (\text{B.8})$$

$$(f_{34})_{22} = -(1/4)(K_n - K_t)\delta_{11} - R\delta\theta_3 K_t/\sqrt{2}, \quad (\text{B.9})$$

$$(f_{34})_{33} = 0, \quad (\text{B.10})$$

where  $R$  is the radius of the spheres. By symmetry, it is clear that  $\delta\theta_1 = 0$ . While the rotational degrees of freedom  $\delta\theta_2$  and  $\delta\theta_3$  do result in a relative tangential displacement at the point of contact between Spheres 1 and 4, this displacement results in equal and opposite contributions to the total force in the  $\hat{e}_1$  direction, and so we have

$$(f_{14})_{11} = (f_{14})_{22} = (f_{14})_{33} = 0. \quad (\text{B.11})$$

Moment equilibrium for Sphere 4 requires that  $R\delta\theta_2 = -R\delta\theta_3 = -\delta_{11}/(5\sqrt{2})$ . Thus, it follows that

$$(f_{24})_{11} = (f_{34})_{11} = -(1/4)(K_n + (3/5)K_t)\delta_{11}, \quad (\text{B.12})$$

$$(f_{24})_{33} = (f_{34})_{22} = -(1/4)(K_n - (3/5)K_t)\delta_{11}. \quad (\text{B.13})$$

Due to the symmetry of the FCC elementary cell, the total forces in the principal direc-

tions  $\hat{e}_1$ ,  $\hat{e}_2$ , and  $\hat{e}_3$  normal to cell faces are

$$F_{11} = 2(f_{12})_{11} + 2(f_{13})_{11} + 4(f_{24})_{11} + 4(f_{34})_{11}, \quad (\text{B.14})$$

$$F_{22} = 2(f_{12})_{22} + 2(f_{23})_{22} + 4(f_{24})_{22} + 4(f_{34})_{22}, \quad (\text{B.15})$$

$$F_{33} = 2(f_{13})_{33} + 2(f_{23})_{33} + 4(f_{24})_{33} + 4(f_{34})_{33}. \quad (\text{B.16})$$

From equations (B.14) – (B.16), it follows that  $F_{11} = -3(K_n + \xi K_t)\delta_{11}$  and  $F_{22} = F_{33} = -(3/2)(K_n - \xi K_t)\delta_{11}$ , with  $\xi = 11/15 \approx 0.733$ . This is the value of  $\xi$  reported in Section 4.3.1.

Note that the value of  $\xi = 11/15 \approx 0.733$  is only valid when the FCC elementary cell is considered alone. If the FCC cell is considered to be a constitutive material element of a larger material array, then the stiffnesses of the inter-particle contacts on the faces of the cell should contribute only half of their full values, as described for the case of no particle rotation at the beginning of this appendix. For the case of unrestrained particle rotation, this leads to  $F_{11} = -2(K_n + \xi K_t)\delta_{11}$  and  $F_{22} = F_{33} = -(K_n - \xi K_t)\delta_{11}$ , with  $\xi = 4/5 = 0.8$ .

The DEM simulations described in Section 4.3.1 performed on a single FCC elementary cell were performed on a single FCC cell in which the inter-particle contact stiffnesses at all contact points were the same. Thus, the value of  $\xi = 11/15 \approx 0.733$  and not the value of  $\xi = 4/5 = 0.8$  was observed in the DEM measurement of Poisson's ratio for a single FCC elementary cell in Section 4.3.1, which is shown in Figure 4.2. We also saw in Section 4.3.1 that when an FCC elementary cell becomes a part of a larger FCC array, particle rotation becomes *partially restrained*, and this leads immediately to  $\xi > 0.8$  (even for a  $2 \times 2 \times 2$  array). Thus, for consistency of presentation, we reported  $F_{11} = -2(K_n + \xi K_t)\delta_{11}$  and  $F_{22} = F_{33} = -(K_n - \xi K_t)\delta_{11}$ , with  $\xi = 11/15 \approx 0.733$  in Section 4.3.1 for a single FCC elementary cell with unrestrained particle rotation subjected to a state of pure uniaxial strain in the  $\hat{e}_1$  direction, in analogy to the case of no particle rotation where the FCC elementary cell is considered to be a constitutive material element of a larger material array.

## Appendix C

# Derivation of the Voigt Estimates of the Isotropic Effective Elastic Moduli for a Locally Cubic Material

In this appendix, we derive the Voigt estimates of the isotropic effective elastic moduli for a statistically isotropic aggregate material composed of randomly oriented (non-isotropic) material subportions. The method employed by Voigt (1928), sometimes called the kinematic method, is the earliest example of the so-called “homogenization” methods commonly employed in the study of composite materials, which include the static method of Reuss (1929) and the self-consistent method of Hershey (1954) and Kröner (1958).

Voigt (1928) assumed that when an aggregate material is subjected to a state of uniform strain, the individual components of the aggregate will be in the same state of strain. It follows that the isotropic fourth-order tensor of effective elastic moduli  $\bar{C}_{ijkl}$  of an isotropic aggregate is simply the orientational average of the elastic modulus tensor of the components:

$$\bar{C}_{ijkl} = \frac{1}{8\pi^2} \int_{\Omega} C_{ijkl} d\Omega, \quad (\text{C.1})$$

where  $d\Omega = \sin\theta d\varphi d\theta d\psi$  is the differential solid angle of the unit sphere  $\Omega$ , and  $\varphi$ ,  $\theta$ , and  $\psi$  are the Euler angles (e.g., Lubarda, 2002).

Note that a linear elastic material is isotropic if its behavior does not depend on its orientation. In other words, a linear elastic material is isotropic if its fourth-order tensor of second-order elastic moduli  $C_{ijkl}$  is invariant under coordinate rotations. If a linear elastic material possessed cubic symmetry, then that material is characterized by only three elastic constants  $C_1 = C_{1111}$ ,  $C_2 = C_{1122}$ , and  $C_3 = C_{1212}$ . A necessary and sufficient condition for a linear elastic material to be isotropic is that the material possesses cubic symmetry *and* that

$$C_1 - C_2 = 2C_3. \quad (\text{C.2})$$

It follows that an isotropic linear elastic material is characterized by the two elastic constants  $C_1$  and  $C_2$  (or  $C_2$  and  $C_3$ ). Note that the elastic constants obtained in Appendix A indicate that the cubic Bravais lattices are not isotropic, except in some special cases such as  $K_t = K_n$  for an FCC or SC particulate material.

In the following Sections C.1 and C.2, we present our own alternative derivation of the homogenization method first derived by Voigt (1928). We apply this technique to find the isotropic effective elastic constants  $\bar{C}_1$  and  $\bar{C}_2$  for a statistically isotropic aggregate material composed of randomly oriented subportions having locally cubic symmetry with cubic elastic constants  $C_1$ ,  $C_2$ , and  $C_3$ . In fact, the author derived the results of this appendix before he was aware of the results of Voigt (1928), Reuss (1929), or Hershey (1954) and Kröner (1958). The derivation is included here partly for the sake of curiosity, but also as an example of an alternative derivation of one of the standard homogenization methods.

## C.1 Averaging Pure Uniaxial Strain

Consider the state of pure uniaxial strain in which the only nonzero component of the strain tensor is  $\epsilon_{11}$ . Let  $a_{ij}$  be the transformation tensor between the 123 and 1'2'3' coordinate systems, where the direction of 1' relative to the 123 coordinate system is given by the unit vector  $n_i = a_{1i}$ . Then the rotated strain tensor representing a single normal strain component in the 1' direction is given by:

$$\epsilon'_{ij} = a_{mi}a_{nj}\epsilon_{mn} = a_{1i}a_{1j}\epsilon_{11} = n_in_j\epsilon_{11}. \quad (\text{C.3})$$

To obtain the corresponding stress in the same direction as the strain, we compute

$$\sigma'_{11} = n_in_j\sigma_{ij} = n_in_jC_{ijkl}\epsilon'_{kl}. \quad (\text{C.4})$$

If the tensor  $C_{ijkl}$  were invariant under rotation, then we would have  $\sigma'_{11} = C_{1111}\epsilon_{11} = \sigma_{11}$ .

In any case, we have

$$\sigma'_{11} = n_in_jC_{ijkl}\epsilon'_{kl} = n_in_jn_kn_lC_{ijkl}\epsilon_{11} = C'_{1111}\epsilon_{11}. \quad (\text{C.5})$$

and so

$$C'_{1111} = n_in_jn_kn_lC_{ijkl}. \quad (\text{C.6})$$

We propose to obtain an isotropic effective elastic constant  $\bar{C}_1 = \bar{C}_{1111}$  by averaging  $C'_{1111}$  over all unit vectors  $n_i$ , assuming that the average stress  $\bar{\sigma}_{11}$  over all unit vectors  $n_i$  is given by

$$\bar{\sigma}_{11} = \langle \sigma'_{11} \rangle_{\|\vec{n}\|=1} = \langle n_in_jn_kn_lC_{ijkl} \rangle_{\|\vec{n}\|=1}\epsilon_{11} = \bar{C}_{1111}\epsilon_{11}. \quad (\text{C.7})$$

This assumption is equivalent to the Voigt hypothesis. If we further assume that the tensor

$C_{ijkl}$  possesses cubic symmetry, then

$$\begin{aligned}
n_i n_j n_k n_l C_{ijkl} &= n_1 n_1 n_1 n_1 C_{1111} + 2n_1 n_1 n_2 n_2 C_{1122} + 2n_1 n_1 n_3 n_3 C_{1133} \\
&+ n_2 n_2 n_2 n_2 C_{2222} + 2n_2 n_2 n_3 n_3 C_{2233} + n_3 n_3 n_3 n_3 C_{3333} \\
&+ 4n_2 n_3 n_2 n_3 C_{2323} + 4n_1 n_3 n_1 n_3 C_{1313} + 4n_1 n_2 n_1 n_2 C_{1212} \\
&= C_1 (n_1^4 + n_2^4 + n_3^4) \\
&+ (2C_2 + 4C_3) (n_1^2 n_2^2 + n_1^2 n_3^2 + n_2^2 n_3^2).
\end{aligned} \tag{C.8}$$

If we let

$$n_1 = \cos \theta, \quad n_2 = \sin \theta \cos \phi, \quad \text{and} \quad n_3 = \sin \theta \sin \phi, \tag{C.9}$$

then

$$\begin{aligned}
\bar{C}_1 &= \langle n_i n_j n_k n_l C_{ijkl} \rangle_{\|\vec{n}\|=1} \\
&= \frac{1}{4\pi} \int_0^{2\pi} \int_0^\pi [C_1 (n_1^4 + n_2^4 + n_3^4) + (2C_2 + 4C_3) (n_1^2 n_2^2 + n_1^2 n_3^2 + n_2^2 n_3^2)] \sin \theta \, d\theta d\phi \\
&= \frac{1}{4\pi} \int_0^{2\pi} \int_0^\pi C_1 [\cos^4 \theta \sin \theta + (\sin^4 \phi + \cos^4 \phi) \sin^5 \theta] \\
&\quad + (2C_2 + 4C_3) [\cos^2 \theta \sin^3 \theta + \cos^2 \phi \sin^2 \phi \sin^5 \theta] \, d\theta d\phi \\
&= \frac{3}{5} C_1 + \frac{2}{5} C_2 + \frac{4}{5} C_3.
\end{aligned} \tag{C.10}$$

Thus we have obtained our first isotropic effective elastic constant:

$$\bar{C}_1 = \frac{3}{5} C_1 + \frac{2}{5} C_2 + \frac{4}{5} C_3. \tag{C.11}$$

## C.2 Averaging Pure Volumetric Strain

Consider the state of pure volumetric strain  $\epsilon_{ij} = \epsilon\delta_{ij}$ . Let  $a_{ij}$  be the transformation tensor between the 123 and 1'2'3' coordinate systems, where the direction of 1' relative to the 123 coordinate system is given by the unit vector  $n_i = a_{1i}$ . This time, we have

$$\epsilon'_{ij} = a_{mi}a_{nj}\epsilon_{mn} = a_{mi}a_{nj}\epsilon\delta_{mn} = a_{ni}a_{nj}\epsilon = \epsilon\delta_{ij}. \quad (\text{C.12})$$

As expected,  $\epsilon_{ij}$  is invariant under rotation. So

$$\sigma'_{11} = n_in_j C_{ijkl}\epsilon\delta_{kl} = n_in_j C_{ijkk}\epsilon = (C'_{1111} + C'_{1122} + C'_{1133})\epsilon. \quad (\text{C.13})$$

If we apply the Voigt hypothesis, then

$$\bar{\sigma}_{11} = \langle \sigma'_{11} \rangle_{\|\vec{n}\|=1} = \langle n_in_j C_{ijkk} \rangle_{\|\vec{n}\|=1} \epsilon = (\bar{C}_{1111} + \bar{C}_{1122} + \bar{C}_{1133})\epsilon. \quad (\text{C.14})$$

If we further assume that the tensor  $C_{ijkl}$  possesses cubic symmetry, then

$$\begin{aligned} n_in_j C_{ijkk} &= n_1 n_1 (C_{1111} + C_{1122} + C_{1133}) \\ &\quad + n_2 n_2 (C_{2211} + C_{2222} + C_{2233}) \\ &\quad + n_3 n_3 (C_{3311} + C_{3322} + C_{3333}) \\ &= (n_1^2 + n_2^2 + n_3^2)(C_1 + 2C_2) \\ &= (C_1 + 2C_2). \end{aligned} \quad (\text{C.15})$$

So if we denote our second isotropic effective elastic constant as  $\bar{C}_2 = \bar{C}_{1122} = \bar{C}_{1133}$ , then

we have

$$\bar{C}_1 + 2\bar{C}_2 = C_1 + 2C_2. \quad (\text{C.16})$$

Using equations (C.11) and (C.16), we can solve for our second isotropic effective elastic constant:

$$\bar{C}_2 = \frac{1}{5}C_1 + \frac{4}{5}C_2 - \frac{2}{5}C_3. \quad (\text{C.17})$$

Since there are only two independent elastic constants for an isotropic linear elastic material, we are done.

### C.3 Isotropic Effective Elastic Constants

To summarize, given a statistically isotropic aggregate material composed of randomly oriented subportions having locally cubic symmetry with cubic elastic constants

$$C_1 = C_{1111} = C_{2222} = C_{3333}, \quad (\text{C.18})$$

$$C_2 = C_{1122} = C_{1133} = C_{2233}, \quad (\text{C.19})$$

$$C_3 = C_{1212} = C_{1313} = C_{2323}, \quad (\text{C.20})$$

then the *isotropic effective* elastic constants  $\bar{C}_1$ ,  $\bar{C}_2$ , and  $\bar{C}_3$  for the statistically isotropic aggregate material are:

$$\bar{C}_1 = \frac{3}{5}C_1 + \frac{2}{5}C_2 + \frac{4}{5}C_3, \quad (\text{C.21})$$

$$\bar{C}_2 = \frac{1}{5}C_1 + \frac{4}{5}C_2 - \frac{2}{5}C_3, \quad (\text{C.22})$$

$$\bar{C}_3 = \frac{1}{5}C_1 - \frac{1}{5}C_2 + \frac{3}{5}C_3, \quad (\text{C.23})$$

with  $\bar{C}_1 - \bar{C}_2 = 2\bar{C}_3$ . Notice from equations (C.21), (C.22), and (C.23) that if  $C_1 - C_2 = 2C_3$  (that is, if the cubic material in the aggregate is already isotropic) then

$$\bar{C}_1 = C_1, \quad \bar{C}_2 = C_2, \quad \text{and} \quad \bar{C}_3 = C_3. \quad (\text{C.24})$$

We also note that while the derivation of this appendix was performed for a statistically isotropic material with locally *cubic* symmetry, the same technique could have been applied to find the isotropic effective elastic constants for any locally non-isotropic linear elastic material. We can use equations (C.21), (C.22), and (C.23) to determine Poisson's ratio  $\bar{\nu}$  and the bulk modulus  $\bar{\kappa}$  for the statistically isotropic material as follows:

$$\bar{\nu} = \frac{\bar{C}_2}{\bar{C}_1 + \bar{C}_2} = \frac{\bar{C}_2}{2(\bar{C}_2 + \bar{C}_3)} = \frac{C_1 + 4C_2 - 2C_3}{4C_1 + 6C_2 + 2C_3}, \quad (\text{C.25})$$

$$\bar{\kappa} = \frac{1}{3}(\bar{C}_1 + 2\bar{C}_2) = \frac{1}{3}(3\bar{C}_2 + 2\bar{C}_3) = \frac{1}{3}(C_1 + 2C_2). \quad (\text{C.26})$$



## Appendix D

# Derivation of the Mohr-Coulomb Yield (Failure) Criterion for an Isotropic Particulate Material

In this appendix, we derive the Mohr-Coulomb yield (or failure) criterion for an isotropic non-cohesive particulate material. Consider an arbitrarily oriented plane in an isotropic particulate material with unit normal vector  $\mathbf{n}$ . The stress vector acting on the plane is given by

$$\mathbf{t}_{\mathbf{n}} = \boldsymbol{\sigma} \mathbf{n}, \quad (\text{D.1})$$

where  $\boldsymbol{\sigma}$  is the (Cauchy) stress tensor, as shown in Figure D.1. Let  $\mathbf{e}_1$ ,  $\mathbf{e}_2$ , and  $\mathbf{e}_3$  be the principal directions of  $\boldsymbol{\sigma}$  and let  $\sigma_1$ ,  $\sigma_2$ , and  $\sigma_3$  be the principal stress. So, in matrix form,

$$[\boldsymbol{\sigma}] = \begin{bmatrix} \sigma_1 & 0 & 0 \\ 0 & \sigma_2 & 0 \\ 0 & 0 & \sigma_3 \end{bmatrix} \quad \text{with respect to } (\mathbf{e}_1, \mathbf{e}_2, \mathbf{e}_3). \quad (\text{D.2})$$

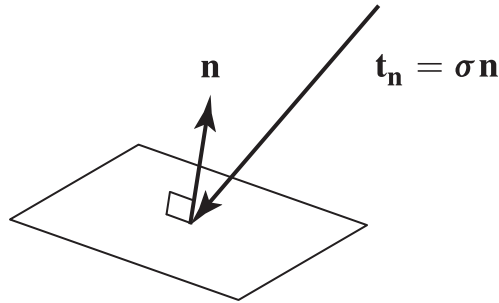


Figure D.1: Stress vector  $\mathbf{t}_n$  acting on a plane with unit normal vector  $\mathbf{n}$ .

If  $\mathbf{n} = n_1\mathbf{e}_1 + n_2\mathbf{e}_2 + n_3\mathbf{e}_3$  then  $\mathbf{t}_n = n_1\sigma_1\mathbf{e}_1 + n_2\sigma_2\mathbf{e}_2 + n_3\sigma_3\mathbf{e}_3$ . The magnitude of the component of  $\mathbf{t}_n$  normal to the plane is

$$\sigma_n = \mathbf{n} \cdot \mathbf{t}_n = \mathbf{n} \cdot \sigma \mathbf{n} = n_1^2\sigma_1 + n_2^2\sigma_2 + n_3^2\sigma_3 \quad (\text{D.3})$$

and the magnitude of  $\mathbf{t}_n$  is

$$\sigma = |\mathbf{t}_n| = \sqrt{\sigma \mathbf{n} \cdot \sigma \mathbf{n}} = \sqrt{n_1^2\sigma_1^2 + n_2^2\sigma_2^2 + n_3^2\sigma_3^2}. \quad (\text{D.4})$$

The magnitude of the component of  $\mathbf{t}_n$  tangent to the plane is then

$$\sigma_t = \sqrt{\sigma^2 - \sigma_n^2}, \quad (\text{D.5})$$

as shown in Figure D.2.

The ‘‘Coulomb friction’’ criterion for sliding on the plane with unit normal  $\mathbf{n}$  is simply:

$$\sigma_t < \mu\sigma_n \quad \Rightarrow \quad \text{no sliding}, \quad \text{and} \quad \sigma_t = \mu\sigma_n \quad \Rightarrow \quad \text{sliding} = \text{failure}, \quad (\text{D.6})$$

where  $\mu$  is the the constant coefficient of (Coulomb) friction on the plane. According to this criterion, an isotropic particulate material will *not* slide (i.e., yield) on a plane with unit

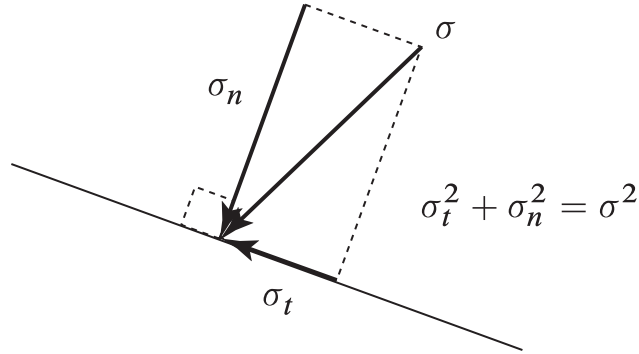


Figure D.2: Components of the stress vector  $\mathbf{t}_n$  acting normal and tangent to the plane with unit normal vector  $\mathbf{n}$ .

normal  $\mathbf{n}$  if and only if

$$\frac{\sigma_t}{\sigma_n} < \mu \quad \Leftrightarrow \quad \frac{\sqrt{\sigma^2 - \sigma_n^2}}{\sigma_n} < \mu \quad \Leftrightarrow \quad \frac{\sigma^2 - \sigma_n^2}{\sigma_n^2} < \mu^2 \quad \Leftrightarrow \quad \frac{\sigma^2}{\sigma_n^2} < 1 + \mu^2. \quad (\text{D.7})$$

Since  $1 + \mu^2$  is a constant, it follows that sliding (i.e., yielding) will occur on the plane where  $\sigma^2/\sigma_n^2$  is maximum. If the principal stresses  $\sigma_1$ ,  $\sigma_2$ , and  $\sigma_3$  are known, then

$$\frac{\sigma^2}{\sigma_n^2} = f(n_1, n_2, n_3) = \frac{\sigma_1^2 n_1^2 + \sigma_2^2 n_2^2 + \sigma_3^2 n_3^2}{(\sigma_1 n_1^2 + \sigma_2 n_2^2 + \sigma_3 n_3^2)^2}. \quad (\text{D.8})$$

We wish to find the triple  $(n_1, n_2, n_3)$  for which the function  $f$  attains its maximum value, subject to the constraint

$$n_1^2 + n_2^2 + n_3^2 = 1. \quad (\text{D.9})$$

So we have

$$d(n_1^2 + n_2^2 + n_3^2) = n_1 dn_1 + n_2 dn_2 + n_3 dn_3 = 0 \quad (\text{D.10})$$

and we set

$$df = d\left(\frac{\sigma^2}{\sigma_n^2}\right) = \frac{\partial}{\partial n_1} \left(\frac{\sigma^2}{\sigma_n^2}\right) dn_1 + \frac{\partial}{\partial n_2} \left(\frac{\sigma^2}{\sigma_n^2}\right) dn_2 + \frac{\partial}{\partial n_3} \left(\frac{\sigma^2}{\sigma_n^2}\right) dn_3 = 0. \quad (\text{D.11})$$

By the method of Lagrange Multipliers, if we let

$$\frac{\partial}{\partial n_1} \left( \frac{\sigma^2}{\sigma_n^2} \right) = \lambda n_1, \quad \frac{\partial}{\partial n_2} \left( \frac{\sigma^2}{\sigma_n^2} \right) = \lambda n_2, \quad \text{and} \quad \frac{\partial}{\partial n_3} \left( \frac{\sigma^2}{\sigma_n^2} \right) = \lambda n_3, \quad (\text{D.12})$$

then equation (D.11) is satisfied if equation (D.10) is enforced. Computing the partial derivatives in equation (D.12) gives:

$$\frac{\partial}{\partial n_1} \left( \frac{\sigma^2}{\sigma_n^2} \right) = \frac{2n_1 [\sigma_1^2 (\sigma_1 n_1^2 + \sigma_2 n_2^2 + \sigma_3 n_3^2) - 2\sigma_1 (\sigma_1^2 n_1^2 + \sigma_2^2 n_2^2 + \sigma_3^2 n_3^2)]}{(\sigma_1 n_1^2 + \sigma_2 n_2^2 + \sigma_3 n_3^2)^3}, \quad (\text{D.13})$$

$$\frac{\partial}{\partial n_2} \left( \frac{\sigma^2}{\sigma_n^2} \right) = \frac{2n_2 [\sigma_2^2 (\sigma_1 n_1^2 + \sigma_2 n_2^2 + \sigma_3 n_3^2) - 2\sigma_2 (\sigma_1^2 n_1^2 + \sigma_2^2 n_2^2 + \sigma_3^2 n_3^2)]}{(\sigma_1 n_1^2 + \sigma_2 n_2^2 + \sigma_3 n_3^2)^3}, \quad (\text{D.14})$$

$$\frac{\partial}{\partial n_3} \left( \frac{\sigma^2}{\sigma_n^2} \right) = \frac{2n_3 [\sigma_3^2 (\sigma_1 n_1^2 + \sigma_2 n_2^2 + \sigma_3 n_3^2) - 2\sigma_3 (\sigma_1^2 n_1^2 + \sigma_2^2 n_2^2 + \sigma_3^2 n_3^2)]}{(\sigma_1 n_1^2 + \sigma_2 n_2^2 + \sigma_3 n_3^2)^3}. \quad (\text{D.15})$$

Equations (D.12) – (D.15) can be solved simultaneously with the constraint equation (D.9) to obtain the following stationary points  $(n_1, n_2, n_3)$  in terms of  $\sigma_1$ ,  $\sigma_2$ , and  $\sigma_3$ :

$$(\pm 1, 0, 0), \quad (0, \pm 1, 0), \quad (0, 0, \pm 1), \quad (\text{D.16})$$

$$\left( \pm \sqrt{\frac{\sigma_2}{\sigma_1 + \sigma_2}}, \pm \sqrt{\frac{\sigma_1}{\sigma_1 + \sigma_2}}, 0 \right), \quad (\text{D.17})$$

$$\left( \pm \sqrt{\frac{\sigma_3}{\sigma_1 + \sigma_3}}, 0, \pm \sqrt{\frac{\sigma_1}{\sigma_1 + \sigma_3}} \right), \quad (\text{D.18})$$

$$\left( 0, \pm \sqrt{\frac{\sigma_3}{\sigma_2 + \sigma_3}}, \pm \sqrt{\frac{\sigma_2}{\sigma_2 + \sigma_3}} \right). \quad (\text{D.19})$$

The first (six) stationary points given by equation (D.16) are obviously minimal, since they result in no tangential stress. Thus, the maximal stationary points are given by equations (D.17) – (D.19). Substituting the maximal stationary points back into the yield criterion

(D.7) gives:

$$\frac{|\sigma_1 - \sigma_2|}{2\sqrt{\sigma_1\sigma_2}} < \mu, \quad \frac{|\sigma_1 - \sigma_3|}{2\sqrt{\sigma_1\sigma_3}} < \mu, \quad \text{and} \quad \frac{|\sigma_2 - \sigma_3|}{2\sqrt{\sigma_2\sigma_3}} < \mu. \quad (\text{D.20})$$

Equation (D.20) defines the interior of the Mohr-Coulomb yield surface in three-dimensional principal stress space, where it is assumed that the principal stresses are in compression. The Mohr-Coulomb yield surface is shown in Figure D.3 on the constant pressure plane  $\sigma_1 + \sigma_2 + \sigma_3 = 3p$ .

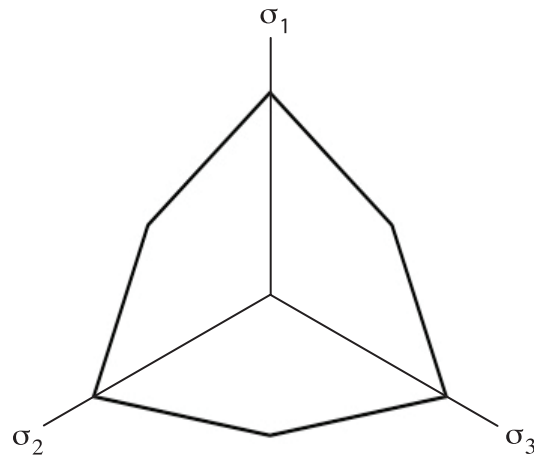


Figure D.3: The Mohr-Coulomb yield surface on the constant pressure plane (the  $\pi$ -plane)  $\sigma_1 + \sigma_2 + \sigma_3 = 3p$ , with the principal stresses  $\sigma_1$ ,  $\sigma_2$ , and  $\sigma_3$  labeled positive in compression.



## Appendix E

# Discrete Element Method Critical Time Step Size

In this appendix, we obtain sharp lower bounds on the critical time step size for the discrete element method (DEM), in 2-D and in 3-D, using a method known as Gerschgorin's bound. The critical time step is the largest stable time step that can be used during a DEM simulation, based on the standard stability criterion for the central difference explicit time integration scheme applied to an undamped linear system,  $\Delta t_{\text{crit}} = 2/\omega_{\text{max}}$ , where  $\omega_{\text{max}}$  is the maximum natural frequency of the stiffness and mass matrices associated with the system (Cook et al., 2002). This stability criterion is also valid for other common second-order explicit time integration schemes, such as "Velocity Verlet" or "leapfrog" (Frenkel and Smit, 2002, Strang, 2007). During a DEM simulation, internal forces are evaluated on an element-by-element basis, and hence the stiffness matrix for the system is never formed. However, stiffness matrices can be constructed for specific arrangements of DEM elements in contact, in 2-D and in 3-D, and these stiffness matrices can be used to determine  $\omega_{\text{max}}$  for the specific arrangements. In larger systems of DEM elements containing these specific arrangements, the imposition of constraints raises the natural frequencies of the subsystems, so  $\omega_{\text{max}}$  for

the entire system should be bounded by  $\omega_{\max}$  for the specific (unconstrained) arrangements of DEM elements in contact, as noted by Tavaréz and Plesha (2007).

If the governing equations for a system of DEM elements in contact (having a specific geometric arrangement and assuming linear elastic response) is written in matrix form as

$$\mathbf{M}\ddot{\mathbf{u}} + \mathbf{K}\mathbf{u} = \mathbf{f} \quad (\text{E.1})$$

then the natural frequencies  $\omega$  of the system are obtained from the following standard eigenvalue problem:

$$(\mathbf{M}^{-1/2}\mathbf{K}\mathbf{M}^{-1/2} - \omega^2\mathbf{I})\mathbf{x} = \mathbf{0}. \quad (\text{E.2})$$

While this eigenvalue problem may not be easy to solve *a priori* in terms of system parameters such as the inter-element normal and tangential contact stiffnesses  $k_n$  and  $k_t$  and the element radius  $r$ , an upper bound on the eigenvalue  $\lambda_{\max} = \omega_{\max}^2$  can be obtained analytically by a theorem known as Gerschgorin's bound (Isaacson and Keller, 1966).

Gerschgorin's bound states that for the standard eigenvalue problem

$$(\mathbf{A} - \lambda\mathbf{I})\mathbf{x} = \mathbf{0} \quad (\text{E.3})$$

where  $\mathbf{A}$  is an  $N \times N$  matrix, the eigenvalues  $\lambda$  are bounded by  $\lambda_{\max} \leq \max(G_{ii})$ , where

$$G_{ii} = A_{ii} + \sum_{j=1, j \neq i}^N |A_{ij}| \quad i = 1, \dots, N \quad (\text{no sum on } i). \quad (\text{E.4})$$

## E.1 Critical Time Step Size for 2-D DEM

First we determine a lower bound on the critical time step size for several different arrangements of 2-D DEM elements based on the Gerschgorin bound. For earlier treatments of this

problem, see Tavaréz and Plesha (2007) and O’Sullivan and Bray (2004). Contact forces between DEM elements are modeled by linear springs of stiffness  $k_n$  and  $k_t$  in the directions normal and tangent to the contacting surfaces, as shown in Figure E.1 at the left. In

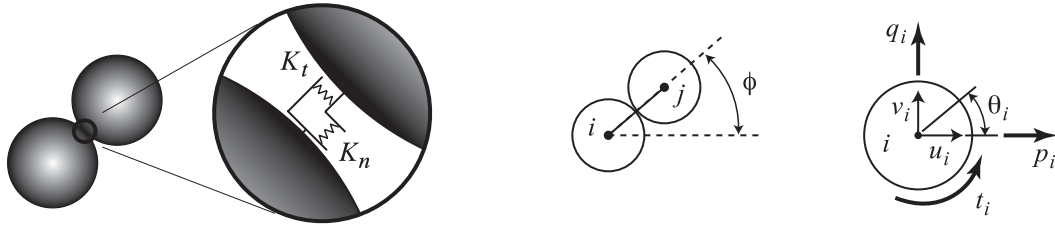


Figure E.1: Left: Linear spring contact model for spherical DEM elements. Center: Geometry of two 2-D DEM elements  $i$  and  $j$  in contact. Right: DOF  $u_i$ ,  $v_i$ , and  $\theta_i$ , forces  $p_i$  and  $q_i$ , and moment (torque)  $t_i$  for a single 2-D DEM element  $i$ .

Figure E.1 at the right, the geometry and degrees of freedom (DOF) of two contacting 2-D DEM elements are shown. The stiffness matrix  $\mathbf{K}$  for two 2-D DEM elements  $i$  and  $j$  in contact is given in block matrix form by

$$\mathbf{K} = \begin{bmatrix} \mathbf{K}_{ij} & -\mathbf{K}_{ij} \\ -\mathbf{K}_{ij} & \mathbf{K}_{ij} \end{bmatrix} \quad (\text{E.5})$$

where

$$\mathbf{K}_{ij} = \begin{bmatrix} (k_n c^2 + k_t s^2) & (k_n - k_t)cs & -k_t sr \\ (k_n - k_t)cs & (k_n s^2 + k_t c^2) & k_t cr \\ -k_t sr & k_t cr & k_t r^2 \end{bmatrix} \quad (\text{E.6})$$

where  $s = \sin \phi$  and  $c = \cos \phi$ , where  $\phi$  is given in Figure E.1,  $r$  is the radius of both DEM elements, and  $k_n$  and  $k_t$  are the normal and tangential stiffnesses at the contact point. The vector of DOF and the vector of forces and moments on the two DEM elements shown in

Figure E.1 are related by

$$\mathbf{K} \begin{Bmatrix} u_i \\ v_i \\ \theta_i \\ u_j \\ v_j \\ \theta_j \end{Bmatrix} = \begin{Bmatrix} p_i \\ q_i \\ t_i \\ p_j \\ q_j \\ t_j \end{Bmatrix}. \quad (\text{E.7})$$

### E.1.1 Single Pair of DEM Elements (2-D)

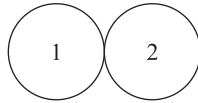


Figure E.2: A single pair of 2-D DEM elements in contact.

If we consider a single pair of contacting DEM elements with radius  $r$  labelled 1 and 2 as shown in Figure E.2, then the stiffness matrix for the system is given in block matrix form by

$$\mathbf{K} = \begin{bmatrix} \mathbf{K}_{12} & -\mathbf{K}_{12} \\ -\mathbf{K}_{12} & \mathbf{K}_{12} \end{bmatrix} \quad (\text{E.8})$$

where

$$\mathbf{K}_{12} = \begin{bmatrix} k_n & 0 & 0 \\ 0 & k_t & k_t r \\ 0 & k_t r & k_t r^2 \end{bmatrix}. \quad (\text{E.9})$$

If the diagonal mass matrix for the pair of DEM elements is given by

$$\mathbf{M} = \begin{bmatrix} \mathbf{M}_1 & 0 \\ 0 & \mathbf{M}_2 \end{bmatrix}, \quad \mathbf{M}_1 = \mathbf{M}_2 = \begin{bmatrix} m & 0 & 0 \\ 0 & m & 0 \\ 0 & 0 & I \end{bmatrix}, \quad (\text{E.10})$$

then the standard eigenvalue problem associated with the natural frequencies  $\omega$  of the system is

$$(\mathbf{M}^{-1/2}\mathbf{K}\mathbf{M}^{-1/2} - \omega^2\mathbf{I}) \mathbf{x} = \mathbf{0}. \quad (\text{E.11})$$

If we let  $\mathbf{A} = \mathbf{M}^{-1/2}\mathbf{K}\mathbf{M}^{-1/2}$ , then from equation (E.4) we obtain the following Gerschgorin bound on  $\omega^2$ , with  $I = (2/5)mr^2$ :

$$G_{11} = G_{44} = \frac{2k_n}{m} \quad (\text{E.12})$$

$$\begin{aligned} G_{22} = G_{55} &= \frac{2k_t}{m} + \frac{2k_tr}{\sqrt{m}\sqrt{I}} \\ &= \frac{5.162k_t}{m} \end{aligned} \quad (\text{E.13})$$

$$\begin{aligned} G_{33} = G_{66} &= \frac{2k_tr^2}{I} + \frac{2k_tr}{\sqrt{m}\sqrt{I}} \\ &= \frac{8.162k_t}{m} \end{aligned} \quad (\text{E.14})$$

If  $0.245k_n \leq k_t$ , then  $\max(G_{ii}) = G_{33} = G_{66}$ , and we have

$$\text{Pair: } \omega_{\max} \leq 2.857\sqrt{\frac{k_t}{m}} \Rightarrow \Delta t_{\text{crit}} = \frac{2}{\omega_{\max}} \geq 0.7\sqrt{\frac{m}{k_t}}. \quad (\text{E.15})$$

Note that the condition  $0.245k_n \leq k_t$  is not at all unusual. Indeed, assuming Hertz-Mindlin contact between spheres composed of a stable elastic material with positive Poisson's ratio, the ratio  $k_t/k_n$  must lie between 2/3 and 1, or roughly  $0.667k_n \leq k_t \leq k_n$ .

## E.1.2 Triangular Configuration of DEM Elements

If we consider a triangular configuration of three contacting DEM elements with radius  $r$  labelled 1, 2, and 3 as shown in Figure E.3, then the stiffness matrix for the system is given

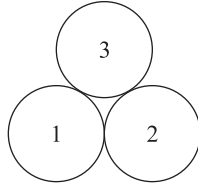


Figure E.3: A triangular configuration of three 2-D DEM elements in contact.

in block matrix form by

$$\mathbf{K} = \begin{bmatrix} \mathbf{K}_{12} + \mathbf{K}_{13} & -\mathbf{K}_{12} & -\mathbf{K}_{13} \\ -\mathbf{K}_{12} & \mathbf{K}_{12} + \mathbf{K}_{23} & -\mathbf{K}_{23} \\ -\mathbf{K}_{13} & -\mathbf{K}_{23} & \mathbf{K}_{23} + \mathbf{K}_{13} \end{bmatrix} \quad (\text{E.16})$$

where

$$\mathbf{K}_{12} = \begin{bmatrix} k_n & 0 & 0 \\ 0 & k_t & k_t r \\ 0 & k_t r & k_t r^2 \end{bmatrix}, \quad (\text{E.17})$$

$$\mathbf{K}_{13} = \begin{bmatrix} \frac{1}{4}(k_n + 3k_t) & \frac{\sqrt{3}}{4}(k_n - k_t) & -\frac{\sqrt{3}}{2}k_t r \\ \frac{\sqrt{3}}{4}(k_n - k_t) & \frac{1}{4}(3k_n + k_t) & \frac{1}{2}k_t r \\ -\frac{\sqrt{3}}{2}k_t r & \frac{1}{2}k_t r & k_t r^2 \end{bmatrix}, \quad (\text{E.18})$$

$$\mathbf{K}_{23} = \begin{bmatrix} \frac{1}{4}(k_n + 3k_t) & -\frac{\sqrt{3}}{4}(k_n - k_t) & -\frac{\sqrt{3}}{2}k_t r \\ -\frac{\sqrt{3}}{4}(k_n - k_t) & \frac{1}{4}(3k_n + k_t) & -\frac{1}{2}k_t r \\ -\frac{\sqrt{3}}{2}k_t r & -\frac{1}{2}k_t r & k_t r^2 \end{bmatrix}, \quad (\text{E.19})$$

$$\mathbf{K}_{12} + \mathbf{K}_{13} = \begin{bmatrix} \frac{1}{4}(5k_n + 3k_t) & \frac{\sqrt{3}}{4}(k_n - k_t) & -\frac{\sqrt{3}}{2}k_t r \\ \frac{\sqrt{3}}{4}(k_n - k_t) & \frac{1}{4}(3k_n + 5k_t) & \frac{3}{2}k_t r \\ -\frac{\sqrt{3}}{2}k_t r & \frac{3}{2}k_t r & 2k_t r^2 \end{bmatrix}, \quad (\text{E.20})$$

$$\mathbf{K}_{12} + \mathbf{K}_{23} = \begin{bmatrix} \frac{1}{4}(5k_n + 3k_t) & -\frac{\sqrt{3}}{4}(k_n - k_t) & -\frac{\sqrt{3}}{2}k_t r \\ -\frac{\sqrt{3}}{4}(k_n - k_t) & \frac{1}{4}(3k_n + 5k_t) & \frac{1}{2}k_t r \\ -\frac{\sqrt{3}}{2}k_t r & \frac{1}{2}k_t r & 2k_t r^2 \end{bmatrix}, \quad (\text{E.21})$$

$$\mathbf{K}_{23} + \mathbf{K}_{13} = \begin{bmatrix} \frac{1}{2}(k_n + 3k_t) & 0 & -\sqrt{3}k_t r \\ 0 & \frac{1}{2}(3k_n + k_t) & 0 \\ -\sqrt{3}k_t r & 0 & 2k_t r^2 \end{bmatrix}. \quad (\text{E.22})$$

If the diagonal mass matrix for this configuration of DEM elements is given by

$$\mathbf{M} = \begin{bmatrix} \mathbf{M}_1 & 0 & 0 \\ 0 & \mathbf{M}_2 & 0 \\ 0 & 0 & \mathbf{M}_3 \end{bmatrix}, \quad \mathbf{M}_1 = \mathbf{M}_2 = \mathbf{M}_3 = \begin{bmatrix} m & 0 & 0 \\ 0 & m & 0 \\ 0 & 0 & I \end{bmatrix}, \quad (\text{E.23})$$

then the standard eigenvalue problem associated with the natural frequencies  $\omega$  of the system is

$$(\mathbf{M}^{-1/2} \mathbf{K} \mathbf{M}^{-1/2} - \omega^2 \mathbf{I}) \mathbf{x} = \mathbf{0}. \quad (\text{E.24})$$

If we let  $\mathbf{A} = \mathbf{M}^{-1/2}\mathbf{K}\mathbf{M}^{-1/2}$ , and if we assume that  $k_t \leq k_n$  (so that  $|k_n - k_t| = k_n - k_t$ ), then from equation (E.4) we obtain the following Gerschgorin bound on  $\omega^2$ , with  $I = (2/5)mr^2$ :

$$G_{11} = G_{44} = \frac{3.366k_n + 3.373k_t}{m} \quad (\text{E.25})$$

$$G_{22} = \frac{2.366k_n + 6.377k_t}{m} \quad (\text{E.26})$$

$$G_{33} = \frac{17.482k_t}{m} \quad (\text{E.27})$$

$$G_{55} = \frac{2.366k_n + 4.796k_t}{m} \quad (\text{E.28})$$

$$G_{66} = \frac{15.901k_t}{m} \quad (\text{E.29})$$

$$G_{77} = \frac{1.866k_n + 7.611k_t}{m} \quad (\text{E.30})$$

$$G_{88} = \frac{3.866k_n + 1.715k_t}{m} \quad (\text{E.31})$$

$$G_{99} = \frac{17.058k_t}{m} \quad (\text{E.32})$$

Once again, if  $0.245k_n \leq k_t$  then  $\max(G_{ii}) = G_{33}$ , and so for  $0.245k_n \leq k_t \leq k_n$  we have

$$\text{Triangular: } \omega_{\max} \leq 4.181\sqrt{\frac{k_t}{m}} \Rightarrow \Delta t_{\text{crit}} = \frac{2}{\omega_{\max}} \geq 0.478\sqrt{\frac{m}{k_t}}. \quad (\text{E.33})$$

Note that the condition  $0.245k_n \leq k_t \leq k_n$  is not unusual, since assuming Hertz-Mindlin contact between spheres composed of a stable elastic material with positive Poisson's ratio, the ratio  $k_t/k_n$  must lie between  $2/3$  and  $1$ , or roughly  $0.667k_n \leq k_t \leq k_n$ .

### E.1.3 Hexagonal Close-Packing of DEM Elements (2-D)

If we consider a 2-D hexagonal close-packed configuration of seven contacting 2-D DEM elements with radius  $r$  labelled 1 through 7 as shown in Figure E.4, then the stiffness matrix



where

$$\mathbf{K}_{12} = \mathbf{K}_{37} = \mathbf{K}_{45} = \mathbf{K}_{67} = \begin{bmatrix} k_n & 0 & 0 \\ 0 & k_t & k_t r \\ 0 & k_t r & k_t r^2 \end{bmatrix}, \quad (\text{E.35})$$

$$\mathbf{K}_{17} = \mathbf{K}_{23} = \mathbf{K}_{47} = \mathbf{K}_{56} = \begin{bmatrix} \frac{1}{4}(k_n + 3k_t) & \frac{\sqrt{3}}{4}(k_n - k_t) & -\frac{\sqrt{3}}{2}k_t r \\ \frac{\sqrt{3}}{4}(k_n - k_t) & \frac{1}{4}(3k_n + k_t) & \frac{1}{2}k_t r \\ -\frac{\sqrt{3}}{2}k_t r & \frac{1}{2}k_t r & k_t r^2 \end{bmatrix}, \quad (\text{E.36})$$

$$\mathbf{K}_{27} = \mathbf{K}_{34} = \mathbf{K}_{57} = \mathbf{K}_{16} = \begin{bmatrix} \frac{1}{4}(k_n + 3k_t) & -\frac{\sqrt{3}}{4}(k_n - k_t) & -\frac{\sqrt{3}}{2}k_t r \\ -\frac{\sqrt{3}}{4}(k_n - k_t) & \frac{1}{4}(3k_n + k_t) & -\frac{1}{2}k_t r \\ -\frac{\sqrt{3}}{2}k_t r & -\frac{1}{2}k_t r & k_t r^2 \end{bmatrix}, \quad (\text{E.37})$$

$$\mathbf{K}_{12} + \mathbf{K}_{16} + \mathbf{K}_{17} =$$

$$\mathbf{K}_{12} + \mathbf{K}_{23} + \mathbf{K}_{27} =$$

$$\mathbf{K}_{23} + \mathbf{K}_{34} + \mathbf{K}_{37} =$$

$$\mathbf{K}_{34} + \mathbf{K}_{45} + \mathbf{K}_{47} =$$

$$\mathbf{K}_{45} + \mathbf{K}_{56} + \mathbf{K}_{57} =$$

$$\mathbf{K}_{56} + \mathbf{K}_{16} + \mathbf{K}_{67} = \begin{bmatrix} \frac{3}{2}(k_n + k_t) & 0 & -\sqrt{3}k_t r \\ 0 & \frac{3}{2}(k_n + k_t) & k_t r \\ -\sqrt{3}k_t r & k_t r & 3k_t r^2 \end{bmatrix}, \quad (\text{E.38})$$

$$\mathbf{K}_{17} + \mathbf{K}_{27} + \mathbf{K}_{37} + \mathbf{K}_{47} + \mathbf{K}_{57} + \mathbf{K}_{67} = \begin{bmatrix} 3(k_n + k_t) & 0 & -2\sqrt{3}k_t r \\ 0 & 3(k_n + k_t) & 2k_t r \\ -2\sqrt{3}k_t r & 2k_t r & 6k_t r^2 \end{bmatrix}. \quad (\text{E.39})$$

If the diagonal mass matrix for this configuration of DEM elements is given as before, then the standard eigenvalue problem associated with the natural frequencies  $\omega$  of the system is

$$(\mathbf{M}^{-1/2}\mathbf{K}\mathbf{M}^{-1/2} - \omega^2\mathbf{I}) \mathbf{x} = \mathbf{0}. \quad (\text{E.40})$$

If we let  $\mathbf{A} = \mathbf{M}^{-1/2}\mathbf{K}\mathbf{M}^{-1/2}$ , and if we assume that  $k_t \leq k_n$  (so that  $|k_n - k_t| = k_n - k_t$ ), then from equation (E.4) we obtain the following Gerschgorin bound on  $\omega^2$ , with  $I = (2/5)mr^2$ :

$$G_{1,1} = G_{4,4} = G_{7,7} = G_{10,10} = G_{13,13} = G_{16,16} = \frac{3.866k_n + 9.298k_t}{m} \quad (\text{E.41})$$

$$G_{2,2} = G_{5,5} = G_{8,8} = G_{11,11} = G_{14,14} = G_{17,17} = \frac{3.866k_n + 6.877k_t}{m} \quad (\text{E.42})$$

$$G_{3,3} = G_{6,6} = G_{9,9} = G_{12,12} = G_{15,15} = G_{18,18} = \frac{25.221k_t}{m} \quad (\text{E.43})$$

$$G_{19,19} = \frac{7.732k_n + 15.222k_t}{m} \quad (\text{E.44})$$

$$G_{20,20} = \frac{7.732k_n + 13.754k_t}{m} \quad (\text{E.45})$$

$$G_{21,21} = \frac{50.441k_t}{m} \quad (\text{E.46})$$

If  $0.22k_n \leq k_t$  then  $\max(G_{ii}) = G_{21,21}$ , and so for  $0.22k_n \leq k_t \leq k_n$  we have

$$\text{Hexagonal: } \omega_{\max} \leq 7.102\sqrt{\frac{k_t}{m}} \Rightarrow \Delta t_{\text{crit}} = \frac{2}{\omega_{\max}} \geq 0.282\sqrt{\frac{m}{k_t}}. \quad (\text{E.47})$$

#### E.1.4 Discussion (2-D)

Note that, although the result given in equation (E.47) is only a lower bound on the critical time step, meaning that the true critical time step could be larger than the value predicted by equation (E.47), this value is significantly lower than the result of Tavarez and Plesha (2007), who obtained

$$\Delta t_{\text{crit}}^{\text{T\&P}} = 0.5\sqrt{\frac{m}{k_n}}, \quad (\text{E.48})$$

for the same hexagonal close-packing that we have considered, assuming that  $k_n = k_t$ . (Tavarez and Plesha (2007) use the mass moment of inertia of a disk rather than that of a sphere in their calculations, which makes a slight difference, but does not remove the discrepancy – see below.) The estimate given in equation (E.47) is also lower than the result of O’Sullivan and Bray (2004), who obtained

$$\Delta t_{\text{crit}}^{\text{O’S\&B}} \approx 0.4 \sqrt{\frac{m}{k}}, \quad (\text{E.49})$$

again assuming that  $k_n = k_t = k$ . What is perhaps most striking about our result is the fact that equation (E.47) does not depend on  $k_n$  at all for a very large range of  $k_t/k_n$  ( $0.22 \leq k_t/k_n \leq 1.0$ ). Of course, as the authors point out in Tavarez and Plesha (2007), the assumption that  $k_n = k_t$  only leads to a more conservative estimate of  $\Delta t_{\text{crit}}$  in any particular equation, since generally  $k_t \leq k_n$ . Also note that equations (E.15), (E.33), and (E.47) are increasingly restrictive on the critical time step size. This increasing restriction on the critical time step size follows the increase in the largest coordination number of any element in each assembly. This suggests that the critical time step size will be further reduced if a configuration of close-packed DEM elements of different sizes is considered in which the largest coordination number for an element is larger than that of a hexagonal close-packing. The same observation was made by O’Sullivan and Bray (2004).

It is worth pointing out that the stability condition  $\Delta t_{\text{crit}} = 2/\omega_{\text{max}}$  is usually associated with the central difference explicit time integration scheme. However, many DEM codes today (e.g., the open source code LAMMPS developed at Sandia National Laboratories, described in Section 9.3) do not use the central difference time integration scheme, but rather follow molecular dynamics codes in using the so-called “Velocity Verlet” time integration scheme, which is really just a form of the “leapfrog” scheme. Luckily, it can be shown (e.g., Strang, 2007) that the stability condition for the leapfrog scheme is the same as that for the

central difference scheme:  $\Delta t_{\text{crit}} = 2/\omega_{\text{max}}$ .

It is also worth pointing out that most DEM codes today (e.g., the open source code LAMMPS) model 2-D discrete elements as spheres rather than disks, because these codes model a 2-D DEM simulation as a constrained 3-D simulation, which is why we have used the value of  $I = (2/5)mr^2$  for the mass moments of inertia of the discrete elements in the calculations of the preceding subsections. If we had used a value of  $I = (1/2)mr^2$  for the mass moments of inertia of the discrete elements, assuming that the discrete elements were modeled as *disks*, then the resulting Gerschgorin bounds on the critical time step derived in the preceding subsections would have been:

$$\text{Pair (disks):} \quad G_{33} = G_{66} = \frac{6.828k_t}{m} \Rightarrow \Delta t_{\text{crit}} = \frac{2}{\omega_{\text{max}}} \approx 0.765\sqrt{\frac{m}{k_t}}. \quad (\text{E.50})$$

$$\text{Triangular (disks):} \quad G_{33} = \frac{14.692k_t}{m} \Rightarrow \Delta t_{\text{crit}} = \frac{2}{\omega_{\text{max}}} \approx 0.522\sqrt{\frac{m}{k_t}}. \quad (\text{E.51})$$

$$\text{Hexagonal (disks):} \quad G_{21,21} = \frac{42.283k_t}{m} \Rightarrow \Delta t_{\text{crit}} = \frac{2}{\omega_{\text{max}}} \approx 0.308\sqrt{\frac{m}{k_t}}. \quad (\text{E.52})$$

For comparison, we repeat the Gerschgorin bounds on the critical time step derived in the preceding subsections for spherical discrete elements, which are slightly more restrictive (the critical time steps for 2-D arrangements of spheres are about 10% smaller than the corresponding critical time steps for 2-D arrangements of disks):

$$\text{Pair (spheres):} \quad G_{33} = G_{66} = \frac{8.162k_t}{m} \Rightarrow \Delta t_{\text{crit}} = \frac{2}{\omega_{\text{max}}} \approx 0.7\sqrt{\frac{m}{k_t}}. \quad (\text{E.53})$$

$$\text{Triangular (spheres):} \quad G_{33} = \frac{17.482k_t}{m} \Rightarrow \Delta t_{\text{crit}} = \frac{2}{\omega_{\text{max}}} \approx 0.478\sqrt{\frac{m}{k_t}}. \quad (\text{E.54})$$

$$\text{Hexagonal (spheres):} \quad G_{21,21} = \frac{50.441k_t}{m} \Rightarrow \Delta t_{\text{crit}} = \frac{2}{\omega_{\text{max}}} \approx 0.282\sqrt{\frac{m}{k_t}}. \quad (\text{E.55})$$

Equations (E.50) – (E.55) are valid for  $0.25k_n \leq k_t \leq k_n$ , where  $k_n$  and  $k_t$  are the normal and tangential contact spring stiffnesses, respectively, and  $m$  is the element mass. Note again

that the condition  $0.25k_n \leq k_t \leq k_n$  is not unusual. Indeed, assuming Hertz-Mindlin contact between spheres composed of a stable elastic material with positive Poisson's ratio, the ratio  $k_t/k_n$  must lie between  $2/3$  and  $1$ , or roughly  $0.667k_n \leq k_t \leq k_n$ .

## E.2 Critical Time Step Size for 3-D DEM

We now turn our attention to determining the Gerschgorin bounds on the critical time step size for various arrangements of 3-D DEM elements in contact. We begin by developing the stiffness matrix for two arbitrarily oriented 3-D DEM elements in contact, where the contact forces between the DEM elements are modeled by linear springs of stiffness  $k_n$  and  $k_t$  in the directions normal and tangent to the plane of contact, as shown in Figure E.5 at the left. In Figure E.5 at the center and right, the geometry and degrees of freedom (DOF)

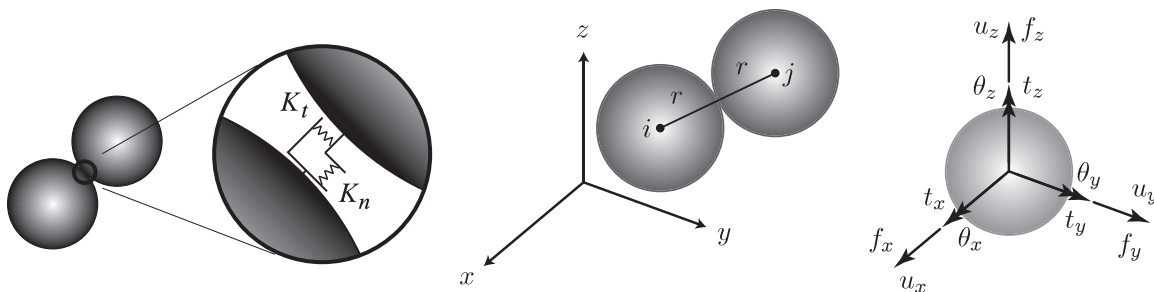


Figure E.5: Left: Linear spring contact model for spherical DEM elements. Center: Geometry of two 3-D DEM elements  $i$  and  $j$  in contact. Right: Translational DOF  $u_x$ ,  $u_y$ ,  $u_z$ , rotational DOF  $\theta_x$ ,  $\theta_y$ ,  $\theta_z$ , forces  $f_x$ ,  $f_y$ ,  $f_z$ , and moments (torques)  $t_x$ ,  $t_y$ ,  $t_z$  for a single 3-D DEM element.

of two contacting 3-D DEM elements are shown. There are three translational DOF for each element:  $u_x$ ,  $u_y$ ,  $u_z$ , and there are three rotational DOF for each element:  $\theta_x$ ,  $\theta_y$ ,  $\theta_z$ , which correspond to small rotations about each of the axes relative to an initial reference position. Corresponding to the translational DOF, each element experiences three forces:  $f_x$ ,  $f_y$ ,  $f_z$ , and corresponding to the rotational DOF, each element experiences three moments

or torques:  $t_x, t_y, t_z$ .

To obtain the stiffness matrix for two 3-D DEM elements in contact, we must determine the relationships between the translational and rotational DOF and the forces and moments on the elements. For elements  $i$  and  $j$  in contact, let the unit vector in the direction from the center of element  $i$  to the center of element  $j$  be written as

$$\mathbf{e}_n = c_x \mathbf{i} + c_y \mathbf{j} + c_z \mathbf{k} \quad (\text{E.56})$$

where  $c_x, c_y$ , and  $c_z$  are the direction cosines, given by  $c_x = (x^j - x^i)/(2r)$ ,  $c_y = (y^j - y^i)/(2r)$ , and  $c_z = (z^j - z^i)/(2r)$ , where  $(x^i, y^i, z^i)$  and  $(x^j, y^j, z^j)$  are the coordinates of the elements  $i$  and  $j$ , respectively, and where  $r$  is the radius of both DEM elements.

The displacement vector  $\mathbf{u}^i$  of element  $i$  is given in terms of that element's translational DOF as

$$\mathbf{u}^i = u_x^i \mathbf{i} + u_y^i \mathbf{j} + u_z^i \mathbf{k} \quad (\text{E.57})$$

and the rotation vector  $\Theta^i$  of element  $i$  is given in terms of that element's rotational DOF as

$$\Theta^i = \theta_x^i \mathbf{i} + \theta_y^i \mathbf{j} + \theta_z^i \mathbf{k} \quad (\text{E.58})$$

Let element  $j$  be fixed. Then the relative displacement vector  $\mathbf{u}_n$  normal to the plane of contact between elements  $i$  and  $j$  is given by

$$\begin{aligned} \mathbf{u}_n &= (\mathbf{u}^i \cdot \mathbf{e}_n) \mathbf{e}_n = (c_x^2 u_x^i + c_x c_y u_y^i + c_x c_z u_z^i) \mathbf{i} \\ &\quad + (c_x c_y u_x^i + c_y^2 u_y^i + c_y c_z u_z^i) \mathbf{j} \\ &\quad + (c_x c_z u_x^i + c_y c_z u_y^i + c_z^2 u_z^i) \mathbf{k} \end{aligned} \quad (\text{E.59})$$

and the relative displacement vector  $\mathbf{u}_t$  tangent to the plane of contact *due to translational*

*DOF only* is given by

$$\begin{aligned}
\mathbf{u}_t = \mathbf{u}^i - \mathbf{u}_n &= ((c_y^2 + c_z^2)u_x^i - c_x c_y u_y^i - c_x c_z u_z^i)\mathbf{i} \\
&+ (-c_x c_y u_x^i + (c_x^2 + c_z^2)u_y^i - c_y c_z u_z^i)\mathbf{j} \\
&+ (-c_x c_z u_x^i - c_y c_z u_y^i + (c_x^2 + c_y^2)u_z^i)\mathbf{k}
\end{aligned} \tag{E.60}$$

where we have used the fact that  $c_x^2 + c_y^2 + c_z^2 = 1$ .

The position vector  $\mathbf{r}$  from the center of element  $i$  to the point of contact between elements  $i$  and  $j$  is given by

$$\mathbf{r} = r\mathbf{e}_n = rc_x\mathbf{i} + rc_y\mathbf{j} + rc_z\mathbf{k} \tag{E.61}$$

and the relative displacement vector  $\mathbf{u}_t^\theta$  at the point of contact *due to rotational DOF* is given by

$$\begin{aligned}
\mathbf{u}_t^\theta = \boldsymbol{\Theta}^i \times \mathbf{r} &= (rc_z\theta_y^i - rc_y\theta_z^i)\mathbf{i} \\
&+ (rc_x\theta_z^i - rc_z\theta_x^i)\mathbf{j} \\
&+ (rc_y\theta_x^i - rc_x\theta_y^i)\mathbf{k}
\end{aligned} \tag{E.62}$$

The total relative tangential displacement vector at the point of contact between elements  $i$  and  $j$  is given by  $\mathbf{u}_t^{\text{total}} = \mathbf{u}_t + \mathbf{u}_t^\theta$ .

Thus, the contact force vector  $\mathbf{f}$  between elements  $i$  and  $j$  is

$$\mathbf{f} = \mathbf{f}_n + \mathbf{f}_t = k_n\mathbf{u}_n + k_t\mathbf{u}_t^{\text{total}} \tag{E.63}$$

and the contact moment vector  $\mathbf{t}$  between elements  $i$  and  $j$  is

$$\mathbf{t} = \mathbf{r} \times \mathbf{f}_t = \mathbf{r} \times k_t\mathbf{u}_t^{\text{total}} \tag{E.64}$$

It follows that the stiffness matrix  $\mathbf{K}$  for two 3-D DEM elements  $i$  and  $j$  in contact can be written in block matrix form by

$$\mathbf{K} = \begin{bmatrix} \mathbf{K}_{ij} & -\mathbf{K}_{ij} \\ -\mathbf{K}_{ij} & \mathbf{K}_{ij} \end{bmatrix} \quad (\text{E.65})$$

where

$$\mathbf{K}_{ij} = \begin{bmatrix} \mathbf{K}_{ij}^{uu} & \mathbf{K}_{ij}^{u\theta} \\ -\mathbf{K}_{ij}^{u\theta} & \mathbf{K}_{ij}^{\theta\theta} \end{bmatrix} \quad (\text{E.66})$$

with

$$\mathbf{K}_{ij}^{uu} = \begin{bmatrix} k_n c_x^2 + k_t (c_y^2 + c_z^2) & (k_n - k_t) c_x c_y & (k_n - k_t) c_x c_z \\ (k_n - k_t) c_x c_y & k_n c_y^2 + k_t (c_x^2 + c_z^2) & (k_n - k_t) c_y c_z \\ (k_n - k_t) c_x c_z & (k_n - k_t) c_y c_z & k_n c_z^2 + k_t (c_x^2 + c_y^2) \end{bmatrix} \quad (\text{E.67})$$

$$\mathbf{K}_{ij}^{u\theta} = \begin{bmatrix} 0 & k_t r c_z & -k_t r c_y \\ -k_t r c_z & 0 & k_t r c_x \\ k_t r c_y & -k_t r c_x & 0 \end{bmatrix} \quad (\text{E.68})$$

$$\mathbf{K}_{ij}^{\theta\theta} = \begin{bmatrix} k_t r^2 (c_y^2 + c_z^2) & -k_t r^2 c_x c_y & -k_t r^2 c_x c_z \\ -k_t r^2 c_x c_y & k_t r^2 (c_x^2 + c_z^2) & -k_t r^2 c_y c_z \\ -k_t r^2 c_x c_z & -k_t r^2 c_y c_z & k_t r^2 (c_x^2 + c_y^2) \end{bmatrix} \quad (\text{E.69})$$

where  $c_x = (x^j - x^i)/(2r)$ ,  $c_y = (y^j - y^i)/(2r)$ ,  $c_z = (z^j - z^i)/(2r)$ ,  $r$  is the radius of both DEM elements, and  $k_n$  and  $k_t$  are the normal and tangential stiffnesses at the contact point.

The vector of DOF and the vector of forces and moments on the two DEM elements

shown in Figure E.5 are related by

$$\mathbf{K} \begin{Bmatrix} \mathbf{u}^i \\ \Theta^i \\ \mathbf{u}^j \\ \Theta^j \end{Bmatrix} = \begin{Bmatrix} \mathbf{f}^i \\ \mathbf{t}^i \\ \mathbf{f}^j \\ \mathbf{t}^j \end{Bmatrix} \quad (\text{E.70})$$

### E.2.1 Single Pair of DEM Elements (3-D)



Figure E.6: A single pair of 3-D DEM elements in contact.

If we consider a single pair of contacting 3-D DEM elements with radius  $r$  labelled 1 and 2 as shown in Figure E.6, then the stiffness matrix for the system is given in block matrix form by

$$\mathbf{K} = \begin{bmatrix} \mathbf{K}_{12} & -\mathbf{K}_{12} \\ -\mathbf{K}_{12} & \mathbf{K}_{12} \end{bmatrix} \quad (\text{E.71})$$

where

$$\mathbf{K}_{12} = \begin{bmatrix} k_n & 0 & 0 & 0 & 0 & 0 \\ 0 & k_t & 0 & 0 & 0 & k_tr \\ 0 & 0 & k_t & 0 & -k_tr & 0 \\ 0 & 0 & 0 & 0 & 0 & 0 \\ 0 & 0 & -k_tr & 0 & k_tr^2 & 0 \\ 0 & k_tr & 0 & 0 & 0 & k_tr^2 \end{bmatrix}. \quad (\text{E.72})$$

If the diagonal mass matrix for the pair of DEM elements is given by

$$\mathbf{M} = \begin{bmatrix} \mathbf{M}_1 & 0 \\ 0 & \mathbf{M}_2 \end{bmatrix}, \quad \mathbf{M}_1 = \mathbf{M}_2 = \begin{bmatrix} m & 0 & 0 & 0 & 0 & 0 \\ 0 & m & 0 & 0 & 0 & 0 \\ 0 & 0 & m & 0 & 0 & 0 \\ 0 & 0 & 0 & I & 0 & 0 \\ 0 & 0 & 0 & 0 & I & 0 \\ 0 & 0 & 0 & 0 & 0 & I \end{bmatrix}, \quad (\text{E.73})$$

then the standard eigenvalue problem associated with the natural frequencies  $\omega$  of the system is

$$(\mathbf{M}^{-1/2} \mathbf{K} \mathbf{M}^{-1/2} - \omega^2 \mathbf{I}) \mathbf{x} = \mathbf{0}. \quad (\text{E.74})$$

If we let  $\mathbf{A} = \mathbf{M}^{-1/2} \mathbf{K} \mathbf{M}^{-1/2}$ , then from equation (E.4) we obtain the following Gerschgorin bound on  $\omega^2$ , with  $I = (2/5)mr^2$ :

$$G_{1,1} = G_{7,7} = \frac{2k_n}{m} \quad (\text{E.75})$$

$$G_{2,2} = G_{3,3} = G_{8,8} = G_{9,9} = \frac{2k_t}{m} + \frac{2k_t r}{\sqrt{m}\sqrt{I}} \\ = \frac{5.162k_t}{m} \quad (\text{E.76})$$

$$G_{5,5} = G_{6,6} = G_{11,11} = G_{12,12} = \frac{2k_t r^2}{I} + \frac{2k_t r}{\sqrt{m}\sqrt{I}} \\ = \frac{8.162k_t}{m} \quad (\text{E.77})$$

If  $0.245k_n \leq k_t$ , then  $\max(G_{ii}) = G_{5,5} = G_{6,6} = G_{11,11} = G_{12,12}$ , and we have

$$\text{Pair: } \omega_{\max} \leq 2.857 \sqrt{\frac{k_t}{m}} \Rightarrow \Delta t_{\text{crit}} = \frac{2}{\omega_{\max}} \geq 0.7 \sqrt{\frac{m}{k_t}}, \quad (\text{E.78})$$

which is the same as the result for a single pair of DEM elements in 2-D, given by equation

(E.15).

## E.2.2 Tetrahedral Configuration of DEM Elements

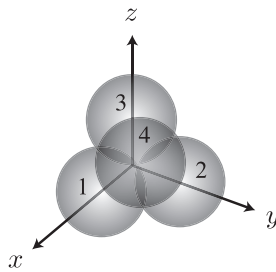


Figure E.7: A tetrahedral configuration of four 3-D DEM elements in contact.

If we consider a tetrahedral configuration of four contacting DEM elements with radius  $r$  labelled 1, 2, 3, and 4 with coordinates

$$1 : (\sqrt{2}r, 0, 0) \quad 2 : (0, \sqrt{2}r, 0) \quad 3 : (0, 0, \sqrt{2}r) \quad 4 : (\sqrt{2}r, \sqrt{2}r, \sqrt{2}r) \quad (\text{E.79})$$

as shown in Figure E.7, then the stiffness matrix for the system is given in block matrix form by

$$\mathbf{K} = \begin{bmatrix} \mathbf{K}_{12} + \mathbf{K}_{13} + \mathbf{K}_{14} & -\mathbf{K}_{12} & -\mathbf{K}_{13} & -\mathbf{K}_{14} \\ -\mathbf{K}_{12} & \mathbf{K}_{12} + \mathbf{K}_{23} + \mathbf{K}_{24} & -\mathbf{K}_{23} & -\mathbf{K}_{24} \\ -\mathbf{K}_{13} & -\mathbf{K}_{23} & \mathbf{K}_{13} + \mathbf{K}_{23} + \mathbf{K}_{34} & -\mathbf{K}_{34} \\ -\mathbf{K}_{14} & -\mathbf{K}_{24} & -\mathbf{K}_{34} & \mathbf{K}_{14} + \mathbf{K}_{24} + \mathbf{K}_{34} \end{bmatrix} \quad (\text{E.80})$$

where

$$\mathbf{K}_{12} = \begin{bmatrix} \frac{1}{2}(k_n + k_t) & -\frac{1}{2}(k_n - k_t) & 0 & 0 & 0 & -\frac{\sqrt{2}}{2}k_t r \\ -\frac{1}{2}(k_n - k_t) & \frac{1}{2}(k_n + k_t) & 0 & 0 & 0 & -\frac{\sqrt{2}}{2}k_t r \\ 0 & 0 & k_t & \frac{\sqrt{2}}{2}k_t r & \frac{\sqrt{2}}{2}k_t r & 0 \\ 0 & 0 & \frac{\sqrt{2}}{2}k_t r & \frac{1}{2}k_t r^2 & \frac{1}{2}k_t r^2 & 0 \\ 0 & 0 & \frac{\sqrt{2}}{2}k_t r & \frac{1}{2}k_t r^2 & \frac{1}{2}k_t r^2 & 0 \\ -\frac{\sqrt{2}}{2}k_t r & -\frac{\sqrt{2}}{2}k_t r & 0 & 0 & 0 & k_t r^2 \end{bmatrix} \quad (\text{E.81})$$

$$\mathbf{K}_{13} = \begin{bmatrix} \frac{1}{2}(k_n + k_t) & 0 & -\frac{1}{2}(k_n - k_t) & 0 & \frac{\sqrt{2}}{2}k_t r & 0 \\ 0 & k_t & 0 & -\frac{\sqrt{2}}{2}k_t r & 0 & -\frac{\sqrt{2}}{2}k_t r \\ -\frac{1}{2}(k_n - k_t) & 0 & \frac{1}{2}(k_n + k_t) & 0 & \frac{\sqrt{2}}{2}k_t r & 0 \\ 0 & -\frac{\sqrt{2}}{2}k_t r & 0 & \frac{1}{2}k_t r^2 & 0 & \frac{1}{2}k_t r^2 \\ \frac{\sqrt{2}}{2}k_t r & 0 & \frac{\sqrt{2}}{2}k_t r & 0 & k_t r^2 & 0 \\ 0 & -\frac{\sqrt{2}}{2}k_t r & 0 & \frac{1}{2}k_t r^2 & 0 & \frac{1}{2}k_t r^2 \end{bmatrix} \quad (\text{E.82})$$

$$\mathbf{K}_{14} = \begin{bmatrix} k_t & 0 & 0 & 0 & \frac{\sqrt{2}}{2}k_t r & -\frac{\sqrt{2}}{2}k_t r \\ 0 & \frac{1}{2}(k_n + k_t) & \frac{1}{2}(k_n - k_t) & -\frac{\sqrt{2}}{2}k_t r & 0 & 0 \\ 0 & \frac{1}{2}(k_n - k_t) & \frac{1}{2}(k_n + k_t) & \frac{\sqrt{2}}{2}k_t r & 0 & 0 \\ 0 & -\frac{\sqrt{2}}{2}k_t r & \frac{\sqrt{2}}{2}k_t r & k_t r^2 & 0 & 0 \\ \frac{\sqrt{2}}{2}k_t r & 0 & 0 & 0 & \frac{1}{2}k_t r^2 & -\frac{1}{2}k_t r^2 \\ -\frac{\sqrt{2}}{2}k_t r & 0 & 0 & 0 & -\frac{1}{2}k_t r^2 & \frac{1}{2}k_t r^2 \end{bmatrix} \quad (\text{E.83})$$

$$\mathbf{K}_{23} = \begin{bmatrix} k_t & 0 & 0 & 0 & \frac{\sqrt{2}}{2}k_tr & \frac{\sqrt{2}}{2}k_tr \\ 0 & \frac{1}{2}(k_n + k_t) & -\frac{1}{2}(k_n - k_t) & -\frac{\sqrt{2}}{2}k_tr & 0 & 0 \\ 0 & -\frac{1}{2}(k_n - k_t) & \frac{1}{2}(k_n + k_t) & -\frac{\sqrt{2}}{2}k_tr & 0 & 0 \\ 0 & -\frac{\sqrt{2}}{2}k_tr & -\frac{\sqrt{2}}{2}k_tr & k_tr^2 & 0 & 0 \\ \frac{\sqrt{2}}{2}k_tr & 0 & 0 & 0 & \frac{1}{2}k_tr^2 & \frac{1}{2}k_tr^2 \\ \frac{\sqrt{2}}{2}k_tr & 0 & 0 & 0 & \frac{1}{2}k_tr^2 & \frac{1}{2}k_tr^2 \end{bmatrix} \quad (\text{E.84})$$

$$\mathbf{K}_{24} = \begin{bmatrix} \frac{1}{2}(k_n + k_t) & 0 & \frac{1}{2}(k_n - k_t) & 0 & \frac{\sqrt{2}}{2}k_tr & 0 \\ 0 & k_t & 0 & -\frac{\sqrt{2}}{2}k_tr & 0 & \frac{\sqrt{2}}{2}k_tr \\ \frac{1}{2}(k_n - k_t) & 0 & \frac{1}{2}(k_n + k_t) & 0 & -\frac{\sqrt{2}}{2}k_tr & 0 \\ 0 & -\frac{\sqrt{2}}{2}k_tr & 0 & \frac{1}{2}k_tr^2 & 0 & -\frac{1}{2}k_tr^2 \\ \frac{\sqrt{2}}{2}k_tr & 0 & -\frac{\sqrt{2}}{2}k_tr & 0 & k_tr^2 & 0 \\ 0 & \frac{\sqrt{2}}{2}k_tr & 0 & -\frac{1}{2}k_tr^2 & 0 & \frac{1}{2}k_tr^2 \end{bmatrix} \quad (\text{E.85})$$

$$\mathbf{K}_{34} = \begin{bmatrix} \frac{1}{2}(k_n + k_t) & \frac{1}{2}(k_n - k_t) & 0 & 0 & 0 & -\frac{\sqrt{2}}{2}k_tr \\ \frac{1}{2}(k_n - k_t) & \frac{1}{2}(k_n + k_t) & 0 & 0 & 0 & \frac{\sqrt{2}}{2}k_tr \\ 0 & 0 & k_t & \frac{\sqrt{2}}{2}k_tr & -\frac{\sqrt{2}}{2}k_tr & 0 \\ 0 & 0 & \frac{\sqrt{2}}{2}k_tr & \frac{1}{2}k_tr^2 & -\frac{1}{2}k_tr^2 & 0 \\ 0 & 0 & -\frac{\sqrt{2}}{2}k_tr & -\frac{1}{2}k_tr^2 & \frac{1}{2}k_tr^2 & 0 \\ -\frac{\sqrt{2}}{2}k_tr & \frac{\sqrt{2}}{2}k_tr & 0 & 0 & 0 & k_tr^2 \end{bmatrix} \quad (\text{E.86})$$

If the diagonal mass matrix for the tetrahedral configuration of DEM elements is given by

$$\mathbf{M} = \begin{bmatrix} \mathbf{M}_1 & 0 & 0 & 0 \\ 0 & \mathbf{M}_2 & 0 & 0 \\ 0 & 0 & \mathbf{M}_3 & 0 \\ 0 & 0 & 0 & \mathbf{M}_4 \end{bmatrix}, \quad \mathbf{M}_1 = \mathbf{M}_2 = \mathbf{M}_3 = \mathbf{M}_4 = \begin{bmatrix} m & 0 & 0 & 0 & 0 & 0 \\ 0 & m & 0 & 0 & 0 & 0 \\ 0 & 0 & m & 0 & 0 & 0 \\ 0 & 0 & 0 & I & 0 & 0 \\ 0 & 0 & 0 & 0 & I & 0 \\ 0 & 0 & 0 & 0 & 0 & I \end{bmatrix}, \quad (\text{E.87})$$

then the standard eigenvalue problem associated with the natural frequencies  $\omega$  of the system is

$$(\mathbf{M}^{-1/2} \mathbf{K} \mathbf{M}^{-1/2} - \omega^2 \mathbf{I}) \mathbf{x} = \mathbf{0}. \quad (\text{E.88})$$

If we let  $\mathbf{A} = \mathbf{M}^{-1/2} \mathbf{K} \mathbf{M}^{-1/2}$ , and if we assume that  $k_t \leq k_n$  (so that  $|k_n - k_t| = k_n - k_t$ ), then from equation (E.4) we obtain the following Gerschgorin bound on  $\omega^2$ , with  $I = (2/5)mr^2$ :

$$\begin{aligned} G_{1,1} = G_{2,2} = G_{3,3} = G_{19,19} = G_{20,20} = G_{21,21} &= \frac{4k_n + 2k_t}{m} + \frac{4\sqrt{2}k_t r}{\sqrt{m}\sqrt{I}} \\ &= \frac{4k_n + 10.944k_t}{m} \end{aligned} \quad (\text{E.89})$$

$$\begin{aligned} G_{7,7} = G_{8,8} = G_{13,13} = G_{14,14} &= \frac{4k_n + 2k_t}{m} + \frac{3\sqrt{2}k_t r}{\sqrt{m}\sqrt{I}} \\ &= \frac{4k_n + 8.708k_t}{m} \end{aligned} \quad (\text{E.90})$$

$$\begin{aligned} G_{9,9} = G_{15,15} &= \frac{4k_n + 2k_t}{m} + \frac{2\sqrt{2}k_t r}{\sqrt{m}\sqrt{I}} \\ &= \frac{4k_n + 6.472k_t}{m} \end{aligned} \quad (\text{E.91})$$

$$\begin{aligned}
G_{4,4} = G_{5,5} = G_{6,6} = G_{22,22} = G_{23,23} = G_{24,24} &= \frac{6k_t r^2}{I} + \frac{4\sqrt{2}k_t r}{\sqrt{m}\sqrt{I}} \\
&= \frac{23.944k_t}{m}
\end{aligned} \tag{E.92}$$

$$\begin{aligned}
G_{10,10} = G_{11,11} = G_{16,16} = G_{17,17} &= \frac{6k_t r^2}{I} + \frac{3\sqrt{2}k_t r}{\sqrt{m}\sqrt{I}} \\
&= \frac{21.708k_t}{m}
\end{aligned} \tag{E.93}$$

$$\begin{aligned}
G_{12,12} = G_{18,18} &= \frac{6k_t r^2}{I} + \frac{2\sqrt{2}k_t r}{\sqrt{m}\sqrt{I}} \\
&= \frac{19.472k_t}{m}
\end{aligned} \tag{E.94}$$

If  $0.308k_n \leq k_t$  then  $\max(G_{ii}) = G_{6,6} = G_{24,24}$ , and so for  $0.308k_n \leq k_t \leq k_n$  we have

$$\text{Tetrahedral: } \omega_{\max} \leq 4.893\sqrt{\frac{k_t}{m}} \Rightarrow \Delta t_{\text{crit}} = \frac{2}{\omega_{\max}} \geq 0.409\sqrt{\frac{m}{k_t}}. \tag{E.95}$$

Note that the condition  $0.308k_n \leq k_t \leq k_n$  is not unusual, since assuming Hertz-Mindlin contact between spheres composed of a stable elastic material with positive Poisson's ratio, the ratio  $k_t/k_n$  must lie between  $2/3$  and  $1$ , or roughly  $0.667k_n \leq k_t \leq k_n$ .

### E.2.3 Hexagonal Close-Packing of DEM Elements (3-D)

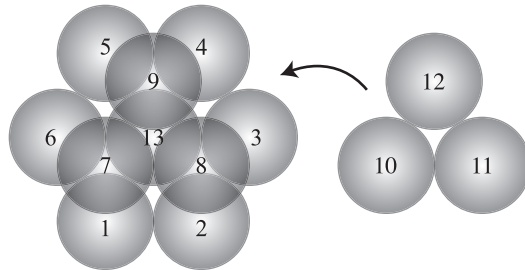


Figure E.8: A hexagonal close-packed configuration of thirteen 3-D DEM elements in contact.

If we consider a 3-D hexagonal close-packed configuration of thirteen contacting 3-D DEM

elements with radius  $r$  labelled 1 – 13 with coordinates

$$\begin{aligned}
 1 &: (-r, -\sqrt{3}r, 0) & 2 &: (r, -\sqrt{3}r, 0) & 3 &: (2r, 0, 0) \\
 4 &: (r, \sqrt{3}r, 0) & 5 &: (-r, \sqrt{3}r, 0) & 6 &: (-2r, 0, 0) \\
 7 &: \left(-r, -\frac{\sqrt{3}r}{3}, \frac{2\sqrt{6}r}{3}\right) & 8 &: \left(r, -\frac{\sqrt{3}r}{3}, \frac{2\sqrt{6}r}{3}\right) & 9 &: \left(0, \frac{2\sqrt{3}r}{3}, \frac{2\sqrt{6}r}{3}\right) \\
 10 &: \left(-r, -\frac{\sqrt{3}r}{3}, -\frac{2\sqrt{6}r}{3}\right) & 11 &: \left(r, -\frac{\sqrt{3}r}{3}, -\frac{2\sqrt{6}r}{3}\right) & 12 &: \left(0, \frac{2\sqrt{3}r}{3}, -\frac{2\sqrt{6}r}{3}\right) \\
 13 &: (0, 0, 0) & & & & 
 \end{aligned} \tag{E.96}$$

as shown in Figure E.8, then the stiffness matrix for the system will be a  $78 \times 78$  matrix, which even in block matrix form would be unwieldy to write. However, in analogy to the 2-D case we strongly expect the critical natural frequencies of the system to be associated with the central element 13, which is in contact with every other element in the system. Thus, for the purposes of the Gerschgorin bound, we need only analyze the six rows of the thirteenth (and final) row of the  $13 \times 13$  block stiffness matrix:

$$\mathbf{K}_{(13,*)} = \begin{bmatrix} -\mathbf{K}_{1,13} & -\mathbf{K}_{2,13} & \dots & -\mathbf{K}_{12,13} & \mathbf{K}_{1,13} + \mathbf{K}_{2,13} + \dots + \mathbf{K}_{12,13} \end{bmatrix} \tag{E.97}$$

where

$$\mathbf{K}_{3,13} = \mathbf{K}_{6,13} = \begin{bmatrix} k_n & 0 & 0 & 0 & 0 & 0 \\ 0 & k_t & 0 & 0 & 0 & \mp k_t r \\ 0 & 0 & k_t & 0 & \pm k_t r & 0 \\ 0 & 0 & 0 & 0 & 0 & 0 \\ 0 & 0 & \pm k_t r & 0 & k_t r^2 & 0 \\ 0 & \mp k_t r & 0 & 0 & 0 & k_t r^2 \end{bmatrix}, \tag{E.98}$$

$$\mathbf{K}_{1,13} = \mathbf{K}_{4,13} = \begin{bmatrix} \frac{1}{4}(k_n + 3k_t) & \frac{\sqrt{3}}{4}(k_n - k_t) & 0 & 0 & 0 & \mp \frac{\sqrt{3}}{2}k_t r \\ \frac{\sqrt{3}}{4}(k_n - k_t) & \frac{1}{4}(3k_n + k_t) & 0 & 0 & 0 & \pm \frac{1}{2}k_t r \\ 0 & 0 & k_t & \pm \frac{\sqrt{3}}{2}k_t r & \mp \frac{1}{2}k_t r & 0 \\ 0 & 0 & \pm \frac{\sqrt{3}}{2}k_t r & \frac{3}{4}k_t r^2 & -\frac{\sqrt{3}}{4}k_t r^2 & 0 \\ 0 & 0 & \mp \frac{1}{2}k_t r & -\frac{\sqrt{3}}{4}k_t r^2 & \frac{1}{4}k_t r^2 & 0 \\ \mp \frac{\sqrt{3}}{2}k_t r & \pm \frac{1}{2}k_t r & 0 & 0 & 0 & k_t r^2 \end{bmatrix}, \quad (\text{E.99})$$

$$\mathbf{K}_{2,13} = \mathbf{K}_{5,13} = \begin{bmatrix} \frac{1}{4}(k_n + 3k_t) & -\frac{\sqrt{3}}{4}(k_n - k_t) & 0 & 0 & 0 & \mp \frac{\sqrt{3}}{2}k_t r \\ -\frac{\sqrt{3}}{4}(k_n - k_t) & \frac{1}{4}(3k_n + k_t) & 0 & 0 & 0 & \mp \frac{1}{2}k_t r \\ 0 & 0 & k_t & \pm \frac{\sqrt{3}}{2}k_t r & \pm \frac{1}{2}k_t r & 0 \\ 0 & 0 & \pm \frac{\sqrt{3}}{2}k_t r & \frac{3}{4}k_t r^2 & \frac{\sqrt{3}}{4}k_t r^2 & 0 \\ 0 & 0 & \pm \frac{1}{2}k_t r & \frac{\sqrt{3}}{4}k_t r^2 & \frac{1}{4}k_t r^2 & 0 \\ \mp \frac{\sqrt{3}}{2}k_t r & \mp \frac{1}{2}k_t r & 0 & 0 & 0 & k_t r^2 \end{bmatrix}, \quad (\text{E.100})$$

$$\mathbf{K}_{7,13} = \begin{bmatrix} \frac{1}{4}(k_n + 3k_t) & \frac{\sqrt{3}}{12}(k_n - k_t) & -\frac{\sqrt{6}}{6}(k_n - k_t) & 0 & -\frac{\sqrt{6}}{3}k_t r & -\frac{\sqrt{3}}{6}k_t r \\ \frac{\sqrt{3}}{12}(k_n - k_t) & \frac{1}{12}(k_n + 11k_t) & -\frac{\sqrt{2}}{6}(k_n - k_t) & \frac{\sqrt{6}}{3}k_t r & 0 & \frac{1}{2}k_t r \\ -\frac{\sqrt{6}}{6}(k_n - k_t) & -\frac{\sqrt{2}}{6}(k_n - k_t) & \frac{1}{3}(2k_n + k_t) & \frac{\sqrt{3}}{6}k_t r & -\frac{1}{2}k_t r & 0 \\ 0 & \frac{\sqrt{6}}{3}k_t r & \frac{\sqrt{3}}{6}k_t r & \frac{3}{4}k_t r^2 & -\frac{\sqrt{3}}{12}k_t r^2 & \frac{\sqrt{6}}{6}k_t r^2 \\ -\frac{\sqrt{6}}{3}k_t r & 0 & -\frac{1}{2}k_t r & -\frac{\sqrt{3}}{12}k_t r^2 & \frac{11}{12}k_t r^2 & \frac{\sqrt{2}}{6}k_t r^2 \\ -\frac{\sqrt{3}}{6}k_t r & \frac{1}{2}k_t r & 0 & \frac{\sqrt{6}}{6}k_t r^2 & \frac{\sqrt{2}}{6}k_t r^2 & \frac{1}{3}k_t r^2 \end{bmatrix}, \quad (\text{E.101})$$

$$\mathbf{K}_{8,13} = \begin{bmatrix} \frac{1}{4}(k_n + 3k_t) & -\frac{\sqrt{3}}{12}(k_n - k_t) & \frac{\sqrt{6}}{6}(k_n - k_t) & 0 & -\frac{\sqrt{6}}{3}k_tr & -\frac{\sqrt{3}}{6}k_tr \\ -\frac{\sqrt{3}}{12}(k_n - k_t) & \frac{1}{12}(k_n + 11k_t) & -\frac{\sqrt{2}}{6}(k_n - k_t) & \frac{\sqrt{6}}{3}k_tr & 0 & -\frac{1}{2}k_tr \\ \frac{\sqrt{6}}{6}(k_n - k_t) & -\frac{\sqrt{2}}{6}(k_n - k_t) & \frac{1}{3}(2k_n + k_t) & \frac{\sqrt{3}}{6}k_tr & \frac{1}{2}k_tr & 0 \\ 0 & \frac{\sqrt{6}}{3}k_tr & \frac{\sqrt{3}}{6}k_tr & \frac{3}{4}k_tr^2 & \frac{\sqrt{3}}{12}k_tr^2 & -\frac{\sqrt{6}}{6}k_tr^2 \\ -\frac{\sqrt{6}}{3}k_tr & 0 & \frac{1}{2}k_tr & \frac{\sqrt{3}}{12}k_tr^2 & \frac{11}{12}k_tr^2 & \frac{\sqrt{2}}{6}k_tr^2 \\ -\frac{\sqrt{3}}{6}k_tr & -\frac{1}{2}k_tr & 0 & -\frac{\sqrt{6}}{6}k_tr^2 & \frac{\sqrt{2}}{6}k_tr^2 & \frac{1}{3}k_tr^2 \end{bmatrix}, \quad (\text{E.102})$$

$$\mathbf{K}_{10,13} = \begin{bmatrix} \frac{1}{4}(k_n + 3k_t) & \frac{\sqrt{3}}{12}(k_n - k_t) & \frac{\sqrt{6}}{6}(k_n - k_t) & 0 & \frac{\sqrt{6}}{3}k_tr & -\frac{\sqrt{3}}{6}k_tr \\ \frac{\sqrt{3}}{12}(k_n - k_t) & \frac{1}{12}(k_n + 11k_t) & \frac{\sqrt{2}}{6}(k_n - k_t) & -\frac{\sqrt{6}}{3}k_tr & 0 & \frac{1}{2}k_tr \\ \frac{\sqrt{6}}{6}(k_n - k_t) & \frac{\sqrt{2}}{6}(k_n - k_t) & \frac{1}{3}(2k_n + k_t) & \frac{\sqrt{3}}{6}k_tr & -\frac{1}{2}k_tr & 0 \\ 0 & -\frac{\sqrt{6}}{3}k_tr & \frac{\sqrt{3}}{6}k_tr & \frac{3}{4}k_tr^2 & -\frac{\sqrt{3}}{12}k_tr^2 & -\frac{\sqrt{6}}{6}k_tr^2 \\ \frac{\sqrt{6}}{3}k_tr & 0 & -\frac{1}{2}k_tr & -\frac{\sqrt{3}}{12}k_tr^2 & \frac{11}{12}k_tr^2 & -\frac{\sqrt{2}}{6}k_tr^2 \\ -\frac{\sqrt{3}}{6}k_tr & \frac{1}{2}k_tr & 0 & -\frac{\sqrt{6}}{6}k_tr^2 & -\frac{\sqrt{2}}{6}k_tr^2 & \frac{1}{3}k_tr^2 \end{bmatrix}, \quad (\text{E.103})$$

$$\mathbf{K}_{11,13} = \begin{bmatrix} \frac{1}{4}(k_n + 3k_t) & -\frac{\sqrt{3}}{12}(k_n - k_t) & -\frac{\sqrt{6}}{6}(k_n - k_t) & 0 & \frac{\sqrt{6}}{3}k_tr & -\frac{\sqrt{3}}{6}k_tr \\ -\frac{\sqrt{3}}{12}(k_n - k_t) & \frac{1}{12}(k_n + 11k_t) & \frac{\sqrt{2}}{6}(k_n - k_t) & -\frac{\sqrt{6}}{3}k_tr & 0 & -\frac{1}{2}k_tr \\ -\frac{\sqrt{6}}{6}(k_n - k_t) & -\frac{\sqrt{2}}{6}(k_n - k_t) & \frac{1}{3}(2k_n + k_t) & \frac{\sqrt{3}}{6}k_tr & \frac{1}{2}k_tr & 0 \\ 0 & -\frac{\sqrt{6}}{3}k_tr & \frac{\sqrt{3}}{6}k_tr & \frac{3}{4}k_tr^2 & \frac{\sqrt{3}}{12}k_tr^2 & \frac{\sqrt{6}}{6}k_tr^2 \\ \frac{\sqrt{6}}{3}k_tr & 0 & \frac{1}{2}k_tr & \frac{\sqrt{3}}{12}k_tr^2 & \frac{11}{12}k_tr^2 & -\frac{\sqrt{2}}{6}k_tr^2 \\ -\frac{\sqrt{3}}{6}k_tr & -\frac{1}{2}k_tr & 0 & \frac{\sqrt{6}}{6}k_tr^2 & -\frac{\sqrt{2}}{6}k_tr^2 & \frac{1}{3}k_tr^2 \end{bmatrix}, \quad (\text{E.104})$$

$$\mathbf{K}_{9,13} = \mathbf{K}_{12,13} = \begin{bmatrix} k_t & 0 & 0 & 0 & \mp \frac{\sqrt{6}}{3} k_t r & \frac{\sqrt{3}}{3} k_t r \\ 0 & \frac{1}{3}(k_n + 2k_t) & \pm \frac{\sqrt{2}}{3}(k_n - k_t) & \pm \frac{\sqrt{6}}{3} k_t r & 0 & 0 \\ 0 & \pm \frac{\sqrt{2}}{3}(k_n - k_t) & \frac{1}{3}(2k_n + k_t) & -\frac{\sqrt{3}}{3} k_t r & 0 & 0 \\ 0 & \pm \frac{\sqrt{6}}{3} k_t r & -\frac{\sqrt{3}}{3} k_t r & k_t r^2 & 0 & 0 \\ \mp \frac{\sqrt{6}}{3} k_t r & 0 & 0 & 0 & \frac{2}{3} k_t r^2 & \mp \frac{\sqrt{2}}{3} k_t r^2 \\ \frac{\sqrt{3}}{3} k_t r & 0 & 0 & 0 & \mp \frac{\sqrt{2}}{3} k_t r^2 & \frac{1}{3} k_t r^2 \end{bmatrix}, \quad (\text{E.105})$$

and the sum is (surprisingly):

$$\mathbf{K}_{1,13} + \mathbf{K}_{2,13} + \dots + \mathbf{K}_{12,13} = \begin{bmatrix} 4k_n + 8k_t & 0 & 0 & 0 & 0 & 0 \\ 0 & 4k_n + 8k_t & 0 & 0 & 0 & 0 \\ 0 & 0 & 4k_n + 8k_t & 0 & 0 & 0 \\ 0 & 0 & 0 & 8k_t r^2 & 0 & 0 \\ 0 & 0 & 0 & 0 & 8k_t r^2 & 0 \\ 0 & 0 & 0 & 0 & 0 & 8k_t r^2 \end{bmatrix}. \quad (\text{E.106})$$

If the diagonal mass matrix for the 3-D hexagonal close-packed configuration of thirteen DEM elements shown in Figure E.8 is given by

$$\mathbf{M} = \begin{bmatrix} \mathbf{M}_1 & & 0 \\ & \ddots & \\ 0 & & \mathbf{M}_{13} \end{bmatrix}, \quad \mathbf{M}_1 = \dots = \mathbf{M}_{13} = \begin{bmatrix} m & 0 & 0 & 0 & 0 & 0 \\ 0 & m & 0 & 0 & 0 & 0 \\ 0 & 0 & m & 0 & 0 & 0 \\ 0 & 0 & 0 & I & 0 & 0 \\ 0 & 0 & 0 & 0 & I & 0 \\ 0 & 0 & 0 & 0 & 0 & I \end{bmatrix}, \quad (\text{E.107})$$

then the standard eigenvalue problem associated with the natural frequencies  $\omega$  of the system

is

$$(\mathbf{M}^{-1/2}\mathbf{K}\mathbf{M}^{-1/2} - \omega^2\mathbf{I}) \mathbf{x} = \mathbf{0}. \quad (\text{E.108})$$

If we let  $\mathbf{A} = \mathbf{M}^{-1/2}\mathbf{K}\mathbf{M}^{-1/2}$ , and if we assume that  $k_t \leq k_n$  (so that  $|k_n - k_t| = k_n - k_t$ ), then from equation (E.4) we obtain the following Gerschgorin bound on  $\omega^2$ , with  $I = (2/5)mr^2$ :

$$\begin{aligned} G_{73,73} &= \frac{11.942k_n + 12.058k_t}{m} + \frac{10.672k_tr}{\sqrt{m}\sqrt{I}} \\ &= \frac{11.942k_n + 28.932k_t}{m} \end{aligned} \quad (\text{E.109})$$

$$\begin{aligned} G_{74,74} &= \frac{12.195k_n + 11.805k_t}{m} + \frac{10.899k_tr}{\sqrt{m}\sqrt{I}} \\ &= \frac{12.195k_n + 29.038k_t}{m} \end{aligned} \quad (\text{E.110})$$

$$\begin{aligned} G_{75,75} &= \frac{11.519k_n + 12.481k_t}{m} + \frac{11.774k_tr}{\sqrt{m}\sqrt{I}} \\ &= \frac{11.519k_n + 31.097k_t}{m} \end{aligned} \quad (\text{E.111})$$

$$\begin{aligned} G_{76,76} &= \frac{19.942k_tr^2}{I} + \frac{10.672k_tr}{\sqrt{m}\sqrt{I}} \\ &= \frac{66.729k_t}{m} \end{aligned} \quad (\text{E.112})$$

$$\begin{aligned} G_{77,77} &= \frac{20.195k_tr^2}{I} + \frac{10.899k_tr}{\sqrt{m}\sqrt{I}} \\ &= \frac{67.720k_t}{m} \end{aligned} \quad (\text{E.113})$$

$$\begin{aligned} G_{78,78} &= \frac{19.519k_tr^2}{I} + \frac{11.774k_tr}{\sqrt{m}\sqrt{I}} \\ &= \frac{67.414k_t}{m} \end{aligned} \quad (\text{E.114})$$

If  $0.315k_n \leq k_t$  then  $\max(G_{ii}) = G_{77,77}$ , and so for  $0.315k_n \leq k_t \leq k_n$  we have

$$\text{Hexagonal: } \omega_{\max} \leq 8.229\sqrt{\frac{k_t}{m}} \Rightarrow \Delta t_{\text{crit}} = \frac{2}{\omega_{\max}} \geq 0.243\sqrt{\frac{m}{k_t}}. \quad (\text{E.115})$$

## E.2.4 Discussion (3-D)

In summary, we have found that for 3-D DEM, the critical time step size is bounded by Gerschgorin's Theorem for the following configurations

$$\text{Pair (3-D):} \quad G_{6,6} = G_{12,12} = \frac{8.162k_t}{m} \Rightarrow \Delta t_{\text{crit}} = \frac{2}{\omega_{\text{max}}} \approx 0.7 \sqrt{\frac{m}{k_t}}. \quad (\text{E.116})$$

$$\text{Tetrahedral (3-D):} \quad G_{6,6} = G_{24,24} = \frac{23.944k_t}{m} \Rightarrow \Delta t_{\text{crit}} = \frac{2}{\omega_{\text{max}}} \approx 0.409 \sqrt{\frac{m}{k_t}}. \quad (\text{E.117})$$

$$\text{Hexagonal (3-D):} \quad G_{77,77} = \frac{67.720k_t}{m} \Rightarrow \Delta t_{\text{crit}} = \frac{2}{\omega_{\text{max}}} \approx 0.243 \sqrt{\frac{m}{k_t}}. \quad (\text{E.118})$$

Equations (E.116) – (E.118) are valid for  $0.32k_n \leq k_t \leq k_n$ , where  $k_n$  and  $k_t$  are the normal and tangential contact spring stiffnesses, respectively, and  $m$  is the element mass. Note that the condition  $0.32k_n \leq k_t \leq k_n$  is not unusual, since assuming Hertz-Mindlin contact between spheres composed of a stable elastic material with positive Poisson's ratio, the ratio  $k_t/k_n$  must lie between  $2/3$  and  $1$ , or roughly  $0.667k_n \leq k_t \leq k_n$ . Moreover, since the hexagonal close-packing is the tightest attainable packing for uniform spheres in 3-D, it is reasonable to conjecture that the critical time step size given in equation (E.118) is safe for any 3-D DEM simulation. Also note that the Gerschgorin bound provides a conservative estimate for the critical time step size, and the actual maximum critical time step may be larger than the estimates derived here.

For comparison, we note that O'Sullivan and Bray (2004) obtained the following estimate for the critical time step size in 3-D DEM simulations:

$$\Delta t_{\text{crit}}^{\text{O'S\&B}} \approx 0.3 \sqrt{\frac{m}{k}}, \quad (\text{E.119})$$

where it was assumed that  $k_n = k_t = k$ . Note that the value of the critical time step size given in equation (E.118) is lower than the result of O'Sullivan and Bray (2004). Thus,

our result is more conservative than theirs. It is also noteworthy that, in the presence of velocity dependent damping, the critical time step size may be further reduced. Interestingly, since the method used by O’Sullivan and Bray (2004) to obtain their critical time step was approximate, they recommended applying a “factor of safety” to the value given in equation (E.119), and thus they recommended using a critical time step size of  $\Delta t_{\text{crit}} \approx 0.2\sqrt{m/k}$ , which corresponds roughly to our result. The justification for their “factor of safety”, however, was heuristic, and it was not proven to provide a strictly conservative bound on the critical time step size. Thus, our result (E.118) is both significant and original. What is perhaps most striking about our result is the fact that equation (E.118) does not depend on  $k_n$  for a very large range of  $k_t/k_n$  ( $0.32 \leq k_t/k_n \leq 1.0$ ). Also, anecdotal evidence suggests that a time step size of  $\Delta t \approx 0.2\sqrt{m_{\text{min}}/k_{\text{max}}}$  is indeed necessary to run (reliably) stable 3-D DEM simulations using the open source code LAMMPS, described in Section 9.3.



# Bibliography

- A. Anandarajah. Sliding and rolling constitutive theory for granular materials. *J. Eng. Mech.*, 130(6):665–680, 2004.
- A. Anandarajah. Critical state of granular materials based on the sliding-rolling theory. *J. Geotech. Geoenviron. Eng.*, 134(1):125–135, 2008.
- J. E. Andrade and X. Tu. Multiscale framework for behavior prediction in granular media. *Mechanics of Materials*, 41:652–669, 2009.
- R. Bachrach, J. Dvorkin, and A. M. Nur. Seismic velocities and Poisson’s ratio of shallow unconsolidated sands. *Geophysics*, 65(2):559–564, 2000.
- K. Bagi. Stress and strain in granular assemblies. *Mechanics of Materials*, 22:165–177, 1996.
- B. Balendran and S. Nemat-Nasser. Double sliding model cyclic deformation of granular materials, including dilatancy effects. *J. Mech. Phys. Solids*, 41:573–612, 1993.
- J. P. Bardet. Lode dependences for isotropic pressure-sensitive elastoplastic materials. *J. Appl. Mech.*, 57:498–506, 1990.
- J.-P. Bardet. *Experimental Soil Mechanics*. Prentice Hall, 1997.
- J.-P. Bardet and I. Vardoulakis. The asymmetry of stress in granular media. *Int. J. Solids Struct.*, 38:353–367, 2001.

- R. J. Bathurst and L. Rothenburg. Micromechanical aspects of isotropic granular assemblies with linear contact interactions. *Journal of Applied Mechanics*, 55:17–23, 1988.
- J. F. W. Bishop and R. Hill. A theory of plastic distortion of a polycrystalline aggregate under combined stresses. *Phil. Mag.*, 42:414–427, 1951a.
- J. F. W. Bishop and R. Hill. A theoretical derivation of the plastic properties of a polycrystalline face-centered metal. *Phil. Mag.*, 42:1298–1307, 1951b.
- R. I. Borja and J. R. Wren. Micromechanics of granular media Part I: Generation of overall constitutive equation for assemblies of circular disks. *Comput. Methods Appl. Mech. Engrg.*, 127:13–36, 1995.
- B. Budiansky and T. Y. Wu. Theoretical prediction of plastic strains of polycrystals. In *Proc. 4th U.S. Nat. Congr. Appl. Mech.*, pages 1175–1185, 1962.
- F. Calvetti and F. Emeriault. Interparticle forces distribution in granular materials: link with the macroscopic behaviour. *Mechanics of Cohesive-Frictional Materials*, 4:247–279, 1999.
- F. F. Camargo, H. Wen, T. Edil, and Y.-H. Son. Comparative assessment of crushed aggregates and bound/unbound recycled asphalt pavement as base materials. *International Journal of Pavement Engineering*, 14(3):223–230, 2013.
- B. Cambou. Micromechanical approach in granular materials. In Bernard Cambou, editor, *Behaviour of Granular Materials*, number 385 in CISM Courses and Lectures, pages 171–216. CISM, Udine, 1998.
- B. Cambou, Ph. Dubujet, F. Emeriault, and F. Sidoroff. Homogenization for granular materials. *European Journal of Mechanics, A/solids*, 14(2):225–276, 1995.

- B. Cambou, M. Chaze, and F. Dedeker. Change of scale in granular materials. *European Journal of Mechanics, A/solids*, 19:999–1014, 2000.
- A. B. Cerato and A. J. Lutenecker. Specimen size and scale effects of direct shear box tests of sands. *Geotechnical Testing Journal*, 29(6):1–10, 2006.
- C. S. Chang and J. Gao. Second-gradient constitutive theory for granular material with random packing structure. *Int. J. Solids Struct.*, 32(16):2279–2293, 1995.
- C. S. Chang and P.-Y. Hicher. An elasto-plastic model for granular materials with microstructural consideration. *Int. J. Solids Struct.*, 42:4258–4277, 2005.
- C. S. Chang and C. L. Liao. Constitutive relations for particulate medium with the effect of particle rotation. *Int. J. Solids Struct.*, 26:437–453, 1990.
- C. S. Chang and A. Misra. Theoretical and experimental study of regular packings of granules. *J. Eng. Mech.*, 115(4):704–720, 1989.
- C. S. Chang and A. Misra. Application of uniform strain theory to heterogeneous granular solids. *J. Eng. Mech.*, 116(10):2310–2328, 1990.
- C. S. Chang, A. Misra, and S. Sundaram. Micromechanical modelling of cemented sands under low amplitude oscillations. *Géotechnique*, 40(2):251–263, 1990.
- C. S. Chang, S. J. Chao, and Y. Chang. Estimates of elastic moduli for granular material with anisotropic random packing structure. *Int. J. Solids Struct.*, 32(14):1989–2008, 1995.
- F. Chen, E. C. Drumm, and G. Guiochon. Prediction/verification of particle motion in one dimension with the discrete-element method. *Int. J. Geomech.*, 7(5):344–352, 2007.
- Y. P. Cheng and N. H. Minh. DEM investigation of particle size distribution effect on direct shear behaviour of granular agglomerates. In *Powders and Grains 2009, Proceedings of*

- the 6th International Conference on Micromechanics of Granular Media*, pages 401–404, 2009.
- G.-C. Cho, J. Dodds, and J. C. Santamarina. Particle shape effects on packing density, stiffness, and strength: Natural and crushed sands. *J. Geotech. Geoenviron. Eng.*, 132(5): 591–602, 2006.
- R. D. Cook, D. S. Malkus, M. E. Plesha, and R. J. Witt. *Concepts and Applications of Finite Element Analysis*. John Wiley and Sons, 2002.
- W. L. Cooper. Communication of stresses by chains of grains in high-speed particulate media impacts. In *Dynamic Behavior of Materials, Volume 1: Conference Proceedings of the Society for Experimental Mechanics Series*, pages 99–107. Springer, 2011.
- L. Cui and C. O’Sullivan. Exploring the macro- and micro-scale response of an idealised granular material in the direct shear apparatus. *Géotechnique*, 56(7):455–468, 2006.
- P. A. Cundall and O. D. L. Strack. A discrete numerical model for granular assemblies. *Géotechnique*, 29(1):47–65, 1979.
- H. K. Dang and M. A. Meguid. Algorithm to generate a discrete element specimen with predefined properties. *Int. J. Geomech.*, 10(2):85–91, 2010.
- F. Delyon, D. Dufresne, and Y.E. Levy. Physique et genie civil: deux illustrations simples. Mécanique des milieux granulaires. *Annales des Ponts et Chaussées*, numero special:53–60, 1990.
- H. Deresiewicz. Mechanics of granular matter. In H. L. Dryden and Th. von Kármán, editors, *Advances in Applied Mechanics*, volume 5, pages 233–306. Academic Press Inc., New York, 1958a.

- H. Deresiewicz. Stress-strain relations for a simple model of a granular medium. *J. Appl. Mech.*, 25:402–406, 1958b.
- F. Di Maio and A. Di Renzo. DEM-CFD simulations of fluidized beds with application in mixing dynamics. *KONA*, 25:205–216, 2007.
- A. Di Renzo and F. Di Maio. Comparison of contact-force models for the simulation of collisions in DEM-based granular flow codes. *Chemical Engineering Science*, 59:525–541, 2004.
- K. Duffaut, M. Landrø, and R. Sollie. Using Mindlin theory to model friction-dependent shear modulus in granular media. *Geophysics*, 75(3):E143–E152, 2010.
- J. Duffy and R. D. Mindlin. Stress-strain relations and vibrations of a granular medium. *J. Appl. Mech.*, 24:585–593, 1957.
- O. Durán, N. P. Kruyt, and S. Luding. Analysis of three-dimensional micro-mechanical strain formulations for granular materials: Evaluation of accuracy. *Int. J. Solids Struct.*, 47(2):251–260, 2010.
- D. Elata and J. G. Berryman. Contact force-displacement laws and the mechanical behavior of random packs of identical spheres. *Mechanics of Materials*, 24:229–240, 1996.
- F. Emeriault and B. Cambou. Micromechanical modelling of anisotropic non-linear elasticity of granular medium. *Int. J. Solids Struct.*, 33(18):2591–2607, 1996.
- F. Emeriault, B. Cambou, and A. Mahboubi. Homogenization for granular materials, non reversible behaviour. *Mechanics of Cohesive-Frictional Materials*, 1:199–218, 1996.
- W. G. Field. Towards the statistical definition of a granular mass. In *Proceedings of 4th Australia-New Zealand conf. on soil mechanics and found. eng.*, pages 143–148, 1963.

- J. A. Fleischmann, W. J. Drugan, and M. E. Plesha. Direct micromechanics derivation and DEM confirmation of the elastic moduli of isotropic particulate materials, Part I: No particle rotation. *J. Mech. Phys. Solids*, 61(7):1569–1584, 2013a.
- J. A. Fleischmann, W. J. Drugan, and M. E. Plesha. Direct micromechanics derivation and DEM confirmation of the elastic moduli of isotropic particulate materials, Part II: Particle rotation. *J. Mech. Phys. Solids*, 61(7):1585–1599, 2013b.
- J. A. Fleischmann, M. E. Plesha, and W. J. Drugan. Quantitative comparison of two-dimensional and three-dimensional discrete element simulations of nominally two-dimensional shear flow. *Int. J. Geomech.*, 13(3):205–212, 2013c.
- D. Frenkel and B. Smit. *Understanding Molecular Simulation: From Algorithms to Applications*. Elsevier, 2002.
- J. D. Goddard. From granular matter to generalized continuum. In G. Capriz, P. Giovine, and P.M. Mariano, editors, *Mathematical Models of Granular Matter*, number 1937 in Lecture Notes in Mathematics, pages 1–22. Springer, 2008.
- M. Guler, T. B. Edil, and P. J. Bosscher. Measurement of particle movement in granular soils using image analysis. *Journal of Computing in Civil Engineering*, 13(2):116–122, 1999.
- Z. Hashin and S. Shtrikman. On some variational principles in anisotropic and nonhomogeneous elasticity. *J. Mech. Phys. Solids*, 10:335–342, 1962.
- R. F. S. Hearmon. *An introduction to applied anisotropic elasticity*. Oxford University Press, 1961.
- R. J. Henderson, H. W. Chandler, A. R. Akisanya, C. M. Chandler, and S. A. Nixon. Micro-mechanical modelling of powder compaction. *J. Mech. Phys. Solids*, 49:739–759, 2001.

- A. V. Hershey. The elasticity of an isotropic aggregate of anisotropic cubic crystals. *J. Appl. Mech.*, 21:236–240, 1954.
- P.-Y. Hicher and C. S. Chang. A microstructural elastoplastic model for unsaturated granular materials. *Int. J. Solids Struct.*, 44:2304–2323, 2007.
- R. Hill. The mechanics of quasi-static plastic deformation in metals. In G.K. Batchelor and R.M. Davies, editors, *Surveys in Mechanics – The G.I. Taylor 70th Anniversary Volume*, pages 7–31. Cambridge University Press, 1956.
- R. Hill. Continuum micro-mechanics of elastoplastic polycrystals. *J. Mech. Phys. Solids*, 13: 89–101, 1965.
- R. Holtzman, D. B. Silin, and T. W. Patzek. Mechanical properties of granular materials: A variational approach to grain-scale simulations. *Int. J. Numer. Anal. Meth. Geomech.*, 33:391–404, 2009.
- R. Holtzman, D. B. Silin, and T. W. Patzek. Frictional granular mechanics: A variational approach. *Int. J. Numer. Meth. Engng*, 81:1259–1280, 2010.
- W. Humphrey, A. Dalke, and K. Schulten. VMD – Visual Molecular Dynamics. *Journal of Molecular Graphics*, 14:33–38, 1996.
- J. W. Hutchinson. Elastic-plastic behavior of polycrystalline metals and composites. *Proc. Roy. Soc. Lond. A*, 319:247–272, 1970.
- B. Indraratna, D. Ionescu, and H. D. Christie. Shear behavior of railway ballast based on large-scale triaxial tests. *J. Geotech. Geoenviron. Eng.*, 124(5):439–449, 1998.
- E. Isaacson and H. B. Keller. *Analysis of Numerical Methods*. John Wiley and Sons, 1966.

- J. Jenkins, D. Johnson, L. La Ragione, and H. Makse. Fluctuations and the effective moduli of an isotropic, random aggregate of identical, frictionless spheres. *J. Mech. Phys. Sol.*, 53:197–225, 2005.
- J. T. Jenkins, P. A. Cundall, and I. Ishibashi. Micromechanical modeling of granular materials with the assistance of experiments and numerical simulations. In J. Biarez and R. Gourvès, editors, *Powders and Grains*, pages 257–264. Balkema, Rotterdam, 1989.
- R. P. Jensen, P. J. Bosscher, M. E. Plesha, and T. B. Edil. DEM simulation of granular media - structure interface: Effects of surface roughness and particle shape. *Int. J. Numer. Anal. Meth. Geomech.*, 23:531–547, 1999.
- R. P. Jensen, T. B. Edil, P. J. Bosscher, M. E. Plesha, and N. Ben Kahla. Effect of particle shape on interface behavior of DEM-simulated granular materials. *Int. J. Geomech.*, 1:1–19, 2001a.
- R. P. Jensen, M. E. Plesha, T. B. Edil, P. J. Bosscher, and N. Ben Kahla. DEM simulation of particle damage in granular media - structure interfaces. *Int. J. Geomech.*, 1:21–39, 2001b.
- L. Jing and O. Stephansson. *Fundamentals of Discrete Element Methods for Rock Engineering: Theory and Applications*. Elsevier B.V., 2007.
- W. R. Ketterhagen, M. T. am Ende, and B. C. Hancock. Process modeling in the pharmaceutical industry using the discrete element method. *Journal of Pharmaceutical Sciences*, 98(2):442–470, 2009.
- E. Kröner. Berechnung der elastischen Konstanten des Vielkristalls aus den Konstanten des Einkristalls. *Z. für Phys.*, 151:504–518, 1958.
- E. Kröner. Zur plastischen Verformung des Vielkristalls. *Acta Metall.*, 9:155–161, 1961.

- N. P. Kruyt. Statics and kinematics of discrete Cosserat-type granular materials. *Int. J. Solids Struct.*, 40:511–534, 2003.
- N. P. Kruyt. Three-dimensional lattice-based dispersion relations for granular materials. In J. Goddard, J. T. Jenkins, and P. Giovine, editors, *IUTAM-ISIMM Symposium on Mathematical Modeling and Physical Instances of Granular Flows*, pages 405–415. American Institute of Physics, 2010.
- N. P. Kruyt and L. Rothenburg. Micromechanical bounds for the effective elastic moduli of granular materials. *Int. J. Solids Struct.*, 39:311–324, 2002.
- N. P. Kruyt and L. Rothenburg. Kinematic and static assumptions for homogenization in micromechanics of granular materials. *Mechanics of Materials*, 36:1157–1173, 2004.
- N. P. Kruyt, I. Agnolin, S. Luding, and L. Rothenburg. Micromechanical study of elastic moduli of loose granular materials. *J. Mech. Phys. Sol.*, 58:1286–1301, 2010.
- M. R. Kuhn. Micro-mechanics of fabric and failure in granular materials. *Mechanics of Materials*, 42:827–840, 2010.
- LAMMPS. <<http://lammps.sandia.gov>>.
- H. Lee, A. S. Gillman, and K. Matouš. Computing overall elastic constants of polydisperse particulate composites from microtomographic data. *J. Mech. Phys. Sol.*, 59:1838–1857, 2011.
- C. L. Liao, T.-P. Chang, D.-H. Young, and C. S. Chang. Stress-strain relationship for granular materials based on the hypothesis of best fit. *Int. J. Solids Struct.*, 34(31/32): 4087–4100, 1997.
- S. H. Liu. Simulating a direct shear box test by DEM. *Canadian Geotechnical Journal*, 43: 155–168, 2006.

- S. H. Liu, D. Sun, and H. Matsuoka. On the interface friction in direct shear test. *Computers and Geotechnics*, 32:317–325, 2005.
- A. E. H. Love. *A treatise on the mathematical theory of elasticity*. Cambridge University Press, 1927.
- V. A. Lubarda. New estimates of the third-order elastic constants for isotropic aggregates of cubic crystals. *J. Mech. Phys. Solids*, 45(4):471–490, 1997.
- V. A. Lubarda. *Elastoplasticity Theory*. CRC Press, 2002.
- H. Matsuoka and D. Sun. *The SMP Concept-Based 3D Constitutive Models for Geomaterials*. Taylor and Francis, 2006.
- M. M. Mehrabadi, B. Loret, and S. Nemat-Nasser. Incremental constitutive relations for granular materials based on micromechanics. *Proceedings: Mathematical and Physical Sciences*, 441(1913):433–463, 1993.
- J. K. Mitchell and K. Soga. *Fundamentals of Soil Behavior*. John Wiley and Sons, 2005.
- S. Nemat-Nasser. *Plasticity: A Treatise on Finite Deformation of Heterogeneous Inelastic Materials*. Cambridge University Press, 2004.
- S. Nemat-Nasser and J. Zhang. Constitutive relations for cohesionless frictional granular materials. *Journal of Plasticity*, 18:531–547, 2002.
- T. Ng. Discrete element method simulations of the critical state of a granular material. *Int. J. Geomech.*, 9(5):209–216, 2009.
- M. Oda. Co-ordination number and its relation to shear strength of granular materials. *Soils and Foundations*, 17(2):29–42, 1977.

- M. Oda. A micro-deformation model for dilatancy of granular materials. In C.S. Chang, A. Misra, R.Y. Liang, and M. Babic, editors, *Mechanics of Deformation and Flow of Particulate Materials*, pages 24–37. ASCE, 1997.
- A. D. Orlando, D. M. Hanes, and H. H. Shen. Scaling effects in direct shear tests. In *Powders and Grains 2009, Proceedings of the 6th International Conference on Micromechanics of Granular Media*, pages 413–416, 2009.
- C. O’Sullivan. Particle-based discrete element modeling: Geomechanics perspective. *Int. J. Geomech.*, 11(6):449–464, 2011.
- C. O’Sullivan and J. D. Bray. Selecting a suitable time step for discrete element simulations that use the central difference time integration scheme. *Engineering Computations*, 21(2-4):278–303, 2004.
- C. O’Sullivan and L. Cui. Micromechanics of granular material response during load reversals: Combined DEM and experimental study. *Powder Technology*, 193:289–302, 2009.
- C. O’Sullivan, J. D. Bray, and M. Riemer. Examination of the response of regularly packed specimens of spherical particles using physical tests and discrete element simulations. *J. Eng. Mech.*, 130(10):1140–1150, 2004.
- N. Ouchiyama and T. Tanaka. Estimation of the average number of contacts between randomly mixed solid particles. *Ind. Eng. Chem. Fundam.*, 19:338–340, 1980.
- ParaView. <<http://paraview.org>>.
- S. Plimpton. Fast parallel algorithms for short range molecular dynamics. *Journal of Computational Physics*, 117:1–19, 1995.
- P. P. Procházka and J. Šejnoha. Extended Hashin-Shtrikman variational principles. *Applications of Mathematics*, 49(4):357–372, 2004.

- A. Reuss. Calculation of flow limits of mixed crystals on the basis of the plasticity of single crystals. *Zeitschrift für angewandte Mathematik und Mechanik*, 9:49, 1929.
- M. Šejnoha and J. Zeman. Overall viscoelastic response of random fibrous composites with statistically quasi uniform distribution of reinforcements. *Computer Methods in Applied Mechanics and Engineering*, 191(44):5027–5044, 2002.
- F. Sidoroff, B. Cambou, and A. Mahboubi. Contact force distribution in granular media. *Mechanics of Materials*, 16:83–89, 1993.
- L. E. Silbert. Stress response inside perturbed particle assemblies. *Granular Matter*, 12(1):135–142, 2010.
- L. E. Silbert, D. Ertas, G. S. Grest, T. C. Halsey, D. Levine, and S. J. Plimpton. Granular flow down an inclined plane: Bagnold scaling and rheology. *Physical Review E*, 64(5):051302–1–14, 2001.
- J. C. Simo and T. J. R. Hughes. *Computational Inelasticity*. Springer, 1998.
- A. J. M. Spencer. Isotropic polynomial invariants and tensor functions. In J.P. Boehler, editor, *Applications of tensor functions in solid mechanics*. Springer, 1987.
- G. Strang. *Computational Science and Engineering*. Wellesley-Cambridge Press, 2007.
- A. S. J. Suiker and R. de Borst. Enhanced continua and discrete lattices for modelling granular assemblies. *Phil. Trans. R. Soc. A*, 363(1836):2543–2580, 2005.
- F. A. Tavarez and M. E. Plesha. Discrete element method for modelling solid and particulate materials. *Int. J. Numer. Meth. Engng*, 70:379–404, 2007.
- G. I. Taylor. Plastic strain in metals. *J. Inst. Metals*, 62:307–324, 1938.

- F. Trentadue. An equilibrium-based approach for the micromechanical modelling of a non-linear elastic granular material. *Mechanics of Materials*, 36(4):323–334, 2004.
- P. A. Vermeer and R. de Borst. Non-associated plasticity for soils, concrete and rock. *Heron*, 29(3):1–64, 1984.
- W. Voigt. *Lehrbuch der Kristallphysik*. Teubner, Leipzig, Germany, 1928.
- K. Walton. The effective elastic moduli of a random pack of spheres. *J. Mech. Phys. Sol.*, 35:213–226, 1987.
- J. Wang and M. Gutierrez. Modeling of scale effects on the micromechanics of granular media under direct shear condition. In *Powders and Grains 2009, Proceedings of the 6th International Conference on Micromechanics of Granular Media*, pages 365–368, 2009.
- J. R. Willis. Bounds and self-consistent estimates for the overall properties of anisotropic composites. *J. Mech. Phys. Solids*, 25:185–202, 1977.
- Y. Yan and S. Ji. Discrete element modeling of direct shear tests for a granular material. *Int. J. Numer. Anal. Meth. Geomech.*, 34:978–990, 2010.
- E. Yanagisawa. Influence of void ratio and stress condition on the dynamic shear modulus of granular media. In M. Shahinpoor, editor, *Advances in the mechanics and the flow of granular materials*, pages 947–960. Gulf Publishing, Houston, 1983.
- L. Zhang and C. Thornton. DEM simulations of the direct shear test. In *15th ASCE Engineering Mechanics Conference*, 2002.
- X. Zhao. *A Numerical Investigation of the Effects of Loading Conditions on Soil Response*. PhD thesis, North Carolina State University, 2009.

- J. Zhou and A. D. Dinsmore. A statistical model of contacts and forces in random granular media. *J. Stat. Mech.*, 5(L05001):1–9, 2009.
- Q. Zhou, B. Helenbrook, and H. H. Shen. A computational study of the micromechanics under pre- and post- failure in a 2-D direct shear test. In *Powders and Grains 2009, Proceedings of the 6th International Conference on Micromechanics of Granular Media*, pages 405–408, 2009.